

Geometric and Electronic Structure/Function Correlations in Non-Heme Iron Enzymes

Edward I. Solomon,* Thomas C. Brunold, Mindy I. Davis, Jyllian N. Kemsley, Sang-Kyu Lee, Nicolai Lehnert, Frank Neese, Andrew J. Skulan, Yi-Shan Yang, and Jing Zhou

Department of Chemistry, Stanford University, Stanford, California 94305-5080

Received September 29, 1999

Contents

I. Introduction	235
II. Mononuclear Non-Heme Iron	237
A. Spectroscopic Methodology	237
1. Fe ^{II}	237
2. Fe ^{III}	243
3. Quantum Chemical Calculations of Molecular Properties	251
B. Substrate Activation	251
1. Lipoxygenases	251
2. Intradiol Dioxygenases	257
3. Comparison of Strategies	263
C. O ₂ Activation	264
1. Extradial Dioxygenases	264
2. Pterin-Dependent Hydroxylases	269
3. α -Ketoglutarate-Dependent and Related Enzymes	273
4. Rieske-Type Dioxygenases	278
5. Bleomycin	281
6. General Strategy	285
D. O ₂ Intermediates and Analogues	286
1. Model Systems	286
2. Intermediates	290
III. Binuclear Non-Heme Iron	294
A. Spectroscopic Methodology	294
1. [Fe ^{III}] ₂	294
2. [Fe ^{II}] ₂	300
B. Reversible O ₂ Binding to Hemerythrin	306
C. O ₂ Activation	311
1. Methane Monooxygenase	311
2. Ribonucleotide Reductase	318
3. Δ^9 Desaturase	324
4. General Strategy	328
D. O ₂ Intermediates	329
1. Peroxo Intermediates	329
2. High-Valent Intermediates	331
3. Conversion of Peroxo Intermediates into High-Valent Fe–Oxo–Fe Species	333
IV. Concluding Comments	336
V. Abbreviations	336
VI. Acknowledgments	337
VII. References	337

I. Introduction

In recent years, significant progress has been made in understanding the geometric and electronic struc-

tures of the active sites of non-heme iron enzymes and the contributions of these sites to molecular mechanisms. Tables 1 and 2 present fairly complete lists of the presently known key classes of mononuclear and binuclear non-heme iron enzymes. As indicated in the tables, these enzymes participate in a range of reactions as extensive as those found in heme chemistry but are generally much less well understood. For most of the enzymes one of the reactants is dioxygen. The uncatalyzed reactions of O₂ with organic substrates are thermodynamically favorable but kinetically slow since they are spin forbidden and the one-electron reduction potential of O₂ is low. In the mononuclear non-heme iron enzymes, these reactions are catalyzed either by a high-spin ferrous site which is involved in dioxygen activation or by a high-spin ferric site which activates substrates. For some of the ferrous enzymes, an additional organic cofactor, α -ketoglutarate or pterin, participates in a coupled reaction with dioxygen where both the substrate and cosubstrate are oxygenated. Thus far, the only well-characterized oxygen intermediate is that for bleomycin, activated bleomycin, which is kinetically competent to cleave DNA in a hydrogen-atom abstraction reaction. In the binuclear non-heme iron enzymes, a diferrous site is involved in reversible O₂ binding to hemerythrin and O₂ activation in ribonucleotide reductase, methane monooxygenase, and Δ^9 desaturase. These show interesting structural differences which could contribute to differences in reactivity (vide infra). Hemerythrin has five histidine ligands, while methane monooxygenase, ribonucleotide reductase, and Δ^9 desaturase are rich in donor oxygen ligands. It had been thought that the strong donor ligation in the latter enzymes activates the sites for dioxygen reactivity; however, a series of membrane desaturases and monooxygenases has recently been determined to have binuclear iron sites which appear to be rich in histidine ligation. Dioxygen binding to hemerythrin involves transfer of two electrons and a proton to O₂ binding at a single iron center, and oxygen intermediates **P**, **Q**, and **X** (vide infra) have been observed in ribonucleotide reductase, Δ^9 desaturase, and methane monooxygenase. An oxygen intermediate has also been observed at the binuclear ferroxidase site in ferritin, which appears to have structural and functional similarities to the binuclear iron site in rubrerythrin. Mononuclear non-heme iron sites are also involved in superoxide dismutation (SOD, Fe^{II}



From left to right: Jing Zhou, Mindy I. E. Davis, Yi-Shan Yang, Edward I. Solomon, Jyllian N. Kemsley, Nicolai Lehnert, Andrew Skulan, and Sang-Kyu Lee. Side photographs: (top) Thomas C. Brunold and (bottom) Frank Neese. Background: "Gates of Hell", Rodin Sculpture Garden, Stanford.

Edward I. Solomon grew up in North Miami Beach, FL, received his Ph.D. from Princeton University (with D. S. McClure), and was a postdoctoral fellow at the H. C. Ørsted Institute (with C. J. Ballhausen) and then at Caltech (with H. B. Gray). He was a professor at MIT until 1982. He then moved to Stanford University where he is now the Monroe E. Spaght Professor of Humanities and Sciences. His research is in the fields of physical-inorganic and bioinorganic chemistry with emphasis on the application of a wide variety of spectroscopic methods to elucidate the electronic structures of transition-metal complexes and their contributions to physical properties and reactivity.

Thomas C. Brunold (Diploma in Chemistry, University of Bern, Switzerland; Ph.D. in Chemistry, University of Bern, Switzerland) did graduate research with Professor Hans U. Güdel. From 1997 to 1999, he was a postdoctoral fellow in Professor Solomon's lab studying oxygen intermediates and models of binuclear non-heme iron enzymes, and manganese catalase. Since August 1999, he has been an Assistant Professor at the University of Wisconsin—Madison where he employs a wide range of spectroscopic methods to study structure and function of bioorganometallic species, metal complex interactions with nucleic acids, and second-sphere effects on metalloprotein active sites.

Mindy I. E. Davis (B.S. in Chemistry/Minor in Biology from MIT) did undergraduate research with Professor Stephen J. Lippard on biomimetic models for binuclear metalloproteins. She worked at Unilever and at Kodak as a Kodak Scholar. Her Ph.D. research at Stanford University combines bioinorganic spectroscopy with theory to study the intra- and extradiol dioxygenases.

Jyllian N. Kemsley (B.A. in Chemistry from Amherst College) worked with Professor David Dooley on amine oxidase and Professor Joan Broderick on lipoxygenase at Amherst and did process analytical research for two years at Merck Research Laboratories. She is now a Ph.D. student at Stanford University, working on pterin-dependent hydroxylases and bleomycin.

and Fe^{III}), hydrolysis (deformylase, Fe^{II}), and hydration (nitrile hydratase, low-spin Fe^{III}), and a binuclear non-heme iron center catalyzes phosphate ester hydrolysis (purple acid phosphatase, $\text{Fe}^{\text{III}}\text{Fe}^{\text{II}}$).

Crystal structures are now available for many of these classes of enzymes (vide infra) and provide the starting point for an in-depth understanding of function. Spectroscopy plays a key complementary role in obtaining molecular-level insight into catalytic mechanisms, but spectroscopic features have been much less accessible for the non-heme iron enzymes relative to the heme enzymes. Non-heme iron active sites have imidazole, carboxylate, water-derived, and,

Sang-Kyu Lee (B.S. in Chemistry from Lehigh University, Ph.D. from the University of Minnesota) was a graduate student with Professor John D. Lipscomb working on MMO. Sang-Kyu has since joined Professor Solomon as a postdoctoral fellow studying multicopper enzymes with MMO as a continuing hobby.

Nicolai Lehnert (Diploma in Chemistry from Heinrich-Heine-Universität Düsseldorf, Germany; Ph.D. from Johannes-Gutenberg-Universität Mainz, Germany) did undergraduate research with Professor Hans-Herbert Schmidtke on the spectroscopy of osmium(IV) complexes and graduate research with Professors Felix Tuczek and Philipp Gütllich performing spectroscopic and theoretical studies on nitrogenase model complexes. Since 1999, he has been a postdoctoral fellow in Professor Solomon's group where he is working on non-heme iron enzymes and their oxygen intermediates.

Frank Neese (Ph.D. in Biology from Konstanz University, Germany) did his graduate research with Professor Peter Kroneck on copper proteins. He then joined the group of Professor Solomon as a postdoctoral fellow to experimentally and theoretically study non-heme iron centers and their oxygen intermediates. In 1999 he returned to Konstanz to work on his Habilitation which focuses on the electron structure, spectroscopy, and mechanism of bacterial metalloproteins in the nitrogen cycle. Frank is also developing a large-scale molecular orbital program and other approaches for the study of transition-metal spectroscopy.

Andrew J. Skulan (B.A. in Chemistry and Physics from Kalamazoo College) studied magnetism in binuclear complexes with Professors Thomas J. Smith and Thomas R. Askew as an undergraduate student. He is now a Ph.D. student and NSF Predoctoral Fellow investigating oxygen activation and formation in binuclear iron and manganese enzymes and model systems.

Yi-Shan Yang (B.S. in Chemistry from National Sun, Yat-sen University, Kaohsiung, Taiwan, R.O.C.) did physical inorganic research for one year at the Institute of Chemistry, Academia Sinica, in Taipei, Taiwan, R.O.C., and is presently a Ph.D. student studying oxygen-activating binuclear non-heme iron enzymes and purple acid phosphatases.

Jing Zhou (B.S. in Chemistry from Fudan University, Shanghai, China; M.A. in Biochemistry from Temple University) did undergraduate research with Professor Anren Jiang on polytungstates. He is presently a Ph.D. student studying non-heme iron enzymes including α -ketoglutarate-dependent enzymes, ethylene-forming enzyme, and lipoxygenases.

in some cases (the intradiol dioxygenases and purple acid phosphatases), phenolate ligation and do not exhibit the intense ligand $\pi \rightarrow \pi^*$ absorption features of heme sites. The reduced (Fe^{II}) sites do not exhibit charge transfer (CT) transitions and are generally not detectable by electron paramagnetic resonance (EPR), and while the oxidized sites (Fe^{III}) do exhibit EPR signals reflecting spin Hamiltonian parameters and CT features, their information content has not been developed. The binuclear sites have the additional structural feature of bridging ligation (carboxylate and oxo or hydroxo) which complicates the ground-state properties and contributes to the two-electron reactivity.

This review develops the methodologies required to study ferrous (magnetic circular dichroism spectroscopy) and ferric (electron paramagnetic resonance, magnetic circular dichroism, resonance Raman, and electronic absorption spectroscopies) active sites and then applies these to obtain geometric and electronic structural insight into the reactions of many of the mononuclear non-heme iron enzymes contained in Table 1. On the basis of these studies,

Table 1. Mononuclear Non-Heme Iron Enzymes

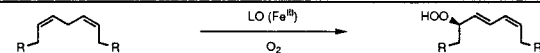
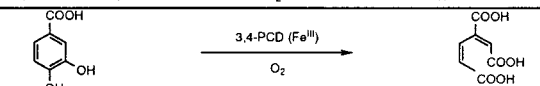
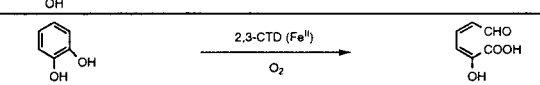
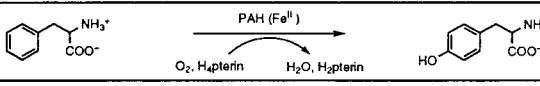
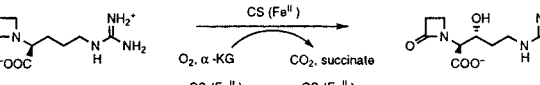
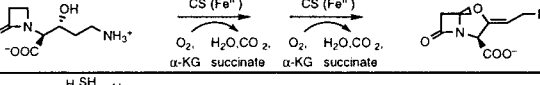
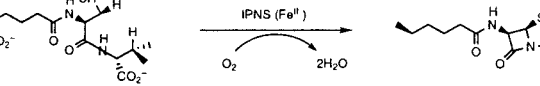
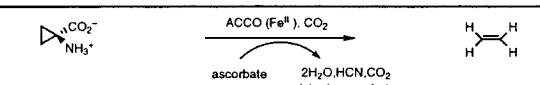
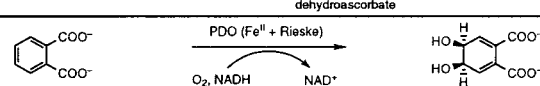
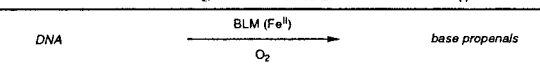
reaction type	representative enzyme	catalytic reaction	review section
hydroperoxidation	lipoxygenases		II.B.1
intradiol dioxygenation	protocatechuate 3,4-dioxygenase		II.B.2
extradiol dioxygenation	catechol 2,3-dioxygenase		II.C.1
pterin-dependent hydroxylation	phenylalanine hydroxylase		II.C.2
α-ketoglutarate-dependent hydroxylation	clavaminate synthase		II.C.3
α-ketoglutarate-dependent 4e ⁻ oxidation	clavaminate synthase		II.C.3
4e ⁻ oxidative ring closure	isopenicillin N-synthase		II.C.3
ascorbate-dependent 2e ⁻ oxidation	1-aminocyclopropane carboxylic acid oxidase		II.C.3
cis-hydroxylation	phthalate dioxygenase		II.C.4
H• abstraction	bleomycin		II.C.5

Table 2. Binuclear Non-Heme Iron Proteins

reaction type	representative enzyme	catalytic reaction	review section/ref
reversible dioxygen binding	hemerythrin	$[\text{Fe}^{\text{II}}\text{Fe}^{\text{II}}] + \text{O}_2 \rightleftharpoons [\text{Fe}^{\text{III}}\text{Fe}^{\text{III}}] - \text{OOH}$	III.B.1
hydroxylation ^a	methane monooxygenase	$[\text{Fe}^{\text{II}}\text{Fe}^{\text{II}}] + \text{CH}_4 \xrightarrow{+\text{O}_2} [\text{Fe}^{\text{III}}\text{Fe}^{\text{III}}] + \text{CH}_3\text{OH}/\text{H}_2\text{O}$	III.C.1
1-e ⁻ oxidation	ribonucleotide diphosphate reductase	$[\text{Fe}^{\text{II}}\text{Fe}^{\text{II}}] + \text{Tyr} \xrightarrow{+\text{O}_2} [\text{Fe}^{\text{III}}\text{Fe}^{\text{III}}] + \text{Tyr}^\bullet$	III.C.2
desaturation	stearoyl-acyl carrier protein Δ ⁹ -desaturase	$[\text{Fe}^{\text{II}}\text{Fe}^{\text{II}}] + \text{stearoyl ACP} \xrightarrow{+\text{O}_2} [\text{Fe}^{\text{III}}\text{Fe}^{\text{III}}] + \text{oleoyl ACP}$	III.C.3
hydrolysis of phosphate ester	purple acid phosphatase	$[\text{Fe}^{\text{II}}\text{Fe}^{\text{III}}] + \text{ROHPO}_3 \xrightarrow{+\text{H}_2\text{O}} [\text{Fe}^{\text{II}}\text{Fe}^{\text{III}}] + \text{H}_3\text{PO}_4$	1,2
NADH peroxidation	rubrerythrin	$[\text{Fe}^{\text{II}}\text{Fe}^{\text{II}}] + \text{H}_2\text{O}_2 \xrightarrow{+\text{O}_2} [\text{Fe}^{\text{III}}\text{Fe}^{\text{III}}]$	3–5
ferroxidation	ferritin	$[\text{Fe}^{\text{II}}\text{Fe}^{\text{II}}] \xrightarrow{+\text{O}_2} [\text{Fe}^{\text{III}}\text{Fe}^{\text{III}}]$	6–9

^a There is also an alkene monooxygenase which contains a binuclear non-heme iron active site and a Rieske-type [2Fe–2S] cluster. The final products are epoxides (ref 10).

a general mechanistic strategy utilized by many of the non-heme ferrous enzymes has developed which is summarized in section II.C.6. We then describe the new electronic structural features associated with binuclear iron sites with bridging ligation and consider these contributions to the reactivity of the enzymes listed in Table 2. Geometric and electronic structure contributions to the dioxygen reactivity of the binuclear ferrous enzymes are summarized in section III.C.4. As a general theme of this review, we consider what is presently known about oxygen intermediates in the proteins and related non-heme iron model complexes. The focus is on possible parallels to O₂ activation by heme systems, which are thought to involve heterolytic cleavage of the O–O bond of peroxide to generate a high-valent iron–oxo

intermediate (compound I; Fe^{IV}=O, porphyrin radical), and whether such a high-valent iron–oxo intermediate would be stable in the different non-heme protein environments.

II. Mononuclear Non-Heme Iron

A. Spectroscopic Methodology

1. Fe^{II}

The electronic structure of octahedral high-spin Fe^{II} centers is described by the left-hand side of the d⁶ Tanabe–Sugano diagram in Figure 1. The ground state is ⁵T_{2g} (with S = 2). Since d → d transitions are parity forbidden one anticipates observing only electronic transitions to spin-allowed excited states. For

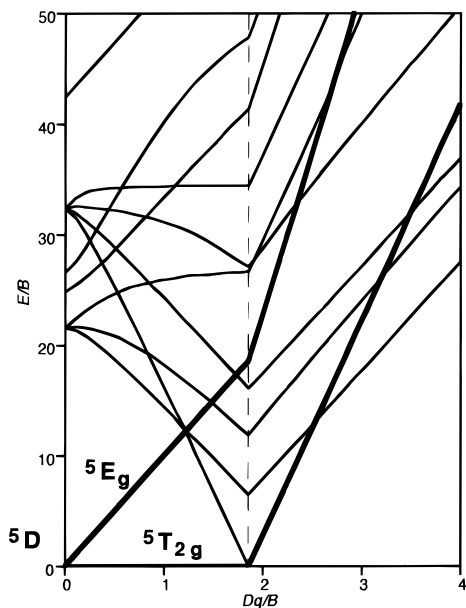


Figure 1. The d^6 Tanabe–Sugano diagram. Quintet states providing spin-allowed transitions are in bold.

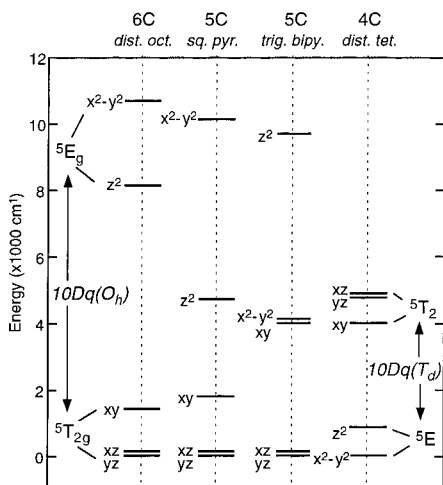


Figure 2. Theoretical LF splittings of d-orbitals for different Fe^{II} coordination environments.

Fe^{II} , this is the 5E_g state which is at $10Dq$. For biologically relevant nitrogen and oxygen ligation, $10Dq$ is approximately $10\,000\text{ cm}^{-1}$. Both the 5E_g excited state and the ${}^5T_{2g}$ ground state are orbitally degenerate and will split in energy in the low-symmetry environment of a non-heme protein active site. The splittings of the ${}^5T_{2g}$ and 5E_g states are directly related to the lifting of the degeneracy of the t_{2g} (d_{xz} , d_{yz} , d_{xy}) and e_g (d_{z^2} , $d_{x^2-y^2}$) orbital sets, respectively, in low-symmetry environments. This splitting is given by ligand-field (LF) theory as summarized in Figure 2.^{11–14} In distorted six-coordinate (6C) sites the 5E_g state will split by up to 2000 cm^{-1} . Removal of one ligand produces a five-coordinate (5C) square-pyramidal environment and a LF splitting of the 5E state of $\sim 5000\text{ cm}^{-1}$, producing transitions at $>10\,000$ and $\sim 5000\text{ cm}^{-1}$. Distortion to a trigonal-bipyramidal 5C structure changes the LF and lowers the energy of the transitions to $<10\,000$ and $<5000\text{ cm}^{-1}$. For a four-coordinate (4C) distorted-tetrahedral environment, $10Dq(T_d) \approx -4/9\,10Dq(O_h)$, and thus, there are only low-energy LF

excited states resulting in transitions around 5000 cm^{-1} . The splitting of the 3-fold orbital degeneracy of the octahedral ${}^5T_{2g}$ ground state in low symmetry is considered later in this section. From Figure 2 it can be seen that the LF transitions are diagnostic of active-site structure. However, these transitions are weak and in the $12000\text{--}5000\text{ cm}^{-1}$ (near-IR) range and will be obscured in absorption due to contributions from buffer and protein vibrations. Alternatively, high-spin Fe^{II} is paramagnetic with an $S = 2$ ground state and will exhibit a \mathbf{C} -term magnetic circular dichroism (MCD) signal which at low temperature (LT) is 2–3 orders of magnitude more intense than the MCD signals associated with the diamagnetic background.

This can be seen from the general expression for MCD intensity^{15–18}

$$\frac{\Delta A}{E} = \text{const} \cdot \beta H \left[\mathbf{A}_1 \left(\frac{-\partial f(E)}{\partial E} \right) + \left(\mathbf{B}_0 + \frac{\mathbf{C}_0}{kT} \right) f(E) \right] \quad (1)$$

where ΔA is the difference in absorbance of left (A_l) and right (A_r) circularly polarized light ($\Delta A = A_l - A_r$), E is the energy of the incident light, β is the Bohr magneton, H is the strength of the applied magnetic field,¹⁹ and $f(E)$ is the absorption band shape. The three terms \mathbf{A}_1 , \mathbf{B}_0 , and \mathbf{C}_0 describe the three different mechanisms giving rise to MCD intensity. Note that eq 1 is valid only when the thermal energy (kT) is larger than the energy splittings of the sublevels of the ground state. For the \mathbf{A}_1 -term, the following equation has been derived^{15–18}

$$\mathbf{A}_1 = \frac{1}{d_A} \sum \left(\langle J | \mu_z | J \rangle - \langle A | \mu_z | A \rangle \right) \left([M_-^{AJ}]^2 - [M_+^{AJ}]^2 \right) \quad (2)$$

Here, $|J\rangle$ is the excited state of the corresponding MCD transition and $|A\rangle$ is the ground state where d_A is the ground-state degeneracy, μ_z is the Zeeman operator ($\mu_z = \mathbf{L}_z + 2\mathbf{S}_z$) and the M_i 's are electric transition dipole moments for left (M_+) and right (M_-) circularly polarized light, respectively. According to eq 2, the system needs either a degenerate ground or excited state for \mathbf{A} -term intensity. Since in eq 1 $\partial f(E)/\partial E$ is the first derivative of the absorption band, the \mathbf{A} -term signal has a derivative shape. The \mathbf{B}_0 -term is given by the equation^{15–18}

$$\mathbf{B}_0 = \frac{2}{d_A} \text{Re} \sum \left[\sum_{K; K \neq J} \frac{\langle J | \mu_z | K \rangle}{\Delta E_{KJ}} \left([M_-^{AJ}] \cdot [M_+^{KA}] - [M_+^{AJ}] \cdot [M_-^{KA}] \right) + \sum_{K; K \neq J} \frac{\langle K | \mu_z | A \rangle}{\Delta E_{KA}} \left([M_-^{AJ}] \cdot [M_+^{JK}] - [M_+^{AJ}] \cdot [M_-^{JK}] \right) \right] \quad (3)$$

\mathbf{B} -term intensity arises from field-induced mixing with an intermediate state, $|K\rangle$, which must be close in energy to either the ground or the excited state in order for this mechanism to be effective. Since the \mathbf{B} -term signal is proportional to $f(E)$, it has an absorption band shape. Note from eq 1 that both \mathbf{A} -

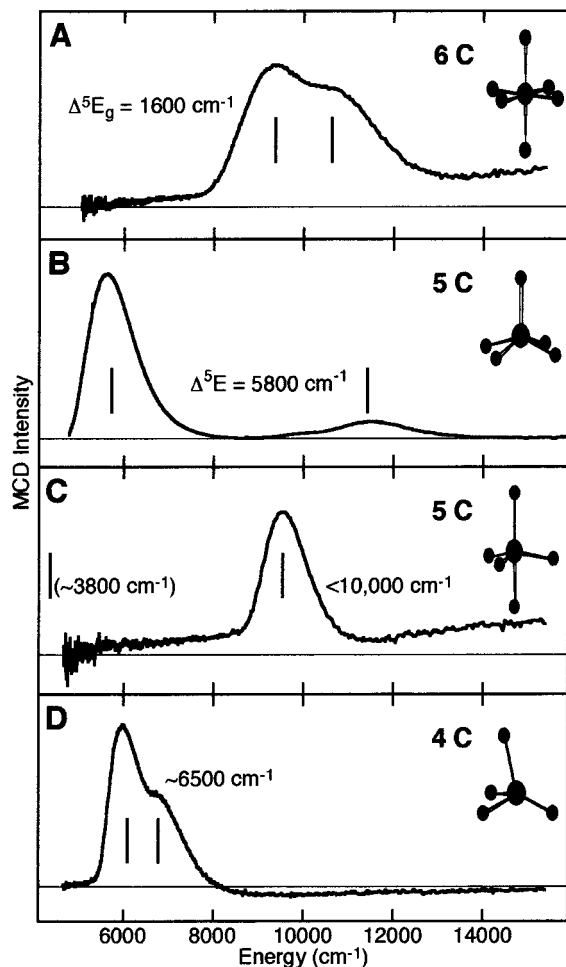


Figure 3. LT MCD spectra of representative structurally defined Fe^{II} model complexes. (A) 6C, octahedral [Fe(H₂O)₆](SiF₆). (B) 5C, square-pyramidal [Fe(HB(3,5-Pr₂pz)₃)(OAc)]. (C) 5C, trigonal-bipyramidal [Fe(tris(2-(dimethylamino)ethyl)amine)Br]⁺. (D) 4C, tetrahedral [Fe(HB(3,5-Pr₂pz)₃)(Cl)]. (Adapted from ref 14.)

and **B**-terms are temperature independent. The expression for the **C**₀-term has the form^{15–18}

$$C_0 = \frac{-1}{d_A} \sum \langle A | \mu_z | A \rangle ([M_-^{AJ}]^2 - [M_+^{AJ}]^2) \quad (4)$$

Importantly, a degenerate ground state is necessary for the occurrence of **C**-term intensity corresponding to a paramagnetic system. As with the **B**-term, the **C**-term has an absorption band shape; however, from eq 1, the **C**-term intensity is proportional to 1/*T*. This leads to a great enhancement of **C**-term intensity at LT compared to **A**- and **B**-term signals. For paramagnetic transition-metal complexes, the observed MCD intensity may be due to all three mechanisms but at LT the **C**-term dominates.²⁰

We have now studied 25 structurally defined ferrous model complexes with LT MCD and found experimental spectra consistent with the LF predictions in Figure 2.¹⁴ From Figure 3A, distorted 6C sites exhibit two LF transitions split by less than 2000 cm⁻¹ in the ~10 000 cm⁻¹ region. Five-coordinate square-pyramidal sites exhibit LF transitions in the > 10 000 and ~5000 cm⁻¹ regions (Figure 3B). For trigonal-bipyramidal 5C sites, these transitions

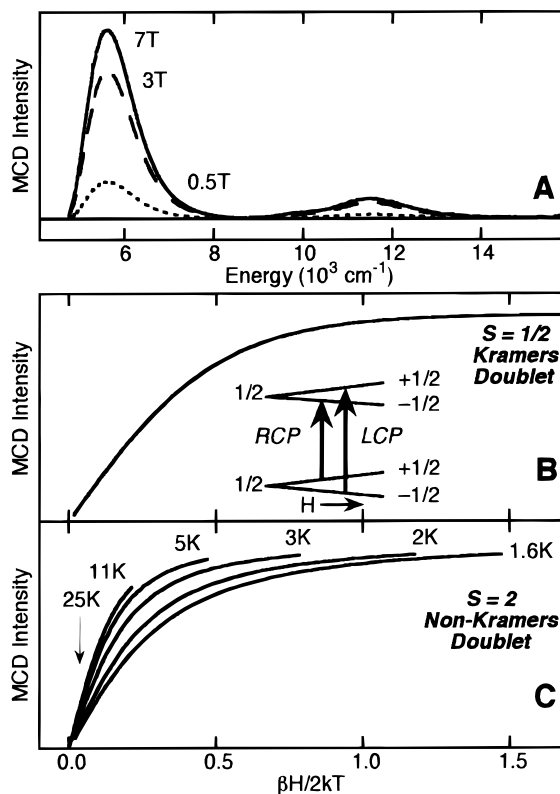


Figure 4. (A) Field dependence of MCD signal. (B) Saturation magnetization MCD for an *S* = 1/2 Kramer's doublet; signal as a function of field and temperature. Inset shows Kramer's doublet in a magnetic field and MCD transitions. (C) Saturation magnetization MCD for an *S* = 2 non-Kramers doublet with signal as a function of field at 5 K.

shift to <10 000 and <5000 cm⁻¹ (Figure 3C) and the distorted tetrahedral complexes exhibit only low-energy LF transitions in their LT MCD spectra (Figure 3D).

We next use the temperature and field dependence of the MCD signal to probe the splitting of the 5T_{2g} ground state.^{11,13,21} In accordance with eq 1, Figure 4A shows that, at LT, increasing the magnetic field increases the MCD signal. This MCD intensity is plotted as a function of increasing field and decreasing temperature in Figure 4B. From Figure 4B, the MCD signal of a paramagnetic center first increases as temperature decreases ($\propto 1/T$) or magnetic field increases; however, this signal eventually levels off at high field and LT and is saturated. The origin of this saturation magnetization behavior (not included in eq 1) can be easily understood from consideration of the **C**-term MCD behavior of a Kramer's doublet (Figure 4B inset). Both the ground and excited states are *S* = 1/2 and will split into *M_S* = -1/2 and +1/2 levels with increasing magnetic field. The selection rules for MCD predict two transitions of equal magnitude but opposite signs (i.e., left- and right-circularly polarized) to a given excited state. At high temperature and low field, these will mostly cancel and one observes a weak MCD signal. As temperature decreases and field increases, Boltzmann population of the higher sublevel decreases, cancellation no longer occurs, and the **C**-term MCD signal increases in intensity. Eventually only the lowest

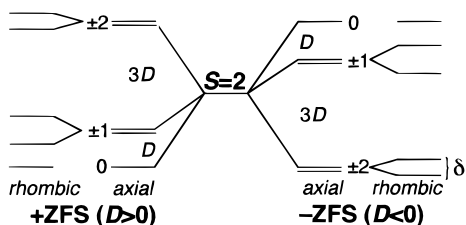


Figure 5. Energy splittings of the $S = 2$ sublevels for +ZFS (left) and -ZFS (right). (Adapted from refs 13 and 21.)

component of the ground state is populated and the signal no longer increases with decreasing temperature or increasing magnetic field; this leads to the *nonlinear* and eventual saturation magnetization behavior observed in Figure 4B.

For a Kramers doublet, the saturation behavior can be expressed by the following Brillouin-like function which includes orientation averaging^{12,13,17,22,23}

$$\Delta\epsilon = A_{\text{sat}} \left\{ \int_0^{\pi/2} \frac{\cos^2 \phi \sin \phi}{\Gamma} g_{\parallel} \times \tanh \left[\frac{\Gamma \beta H}{2kT} \right] d\phi - \sqrt{2} \frac{M_z}{M_{xy}} \int_0^{\pi/2} \frac{\sin^3 \phi}{\Gamma} g_{\perp} \times \tanh \left[\frac{\Gamma \beta H}{2kT} \right] d\phi \right\} \quad (5)$$

where A_{sat} is the maximum C -term intensity at saturation, ϕ is the angle between the applied magnetic field and the g -tensor's²⁴ principal (z) axis (vide infra), g_{\parallel} and g_{\perp} are effective g -values of the doublet with g_{\parallel} being the g -value along the z -axis, M_z and M_{xy} are the polarizations of the MCD transition, and Γ is defined as

$$\Gamma = \sqrt{(g_{\parallel} \cos \phi)^2 + (g_{\perp} \sin \phi)^2} \quad (6)$$

As anticipated by eq 5, the saturation magnetization curves for an $S = 1/2$ ion obtained at different temperatures with increasing applied magnetic fields superimpose when plotted as a function of $\beta H/2kT$ as shown in Figure 4B. This, however, is not the case for high-spin ferrous active sites.^{11–13} As shown in Figure 4C, saturation magnetization data obtained at different temperatures do not overlay but instead form a nested set of curves.²⁵ This nesting derives from the non-Kramers nature of the $S = 2$ ground state.^{11,13,26}

This ground state is 5-fold degenerate in M_S values ($0, \pm 1, \pm 2$), and this sublevel degeneracy will split in the low-symmetry protein environment due to zero-field splitting (ZFS). An axial distortion produces the DS_z^2 term in the spin Hamiltonian in eq 7²⁷

$$\mathbf{H} = D(\mathbf{S}_z^2 - \frac{1}{3}\mathbf{S}^2) + E(\mathbf{S}_x^2 - \mathbf{S}_y^2) \quad (7)$$

with D and E being the axial and rhombic ZFS parameters, respectively, and the \mathbf{S} are spin operators. For a +ZFS state, corresponding to a strong LF along the z -axis, the $M_S = 0$ sublevel is lowest in energy and ± 1 is at D and ± 2 is at $3D$ energy units above this (Figure 5, left). For a $-D$ (weak axial LF) case, the $M_S = \pm 2$ is lowest in energy (Figure 5, right). For a rhombic site, as anticipated for a non-heme protein environment, the rhombic ZFS param-

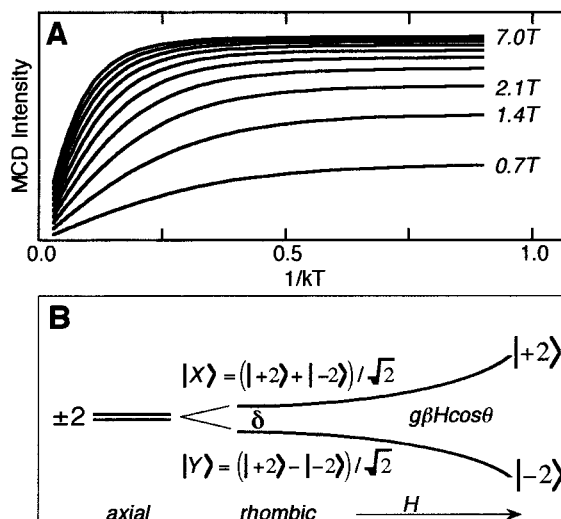


Figure 6. (A) Data from Figure 4C replotted as a function of $1/kT$ for fixed magnetic fields. (B) Rhombic and magnetic field splitting and mixing of an $M_S = \pm 2$ non-Kramers doublet. (Adapted from refs 13 and 21.)

eter E is nonzero and this will split the degeneracy of the $M_S = \pm 2$ sublevels by an amount δ even in the absence of a magnetic field. This splitting will occur only for a non-Kramers doublet and often leads to the lack of an EPR signal. It is also the origin of the nested saturation magnetization curves in Figure 4C.^{11,13}

This can be observed from a replot of the data in Figure 4C to separate the effects of temperature and magnetic field. Figure 6A shows the increase in the MCD signal with decreasing temperature for a series of fixed magnetic fields. At LT (right side of Figure 6A) the signal saturates, indicating that only the lowest component of the ground state is populated. It is important to note that at increasing fields the MCD saturation intensity at LT increases in a nonlinear fashion and eventually levels off at high magnetic fields. This indicates that the wave function of the lowest component of the ground state is changing with magnetic field. This is exactly the behavior expected for a non-Kramers doublet. As shown in Figure 6B, rhombic ZFS both splits the energy of the $M_S = \pm 2$ and mixes these wave functions. As the magnetic field increases, the sublevels split in energy by the amount $g_{\parallel} \beta H$ due to the Zeeman effect. The wave functions also change and become pure $M_S = -2$ for the lowest energy sublevel and $+2$ for the higher energy sublevel and thus MCD active at high magnetic field.²⁸

One can take this non-Kramers doublet model and allow for orientation averaging for a frozen protein solution to fit the nested saturation magnetization data, Figure 4C. For a xy -polarized MCD transition, for example, the appropriate expression is^{11,13}

$$\Delta\epsilon = A_{\text{sat}} \int_0^{\pi/2} \frac{\cos^2 \phi \sin \phi}{\sqrt{\delta^2 + (g_{\parallel} \beta H \cos \phi)^2}} g_{\parallel} \beta H \times \tanh \left[\frac{\sqrt{\delta^2 + (g_{\parallel} \beta H \cos \phi)^2}}{2kT} \right] d\phi \quad (8)$$

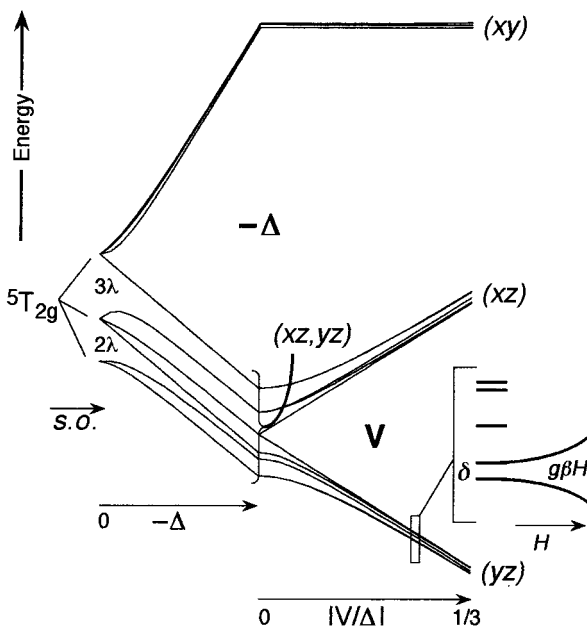


Figure 7. LF theory for the ${}^5T_{2g}$ ground state of a $-ZFS$ system. Inset expands region indicated and includes the magnetic field effects given by the last term in eq 7. (Adapted from ref 13.)

Applying eq 8 to the variable-temperature, variable-field (VTVH) MCD data in Figure 4C, the spin Hamiltonian parameters (δ , g_i) for the non-Kramers doublet ground state can be derived. Thus, we have used an excited state to obtain EPR parameters for an EPR nondetectable non-Kramers ground state.

We are then interested in the information content of these spin Hamiltonian parameters in terms of the orbital energy splitting of the ${}^5T_{2g}$ state by the LF of the protein active site. From Figure 7, the 3-fold orbital degeneracy of the ${}^5T_{2g}$ state (corresponding to the extra electron in the d_{xy} , d_{xz} , or d_{yz} orbital) gives an orbital angular momentum contribution to this ground state. This will spin-orbit couple (SOC) to the $S = 2$ spin state to produce a splitting of the ${}^5T_{2g}$ state in octahedral symmetry into 7-, 5-, and 3-fold degenerate spin-orbit levels (the last being lowest in energy on the left of Figure 7 where λ is the many-electron SOC parameter). The orbital degeneracy of the ${}^5T_{2g}$ state will also split due to the low-symmetry protein environment, with Δ defining the axial splitting of the d_{xy} relative to the d_{yz} and d_{xz} orbitals (the latter lowest for a weak-axial interaction) and V defining the rhombic splitting of d_{xz} relative to d_{yz} . Combining these d-orbital splittings with SOC in LF calculations with the Hamiltonian¹³

$$H({}^5T_{2g}) = \lambda(\vec{L} \cdot \vec{S}) + \Delta(L_z^2 - 1/3L^2) + V(L_x^2 - L_y^2) + \beta(\mu_x H_x + \mu_y H_y + \mu_z H_z) \quad (9)$$

(neglecting spin-spin interactions which are expected to be small; $\mu_i = \mathbf{L}_i + 2\mathbf{S}_i$) leads to the energy diagram on the right side of Figure 7 with a rhombically split non-Kramers doublet ground state (Figure 7, inset). Using this model we can calculate g_i and δ , the spin Hamiltonian parameters of the non-Kramers doublet, as a function of the axial (Δ) and rhombic (V) splitting of the t_{2g} set of d-orbitals. This

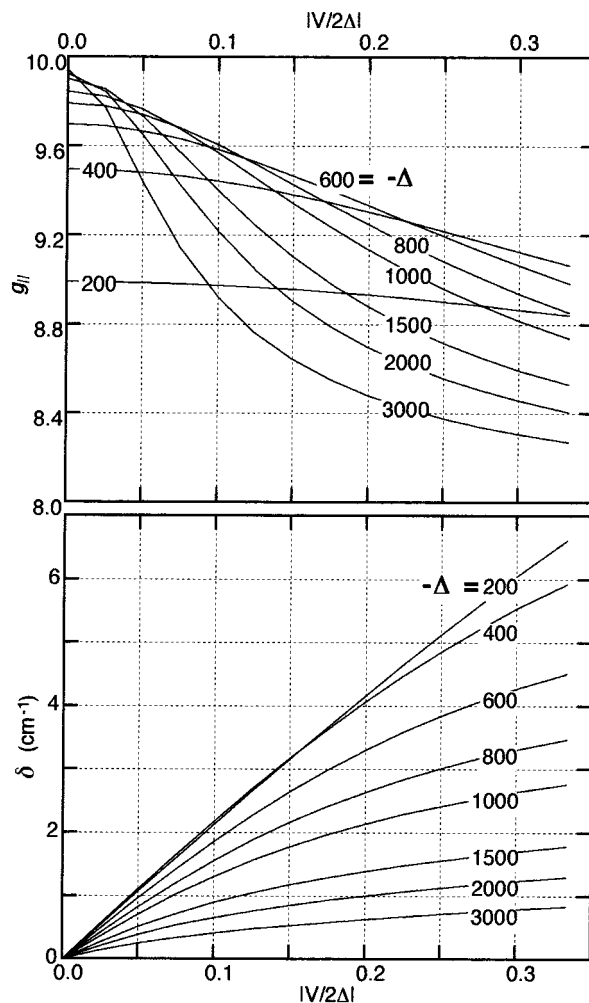


Figure 8. Relationship between δ and g_i and the LF parameters $-\Delta$ and V for the ${}^5T_{2g}$ ground state of a system with $-ZFS$. (Reprinted with permission from ref 13. Copyright 1995 Elsevier Science.)

gives the diagrams in Figure 8. These diagrams allow experimentally obtained values of δ and g_i to be used to determine Δ and V and thus the splitting of the t_{2g} set of orbitals by the LF of the ferrous site. At this point it should be noted that observation of reduced nesting in the VTVH MCD saturation magnetization data (e.g., Figure 4C) indicates a smaller value of δ . This in turn is associated with an increase in the value of Δ (Figure 8) and hence an increase in the axial splitting of the t_{2g} orbitals, as would be observed, for example, in going from a 6C to a 5C site.

The above analysis has considered a weak axial distortion giving a $-ZFS$. For the $+ZFS$ case, the $M_S = 0$ sublevel is lowest in energy and the $M_S = \pm 1$ are at an energy D in the absence of a rhombic splitting (Figure 5, left). The VTVH MCD data for a $+D$ case are similar to that for a $-D$ but with a very large nesting (Figure 9A). This derives from the fact that when the magnetic field is not parallel to the z -axis, the $M_S = 0$ and one component of the $M_S = \pm 1$ behave very much like the $M_S = \pm 2$ non-Kramers doublet: they split with $g \approx 8$ and the wavefunctions change in the same way with the applied magnetic field (Figure 9B). The major difference is that at zero magnetic field the splitting is the axial parameter D

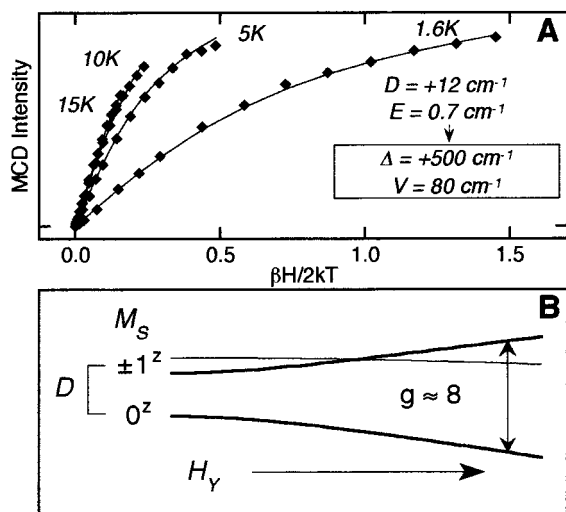


Figure 9. (A) z-Polarized ($H||y$) saturation magnetization data for the + D complex $\text{FeSiF}_6 \cdot 6\text{H}_2\text{O}$. (B) Magnetic field ($H||y$) splitting of a +ZFS system. (Adapted from ref 21.)

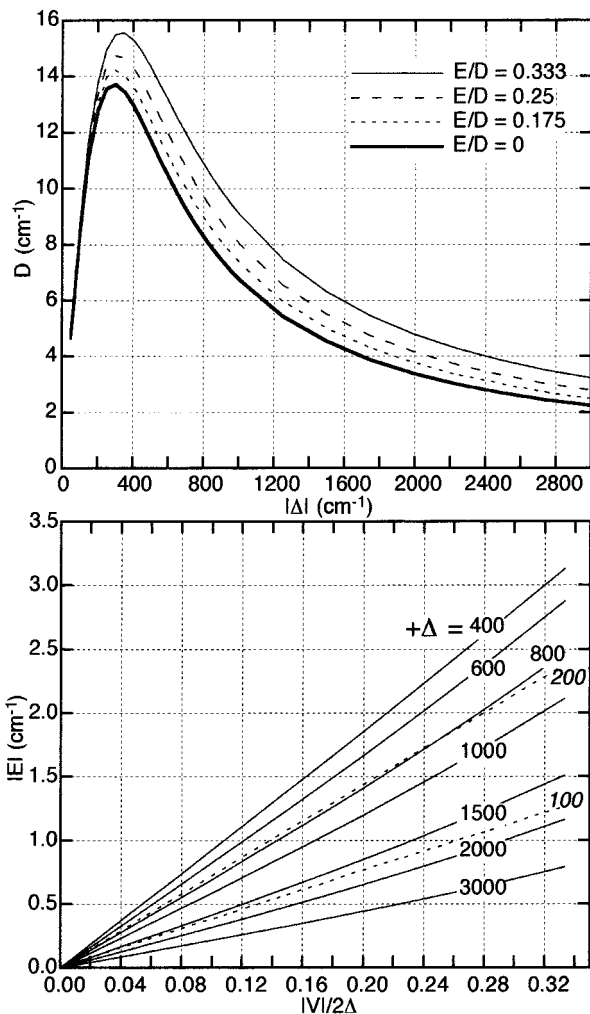


Figure 10. Relationship between the spin Hamiltonian parameters D and E and the LF parameters $+\Delta$ and V for the ${}^5T_{2g}$ ground state of a system with +ZFS. (Reprinted with permission from ref 13. Copyright 1995 Elsevier Science.)

rather than the rhombic δ and D is much larger leading to the increased nesting (i.e., compare Figure 9A to Figure 4C).¹³ Thus, from the nature of the saturation magnetization data, one can recognize a

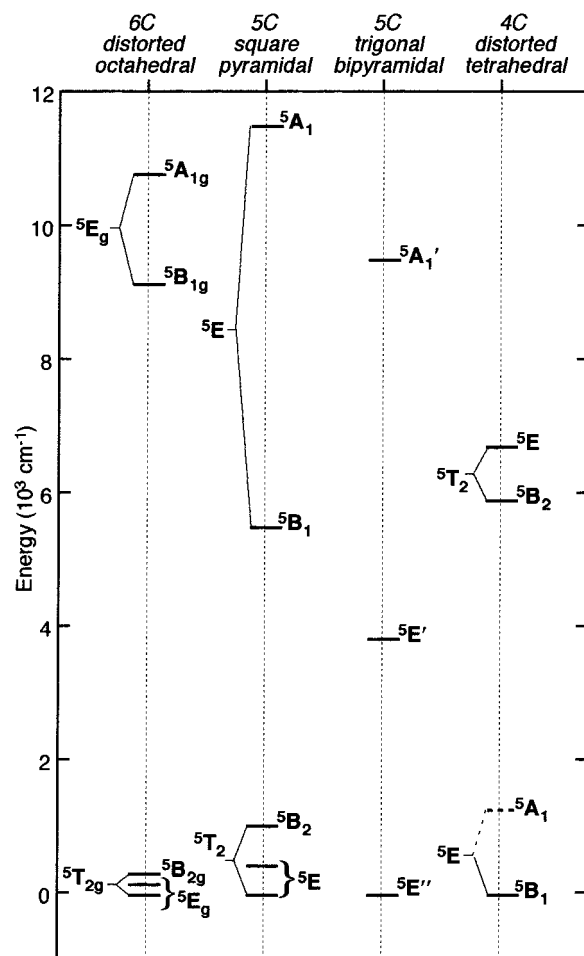


Figure 11. Experimentally determined LF splittings for the complexes shown in Figure 3. (Adapted from ref 14.)

+ D (strong axial) case and use the + D model in Figure 9B with orientation averaging for the frozen protein solution to obtain the spin Hamiltonian parameters. Figure 10 gives the correlation of D and E to the axial (Δ) and rhombic (V) splittings of the t_{2g} set of d-orbitals.

Thus, for the compounds in Figure 3, the VTVH MCD data allow one to obtain the experimental LF splittings of the five d-orbitals at the non-heme ferrous active site.¹⁴ The corresponding state splittings are given in Figure 11. The LF splittings provide a direct probe of active-site geometric and electronic structure and can be used to obtain molecular-level insight into the catalytic mechanism. A more detailed development of the Fe^{II} MCD methodology is presented in ref 13.

Additional spectroscopic methods that have been applied to the study of non-heme Fe^{II} active sites include Mössbauer and X-ray absorption spectroscopy (XAS). The isomer shift (δ_{Fe}) is characteristic of s-electron charge density at the nucleus and is typically found for high-spin Fe^{II} in the range from 0.8 to 1.6 mm s^{-1} . In addition, for low-symmetry environments, large quadrupole splittings ΔE_Q are observed.^{29,30} In the case of non-heme iron systems with N- and O-based ligands, δ_{Fe} is expected to be $>1.2 \text{ mm s}^{-1}$ for 6C or 5C Fe^{II} sites and $<1 \text{ mm s}^{-1}$ for 4C Fe^{II} sites.³¹ δ_{Fe} decreases if N or O ligands are replaced by a more covalent ligand such as S.

Table 3. Mössbauer Parameters for Fe^{II} Enzymes

Fe ^{II} enzyme	coord. no.	δ_{Fe} (mm s ⁻¹)	ΔE_{Q} (mm s ⁻¹)	temp (K)	ref
bleomycin	6	1.22	2.83	4.2	34,35
isopenicillin <i>N</i> -synthase	6	1.30	2.70	4.2	36
isopenicillin <i>N</i> -synthase, substrate-bound	5	1.10	3.40	4.2	36
lipoxygenase, soybean	6	1.10	3.08	4.2	37
phenylalanine hydroxylase	6	1.23	2.85	4.2	38
protocatechuate 4,5-dioxygenase	5	1.28	2.22	4.2	39
protocatechuate 4,5-dioxygenase, substrate-bound	5	1.27	2.33	4.2	39
tyrosine hydroxylase	5/6	1.26	2.68	1.8	40–42

Table 4. XAS Pre-edge Parameters for Fe^{II} Enzymes

Fe ^{II} enzyme	coord. no.	pre-edge energy (eV)	pre-edge area ^a	ref
bleomycin	6	7111.4/7113.6		43
catechol 2,3-dioxygenase	5		10.1	44
catechol 2,3-dioxygenase, substrate-bound	5		11.1	44
isopenicillin <i>N</i> -synthase	6	7112	8	45
isopenicillin <i>N</i> -synthase, substrate-bound	5	7112	12	45
lipoxygenase, soybean	6	7111.5/7113.1	8.4	46
lipoxygenase, rabbit	6	7111.8/7113.1	8.2	46
lipoxygenase, human	6	7111.7/7113.3	8.4	46
phenylalanine hydroxylase	6	7111.7/7113.6	9.9	47
phenylalanine hydroxylase, substrate-bound	6	7111.8/7113.6	8.2	47
protocatechuate 3,4-dioxygenase, chemically reduced	6	7111.8/7113.4	8.8	48
tyrosine hydroxylase	5/6		6.9	41

^a Pre-edge intensities may vary slightly due to different spectral fitting procedures employed in different laboratories.

Examples of Mössbauer parameters for some Fe^{II} enzymes are listed in Table 3. In the X-ray absorption spectra the 1s → 3d pre-edge transition energy and intensity distribution over the dⁿ⁺¹ final state multiplets are characteristic of oxidation state and geometry.^{32,33} Six-coordinate Fe^{II} complexes have a low total pre-edge intensity with a pre-edge shape that is broad and flat. This intensity derives solely from an electric quadrupole mechanism. In contrast, 5C and 4C Fe^{II} sites typically have two pre-edge peaks with a higher total pre-edge intensity. These can be distinguished by the intensity distribution over the pre-edge region: distorted tetrahedral structures show two intense peaks, while square-pyramidal structures have one intense and one weak peak with the weak transition at higher energy. This intensity increase and its distribution over the peaks reflects symmetry-specific 4p mixing in a noncentrosymmetric environment. XAS pre-edge results for selected non-heme Fe^{II} proteins are summarized in Table 4.

2. Fe^{III}

The Tanabe–Sugano diagram in Figure 12 gives the energies of the different LF states of Fe^{III} relative to the ground state as a function of the LF parameter $10Dq(O_h)$, both axes normalized to the electron–electron repulsion parameter B .⁴⁹ For the free Fe^{III} ion, B is about 1050 cm⁻¹⁵⁰ but it is reduced in coordination compounds due to covalency. For Figure 12, a reasonable value of $B = 750$ cm⁻¹ has been applied. The free Fe^{III} ion has a d⁵ electron configuration which leads to a ⁶S atomic ground state and a large number of quartet and doublet excited states (atomic terms, Figure 12, left) which differ in electron distribution among the d-orbitals and hence in electron–electron repulsion. In an octahedral LF, the five d-orbitals are split into a 3-fold degenerate t_{2g} set and a 2-fold degenerate e_g set by an energy equal to the LF parameter $10Dq$. Going from the left to the right

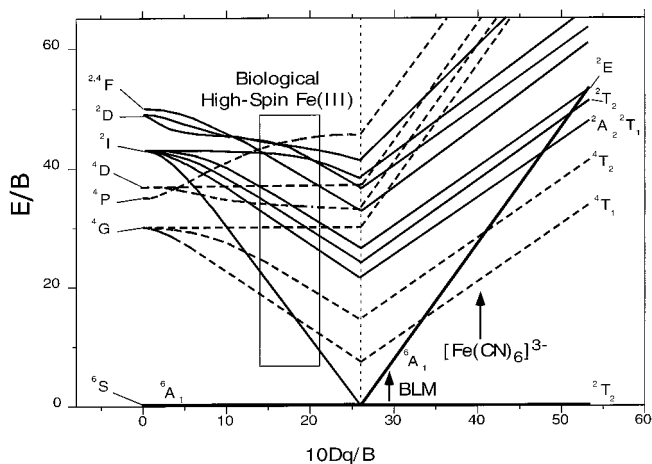


Figure 12. The d⁵ Tanabe–Sugano diagram. Typical LF strengths of biological non-heme ferric centers are indicated.

in the Tanabe–Sugano diagram, $10Dq$ increases continuously, which leads to an increasing splitting of the d-functions and hence an energy splitting of the orbitally degenerate excited atomic terms. When $10Dq$ is small ($< 26B$), the Fe^{III} remains in the high-spin ⁶A_{1g} ground state corresponding to a (t_{2g})³(e_g)² electron configuration with maximum multiplicity (all five d-orbitals are singly occupied). Typical LF strengths for biological high-spin Fe^{III} sites are 10000–16000 cm⁻¹ (Figure 12). At $10Dq \approx 20$ 000 cm⁻¹, the ²T_{2g} state corresponding to a low-spin (t_{2g})⁵ configuration crosses the high-spin ⁶A_{1g} state and becomes the ground state. Only a few biologically relevant non-heme low-spin Fe^{III} systems are known; for example, bleomycin (BLM) exhibiting a $10Dq$ value of 20 600 cm⁻¹ (i.e., $10Dq/B = 27.5$), therefore being close to the spin-crossover region. Another known low-spin non-heme Fe^{III} enzyme is nitrile hydratase which also has sulfur-based ligands. A

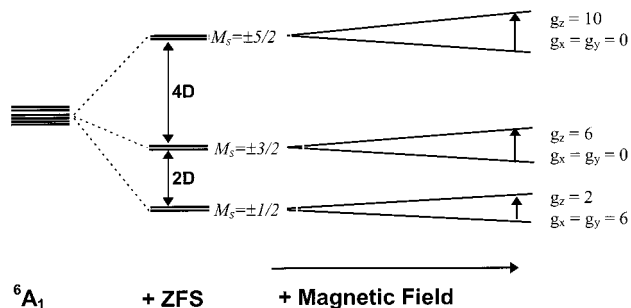


Figure 13. Axial ZFS for high-spin ferric centers with $D > 0$ and Zeeman splitting of the resulting doublets with H parallel and perpendicular to the z -axis of the ZFS tensor and $D > h\nu$ of the microwaves ($\sim 0.33 \text{ cm}^{-1}$ at X band). (Adapted from ref 169.)

classic example of a low-spin system is hexacyanoferrate(III) having a $10Dq$ of about $30\,000 \text{ cm}^{-1}$.

a. High-Spin Fe^{III} . 1. Ground-State Properties. The ${}^6\text{A}_{1g}$ ground state of high-spin Fe^{III} has a total spin $S = 5/2$ corresponding to a Kramers system and can be probed with EPR spectroscopy. Its 6-fold degeneracy in M_S values can be split in energy even in zero magnetic field (due to SOC with excited states, vide infra). In the case of an axially distorted octahedral system, three doubly degenerate states result corresponding to the magnetic spin quantum numbers $M_S = \pm 5/2, \pm 3/2, \pm 1/2$. This ZFS is given in terms of the parameter D in eq 7 and Figure 13. Applying a magnetic field removes the remaining degeneracy and splits the corresponding $M_S = \pm 5/2, \pm 3/2, \pm 1/2$ doublets proportional to the strength of the field, $|\vec{H}|$. Generalizing eq 7 to include the Zeeman effect gives²⁷

$$\mathbf{H} = \vec{\mathbf{S}}\mathbf{D}\vec{\mathbf{S}} + \beta\vec{H}\mathbf{g}\vec{\mathbf{S}} \quad (10)$$

where \mathbf{D} is the ZFS tensor, $\vec{\mathbf{S}}$ is the spin operator, β is the Bohr magneton, H is the magnetic field strength, and \mathbf{g} is the g tensor. Assuming coaxial \mathbf{D} and \mathbf{g} tensors, eq 10 can be written as²⁷

$$\mathbf{H} = D(\mathbf{S}_z^2 - \frac{1}{3}\mathbf{S}^2) + E(\mathbf{S}_x^2 - \mathbf{S}_y^2) + \beta(g_x H_x \mathbf{S}_x + g_y H_y \mathbf{S}_y + g_z H_z \mathbf{S}_z) \quad (11)$$

Here, D and E are again the axial and rhombic ZFS parameters which are related to the elements of the diagonalized \mathbf{D} tensor by eq 12 (a "proper coordinate system" is chosen such that $0 \leq E \leq \frac{1}{3}D$)

$$D = D_{zz} - \frac{1}{2}(D_{xx} + D_{yy}) \quad E = \frac{1}{2}(D_{xx} - D_{yy}) \quad (12)$$

The sign of the axial splitting parameter D is directly related to the geometry of the complex (vide infra). Note that for Kramers doublets the degeneracy of the $\pm M_S$ doublets is not lifted in a rhombic field ($E \neq 0$, vide supra). Applying the spin Hamiltonian (eq 11) to the $S = 5/2$ system gives a 6×6 matrix whose solutions (eigenvalues and eigenfunctions) depend on the strength and orientation of the magnetic field. Hence, for an exact solution, the spin Hamiltonian matrix must be diagonalized at every field. This leads to a rather complex pattern of the resulting terms.^{51–53} In case that $|D| \gg g\beta H$, a useful approximation is to solve the field-free spin Hamiltonian matrix (setting

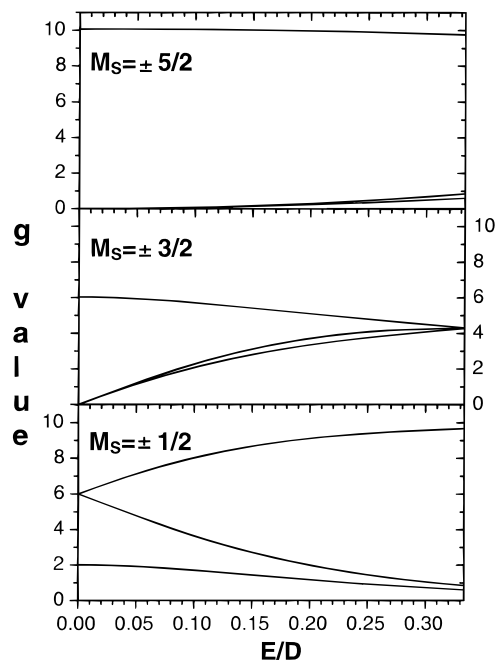


Figure 14. Resonance positions observed in high-spin ferric EPR spectra as a function of the E/D ratio. (Adapted from ref 169.)

\vec{H} to zero) and treat the resulting three doublets as three independent pseudo $S = 1/2$ systems. Each doublet is then subjected to a magnetic field and the Zeeman splittings are calculated. Figure 13 (right) includes the results in a schematic way for an axial system with the field parallel and perpendicular to the principal (z) axis of the ZFS tensor.

These ground-state splittings can be probed with EPR spectroscopy, which allows the detection of magnetic dipole transitions in the microwave region. Note that the splittings induced by the magnetic field are in the range of $0\text{--}1 \text{ cm}^{-1}$, whereas typical D values for Fe^{III} high-spin systems are found between -2 and 2 cm^{-1} . Using the model of three independent pseudo $S = 1/2$ doublets, the EPR transition energies are expressed as effective g -values ($g_{\text{eff}} = \tilde{g}$) calculated from the resonance energy with the relation $\tilde{g} = 0.7147\nu/H_{\text{res}}$, where ν is the operating frequency of the EPR spectrometer and H_{res} is the resonance position of the field in Gauss. Figure 14 shows the \tilde{g} values of the three doublets as a function of the E/D ratio ($0 \leq E \leq \frac{1}{3}D$), and Figure 15 contains typical EPR spectra observed for pure axial ($E/D = 0$), distorted axial ($E/D = 0.05$), and rhombic ($E/D = 1/3$) systems. Since the splittings are small compared to the thermal energy (kT) even at liquid nitrogen temperature, the EPR spectra normally contain contributions of all three doublets and the temperature dependence of the different signals can be used to calculate D . For each doublet, three \tilde{g} values corresponding to the three principal axes (x, y, z) are observed in (frozen) solutions due to the random orientation of individual molecules relative to the direction of the external magnetic field, \vec{H} .

Origin and Interpretation of Zero-Field Splittings in High-Spin Ferric Complexes. Compared to the ZFSs of high-spin ferrous centers developed in section II.A.1, the interpretation of the \mathbf{D} tensor in high-spin

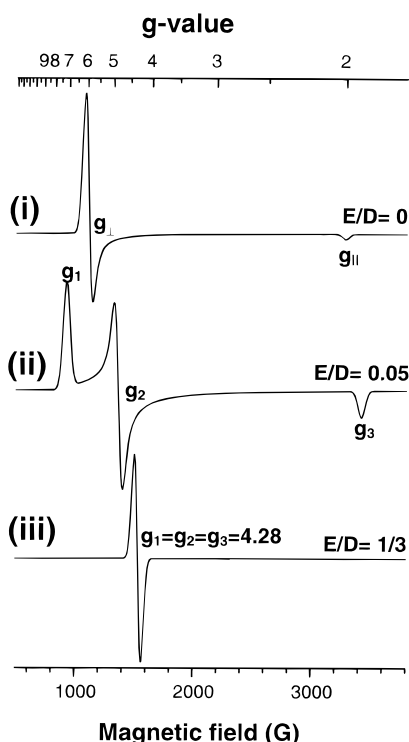


Figure 15. Three typical high-spin ferric EPR spectra: (i) purely axial case ($D > 0$); (ii) intermediate situation; and (iii) purely rhombic case ($E/D = 1/3$). (Adapted from ref 169.)

ferric centers is rather more subtle.^{54–56} Since for the high-spin d^5 configuration the lowest term is ${}^6A_{1g}$, there is no in-state orbital angular momentum and no LF excited states of the same multiplicity are present. Therefore, the SOC interaction is not large in contrast to the case of the ferrous centers where the triply degenerate (or barely split) ${}^5T_{2g}$ term is lowest. Consequently, the g shifts are very small (< 0.01) and the ZFSs are usually moderate for non-heme ferric sites (-2 to 2 cm^{-1}). This may be compared to ZFSs of high-spin ferric hemes which are about 10 cm^{-1} .⁵⁷ The lowest-energy LF excited states that are available for SOC interactions with the ground state in high-spin ferric centers are of quartet multiplicity (see Tanabe–Sugano diagram in Figure 12, left). In cubic systems these are ${}^4T_{1g}$ and ${}^4T_{2g}$ states, both triply orbitally degenerate. Of these two states, only ${}^4T_{1g}$ can SOC to the ${}^6A_{1g}$ ground state and thereby gives rise to the observed ZFS.⁵⁴ However, for exact cubic symmetry, the three principal values of the \mathbf{D} tensor are necessarily equal and, therefore, no splitting is observable by EPR spectroscopy.⁵⁸ Thus, the observed ZFS as expressed by the parameters D and E/D reflects a rather subtle interplay between various interactions that lift the cubic symmetry of the electronic wave functions. The most important of these are (a) low-symmetry one-electron orbital energy splittings that give rise to ${}^4T_{1g}$ state splittings and thus slightly different SOC of the ${}^4T_{1g}$ components with the ${}^6A_{1g}$ ground state and (b) differential covalencies of the d-orbitals that individually change SOC matrix elements by attenuating the metal contribution to the SOC. Low-symmetry splittings arise from geometric distortions and can be rationalized with standard LF theoretical

Table 5. Geometry Contribution to the Sign of D in High-Spin Ferric Complexes

site symmetry	distortion	contribution to D
octahedral (O_h)	weak-axial D_{4h}	positive
	strong-axial D_{4h}	negative
tetrahedral (T_d)	flattened-tetrahedron D_{2d}	positive
	elongated-tetrahedron D_{2d}	negative
trigonal-bipyramidal (D_{3h})	similar to strong-axial O_h	negative
square pyramidal (C_{4v})	best viewed as weak-axial O_h	positive

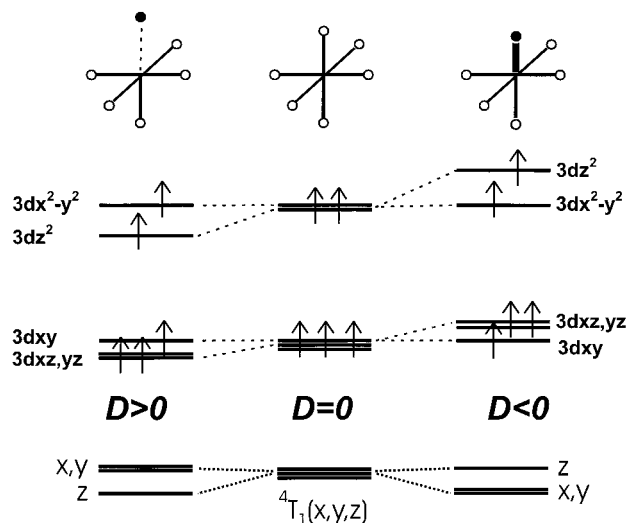


Figure 16. Relationship between the electronic structure of a high-spin ferric center (energy splittings of the d-orbitals and of the 4T_1 LF excited state) and the sign of D . Left: weak axial-ligand case. Right: strong axial-ligand case. (Adapted from ref 169.)

arguments, while the covalency effects require molecular orbital approaches. Often the two effects work in opposite directions such that the prediction of the sign of D from theory is difficult. For low-symmetry distortions, the splittings of the σ -antibonding orbitals usually dominate and give rise to the patterns collected in Table 5 and illustrated in Figure 16 for the case of a distorted octahedron. In many cases these distortions will dominate the D values. However, in cases of highly covalent bonds, i.e., with electronically soft ligands, the covalency effects may reverse the sign of D . An example of this behavior is the complex $\text{Fe}(\text{SR})_4^-$ where the observed distortion would imply $D < 0$ but the observed D is clearly positive.^{55,59} Another example is the $[\text{Fe}(\text{EDTA})(\text{O}_2)]^{3-}$ complex⁶⁰ that will be analyzed in section II.D.

Mössbauer Spectroscopy. High-spin Fe^{III} has characteristic Mössbauer features with an isomer shift δ_{Fe} from about $+0.1$ to $+0.5$ mm s^{-1} (vs metallic iron). Since all five d-orbitals are singly occupied, the quadrupole splitting ΔE_Q is 0 mm s^{-1} in cubic symmetry. However, in low-symmetry environments, a quadrupole splitting may be induced by anisotropic covalency and/or the net charges of surrounding ligands.^{29,30} Applying Mössbauer spectroscopy in a magnetic field, the ZFS parameters as described above can be probed by temperature- and field-dependent experiments.³¹ Moreover, the iron hyperfine parameters can be determined with this method.

Table 6. LF Transition Energies (in cm^{-1}) (Adapted from ref 63)

High-Spin Fe^{III}						
coord. no.	compound	sym. ^a	${}^4\text{T}_{1g}$	${}^4\text{T}_{2g}$	${}^4\text{A}_{1g}$	${}^4\text{E}_g$
6	$[\text{Fe}(\text{urea})_6]^{3+}$	O_h	12 500	17 100	23 100	23 400
	$[\text{Fe}(\text{H}_2\text{O})_6]^{3+}$	O_h	12 600	18 500	24 300	24 600
	$[\text{FeF}_6]^{3-}$	O_h	14 200	19 700		25 400
5	$[\text{Fe}(\text{N}_3)_5]^{2-}$	D_{3h}^b	14 000	16 100		
4	$[\text{FeCl}_4]^{-c}$	T_d	12 890(z)	15 210(z)		18 200
			14 240(xy)	16 050(xy)		
Low-Spin Fe^{III}						
coord. no.	compound	sym. ^a	${}^4\text{T}_{1g}$	${}^4\text{T}_{2g}$	${}^2\text{A}_{2g}/{}^2\text{T}_{1g}$	${}^2\text{E}_g$
6	$[\text{Fe}(\text{CN})_6]^{3-}$	O_h	20 000	28 740	31 000	36 600

^a Idealized symmetry of the metal and its first coordination sphere. ^b In the trigonal-bipyramidal system, the lowest energy LF states are ${}^4\text{E}'$ and ${}^4\text{E}'$, respectively. ^c See ref 64.

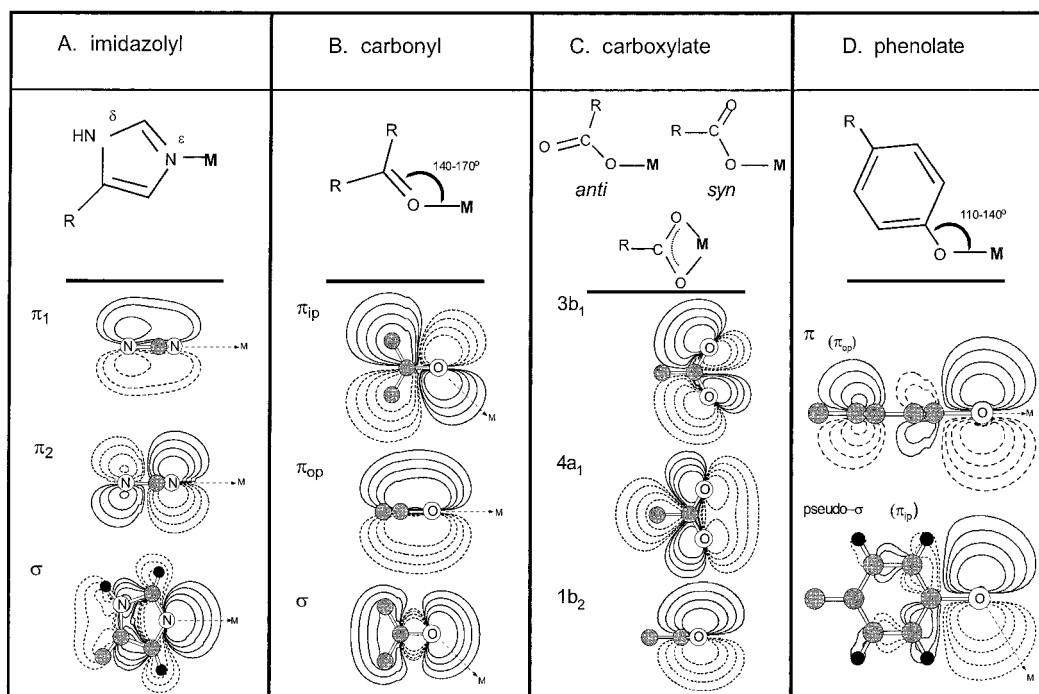
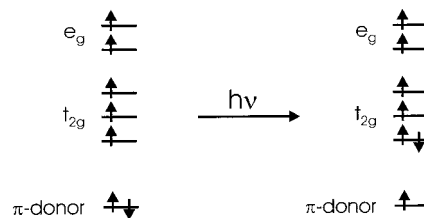


Figure 17. Frontier orbitals of important amino acid (i.e., endogenous) ligands in non-heme environments. (Reprinted with permission from ref 699. Copyright 1996 American Chemical Society.)

2. Excited-State Properties. From the weak-field side of the Tanabe–Sugano diagram in Figure 12 all LF transitions to excited states are spin-forbidden and, hence, have low intensities with ϵ below $1 \text{ M}^{-1} \text{ cm}^{-1}$. Table 6 shows typical LF excitation energies for high-spin complexes with $10Dq$ values comparable to the biological non-heme systems including different geometries. Note that the energies of the first excited states ${}^4\text{T}_{1g}$ and ${}^4\text{T}_{2g}$ are inversely proportional to the LF strength: when $10Dq$ is lowered, these states are raised in energy. Since the corresponding transitions appearing around $12\,000 \text{ cm}^{-1}$ have such low intensities, they cannot be observed in absorption in diluted protein solutions and it is difficult to make unequivocal assignments from MCD spectra.¹² Therefore, in contrast to Fe^{II} systems, the LF transitions are not useful as a probe of the electronic structure of high-spin Fe^{III} centers.

Due to the fact that the ferric ion has a high effective nuclear charge, the d-orbitals become substantially stabilized compared to Fe^{II} . Thus, ligand-to-metal CT (LMCT) transitions are much lower in

Scheme 1

energy and frequently fall in the visible region of the spectrum.⁶¹ These transitions are spin- and electric dipole-allowed and have large intensities of $\epsilon > 1000 \text{ M}^{-1} \text{ cm}^{-1}$. Figure 17 shows the valence orbitals of the most important endogenous ligands in non-heme iron proteins. All four amino acids have π -donor orbitals at high energy which interact with the iron t_{2g} functions, and this will lead to reasonably intense $\pi \rightarrow t_{2g}$ CT transitions as illustrated in Scheme 1. In case of histidine, for example, the corresponding CT absorption is observed at about 350 nm. Importantly,

the intensities of electronic transitions are directly related to the transition density of the molecular orbitals involved. Considering a transition between two orbitals with one being the bonding and the other being the antibonding combination of two fragment orbitals (for example, one fragment function could be a metal-d and the other one a ligand-donor orbital), the intensity of the corresponding absorption has its maximum when the interaction between the fragment orbitals is largest. This means both resulting bonding and antibonding functions have equal contributions of both fragments. Alternatively, if the interaction between the fragment orbitals is zero, the CT transition has zero intensity. Thus, the CT intensity is a probe of metal–ligand covalency. Evaluation of the corresponding absorptions is especially useful in a series of related compounds in order to determine relative covalencies.⁶² It is also possible to calculate the metal–ligand covalency by ab initio electronic structure methods (section II.A.3). Comparison with experimental data along a series of complexes can then be used for band assignments or, alternatively, to evaluate bonding descriptions. This is of special interest for the characterization of intermediates (section II.D).

VTVH MCD and Determination of CT Polarizations. As pointed out in section II.A.1, MCD spectroscopy in the LF region has developed into a major tool for the study of spectroscopically difficult mononuclear Fe^{II} sites. A similar utility has not been demonstrated for high-spin ferric sites mainly because the spin-forbidden LF bands are very weak in MCD spectra and do not correlate as strongly with the geometry of the site relative to the ferrous case. Attention is therefore focused on the information content of the spin-allowed CT transitions. Since the MCD spectrum is a signed quantity the technique is particularly powerful in resolving distinct electronic transitions under broad absorption envelopes. At LT the MCD spectra are dominated by the temperature-dependent C-term contribution. The variation of the C-term intensity for a given band as a function of the magnetic field and temperature for a sample of randomly oriented molecules with a general spin ground state *S* has recently been shown to be given by⁶⁵

$$\frac{I^{\text{MCD}}}{E} = \frac{\gamma}{4\pi S} \int \int \sum_i N_i \langle I_z \langle \mathbf{S}_i \rangle_i M_{xy} + I_y \langle \mathbf{S}_i \rangle_i M_{xz} + I_x \langle \mathbf{S}_i \rangle_i M_{yz} \rangle \sin \theta \, d\theta \, d\phi \quad (13)$$

Here, *E* is the photon energy and γ a collection of constants. The summation *i* is over all sublevels of the ground state with Boltzmann population *N_i* and spin expectation values $\langle \mathbf{S}_i \rangle_i$. The *I_s* are the direction cosines that describe the orientation of the applied magnetic field in the molecular coordinate system with the angles θ and ϕ . The *M_s* are effective transition dipole moment products that depend on the electronic structure of the complex and the particular transition studied (vide supra). Equation 13 is a convenient parametrization of MCD data because the Boltzmann populations and spin expectation values can be easily generated from a spin Hamiltonian (eq 11) which fits the EPR data, and

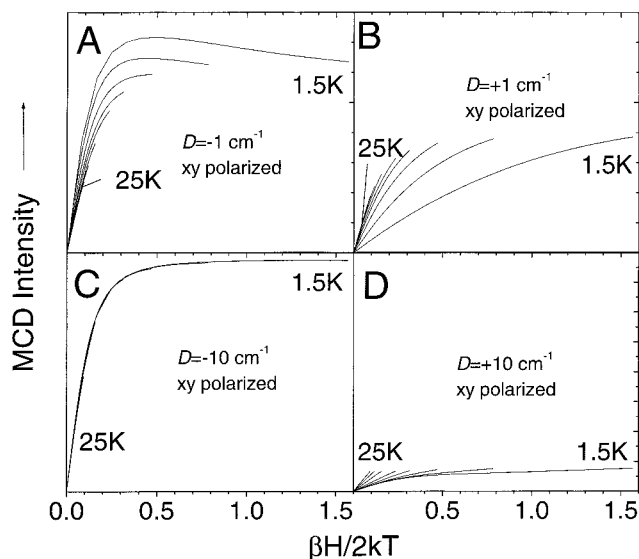


Figure 18. Dependence of the VTVH MCD behavior of a high-spin ferric center as a function of the sign and magnitude of *D*. (Adapted from ref 65.)

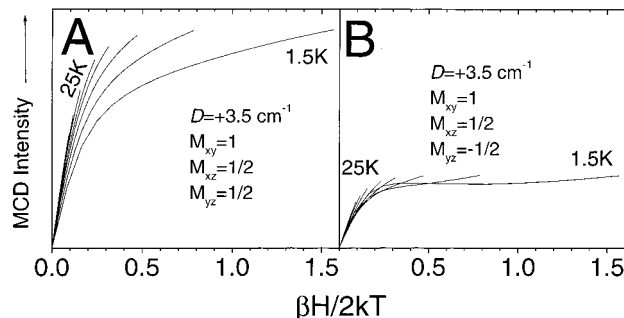


Figure 19. Dependence of the VTVH MCD behavior of a high-spin ferric center as a function of absorption band polarizations. (Adapted from ref 65.)

the only unknowns (fit parameters) are therefore the transition dipole moment products. Test calculations have shown that in the case of high-spin *d⁵* systems, the MCD C-term response is a weak function of *E/D*, a strong function of the sign of *D*, and only moderately sensitive to the absolute magnitude of *D* as illustrated in Figure 18.^{65,66} The transition dipole moment products that can be of either sign, however, strongly influence the MCD behavior and can give rise to an extremely complex pattern (an example is given in Figure 19). This will vary with the band being studied for a given ferric site, and this is also observed experimentally. This strong dependence allows one to obtain the polarizations of optical transitions in samples of randomly oriented molecules in frozen solutions. Therefore, VTVH MCD data fit by eq 13 can give insight into the assignment of the observed CT features, the properties of which are directly related to the specifics of metal–ligand bonding and thus to the chemical properties of the site. In the limit of large ZFS (relative to the Zeeman energy), eq 13 reduces in the linear regime to

$$\frac{I^{\text{MCD}}}{E} = \frac{\gamma}{4\pi S} \sum_d \alpha_d \frac{\beta H}{kT} \{ \tilde{g}_z^{(d)} M_{xy} + \tilde{g}_y^{(d)} M_{xz} + \tilde{g}_x^{(d)} M_{yz} \} \quad (14)$$

where α_d is the fractional population of the *d*th

Kramers doublet and $\tilde{g}_{x,y,z}^{(d)}$ are the known effective g -values of the d th Kramers doublet. Equation 14 shows that the effective g -value *perpendicular* to the plane of polarization of the transition determines the slope of the MCD magnetization curve in the linear limit. Similar equations have been used by several workers to obtain information about the ground-state spin Hamiltonian parameters.^{23,67} The microscopic interpretation of the transition dipole moment products requires a detailed analysis of SOC and when carried through allows prediction of \mathbf{C} -term signs that give further information about the electronic structure of the complex and aids in band assignments. There are three physically distinct mechanisms that contribute to \mathbf{C} -term intensity:^{65,68} (a) SOC of the ground state A to the excited state J that is studied, (b) SOC of the ground state with intermediate excited states K of the same spin, and (c) SOC of the excited state J with intermediate excited states K of the same spin. Mechanism a is generally weak. Since the CT states in high-spin ferric complexes are usually relatively high in energy (>15000 – 20000 cm^{-1}), mechanism c will usually dominate their MCD spectra. This mechanism leads to a sum rule that states that the SOC between states J and K gives rise to oppositely signed \mathbf{C} -terms for the transitions $A \rightarrow J$ and $A \rightarrow K$. Therefore, positively as well as negatively signed bands are expected and commonly the MCD spectra of high-spin ferric complexes show rich structure. For the interpretation of the effective polarization it is important that the underlying spin Hamiltonian is formulated in the principal axis system of the \mathbf{D} tensor such that the polarizations according to eqs 13 and 14 are expressed in this coordinate system. Experimentally, this coordinate system can, in principle, be obtained from single-crystal EPR measurements. However, because this information is usually not available, theoretical procedures have been devised that allow the determination of the D and ED values and the \mathbf{D} tensor orientation from semiempirical configuration interaction (CI) calculations.⁵⁶

Determination of Excited-State Distortions with Resonance Raman Spectroscopy. Absorption of a photon excites a molecule to a high-energy state, and the following geometric relaxation leads to a change of its structure which can be expressed by displacements along the different ground-state normal coordinates. Importantly, these displacements lead to vibrational progressions on absorption bands (i.e., the band shape) and the resonance Raman (rR) effect.⁶⁹ Therefore, rR is a powerful tool for determining structural changes in excited states relative to the ground state. Since in the case of solids or liquids absorption bands usually show little vibrational structure, rR is the best source of information about these structural distortions. To access the information contained in rR spectra, excitation profiles have to be recorded. The displacement of the excited-state energy surface along each normal mode is individually probed by measuring the relative intensity of the corresponding mode compared to an internal standard at different excitation energies in the region of absorption (for an example, see section II.D). Once

an absorption spectrum and the rR profiles for a compound are obtained, the time-dependent theory developed by Lee, Tannor, and Heller^{70–73} can be used to determine the excited-state distortions along the different normal modes. Compared to the time-independent formalism based on the quantum theoretical dispersion formula developed by Kramers, Heisenberg, and Dirac,^{74–77} Heller theory has the advantage of being much simpler to compute.

The formulation of the rR effect in the time domain is based on the overlap between a propagating (in time) wave packet in the displaced excited state which is created by the electronic excitation and the vibrational functions of the electronic ground state. The explicit multidimensional expression for the intensity of an electronic absorption can be written as⁷³

$$I^{\text{ABS}} \propto E_L \sum_j M_{0 \rightarrow j}^2 \int_{-\infty}^{+\infty} e^{i(E_L - E_0)t - \Gamma_j |t|/\hbar} \prod_p e^{-(1/2)(\Delta_p^j)^2 [1 - \exp(-i\omega_p t)]} dt \quad (15)$$

where E_L is the energy of the incident light, $M_{0 \rightarrow j}$ is the transition dipole moment, and E_{0j} is the energy of the pure electronic transition from $0 \rightarrow j$, Γ_j describes the homogeneous line width of this transition, Δ_p^j is the dimensionless displacement of normal coordinate p in the excited state j which is related to the Huang–Rhys parameter S_p^j by $S_p^j = 1/2(\Delta_p^j)^2$, and $\hbar\omega_p$ is the energy of the p th normal mode. The corresponding expression for the rR intensity of the fundamental transition ($0 \rightarrow 1$) in the k th normal mode is given by⁷³

$$I_k^{\text{rR}} \propto E_L E_S^3 \left| \sum_j M_{0 \rightarrow j}^4 \int_0^{+\infty} e^{i(E_L - E_0)t - \Gamma_j |t|/\hbar} (1/4 \Delta_k^j) \cdot (e^{i\omega_k t} - 1) \prod_p e^{-(1/2)(\Delta_p^j)^2 [1 - \exp(-i\omega_p t)]} dt \right|^2 \quad (16)$$

where E_S is the energy of the scattered light. Equations 15 and 16 depend on the approximations that all potentials are harmonic and the normal coordinates and their vibrational frequencies of the ground and the excited state are identical. The effect of small deviations should, in general, be negligible. Fitting the experimental data (absorption spectrum and rR profiles) simultaneously with eqs 15 and 16 allows the determination of the displacements Δ_p^j along each normal coordinate p in the excited state j . An example of the application of the Heller theory is given in Figure 20. Panel A shows the rR data of the complex $[\text{Fe}(\text{EDTA})(\text{O}_2)]^{3-}$ (which is evaluated in detail in section II.D.1) and panel B the absorption spectrum both along with their simultaneous fits using eqs 15 and 16.⁶⁰ With knowledge of the mass-weighted eigenvectors \vec{I}_p from a normal coordinate analysis (NCA), the actual displacement δ_i along an internal coordinate i (bond length, bond angle, or dihedral angle) in the excited state can be calculated from the dimensionless but signed parameter Δ_p^j with the equation

$$\delta_i = \sum_p \sqrt{\frac{\hbar v_p}{\lambda_p}} \cdot \vec{I}_{p,i} \cdot \Delta_p^j \quad (17)$$

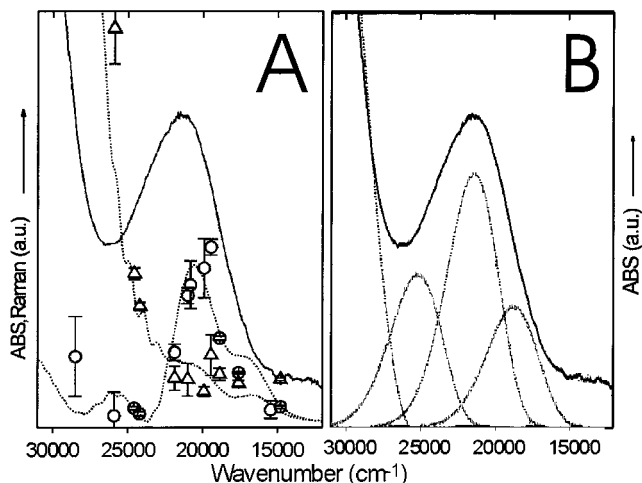


Figure 20. Simultaneous fit of rR profiles (panel A) and absorption spectra (panel B) with Heller theory^{70,71} using the example of $[\text{Fe}(\text{EDTA})(\text{O}_2)]^{3-}$. Circles: experimental resonance profile of $\nu(\text{OO})$; triangles: experimental profile of $\nu(\text{FeO})$. The dotted lines represent the fitted curves using the electronic absorption features indicated in (B). (Reprinted with permission from ref 60. Copyright 1998 American Chemical Society.)

with ν_p being the vibrational frequency and λ_p the eigenvalue of normal mode p from NCA. In this way, the geometry of the excited state relative to the ground state can be evaluated.⁷³ This derives from the change in electronic structure associated with the transition. Thus, rR probes the nature of the electronic transition responsible for the resonance enhancement.

b. Low-Spin Fe^{III} . 1. *Ground-State Properties.* EPR spectra of low-spin ferric complexes frequently show a rhombic pattern ($g_x \neq g_y \neq g_z$) with very large g shifts in the range ~ 1 –4. The theory for this behavior was first developed by Griffith and elaborated by others, mainly in the context of low-spin heme ferric sites.^{50,78–84} Griffith's model focuses on the three orbital components of the low-symmetry split ${}^2\text{T}_{2g}$ ground term (Tanabe–Sugano diagram; Figure 12, right) which undergoes in-state SOC that dominates the g shifts. An orthorhombic low-symmetry distortion will lift the degeneracy of the t_{2g} orbital set in a way that can be described by the two LF parameters V and Δ that are defined in Figure 7. A convenient relation between the g shifts, V , Δ , and the one-electron SOC constant ζ_{Fe} has been developed by Taylor.⁸¹ In this model the LF parameters are obtained from the g -values as

$$\frac{V}{\zeta_{\text{Fe}}} = \frac{g_x}{g_x + g_y} + \frac{g_y}{g_z - g_x}$$

$$\frac{\Delta}{\zeta_{\text{Fe}}} = \frac{g_x}{g_z + g_y} + \frac{g_z}{g_y - g_x} - \frac{1}{2} \frac{V}{\zeta_{\text{Fe}}} \quad (18)$$

Plots of Δ/ζ_{Fe} versus V/Δ have been used to characterize the axial ligands of low-spin ferric hemoproteins.^{83,85–88} Another use of these equations is to predict approximate energies for the positions of the first two LF bands that correspond to transitions within the low-symmetry split ${}^2\text{T}_{2g}$ ground term. A reason-

able estimate for the SOC constant of free Fe^{III} is about 460 cm^{-1} ,⁸⁹ which is reduced to 380 – 400 cm^{-1} in complexes by covalency effects. Another result of the theory is the relation $g_x^2 + g_y^2 + g_z^2 \leq 16$ that may be used to estimate the position of the third g -value if only two are experimentally observed and to quantify low-spin ferric EPR spectra.⁹⁰ However, $g_x^2 + g_y^2 + g_z^2 > 16$ sometimes occurs for reasons that remain to be elucidated. Note that in cases where the lowest Kramers doublet is close to being orbitally degenerate, the g -values can be both positive and negative (page 363 in ref 50 and ref 91); ambiguities about the signs of the g -values arise, and additional information is necessary to establish the LF parameters.^{81,83} There are less data available for low-spin non-heme ferric sites. A representative collection of heme and non-heme low-spin ferric g -values is given in Table 7 together with values for Δ/ζ_{Fe} and V/Δ . Many of the non-heme sites have significantly larger values for Δ/ζ_{Fe} than the heme systems, particularly the complexes with Schiff-base ligands and the non-heme peroxy complexes. Interestingly, activated BLM (ABLM) and its analogue $[\text{Fe}(\text{PMA})(\text{OOH})]^+$ show the smallest value for Δ/ζ_{Fe} among the alkyl- and hydroperoxide complexes. This behavior is a direct consequence of the unique electronic structure of activated bleomycin and will be discussed in section II.D.

Mössbauer Spectroscopy. Typical isomer shifts for low-spin Fe^{III} range from -0.2 to $+0.1 \text{ mm s}^{-1}$.^{29,30} In a perfect octahedron, the quadrupole splitting is zero because the hole in the t_{2g} shell is delocalized among all three corresponding d-orbitals. When the degeneracy of the d-functions is lifted (as required by the Jahn–Teller theorem), a quadrupole splitting occurs. In addition to the contributions already discussed for the high-spin case, there is also an electronic contribution since now the hole is localized, leading to an anisotropic distribution of d-electron density. Thus, quite large quadrupole splittings may appear for low-spin Fe^{III} relative to corresponding high-spin complexes. Similar to the high-spin case, Mössbauer spectroscopy in a magnetic field can be used to determine g -values (to complement EPR) and iron hyperfine parameters.

2. *Excited-State Properties.* The right-hand side of the Tanabe–Sugano diagram presented in Figure 12 gives the LF excited states of low-spin Fe^{III} , which has a ${}^2\text{T}_{2g}$ ground state in a strong octahedral LF. Since the first two excited states are quartets (${}^4\text{T}_{1g}$ and ${}^4\text{T}_{2g}$), the corresponding transitions are spin-forbidden and have low absorption intensities and, hence, should be difficult to detect, especially in dilute protein solutions. Since non-heme Fe^{III} low-spin systems have LF strengths very close to the spin-crossover region, the transitions to the quartet states should have energies very similar to those of Fe^{III} high-spin systems (vide supra). The lowest energy excited doublet states (${}^2\text{A}_{2g}$ and ${}^2\text{T}_{1g}$) corresponding to a $(t_{2g})^4(e_g)^1$ configuration give rise to spin-allowed transitions which appear above $25\,000 \text{ cm}^{-1}$. These absorptions can also be difficult to detect since complexes with strong π -donors have intense CT bands in this energy region, masking weaker transitions. In this case, MCD is the proper method to

Table 7. *g*-Values and Deduced Crystal-Field Parameters for a Representative Collection of Non-Heme and Heme Low-Spin Ferric Model Complexes and Active Sites

compound ^a	ligation	<i>g_z</i>	<i>g_y</i>	<i>g_x</i>	$\Delta/\zeta_{\text{Fe}}^b$	V/Δ^b	ref
Small Inorganic Complexes							
Fe(CN) ₆	6CN ⁻	2.35	2.10	0.91	1.34	1.23	92
Fe(phen) ₃	6N	2.69	2.69	1.51	1.28	2.00	93
Fe(bpy) ₂ (CN) ₂	4N, 2CN ⁻	2.63	2.63	1.42	1.22	2.00	94
Fe(cyclam) ₂ (N ₃) ₂	4N, 2N ₃ ⁻	2.40	2.31	1.91	3.84	1.33	95
Schiff-Base Ligands							
Fe[N ₄](Meim) ₂	[N ₄] ²⁻ (Meim) ₂	2.10	2.04	1.99	32.96	0.57	96
Fe[N ₂ O ₂](im) ₂	[N ₄] ²⁻ (im) ₂	2.40	2.10	1.94	12.93	0.38	97
[Fe(ADIT) ₂] ⁺	4N, 2S	2.19	2.13	2.01	12.56	0.97	98
[Fe(PyPep) ₂] ⁻	4N, 2S	2.22	2.14	1.98	9.64	0.97	99
Biomolecules							
FeBLM	5N, 1OH ⁻	2.41	2.18	1.90	6.49	0.71	100
nitrite hydratase	2S, 3N, 1O	2.28	2.14	1.97	10.18	0.72	101
Peroxo Complexes							
activated bleomycin	5N, 1OOH ⁻	2.26	2.17	1.94	6.65	1.08	100
[Fe(TPA)(OH ₂)(OO ^t Bu)] ²⁺	4N, 1O, 1OOR ⁻	2.19	2.14	1.98	8.82	1.20	102
[Fe(N4Py)(OOH)] ²⁺	5N, 1OOH ⁻	2.17	2.12	1.98	10.15	1.14	103
[Fe(PMA)(OO ^t Bu)] ⁺	5N, 1OOR ⁻	2.28	2.18	1.93	6.22	1.07	104
[Fe(L)(OOH)] ²⁺	5N, 1OOH ⁻	2.15	2.13	1.98	8.29	1.56	105
[Fe(L ²)(OOH)] ²⁺	5N, 1OOH ⁻	2.19	2.12	1.95	8.69	1.06	106
Heme Models							
Fe(TPP)(Ome) ₂	P, 2 ⁻ Ome	2.49	2.165	1.91	8.27	0.50	107
Fe(TPP)(imH) ₂	P, 2imH	2.92	2.30	1.56	3.24	0.61	108
Fe(TPP)(im) ₂	P, 2im	2.73	2.28	1.76	4.25	0.63	108
Heme Proteins							
myoglobin-CN ⁻	P, His, CN ⁻	3.45	1.89	0.93	3.30	0.27	109
myoglobin-OH ⁻	P, His, OH ⁻	2.61	2.19	1.82	5.85	0.53	110
myoglobin-N ₃ ⁻	P, His, N ₃ ⁻	2.80	2.25	1.75	4.70	0.52	110
myoglobin-SH ⁻	P, His, SH ⁻	2.56	2.24	1.84	5.03	0.69	109
Cyt <i>c</i> (horse heart, pD = 6.6)	Met, His	3.07	2.23	1.26	2.66	0.55	109
Cyt <i>c</i> (horse heart, pD = 11)	Lys, His	3.33	2.05	[1.13]	3.25	0.35	109
Cyt <i>P</i> ₄₅₀	P, Cys, 1O	2.41	2.26	1.93	5.15	0.99	111
Cyt <i>b</i> ₅	P, 2His	3.03	2.23	1.93	9.26	0.25	110
sulfite reductase	P, His, Cys	2.44	2.36	1.77	2.55	1.52	112

^a im = imidazole; imH = protonated form of imidazole; Meim = methylimidazole; [N₄]²⁻, [N₂O₂]²⁻ = macrocyclic Schiff-base ligands depicted in ref 113; P = porphyrin-type ligand; TPP = tetraphenylporphyrin; bpy = bipyridine; phen = phenanthroline; PyPep = *N*-2-mercaptophenyl-2'-pyridinecarboxamide; ADIT = 6-amino-2,3-dimethyl-4-azahex-3-ene-2-thiolato. ^b All *g*-values have been assumed positive in the calculation of Δ/ζ_{Fe} and Δ/V , and some of the complexes are not in a "proper" coordinate system in the sense discussed by Taylor in ref 81. For this reason, Fe(phen)₃ and Fe(bpy)₂(CN)₂ have $V/\Delta = 2$ instead of 0.

probe the LF excited states since they distinctly gain intensity compared to the CT absorptions in the MCD experiment.¹¹⁴ Moreover, CT transitions can be identified using rR spectroscopy since LF excited states are weaker in intensity and exhibit smaller structural distortions relative to the ground state and, therefore, do not give rise to significant resonance enhancement.

In low-symmetry environments, the degeneracy of the d-orbitals is lifted, leading to a splitting of the electronic states. The *t*_{2g} splittings can easily be probed with EPR spectroscopy (vide supra) and the corresponding parameters Δ (axial distortion) and V (rhombic distortion, Figure 7) can be determined. Moreover, an axial distortion also leads to a splitting of the *e*_g orbitals which is expressed with the parameter Δ_{eg} . Figure 21 illustrates the effect of Δ , V , and Δ_{eg} on the lowest-energy LF states. On the left side, part of the Tanabe–Sugano diagram (Figure 12) is reproduced, showing the term energies as a function of increasing $10Dq$. At the spin-crossover point, $10Dq$ is left constant (at 21 000 cm⁻¹) and the splittings of the terms induced by the parameters Δ , V , and Δ_{eg} are successively shown as indicated on the x-axis of Figure 21: first, Δ is introduced (range 0–3000 cm⁻¹),

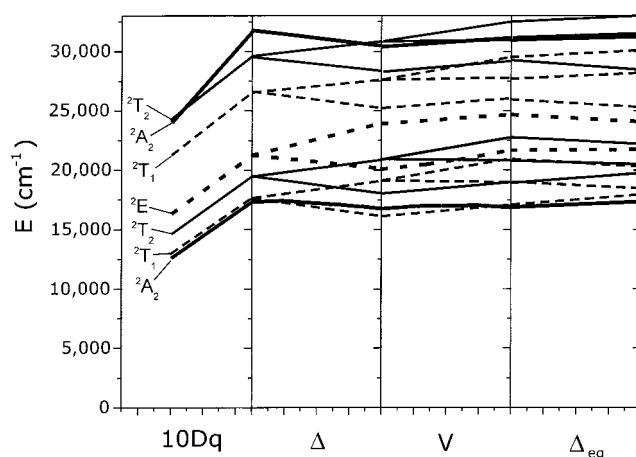
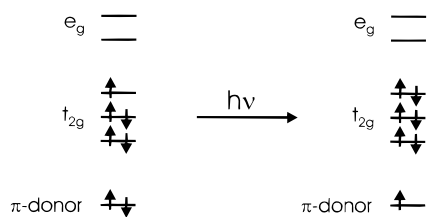


Figure 21. Energy splitting of the lowest-energy excited doublet states of a low-spin ferric center as a function of the parameters Δ , V , and Δ_{eg} (see text).

then V (at $\Delta = 3000$ cm⁻¹; range 0–2000 cm⁻¹), and finally Δ_{eg} (at $\Delta = 3000$ cm⁻¹; $V = 2000$ cm⁻¹; range 0–2000 cm⁻¹). Since V and Δ are independently fixed by EPR experiments (vide supra), the observed LF pattern is basically determined by the two fit parameters $10Dq$ and Δ_{eg} . Thus, provided that a number of

Scheme 2

LF excited states are observed, a complete experimental picture of the ferric d-orbital splittings can be obtained.

Since low-spin Fe^{III} has a ${}^2\text{T}_{2g}$ ground state corresponding to a $(t_{2g})^5$ configuration, CT transitions exciting one electron to the t_{2g} orbitals, as illustrated in Scheme 2, lead to a completely filled t_{2g} final state. In principle, these CT absorptions are similar to the high-spin case, as described above (Scheme 1), but there is now only one hole in the t_{2g} levels, meaning that the number of CT transitions into these orbitals is reduced. Only one intense absorption feature should appear. In low-symmetry environments where the orbital degeneracy of the ground state is lifted, the VTVH MCD data of these absorptions show typical $S = 1/2$ behavior. In contrast, CT excitation into the e_g orbitals lead to multiplets and thus a more complex absorption pattern. Since these transitions are higher in energy by $10Dq$ (about $20\,000\text{ cm}^{-1}$), they are well separated and do not complicate the analysis of the ligand $\pi \rightarrow t_{2g}$ CT transitions.

3. Quantum Chemical Calculations of Molecular Properties

For high-spin ferrous centers the d-manifold is well separated from the ligand valence orbitals. Thus, the covalency is low and energy splittings are well described by LF theory. For ferric sites, the higher effective nuclear charge (and spin polarization for the high-spin case) greatly lowers the energy of the d-manifold into the region of the ligand valence orbitals, leading to high covalency and requiring molecular orbital approaches to describe electronic structure.

Quantum chemical calculations are very useful for determining the electronic structure of molecules and their properties: bonding schemes, covalencies, geometries, vibrational frequencies, transition energies, and intensities as well as magnetic coupling parameters. Moreover, reaction mechanisms or structure/reactivity relationships can be evaluated by calculating transition states or complete reaction profiles.^{115–118} Once a quantum chemical method (a theoretical method combined with a basis set) has proven to be reliable for the calculation of specific properties, it can be applied to related systems where experimental data are limited. However, as should be stressed at this point, the comparison with experiment is absolutely necessary. This is especially important when extrapolations to reaction mechanisms are involved.

Many different quantum chemical methods are available for the calculation of transition-metal compounds. For ground-state properties such as geometries or vibrational frequencies, the various density functional methods (DFT) are most favorable since

Hartree–Fock (HF) calculations normally give a much too ionic bonding description, and on the other hand, the correlated methods such as CI or coupled cluster (CC) are still too time-consuming for large systems. Geometries with average errors in bond lengths of $\pm 0.05\text{ \AA}$ are obtained from calculations using gradient-corrected exchange and correlation functionals.^{116,119,120} For vibrational frequencies, Becke's three-parameter hybrid functional (B3) combined with a gradient-corrected correlation functional gives very good results.^{121,122} The calculation of transition energies is a more severe problem, which, in principle, requires the CI formalism. In this area, the semiempirical CI methods such as INDO/S-CI have proven to be very useful, giving good results at low time consumption.¹¹⁷ On the other hand, transition energies can be calculated with DFT using the Slater transition state¹²³ or time-dependent perturbation theory,¹²⁴ but these treatments are still restricted to single-determinantal wave functions and therefore cannot correctly be applied to multiplet problems such as LF transitions.

For reaction mechanisms and transition states where experimental data are often limited and calculations are the only source of information, it is of critical importance to make sure that the participating species are treated well by the chosen theoretical method. For the calculation of reaction energies, kinetic barriers, or thermodynamic properties, B3 combined with a gradient-corrected correlation functional has given good results.¹²² Compared to this, the other density functional methods are slightly inferior but have also been successfully applied to problems in transition-metal chemistry.

B. Substrate Activation

1. Lipoxygenases

Biochemical Characterization. Lipoxygenases (LOs, EC 1.13.11.12) are non-heme iron dioxygenases that catalyze the regio- and stereospecific hydroperoxidation of 1,4-*Z,Z*-pentadiene-containing polyunsaturated carboxylic acids (Table 1).^{125–129} LOs occur in all plants and animals and some lower organisms (alga, molds, and corals) but have not yet been found in bacteria or yeast.¹³⁰ LOs are usually classified according to their positional specificity for arachidonic acid, a major substrate of LOs in mammalian systems. 5-LOs are involved in the biosynthesis of leukotrienes and lipoxins which are mediators of anaphylactic and inflammatory disorders.¹²⁸ 5-LOs or their products may also be important for transcription regulation.¹³¹ 15-LOs initiate organelle degradation by pore formation in organelle membranes, which are important during differentiation of specific cell types such as reticulocytes.¹³² 12-LOs may play a role in tumor cell metastasis.¹³³ Therefore, specific inhibitors of various LOs would be important in the therapy of asthma and other inflammatory diseases which are aspirin-insensitive.^{134,135} An understanding of the structure of the LOs and the mechanism of the reaction they catalyze forms the basis for rational drug design.

The predominant substrates of LOs in plants are generally linoleic and linolenic acids. The products

Table 8. Experimental Enzyme Kinetic Parameters (Reprinted with permission from ref 143. Copyright 1998 American Chemical Society)

enzyme	k_{cat} (s^{-1})	K_{m} (mM)	$k_{\text{cat}}/K_{\text{m}}$ ($\text{s}^{-1} \text{mM}^{-1}$)	$(k_{\text{cat}}/K_{\text{m}})^{\text{H}}/(k_{\text{cat}}/K_{\text{m}})^{\text{D}}$	K_{i} (mM oleic acid)	ref
WT SLO-1	280 ± 8	11 ± 2	25 ± 5	48 ± 5	22 ± 2	144,145
WT 15-HLO	6.2 ± 0.1	7.8 ± 0.5	0.79 ± 0.06	59 ± 6	not determined	146
N694H SLO-1	10 ± 2	4 ± 1	2.5 ± 1.1	60 ± 9	8 ± 1	143

Table 9. Summary of Rate and Equilibrium Constants for Scheme 3 (Adapted from ref 151 and references therein)

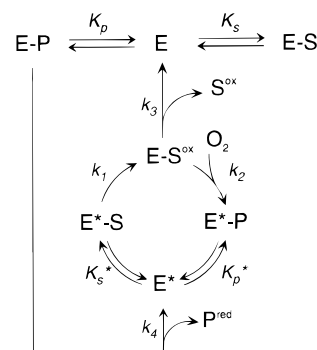
k_1 (s^{-1})	k_2 ($\text{M}^{-1} \text{s}^{-1}$)	k_3 (s^{-1})	k_4 (s^{-1})	K_{S} (μM)	K_{S^*} (μM)	K_{P} (μM)	K_{P^*} (μM)
200–350	$\sim 10^9$	2400	250	20	15–23	16	24

of the plant LOs are further metabolized by an array of enzymes to produce jasmonic acid and other plant hormones which are involved in plant growth and development, senescence, and responses to wounding and pathogen infection.¹²⁶ The three isozymes isolated from mature soybean seeds are designated as soybean LO-1 (SLO-1), SLO-2, and SLO-3.¹³⁶ They have different pH profiles for activity and different regiospecificity. Due to its abundance in soybean seed, ease of purification, and stability, SLO-1, a 15-LO, has been used in the majority of studies of LO kinetics and mechanism.

All LOs are monomers containing one iron atom. The plant LOs have a higher molecular weight (MW \approx 96 kDa) than their mammalian counterparts (MW \approx 75 kDa).¹²⁷ Sequence alignment of known LOs shows the conservation of a set of histidines which are clustered in a His(X)4His(X)4His(X)17His motif.¹³⁷ The highlighted histidines correspond to His499 and His504 in SLO-1 and His 361 and His366 in 15-rabbit LO (15-RLO) where the former have been identified as Fe^{II} ligands by site-directed mutagenesis.¹³⁸ Near the C-terminus, there is another highly conserved region which contains a His(X)3(His/Asn) motif. The first histidine is at position 690, followed by an asparagine at position 694 in SLO-1, and in 15-RLO they are His541 and His 545.^{139–141} This asparagine is conserved in all plant LOs with one exception, all mammalian 5-LOs, murine platelet 12-LO, and human platelet 12-LO, but is replaced by a histidine in the rest of mammalian 12-LOs and all mammalian 15-LOs.¹³⁷ The C-terminus is an isoleucine which is conserved among all LOs except rat leukocyte 5-LO, where it is replaced by a valine.¹⁴² The fact that the members of the LO family share high sequence homology around the iron-binding site indicates that SLO-1 may serve as a reference for the iron-binding site in all LOs.

Kinetics. Table 8 lists the k_{cat} and K_{m} from steady-state kinetic studies for SLO-1, 15-human LO (15-HLO), and N694H SLO-1, the latter being a mutant of SLO-1 where the Asn694 has been replaced by a histidine.¹⁴³ The k_{cat} for 15-HLO is significantly lower than that for SLO-1, and k_{cat} for N694H SLO-1 is an intermediate between the two.

Insight into the catalytic mechanism of LO mostly derives from detailed steady-state and pre-steady-state studies on SLO-1.^{147–152} These results are summarized in Scheme 3, and the associated kinetic parameters are listed in Table 9. As isolated, LO contains a single ferrous ion, which is stable under aerobic conditions. Treatment of Fe^{II} LO (E in Scheme

Scheme 3^a

^a Abbreviations: E and E*, Fe^{II} and Fe^{III} LO, respectively; S, substrate; P, product; S^{ox} and P^{red}, oxidized and reduced forms of S and P (radical compounds); K_{S} , K_{P} , K_{S^*} , and K_{P^*} , equilibrium dissociation constants of E-S, E-P, E*-S, and E*-P, respectively; k_1 , k_3 , and k_4 , monomolecular rate constants; k_2 , bimolecular rate constant (Reprinted with permission from ref 150. Copyright 1993 American Chemical Society.)

3) with hydroperoxide product, 13-(S)-hydroperoxy-9,11-(E,Z)-octadecadienoic acid (13-HPOD, P in Scheme 3), results in the oxidation (k_4) of Fe^{II} LO to Fe^{III} LO (E*). The E* catalyzes the first step of the reaction, namely, hydrogen-atom abstraction from S to form the radical S^{ox} (k_1). In the second reaction step, insertion of O₂ at C-1 or C-5 of the pentadiene system leads to the formation of P (k_2). Hydrogen abstraction is coupled to reduction of the Fe^{III} to Fe^{II} , while O₂ insertion is accompanied by its reoxidation to Fe^{III} . S and P compete for a single binding site on both Fe^{II} and Fe^{III} LO. Under anaerobic conditions, the radicals S^{ox} dissociate from the enzyme and dimerize (k_3). This model can explain the lag phase present in steady-state kinetic experiments with SLO-1. This is due to the fact that Fe^{II} LO does not react with substrate. However, the as-isolated enzyme contains a small amount of active ferric sites. Upon aerobic treatment with substrate, these few ferric sites generate the hydroperoxide product which then oxidizes the remaining ferrous to active ferric enzyme. Hence, the lag-phase is due to this initial build-up of active ferric enzyme.

The reaction of the ferric SLO-1 with the hydroperoxide product HPOD leads to a species with an absorption maximum at 580 nm (purple SLO-1) and a lifetime of several minutes at 4 °C. Although stopped-flow spectrophotometric experiments have been performed,¹⁴⁸ it is still a matter of discussion whether this purple species is directly involved in the catalytic cycle. This would require a reorientation of the fatty acid peroxy radical in order for the peroxy

oxygen to interact directly with the iron center, which is necessary for the occurrence of the 580 nm CT band. Alternatively, purple LO could be the dead-end enzyme-product complex.

The hydrogen abstraction rate constant k_1 in Scheme 3 has a large isotopic effect at the C-13 position of linoleic acid.^{144,153–155} A number of steps are partially rate-limiting at room temperature: substrate binding, a H₂O/D₂O-sensitive step, and C–H bond cleavage.¹⁴⁴ At lower temperatures, the solvent-sensitive step dominates the reaction, whereas at higher temperatures, the hydrogen abstraction step is rate-limiting. Most recently, this isotopic effect has been separated into the primary and secondary components using singly deuterated linoleic acid as the substrate.¹⁵⁶ These results have been interpreted in terms of a tunneling mechanism of hydrogen-atom transfer.^{144,156}

Structure. Crystal structures are available for the ferrous form of two of the SLOs. SLO-1 has been characterized by Boyington et al. at 2.6 Å resolution at room temperature (PDB ID: 2SBL)¹³⁹ and by Minor et al. at 1.4 Å resolution at 100 K (PDB ID: 1YGE).¹⁴⁰ Recently, the structure of SLO-3 has been obtained by Skrzypczak-Jankun et al. at room temperature at a resolution of 2.6 Å (PDB ID: 1LNH).¹⁵⁷ For mammalian LOs, one structure is available for the inhibited ferrous form of reticulocytic rabbit 15-LO (15-RLO) obtained by Gillmor et al. at 2.4 Å resolution at liquid N₂ temperature (PDB ID: 1LOX).¹⁴¹ In the following, the structures of SLO-1 and SLO-3 are discussed and then compared with that of 15-RLO.

The two structures of SLO-1, 2SBL and 1YGE, give a uniform description of the proteins' overall structure: its spatial shape is an ellipsoid of dimensions 90 × 65 × 60 Å with two domains. Domain I (146 amino acids) is an eight-stranded antiparallel β-barrel containing the N-terminus. Since it has been found that β-barrels are essential in proteins that bind to lipids,^{140,158} this part of the enzyme could be important for molecular recognition in catalysis and/or proteolysis.¹⁵⁷ Domain II (693 amino acids) is only loosely connected to Domain I and consists of a bundle of 20 (1YGE) or 23 (2SBL) helices, respectively. This domain contains the active site of the enzyme with one bound iron cofactor and the substrate-binding cavity.

The structure of the iron-binding site in SLO-1 is different in 2SBL and 1YGE. This could be related to the different conditions for crystallization or the effect of having a mixture of site structures on the refinement of the data (vide infra). There are also differences in the definition of an acceptable Fe^{II}–ligand bond length. In 2SBL, the iron atom is surrounded by three histidine ligands (His499, His504, and His690) bound with their ε-N and the C-terminal isoleucine (Ile839) bound with one carboxylate oxygen leading to a highly distorted octahedral coordination sphere with two open sites (Figure 22A). In addition, an asparagine (Asn694) occupies one of the open positions with its carbonyl oxygen but at a nonbonding distance of 3.2 Å. In 1YGE, an additional water ligand is found at 2.6 Å and the Asn694 is about 3.1

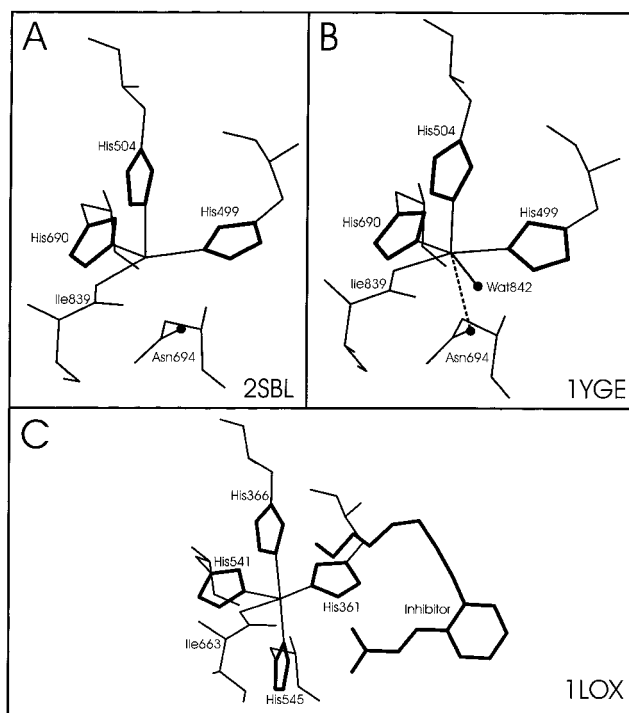


Figure 22. Structures of the active site of ferrous LO. Panel A: SLO-1 according to Boyington et al.¹³⁹ with a 4C iron site. Panel B: SLO-1 according to Minor et al.¹⁴⁰ The oxygen atoms of Asn694 (A, B) and a water molecule (B) are >2.5 Å away from iron. Panel C: 15-RLO according to Gillmor et al. with an inhibitor bound. (Structures were generated using the crystallographic coordinates from PDB files 2SBL, 1YGE, and 1LNH, respectively.)

Å away from the iron. This asparagine is therefore regarded as a weak ligand, resulting in a distorted octahedron with a 6C Fe^{II} site as shown in Figure 22B. The water molecule is stabilized by a hydrogen bond with the unbound carboxylate oxygen of Ile839. Both crystal structures show two possible channels for substrate access to the active center. The larger of these two cavities (II) is thought to be the fatty acid binding site.¹⁴⁰ It is bent by ~120° as it passes the water ligand of Fe^{II} with His499, His504, and Ile839 being directly adjacent to its interior. Asn694 and His690 have no direct contact, but Asn694 is connected to cavity II by a hydrogen-bonding chain including Gln697 and Gln495.

SLO-3 and SLO-1 share 72% sequence identity, and their overall structures are very similar; again, two domains are observed for 1LNH which have similar properties as those described for SLO-1. The iron binding site of SLO-3 consists of three histidines (His518, His523, and His709) and the carboxylate oxygen of the C-terminal Ile857. Another two potential ligands are Asn713 (pointing with the carbonyl oxygen to iron) and a water molecule both found at nonbonding distances of ~3 Å. Therefore, the Fe^{II} atom has a distorted octahedral coordination environment with two vacant positions which is intermediate between the two SLO-1 structures described above. Note that Asn713 and the water molecule can move to a bonding distance with iron without any disturbance of their environment. In SLO-3, three channels approaching the active site are found; two are very similar in shape to cavities I and II of SLO-

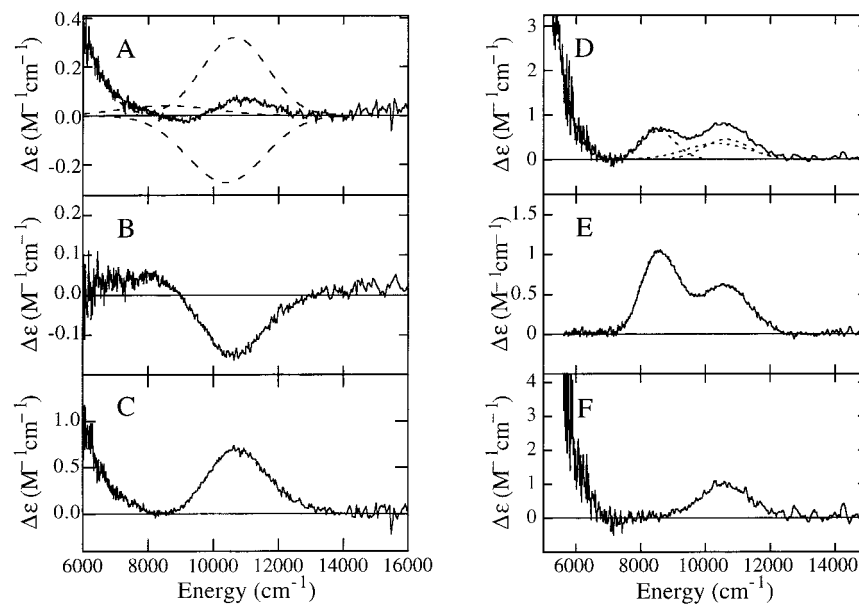


Figure 23. CD (277 K) and MCD (5 K, 7 T) spectra of SLO-1. (A) CD of resting SLO-1 with Gaussian components shown in dashed lines. (B) CD of SLO-1 in 50% (v/v) glycerol- d_3 ; (C) A - (0.6 \times C) and renormalized. (D) MCD of SLO-1 in saturated sucrose with Gaussian fitting components shown in dashed lines. (E) MCD of SLO-1 in 50% (v/v) glycerol- d . (F) Spectrum D - (0.6 \times E) and renormalized. (Reprinted with permission from ref 46. Copyright 1995 American Chemical Society.)

1, although some sequence differences occur. The additional cavity III and cavity II are believed to be involved in substrate delivery to the active site. This greater flexibility of substrate binding in SLO-3 could account for the different regio- and stereoselectivity of SLO-3¹⁵⁷ which produces 9- and 13-hydroperoxides (diastereomers), whereas SLO-1 gives predominantly the 13(*S*)-hydroperoxide.¹⁵⁹

Although the sequence identity between mammalian and plant LOs is only about 25%, the spatial shape of 15-RLO is very similar to soybean LOs but its overall structure is much more compact. 15-RLO consists of two domains: one small N-terminal β -barrel domain (115 amino acids) and the C-terminal domain (548 amino acids) which contains the active site and the substrate-binding cavities. The Fe^{II} atom is coordinated by four histidine ligands (His361, His366, and His541 with their ϵ -N atoms and His545 with its δ -N atom) and the C-terminal carboxylate oxygen of Ile663. Importantly, the asparagine ligand in the plant LOs is substituted by a histidine at a bonding distance of 2.3 Å (His545, Figure 22C). No water molecule is observed in the vacant sixth coordination position of the octahedral environment of iron. Importantly, the crystal structure 1LOX has an inhibitor bound blocking that position (Figure 22C), which allows identification of the substrate-binding pocket in 15-RLO. The orientation of this channel with respect to the active site is analogous to cavity II in SLO-1 and SLO-3.

Further insight into important substrate–amino acid residue interactions upon binding has been obtained by site-directed mutagenesis.¹⁴⁶ Mutagenesis has also been used to propose a model for the positional specificity of the mammalian 5-, 12-, and 15-LOs.¹⁴¹ In 1LOX, two amino acids with large residues have been identified on the bottom of the boot-shaped substrate-binding pocket: Ile418 and Met419. By substitution of these amino acids in 15-

LO with the corresponding residues of 12-LO, the former is endowed with 12-LO properties.¹⁶⁰ Therefore, positional specificity seems to be due to the volume of the binding site, especially the length of the cavity determining how deep the substrate penetrates into the pocket and, hence, which carbon atom is oriented toward the iron active site.¹⁴¹

Spectroscopy. There have been a limited number of spectroscopic studies aimed at defining the geometric and electronic structure of the ferrous site of SLO-1. Magnetic susceptibility measurements show that the ferrous active-site ground state is high-spin with $S = 2$.¹⁶¹ X-ray absorption¹⁶² and Mössbauer studies³⁷ predicted a distorted octahedral geometry; however, these studies now appear to have been complicated by solvent effects (vide infra). Figure 23A shows the near-IR CD spectrum of resting SLO-1.⁴⁶ There is a low-energy feature at $<5000\text{ cm}^{-1}$ and a second feature at $10\,700\text{ cm}^{-1}$ with a shoulder at $\sim 8000\text{ cm}^{-1}$. The near-IR MCD spectrum of resting SLO-1 is shown in Figure 23D and has three positive peaks at <5500 , 9200 , and $10\,500\text{ cm}^{-1}$. Since no LF geometry of a single high-spin ferrous site can give rise to more than two $d \rightarrow d$ transitions in the $4000\text{--}13000\text{ cm}^{-1}$ region (section II.A.1), resting SLO-1 must exist as a mixture of more than one form. Anaerobic addition of substrate linoleate or the addition of methanol, ethanol, ethylene glycol, or glycerol to resting SLO-1 produces a dramatic change in the near-IR CD spectrum, as shown in Figure 23B, and results in the LT MCD spectrum shown in Figure 23E. Simultaneous Gaussian fitting of the CD and MCD spectra indicates a positive band at 8600 cm^{-1} and a negative band at $10\,300\text{ cm}^{-1}$ in the CD spectrum and two positive bands in the MCD spectrum, which are consistent with a 6C ferrous site with distorted octahedral geometry. Subtraction of 60% of the 6C species signal intensity from the resting spectra and renormalization gives the CD and

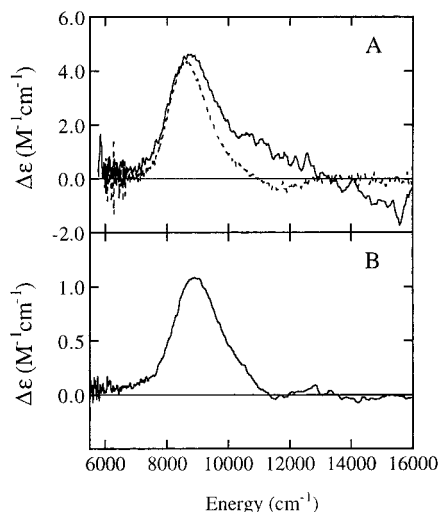


Figure 24. (A) Near-IR MCD spectra at 6 T and 4.2 K of resting 15-RLO in 20 mM sodium phosphate, pD 7.0 + 50%(v/v) glycerol- d_3 (dashed line ($\times 2$)) and near-IR MCD spectra at 7 T and 4.2 K of resting 15-HLO in 20 mM sodium phosphate, pD 7.0 + 50%(v/v) glycerol- d_3 . (B) Near-IR MCD spectra at 7 T and 5.0 K of resting N694H SLO-1 in 50 mM CHES, pD 9.0 + 50%(v/v) glycerol- d_3 . (Reprinted with permission from refs 46 and 143. Copyright 1995 and 1998 American Chemical Society.)

MCD spectra shown in Figure 23C and F, respectively. The spectra of this species, also present in resting SLO-1, have two positive $d \rightarrow d$ bands at ~ 5000 and $10\,600\text{ cm}^{-1}$ which are consistent with a 5C square-pyramidal geometry. Therefore, CD and MCD studies show that resting SLO-1 exists as an $\sim 40/60\%$ mixture of 5C and 6C species. The addition of monoprotic alcohols, polyprotic alcohols, or substrate linoleate to resting SLO-1 shifts the 5C-plus-6C mixture of resting SLO-1 to a purely 6C form.

CD and MCD studies on human recombinant 15-LO (15-HLO), rabbit reticulocyte 15-LO (15-RLO),⁴⁶ and N694H SLO-1¹⁴³ provide further information about the protein ligand responsible for this *coordination flexibility* at the Fe^{II} active site. In contrast to SLO-1, glycerol does not perturb the near-IR CD spectra of resting 15-HLO, 15-RLO, or N694H SLO-1. Their LT MCD spectra are shown in Figure 24. For 15-HLO and 15-RLO, a band at $\sim 8700\text{ cm}^{-1}$ with a shoulder at $\sim 10\,500\text{ cm}^{-1}$ indicates a 6C ferrous site. The similar MCD spectrum of N694H SLO-1 (band at $\sim 9000\text{ cm}^{-1}$ and shoulder at $\sim 11\,000\text{ cm}^{-1}$) is also consistent with a 6C ferrous site in the enzyme. Therefore, substitution of asparagine with histidine leads to a pure 6C Fe^{II} site in these mammalian LOs and N694H SLO-1.

VTVH MCD studies of resting SLO-1 (6C species) and N694H SLO-1 give almost the same ground-state properties (Figure 25A,B), which are very different to those of 15-HLO and 15-RLO (Figure 25C).^{46,143} The SLO-1 and N694H SLO-1 data show a much larger degree of nesting than that observed for 15-RLO. Analyses of these data give $\delta = 13\text{ cm}^{-1}$, $\tilde{g} = 8$ for the 6C species of SLO-1 and N694H SLO-1 and $\delta = 4\text{ cm}^{-1}$, $\tilde{g} = 9$ for 15-RLO. The δ values are consistent with the t_{2g} orbital splittings shown in the insets of Figure 25, and the difference can be attributed to a stronger histidine ligand in the mam-

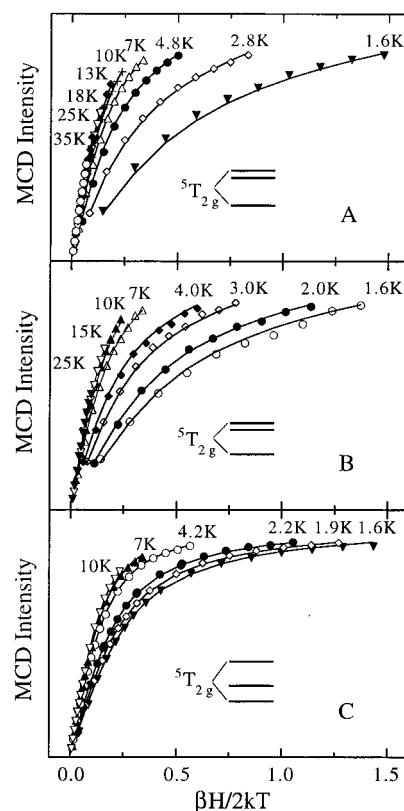


Figure 25. VTVH MCD data for (A) resting SLO-1 obtained for the 8600 cm^{-1} ; (B) resting N694H SLO-1 obtained at 9090 cm^{-1} ; (C) resting 15-RLO at 8600 cm^{-1} . The insets give the ${}^5T_{2g}$ ground-state splittings obtained from the saturation magnetization data. (Reprinted with permission from refs 46 and 143. Copyright 1995 and 1998 American Chemical Society.)

malian enzymes replacing the asparagine ligand in SLO-1 at the axial direction of the Fe^{II} site. However, this histidine in N694H SLO-1 is a weaker ligand than that in the mammalian enzymes, as shown by the larger nesting behavior of its VTVH MCD data, indicating that it is not in its most favorable conformation for binding to the Fe^{II} atom in SLO-1. This is likely due to its evolutionary optimization for asparagine. Fe K-edge XAS and extended X-ray absorption fine structure (EXAFS) studies of Fe^{II} SLO-1, 15-HLO, and 15-RLO in glycerol⁴⁶ and the solvent effect on Fe^{II} in SLO-1¹⁶³ are also consistent with the above results from CD and MCD studies.

Correlating the spectroscopic studies to the two crystal structures of SLO-1, the potential ligand that would show coordination flexibility is Asn694O δ 1, which is 3.2 \AA away in 2SBL and 3.1 \AA away in 1YGE from the Fe^{II} . Spectroscopically, both of these distances place Asn694O δ 1 too far from the ferrous ion to be a reasonable ligand. There is significant disorder in the distance between the side chain amide oxygen of Asn694 and the Fe^{II} ion in the crystal structure.¹⁴⁰ This would be consistent with the CD and MCD studies of resting SLO-1, which show that the enzyme exists as a mixture of 5C and 6C species. Substitution of the weak asparagine ligand by a stronger histidine ligand, as in mammalian 15-LOs and N694H SLO-1, would result in a pure 6C environment with histidine bound more strongly to the Fe^{II} ion. This is experimentally observed from the

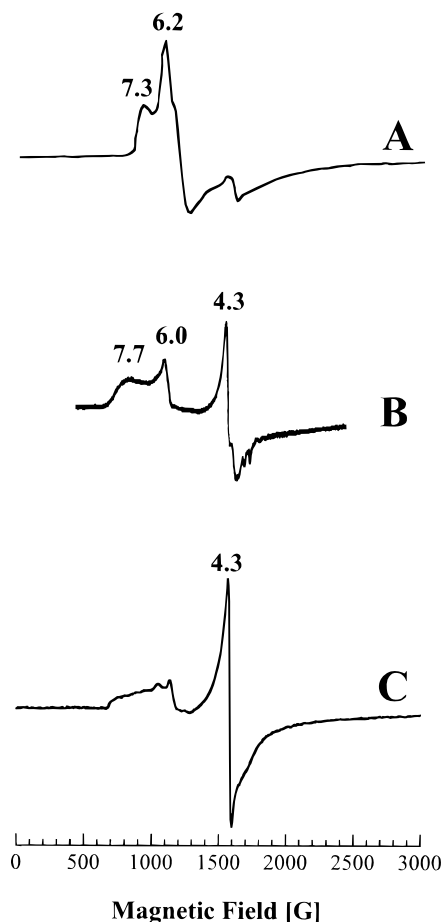


Figure 26. EPR spectra of ferric LO. (A) SLO-1; (B) N694H SLO-1 mutant; (C) 15-RLO. (Adapted from refs 12, 170, and 143.)

CD, MCD, and X-ray absorption results on 15-HLO, 15-RLO, and N694H SLO-1. The stronger Fe^{II} -His bond is also seen in the X-ray crystal structure of 15-RLO (vide supra).¹⁴¹ Finally, the side chain of Asn694 in SLO-1 is related to the substrate-binding cavity through a hydrogen-bonding network (vide supra). The binding of substrate or alcohols in this cavity could interrupt this network and result in a stronger interaction between the Asn694 amide oxygen and the Fe^{II} ion, thus shifting the 5C-plus-6C mixture to a pure 6C species.

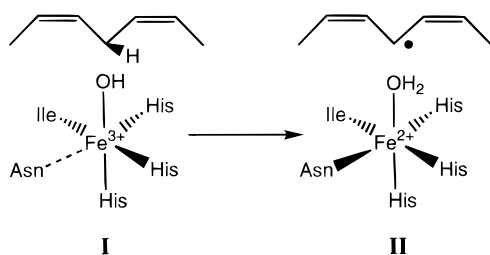
As developed in section II.A.2.a.1, the ground-state properties of Fe^{III} can be probed with EPR spectroscopy. Figure 26A shows the EPR spectrum of the ferric form of wild-type (WT) SLO-1 in sodium borate buffer at pH 9.¹² Signals at effective g -values of 7.33, 6.21, 5.84, and 4.28 are observed which determine the ferric ion to be in the high-spin state. This has also been shown by magnetic susceptibility¹⁶⁴ and Mössbauer spectroscopy.³⁷ Moreover, the occurrence of multiple EPR signals indicates the presence of more than one Fe^{III} high-spin species. For the more rhombic component ($\tilde{g} \approx 7.3$ – 7.5) a D value of $2 \pm 1 \text{ cm}^{-1}$ has been determined¹⁶⁵ with $E/D = 0.065$,¹⁶⁶ and the axial species ($\tilde{g} \approx 6.2$, 5.8) has been fitted with $D = 1.7 \pm 0.5 \text{ cm}^{-1}$ ^{12,165} and $E/D \approx 0.01$.^{12,166} In both cases, the $M_S = \pm 1/2$ doublet is lowest in energy ($D > 0$), giving rise to transitions with effective g -values as shown in Figure 14. The species at $\tilde{g} \approx 4.3$ has

been attributed to impurities.¹⁶⁷ The relative amount of the axial and the more rhombic component associated with the enzyme depends on the type and concentration of buffer, pH, purification, and storage time.¹⁶⁶ A freshly prepared sample of ferric WT SLO-1 in 0.2 M phosphate buffer at pH 6.8, for example, contains 93% of the more rhombic species. The fact that all EPR features have very large line widths has been taken as evidence that each observed signal itself could be associated with more than one species.¹⁶⁶ In summary, WT SLO-1 shows a complex EPR pattern with multiple contributions of iron centers with slightly different environments. Nevertheless, all signals are more or less axial, which is surprising for an iron center in a low-symmetry non-heme environment. In this case one would expect a rhombic signal due to the complete lifting of the degeneracy of the 4T_1 state. However, because the Asn694 ligand is very weak (Figure 16), the z component of 4T_1 is greatly separated in energy from the x and y components and D predominates over the rhombic splitting E . In addition, using ^{17}O -labeled water, it has been found from EPR spectroscopy that in WT SLO-1 at least one water-derived ligand is bound to the ferric site.¹⁶⁸ The ground-state properties of LO have also been probed with XAS/EXAFS,^{162,163,169} which indicates the existence of one short Fe–O bond in ferric SLO-1 (1.88 \AA)¹⁶³ that has been assigned to a coordinated hydroxide.

In the mammalian 15-LOs, the weak asparagine ligand is replaced by histidine, which should give rise to a stronger interaction with Fe^{III} . Figure 26C shows the corresponding EPR data of WT rabbit 15-RLO in 10 mM bis-Tris, 0.2 M NaCl buffer at pH 6.8.¹⁷⁰ The spectrum is dominated by a rhombic Fe^{III} species ($E/D = 0.32$, quantitated to about 80%) with signals at $\tilde{g} = 4.3$ and 9.5 (weak). In addition, small features around $\tilde{g} = 6$ – 7 are observed which account for about 20% of iron and are attributed to oxidized sites that also have product bound. For the rhombic species a $|D|$ value of about 1.0 cm^{-1} has been determined.¹⁷⁰ The fact that the iron site in WT 15-RLO has a rhombic EPR spectrum shows that histidine is also a stronger ligand than asparagine at the Fe^{III} oxidized state of the enzyme. Thus, all three components of the 4T_1 excited state are approximately equally split in energy.

The EPR spectrum of N694H SLO-1 in 100 mM borate, 0.2 M NaCl buffer at pH 9.2 is shown in Figure 26B.¹⁴³ Signals are found at effective g -values of 7.7, 6.0, and 4.3 which are fitted with axial ($\tilde{g} = 6$, D estimated to $\sim 2 \text{ cm}^{-1}$, $E/D = 0$), more rhombic ($\tilde{g} = 7.7$, $D = 2 \pm 1 \text{ cm}^{-1}$, $E/D = 0.08$), and rhombic ($\tilde{g} = 4.3$, $|D| = 1 \pm 0.2 \text{ cm}^{-1}$, $E/D = 0.33$) species. Quantitation of the EPR features shows that as in case of WT SLO-1, the signals close to the axial limit dominate (about 90% for the axial plus more rhombic components).¹⁴³ This indicates that the histidine in N694H SLO-1 is not as strong a ligand as in WT 15-RLO, which is in accordance with modeling studies¹⁷¹ and a crystal structure of the corresponding Fe^{II} form of this mutant^{157,172} showing that due to the orientation of the protein chain, His694 is at a distance of 2.8 \AA from iron, which indicates a weak interaction.

Scheme 4



In case of WT Fe^{III} SLO-1, weak LF transitions have been observed in the MCD spectrum¹² but their information content in terms of the coordination environment of iron is not as high as in case of Fe^{II} (vide supra). A prominent spectroscopic feature in ferric LOs is an absorption feature around 350 nm that is observed when ferrous enzyme is oxidized. This band is attributed to an imidazole (His) to Fe^{III} CT transition.¹² To resolve this transition from the protein envelope, UV-vis CD spectroscopy has been applied showing features at 425 (WT SLO-1) and 400 nm (N694H SLO-1).^{143,173} The energies of these CD bands reflect the ease of reduction of the iron center and thus provide a probe of the relative reduction potentials (E°) of the metals in both enzymes (vide infra).

Molecular Mechanism. As isolated, LO contains a single ferrous ion which is activated to ferric by the hydroperoxide product. The intermediate formed by the reaction of the ferric enzyme with substrate has not been characterized, although most of the researchers favor a mechanism of homolytic cleavage of the C–H bond to produce a substrate radical and a ferrous species.¹⁶⁹ Heterolytic cleavage of the C–H bond to produce a carbanion coordinated to the ferric center and a hybrid mechanism in which the formation of an organoiron complex follows the hydrogen-atom abstraction step have also been proposed.^{174–176}

This hydrogen-atom abstraction reaction is the key step of the LO mechanism and is shown in Scheme 4, where the ferric hydroxide species (I) abstracts a hydrogen atom from linoleic acid, generating the ferrous–water species (II) and the substrate radical which subsequently reacts with oxygen to form the hydroperoxide product. The driving force of the hydrogen-atom abstraction can be related to the strength of the OH bond produced in the abstraction intermediate (species II), which through a Born scheme is related to the reduction potential of the Fe^{III}/Fe^{II} couple (E°) and the pK_a of the abstracted proton in the ferrous species II.^{143,169,177} A high reduction potential and a high pK_a of the bound water in the reduced species II increases the hydrogen-atom abstraction driving force and thus the catalytic rate. The structural changes observed in the spectroscopies of SLO-1, 15-HLO/RLO, and N694H SLO-1 can strongly affect the reduction potentials and the pK_a 's of the reduced species II and hence k_{cat} . Increasing the donor ability of the varied axial ligand will reduce the effective nuclear charge on iron and thus the inductive effect on the coordinated water in species II and hence raise the pK_a . MCD studies on the pH dependence places a lower limit of the pK_a of the coordinated water in the ferrous species II of 11.5 in

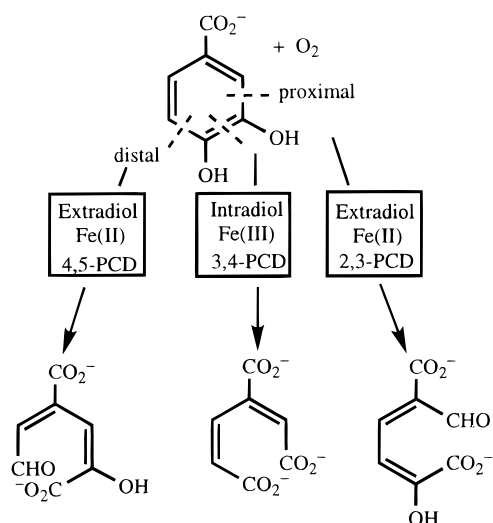
WT SLO-1. For N694H SLO-1 and 15-HLO, replacement of the asparagine with the stronger histidine ligand, which is a better donor, should raise the pK_a of the coordinated water in the ferrous species II even further, which would increase k_{cat} , opposite to what is observed (Table 8). Therefore, the reduction potentials of the three enzymes must overcome the pK_a change in determining the catalytic rate. Reducing the donor ability of the varied ligand on the iron should destabilize the oxidized site more than the reduced site and raise E° . The EPR studies show that the interaction of the axial Asn ligand with the ferric ion in WT SLO-1 is very weak as the signal is close to the axial limit. In contrast, interaction of the corresponding histidine ligand is strong in 15-RLO based on its rhombic Fe^{III} EPR signal. N694H SLO-1 has a 6C Fe^{III} site as determined from MCD spectroscopy. Nevertheless, the mutant has a weaker axial histidine interaction than the mammalian enzymes based on the larger nesting behavior of its VTVH data and its more axial EPR signal. Thus, one would expect that the ferric site in WT SLO-1 is easiest to reduce (highest E° , >600 mV)¹⁷⁸ and that 15-RLO has the lowest E° with N694H SLO-1 in between. The trend in E° can also be evaluated from the relative energies of the His-to-Fe^{III} CT bands in the CD spectrum. The LMCT band is found to be at higher energy for N694H SLO-1 (~400 nm (25 000 cm⁻¹)) as compared to WT SLO-1 (~425 nm (23 800 cm⁻¹)), signifying a shift to lower reduction potential (E°) for N694H SLO-1. This CT energy increase correlates to a ~100 mV change, which would decrease k_{cat} by a factor of ~50, consistent with the fact that $k_{cat} = 10 \text{ s}^{-1}$ for N694H SLO-1 is 28 times lower than that of WT SLO-1 ($k_{cat} = 280 \text{ s}^{-1}$). As expected, k_{cat} is smallest for the mammalian 15-LOs (k_{cat} for 15-HLO = 6.2 s⁻¹).¹⁴³ Recently, two ferric model complexes have been found to carry out similar hydrogen-atom abstraction chemistry.^{179,180}

The pentadienyl radical generated from the hydrogen abstraction step should react with dioxygen on the side of the substrate that is opposite to iron. A peroxy radical is formed which would oxidize the ferrous site back to the active ferric state and be reduced to the hydroperoxide product.¹⁷⁶ Under anaerobic conditions, the pentadienyl radical would diffuse out of the protein and dimerize as is observed.¹⁸¹

2. Intradiol Dioxygenases

Biochemical Characterization. Aromatic ring-cleaving dioxygenases occur predominantly in aerobic soil bacteria but are also found in vertebrates. These enzymes, which are important in the degradation of lignin, terpene, tannin, and xenobiotic pollutants in bacteria and in tryptophan and tyrosine catabolism in mammals, insert both atoms from dioxygen into the substrate aromatic ring leading to ring cleavage.^{182–185} This class of enzymes is divided into intra- and extradiol dioxygenases based on the position of ring cleavage, which correlates to the metal ion oxidation state as shown in Scheme 5. From sequence homology comparisons, the intra- and extradiol dioxygenases have evolved independently;^{186–188} however, there is at least one case where a slow substrate (3-chloro-

Scheme 5

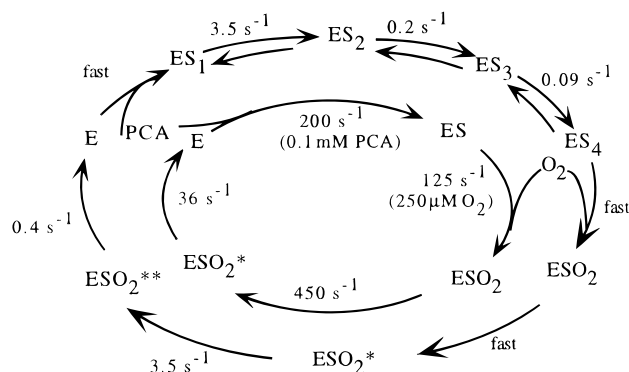


catechol) was cleaved by an intradiol dioxygenase in an extradiol fashion indicating that the redox state is not the sole determining factor in specificity.¹⁸⁹

Intradiol dioxygenases cleave a more limited set of aromatic substrates than do extradiol dioxygenases. The most well-studied intradiol dioxygenases are protocatechuate 3,4-dioxygenases (3,4-PCD, EC 1.13.11.3), which have been characterized by extensive crystallographic studies; catechol 1,2-dioxygenases (pyrocatechase; 1,2-CTD, EC 1.13.11.1); and chlorocatechol 1,2-dioxygenases (1,2-CCD, EC 1.13.11.1). These enzymes cleave catecholic substrates to produce muconic acid derivatives. The 3,4-PCD enzymes, found in divergent bacterial sources, usually consist of 4–12 $\alpha\beta\text{Fe}^{\text{III}}$ protomer units.^{188,190–193} The α - and β -subunits exhibit a high degree of sequence homology, including conserved iron-binding residues, and a range of molecular weights from 22 to 24 kDa for the α -subunit and from 25 to 40 kDa for the β -subunit. 1,2-CTD and 1,2-CCD (also referred to as Type I and Type II 1,2-CTDs, respectively) have two subunits, usually $\alpha_2\text{Fe}_2$, $\alpha_2\text{Fe}$, or occasionally $\alpha\beta\text{Fe}_2$, and have conserved active-site residues.^{192–194} 1,2-CCDs have evolved to cleave chlorinated catechol rings, a class of enzymes being studied for their potential use in bioremediation.^{195,196} The subunit molecular weights are 34–40 kDa for 1,2-CTDs and 27–30 kDa for 1,2-CCDs. Comparison of 3,4-PCD to 1,2-CTD and 1,2-CCD indicates that there is high sequence homology and likely a common ancestor for these intradiol dioxygenases.^{192,193,197}

Kinetics. Steady-state kinetics of 3,4-PCD reveals an ordered mechanism whereby substrate binding must precede O_2 reactivity (inner reaction cycle of Scheme 6).¹⁹⁰ 3,4-PCD preferentially cleaves 3,4-dihydroxyphenylacetate (protocatechuate, PCA), and the addition of a CH_2 or CH_2CH_2 group between the ring and the carboxylate of PCA (yielding homoprotocatechuate, HPCA, or dihydroxyphenylpropionate, DHPP, respectively) leads to a drop in the reaction rate to $<1\%$.¹⁹⁸ 3,4-PCD binds catechol very poorly, and turnover is at the limit of detection.^{191,199} Electron-donating groups on the substrate accelerate dioxygen attack (vide infra).¹⁹⁰ For 3,4-PCD from *Pseudomonas*

Scheme 6. Kinetics Scheme for 3,4-PCD (inner circle) and for Y447H 3,4-PCD (outer circle) (Reprinted with permission from ref 211. Copyright 1998 American Chemical Society)



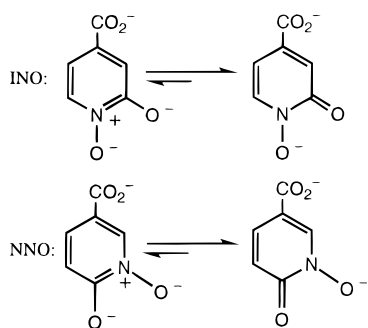
putida, $K_m(\text{O}_2)$ is 43 μM , $K_m(\text{PCA})$ is 30 μM , and k_{cat}/K_m for PCA is within 2 orders of magnitude of the diffusion-controlled limit.²⁰⁰ The reaction of the substrate-bound forms of 3,4-PCD and 1,2-CTD with dioxygen is dependent on the concentration of O_2 and was studied further using transient kinetics.^{190,201,202}

From stopped-flow studies, the reaction of the 3,4-PCD–PCA with dioxygen occurs with the formation of two intermediates, ESO_2 and ESO_2^* .^{190,198} ESO_2 forms and decays in milliseconds, and ESO_2^* forms with the same rate as the decay of ESO_2 . ESO_2^* decays slowly, at the turnover rate of the enzyme, indicating that it is the rate-determining step. Chemical quenching experiments suggest that it is the enzyme–product complex, making product release rate-determining ($\sim 36 \text{ s}^{-1}$).²⁰³ Two intermediates are also observed in the catalytic cycle of 1,2-CTD from *Pseudomonas arvilla* and exhibit some differences relative to 3,4-PCD.^{201,202}

The active site of 3,4-PCD contains an axial tyrosine that dissociates upon substrate binding, as indicated by X-ray crystallography (vide infra). Mutagenesis studies in which this axial tyrosine was replaced by histidine (Y447H) led to a stable and active mutant, which has provided additional mechanistic insight. Compared to the WT enzyme, $K_m(\text{O}_2)$ is lower ($<6 \mu\text{M}$), $K_m(\text{PCA})$ is 10-fold lower, k_{cat}/K_m for PCA decreases 45–50-fold, and the turnover number decreases by 600-fold at 25 °C.²⁰⁰ The substrate-binding step slows down significantly and becomes the rate-determining step. Several intermediates are observed in the substrate-binding process for Y447H (outer reaction cycle of Scheme 6).²⁰⁰ The absorption spectrum of the final substrate-bound form is nearly identical to that of the ES complex of the WT enzyme. It is believed that the WT enzyme also proceeds through at least some of these intermediates, which are not observed due to the fast binding of substrate to the WT enzyme. The substrate complex of Y447H reacts rapidly with O_2 and proceeds in a fashion similar to the native enzyme up to ESO_2^* formation.²⁰⁰ The decay of ESO_2^* is 100-fold slower and occurs in two phases.²⁰⁰ These intermediates may also occur in the WT enzyme but at rates too rapid for detection.

To gain further insight into the substrate-binding process, the potent inhibitors 2-hydroxyisonicotinic

Scheme 7



acid *N*-oxide (INO) and 6-hydroxynicotinic acid *N*-oxide (NNO) were studied (Scheme 7).^{204–206} These tautomeric inhibitors preferentially bind to 3,4-PCD in their ketonized form, i.e., with the hydroxyl CO group as a double bond.²⁰⁵ The reaction of dioxygen with the substrate ring is spin-forbidden, and it has been proposed that substrate ketonization, with some charge donation to the iron, would allow the dioxygen to attack the aromatic ring and cleave it in an intradiol fashion. If ketonization of the substrate occurs, then INO and NNO are excellent transition-state analogues. INO and NNO proceed through at least three enzyme-associated states before forming, essentially irreversibly, complexes with 3,4-PCD. EPR hyperfine broadening shows that Fe^{III}-bound water dissociates and then reassociates during these steps.²⁰⁴

Structure. There are numerous crystallographic results available for 3,4-PCD from *P. putida*. Structures of the substrate-, inhibitor-, transition-state analog-, and small molecule-bound forms have been instrumental in elucidating potential structures for the intermediates of the intradiol dioxygenases. The crystal structure of 3,4-PCD at 2.15 Å resolution indicates that the enzyme is highly symmetric with numerous 2- and 3-fold axes. There is a narrow solvent-filled channel through the 3-fold axes at the interface of the two subunits that leads to the solvent binding site on the iron and allows for solvent

exchange. A solvent-filled pocket adjacent to the active site appears ready to orient the plane of the incoming substrate to coordinate along the axial direction. The active site occurs at the subunit interface; however, all of the ligands originate from the β -subunit. 3,4-PCD has a 5C distorted trigonal-bipyramidal active site with Tyr447 and His462 coordinated in the axial positions, and His460, Tyr408, and water (i.e., hydroxide) are coordinated in the equatorial plane (Figure 27A).^{207,208} The largest distortion from trigonal bipyramidal is in the equatorial plane: the angle between the equatorial Tyr408 and His460 is reduced from 120° to ~93°, while the angle between this histidine and OH⁻ is ~141°.

To understand the substrate-binding steps, a series of coordinated inhibitors and substrates were structurally characterized. It is believed that the substrate may bind initially to 3,4-PCD in a monodentate fashion before forming the stable bidentate complex (vide infra). The crystal structure of the enzyme complex with the low-affinity monodentate inhibitor, 3-iodo-4-hydroxybenzoate (IHB), indicates that the inhibitor replaces the equatorial OH⁻, forming a 5C complex (Figure 27B).²⁰⁹ In contrast, the high-affinity monodentate inhibitor, 3-fluoro-4-hydroxybenzoate (FHB), binds associatively in the equatorial plane forming a 6C complex (Figure 27C).²⁰⁹ These differences in geometry have been proposed to be due to different hydrogen-bonding interactions in the active site.²⁰⁹

The crystal structure of the PCA complex of 3,4-PCD shows that the substrate binds to the iron in a bidentate fashion, replacing the axial Tyr447 and the equatorial OH⁻ (Figure 27D).²⁰⁶ The plane of the PCA ring is rotated ~18° relative to the plane of the FHB inhibitor. The site becomes square pyramidal with the open position trans to His460. Tyr447 rotates ~100° and is stabilized by hydrogen bonding to nearby Tyr16 and Asp413. There are a number of conserved residues in the substrate-binding pocket thought to be important in stabilizing the substrate.²⁰⁶ The plane of the substrate is aligned in the

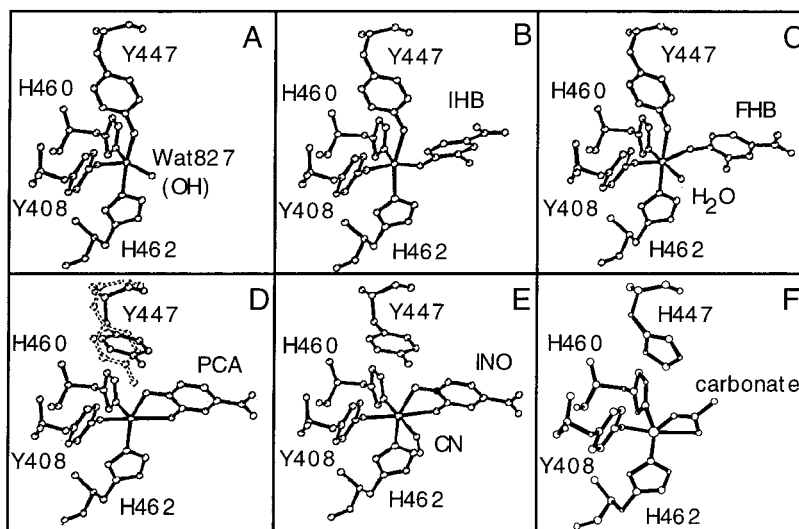


Figure 27. Active-site X-ray crystallographic structures of (A) 3,4-PCD, (B) 3,4-PCD–IHB, (C) 3,4-PCD–FHB, (D) 3,4-PCD–PCA, (E) 3,4-PCD–INO–CN, and (F) Y447H 3,4-PCD. (Structures were generated using crystallographic coordinates from PDB files 2PCD, 3PCI, 3PCF, 3PCA, 3PCL, 3PCD, respectively. Adapted from ref 211.)

pocket by hydrophobic residues: Gly14, Pro15, Trp449, and Ile491. Two of these, Pro15 and Ile491, are reported to prevent the formation of a planar five-membered chelate, perhaps stabilizing the asymmetrically bound substrate (vide infra).²⁰⁶ The substrate has hydrogen bonds from the carboxylate to Tyr324 and from the O3 to Arg457. There is a spherical cavity adjacent to the substrate and the iron with the rotated Tyr447 forming the top. If dioxygen enters this cavity, it could align along the substrate bond to be cleaved.

The slowly metabolized substrate HPCA has been an important replacement for PCA in many of the spectroscopic studies. The X-ray crystallographic structure of HPCA bound to 3,4-PCD shows that, like PCA, it forms a 5C complex.²¹⁰ The two possible orientations of HPCA (via the O3 or O4 of the substrate trans to Tyr408) could not be resolved in the 2.4 Å resolution crystal structure, but rR studies show that both PCA and HPCA align in a similar manner in the active site.²¹⁰ Both substrates bind asymmetrically, with the longer bond (~0.3 Å longer) trans to the equatorial Tyr408. This bonding difference is thought to be due to the stronger trans effect of Tyr408 relative to His462.

The asymmetry in substrate–iron bonds, which has been proposed to be due to ketonization, was explored with the substrate analogues, INO and NNO. These analogues bind to the active site of 3,4-PCD in a bidentate fashion and retain the bound solvent forming a 6C site.²⁰⁶ The rings of INO and PCA overlay in the active site. INO is also bound asymmetrically with the long bond (2.43 Å) trans to the equatorial tyrosine and with the short bond (2.01 Å) trans to His462. The retention of the bound solvent has been suggested to be required to maintain the charge neutrality of the active site, a theme which is emerging as an important attribute of the intradiol dioxygenases.^{48,211}

To model the dioxygen intermediate, the structure of the CN⁻ complex of 3,4-PCD–INO was determined.²⁰⁶ CN⁻ replaces the bound water, and the Fe–CN angle is quite bent (145°) compared to the usual preferred linear binding mode. This appears to be due to the constraints of the active-site cavity whereby the distal end of the CN⁻ is hydrogen-bonded to Tyr16 and water (Figure 27E).²⁰⁶ This bent structure weakens the Fe–CN bond based on the lack of hyperfine coupling from ¹³CN.²¹¹ Assuming the geometry of CN⁻ binding is a good model for that of O₂ binding, preference for adopting a bent angle for small molecules would be expected to aid the reaction with dioxygen proposed to proceed via an Fe–O–O–PCA peroxy intermediate (vide infra).²¹¹

The 3,4-PCD Y447H mutant, important in elucidating additional kinetic steps, has also been crystallographically characterized (Figure 27F).²⁰⁰ The axial His447 does not bind to the iron center and appears to be replaced by (H)CO₃⁻. Since substrate replaces Y447 and hydroxide in the WT enzyme and in the Y447H mutant these positions are substituted with a bidentate carbonate, the kinetics of substrate binding should be changed as discussed above. Whether the additional kinetic steps observed for the

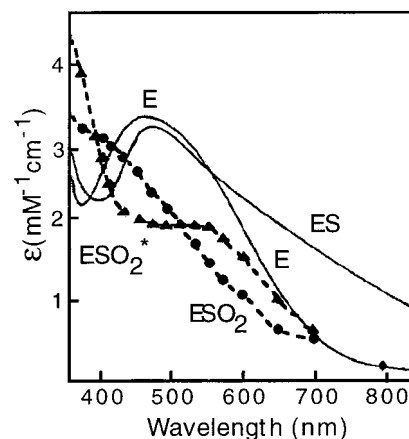


Figure 28. UV–vis spectra of 3,4-PCD, 3,4-PCD–PCA, and the two intermediates, labeled E, ES, ESO₂, and ESO₂*, respectively. (Reprinted with permission from ref 190. Copyright 1981 American Society for Biochemistry and Molecular Biology.)

Y447H mutant occur in the WT enzyme remains to be evaluated.

There are currently no crystal structures of 1,2-CTD enzymes, but comparison of their sequences with those of the crystallographically characterized 3,4-PCDs provides insight into substrate specificity. Tyr324, which hydrogen bonds to the carboxylate of PCA, is replaced by phenylalanine or tryptophan in most 1,2-CTDs. The positively charged residues Arg133, Lys325, and Arg450 are replaced by acidic residues in most 1,2-CTDs. These substitutions suggest that Types I and II 1,2-CTDs would have increased affinity for hydrophobic substrates.¹⁸⁵ The residues of the putative O₂ binding cavity (Gly14, Pro15, Tyr16, Trp400, Tyr447) are conserved in all 3,4-PCDs and related enzymes, although in some 1,2-CTDs Tyr16 is replaced by leucine.

Spectroscopy. Spectroscopy was important in identifying the active-site ligands prior to crystallography.^{191,205,212–216} Now spectroscopic data can be used in conjunction with crystallography to obtain geometric and electronic structure insight into the reaction mechanism. 3,4-PCD from *Brevibacterium fuscum* was used for most of these spectroscopic studies. 3,4-PCD has a very sharp rhombic ($|E/D| = 0.33$) $S = 5/2$ EPR signal at $g = 4.3$ and a much weaker signal at $g = 9.67$.²¹⁷ From the temperature dependence of the $g = 4.3$ EPR signal, $|D|$ is 1.6 cm⁻¹ for 3,4-PCD from *P. putida* and 1.2 cm⁻¹ for 3,4-PCD from *B. fuscum*.^{199,217,218}

3,4-PCD has a distinctive burgundy color ($\lambda_{\text{max}} = 460$ nm, $\epsilon = 2.9\text{--}3.2$ mM⁻¹ cm⁻¹ Fe⁻¹)¹⁹¹ characteristic of tyrosine-to-Fe^{III} CT transitions (Figure 28). The Raman spectra taken in resonance with this band show features characteristic of the two tyrosine ligands: ν_{CO} of 1254 and 1266 cm⁻¹ and δ_{CH} of 1172 and 1180 cm⁻¹ (Figure 29, inset).²¹² rR profiles show that the two ν_{CO} and two δ_{CH} features have different enhancement profiles (Figure 29). The higher frequency modes (1266 and 1180 cm⁻¹) show a maximum enhancement near 500 nm (20 000 cm⁻¹), while the lower frequency modes (1254 and 1172 cm⁻¹) show a maximum enhancement near 450 nm (25 000 cm⁻¹). The higher frequency Raman modes show an

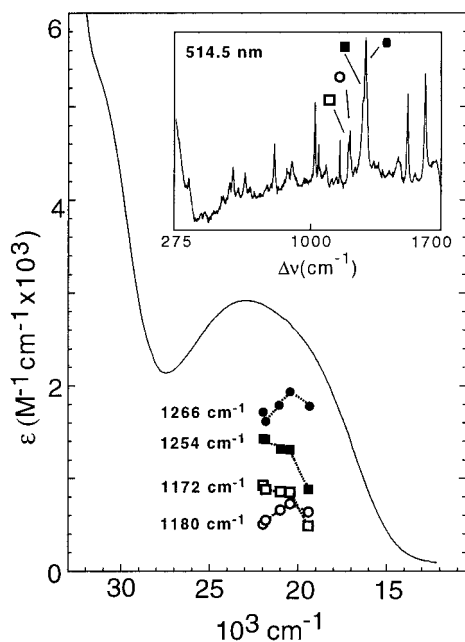
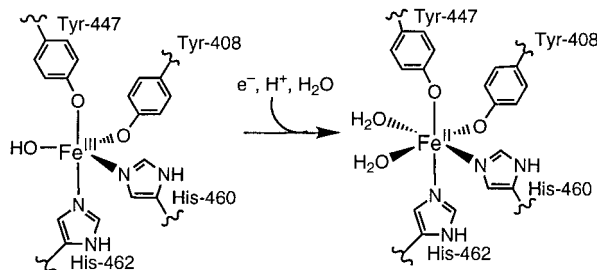


Figure 29. rR profiles of axial δ_{CH} (○), axial ν_{CO} (●), equatorial δ_{CH} (□), and equatorial ν_{CO} (■) for 3,4-PCD overlaid on the absorption spectrum using excitation at 514.5 nm with the four profiled peaks labeled. (Reprinted with permission from ref 212. Copyright 1992 American Chemical Society.)

isotope shift upon replacement of H_2O with D_2O and by addition of exogenous ligands. The 500 nm band is assigned to a LMCT transition from the axial tyrosine since this residue is more solvent-accessible, consistent with X-ray crystallography.^{207,208,212} This assignment of the 500 and 450 nm LMCT transitions as arising from the axial and equatorial tyrosines, respectively, has recently been confirmed using a combination of absorption, CD and MCD spectroscopies, and theoretical calculations.²¹⁹

Utilizing the high-spin Fe^{III} VTVH MCD and ZFS methodologies recently developed (section II.A.2),^{56,65} a detailed understanding of the geometric and electronic structure of the active site is emerging and should provide insight into the nature of Fe^{III} –tyrosinate bonding and dioxygenase reactivity.²¹⁹ The valence orbitals of a phenolate are the three oxygen 2p orbitals. One does not significantly participate in bonding to the iron because it is involved in the C–O σ -bond and is therefore at much lower energy. The other two O valence orbitals, which are perpendicular to the C–O bond, the in-plane (π_{ip}) and out-of-plane (π_{op}) oxygen p-orbitals, are split in energy due to the differences in conjugation into the ring (Figure 17). The π_{op} is at slightly higher energy than the π_{ip} orbital for a free phenolate. For Fe^{III} in a trigonal-bipyramidal LF, the d-orbitals split in energy with $d_z^2 > d_{x^2-y^2}, d_{xy} > d_{yz}, d_{xz}$ with the degenerate orbitals further split in the low-symmetry protein site. The donor interaction of the phenolate with the ferric site is determined by the overlap of the π_{ip} and π_{op} orbitals with these d-orbitals and will depend on the Fe–O–C_{tyr} angle and the Fe–O–C–C_{tyr} dihedral angle. From protein crystallography, Fe–O–C_{tyr axial} $\approx 148^\circ$ and Fe–O–C_{tyr equatorial} $\approx 133^\circ$ and both of the dihedral angles are $\sim 24\text{--}26^\circ$. Thus, the π_{ip} and π_{op} orbitals will be involved in both σ - and π -donor

Scheme 8. Reduction Scheme for 3,4-PCD
(Reprinted with permission from ref 48. Copyright 1999 American Chemical Society)



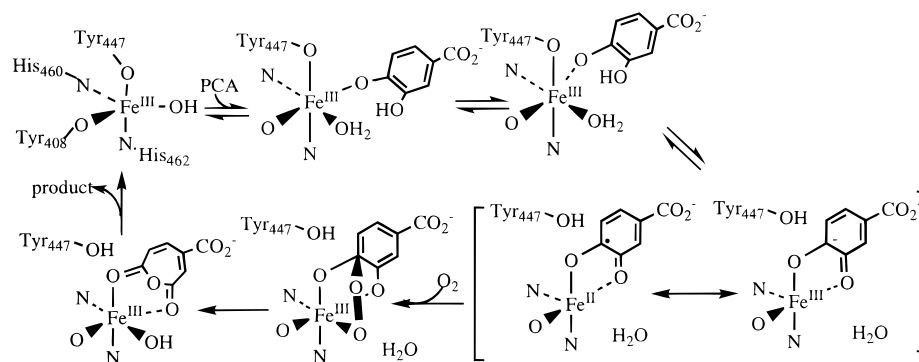
interactions with more than one d-orbital. Elucidating details of these bonds now requires quantitative correlation of spectroscopy and electronic calculations.²¹⁹

In addition to the two tyrosinates, the two coordinated histidines and bound solvent can be observed spectroscopically. The Fourier-transformed EXAFS data show a prominent outer-shell peak at 3.3 Å, indicative of histidine ligation. Solvent ligation was implied by EPR hyperfine line-broadening with H_2^{17}O and by relaxation in the ^1H NMR.^{205,214,216} Two separate EXAFS studies indicated three ligands at 1.88–1.90 Å and two at 2.08–2.10 Å.^{48,215} The three short ligands were assigned to the two phenolates and the solvent and the longer bonds to the two histidines. The short bond length of the solvent is most consistent with the solvent being deprotonated (i.e., OH^-) and hence a neutral active site. 1,2-CCD and hydroxyquinol 1,2-dioxygenase (1,2-HQD) were both found to be 5C and similar to 3,4-PCD by XAS.²²⁰

Chemical reduction of 3,4-PCD produces a high-spin ferrous center. LF CD and MCD spectra indicate that the site is 6C with an excited-state $^5\text{E}_g$ splitting of 2033 cm^{-1} .⁴⁸ XAS pre-edge intensity distribution and splitting pattern also indicate that the site increases in coordination number upon reduction.⁴⁸ A model for the reduced site was proposed, where an additional solvent coordinates and at least one of the ligands (i.e., hydroxide) becomes protonated, suggesting that the retention of charge neutrality and dynamic changes in the active site are important features of this enzyme class (Scheme 8). Protonation of one of the ligands and an increase in coordination number upon reduction is also observed for the other mononuclear enzyme involved in substrate activation, LO (section II.B.1). In both enzymes the active-site hydroxide presumably protonates upon reduction, decreasing its ligand donor strength, which is compensated for by the increase in coordination number.

Upon anaerobic substrate binding to ferric 3,4-PCD, a new broad low-energy feature appears at $\sim 600\text{ nm}$ (Figure 28) and there are changes in the high-energy region, as seen in the UV–vis absorption, CD, and MCD studies.¹⁹⁰ Raman excitation into the new low-energy band indicates that it arises from catecholate-to-iron CT.²¹⁰ rR spectra of 3,4-PCD–HPCA taken at 514 and 580 nm show new features at 544, 560, 640, 1320, and 1470 cm^{-1} which have been shown to be indicative of chelated Fe^{III} –

Scheme 9



catecholate.^{221–224} EPR, Mössbauer, and XAS spectroscopies indicate that the 5C substrate-bound site has become more axial but remains ferric.^{199,215,218} The 3,4-PCD–PCA complex is very heterogeneous and consists of species with $|E/D|$ ranging from 0 to 0.33 with $|D| \geq 1 \text{ cm}^{-1}$.^{199,218} The complex with HPCA is much more homogeneous, with 90% of the sample consisting of a species with $|E/D| = 0.33$ and 5% consisting of a species with $|E/D| = 0.02$. Proton NMR spectra of 4-methylcatechol bound to 3,4-PCD and 1,2-CTD exhibit large downfield shifts of the methyl resonances to 50 and 100 ppm, respectively. This indicates a large amount of spin delocalization into the ring.^{225,226} The difference in the ¹H NMR shift of the substrate resonances for the two enzymes, 3,4-PCD and 1,2-CTD, has been attributed to monodentate binding of substrate to 1,2-CTD and needs further study.^{225,226} XAS of 1,2-CCD and 1,2-HQD substrate-bound complexes showed that they too remain 5C upon substrate binding.²²⁰

The intermediate ESO₂ is characterized by a bleached optical spectrum ($\lambda_{\text{max}} = 400 \text{ nm}$), while the product complex ESO₂* is purple ($\lambda_{\text{max}} = 540 \text{ nm}$) (Figure 28).¹⁹⁰ The absorption spectrum of the complex with INO resembles that of ESO₂ and not ES. Small-molecule binding studies were used to gain spectroscopic insight into the intermediate and to correlate with the mechanistic order observed in the kinetics. Chemically reduced 3,4-PCD binds NO to form an $S = 3/2$ species. The EPR spectrum of 3,4-PCD–NO is the same as that of 3,4-PCD–NO–PCA (where NO is added before PCA) but is different from 3,4-PCD–PCA–NO (where PCA is added before NO).²²⁷ This indicates that substrate does not bind to the site once NO is bound. There is much larger rhombicity in 3,4-PCD–PCA–NO than in 3,4-PCD–NO ($|E/D| = 0.055$, D not determined for 3,4-PCD–NO; $|E/D| = 0.175$, $D = +3\text{--}5 \text{ cm}^{-1}$ for 3,4-PCD–PCA–NO). In the 3,4-PCD–PCA–NO complex, EPR hyperfine broadening is observed when the substrate C4 hydroxyl group is labeled but not when the label is at the C3 position, indicating that the substrate may be bound in a monodentate fashion in the NO complex.²²⁷ Whether this change from the chelated substrate complex observed in the crystallography (Figure 27D) to the monodentate substrate observed in the presence of NO is mechanistically relevant remains to be evaluated.

Molecular Mechanism. The reaction of the intradiol dioxygenases shows a sequential order, with

substrate binding before dioxygen. The range of conformations seen for inhibitors and substrates, the series of steps observed in the Y447H mutant, and the heterogeneity of rapidly frozen 3,4-PCD–PCA samples has led to the proposal that 3,4-PCD binds substrate in three steps. These steps in Scheme 9 are the initial weak binding through PCA O4 similar to IHB, then a rotation deeper into the binding pocket similar to FHB, and finally the chelated structure seen in the 5C substrate-bound forms.^{211,228} The first step is supported by computer modeling that assumes no change in the active site, which suggests that only O4 would bind and O3 would point into an adjacent pocket which contains residues to stabilize it.²¹¹ Since substrate has been established to bind as a dianion, two protons must be absorbed by the active site ($pK_a \approx 8.8, 11.7$).²²⁹ The most convenient bases are the departing tyrosinate and hydroxide. The lack of the active-site base would be a possible reason that the binding of substrate in the Y447H 3,4-PCD mutant is slower.

In the resulting 3,4-PCD–PCA complex (discussed in detail below) there is a pocket capable of binding small molecules. If O₂ binds here it would be aligned along the bond to be cleaved. A bridged peroxide intermediate (Scheme 9) was proposed on the basis of some very interesting $[\text{Ir}^{\text{III}}(\text{triphos})(\text{substrate})]^+$ and $[\text{Rh}^{\text{III}}(\text{triphos})(\text{substrate})]^+$ model complexes.^{230–233} These complexes have been shown to reversibly bind oxygen. EPR spectra indicated that the Rh^{III} complex formed a semiquinone–superoxide species.²³³ The $[\text{Ir}^{\text{III}}(\text{triphos})(\text{OO})(\text{phenSQ})]^+$ complex was crystallographically characterized and shown to be a peroxide intermediate bridged from the substrate to the metal center with an Ir–O–O angle of 111–114°. ²³⁰ In contrast to the ES complexes, the substrates in these model complexes are not bound very asymmetrically and the reaction rate is quite slow. In the protein, dioxygen is expected to react with substrate first and then the distal O could bind to the open coordination position on the iron, which has been found to coordinate small molecules such as CN[−]. This would allow the second O from dioxygen to be retained as required by the reaction stoichiometry. The peroxide intermediate would be expected to have a bent Fe–O–O–PCA angle consistent with the shape of the cavity, the bent angle of Fe–CN (145°), and the bent angle observed in 3,4-PCD–NO EXAFS studies (<160°).²³⁴ Whether the substrate remains chelated as in the Ir^{III} model complex or becomes monodentate

as seen in the 3,4-PCD-PCA-NO EPR studies, the 1,2-CTD ^1H NMR studies, and some model EPR studies²³⁵ remains to be determined.

There are two proposed reactions of the peroxy-bound species to form products, which proceed through either a dioxetane or an anhydride intermediate.^{217,236} If the reaction proceeded through a dioxetane intermediate, 100% retention of the label would be expected, but there is a loss of label in studies on 1,2-CTD or 3,4-PCD (~26% and ~50%, respectively) with the slow substrate pyrogallol.^{237,238} (Note that no label is lost using catechol with 1,2-CTD; this has been attributed to the rapid reaction rate not allowing sufficient time for exchange.²⁰¹) The loss of label has been used to argue for an anhydride intermediate where the Fe-OH group (Scheme 9) can exchange with solvent. This anhydride intermediate could then form product via a Criegee rearrangement.²³⁸ However, the formation of an 1,2-epoxide has also been proposed and is not ruled out by the labeling studies.¹⁸²

Returning to the substrate complex, 3,4-PCD-PCA, it has been shown that electron-donating substituents on the substrate ring accelerate the rate of reaction for the intradiol dioxygenases.^{190,201} This is consistent with several possible substrate activation mechanisms (brackets in Scheme 9): Fe^{II}-semiquinone formation with dioxygen attack on the iron, Fe^{II}-semiquinone formation with dioxygen attack on the substrate, and Fe^{III}-ketonized substrate formation with dioxygen attack on the substrate. Some insight has come from protein and model studies.

The structure/activity relationship for the rate of conversion of C4-substituted catechols by 1,2-CTD from *P. putida* has been examined.²³⁹ Substituents (methyl, fluoro, chloro, bromo) at C4 or C4 and C5 decrease the rate of conversion. The reaction rates were compared to the energy of the highest occupied molecular orbital (E_{HOMO}) of the substrates since from frontier molecular orbital theory this is one contribution to the reactivity of nucleophiles. The charge on the catechol oxygen atoms was fixed at -0.8 per oxygen, and only the monoanionic form of the substrates were considered. A linear relationship was obtained between $\ln(k_{\text{cat}})$ and the calculated E_{HOMO} .²³⁹ This was interpreted to indicate that the rate-determining step of the reaction is dependent on the nucleophilic reactivity of the substrate, consistent with the structures in the brackets in Scheme 9. However, since the rate-determining step for this enzyme and for 3,4-PCD has been shown to be product release,^{190,201,202} how this trend relates to the oxygen reactivity is not clear.

Functional ferric model complexes have been synthesized, some of which afford both intra- and extradiol cleavage products while others yield just intra- or extradiol products.²⁴⁰⁻²⁴⁷ This again demonstrates that the redox state is not the sole determinant of intradiol versus extradiol dioxygenase reactivity. The high-spin $[\text{Fe}^{\text{III}}(\text{L})\text{DBC}]^+$ model series (where L = series of tetradentate tripodal ligands) are 6C with the doubly deprotonated catechol derivative, di-*tert*-butylcatechol (DBC), bound in a bidentate fashion.^{248,249} The reaction rate increases as the center

becomes more Lewis acidic and as the half-wave potential, $E_{1/2}$, increases. The increased rate is associated with a decrease in the energy of the catecholate-to-iron LMCT transition.²⁴⁹ One member of this series $[\text{Fe}^{\text{III}}(\text{TPA})\text{DBC}]^+$ is very reactive, although the difference between the two Fe-substrate bond lengths is very small (0.1 Å) compared to the protein site (0.3 Å, *vide supra*). X-ray crystallography and proton NMR spectroscopy suggest semiquinone character in the bound substrate and a strong iron-catecholate interaction, indicating perhaps some Fe^{II}-semiquinone character (left resonance structure in Scheme 9).^{249,250} Spin delocalization onto the substrate was quantified by the contact shifts of the 4-H and 6-H resonance in ^1H NMR. As the iron center becomes more Lewis acidic, the isotropic shifts of the protons become more like a semiquinone. Corresponding Ga^{III} complexes, with approximately the same Lewis acidity, do not exhibit fast rates or high specificities.²⁴⁹ Therefore, Fe^{III} plays more of a role than just that of a Lewis acid.

The substrate asymmetry observed in the protein EXAFS and X-ray crystallographic studies indicates that there may be some substrate ketonization.^{206,210,234,251} This is supported by the high binding affinity of the transition state analogues, INO and NNO.²⁰⁵ Additionally, the UV-vis absorption spectrum of ESO₂ resembles that of 3,4-PCD-INO.^{190,205}

Despite the wealth of information provided by the crystallographic, spectroscopic, and model studies, there are still a number of key points that must be elucidated to understand intradiol dioxygenase catalysis on a molecular level. The role of the tyrosine that dissociates may be to raise E° and partly modulate the CT from the catechol to the iron (inducing an Fe^{II}-semiquinone character). The electronic structure of the site may lead to the asymmetric binding of catechol via the trans effect. The effect on activity of ketonization and charge donation from the catecholate to the iron needs further study. The nature of the intermediate and whether it is a tribridged peroxy species as in the Ir^{III} model complex or a doubly bridged peroxy complex as suggested by the monodentate substrate-NO studies remains to be demonstrated. Furthermore, the factors that lead to intradiol versus extradiol cleavage products are yet to be fully understood.

3. Comparison of Strategies

Both the lipoygenases and intradiol dioxygenases activate substrate with a non-heme ferric site. However, these sites are very different, and this is consistent with the differences in type of substrate and thus the molecular mechanisms of activation. In the lipoygenases, the substrate is a fatty acid with no heteroatom for lone pair coordination to the metal ion. While there has been some consideration of the possible formation of organometallic intermediates in LO catalysis,¹⁷⁴⁻¹⁷⁶ most researchers consider this site to function through H-atom abstraction from a noncoordinated fatty acid substrate. Thus, the role of the metal ion is to abstract efficiently the H atom using an Fe^{III}-OH⁻ to Fe^{II}-OH₂ couple. The electronic features which drive this reaction are the $\text{p}K_{\text{a}}$

Table 10. Representative Extradiol Dioxygenases and Related Fe^{II} Enzymes

enzyme	MW (subunit structure)	source ^a	ref
catechol 2,3-dioxygenase	140 (αFe) ₄	<i>P. arvilla</i>	260,261
3-methylcatechol 2,3-dioxygenase	140 (αFe) ₄	<i>P. putida</i> UCC2	262
chlorocatechol 2,3-dioxygenase	135 (αFe) ₄	<i>P. putida</i>	263
protocatechuate 4,5-dioxygenase	150 ($\alpha\beta$) ₂ Fe	<i>P. testosteroni</i>	39
protocatechuate 2,3-dioxygenase	140 (αFe) ₄	<i>B. macerans</i>	264
homoprotocatechuate 2,3-dioxygenase	140 (αFe) ₄	<i>P. ovalis</i>	265
3,4-dihydroxyphenylacetate 2,3-dioxygenase	140 (αMn) ₄	<i>A. strain Mn-1</i>	255
2,3-dihydroxyphenylpropionate 1,2-dioxygenase	134 (αFe) ₄	<i>E. coli</i>	266
2,6-dichlorohydroquinone dioxygenase	36 (αFe)	<i>S. chlorophenolica</i>	267
2,2',3-trihydroxybiphenyl dioxygenase	32 (αFe)	<i>S. sp strain RW1</i>	268
2,3-dihydroxybiphenyl 1,2-dioxygenase	265 (αFe) ₈	<i>P. sp strain LB400</i>	269
1,2-dihydroxynaphthalene dioxygenase	264 (αFe) ₈	<i>P. paucimobilis</i>	270
homogentisate 1,2-dioxygenase	~380	<i>P. fluorescens</i>	271
gentisate 1,2-dioxygenase	160 (αFe) ₄	<i>P. acidovorans</i>	272,273
3-hydroxyanthranilate 3,4-dioxygenase	33 (αFe)	<i>Homo sapiens</i>	274

^a *P.* = *Pseudomonas*, *S.* = *Spingomonas*, *B.* = *Brevibacterium*, *A.* = *Arthrobacter*.

of the coordinated H₂O and, in particular, the redox potential of the site, both of which must be high. These are achieved by a ligand environment that involves weak-to-moderate asparagine, histidine, and carboxylate donors. Such low donor interactions are reflected by the lack of significant ligand-to-Fe^{III} CT intensity in the visible absorption spectrum of the LOs. The coordination flexibility of the asparagine ligand further decreases its bonding interaction with the oxidized site. These weak donor interactions destabilize the oxidized relative to the reduced site and lead to the high potential required for a large driving force for the H-atom abstraction reaction.

In contrast, the substrates in the intradiol dioxygenases have catecholate groups which are strong σ - and π -donor ligands to Fe^{III} 252 and do directly coordinate to the ferric site in the ES complex. The endogenous ligation of the intradiol site includes two tyrosines which exhibit intense phenolate-to-Fe^{III} CT transitions in the visible region of the absorption spectrum, indicating strong π - and σ -donor interactions with the ferric site (vide supra). These strong donor interactions stabilize the oxidized site and lead to a low reduction potential. Thus, the Fe^{III} state is stabilized by the protein ligation to provide the strong bonding interactions with the catecholate substrate required for catalysis. Several electronic structure mechanisms have been proposed for how this bonding interaction activates the catecholate for reaction with dioxygen (presented in section II.B.2) and for how loss of the tyrosine upon substrate coordination modulates this electronic structure. Detailed spectroscopic studies are required to experimentally evaluate the electronic structure of the ES complex and its role in activating the intradiol dioxygenation reaction of catecholate.

C. O₂ Activation

1. Extradiol Dioxygenases

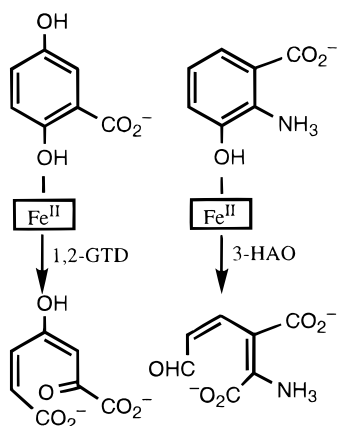
Biochemical Characterization. Extradiol dioxygenases, isolated from many divergent soil bacteria (*Pseudomonads*), have an Fe^{II} active site²⁵³ (or rarely, Mn^{II})^{254–256} and catalyze the insertion of both atoms of dioxygen into catechol (CAT) derivatives, leading to the formation of the ring-cleavage product 2-hy-

droxyacetaldehyde acid.^{182,228,247,257} The extradiol dioxygenases can be further divided into proximal or distal dioxygenases depending on the position of ring cleavage relative to the substituent (Scheme 5). A large effort has focused on the directed evolution of various extradiol dioxygenases for degradation of specific pollutants, such as the recalcitrant polychlorinated biphenyls (PCBs).^{184,258} The bacteria appear to quickly evolve to degrade new substrates, which is likely due to the location of the gene on a plasmid, rather than in the chromosomal DNA, which evolves more slowly.²⁵⁹ This has led to a plethora of extradiol dioxygenases with divergent substrate preferences, some of which are listed in Table 10.

Extradiol dioxygenases can be divided into one- and two-domain enzymes.²⁷⁵ The two-domain enzymes are believed to have originated from a single gene duplication and then divergence to become monocyclic- and bicyclic-cleaving dioxygenases.^{275,276} The majority of extradiol enzymes (including the Mn^{II} enzymes) are two-domain enzymes with the Fe^{II} bound in the C-terminal domain. However, there are two-domain enzymes that are believed to bind the iron in the N-terminal domain.²⁷⁷ The representative bacterial extradiol dioxygenases, 2,3-dihydroxybiphenyl 1,2-dioxygenase (1,2-DHBD, EC 1.13.11.39), catechol 2,3-dioxygenase (2,3-CTD, EC 1.13.11.2, also called metapyrocatechase), and protocatechuate 4,5-dioxygenase (4,5-PCD, EC 1.13.11.8) which have (αFe)₈, (αFe)₄, and $\alpha_2\beta_2\text{Fe}$ quaternary structures, respectively, will be the focus of this review.^{39,278–280}

Sequence alignments of 35 extradiol dioxygenases show that there are nine strictly conserved residues.²⁷⁵ The three metal ligands, His146, His210, and Glu260 (numbering from 1,2-DHBD from *Pseudomonas cepacia* LB400), a motif found in other iron enzymes (vide infra) and referred to as the 2-His-1-carboxylate facial triad,²⁸¹ are strictly conserved. Mutagenesis studies of the Mn^{II} enzymes also indicate a 2-His-1-carboxylate facial triad.²⁸² His195, His241, and Tyr250 are conserved residues in the active-site pocket whose functions are not yet known. The other three conserved residues (Gly28, Leu165, Pro254) are at the N- and C-term interface and are proposed to play a role in protein structure or folding.²⁷⁵

Scheme 10



Other non-heme iron aromatic ring-cleaving dioxygenases that have different substrate specificities but are often grouped with the extradiol dioxygenases have been isolated from bacteria and in some cases also mammals. Two enzymes, homogentisate and gentisate 1,2-dioxygenases (1,2-HGTD, EC 1.13.11.5, and 1,2-GTD, EC 1.13.11.4, respectively), are involved in tyrosine metabolism.^{271,272,283} They contain Fe^{II} and cleave aromatic rings with *para*-hydroxyl groups (Scheme 10). 1,2-GTD cleaves the C1–C2 bond of gentisate (2,5-dihydroxybenzoate), and 1,2-HGTD cleaves the C1–C2 bond of homogentisate, in which a CH₂ group separates the carboxyl group from the ring.²⁷² In humans, a defect in 1,2-HGTD (usually due to a missense mutation) leads to alcaptonuria, a disease characterized by arthritis and urine discoloration.^{284,285} Another non-heme Fe^{II} enzyme, 3-hydroxyanthranilate 3,4-dioxygenase (3-HAO, EC 1.13.11.6, Scheme 10), is involved in tryptophan metabolism and the biosynthesis of pyridine nucleotides in humans, and its product, the toxin quinolinic acid, may be linked to neuronal damage after neurological or inflammatory distress (epilepsy, Huntington's disease, brain trauma, or AIDS).²⁷⁴ While this enzyme is only ~12% homologous to the extradiol dioxygenase 2,3-hydroxyphenylpropionate 1,2-dioxygenase (1,2-DHPPD), there is strong conservation in the region believed to be important for iron binding.²⁸⁶ All of these enzymes contain one non-heme Fe^{II} and cleave aromatic substrates using dioxygen with no other cosubstrates or cofactors.

Kinetics. Steady-state kinetics on 2,3-CTD indicate a bi-uni mechanism, implicating a ternary enzyme–substrate–O₂ complex.²⁸⁷ Consistent with this ordered mechanism, the rate of auto-oxidation of the ferrous site by dioxygen is slow relative to the reaction rate but can vary from enzyme to enzyme.^{268,288,289} The rate of reaction with dioxygen is fast once substrate is bound.^{39,290} Single turnover kinetics are consistent with substrate binding before dioxygen reactivity, and no intermediates have been resolved. In addition to increased dioxygen sensitivity, the substrate complexes of 2,3-CTD and 4,5-PCD more strongly bind NO and N₃[−] (Table 11).²⁹¹ Exposure to H₂O₂ or ferricyanide inactivates these enzymes due to oxidation of the iron, and re-reduction leads to only a partial recovery of activity;^{39,288,292} the reason for this is unknown. For 2,3-CTD, $K_m(\text{CAT})$

Table 11. Kinetic Parameters for 2,3-CTD and 1,2-DHB (Adapted from ref 291)

enzyme	$K_m(\text{O}_2)$	$K_d(\text{NO})$ for E	$K_d(\text{NO})$ for ES
2,3-CTD	7–9 μM	0.2–2 mM	3–4 μM
1,2-DHBD	54–303 μM	360 μM	3 μM

= 1.87 μM , $K_m(\text{O}_2)$ = 7.45 μM , and $k_{\text{cat}} = 278 \text{ s}^{-1}$.²⁹³ For 1,2-GTD, the kinetic parameters are $k_{\text{cat}}/K_m = 430 \times 10^4 \text{ s}^{-1} \text{ M}^{-1}$, $K_m = 85 \mu\text{M}$, and the turnover number is 22000–38500 $\text{min}^{-1} \text{ site}^{-1}$.²⁷²

Both reversible competitive substrate inhibition and mechanism-based inactivation (suicide inhibition) have been observed in 1,2-DHBD.²⁸⁹ This inactivation is gradual; the reaction velocity for 1,2-DHBD decreases to zero prior to the complete exhaustion of either the substrate or dioxygen.²⁸⁹ This phenomenon of suicide inhibition has also been observed in 2,3-CTD.^{294–297} In both enzymes, inactivation is more prominent with slower substrates. An understanding of this process may be relevant to the mechanism of these enzymes and may also aid the development of new enzymes that metabolize slower substrates.

Structure. Crystal structures of 1,2-DHBD have been reported for the following forms: active ferrous (1.9 Å resolution), inactive ferric (1.8 Å resolution), substrate-bound ferrous, and substrate-bound ferric (2.6 Å).^{278,298–300} Recently, the structures of ferrous 2,3-CTD (2.8 Å resolution), ferric 4,5-PCD (2.2 Å resolution), and substrate bound to ferric 4,5-PCD (2.2 Å resolution) have also been determined.^{301,302}

Despite the low sequence homology between 1,2-DHBD and 2,3-CTD, both contain an eight-stranded mixed β -sheet surrounding a large funnel-shaped space lined with hydrophobic residues which forms the putative substrate channel.^{278,302} The active site lies in the center of this channel.³⁰² It was noted that this channel is narrower in 2,3-CTD than in 1,2-DHBD;³⁰² this may help define their different substrate specificities. Also note that 4,5-PCD has a significantly different three-dimensional structure.³⁰¹

Despite global structural differences, the active sites in all of these enzymes consist of the 2-His-1-carboxylate facial triad,²⁸¹ in which the monodentate carboxylate is a glutamate residue; however, the exogenous ligands differ. As indicated by spectroscopy (vide infra), the active site of ferrous 1,2-DHBD is a square pyramid with two exogenous water ligands, His210 and Glu260 as the four equatorial ligands, and His146 as the axial ligand²⁷⁸ (Figure 30A). The two waters have unequal bond lengths of 2.41 and 2.12 Å, with the longer bond length trans to His210. The other bond lengths are 2.15 and 2.25 Å for the two histidines and 1.96 Å for the glutamate. Aerobically oxidized ferric 1,2-DHBD has the same active-site coordination geometry as the reduced site but with slightly altered bond lengths.²⁹⁸ The waters have bond lengths of 2.1 and 2.5 Å. The two histidines have bond lengths of 2.2 and 2.3 Å, and the glutamate is at 2.1 Å. It is interesting to note that in contrast to the intradiol dioxygenases, the change of redox state does not significantly alter the geometry of the site. Ferrous 2,3-CTD has only one exogenous acetone from the buffer bound to the active site, forming a

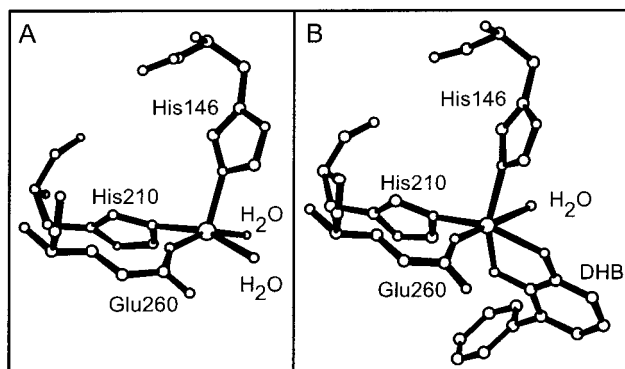


Figure 30. (A) Active-site X-ray crystallographic structure resting ferrous 1,2-DHBD. (B) Active site of ferrous substrate complex 1,2-DHBD-DHB; note that the water ligand has a long bond length of 1.42 Å. (Structures were generated using the crystallographic coordinates from the PDB file 1HAN and from ref 299, respectively.)

distorted tetrahedral site.³⁰² Oxidized 4,5-PCD also has only one exogenous ligand, a water molecule.³⁰¹

The crystal structure of substrate-bound ferrous 1,2-DHBD (1,2-DHBD-DHB, DHB is dihydroxybiphenyl) shows a 6C active site in which the solvent trans to Glu260 has a long bond length of 2.42 Å (Figure 30B).²⁹⁹ Both of the hydroxyl groups of the substrate bind to the iron; one binds to the open axial position of the resting site (Figure 30A) and the other displaces the equatorial water trans to His210. The substrate is bound asymmetrically (1.98 and 2.35 Å): the Fe-O_{substrate} bond trans to His210 and furthest from the site of ring cleavage is longer; this substrate hydroxyl group is proposed to be protonated (vide infra). The crystal structure of ferric 1,2-DHBD-DHB shows that the site is 5C but is trigonal bipyramidal rather than square pyramidal.²⁹⁸ Ferric 1,2-DHBD-3-methylcatechol and ferric 4,5-PCD-PCA have structures that are similar to ferric 1,2-DHBD-DHB.^{298,301}

Spectroscopy. Spectroscopy has been important in identifying the active-site ligands and geometry prior to the crystallography. Spectroscopy continues to provide insight into the molecular mechanism as described below. NMR studies indicate that 2,2',3-trihydroxybiphenyl 1,2-dioxygenase has two solvent-exchangeable protons in the active site which are from the two histidine ligands.³⁰³ CD and MCD studies of 2,3-CTD show two $d \rightarrow d$ transitions, one at 11 240 cm^{-1} and the other at 5220 cm^{-1} (Figure 31), indicative of a 5C square-pyramidal Fe^{II} active site.^{304,305} XAS pre-edge features and EXAFS results for 2,3-CTD are consistent with a 5C site with two histidine ligands and average metal-ligand bond lengths of 2.09 Å.⁴⁴ Another XAS and EXAFS study found that there are six N/O ligands at 2.05 Å.³⁰⁶ The lack of a split in the shell is surprising, since the crystal structure predicts a separation between the longest and shortest bonds of 0.45 Å. VTVH MCD data show nesting which fit to a $M_S = \pm 2$ non-Kramers doublet splitting of $\delta = 4.0 \text{ cm}^{-1}$ and $g_{\parallel} = 8.9$ (Figure 32A). Analysis of the parameters using the $^5T_{2g}$ Hamiltonian (section II.A.1) provide LF ground-state splitting parameters of $\Delta = 600 \text{ cm}^{-1}$ and $|V| \approx 300 \text{ cm}^{-1}$.

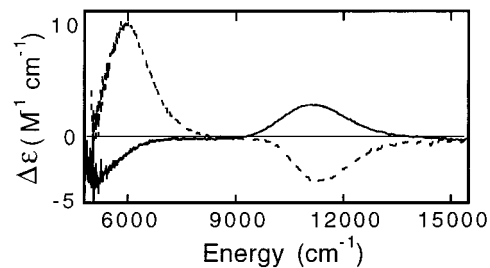


Figure 31. CD spectrum of resting 2,3-CTD (—) and MCD spectrum of resting 2,3-CTD (---) (Adapted from refs 304 and 305.)

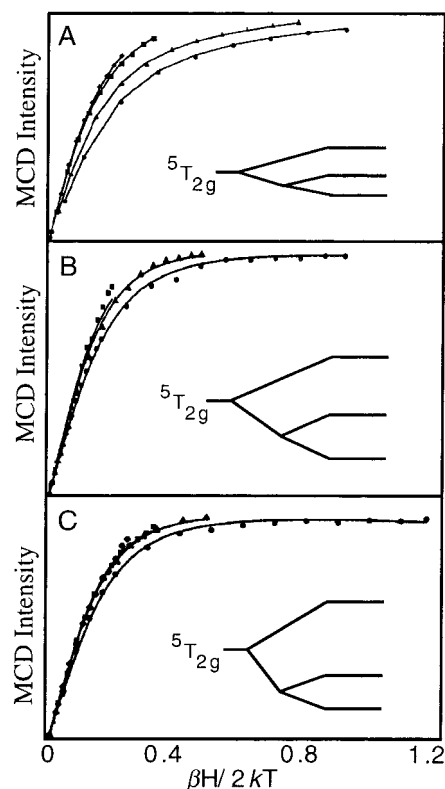


Figure 32. VTVH MCD spectra of (A) 2,3-CTD taken at 890 nm, (B) 2,3-CTD-CAT at 750 nm, and (C) 2,3-CTD-CAT-N₃ at 680 nm. The data are represented by points and the fits to the data by lines. The derived LF splitting of $^5T_{2g}$ is included as an inset on each plot. (Reprinted with permission from ref 304. Copyright 1990 American Chemical Society.)

Magnetic Mössbauer studies of 4,5-PCD reveal that the site remains high-spin ferrous upon substrate binding and that there are no large changes in the active-site parameters.³⁹ Proton NMR experiments on 2,2',3-trihydroxybiphenyl 1,2-dioxygenase suggest that both histidines remain bound but that the site does change.³⁰³ From XAS pre-edge and EXAFS studies, the substrate complex, 2,3-CTD-CAT, is 5C with one atom at 1.93 Å and four atoms at 2.10 Å.⁴⁴ This splitting of the first shell is attributed to the asymmetric binding of the substrate as a monoanion by analogy to monoanionic model complexes.³⁰⁷ Another XAS/EXAFS study indicates that the site was 6C with a split shell.³⁰⁸ Further CD and MCD studies reveal that while the active-site geometry remains square pyramidal, the splittings of the $^5T_{2g}$ and 5E_g orbitals differ from that of the resting enzyme,

indicating the formation of a different square-pyramidal complex.³⁰⁴ VTVH MCD data show much less nesting with $\delta = 2.6 \text{ cm}^{-1}$ and $g_{\parallel} = 8.4$, leading to a large $^5T_{2g}$ ground-state orbital splitting of $\Delta = 1100 \text{ cm}^{-1}$ and $|V| = 704 \text{ cm}^{-1}$ (Figure 32B). From an analysis of the destabilization of the $d_{x^2-y^2}$, d_{xy} , and d_{xz} orbitals upon substrate binding, the substrate was predicted to be bound through both hydroxyl groups, with one in an axial and the other in an equatorial position (relative to the geometry of the resting enzyme, Figure 30A).^{278,298,304} If the weak water ligand observed in the crystal structure²⁹⁹ is the ligand that has no significant bonding interaction with the Fe^{II} in these solution studies, then the square pyramid that is formed (Figure 30B) has Glu260 as the new apical ligand and has the substrate bound in the equatorial plane of the ES complex (relative to the geometry of substrate bound form).

Small-molecule binding studies have been important in providing mechanistic insight into the dioxygen reactivity. Azide, as monitored by CD and MCD, does not bind to 2,3-CTD but does bind to 2,3-CTD-CAT, leading to a new square-pyramidal species.³⁰⁴ The doublet splitting parameters obtained from the VTVH MCD (Figure 32C) are $\delta = 1.8 \text{ cm}^{-1}$, $g_{\parallel} = 8.3$, thus yielding LF splitting parameters of $\Delta = 1500 \text{ cm}^{-1}$ and $|V| = 500 \text{ cm}^{-1}$. This dramatic increase in affinity for small molecules upon substrate binding was also observed with NO.²⁹¹ NO should be a good model for dioxygen binding in the extradiol dioxygenases since it is a neutral molecule which undergoes a redox reaction; the change in its affinity upon the binding of various substrate analogues directly correlates with changes in the rate of oxidation of the iron center by dioxygen.³⁰⁹ Addition of NO to either the resting or substrate-bound forms yields an $S = 3/2$ species, resulting from the antiferromagnetic coupling of high-spin $S = 5/2 \text{ Fe}^{\text{III}}$ with the $S = 1 \text{ NO}^-$.³¹⁰ The EPR spectrum of 2,3-CTD-NO differs from that of 2,3-CTD-CAT-NO:²⁹¹ the nearly axial $g = 4$ signal with $|E/D| = 0.016$ is replaced by two major species with $|E/D| = 0.064$ and 0.037 . This indicates that unlike the intradiol dioxygenases (vide supra), in the case of the extradiol dioxygenases substrate binds independently of NO, implying that they do not compete for the same binding site. The EPR spectra of 2,3-CTD-NO and 4,5-PCD-NO show line-broadening by H_2^{17}O , thus showing that they retain at least one bound solvent molecule.²⁹¹ No H_2^{17}O line-broadening was observed upon binding substrates and NO, indicating the displacement of both water molecules. By using substrates in which the hydroxyl groups were selectively ^{17}O -labeled, it was observed that both oxygen atoms of the substrate can bind to the iron in the ES-NO complex. This suggests that there are three iron binding sites available to exogenous ligands.³⁰⁹ XAS pre-edge and EXAFS studies suggest that NO binding to 2,3-CTD-CAT leads to a 6C complex with a new short bond of 1.74 \AA .⁴⁴

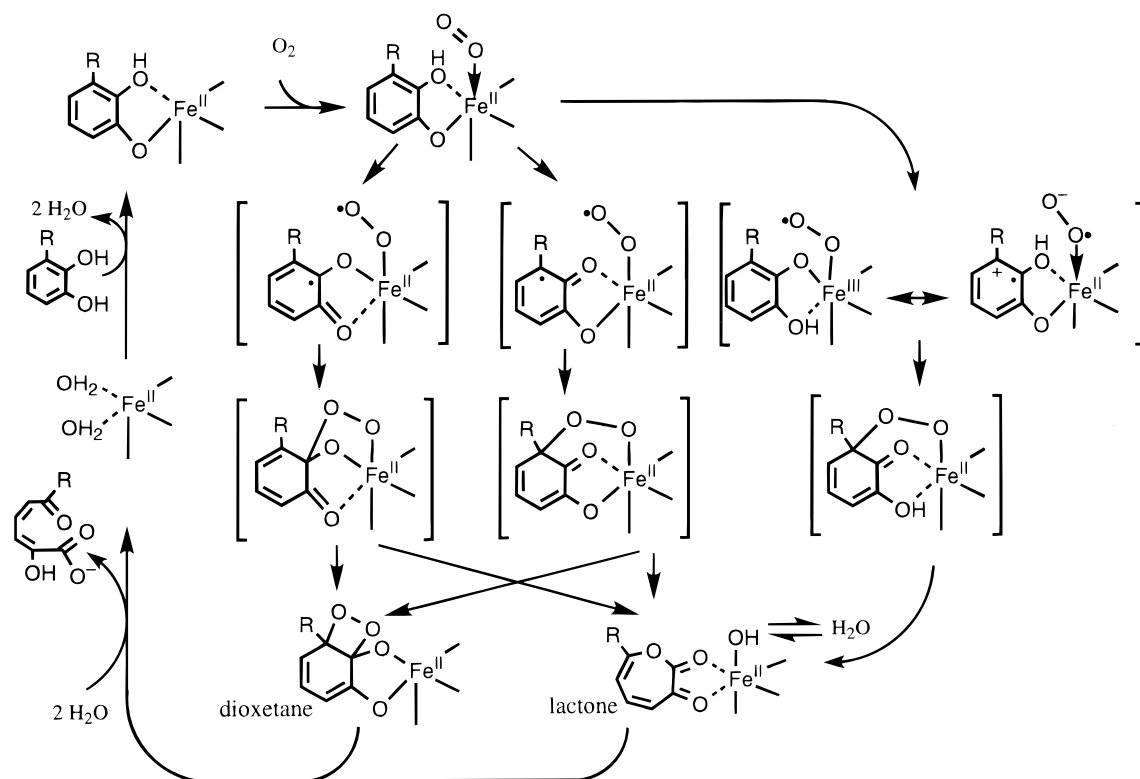
EPR studies on 1,2-GTD, employing selective labeling of each of the substrate (gentisate) substituents with ^{17}O , demonstrate that substrate coordination occurs via the carboxyl and adjacent hydroxyl groups in 1,2-GTD-gentisate-NO, forming a six-

membered chelate ring. As in the extradiol dioxygenases, the affinity for NO increases 100-fold upon substrate binding.²⁸³

Molecular Mechanism. Despite the fact that the extradiol dioxygenases are 5C in the resting ferrous form, in the absence of substrate they are not highly reactive toward dioxygen. An understanding of the electronic structure of the extradiol dioxygenase active site will undoubtedly provide insight into this lack of dioxygen reactivity of a coordinatively unsaturated ferrous center.

Like intradiol dioxygenases, the extradiol dioxygenases and related enzymes appear to have an ordered mechanism in which substrate binds before dioxygen.^{287,291,304} In the first step of the mechanism (Scheme 11), the substrate binds as a monoanion in a bidentate fashion in the open coordination position and both water molecules dissociate, resulting in a new open coordination position on the Fe^{II} . In the next step of the mechanism, dioxygen reacts with the enzyme to form a ternary complex (Scheme 11). Presumably, O_2 binds at the open coordination position, although studies of azide binding to the ES complex by MCD/CD suggest that this ternary complex may be 5C.³⁰⁴ Similar to the dioxygen reaction, the affinity of the enzyme for azide and NO also increases substantially upon substrate binding (vide supra).^{291,304} There are at least three possible mechanisms that would account for this observation: (1) a modulation of the redox potential of the iron center when the substrate binds (i.e., catechol coordination may lower the redox potential);²⁴⁷ (2) the change in orientation of the open coordination position may allow dioxygen better access to the iron or lead to a more favorable O_2 binding pocket due to H bonds or other factors; or (3) the change in the electronic structure upon substrate binding changes the frontier molecular orbital involved in dioxygen reactivity. A change in redox potential, while likely, would not explain the increased binding affinity for azide since this is not a redox process. The other two possibilities have not been evaluated.

It has been proposed that the reaction of dioxygen with the ES complex leads initially to a superoxide species. Two possibilities have been considered for the reduction of the bound dioxygen to superoxide: the extra electron could come from either the substrate or the Fe^{II} . The first possibility would lead to an Fe^{II} -semiquinone-superoxide species which could undergo radical coupling of the semiquinone and superoxide (Scheme 11, center). The second possibility leads to a monodeprotonated Fe^{III} -catecholate-superoxide which could undergo nucleophilic attack by superoxide on the ring (Scheme 11, right).^{182,228} The formation of a superoxide species is supported by the fact that superoxide dismutase decreases the rate of suicide inactivation in 2,3-CTD by 3-fluorocatechol.²⁹⁶ The possibility of a semiquinone-superoxide intermediate was probed by use of a substituted catechol (R of Scheme 11 is a cyclopropyl group, *cis*- and *trans*-2,3-dihydroxyphenyl cyclopropane 1-carboxylic acid).³¹¹ Formation of a cyclopropylmethyl radical during the reaction is expected to lead to fast ring opening and isomerization.³¹² These substrate

Scheme 11. Possible Mechanism for the Extradiol Dioxygenases (Adapted from refs 182, 228, and 315)

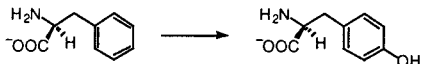
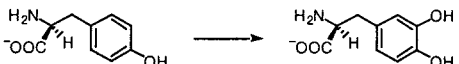

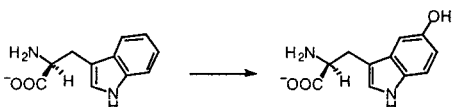

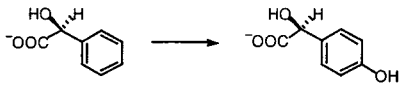
analogues are cleaved by 1,2-DHPPD, and fast isomerization was observed, thus indicating the opening of the cyclopropane ring.³¹¹ Since $^2\text{H}_2\text{O}$ experiments ruled out deprotonation and reprotonation of the cyclopropyl ring, the *cis/trans* isomerization was consistent with a semiquinone radical intermediate (Scheme 11, center).³¹¹ The nucleophilic mechanism is also not supported by the observation that substrates with both electron-donating and -withdrawing functional groups such as hydroxide, chloride, methyl, and methoxy are cleaved by these enzymes.^{185,313} Additionally, 4-nitrocatechol is a competitive inhibitor of 4,5-PCD,³¹⁴ and electron-donating groups that can tautomerize appear to be required for 1,2-GTD.²⁸³ The nucleophilic mechanism does, however, provide a possible explanation for the specificity for extradiol cleavage since the position *ortho* to the long Fe–O_{substrate} bond would be expected to have more partial positive charge and be activated for nucleophilic attack (Scheme 11, right).²²⁸

Both possible electronic mechanisms would lead to an aryl peroxy intermediate. Depending on the formulation of the aryl peroxy intermediate, this can undergo a number of possible reactions (Scheme 11): (1) the formation of an epoxide with subsequent rearrangement to form a lactone, (2) the formation of a peroxy species to the carbon *ortho* to the hydroxyl group with subsequent rearrangement to a dioxetane, (3) the formation of a peroxy species to the carbon *ortho* to the hydroxyl group followed by an acyl migration leading to a lactone, (4) the formation of a peroxy species to the hydroxyl carbon with subsequent rearrangement to a dioxetane species, or (5) the formation of a peroxy species to the hydroxyl carbon followed by an alkenyl migration to form a lactone species.¹⁸² Attack at the carbon adjacent to

the hydroxylated carbon would seem to afford control over the specificity, whereas a peroxy bridge to the hydroxylated carbon could be envisioned to provide intradiol cleavage products as well. Alternatively, the regiospecificity of O₂ attack on the ring was proposed to be controlled by the steric requirements of the active site.¹⁹⁷ For 1,2-DHPPD, ^{18}O -labeling of both water and its substrate, with subsequent analysis of label insertion into the products, was used to examine these possibilities.³¹⁵ When water was labeled, there was some insertion of label into the carboxylate of the product, suggesting that the reaction probably occurred through a lactone with subsequent exchange of the bound hydroxyl group with bulk solvent (Scheme 11).³¹⁵ Consistent with this, when labeled dioxygen was used, there was some loss of label in the product.³¹⁵ However, in similar studies with 1,2-GTD, no label is lost.²⁸³ A seven-membered lactone analogue was in fact hydrolyzed very slowly by the enzyme.³¹⁵

The mechanism of the extradiol dioxygenases and related enzymes is currently not as well understood as that of the intradiol dioxygenases. The lack of O₂ reactivity for a 5C Fe^{II} site and why the affinity for small molecules increases so dramatically upon substrate binding are not clear. Assignment of the electron distribution in the ternary ESO₂ complex and the mechanism of subsequent attack on the ring remain to be determined. The suicide inactivation is not yet well understood and may provide insight into the molecular mechanism. The study of intermediates observed in the reaction of the model complex (*n*-butylN)₄[(CH₃CN)_xFe^{II}P₂W₁₅Nb₃O₆₂] with dioxygen and DBC may provide insight into the protein mechanism.³¹⁶ As indicated above, the ferric model complex, [Fe(TACN)(DBC)Cl]⁺, will do extradiol cleavage,

Table 12. Reactions of the Pterin-Dependent Hydroxylases

enzyme	reaction	references
Phenylalanine hydroxylase (phenylalanine 4-monooxygenase) EC 1.14.16.1		317-319
Tyrosine hydroxylase (tyrosine 3-monooxygenase) EC 1.14.16.2		320
Anthranilate hydroxylase ^a (anthranilate 3-monooxygenase) EC 1.14.16.3		321,322
Tryptophan hydroxylase (tryptophan 3-monooxygenase) EC 1.14.16.4		323,324
Glycerol-ether monooxygenase EC 1.14.16.5		337-339
Mandelate hydroxylase (mandelate 4-monooxygenase) EC 1.14.16.6		325

^a Two NADH/NADPH-dependent enzymes are also often referred to as anthranilate hydroxylase: anthranilate 1,2-dioxygenase (deaminating, decarboxylating), EC 1.14.12.1, the enzyme from *A. niger* requires Fe^{II} while the enzyme from *T. cutaneum* is a flavoprotein; and anthranilate 3-monooxygenase (deaminating), EC 1.14.13.35, also an Fe^{II} enzyme.

indicating that oxidation state is not the sole determining factor for specificity.²⁴⁴ Also, the substrate-bound forms of 1,2-DHBD and 3,4-PCD (section II.B.2) have congruent structures. How the specificity of the position of ring cleavage for the intradiol and extradiol dioxygenases with their preferred substrates is controlled has not yet been determined. Molecular insight into the mechanism should allow the rational design of mutant enzymes and model complexes to degrade specific pollutants.

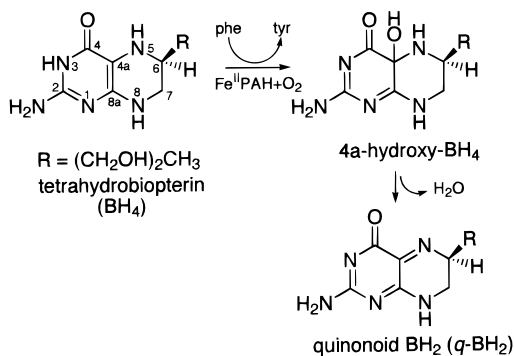
2. Pterin-Dependent Hydroxylases

Biochemical Characterization. Several tetrahydropterin-dependent monooxygenases have been isolated and are listed in Table 12. Five of these enzymes also require mononuclear Fe^{II} for function: phenylalanine hydroxylase (PAH),³¹⁷⁻³¹⁹ tyrosine hydroxylase (TyrH),³²⁰ anthranilate hydroxylase,^{321,322} tryptophan hydroxylase (TrpH),^{323,324} and mandelate hydroxylase.³²⁵ Very little research has been done to characterize the anthranilate and mandelate enzymes; however, the three amino acid hydroxylases (PAH, TyrH, and TrpH) are known to share many physical, structural, and catalytic properties.^{38,326-328} PAH, expressed primarily in the liver and kidney, catalyzes the conversion of L-phenylalanine to L-tyrosine in the rate-limiting step of phenylalanine catabolism. TyrH functions in the rate-limiting step

of catecholamine biosynthesis in the brain, catalyzing the hydroxylation of L-tyrosine to 3,4-dihydroxyphenylalanine (L-Dopa). TrpH hydroxylates L-tryptophan to 5-hydroxytryptophan in the rate-limiting step in the biosynthesis of serotonin, also in the brain. Disruption of TyrH function is suspected to play a role in several neurological disorders, including schizophrenia and Parkinson's disease, while dysfunction of PAH leads to severe mental retardation (phenylketonuria, PKU). Of the PKU-inducing PAH mutants characterized to date, most appear to affect protein stability.³²⁹⁻³³⁴ The three enzymes share extensive sequence homology in their catalytic domains, and it is believed that they have similar hydroxylation mechanisms. It should also be noted that a PAH enzyme has been isolated from *Chromobacterium violaceum*, and the metal requirement for this enzyme is unclear.^{335,336}

Of the three amino acid hydroxylases, PAH has been the most extensively studied due to its relative stability and ease of purification; consequently, this review will focus on PAH with secondary emphasis on TyrH. PAH exists as a dimer or tetramer of identical 51.7 kDa subunits, each of which contains a non-heme iron atom that is required for catalysis.^{340,341} The enzyme is tightly regulated by both L-phenylalanine and pterin cofactor. L-Phenylalanine allosterically activates the enzyme from the resting,

Scheme 12



low-affinity state (PAH^{T}) to the activated, high-affinity state (PAH^{R}) through cooperative binding to an allosteric effector site that is distinct from the enzyme's catalytic site.^{342–345} The $\text{T} \rightarrow \text{R}$ activation is accompanied by a significant structural rearrangement of the protein and promotes tetramer formation.^{344,346} Alternatively, activation can be accomplished by using detergents (e.g., lysolecithin), proteases (e.g., α -chymotrypsin), or sulfhydryl-modifying reagents (e.g., *N*-ethylmaleimide).^{347–349} Additionally, phosphorylation of PAH appears to sensitize the enzyme to allosteric activation by *L*-phenylalanine.³⁵⁰ In contrast, allosteric activation is inhibited by the cofactor tetrahydrobiopterin (BH_4 ; Scheme 12), although pterin analogues lacking the dihydropropyl side chain do not inhibit activation.^{350,351} The regulatory mechanisms of TyrH and TrpH are markedly different from that of PAH, possibly indicating that while the three enzymes share similar catalytic domains, the regulatory domains evolved separately to suit the particular physiological role and location of each enzyme.

Kinetics. As isolated, the active site of PAH is in the Fe^{III} oxidation state, which may be an artifact of purification. BH_4 and analogues reduce the enzyme from the Fe^{III} to the catalytically active Fe^{II} state.^{343,352–354} This reduction is postulated to occur at a site distinct from either the regulatory or catalytic sites.³⁵⁵ The reduction reaction may play a role in vivo to avoid the accumulation of inactive $\text{Fe}^{\text{III}}\text{PAH}$ as the enzyme becomes oxidized once in every 150–200 catalytic turnovers.^{355,356} The stoichiometry of reduction depends on enzyme activation: reduction of $\text{Fe}^{\text{III}}\text{PAH}^{\text{T}}$ consumes two electrons per enzyme subunit, with one electron transferred to Fe^{III} and one to O_2 , while reduction of $\text{Fe}^{\text{III}}\text{PAH}^{\text{R}}$ requires only one electron per subunit.^{318,355,357} Very little is known about the reduction mechanism.³⁸

Despite many years of effort, the hydroxylation mechanism of PAH and its related enzymes is also poorly understood. Fe^{II} , reduced pterin cofactor, and O_2 are required to hydroxylate the appropriate amino acid. A crucial early step toward elucidating the mechanism of PAH was determination of the pterin product, initially thought to be the quinonoid BH_2 ($q\text{-BH}_2$). $q\text{-BH}_2$ is actually produced by dehydration of the initial product of the coupled hydroxylation of PAH, 4a-hydroxy- BH_4 (4a-carbinolamine), as shown in Scheme 12.³⁵⁸ $^{18}\text{O}_2$ studies further demonstrated that dioxygen is partitioned by PAH such that the

hydroxy group added to the 4a-hydroxy- BH_4 and the hydroxylated amino acid comes directly from O_2 .^{359,360} On the basis of regulatory constraints, an ordered sequential mechanism is observed for the resting enzyme with its natural substrates: $\text{L-Phe} + \text{BH}_4 + \text{O}_2$.^{38,351} Using preactivated enzyme, substrates can be added in at least a partially random order. Steady-state analysis has indicated that the binding order for TyrH, however, is $\text{BH}_4 + \text{O}_2 + \text{L-Tyr}$,³⁶¹ although this does not require that O_2 be activated before *L*-tyrosine binds. Both enzymes have an absolute requirement for binding of all three substrates before any coupled hydroxylation product is released. For lysolecithin-activated PAH, the K_m for catalytic binding of *L*-phenylalanine is $180 \mu\text{M}$, within a factor of 2 of the $K_{d,\text{app}}$ ($110 \mu\text{M}$) for the allosteric activator site.^{318,346} The K_m for BH_4 is $3\text{--}21 \mu\text{M}$,^{347,355,362} depending on assay conditions, while the K_m for 6-methyltetrahydropterin (6MPH_4) is $45\text{--}61 \mu\text{M}$.^{318,346} PAH isolated from rat liver has a V_{max} of 22 s^{-1} subunit⁻¹.³⁵⁴ It is notable that for TyrH the K_m 's for tyrosine and for oxygen are dependent on the structure of the pterin cofactor used in the assay.³²⁰ This is consistent with the ordered mechanism above and may indicate a role for the pterin in amino acid binding.

PAH inhibitor studies have generally not been informative since most reversible inhibitors are actually poor substrates that cause significant uncoupling of the PAH reaction, i.e., only the pterin is oxidized. Such alternative substrates range from *L*-methionine and *L*-norleucine to *ortho*-, *meta*-, and *para*-substituted *L*-phenylalanine derivatives, requiring oxygen-atom insertion into alkane and aromatic C–H bonds as well as oxygen-atom transfers to form epoxides or sulfoxides.³⁸ The mechanism of this uncoupled hydroxylation is poorly understood. Although it is generally assumed that the oxidizing species for the uncoupled reaction would be the same as that for the coupled hydroxylation of both cosubstrates,³⁵⁶ there is no evidence that this is in fact the case. Completely uncoupled turnover (e.g., with *L*-tyrosine as substrate) may also have a different mechanism from partially uncoupled turnover (e.g., with *para*-substituted *L*-phenylalanine derivatives).³⁸ The pterin product $q\text{-BH}_2$ is formed from uncoupled hydroxylation, and such turnover also results in oxidation of the iron to the Fe^{III} state.^{355,356} The 4a-hydroxy- BH_4 product has also been observed, although it is not clear whether this is actually a product of the uncoupled reaction in a partially coupled mechanism.^{356,363,364} Production of H_2O_2 rather than complete reduction of O_2 to H_2O during uncoupled pterin oxidation is also controversial.^{356,364}

Structure. Several crystal structures have recently appeared on truncated forms of both PAH and TyrH.³²⁷ The first structure published of PAH consists of the catalytic and C-terminal tetramerization domains of the enzyme, minus the N-terminal regulatory domain. This truncated form of the enzyme represents a fully activated state ($\approx \text{PAH}^{\text{R}}$) in which activity does not increase upon addition of *L*-phenylalanine. The dimeric form of the enzyme is stabilized through interactions of both the catalytic and tetramerization domains,³⁶⁵ while tetramerization oc-

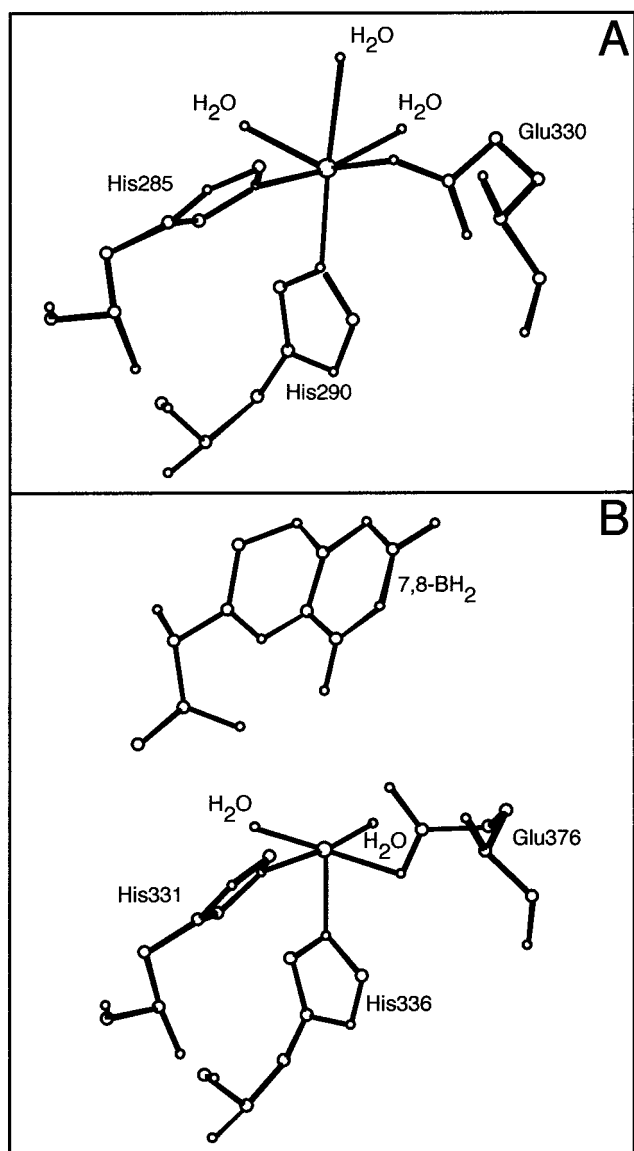


Figure 33. (A) Structure of the active site of Fe^{III}PAH. (B) Structure of the active site of Fe^{III}TyrH with cofactor analogue 7,8-BH₂. (The structures were generated using the crystallographic coordinates from PDB files 1PAH and 2TOH, respectively.)

curs via a “domain swapping arm” that interacts with the other monomers to form an antiparallel coiled-coil structure.³⁶⁶ Within each monomer, the active site is lined primarily with hydrophobic residues and contains one 6C Fe^{III} in a distorted octahedral geometry.³⁶⁵ Site-directed mutagenesis had previously determined that His285 and His290 were required for iron binding;³⁶⁷ in the crystal structure, the iron atom is coordinated to these ligands as well as to Glu330 (monodentate) and three H₂O ligands as shown in Figure 33A. The active-site structure is consistent with the “2-His-1-carboxylate facial triad” postulated to be a common motif for non-heme Fe^{II} enzymes.²⁸¹ Further studies on an alternative truncated form of PAH, with the catalytic and regulatory domains but without the tetramerization domain, indicate that the core of the regulatory domain is far from the active site; however, the N-terminal arm does extend across the catalytic domain to restrict access to the active site.³⁶⁸

The overall protein structure and Fe^{III} coordination of PAH is very similar to that determined for truncated Fe^{III}TyrH, although in Fe^{III}TyrH one of the water ligands appears to be missing.³⁶⁹ A crystal structure has also been reported for truncated Fe^{III}-TyrH with an oxidized BH₄ analogue, 7,8-dihydrobiopterin (7,8-BH₂), bound at the active site.³⁷⁰ The pterin does not bind to the iron, and the closest contact between the pterin and the iron is the C4 carbonyl oxygen at a distance of 3.6 Å as indicated in Figure 33B. A hydroxylated phenylalanine residue was also observed in this structure, and it was proposed to play a role in substrate specificity.^{327,370} Hydroxylation of the phenylalanine, however, was recently shown to be the result of crystallization conditions, and it is not required for full enzyme function.³⁷¹ The pterin overlaps with the binding site of catecholamine inhibitors, as determined by crystal structures of truncated Fe^{III}PAH,³⁷² although the aromatic rings of the pterin and catecholamine are 90° to each other. In general, catechols are competitive inhibitors with respect to the pterin cofactor and are noncompetitive inhibitors with respect to substrate. When bound to the enzyme, they give rise to a blue-green protein solution with LMCT bands around 700 nm, indicating that the catecholamines coordinate to the Fe^{III} center.^{373,374} This is confirmed by the crystal structures, where each catecholamine displaces two of the water ligands to bind in a bidentate fashion to the Fe^{III} atom.

Spectroscopy. As with the crystal structures, most of the spectroscopic data on the iron site of PAH have been collected on the Fe^{III} form of the enzyme rather than the catalytically relevant Fe^{II} oxidation state. The EPR spectrum of the resting Fe^{III} enzyme with no substrates bound at the active site (PAH^T[]) has axial ($g_{\text{eff}} = 6.7$ and 5.4) and rhombic ($g_{\text{eff}} = 4.3$) components consistent with an $S = 5/2$ system.^{346,353} CD and MCD studies provided the first direct analysis of the Fe^{II} site of resting PAH^T[] and showed two $d \rightarrow d$ transitions split by $\sim 1600\text{--}1950\text{ cm}^{-1}$ and centered slightly $< 10\,000\text{ cm}^{-1}$ ($10Dq \approx 9400\text{--}9850\text{ cm}^{-1}$) as presented in Figure 34A.⁴⁷ This is indicative of a distorted-octahedral, high-spin Fe^{II} active site with a first coordination sphere comprised of significant oxygen ligation, consistent with Mössbauer spectroscopy,³⁸ XAS/EXAFS,⁴⁷ and with subsequent analysis of the Fe^{III}PAH crystal structure.³⁶⁵ VTVH MCD data in Figure 34B show limited nesting and were fit with a $M_S = \pm 2$ doublet splitting of $\delta = 2.9\text{ cm}^{-1}$ and $g_{\parallel} = 8.9$.³⁷⁵ The small value of δ is unusual for a 6C site; it can be associated either with π -backbonding, which is not relevant for the endogenous ligands of PAH, or with a site that is relatively axial. Analysis of the spin Hamiltonian gives $^5T_{2g}$ LF ground-state splitting parameters of $\Delta \approx -250\text{ cm}^{-1}$ and $|V| \approx 70\text{ cm}^{-1}$ ($|V/2\Delta| \approx 0.14$), as shown in Figure 34I. Activation of the enzyme by nonphysiological activators does not perturb either the MCD⁴⁷ or the EPR³⁸ spectra of Fe^{II}PAH[] and Fe^{III}PAH[], respectively, indicating that the active site is not affected by activation despite the other structural changes in the enzyme discussed above.

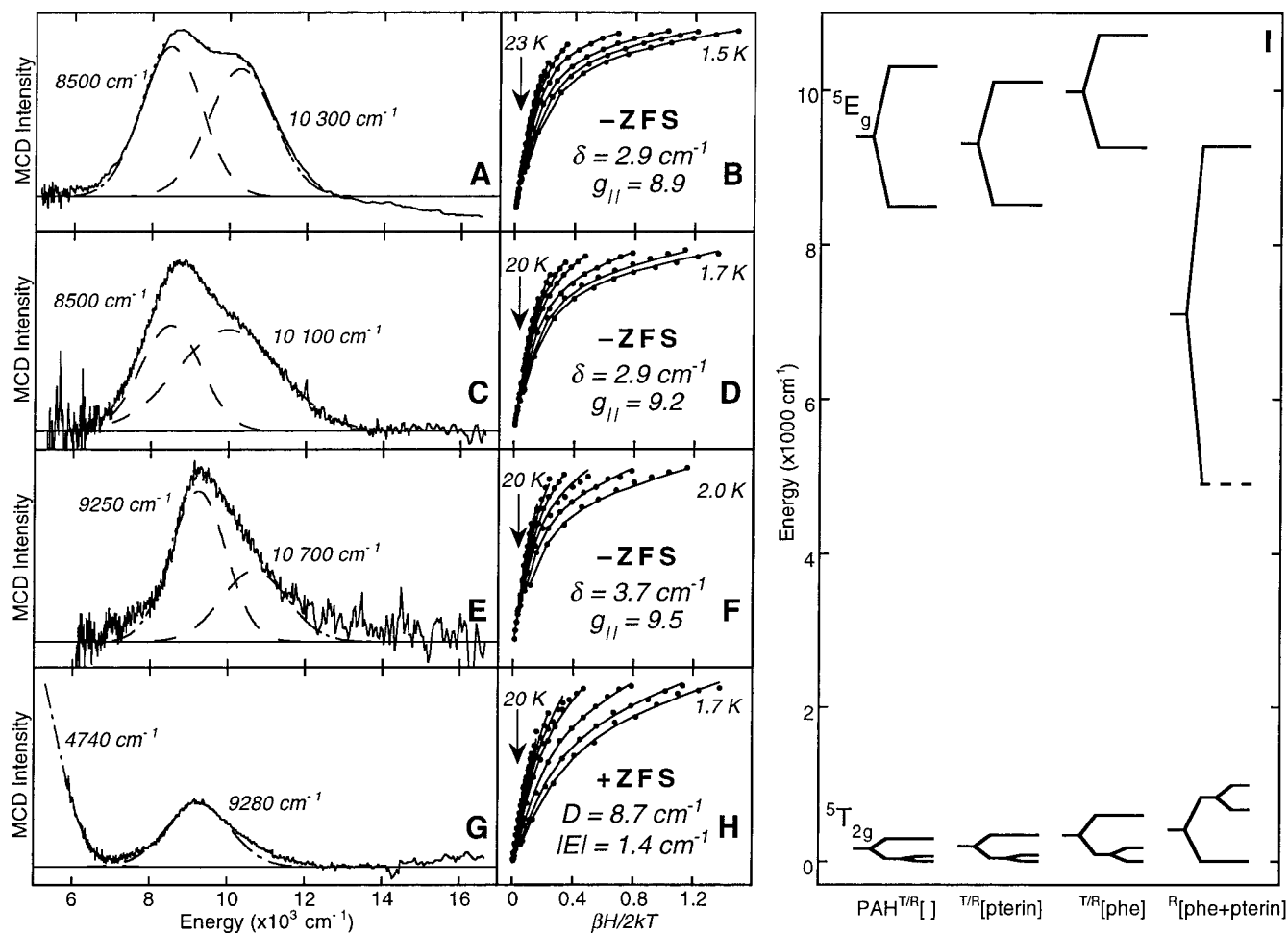


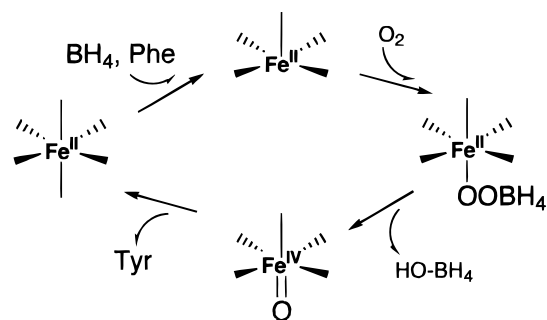
Figure 34. (A) MCD spectrum $\text{PAH}^{\text{T}}[\]$ (—) with Gaussian fit (---) and components (---). (B) VTVH MCD recorded at 8500 cm^{-1} for $\text{PAH}^{\text{T}}[\]$. The best fit (---) to the data (●) was generated by the parameters described in the text. (C) MCD spectrum of $\text{PAH}^{\text{T}}[5\text{-deaza-6-MPH}_4]$. (D) VTVH MCD recorded at 8805 cm^{-1} for $\text{PAH}^{\text{T}}[5\text{-deaza-6-MPH}_4]$. (E) MCD spectrum $\text{PAH}^{\text{R}}[\text{L-Phe}]$. (F) VTVH MCD recorded at 9000 cm^{-1} for $\text{PAH}^{\text{R}}[\text{L-Phe}]$. (G) MCD spectrum $\text{PAH}^{\text{R}}[\text{L-Phe, pterin}]$. (H) VTVH MCD recorded at 6055 cm^{-1} for $\text{PAH}^{\text{R}}[\text{L-Phe, pterin}]$. (I) Experimentally determined d-orbital energy levels. (Adapted from refs 47 and 375.)

CD and MCD spectra of the cofactor analogue 5-deaza-6-MPH₄ bound to $\text{Fe}^{\text{II}}\text{PAH}$ ($\text{Fe}^{\text{II}}\text{PAH}^{\text{T}}[5\text{-deaza-6-MPH}_4]$) show two $d \rightarrow d$ bands with $\Delta^5\text{E}_g \approx 1600\text{--}1900\text{ cm}^{-1}$ and $10Dq \approx 9300\text{--}9850\text{ cm}^{-1}$ (Figure 34C).³⁷⁵ VTVH MCD data in Figure 34D gave $\delta = 2.9\text{ cm}^{-1}$ and $g_{\parallel} = 9.2$, yielding $\Delta = -300\text{ cm}^{-1}$ and $|V| = 80\text{ cm}^{-1}$ (Figure 34I). Again, activation of the enzyme by nonallosteric methods does not affect the CD/MCD spectra. These results are almost identical to those for $\text{Fe}^{\text{II}}\text{PAH}[\]$, above, and demonstrate that pterin binding does not perturb the 6C active site. This is in agreement with the crystal structure of 7,8-BH₂ bound to $\text{Fe}^{\text{III}}\text{TyrH}$,³⁷⁰ along with Mössbauer and XAS results indicating that pterin is close to but not coordinated to the iron.⁴¹

Binding of substrate L-phenylalanine to $\text{Fe}^{\text{II}}\text{PAH}$, however, does affect the active site. The two $d \rightarrow d$ bands observed by CD/MCD shift to slightly higher energy, as shown in Figure 34E, with $10Dq = 9980\text{--}10450\text{ cm}^{-1}$ and $\Delta^5\text{E}_g = 1450\text{--}2000\text{ cm}^{-1}$.⁴⁷ Activation does not affect the substrate-bound site, as the spectra are the same for both $\text{Fe}^{\text{II}}\text{PAH}^{\text{T}}[\text{L-Phe}]$ and $\text{Fe}^{\text{II}}\text{PAH}^{\text{R}}[\text{L-Phe}]$. The VTVH MCD data show greater nesting (Figure 34F) with $\delta = 3.7\text{ cm}^{-1}$ and $g_{\parallel} = 9.5$, leading to greater ground-state orbital splittings of

$\Delta = -500\text{ cm}^{-1}$ and $|V| = 180\text{ cm}^{-1}$ (Figure 34I).³⁷⁵ This reflects a perturbation of the 6C iron site with an increase in LF strength attributed to a rearrangement of the active-site ligation, presumably to allow for proper orientation of substrate in active site. Such a ligand rearrangement is also indicated by EXAFS analysis, showing a shift in the relative number of ligands from the outer to the inner subshell of the first coordination sphere of the Fe^{II} site upon substrate binding.⁴⁷ These results contradict ¹H NMR studies on the Fe^{III} enzyme, concluding that a water molecule is displaced from coordination to the iron upon substrate binding,³⁷⁶ although another NMR study placed the aromatic ring of the phenylalanine in the second coordination sphere of the Co^{II} -substituted enzyme.³⁷⁷ EPR spectra of either $\text{Fe}^{\text{III}}\text{PAH}^{\text{R}}[\text{L-Phe}]$ or $\text{Fe}^{\text{III}}\text{PAH}^{\text{T}}[\text{L-Phe}]$ show the disappearance of the axial signals at $g_{\text{eff}} = 6.7$ and 5.4 characteristic of the resting enzyme, with a new signal appearing at $g_{\text{eff}} = 4.5$.³⁴⁶

Addition of both substrate L-phenylalanine and pterin cofactor to $\text{Fe}^{\text{II}}\text{PAH}$ has also been studied by CD and MCD spectroscopy. For the $\text{Fe}^{\text{II}}\text{PAH}^{\text{R}}[\text{L-phe, pterin}]$ species, a dramatic change is observed in both excited-state and ground-state spectral features. One

Scheme 13. Possible Mechanistic Scheme for PAH

of the higher energy bands (at $\sim 10\,000\text{ cm}^{-1}$) disappears and a new, low-energy band ($< 6500\text{ cm}^{-1}$) is observed in Figure 34G.³⁷⁵ This Fe^{II} site with $10Dq < 8900\text{ cm}^{-1}$ and $\Delta^5E_g > 3100\text{ cm}^{-1}$ is 5C, indicating that the iron has lost a ligand. Additionally, the VTVH MCD data shown in Figure 34H have much greater nesting relative to the other PAH species (Figure 34B, D, and F). Analysis determined that this is due to +ZFS in Fe^{II}PAH^R[L-phe, pterin], with $D = 8.7\text{ cm}^{-1}$ and $|E| = 1.4\text{ cm}^{-1}$, whereas all other Fe^{II}-PAH forms studied have -ZFS as outlined above. This leads to ground-state orbital splittings of $\Delta \approx +825\text{ cm}^{-1}$ and $|V| \approx 315\text{ cm}^{-1}$ as shown in Figure 34I. For a 5C site, the e_g orbitals have a relatively small splitting; combined with +ZFS, this is consistent with a strong-axial square-pyramidal structure.

Molecular Mechanism. The formation of such a 5C site upon substrate and cofactor binding directly implicates the iron in coupled hydroxylation and is also consistent with the ordered mechanism of PAH wherein substrate and cofactor must be present before any product is released.^{38,351} The open coordination position observed for PAH^R[L-phe, pterin] suggests initial reaction of O₂ with Fe^{II} and possible coordination of a peroxy-pterin intermediate to the iron, as indicated in Scheme 13.³⁷⁵ The ligand lost relative to the resting enzyme in Figure 33A is likely one of the H₂O molecules. A 4a-peroxy-BH₄ species has been proposed as an intermediate for PAH,³⁷⁸ but such an intermediate has not been observed. It would be possible to form a formally Fe^{II}-OO-pterin intermediate that subsequently heterolytically cleaves to yield 4a-hydroxy-BH₄ and Fe^{IV}=O, which could then react with the amino acid. A recent study of a non-heme model complex shows evidence for an Fe^{IV}=O intermediate in the hydroxylation of a phenyl group.³⁷⁹ In the crystal structure of TyrH with oxidized pterin (Figure 33B), the distance from the iron to the pterin C4a atom is 5.6 Å, which would allow for O₂ interaction with both the iron and pterin as a peroxy intermediate.³⁷⁰ Although it is generally assumed that the initial reactive species is formed using the pterin cofactor, there is no evidence for this. It should also be noted that the first product released by TyrH is the amino acid product, L-Dopa.³⁶¹

¹⁸O isotope effects were studied as a function of amino acid substrate, pterin derivative, and pH; large effects ($^{18}(V/K) \approx 1.0175$) were seen for TyrH under all conditions.³⁸⁰ This was interpreted to be consistent with a change in the oxygen bond order as the rate-determining step in catalysis. These studies also suggested that formation of an iron-dioxygen species

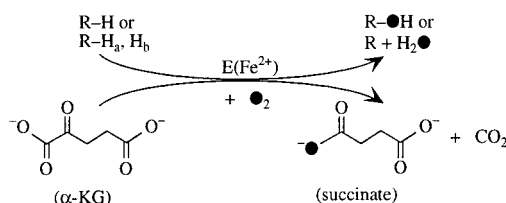
is not rate determining. Steady-state and ²H kinetic isotope effect (KIE) experiments on TyrH have also ruled out amino acid C-H bond cleavage and product release as slow steps in catalysis and indicate that formation of the hydroxylating intermediate is the rate-limiting step.^{361,381} The NIH shift, where the tritium atom in L-[4-³H]Phe migrates to the *meta* position in the tyrosine product, was originally documented in PAH.³⁸² Although an arene oxide is usually suggested to be an intermediate in such migration reactions,³⁷⁸ there is no evidence that this must be the case for PAH.^{38,319} In fact, experiments using 4-methyl-phenylalanine indicated that a *meta*-carbocation is formed.³⁶⁰ Proposed mechanisms generally involve electrophilic attack of an oxygen species at the *para*-position of the aromatic ring.

While progress has been made in establishing and understanding the kinetic order for PAH and TyrH, more research is necessary to further elucidate the molecular mechanism of the pterin-dependent hydroxylases. In particular, the nature of the hydroxylating intermediate and the role of the iron in catalysis have yet to be established. As the mechanism of action of these enzymes is defined, the diseases induced by enzyme mutations will be better understood at a molecular level.

3. α -Ketoglutarate-Dependent and Related Enzymes

Biochemical Characterization. A large class of mononuclear non-heme iron enzymes requires α -ketoglutarate (α -KG or 2-oxoglutarate) as a cosubstrate.³⁸³⁻³⁸⁵ They are present in animals, plants, and microorganisms, where they play key roles in an array of primary and secondary metabolic pathways. Prolyl 3-hydroxylase (EC 1.14.11.7), prolyl 4-hydroxylase (EC 1.14.11.2), and lysyl hydroxylase (EC 1.14.11.4) are involved in posttranslational processing of collagen in animals.³⁸⁶ Prolyl 4-hydroxylase from plants is critical in the synthesis of hydroxyproline-rich glycoproteins which regulate the extensibility and digestibility of the cell wall.³⁸⁷ Aspartyl β -hydroxylase (EC 1.14.11.6) catalyzes the posttranslational hydroxylation of aspartyl residues in several epidermal growth factors in mammalian systems.³⁸⁸ Two α -KG dependent non-heme iron enzymes, ϵ -N-trimethyl-L-lysine hydroxylase (EC 1.14.11.8) and γ -butyrobetaine hydroxylase (EC 1.14.11.1), are critical in the fatty acid biosynthesis.^{389,390} Thymine 7-hydroxylase (EC 1.14.11.6) and pyrimidine deoxyribonucleoside 2'-hydroxylase (EC 1.14.11.3) are important enzymes in pyrimidine metabolism.^{391,392} 2,4-Dichlorophenoxyacetic acid (2,4-D)/ α -KG dioxygenase (TfdA) catalyzes the first step in catabolism of the broadleaf herbicide 2,4-D to form 2,4-dichlorophenol and glyoxylic acid, a reaction thought to proceed via hydroxylation at the 2,4-D methylene group followed by spontaneous breakdown of the hemiacetal product.^{393,394} Most α -KG-dependent iron enzymes are hydroxylases; they catalyze the coupled reaction of hydroxylation of an unactivated C-H bond in a substrate and the oxidative decarboxylation of the cosubstrate α -KG, leading to succinate and CO₂. One atom of dioxygen is incorporated as the hydroxyl group of the product and the other into the carbox-

Scheme 14



ylate group of succinate (Scheme 14). However, some members of this class can catalyze other oxidative reactions of substrate and some are multifunctional. In addition to hydroxylation of thymine to 5-hydroxymethyluracil, thymine 7-hydroxylase catalyzes the following two oxidation steps to form 5-formyl uracil and uracil-5-carboxylic acid.^{391,395} Deacetoxycephalosporin C synthase (DAOCS) catalyzes the first committed step in the biosynthesis of antibiotic cephalosporin, the expansion of the five-membered thiazolidine ring of penicillin N to deacetoxycephalosporin C which contains the characteristic six-membered cepham ring.³⁹⁶ Another important α -KG-dependent iron enzyme in antibiotic biosynthesis is clavamate synthase 2 (CS2), which catalyzes three reactions: (1) the normal hydroxylation of deoxyguanidinoproclavaminc acid (DGPC) to guanidinoproclavaminc acid, (2) oxidative cyclization of proclavaminc acid (PC), and (3) desaturation of dihydroclavaminc acid to clavamic acid (Table 1).^{397–399} In the non-oxygenation reactions, one atom of dioxygen is reduced to water with the two-electron oxidation of the substrate (Scheme 14).

All α -KG-dependent non-heme iron enzymes require ferrous ion, α -KG, and O_2 for reactivity but have different quaternary structures.³⁸³ Prolyl 4-hydroxylase from all animal sources consists of $\alpha_2\beta_2$ subunits with MW = 64 and 60 kDa, respectively.³⁸⁶ Each α -subunit contains one catalytic active site while the role of the β -subunit is complex and multifunctional. Lysyl hydroxylase is a homodimer (α_2) with a total MW = 85 kDa.³⁸³ The active form of DAOCS is a monomer with MW = 34.5 kDa.⁴⁰⁰ CS2 is a monomer of MW = 36 kDa.^{401,402}

Amino acid sequence alignment among the α -KG-dependent iron enzymes shows that only a subclass of these enzymes share high sequence homology.^{385,403} A common motif HisXAspX(53–57)His is found in this subclass. Utilizing site-directed mutagenesis, this motif has been identified as part of the iron-binding site.^{403–405} About 10 amino acid residues from the second histidine in this motif the residues ArgXSer are highly conserved and may be part of the α -KG binding site.^{403–405} These common motifs are also conserved in two non-heme iron enzymes which are not dependent on α -KG: isopenicillin N-synthase (IPNS) and 1-amino-1-cyclopropane carboxylic acid (ACC) oxidase (ACCO, also known as ethylene-forming-enzyme, EFE).⁴⁰³

IPNS plays a key role in antibiotic synthesis in a variety of microorganisms. It catalyzes the transformation of a tripeptide δ -(L- α -aminoadipoyl)-L-cysteiny-D-valine (ACV) into isopenicillin N.^{406,407} In this reaction, substrate ACV is oxidized by four electrons with ring closure and one molecule of dioxygen is

reduced to two water molecules (Table 1). Ethylene is an important messenger molecule in higher plants involved in the wounding and senescence of leaves and flowers, seed germination, and fruit ripening.^{408,409} The final step in the biosynthesis of ethylene is catalyzed by ACCO.^{410,411} Substrate ACC is oxidatively fragmented to form ethylene with concomitant oxidation of the cosubstrate ascorbate to dehydroascorbate (Table 1).⁴¹²

Kinetics. No pre-steady-state kinetic study has appeared for this class of enzymes. Steady-state kinetic studies on prolyl hydroxylase favor an ordered sequential mechanism with the binding of Fe^{II} followed by the sequential binding of α -KG, O_2 , and substrate.^{413,414} In contrast, similar studies on thymine hydroxylase also indicate a sequential ordered mechanism but with substrate binding before O_2 .^{391,395} This difference may be due to the fact that prolyl hydroxylase can catalyze the uncoupled α -KG decarboxylation reaction (vide infra) in the absence of substrate,^{413,415} which complicates the kinetic analysis. Thymine 7-hydroxylase is unable to catalyze the uncoupled reaction unless a substrate analogue is present.^{395,416}

Many enzymes in this class catalyze the reaction where α -KG decarboxylation is uncoupled from the substrate oxidation, either in the absence of substrate or in the presence of a substrate analogue.^{413,415–418} This uncoupled reaction can also occur to a significant extent in the presence of substrate, as demonstrated, for example, by the fact that the formation of CO_2 from decarboxylation of α -KG exceeds substrate formation by 20% for human γ -butyrobetaine hydroxylase.⁴¹⁶ The uncoupled reaction usually leads to enzyme deactivation. The deactivation has an unknown mechanism but possibly results in the oxidation of Fe^{II} to the inactive Fe^{III} form.⁴¹⁹ Ascorbate is usually added in vitro to obtain full catalytic activity, possibly by acting as an alternative electron source in the uncoupled reaction, thus preventing deactivation. It is consumed substoichiometrically in the normal reaction^{415,420} and stoichiometrically⁴¹⁹ in the uncoupled reaction.

Structure. The first crystal structure of an α -KG-dependent iron enzyme was recently reported for DAOCS.⁴²¹ Three forms have been published (Figure 35): apo (i.e., metal removed) DAOCS (PDB ID: 1DCS), the DAOCS complex with Fe^{II} (PDB ID: 1RXF), and the complex of DAOCS with Fe^{II} and α -KG (PDB ID: 1RXG). The overall folding of a jelly roll flanked with helices is the same for all three structures, except that the apo DAOCS exists as a trimer but dissociates into monomers when Fe^{II} and/or α -KG bind. In the DAOCS/ Fe^{II} complex, the Fe^{II} is 6C, ligated by His183, His243, Asp185 (monodentate), and three water molecules. In the DAOCS/ Fe^{II} / α -KG, the cosubstrate binds in a bidentate manner through its 1-carboxylate and 2-oxo groups, replacing two of the water molecules in a new 6C species, consistent with spectroscopic studies on CS2 (vide infra). The 5-carboxylate group of α -KG forms a salt bridge with Arg258 and is H-bonded to Ser260. Both the Fe^{II} endogenous ligands and the α -KG anchors, Arg258 and Ser260, are consistent with sequence alignment.⁴⁰³

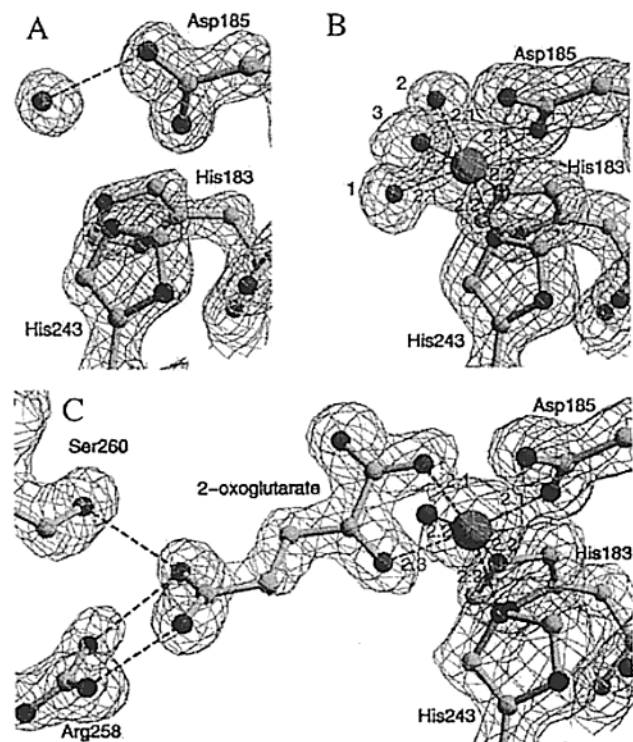


Figure 35. Structure of the active site in DAOCS: (A) the apoenzyme; (B) the complex of DAOCS/Fe^{II}; and (C) the complex of DAOCS/Fe^{II}/α-KG. (Reprinted with permission from Nature (ref 421). Copyright 1998 Macmillan Magazines Ltd.)

Crystal structures of the Mn^{II}-substituted IPNS (PDB ID: 1IPS) as well as structures of the IPNS/Fe^{II}/ACV (PDB ID: 1BK0) and IPNS/Fe^{II}/NO/ACV (PDB ID: 1BLZ) complexes have been reported.^{403,422} IPNS and DAOCS share a common jelly roll β-strand motif where the active site is located. In the IPNS/Mn^{II} structure (Figure 36A), the metal is coordinated by His214, Asp216 (monodentate), His270, Gln330, and two water molecules. In the IPNS/Fe^{II}/ACV structure (Figure 36B), ACV is bound rigidly and is held in a conformation approaching that required for β-lactam formation. The thiolate group of ACV binds directly to the Fe^{II} ion, replacing Gln330. Further, a water molecule trans to Asp216 is lost and Fe^{II} goes 5C. The open coordination site is protected from the binding of a water molecule by the ACV-derived valine isopropyl group. The carboxylate of the valine residue of ACV is H-bonded to Arg279 and Ser281, which through sequence alignment correspond to Arg258 and Ser260 in DAOCS (vide supra). In the IPNS/Fe^{II}/NO/ACV complex (Figure 36C), the NO molecule occupies the open coordination position of the IPNS/Fe^{II}/ACV complex. The oxygen atom of the NO molecule is at an equal distance from both the valine nitrogen and the cysteinyl β-carbon, which must each lose one hydrogen atom to close the β-lactam ring. There is no crystal structure presently available for ACCO.

Spectroscopy. Early EPR studies of prolyl hydroxylase showed an EPR signal at $g = 4.3$,⁴²³ which most certainly came from the inactive high-spin Fe^{III} form of the enzyme. EPR and electron spin-echo envelope modulation (ESEEM) studies on Cu^{II}-substituted TfdA were interpreted as the Cu^{II} oc-

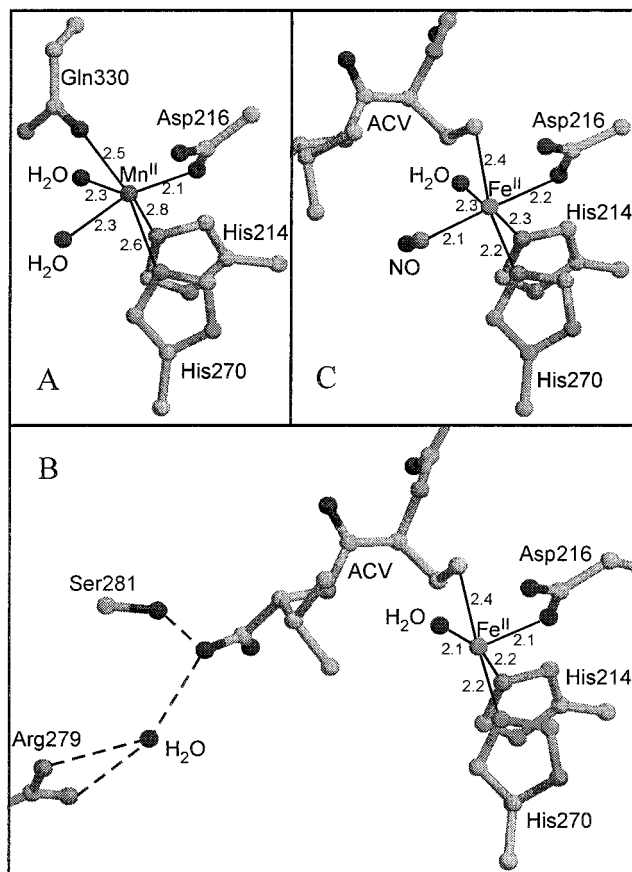


Figure 36. Structure of the active site in IPNS. (A) The complex of IPNS/Mn^{II}. (B) The complex of IPNS/Fe^{II}/ACV. (C) The complex of IPNS/Fe^{II}/ACV/NO. (Structures generated using the crystallographic coordinates from PDB files 1IPS, 1BK0, and 1BLZ, respectively.)

cupying the Fe^{II} binding site and coordinated by two endogenous histidine ligands and four other endogenous or exogenous ligands.⁴²⁴ CD and MCD studies on CS2 provide the first direct spectroscopic information about the nature of the catalytically relevant Fe^{II} active site in an α-KG-dependent iron enzyme.⁴²⁵ A near-IR CD titration demonstrated stoichiometric binding of Fe^{II} to the apo enzyme ($K_m > 5000 \text{ M}^{-1}$). Near-IR MCD of the CS2/Fe^{II} complex (Figure 37A) showed two $d \rightarrow d$ bands at ~ 9000 and $11\,000 \text{ cm}^{-1}$, indicating a distorted 6C ferrous active site. This was subsequently supported by X-ray crystallographic studies on DAOCS/Fe^{II} (vide supra).

The interaction of α-KG with CS2 was also studied by CD titrations, which showed that the affinity of α-KG binding is higher when Fe^{II} is present.⁴²⁵ The CS2/Fe^{II}/α-KG complex shows two $d \rightarrow d$ bands at ~ 8700 and $10\,400 \text{ cm}^{-1}$ in the near-IR MCD spectra (Figure 37B) and a broad CT band from $16\,000$ to $26\,000 \text{ cm}^{-1}$ as well as an α-KG $n \rightarrow \pi^*$ band at $28\,000 \text{ cm}^{-1}$ in the UV-vis absorption/CD/MCD spectra (Figure 38). VTVH MCD of this complex (Figure 37E) showed a smaller ZFS than resting CS2/Fe^{II} (Figure 37D) and thus a larger $^5T_{2g}$ ground-state splitting, indicating the presence of a strong π interaction between α-KG and Fe^{II} (Figure 37G). The metal-to-ligand CT (MLCT) absorption intensity in Figure 38 requires direct orbital overlap between α-KG and Fe^{II}, which requires that α-KG must bind

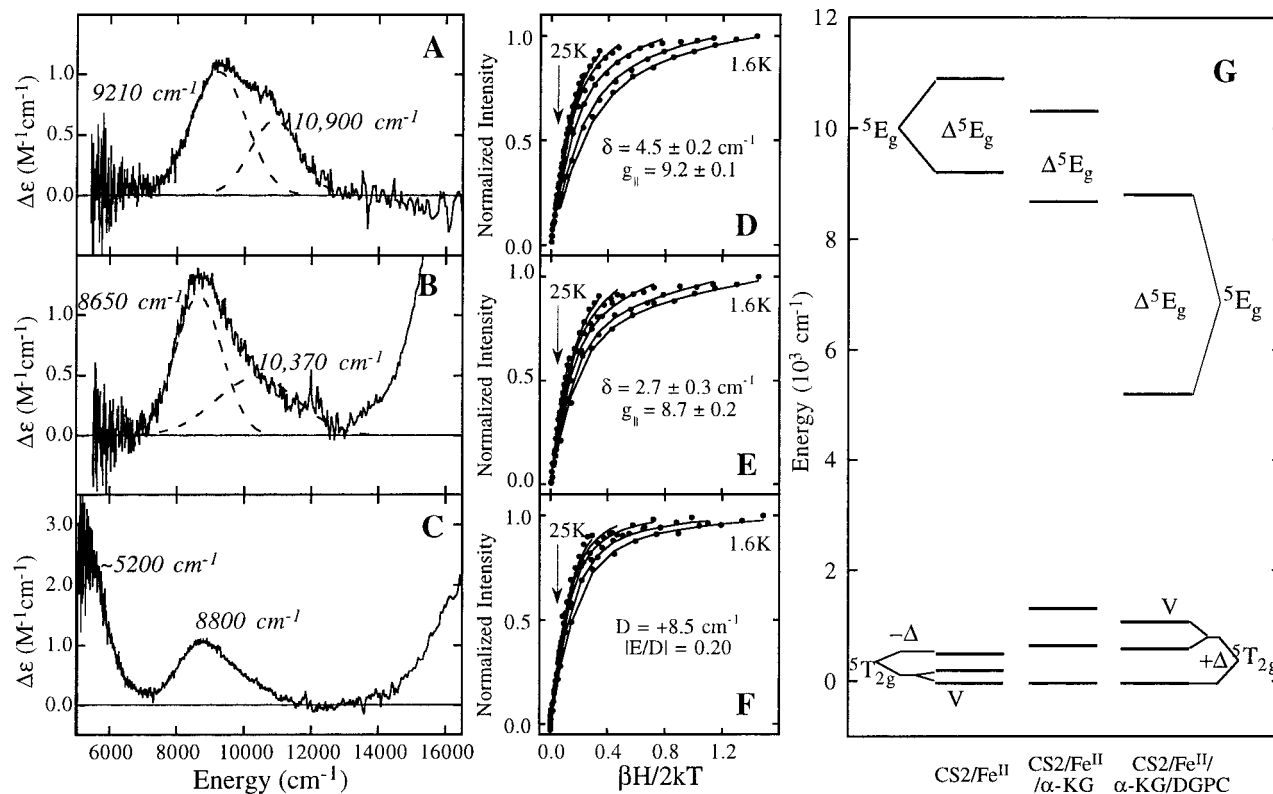


Figure 37. (A) MCD spectrum and its Gaussian components of CS2/Fe^{II}. (B) MCD spectrum and its Gaussian components of CS2/Fe^{II}/α-KG. (C) MCD spectrum of CS2/Fe^{II}/α-KG/DGPC. (D) VTVH MCD data at 9200 cm^{-1} (●) and its best fit (—) for CS2/Fe^{II}. (E) VTVH MCD data at 8550 cm^{-1} (●) and its best fit (—) for CS2/Fe^{II}/α-KG. (F) VTVH MCD data at 6060 cm^{-1} (●) and its best fit (—) for CS2/Fe^{II}/α-KG/DGPC. (G) The d-orbital energy level diagram for the complexes of CS2/Fe^{II}, CS2/Fe^{II}/α-KG, and CS2/Fe^{II}/α-KG/DGPC. (Adapted from refs 425 and 429.)

directly to Fe^{II}. The MLCT intensity also indicates that there is π -back-bonding from the Fe^{II} t_{2g} orbitals into the α-KG π^* orbital. This back-bonding may play a role in activating α-KG for reaction with oxygen by imparting some radical character. The $n \rightarrow \pi^*$ transition of α-KG shifts from 29 000 to 28 000 cm^{-1} upon Fe^{II} binding (Figure 38B), which indicates that the α-keto carboxylate moiety of α-KG becomes much more planar when α-KG binds to Fe^{II}. The above analysis and the comparison with model complexes⁴²⁶ demonstrate that α-KG binds to Fe^{II} in a bidentate fashion producing a new 6C site. Early biochemical studies^{427,428} using a series of α-KG analogues speculated this binding mode, which has also been confirmed by the later crystallographic studies on DAOCS (vide supra). EPR and ESEEM studies on the α-KG interaction with TfdA/Cu^{II} indicated a monodentate binding mode of α-KG.⁴²⁴

Insight into substrate interactions with the Fe^{II} active site also comes from CD/MCD studies.⁴²⁹ When α-KG is absent, binding of the hydroxylation substrate DGPC does not perturb the CD/MCD spectra of the iron site, but when α-KG is present, dramatic changes occur to the spectra: a new $d \rightarrow d$ band at ~5200 cm^{-1} and another at ~8800 cm^{-1} appear (Figures 39 and 37C), indicating the formation of a 5C species. The VTVH MCD data of the complex of CS2/Fe^{II}/α-KG/DGPC (Figure 37F) are best described by a +ZFS model, which indicates that the 5C site is a strong axial, square-pyramidal Fe^{II} site. The MLCT and $n \rightarrow \pi^*$ transitions remain, indicating that α-KG

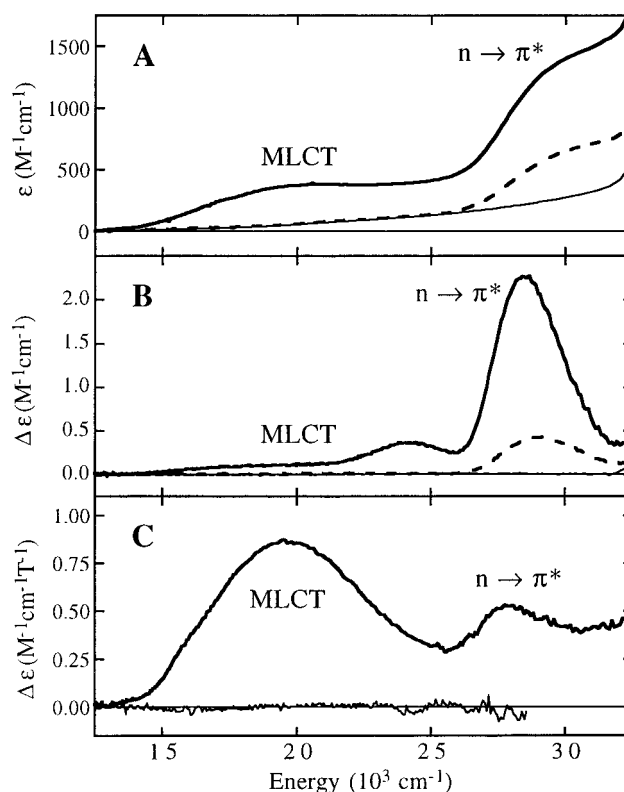


Figure 38. UV-vis absorption (A), CD (B), and MCD (C) spectra of apo-CS2 (light solid line), the complex of CS2/α-KG (dashed line), and the complex of CS2/Fe^{II}/α-KG (heavy solid line). (Adapted from ref 425.)

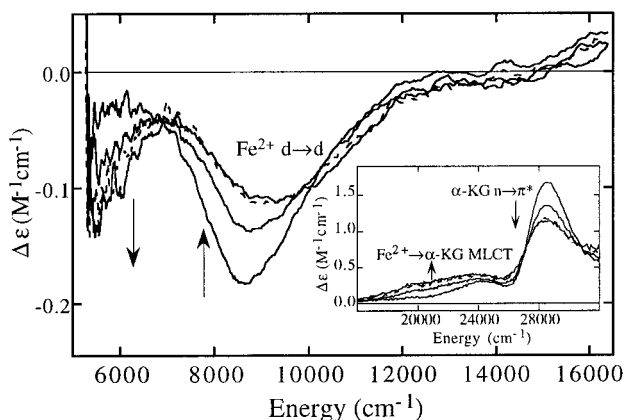


Figure 39. Near-IR CD titration studies of DGPC substrate binding with the CS2/Fe^{II}/α-KG complex at 277 K. Inset: corresponding CD titration spectra in the UV-vis region. (Reprinted with permission from ref 429. Copyright 1998 American Chemical Society.)

still binds to Fe^{II} in a bidentate fashion when the DGPC substrate is bound to the active site (Figure 39, inset). From the asymmetrical shape of the high-energy d → d band at ~8800 cm⁻¹ (Figure 37C) and the different VTVH behavior observed for the two sides of this band (data not shown), it is concluded that a small amount of 6C Fe^{II} species is also present upon substrate binding.⁴³⁰ This may correlate to the fact that the uncoupled reaction occurs even in the presence of substrate at saturating concentration. The effect of PC cyclization substrate binding on the Fe^{II} active site is similar to that of DGPC: a similar 5C site is formed where α-KG remains bound in a bidentate mode.⁴³⁰ This suggests that the hydroxyl group of PC does not coordinate directly to the Fe^{II} and a similar 5C site is formed for both the hydroxylation reaction and the cyclization reaction. There is also a small amount of 6C component present upon PC substrate binding.

Mössbauer spectroscopic studies demonstrated that resting IPNS/Fe^{II} is 6C high-spin Fe^{II}.³⁶ NMR studies on Fe^{II}- or Co^{II}-substituted IPNS identified three nitrogen ligands and a carboxylate ligand.⁴³¹ Two histidine residues were observed by ESEEM on the Cu^{II} complex of IPNS.⁴³² The IPNS/Fe^{II}/NO complex shows a *S* = 3/2 EPR signal (*E/D* = 0.015) which becomes more rhombic (*E/D* = 0.035) when ACV substrate binds.³⁶ The absorption spectrum of the IPNS/Cu^{II}/

ACV complex shows a strong 390 nm band which is assigned as a thiolate-to-Cu^{II} CT transition, indicating ACV may directly bind to the metal.⁴³³ EXAFS on the complex of IPNS/Fe^{II}/ACV indicated a sulfur scatterer at 2.3 Å, and EXAFS studies on the IPNS/Fe^{II}/ACV/NO complex showed evidence of a 1.76 Å scatterer which is assigned to the bound NO.⁴³⁴ These results demonstrate that substrate directly binds to Fe^{II} through the thiolate ligand, which was confirmed by later crystallographic studies (vide supra).⁴⁰³

The first spectroscopic study on ACCO has recently been published using EPR and electron nuclear double resonance (ENDOR) on the ACCO/Fe^{II}/NO/ACC complex.⁴³⁵ The data indicate that in contrast to the α-KG-dependent enzymes, substrate ACC binds directly to the iron through both the amino and the carboxylate groups, in a bidentate mode. Cosubstrate ascorbate does not directly bind to the Fe^{II}.

Molecular Mechanism. As early as 1982, when information on the Fe^{II} coordination environment was very limited, a hypothetical molecular mechanism was proposed for prolyl hydroxylase.⁴³⁶ In light of the recent spectroscopic data on CS2^{425,429,430} and crystallographic studies on DAOCS,⁴²¹ a detailed catalytic mechanism of the α-KG enzymes can be developed (Figure 40). Fe^{II} binds at the active site to form a 6C distorted octahedral site with a coordinatively saturated environment so that it is relatively unreactive toward dioxygen. Cosubstrate α-KG binds in a bidentate fashion to Fe^{II} through its 1-carboxylate and 2-keto groups, forming a nearly planar five-membered ring with the iron. The Fe^{II} site is still 6C and relatively unreactive toward O₂, thus limiting the rate of the uncoupled reaction. Prior to the O₂ reaction, substrate binds to the active site in the proximity of the Fe^{II} ion and the interaction of substrate with the protein matrix results in the dissociation of an Fe^{II} ligand, forming a 5C site with an approximately square-pyramidal geometry. The fact that the open coordination position at the Fe^{II} site only becomes available when both substrate and cosubstrate are present supplies a critical coupling mechanism for the decarboxylation of α-KG and hydroxylation (or oxidation) of substrate. Substrate analogues which bind in a similar manner as the substrate but cannot be hydroxylated or oxidized could also result in an open coordination position, thus facilitating the uncoupled reaction.

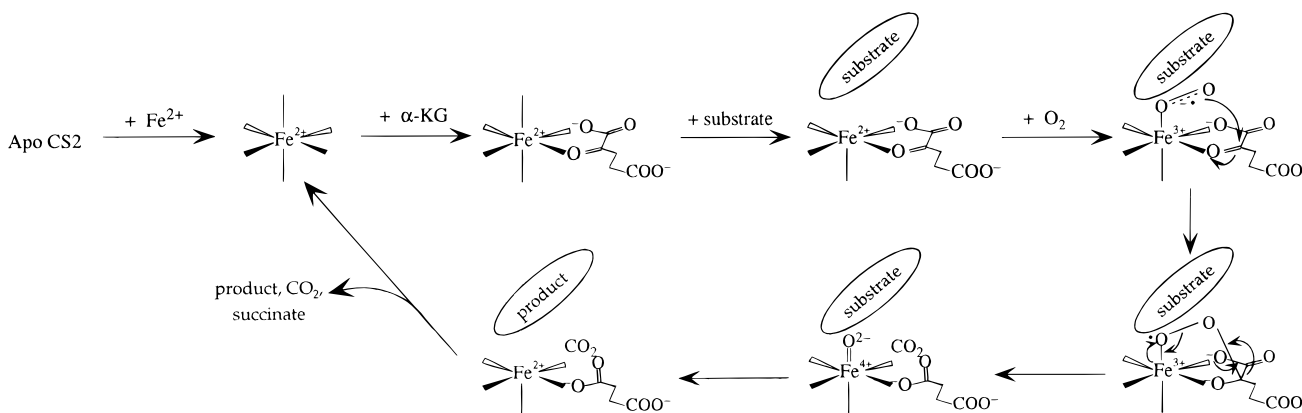


Figure 40. Possible catalytic mechanism for α-KG-dependent non-heme iron enzymes.

O₂ would then react at the open coordination position on the 5C Fe^{II} in a coupled reaction. There would be partial electron transfer (ET) from Fe^{II} to O₂ giving O₂ some superoxo radical anion character (O₂⁻). This would activate O₂ for nucleophilic attack at the α-keto carbon, as indicated by oxygen isotope labeling. This process is facilitated by the low-energy lowest unoccupied molecular orbital (LUMO) π* of the planar α-keto-carboxylate moiety of α-KG in the coordinated structure. The resulting bridged intermediate (Figure 40, bottom right) could undergo a concerted decarboxylation of α-KG and a heterolytic cleavage of the O–O bond, forming an oxo-ferryl (Fe^{IV}=O^{-II}) intermediate. The formation of CO₂ is probably the first irreversible step and the driving force up to this stage of the reaction. An oxo-ferryl intermediate could abstract a hydrogen atom from the substrate and then hydroxylate it in a rebound mechanism or abstract a second hydrogen atom from the substrate, thus producing water and a desaturation product.³⁸⁴ In this model, the hydrogen-atom abstraction step follows the decarboxylation, which is consistent with the deuterium isotopic effects observed for thymine 7-hydroxylase which indicate that an irreversible step (or steps) occurs prior to the C–H bond breaking.³⁹⁵ It has also been shown for prolyl 4-hydroxylase that a substrate-derived radical is generated in the reaction, which is consistent with a rebound mechanism.⁴³⁷ It is important to point out that no oxygen intermediate (i.e., bridged superoxo or oxo-ferryl) has been observed for any α-KG-dependent enzyme. This warrants future theoretical and experimental study.

A detailed molecular mechanism has been proposed for IPNS based on spectroscopic and crystallographic studies.⁴²² Resting IPNS/Fe^{II} is also 6C and thus relatively stable toward dioxygen. Substrate ACV binds directly to Fe^{II} IPNS through its thiolate group, providing an open coordination position at the Fe^{II}. O₂ can then react to form an Fe^{III}-superoxo intermediate. This intermediate is suggested⁴²² to perform the first hydrogen-atom abstraction step and close the β-lactam ring, resulting in the formation of the first water molecule and generating an Fe^{IV}=O^{-II} intermediate, which completes the second ring-closure process by hydrogen-atom abstraction forming a thiazolidine ring.

Previously proposed mechanisms of ACCO involved direct binding of cosubstrate ascorbate to the iron before O₂ as part of the oxygen activation process.^{438,439} The EPR and ESEEM studies of the NO complex of ACCO suggested a quite different molecular mechanism for ACCO.⁴³⁵ An Fe^{III}-superoxo intermediate is proposed. Whether it is preceded by a 6C → 5C process with substrate binding is presently under study.⁴⁴⁰ This intermediate is thought to initiate a radical process by single hydrogen-atom abstraction or electron-coupled proton transfer (PT) from the bound amino group. The resulting substrate radical may undergo spontaneous conversion into products. The role of cosubstrate ascorbate is proposed to reduce the toxic peroxo byproduct to water. Alternatively, the two-electron reduction of Fe^{III}-superoxo by the cosubstrate ascorbate could result

in an Fe^{IV}=O^{-II} intermediate which initiates the radical reaction.⁴³⁵

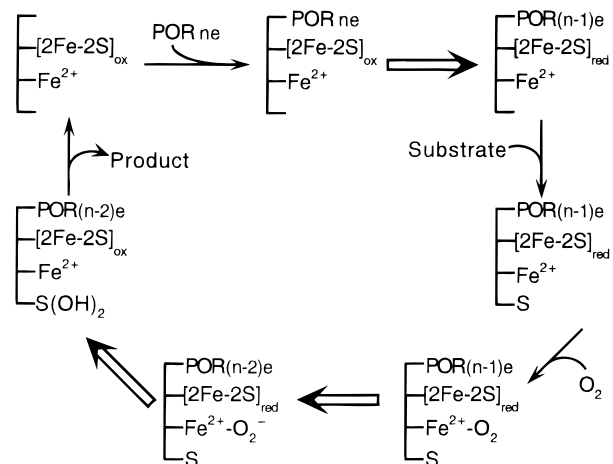
4. Rieske-Type Dioxygenases

Biochemical Characterization. The Rieske iron-sulfur center is a two iron–two sulfur cluster ([2Fe–2S]) which has a 2His (on one iron), 2Cys (on the other iron) coordination environment, instead of the 4Cys present in plant ferredoxins. It plays a key role in the electron transport pathway in membrane-bound cytochrome complexes as well as in some dioxygenases.⁴⁴¹ The latter are mainly comprised of two protein components: a reductase containing flavin and a ferredoxin [2Fe–2S], and a terminal oxygenase containing a Rieske [2Fe–2S] cluster and a non-heme iron active site.⁴⁴² Except for the recently reported alkene monooxygenase that has a binuclear iron site in its terminal oxygenase,¹⁰ most of the Rieske-type oxygenases have a mononuclear iron site, which is believed to be the site of dioxygen activation and substrate oxygenation.^{442,443} The majority of the Rieske-type mononuclear non-heme oxygenases form a family of enzymes which are aromatic-ring-hydroxylating dioxygenases. These catalyze the regio- and stereospecific *cis*-dihydroxylation of an aromatic ring using dioxygen and NAD(P)H (Table 1). Examples include benzene dioxygenase (BDO, EC 1.14.12.3),⁴⁴⁴ phthalate dioxygenase (PDO, EC 1.14.12.7),⁴⁴⁵ toluene dioxygenase (EC 1.14.12.11),⁴⁴⁶ and naphthalene 1,2-dioxygenase (NDO, EC 1.14.12.12),⁴⁴⁷ which initiate the aerobic degradation of aromatic compounds in the soil bacteria and are targets for bioengineering in bioremediation. This step is the first step in the pathway that ultimately leads to ring cleavage by the intra- and extradiol dioxygenases (sections II.B.2 and II.C.1).⁴⁴³ Besides these bacterial dioxygenases, other Rieske-type mononuclear non-heme oxygenases include anthranilate 1,2-dioxygenase (EC 1.14.12.1),⁴⁴⁸ which deaminates and decarboxylates the substrate to produce catechol; chlorophenylacetate 3,4-dioxygenase (EC 1.14.2.13),⁴⁴⁹ which converts substrate to catechol with chloride elimination; and 4-methoxybenzoate *O*-demethylase (putidamonooxin),⁴⁵⁰ which catalyzes the conversion of 4-methoxybenzoic acid to 4-hydroxybenzoic acid and formaldehyde.

The reductase component is usually a monomer (MW = 12–15 kDa) and utilizes flavin to mediate ET from the two-electron donor NAD(P)H to the one-electron acceptor [2Fe–2S] cluster and is specific to each terminal oxygenase; other electron donors do not support efficient oxygenation.⁴⁴² The crystal structure of phthalate dioxygenase reductase is available.⁴⁵¹

The terminal oxygenases are large protein aggregates (MW = 150–200 kDa) containing either multiples of α subunits (BDO α₂, PDO α₄) or an equimolar combination of α and β subunits (toluene dioxygenase α₂β₂, NDO α₃β₃).⁴⁴² The α subunits contain a Rieske [2Fe–2S] cluster and a catalytic non-heme Fe^{II} center. β subunits do not seem to be involved in the catalytic function (vide infra).

Kinetics. Steady-state kinetic studies coupled with various rapid reaction studies of the partial reactions of PDO allowed Ballou et al. to propose a kinetic scheme (Scheme 15).⁴⁴³ On the basis of steady state

Scheme 15^a

^a Abbreviations: POR, phthalate oxygenase reductase; S, substrate, and S(OH)₂, product; *ne*, electrons at POR, *n* = 2, 3. (Taken from phthalate oxygenase, a Rieske iron–sulfur protein from *Pseudomonas cepacia*, by Ballou, D.; Batie, C. In *Oxidase and Related Redox Systems*; Alan R. Liss, Inc.: New York, 1988. Reprinted with permission from Wiley-Liss, Inc., a subsidiary of John Wiley & Sons, Inc.)

studies employing varying concentrations of each component, it is found that the reduced form of the reductase binds to PDO. The substrate binds to PDO after the Rieske cluster is reduced by the bound reductase, which is consistent with the fact that PDO is reduced by the reductase at a similar rate whether substrate is present. Dioxygen reacts after substrate binds, which is consistent with the fact that PDO is relatively unreactive toward dioxygen in the absence of reductase and substrate.

Recent biochemical studies on NDO found that H₂O₂ was released when benzene was used as a substrate analogue, indicating an uncoupling of the reduction of O₂ and substrate dihydroxylation.⁴⁵² Similar uncoupling reactions are observed for both pterin- and α-KG-dependent non-heme iron enzymes (sections II.C.2 and II.C.3, respectively).

Structure. The structure of NDO (PDB ID: 1NDO) was solved at 2.25 Å resolution.⁴⁵³ The enzyme is a hetero hexamer (α₃β₃) and has an overall mushroom shape; the three β subunits form the stem, while the three α subunits form the cap (Figure 41A). Each α subunit contains both a Rieske [2Fe–2S] cluster and a mononuclear Fe site, the distance between which is about 44 Å (Figure 41A). In the Rieske cluster, Fe1 is coordinated by Cys81 and Cys101 and Fe2 by His83 and His104 through their Nδ atom (Figure 41B), consistent with various spectroscopic studies (vide infra). The mononuclear iron, whose oxidation state was not determined, is coordinated by His208, His213, a bidentate Asp362, and a water molecule in a distorted octahedral geometry with one ligand apparently missing (Figure 41B). Interestingly, Asn201 is located along the open ligand position at a distance of 3.75 Å. Asn201 is at the bottom of a narrow gorge, which is lined by hydrophobic residues and is proposed to function in substrate binding. In a recent report,⁴⁵⁴ the refinement of the structure showed that an indole-oxygen intermediate occupies the substrate-binding channel and directly coordi-

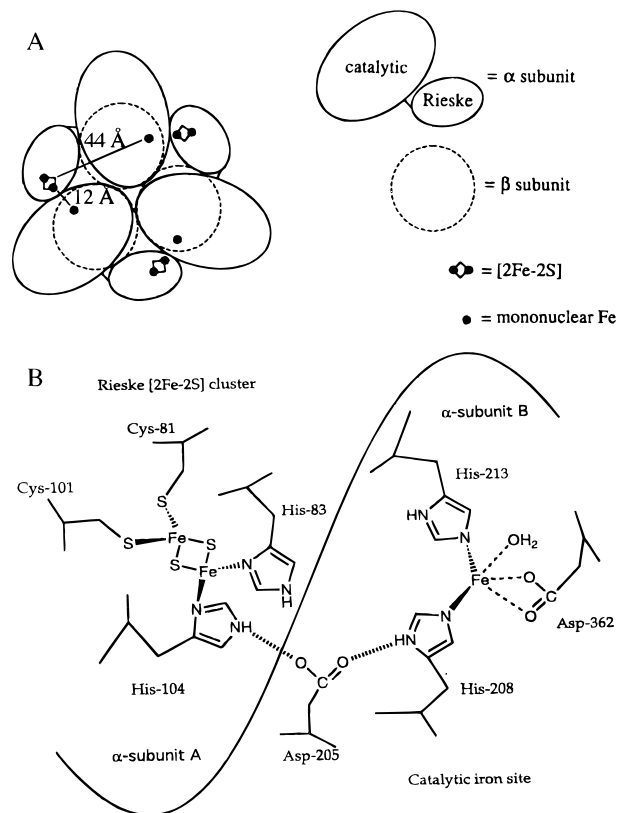


Figure 41. (A) Schematic overall protein structure of NDO showing α and β subunits and the inter- and intra-subunit distance between the Rieske site and the non-heme iron site. (Reprinted with permission from ref 1010. Copyright 1999 Data Trace Publishing Company.) (B) Schematic structure of the Rieske site, the non-heme iron site, and the proposed route of ET between them in NDO. (Adapted from ref 453. Revised by the author.)

nates to the iron atom, whose oxidation state is unknown. Asp205 is H-bonded to the non-heme iron ligand His208 in the same α subunit, as well as to the His104 ligand at the Rieske [2Fe–2S] cluster in a neighboring subunit (Figure 41B). The distance between the Rieske cluster and non-heme iron of the neighboring subunit site is about 12 Å (Figure 41A). From site-directed mutagenesis,⁴⁵⁵ Asp205 plays a key role in ET from the Rieske center to the non-heme iron center during catalysis. A depression close to the Rieske cluster was proposed to be the site for reductase docking.⁴⁵³

Spectroscopy. Many spectroscopic studies have been published on the Rieske cluster in PDO^{456–461} and BDO.^{462,463} The oxidized Rieske cluster [Fe^{III}, Fe^{III}] has strong antiferromagnetic coupling between the two Fe^{III} atoms and thus is diamagnetic (*S*_{tot} = 0) and EPR silent (section III.A.1). The reduced Rieske cluster is paramagnetic (*S*_{tot} = 1/2) due to antiferromagnetic coupling of the localized [Fe^{III}, Fe^{II}] center (*S*₁ = 5/2, *S*₂ = 2) and shows an EPR signal with *g*_z = 2.01–2.02, *g*_y = 1.91–1.92, and *g*_x = 1.72–1.80.⁴⁴¹ Mössbauer spectroscopy⁴⁶⁴ on the reduced Rieske cluster suggested that two noncysteine ligands coordinate to the Fe^{II}, which ENDOR⁴⁶⁵ indicated to be two histidine residues, consistent with the X-ray structure of NDO (vide supra). EXAFS and XANES spectroscopies demonstrated that the Rieske cluster was different in the reduced and oxidized states but

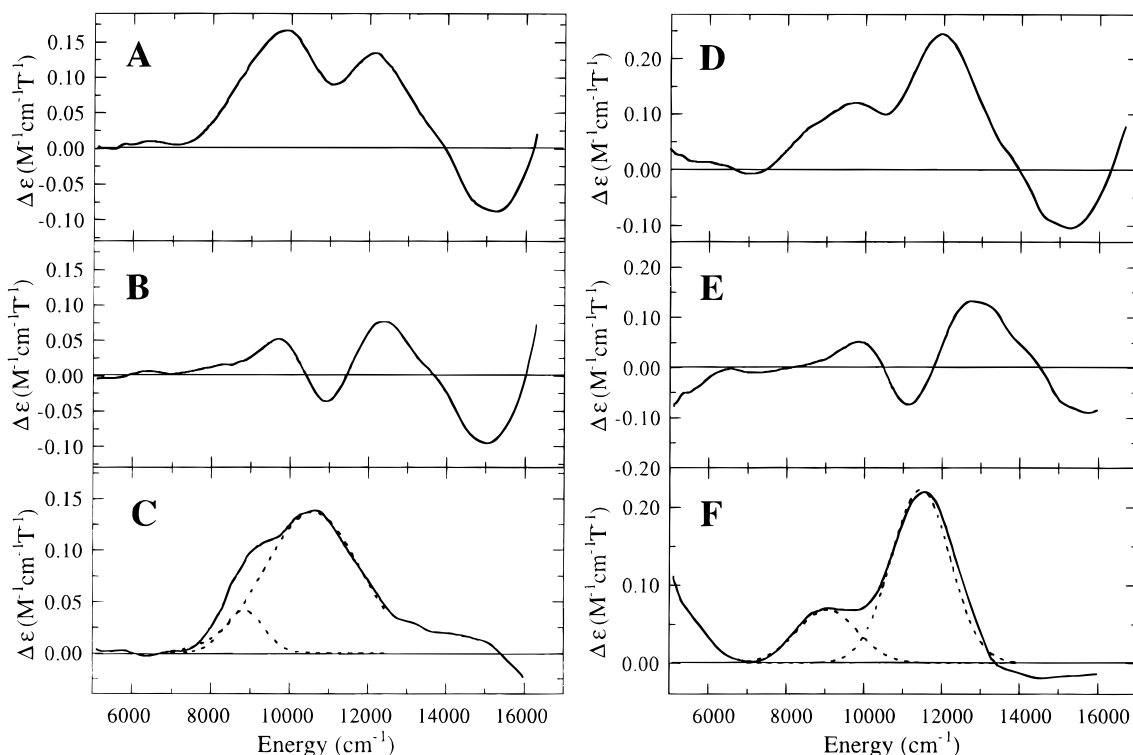


Figure 42. (A) LT MCD spectrum of FePDO. (B) MCD spectrum of the corresponding apoPDO with the Rieske site oxidized. (C) Difference MCD spectrum of FePDO minus apoPDO with the best Gaussian fit. (D) MCD spectrum of the complex of FePDO/phthalate (5 equiv). (E) MCD spectrum of the complex of apoPDO/phthalate (5 equiv) with the Rieske site oxidized. (F) Difference MCD spectrum of FePDO + 5 × phthalate minus the apoPDO/phthalate (5 equiv) with the best Gaussian fit. (Adapted from ref 468.)

not affected by substrate or iron binding at the non-heme site.^{460,461}

Less spectroscopy has been done on the mononuclear non-heme Fe^{II} site. This reflects the fact that the high-spin Fe^{II} site is less spectroscopically accessible than the Rieske cluster and is obscured by the cluster's dominant spectroscopic features. EXAFS and XANES on Co^{II}-substituted (at the non-heme site) PDO indicated a 6C site for the metal ion and that the oxidation state of the Rieske center has only a very small effect on the non-heme site.⁴⁶⁶ Recent EPR studies on Cu^{II}-substituted (at the non-heme site) PDO using ⁶³Cu and ¹⁵N enabled analysis of the Cu^{II} superhyperfine structure which identified two histidine ligands coordinated to the metal.⁴⁶⁷ MCD is complicated by the reduced Rieske center which is paramagnetic and has an intense MCD *C*-term (vide supra). However, the diamagnetic oxidized Rieske center exhibits no MCD *C*-term and allows the measurement of the temperature-dependent MCD spectra of the non-heme iron center. The MCD spectrum of the non-heme Fe^{II} LF region could then be obtained by subtraction of the temperature-independent Rieske background. This was achieved by using the spectrum of the corresponding apo-enzyme (non-heme site depleted) with its Rieske center oxidized as reference.⁴⁶⁸ Figure 42 shows the MCD spectra of PDO with its oxidized Rieske center (A), apo PDO with the non-heme site depleted and the Rieske center oxidized (B), and the difference spectrum (C). The difference spectrum shows two bands at ~8850 and 10 600 cm⁻¹ indicating that the resting enzyme contains a 6C mononuclear high-spin

Fe^{II} ion. Also shown in Figure 42D–F are the corresponding spectra for the addition of phthalate substrate under anaerobic conditions. The difference spectrum shows the presence of three peaks at ~5000, 9070, and 11 500 cm⁻¹, which indicates that two different 5C species are formed upon substrate binding. This is consistent with the fact that in XAS studies of Co^{II}-substituted PDO the pre-edge feature increases in intensity upon substrate binding.⁴⁶⁶ From the MCD studies, it was found that azide binding to Fe^{II} is affected by the binding of the substrate, which indicated a close interaction of the substrate with Fe^{II}.⁴⁶⁸ Nuclear magnetic relaxation dispersion (NMRD) studies on Cu^{II}/Mn^{II}-substituted PDO indicated that there is a water molecule coordinated both in the absence and presence of substrate.⁴⁶⁹

Mechanism. The crystal structure and spectroscopic results provide the basis for molecular-level insight into the catalytic mechanism of this class of enzymes (Figure 43). From the spectroscopy, the resting Fe^{II} site in PDO is 6C. In the crystal structure of NDO, this site appears to be 5C with an asparagine as a distant sixth ligand. This difference may reflect experimental conditions (solution vs crystal) but may also relate to the oxidation state of the metal ion. Upon substrate binding, the MCD spectrum shows that the iron site goes 5C. It is possible that it is the neutral asparagine ligand that dissociates, as appears to also be the case for IPNS. This is in agreement with a recent crystallographic result on a possible intermediate that occupies the substrate-binding pocket near the open coordination position.⁴⁵⁴

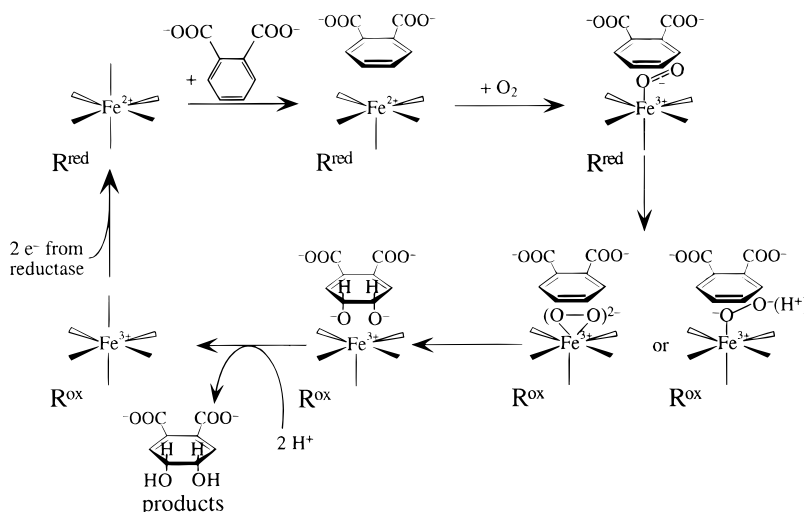


Figure 43. Possible molecular mechanism for PDO. R^{red} : reduced Rieske center. R^{ox} : oxidized Rieske center.

The open coordination site on Fe^{II} upon substrate binding appears to be critical for O_2 activation and the hydroxylation of the substrate. The O_2 reaction at this open coordination position could allow two-electron transfer (one from Fe^{II} and another from the reduced Rieske cluster) to form a peroxo or hydroperoxo intermediate at the non-heme site. The peroxo intermediate may be activated either for direct attack on the unactivated aromatic ring or for heterolytic cleavage to produce an oxo-ferryl intermediate with a bound hydroxide,⁴⁴³ resulting in *cis*-dihydroxylation.

5. Bleomycin

Biochemical Characterization. Investigation of bleomycin (BLM) as a cancer chemotherapy agent began in 1965, and this antibiotic was found to have therapeutic benefit against squamous cell carcinoma and malignant lymphoma.⁴⁷⁰ Much research has been done since then to characterize the drug clinically and chemically, and there are several extensive reviews on the latter.^{471–477} Although BLM is isolated from *Streptomyces verticillus* as a copper complex, it is administered clinically in a metal-free form to reduce irritation and is believed to cleave DNA as an Fe^{II} complex in vivo.⁴⁷⁸ (For a summary of BLM reactivity with other metals, including Cu, Co, Mn, Ru, and V, see ref 476.) The structure of this glycopeptide antibiotic is typically described as having three domains (Figure 44): the bithiazole tail, which intercalates into DNA; the sugar moiety, believed to be involved in drug uptake into cells; and the β -aminoalanine, pyrimidine, and β -hydroxyhistidine groups, collectively known as the metal-binding region. Metal ligands are shown in bold in Figure 44, although there is some controversy regarding the β -aminoalanine and/or mannose carbamoyl ligands (vide infra). Several BLM congeners that differ in the structure of the bithiazole tail terminal amine have been isolated and/or synthesized; the structure of this tail seems to affect the cytotoxicity of the drug. Tissue susceptibility to BLM is apparently dependent on levels of the detoxifying enzyme bleomycin hydrolase, which removes the carbamoylamine from the β -aminoalanine moiety.⁴⁷⁹

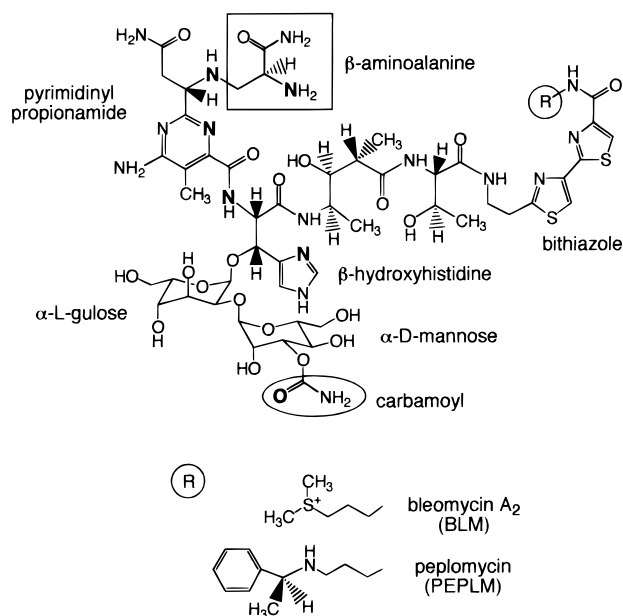


Figure 44. Structure of BLM.

BLM attacks DNA, RNA,^{480,481} cell walls,⁴⁸² and small organic molecules in vitro,^{483,484} although its major cytotoxic effect is through DNA degradation. There are two pathways of BLM-induced DNA cleavage, as shown in Figure 45.^{485–488} Both pathways begin by reaction of an activated BLM species (vide infra) with the $\text{C}4'\text{-H}$ of the deoxyribose to yield a radical centered on the sugar. This radical then reacts with O_2 in pathway A: the DNA strand is cleaved and the final products are 3'-phosphoglycolate and base propenal.⁴⁸⁹ Pathway B is O_2 -independent and yields free nucleic base and the ring-opened sugar.^{485,490} At this point the DNA strand is intact and pathway B results in strand scission only under basic conditions.

BLM preferentially cleaves duplex DNA at GpC and GpT (GpY) sites,^{491,492} where the purine 2-amino group of the DNA strand is critical to site recognition by the BLM metal-binding head.⁴⁹³ Other sites are also cleaved, in the general order of efficiency purine-pyrimidine > purine-purine > pyrimidine-pyrimidine > pyrimidine-purine.⁴⁹⁴ Sequence speci-

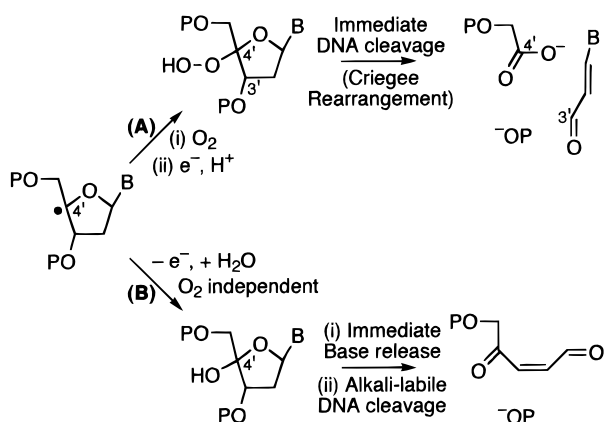


Figure 45. Pathways of DNA cleavage. (A) Immediate strand cleavage to produce base propenal and 5'-phosphate. (B) Free-base release with DNA cleavage under basic conditions, producing 3'-phosphate. (Reprinted with permission from ref 488. Copyright 1995 Elsevier Science.)

ficity, however, does appear to depend at least partially on reaction conditions.⁴⁷⁶ Closely spaced lesions in opposite strands of duplex DNA typically have strong GpY specificity in one strand but not in the other;⁴⁹⁵ thus, location of the second lesion is a consequence of the first. A mechanism has been proposed where partitioning of single-strand versus double-strand cleavage occurs from a common intermediate and for double-strand cleavage BLM must be reactivated to achieve the second break.^{496,497} For RNA degradation, fewer sites are cleaved than in DNA, not all sites have the preferred GpY sequence, cleavage is less efficient, and the mechanism of cleavage is less well understood than that of DNA.^{476,480}

Kinetics. Fe^{II}BLM alone is not competent to cleave DNA. Addition of O₂ to Fe^{II}BLM forms an intermediate, O₂-Fe^{II}BLM or $\cdot\text{O}_2^-$ -Fe^{III}BLM, referred to as oxygenated BLM ($t_{1/2} = 6$ s).^{35,498} The rate of formation of oxygenated BLM is 6.1 M⁻¹ s⁻¹, and the reaction shows first-order dependence on Fe^{II}BLM and O₂.⁴⁹⁸ In the presence of excess DNA, the rate of formation increases by approximately 3-fold and the oxygenated complex is effectively trapped.⁴⁹⁹ Consumption of oxygenated BLM is through a disproportionation reaction, where one oxygenated complex is reduced to activated BLM (ABLM), HOO-Fe^{III}BLM (vide infra), and one is oxidized to Fe^{III}BLM + O₂.⁵⁰⁰⁻⁵⁰³ ABLM is the species capable of cleaving DNA, with $t_{1/2} \approx 2$ min at 4 °C.¹⁰⁰ The formation of ABLM is a first-order reaction in oxygenated BLM, indicating that the bimolecular step in this disproportionation reaction is not rate-limiting.

BLM has an association constant with DNA on the order of 10⁵ M⁻¹,^{504,505} while estimates of the ratio of DNA base pairs to BLM in the cell nucleus are 10⁵⁻⁸:1.^{506,507} This makes it likely that once BLM enters the nucleus, virtually all of it is bound to DNA and it is the DNA-bound species that is activated.⁴⁷⁵ The rate of decay of ABLM is not influenced by the presence or absence of DNA.¹⁰⁰ ABLM can also be formed by the reaction of Fe^{III}BLM with peroxides¹⁰⁰ or other reductants⁵⁰⁸⁻⁵¹⁰ or Fe^{II}BLM with superoxide.⁵¹¹ Alternative reductants to oxygenated BLM are likely the source of ABLM in vivo.

DNA cleavage by ABLM can be broken down into several different events. ABLM reacts with the C4'-H of the deoxyribose, forming a C4' radical on the sugar.⁵¹² The 2'-*pro-R*-H from the deoxyribose is then rapidly released into solvent ($t_{1/2} = 1.8$ min).⁵¹³ Continuing pathway A from Figure 45, DNA strand cleavage follows ($t_{1/2} = 2.5-5$ min), arising from a combination of C3'-C4' and C1'-(ring-O) bond cleavages, with subsequent release of base propenal ($t_{1/2} = 6.7$ min) and formation of the 5'-phosphate ($t_{1/2} = 7.4$ min).⁵¹⁴ Additional O₂ is required for formation of the 3'-phosphoglycolate terminus, while the extra oxygen incorporated into base propenal comes from H₂O.⁵¹⁵ For pathway B, the sugar radical formed after C4'-H attack becomes oxidized to the C4'-hydroxide, with the oxygen coming from H₂O.⁵¹⁶ This rearranges with loss of nucleic base and formation of the ring-opened sugar with a C4'-ketone. Under basic conditions the damaged sugar can undergo backbone cleavage.^{509,517}

Structure. The three-dimensional structure of BLM has been interpreted from the crystal structures of the Cu^{II} complex of the BLM synthetic precursor P-3A and model complexes (Cu^{II}, Co^{III}, Zn^{II})⁵¹⁸⁻⁵²³ and from multinuclear NMR studies with and without a bound oligonucleotide.⁵²⁴⁻⁵⁴³ No crystal structure has been obtained on the complete BLM molecule. It is generally agreed that an imidazole nitrogen of β -hydroxyhistidine, the amide of β -hydroxyhistidine, a pyrimidine nitrogen, and the secondary amine of the β -aminoalanine fragment are bound to the metal in a square-planar arrangement. In terms of how the ligand wraps around the metal, two screw senses have been proposed that depend on the face upon which the axial ligand is positioned on the square plane. The identity of the axial ligands remains controversial, with much of the analysis coming from NMR studies and molecular dynamics modeling on BLM bound to metals other than Fe^{II} (typically Co^{III} and Zn^{II}). Several of the proposed binding arrangements are reproduced in Figure 46. In general, either the primary amine of the β -aminoalanine or the mannose carbamoyl nitrogen is proposed as an axial ligand, with solvent or another bound molecule occupying the sixth site. In contrast, CD and MCD studies on Fe^{II}BLM derivatives have indicated that the primary amine significantly affects the iron coordination sphere and the mannose carbamoyl group also alters the coordination environment of the metal.⁵⁴⁴ NMR analyses of OC-Fe^{II}BLM and Co^{II}-BLM have also implicated the mannose carbamoyl as a sixth ligand along with the β -aminoalanine primary amine.^{524,545}

Along with experiments to elucidate the structure of BLM in solution have come studies on BLM complexed with small DNA oligomers, again using primarily non-Fe^{II} BLM complexes.^{477,528,531,532,534,535,537,540-543} The bithiazole tail binds via partial intercalation with no specific interactions between the tail and the DNA. As previously indicated by experiments with BLM analogues,^{546,547} it is the metal-binding domain that confers sequence specificity rather than the bithiazole tail. Several hydrogen bonds orient the BLM metal-binding domain for reactivity, including

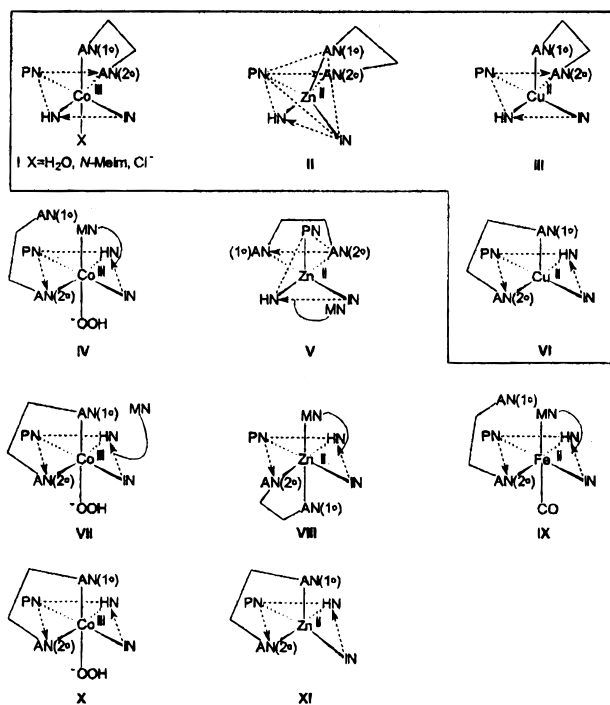


Figure 46. Three-dimensional structures proposed for BLM. Coordinated to the metal centers are the imidazole nitrogen N1 (IN), the amide of β -hydroxyhistidine (NH), the pyrimidine N5 (PN), the secondary amine of β -aminoalanine [AN(2°)], the primary amine of β -aminoalanine [AN(1°)], and/or the mannosyl carbamoyl nitrogen (MN). Crystallographically derived structures (boxed) for several model compounds: (I) $\text{Cu}^{\text{II}}\text{P-3A}$, ref 520, $N\text{-MeIm} = N\text{-methylimidazole}$; (II) ref 522; (III) ref 518; (VI) ref 519. Structures derived from molecular-dynamics calculations: (IV) $\text{HOO-Co}^{\text{III}}\text{PEPLM}$, ref 536; (V) $\text{HOO-Co}^{\text{III}}\text{BLM}$, refs 530 and 534; (VII) $\text{Zn}^{\text{II}}\text{BLM}$, refs 526, 528, and 531; (VIII) $\text{CO-Fe}^{\text{II}}\text{BLM}$, ref 527; (IX) $\text{HOO-Co}^{\text{III}}\text{-deglyco-PEPLM}$, ref 536; (X) $\text{Zn}^{\text{II}}\text{-deglyco-BLM}$, ref 542. (Reprinted with permission from ref 542. Copyright 1998 American Chemical Society.)

two bonds between the BLM pyrimidine and the DNA guanine as shown in Figure 47A.^{535,541,548}

Spectroscopy. Several other spectroscopic techniques have been used to focus on the iron center to determine the geometric and electronic structure of $\text{Fe}^{\text{II}}\text{BLM}$ and subsequent intermediates. Absorption, CD/MCD, XAS/EXAFS, and rR spectroscopies have been used to characterize $\text{Fe}^{\text{II}}\text{BLM}$. The Fe^{II} site is high-spin $S = 2$, and the near-IR CD/MCD spectrum in Figure 48A shows two $d \rightarrow d$ bands split by $2650\text{--}3950\text{ cm}^{-1}$, with $10Dq \approx 10730\text{--}11080\text{ cm}^{-1}$. This is indicative of a 6C distorted octahedral geometry, and the large Δ^5E_g suggests that one axial ligand interaction is weak. The VTVH MCD data have an unusually small nesting for a 6C Fe^{II} site ($\delta = 2.4\text{ cm}^{-1}$, Figure 48B) that can be attributed to a strong metal–ligand π -back-bonding interaction. EXAFS analysis indicated that a relatively short Fe–N bond is present ($2.06\text{--}2.08\text{ \AA}$, versus other Fe–N/O bonds at 2.19 \AA), which would also be consistent with π -back-bonding.⁴³ The presence of π -back-bonding is confirmed by the presence of low-energy, MLCT transitions in the UV–vis region (Figure 49A,B) that are normally not observed in non-heme Fe^{II} active sites but are common for heme systems. From the strong resonance enhancement of the pyrimidine normal

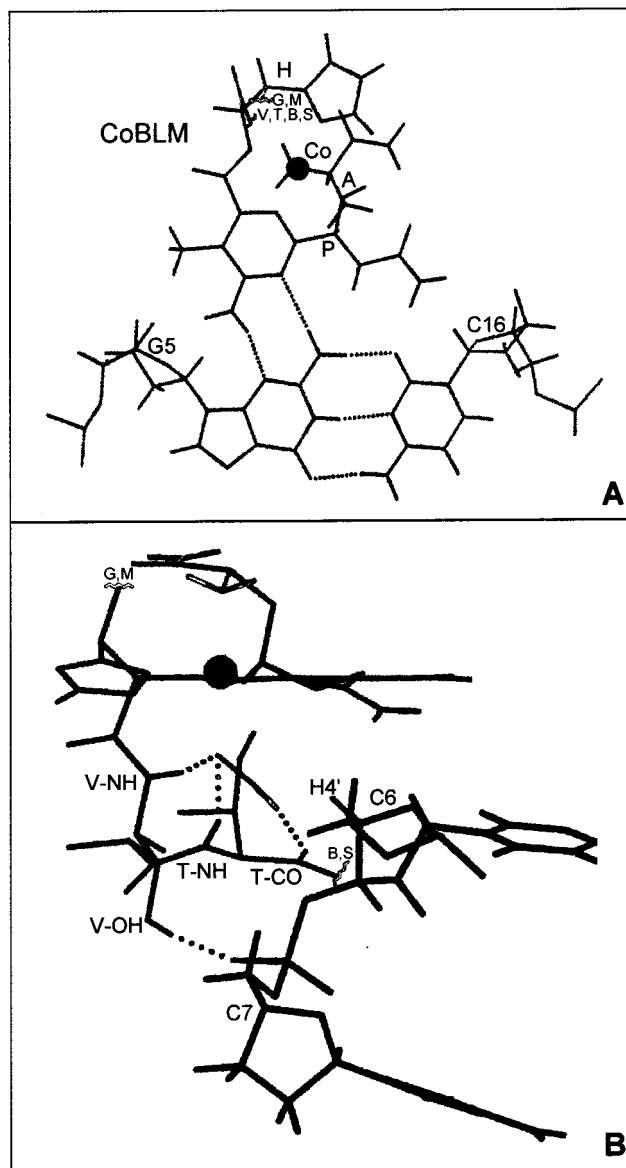


Figure 47. (A) Hydrogen-bonding interactions between BLM and DNA. The P moiety of $\text{Co}^{\text{III}}\text{BLM}$ forms hydrogen bonds with the guanine of DNA. (B) Position of the hydroperoxide oxygens of $\text{Co}^{\text{III}}\text{BLM}$ "green" relative to the $\text{C4}'\text{-H}$ of cytosine, the site of DNA cleavage. For the BLM structure: P = BLM pyrimidinyl propionamide, A = β -aminoalanine, H = β -hydroxyhistidine, T = threonine, V = methylvalerate, GM = glucose and mannose sugars, and VTBS = peptide linker and tail. For DNA: G = guanine and C = cytosine. (Reprinted with permission from ref 535. Copyright 1996 American Chemical Society.)

modes in the Raman spectrum, these transitions were assigned as $\text{Fe}^{\text{II}} \rightarrow$ pyrimidine MLCT transitions (Figure 49C).⁴³

This pyrimidine π -back-bonding was investigated further using CD/MCD spectroscopy to probe several structural derivatives of BLM and its congener PEPLM (Figures 44 and 48; the CD/MCD spectra of PEPLM are identical to BLM⁵⁴⁴), including *iso*-PEPLM (with the mannose 3-*O*-carbamoyl substituent shifted from the 3- to the 2-hydroxyl group) and depyruvamide (DP)–PEPLM (without the β -aminoalanine moiety).⁵⁴⁴ The MCD spectra and VTVH MCD data are shown in Figure 48. Both the energies of the $d \rightarrow d$ bands and the intensity ratio of the two

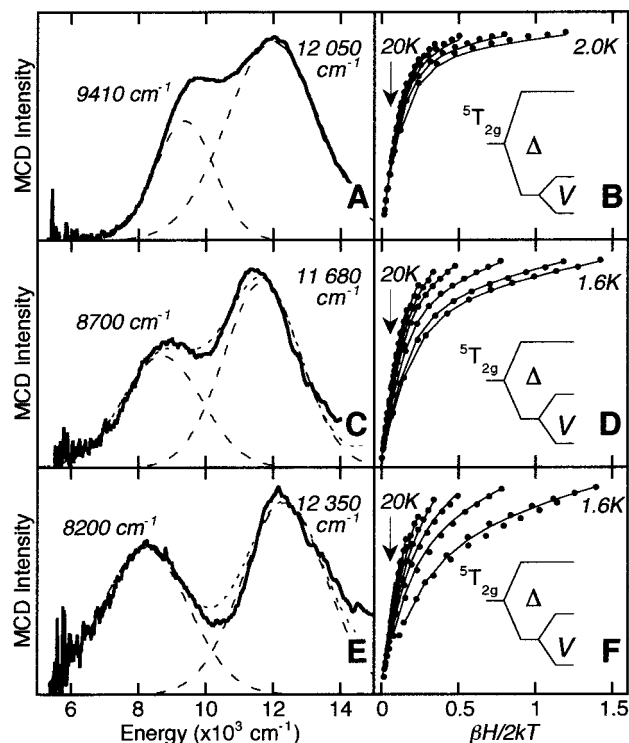


Figure 48. (A) LF MCD and (B) VTVH MCD recorded at $12\,000\text{ cm}^{-1}$. (C) LF MCD and (D) VTVH MCD recorded at $12\,000\text{ cm}^{-1}$ for $\text{Fe}^{\text{II}}\text{iso-PEPLM}$. (E) LF MCD and VTVH MCD recorded at $12\,350\text{ cm}^{-1}$ for $\text{Fe}^{\text{II}}\text{DP-PEPLM}$. The best fits (—) to the VTVH data (●) were generated by the parameters in Table 13. (Adapted from refs 43 and 544.)

bands are altered in these derivatives (Figure 48C,E); the splittings (Δ^5E_g) and $10Dq$ are summarized in Table 13. Additionally, the VTVH MCD data show increased nesting for the *iso*- and DP-PEPLM derivatives (Figure 48D,F); since π -back-bonding is the source of the unusually small nesting for $\text{Fe}^{\text{II}}\text{BLM}$, the increase in nesting indicates that back-bonding is reduced in these derivatives. This is also reflected in changes to the CT bands observed in the UV-vis spectra. Finally, titrations of $\text{Fe}^{\text{II}}\text{BLM}$ and the derivative complexes with the O_2 -analogue N_3^- indicated that there is a single exchangeable site for exogenous ligand binding.⁵⁴⁴

While $\text{Fe}^{\text{III}}\text{BLM}$ is normally a low-spin ($S = 1/2$) complex, at low pH or in phosphate buffer it is high spin ($S = 5/2$). When bound to DNA, $\text{Fe}^{\text{III}}\text{BLM}$ is low-spin $S = 1/2$ with EPR g -values of 2.45, 2.18, and 1.89.^{100,475,498} Binding to DNA also causes changes in the rR spectrum that suggest conformation changes to the drug's metal-binding site.⁵⁴⁹ Preliminary CD/MCD studies have indicated that the spectral changes may reflect a conversion of the Fe^{II} site from 6C →

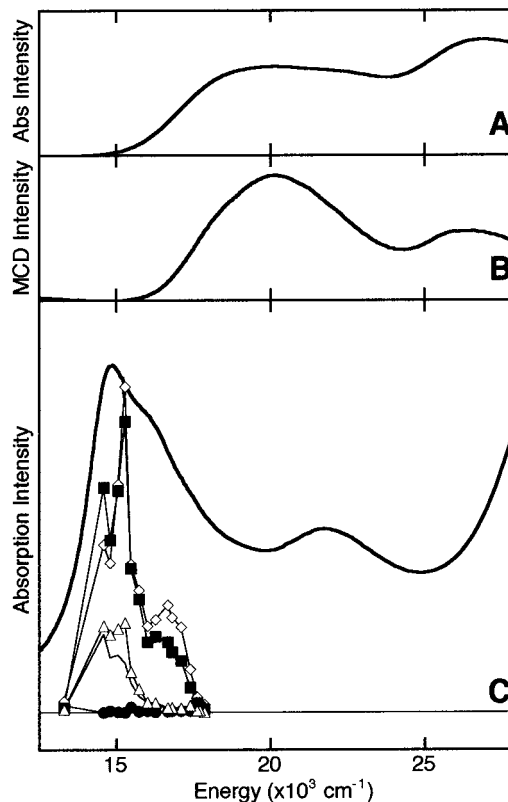


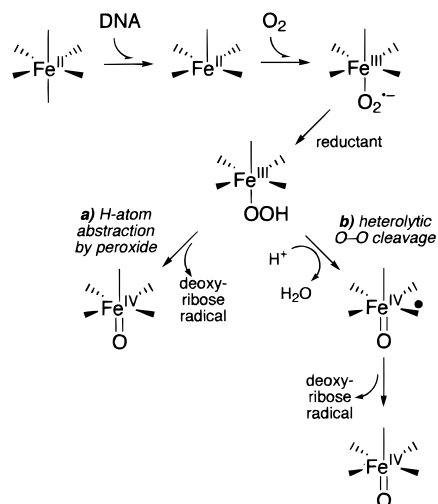
Figure 49. (A) Absorption and (B) MCD spectra of the $\text{Fe}^{\text{II}}\text{BLM}$ CT region. (C) Room-temperature absorption spectrum (—) of the BLM model complex $[\text{Fe}^{\text{II}}\text{PMA}]^+$ and rR profiles of the 680 (▽), 744 (■), 1519 (○), and 1542 (●) cm^{-1} vibrations. (Adapted from ref 43.)

5C upon binding to DNA.⁵⁵⁰ Oxygenated BLM is EPR-silent and was originally thought to be an O_2 - $\text{Fe}^{\text{II}}\text{BLM}$ complex; however, Mössbauer experiments demonstrated that the diamagnetic iron site is low spin with a quadrupole splitting consistent with an Fe^{III} oxidation state.³⁵ Consequently, oxygenated BLM may be better described as a ferric superoxide complex, $^{\bullet}\text{O}_2-\text{Fe}^{\text{III}}\text{BLM}$.

Initial studies on ABLM using EPR,¹⁰⁰ Mössbauer,³⁵ and redox titrations⁵⁵¹ were consistent with this intermediate being a low-spin Fe^{III} species, either a peroxide complex (end-on or side-on) or a monooxygenated species analogous to peroxidase compound I (formally $\text{Fe}^{\text{III}}\text{O}^0$). The XAS preedge region shows an intensity and band ratio consistent with a 6C octahedral Fe^{III} species with no severe distortion around the iron site.⁵⁵² This indicates that a short Fe-O bond ($\sim 1.65\text{ \AA}$) is not present, as would be expected for an $\text{Fe}^{\text{IV}}=\text{O}$ species, and was supported by EXAFS analysis, indicating that ABLM has Fe-N/O bond lengths of 1.89 – 2.03 \AA . Electrospray mass

Table 13. Ground- and Excited-State Parameters for $\text{Fe}^{\text{II}}\text{BLM}$ Derivatives (Adapted from ref 544)

complex	CD/MCD	Δ^5E_g (cm^{-1})	$10Dq$ (cm^{-1})	δ (cm^{-1})	g_{\parallel}	Δ (cm^{-1})	$ V $ (cm^{-1})
$\text{Fe}^{\text{II}}\text{BLM}$	CD	3950	11 080				
	MCD	2640	10 730	2.4	9.3	-800	280
$\text{Fe}^{\text{II}}\text{PEPLM}$	CD	3950	11 075				
	MCD	2630	10 685	2.4	9.3	-900	280
$\text{Fe}^{\text{II}}\text{iso-PEPLM}$	CD	3050	10 525				
	MCD	2980	10 190	4.8	9.0	-600	380
$\text{Fe}^{\text{II}}\text{DP-PEPLM}$	CD	4100	10 450				
	MCD	4150	10 275	4.4	9.2	-600	400

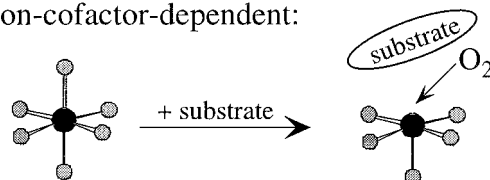
Scheme 16. Possible Mechanistic Scheme for BLM

spectroscopy further established that when ABLM is formed from $\text{H}_2^{18}\text{O}_2$, the activated species contains both labeled oxygen atoms; the mass-to-charge data were also consistent with a hydrogen nucleus accompanying the two peroxide oxygens.⁵⁰¹ X- and Q-band ENDOR using BLM activated in the presence of $^{17}\text{O}_2$ demonstrated hyperfine coupling only to one oxygen, consistent with end-on ligation of hydroperoxide.⁵⁰³ Taken together, these results show that the structure of ABLM is low-spin $\text{HOO-Fe}^{\text{III}}\text{BLM}$ (discussed further in section II.D.2.b).

Molecular Mechanism. As outlined above, the degradation of DNA by BLM begins with the reaction of $\text{Fe}^{\text{II}}\text{BLM}$ and O_2 to form oxygenated BLM ($\text{O}_2^- - \text{Fe}^{\text{III}}\text{BLM}$), which subsequently picks up one electron to form ABLM ($\text{HOO-Fe}^{\text{III}}\text{BLM}$) (Scheme 16). The reductant can be another molecule of oxygenated BLM, which oxidizes to $\text{Fe}^{\text{III}}\text{BLM} + \text{O}_2$, or one of several different reductants including peroxides and superoxides. The reactivity of BLM and its oxygen-bound species is modulated by π -back-bonding to the pyrimidine ring, which decreases the extent of CT to the O_2 in oxygenated BLM. This leads to reversible binding of O_2 in oxygenated BLM and stabilization of this species, the reduction in activity of BLM derivatives with reduced back-bonding interactions,⁵⁴⁴ and the formation of low-spin $\text{Fe}^{\text{II}}\text{BLM}$ complexes with NO and other strong-field ligands.^{34,553} Such complexes are more typical of heme rather than non-heme systems. The $\text{Fe}^{\text{II}}\text{BLM}$ MLCT transitions (Figure 49), however, are less intense and at higher energy relative to heme systems,⁵⁵⁴ indicating that there is less back-bonding to the BLM framework than is observed for the heme tetrapyrrole macrocycle. These characteristics make BLM an important bridge between the chemistry of non-heme and heme active sites.

ABLM, $\text{HOO-Fe}^{\text{III}}\text{BLM}$, is the species which initiates the cleavage of DNA, and experiments with ^3H -labeled DNA showed that $\text{C4}'\text{-H}$ abstraction from the deoxyribose sugar initiates DNA degradation.⁵⁵⁵ Alternatively, $^{18}\text{O}_2$ isotope experiments indicated that ABLM decays through O-O bond cleavage at a rate consistent with DNA cleavage.⁵⁰² For $\text{HOO-Co}^{\text{III}}\text{BLM}$ "green", a possible structural analogue to

non-cofactor-dependent:



cofactor-dependent:

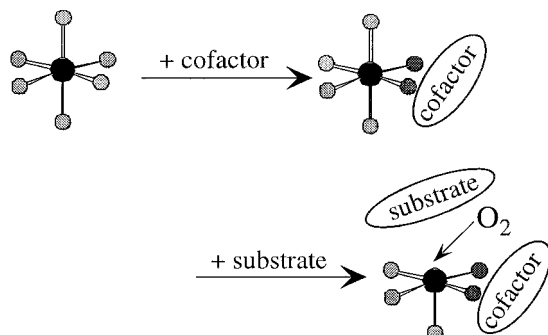


Figure 50. General strategy for mononuclear non-heme O_2 -activating enzymes.

activated $\text{Fe}^{\text{II}}\text{BLM}$, the distal oxygen of the hydroperoxide is 2.5 Å away from the $\text{C4}'\text{-H}$ of cytosine (Figure 47B).⁵³⁵ There are also several hydrogen bonds between the hydroperoxide and the "peptide linker" region of BLM that may assist in positioning the hydroperoxide for H-atom abstraction. This provides a structural basis for the reaction of ABLM with the $\text{C4}'\text{-H}$ of the deoxyribose to initiate DNA cleavage. ABLM abstracts the H atom, going through either heterolytic O-O bond cleavage to form $\text{O}=\text{Fe}^{\text{IV}}\text{BLM}^+ + \text{H}_2\text{O}$ or direct reaction of the hydroperoxide to yield $\text{O}=\text{Fe}^{\text{IV}}\text{BLM}^*$ and the deoxyribose $\text{C4}'$ radical. Section II.D.2.b contains further discussion on the nature of ABLM and the mechanism of DNA cleavage.

6. General Strategy

From the results summarized in the above section, it is clear that a common strategy for dioxygen activation by ferrous sites is emerging, Figure 50. For most of these enzymes the resting ferrous site is 6C, coordinatively saturated, and fairly stable in the presence of O_2 . Upon binding of substrate to the active-site pocket or both cosubstrates in the cases of the cofactor-dependent enzymes, the ferrous site becomes 5C. This provides an open coordination position for the dioxygen to interact with the Fe^{II} to generate a highly reactive iron-oxygen intermediate for the direct hydroxylation of substrate or for the coupled hydroxylation of cosubstrates in the cofactor-dependent enzymes. The $6\text{C} \rightarrow 5\text{C}$ conversion in the presence of a substrate(s) has thus far been observed in PAH, CS2, IPNS, and the Rieske-type oxygenases and also appears to occur in ACCO^{440} and BLM.⁵⁵⁰ Only the extradiol dioxygenases have a 5C ferrous center present in the resting enzyme. However, this is also unreactive with dioxygen in the absence of substrate. The molecular basis for this must still be elucidated (section II.C.1).

As might be anticipated for ferrous active sites, the ligation (except for BLM) is two histidines, carboxyl-

Table 14. Fe^{III}-Alkyl- and Hydroperoxo Model Systems and Comparison with Intermediates

complex	spin	L ^a	CT: λ _{max} (nm) [ε (M ⁻¹ cm ⁻¹)]	g and E/D values	Raman shift (cm ⁻¹)	refs
[Fe(EDTA)(O ₂)] ³⁻ purple LO	hs	N ₂ O ₂ ⁻	520 [530]; 287 [6100]	E/D = 0.21 g = 4.3	459 (FeO); 816 (OO)	60,557,558 559–561
[Fe(bPPa)(OO'Bu)] ²⁺	hs	P ₃ N ₂ O	613 [2000]	E/D = 0.067	873; 838; 629; 469	562
[Fe(6-Me ₃ TPA)(OH ₂)(OO'Bu)] ²⁺	hs	P ₃ N	562 [2000]	g = 4.3	877; 842; 637; 468	102
[Fe(TPA)(OH ₂)(OO'Bu)] ²⁺	ls	P ₃ N	600 [2200]	2.19; 2.14; 1.98	796; 696; 490	102
[Fe(PMA)(OO'Bu)] ⁺	ls	IPrN ₂ N ⁻		2.28; 2.18; 1.93		104
[Fe(BLM)(OOH)] ⁺	ls	IPrN ₂ N ⁻	365; 384	2.26; 2.17; 1.94		100
[Fe(TPA)(solvent)(OOH)] ²⁺	ls	P ₃ N	538 [1000]	2.19; 2.15; 1.97	789; 626	563,564
[Fe(N4Py)(OOH)] ²⁺	ls	P ₄ N	530 [1100]	2.17; 2.12; 1.98	790; 632	103
[Fe(PMA)(OOH)] ⁺	ls	IPrN ₂ N ⁻		2.27; 2.19; 1.94		104
[Fe(L)(OOH)] ²⁺	ls	P ₅	592	2.15; 2.13; 1.98		105
[Fe(L ⁵)(OOH)] ²⁺	ls	P ₃ N ₂	537 [1000]	2.19; 2.12; 1.95		106,565
[Fe(L ⁵)(O ₂)] ⁺	hs	P ₂ N ₂	740 [500]	E/D = 0.08		565

^a Ligation in the cases of special polydentate ligands: P = pyridine; N = amine; O = carbonyl oxygen; O⁻ = carboxylate oxygen(-); I = imidazole; Pr = pyrimidine; N⁻ = amide(-). For lipoxygenase (LO) and bleomycin (BLM), see sections II.B.1 and II.C.5, respectively.

ate, and waters. In IPNS and perhaps the Rieske-type dioxxygenases there is a carbonyl oxygen from an amide residue. These are all relatively weak donors which would favor a high reduction potential for the site, which should be further increased by the 6C → 5C conversion. Since the *E*^o for the O₂ → O₂⁻ couple is low (-0.33 V), one would not expect significant CT from the Fe^{II} to O₂ and thus there should be little superoxide character in the initial O₂-Fe reaction intermediate. The change in ligation associated with substrate coordination to the iron center would modify this charge donation. In three of these enzymes the substrate or cosubstrate directly coordinates to the Fe^{II}: bidentate α-KG, bidentate catecholate, and the thiolate of ACV. The latter two are strong donor ligands (indicated by low-energy LMCT transitions) which should decrease the potential of the iron and increase the superoxide character in the initial O₂-Fe reaction intermediate. The αKG-Fe^{II} bond still needs to be defined.

Since the reduction potential of the O₂ → H₂O₂ couple is fairly high (+0.281 V), the two-electron reduction of O₂ to peroxide is considered in many of the possible reaction mechanisms summarized in this section. In BLM, the second electron derives from an exogeneous reductant (which may be another BLM molecule); in the Rieske-type dioxxygenases this is supplied by the Rieske center, and in the other enzymes considered here either the substrate (catecholate) or the cofactor (BH₄ or αKG) can provide the second electron. The only observed catalytic oxygen intermediate is ABLM, which is a low-spin ferric hydroperoxide complex (vide supra). In the Rieske-type dioxxygenases the two-electron reduction might be expected to generate a high-spin Fe^{III}-peroxide or -hydroperoxide complex. In the other non-heme ferrous enzymes, a substrate-peroxy intermediate bridged to the iron center is generally invoked. The electronic structure/reactivity correlations of these species are considered below.

D. O₂ Intermediates and Analogues

The non-heme iron enzymes discussed above react with O₂ to give intermediates that have been thought to parallel those in heme systems. The reactivity of

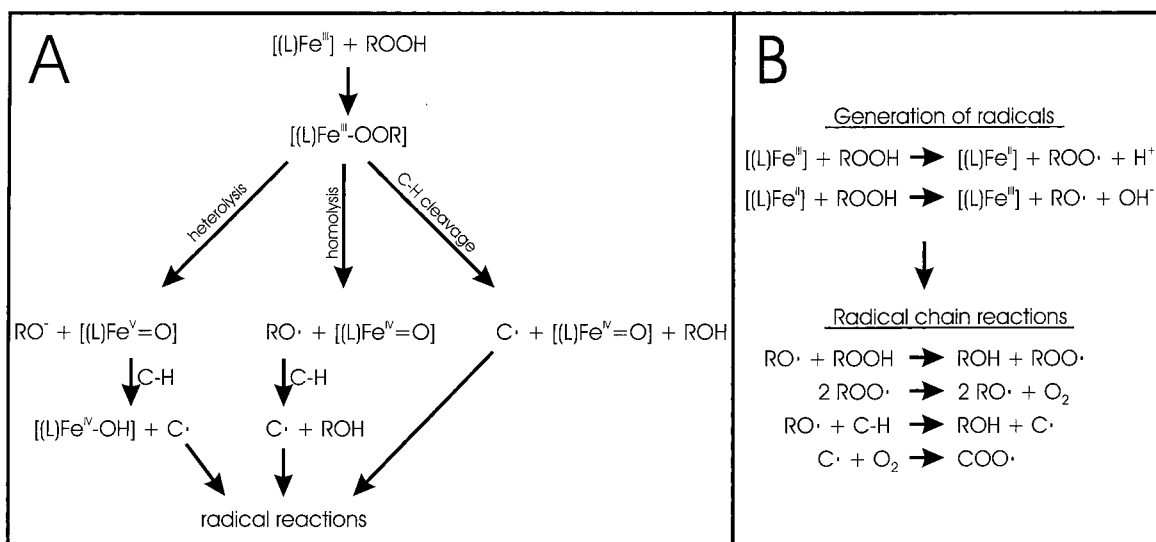
heme-based oxygenases and oxidases involves high-valent iron-oxo species which are thought to be generated from heterolytic O-O bond cleavage of an Fe^{III}-hydroperoxo precursor to form the catalytically active Fe^{IV}=OP⁺ species and a water molecule. The porphyrin ligand (P) is oxidized, which helps to stabilize the high formal charge (Fe^V) on iron. Since no such ligand is present in non-heme environments, the occurrence of such a highly oxidized intermediate is questionable (for a detailed comparison of heme and non-heme reaction mechanisms, see section II.D.2.b). Alternatively, Fe^{IV}=O species may occur in non-heme environments, as recently proposed for model systems.⁵⁵⁶

In case of non-heme iron enzymes, purple LO is the only potential oxygen intermediate that has been spectroscopically characterized (section II.D.2.a). For other enzymes, spectroscopic information about intermediates is quite limited or missing. In the case of 3,4-PCD (section II.B.2), an enzyme-substrate complex with bound O₂ (ESO₂) has been observed but decays in milliseconds.^{190,200,211} Accordingly, spectral insight into the nature of this intermediate has been limited. In addition to these enzyme species, the catalytically relevant non-heme oxygen intermediate ABLM has been investigated in detail (section II.D.2.b). In contrast to the limited information available in the enzymatic reactions, a large number of model complexes with coordinated peroxo (O₂²⁻) and substituted peroxo (ROO⁻, R = H, organic residue) ligands have been reported (see Table 14). The latter serve as potential models for the peroxo intermediates described above. These systems show a rich variety of reactions that have been characterized and correlated with enzymatic activity.²⁴⁷ The systematic evaluation of the various models allows the determination of the electronic and spectroscopic properties of the different coordination modes of peroxide and how this relates to reactivity.

1. Model Systems

In 1956, Cheng and Lott discovered that reaction of Fe^{III}-EDTA with H₂O₂ gives the 6C ferric peroxo (O₂²⁻) complex [Fe(EDTA)(O₂)]³⁻.⁵⁶⁶ The Fe^{III}-EDTA system catalyzes a number of reactions including

Scheme 17

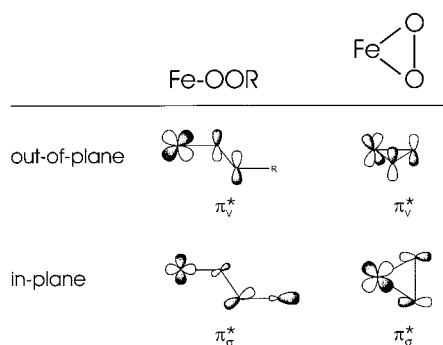


superoxide dismutation,^{557,567} decomposition of H_2O_2 , and organic substrate oxidation (in the presence of H_2O_2) at $pH < 10$.^{568–572} rR spectroscopy with mixed isotope perturbation has shown that the peroxide ligand is bound in a side-on (η^2) fashion.⁵⁵⁸ A number of end-on Fe^{III} -alkylperoxo complexes with non-heme ligand sets have recently been synthesized.^{104,562} Que and co-workers reported the synthesis of a series of 6C end-on *tert*-butyl- and cumylperoxo complexes $[Fe(TPA)(OH_2)(OOR)]^{2+}$.^{573–575} Using the unsubstituted TPA ligand (TPA = tris(2-pyridylmethyl)amine), an Fe^{III} low-spin complex is formed. Introducing steric hindrance by substitution of the TPA ligand (e.g., 6-Me₃TPA) leads to the corresponding high-spin complex.¹⁰² In this case, steric crowding lowers the LF felt by the Fe^{III} relative to the unsubstituted system, an effect which is well-known from spin-crossover compounds.^{576,577} Both the high-spin and low-spin complexes exhibit characteristic spectroscopic features which are discussed below. In the case of hydroperoxide, an end-on low-spin $[Fe(TPA)(\text{solvent})(OOH)]^{2+}$ complex is obtained.^{563,564} Making use of pentadentate ligands with nitrogen donors, a number of similar hydroperoxo complexes have been synthesized and characterized.^{103–106,564,565,578,579} All these systems have low-spin Fe^{III} centers with very similar spectroscopic properties as the corresponding low-spin end-on alkylperoxo complexes, and therefore, it is reasonable to assume that the hydroperoxo ligand is also coordinated end-on (section II.D.1.b). Most recently, there has been evidence in one system that by deprotonation the end-on-coordinated hydroperoxo ligand can be transformed into a side-on peroxo species.⁵⁶⁵ This formally connects the end-on hydroperoxo systems to the $[Fe(EDTA)(O_2)]^{3-}$ complex (section II.D.1.a). None of these iron alkyl- or hydroperoxo complexes has yet been structurally characterized, but X-ray data have been obtained for a number of Mn,⁵⁸⁰ Co,^{581–586} Cu,^{587–590} and Rh⁵⁹¹ systems.

Numerous ferrous and ferric complexes exhibit catalase activity⁵⁹² with H_2O_2 ,^{593,594} C–H bond cleavage and alkane oxidation reactions,^{595,596} or epoxidations of olefins,⁵⁹⁷ but in most of the cases the

corresponding intermediates have not been identified. Insights into these reactivities have been obtained from the above characterized model systems. For the iron-alkylperoxo complexes with the TPA ligand (vide supra) which show H-atom abstraction reactions from alkanes yielding alcohols and ketones, two mechanisms have been discussed in early studies: (a) one similar to P450 chemistry involving a high-valent ferryl $[Fe^{V}=O]$ complex as the active species (Scheme 17A, left)^{573,598–600} and (b) a radical mechanism based on Haber–Weiss decomposition of the alkylhydroperoxide,^{599–601} which in this case is not bound to the iron center. Accordingly, the metal only serves as a catalyst in different redox reactions generating alkylperoxo and alkoxy radicals which then undergo various chain reactions as shown in Scheme 17B. Most recently, new mechanistic insight has been developed in two ligand systems (PMA¹⁰⁴ and TPA^{379,556}), leading to a third possible mechanism based on O–O bond *homolysis*. This generates a high-valent $Fe^{IV}=O$ species and an alkoxy radical which attacks the alkane and, hence, starts a series of radical reactions, as shown in Scheme 17A (middle). In accordance with the mechanistic insight developed from the study of activated bleomycin (section II.D.2.b) and as speculated before,⁶⁰⁰ the coordinated alkylperoxo ligand itself could also be the active species by directly attacking the hydrocarbon and abstracting an H-atom. This would directly generate an alkyl radical and a ferryl $[Fe^{IV}=O]$ species (Scheme 17A, right). In any case, the further course of the different reactions observed (hydrocarbon oxidations, olefin epoxidations, etc.) is not clear, especially since there is some variation depending on the nature of the model system involved. The hydroperoxo complexes described above show similar reactions, but the question remains whether they follow a comparable mechanism. Variations could arise from the reduced stability of the hydroxo radical relative to alkoxy radicals or distinctly different activation barriers for homolytic O–O bond cleavage (section II.D.2.b). Since some of these low-spin hydroperoxo complexes also have DNA degradation capabilities,^{594,602–604} they are considered as model systems for FeBLM. This is

Scheme 18



especially the case for the $[\text{Fe}(\text{PMA})(\text{OOH})]^+$ complex of Mascharak and co-workers with the PMA ligand,⁵⁷⁸ which is a structural model of BLM. The side-on peroxo ligand only has a low reactivity toward organic substrates, but as pointed out recently,⁶⁰ this could be greatly enhanced by protonation of the O_2^{2-} moiety (section II.D.1.a).

a. Side-On Peroxo Complexes. As mentioned above, the purple Fe^{III} -EDTA peroxide system was probably the first non-heme iron oxygen intermediate discovered and remains one of the most intensely studied.^{60,557,558,566,569,605-607} Since the spectral features of the 1:1 adduct between Fe^{III} -EDTA and H_2O_2 at elevated pH (>10) are now reasonably well understood, it provides an important reference for a mononuclear non-heme ferric peroxide complex with a side-on (η^2) peroxide binding mode.⁵⁵⁸

In an octahedral LF, the five d-orbitals of iron are split into a set of three t_{2g} and two e_g functions, which in general form π - and σ -bonds with ligand orbitals, respectively. The free peroxide($2-$) ion has a HOMO set of two π^* orbitals, the degeneracy of which is lifted in the side-on structure by interaction with the d-functions of iron, as illustrated on the right side of Scheme 18; one of the π^* orbitals mediates a δ -bond (labeled π_v^*) whereas the other interaction is of σ -type (π_σ^* orbital). The electronic structure of the side-on ferric peroxide complex $[\text{Fe}(\text{EDTA})(\text{O}_2)]^{3-}$ is dominated by this σ -bond formed between the Fe d_{xy} and peroxide π_σ^* orbitals (Figure 51A). The bonding contributions of π - and δ -symmetry are weak. Importantly, there is no back-bonding between the Fe 3d and peroxide σ^* orbitals that would contribute to a weakening of the O-O bond (Figure 51B). Thus, the O-O bond is significantly stronger than that in the side-on-bound dicopper-peroxide complexes where such a back-bonding interaction has been established.⁶⁰⁸ This is due to the high effective nuclear charge on the ferric ion⁶⁰⁹ and the substantial exchange stabilization of the high-spin d^5 configuration.⁶¹⁰ Thus, the Fe 3d orbitals are energetically much closer to the filled peroxide orbitals than to the high-lying empty σ^* orbital. This weak π -/strong σ -bonding pattern is directly reflected in the CT spectrum of $\eta^2\text{-O}_2^{2-}\text{-Fe}^{\text{III}}$, which shows weak intensity in the visible region and strong CT intensity in the near-UV region (Figure 52, upper left panels II and I, respectively). The CT intensity in the visible region (II) originates primarily from $\pi_v^* \rightarrow \text{Fe}$ CT transitions, which are weak ($\epsilon = 500 \text{ M}^{-1} \text{ cm}^{-1}$) due to the low covalency of the donor and acceptor

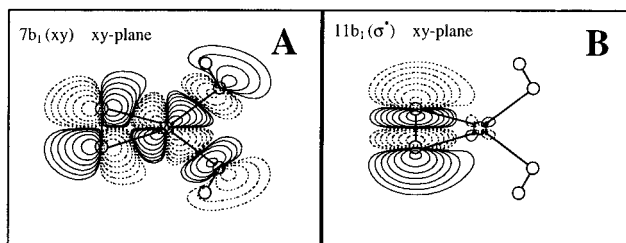


Figure 51. Important orbitals of side-on bound peroxide illustrating the in-plane interaction between Fe^{III} and O_2^{2-} calculated for $[\text{Fe}(\text{EDTA})(\text{O}_2)]^{3-}$. (A) d_{xy} interaction with π_σ^* . B: $\text{O}_2^{2-} \sigma^*$ orbital with essentially no metal character. (Reprinted with permission from ref 60. Copyright 1998 American Chemical Society.)

molecular orbitals, while the strong CT intensity ($\epsilon = 6000 \text{ M}^{-1} \text{ cm}^{-1}$) in the UV region (I) reflects a highly covalent σ -bond (section II.A.2.a.2). This interpretation is supported by a quantitative analysis of rR excitation profiles using time-dependent theory of electronic and rR spectroscopy.⁷⁰ The analysis shows that the O-O vibration (816 cm^{-1}) is strongly enhanced in the visible region (II), indicating ferrous-superoxide-like excited states, while the UV absorption (region I) leads to little enhancement of the O-O stretching vibration but strong enhancement of the Fe-O stretch (459 cm^{-1}), which is consistent with a transition from a strongly bonding to a strongly antibonding molecular orbital (MO).⁶⁰ The vibrational assignments (Table 14) were confirmed by isotope substitutions, and a normal coordinate description classified the O-O and Fe-O stretching vibrations as almost pure modes with little mechanical coupling. Variable-temperature EPR spectroscopy has been used to establish a -ZFS which derives from the high covalency of the Fe-O₂ σ -bond (Figure 51A) which attenuates the magnetic moment in the z-direction. VTVH MCD spectroscopy in conjunction with the newly developed methods for the computation of the orientation of the D -tensor and the analysis of the MCD saturation data (section II.A.2.a.2) were used to establish the polarizations of the CT transitions for a detailed spectral assignment (Figure 52, bottom panels).

This electronic structure description⁶⁰ indicates that the O-O bond of $\eta^2\text{-O}_2^{2-}\text{-Fe}^{\text{III}}$ is not activated for cleavage, consistent with its low reactivity toward organic substrates.⁵⁶⁹ Alternatively, it is rather nucleophilic and strongly activated toward protonation, which would greatly increase the electron affinity of the peroxide and generate a highly reactive species. This could undergo either direct electrophilic attack on substrate or reductive cleavage of the O-O bond through H-atom abstraction. This point requires further study.

b. End-On Alkyl- and Hydroperoxo Complexes. The different high- and low-spin end-on alkylperoxo complexes summarized in Table 14 exhibit very characteristic absorptions at about 550-600 nm with an ϵ of about $2000 \text{ M}^{-1} \text{ cm}^{-1}$. Clearly, these UV-vis absorptions are ligand-to-metal CT transitions from peroxide to iron. In case of the TPA ligand system, a comparison between related Fe^{III} high-spin and low-spin alkylperoxo complexes is possible (Figure 53). Although the intensities of the

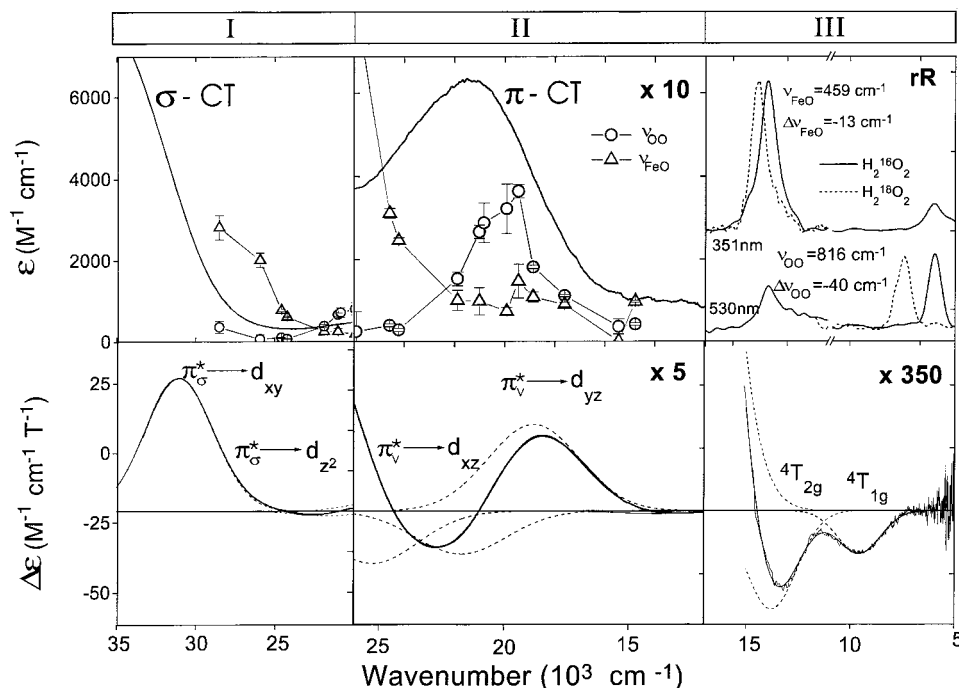


Figure 52. Optical absorption spectra (panels I and II, top), MCD data (panels I–III, bottom), and rR spectra (panel III, top) measured at two different excitation wavelengths of $[Fe(EDTA)(O_2)]^{3-}$. Circles and triangles give experimental rR profiles of $\nu(OO)$ and $\nu(FeO)$, respectively, and solid lines are fits of these profiles to Heller theory. Dashed curves in the bottom panels are Gaussian fits of the MCD bands. (Reprinted with permission from ref 60. Copyright 1998 American Chemical Society.)

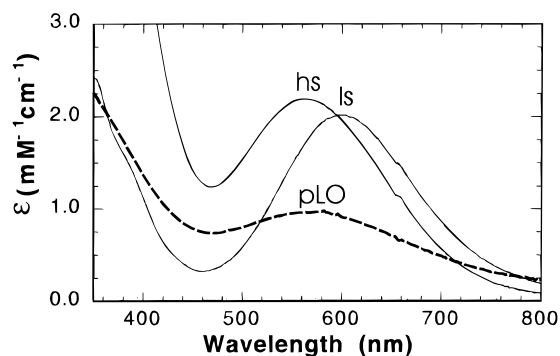


Figure 53. Absorption spectra of $[Fe(6-Me_3TPA)(OH_2)(OO^t-Bu)]^{2+}$ (high-spin, hs) and $[Fe(TPA)(OH_2)(OO^t-Bu)]^{2+}$ (low-spin, ls). (Reprinted with permission from ref 102. Copyright 1997 American Chemical Society.) Superimposed is the spectrum of purple LO (pLO, dashed line).

absorptions are quite similar, the transition of the high-spin system is blue-shifted by more than 1000 cm^{-1} . For the low-spin hydroperoxides, the corresponding absorption appears in the same spectral region (530–600 nm) but with a lower molar extinction coefficient ($\epsilon \approx 1000 M^{-1} cm^{-1}$).

The electronic structures of ferric alkyl- and hydroperoxo complexes are less well developed than that of the side-on peroxide system described above. Nevertheless, a comparison of the corresponding UV–vis spectra (Figure 53 to Figure 52) indicates that the bonding descriptions of these systems are fundamentally different. In case of the side-on coordination mode, the *out-of-plane* π_{ν}^* orbital forms a δ -bond with the d-orbitals of iron as shown in Scheme 18, right top; hence, due to small overlap, the experimental CT intensity in the visible region is low

($\epsilon \approx 500 M^{-1} cm^{-1}$, section II.A.2.a.2). Compared to free peroxide, the degeneracy of the two π^* functions is lifted by interaction with R in the free ROO^- ligand (R = H, organic residue). The orbital orthogonal to the R–O–O plane labeled π_{ν}^* is very similar to the corresponding orbital of free peroxide (Scheme 18, left). In contrast, π_{σ}^* now overlaps with a σ -type function of R leading to a decrease of this orbital in energy and a change in its coefficient on the coordinating O. Therefore, π_{σ}^* is expected to mediate a weaker bonding interaction with the metal than π_{ν}^* . Depending on the dihedral angle of the M–O–O–R moiety, π_{ν}^* forms a σ or π bond with the e_g or t_{2g} orbitals of the metal, respectively. Assuming a dihedral angle of 180° as observed in the structurally defined Cu complex,⁵⁸⁷ the bonding scheme depicted in Scheme 18, left, results. In this case, π_{ν}^* mediates a strong π interaction with the metal. On the basis of this bonding description, the visible absorption band of the alkyl- and hydroperoxo complexes is assigned to a ligand-to-metal CT transition from the *out-of-plane* peroxide π_{ν}^* function to the properly oriented t_{2g} orbital of iron as shown in Scheme 18. This transition is more intense for the end-on coordination mode relative to side-on due to better orbital overlap.

The high- and low-spin end-on alkylperoxo complexes in Table 14 have Raman features at about 800–900 (high-spin) and 700–800 cm^{-1} (low-spin), respectively, which are sensitive to ^{18}O substitution of the alkylperoxide. The Raman spectra cannot unequivocally be assigned because the O–O and C–O stretch of the alkylperoxide are both around 800 cm^{-1} and strongly mixed. Therefore, two corresponding features are observed which both shift on ^{18}O

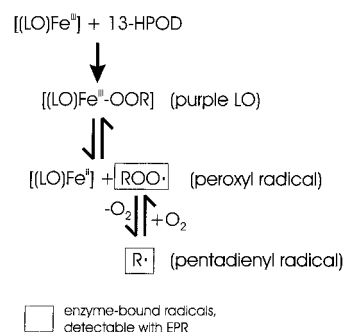
substitution. Nevertheless, the energies of these two peaks are characteristic of Fe^{III} in high-spin versus low-spin complexes, as can be seen from Table 14. The hydroperoxides exhibit only one isotope-sensitive peak in the 800 cm^{-1} region which therefore can be attributed to the O–O stretch. Note that the appearance of this vibration below 800 cm^{-1} also seems to be characteristic for the low-spin Fe^{III} hydroperoxo complexes. The assignments of the other isotope-sensitive features are not clear, but it seems most probable that the peaks around 600 cm^{-1} belong to the Fe–O stretch. For comparison, Table 14 also includes the corresponding features of the $[\text{Fe}(\text{EDTA})(\text{O}_2)]^{3-}$ system.

2. Intermediates

a. Purple Lipoygenase. Purple LO is formed when substrate (linoleic acid) and oxygen or the alkylhydroperoxide product (13-HPOD, section II.B.1) is added to the active, ferric form of the enzyme at reduced temperature. The formation of purple LO is associated with the appearance of an absorption band at 585 nm ($\epsilon \approx 1300\text{ M}^{-1}\text{ cm}^{-1}$, Figure 53) and a rhombic EPR signal at $g_{\text{eff}} = 4.3$.^{559,560,611} In addition, carbon-centered radicals⁶¹² and peroxy radicals⁶¹³ have been detected by EPR spectroscopy in such reaction mixtures (vide infra). Moreover, the appearance of the purple color is associated with dramatic changes in the CD spectrum.¹⁷³ On the basis of the spectroscopic properties of related models (vide supra), these results strongly suggest that *purple LO is an end-on high-spin ferric alkylperoxo complex of the 13-HPOD product coordinated to the iron active center.* Detailed investigations of Nelson and co-workers on the properties of the organic radicals mentioned above have led to mechanistic insight into the formation of purple LO.^{614,615} When ferric LO is treated with 13-HPOD anaerobically, the solution turns purple and LT EPR shows a sharp signal with $g \approx 2$. Using isotope-labeled 13-HPOD (deuterated on the fatty acid backbone or ^{17}O labeled peroxide), the EPR spectrum indicates that the $g = 2$ signal belongs to the pentadienyl radical of the fatty acid. If the experiment is performed in an oxygen atmosphere, the peroxy radical of 13-HPOD is detected with g -values of 2.035/2.008/2.003. At $4\text{ }^\circ\text{C}$, the 585 nm band of purple LO and this $g \approx 2$ signal exhibit the same slow decay behavior over several minutes, proving that both species are related. Importantly, from the isotope-labeling experiments, this peroxy radical exchanges with O_2 . Since the EPR spectra of both the pentadienyl and the peroxy radical show very sharp signals compared to the corresponding free species, it is most probable that they are in an enzyme-bound state which eliminates most conformational degrees of freedom. This is also apparent from the very slow decay of the peroxy radical (vide supra) and the fact that addition of ethanol to purple LO (ethanol is known to bind close to the LO active site) leads to an immediate loss of the EPR signals of the radicals whereas the purple color remains.

Taking these observations together, the formation of purple LO seems to be an equilibrium reaction as shown in Scheme 19. First, the alkylperoxo complex

Scheme 19



is generated which is metastable toward formation of Fe^{II} and a corresponding peroxy radical. This species loses dioxygen, forming a pentadienyl radical which then reversibly binds O_2 . Therefore, depending on the O_2 concentration, the pentadienyl or peroxy radical is the dominant species observed in the EPR spectrum. Finally, the alkylperoxo complex is recovered by reaction of the peroxy radical with the Fe^{II} center. Most recently, Nelson and co-workers have shown that by photolysis the alkylperoxo complex can be reversibly split at 77 K forming an EPR-silent metal center and a new oxygen-containing radical with different properties than the peroxy radical.⁵⁶¹ As discussed in section II.B.1, the role of the purple intermediate in the catalytic cycle of LO is not clear; it could either be an enzyme–product complex or formed by a side reaction that is not directly involved in catalysis.

b. Activated Bleomycin. As presented in section II.C.5, two oxygen intermediates are observed for BLM. When the Fe^{II} complex of BLM is exposed to air, a short-lived intermediate is formed called oxygenated BLM, $[\text{Fe}(\text{BLM})(\text{O}_2)]$.¹⁰⁰ This compound is EPR-silent, but Mössbauer spectroscopy shows that the iron is in the low-spin Fe^{III} oxidation state.³⁵ Therefore, oxygenated BLM is described as an $\text{Fe}^{\text{III}}\text{-superoxide}$ complex with both the Fe^{III} and O_2^- having $S = 1/2$, which are antiferromagnetically coupled leading to a diamagnetic ground state. ABLM has the ability to cleave DNA and is quickly formed from the oxygenated BLM precursor by one-electron reduction. Since ABLM is to date the only non-heme iron–oxygen intermediate that is stable enough for detailed spectroscopic analysis, its electronic structure and reactivity is of considerable interest for the understanding of non-heme iron sites in general. This species has been studied by UV–vis and EPR spectroscopy (Table 14),^{100,616} Mössbauer spectroscopy,³⁵ electrospray mass spectrometry,⁵⁰¹ and XAS.⁵⁵² All these results demonstrate that *activated bleomycin is a low-spin end-on $\text{Fe}^{\text{III}}\text{-hydroperoxo}$ complex, $[\text{Fe}(\text{BLM})(\text{OOH})]$.* Recently, the spectroscopic protocols described in section II.A.2.b were applied to this intermediate, and the results provide fundamental insight into the mechanism of DNA cleavage by FeBLM .

The ground-state studies focus on simulation and analysis of the EPR spectra of $\text{Fe}^{\text{III}}\text{BLM}$ and ABLM that have been described by a number of authors.^{100,503} The g -values were analyzed through a low-spin d^5 LF model (section II.A.2.b) corrected for

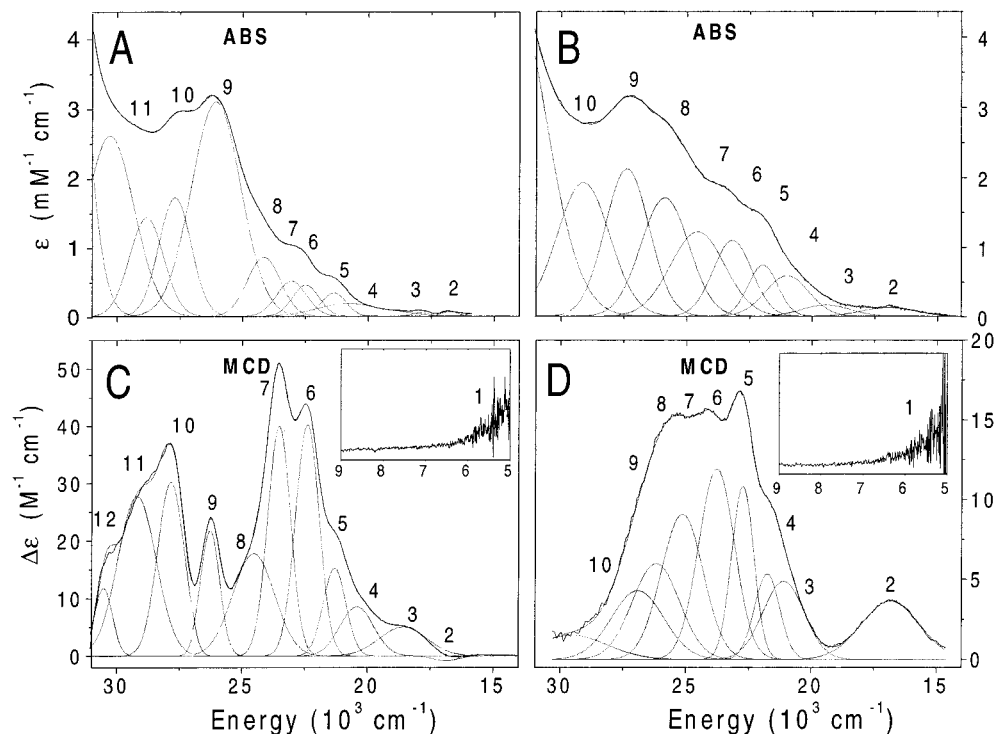


Figure 54. Optical absorption spectra (top panels) and MCD data (bottom panels) of Fe^{III}BLM (left: A, C) and ABLM (right: B, D). Insets give the NIR MCD spectra at increased sensitivity. Gaussians are simultaneous fits of absorption, CD, and MCD spectra.

covalency.^{503,617} The analysis provides the splitting of the t_{2g} set of d_{π} orbitals.⁶¹⁷ This splitting can be evaluated experimentally from the near-IR MCD data which show the highest energy component of the low-symmetry-split (t_{2g})⁵ ${}^2T_{2g}$ ground state (inset in Figure 54C,D). A combination of absorption, CD, and LT MCD spectra, Figure 54, allow the LF transitions to be separated from the CT transitions through their Kuhn anisotropy factors in CD and CD values in MCD. The data in Figure 54 allow the assignment of bands 2–7 as LF transitions to states deriving from the (t_{2g})⁴(e_g)¹ and (t_{2g})³(e_g)² excited configurations where a LF analysis then gives experimental values of $10Dq$, B , and the low-symmetry splitting of the e_g d_{σ} orbitals (section II.A.2.b). Together, these ground- and excited-state spectral studies give the experimental LF splitting of the five d -orbitals of the low-spin ferric active site and how this changes with hydroperoxide binding in ABLM.⁶¹⁷ The results are shown in Figure 55 and indicate that the LFs of the ferric ion in Fe^{III}BLM and ABLM are fairly similar. ABLM has a slightly higher $10Dq$ value, and its t_{2g} orbital set shows a more axial splitting pattern that is also reflected in the EPR spectra of Fe^{III}BLM and ABLM. The CT transitions (bands 8 and above in Figure 54) can then be analyzed to probe specific ligand–metal bonding interactions. rR spectra on Fe^{III}BLM in this region show dominant contributions from the pyrimidine and deprotonated amide ligands.⁶¹⁸ rR excitation profiles through this CT region allow the dominant CT band (band 9, Figure 54A) to be assigned to a deprotonated amide-to-iron CT transition.⁶¹⁷ The considerable intensity of this band ($\epsilon \approx 3200 \text{ M}^{-1} \text{ cm}^{-1}$) shows that the redox-active t_{2g} orbital in

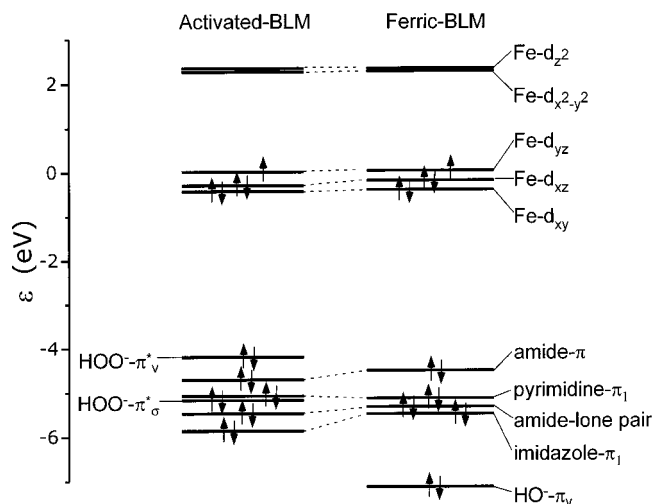


Figure 55. Comparison of Fe^{III}BLM versus ABLM orbital energies. The singularly occupied molecular orbital has been set to 0 eV, and all energies are relative to this. The d -orbital energies were fixed from the LF analysis.

Fe^{III}BLM must be oriented toward the deprotonated amide ligand, which is therefore the dominant π -donor ligand in the BLM donor set. Strikingly, from Figure 54B and D, the absorption and MCD spectra show only limited change upon hydroperoxide binding. This implies that the deprotonated amide dominates over the hydroperoxide as a π donor and also determines the orientation of the redox orbitals in Fe^{III}BLM and ABLM. Therefore, the overlap of the hydroperoxide π_v^* orbital with the hole is poor, which explains the lack of an intense CT band from the hydroperoxide in ABLM. This is an important dif-

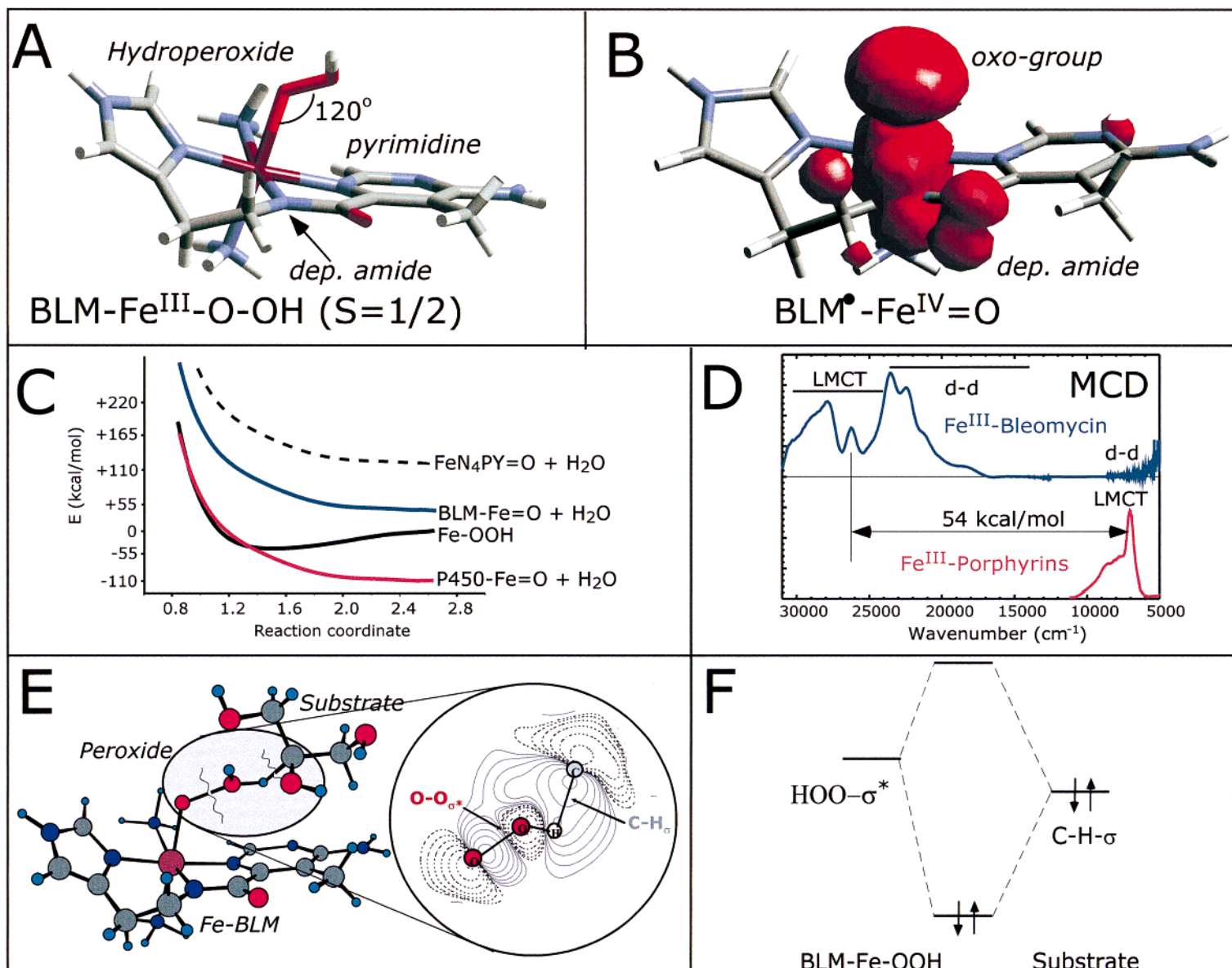


Figure 56. Electronic structure calculations on the mechanism of H-atom abstraction by ABLM. (A) Optimized structure of ABLM at the NDDO/1 level. (B) Total spin density of a putative Fe^V=O intermediate. (C) Schematic potential energy surfaces for heterolytic O–O bond cleavage with different ligand sets and the O–O potential energy curve of ABLM (Fe–OOH). (D) MCD spectra of Fe^{III}BLM and Fe^{III}–porphyrins with deprotonated amide-to-Fe^{III} CT (top) and porphyrin-to-Fe^{III} CT (bottom). (E) Intermediate stage on the reaction coordinate for the direct reaction of ABLM with a C–H bond. (F) The corresponding orbital interaction scheme.

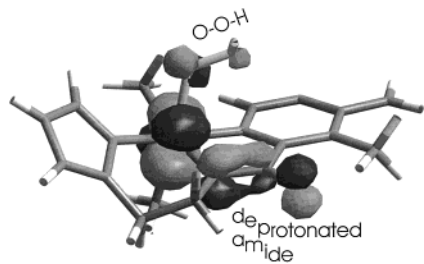


Figure 57. Plot of the SOMO of ABLM showing that the singly occupied t_{2g} orbital of iron mainly interacts with the deprotonated amide ligand.

ference with respect to the low-spin Fe^{III} –hydroperoxo complexes (Table 14), indicating that the π -donor bonding of OOH^- in ABLM is different.

This analysis is further supported by electronic structure calculations. Energy minimization at the NDDO/1 level gave the structure shown in Figure 56A. Alternative structures that differ from Figure 56A were ruled out by comparison of the calculated spectroscopic properties at the INDO/S level. INDO/S, gradient-corrected DFT, and hybrid DFT calculations all predict the redox-active orbital to be mainly π antibonding with the deprotonated amide ligand (Figure 57), in agreement with the analysis of the experimental data. Taken together this allows the construction of the experimentally calibrated bonding scheme for ABLM shown in Figure 55, left.⁶¹⁷

The experimentally evaluated calculations were then extended to address the reactive species in ABLM chemistry that attacks DNA. The accepted mode of reactivity is a hydrogen-atom abstraction from the C_4' position of the DNA ribose sugar.^{472,474,476} Three possible scenarios have been evaluated: (a) heterolytic cleavage of the O–O bond that would lead to a high-valent, formally $\text{Fe}^{\text{V}}=\text{O}$, intermediate that attacks DNA; (b) homolytic cleavage of the O–O bond that would lead to a high-valent, formally $\text{Fe}^{\text{IV}}=\text{O}$, intermediate; and (c) direct reaction of the low-spin Fe^{III} – OOH species with DNA to give a DNA radical, H_2O , and an $\text{Fe}^{\text{IV}}=\text{O}$ species. To date, unambiguous data have not been reported that would allow one to distinguish the three possible mechanisms of DNA cleavage. As is the case for P450 chemistry, the reactive species may be very short-lived and not build up to a sufficient level for direct detection.

Possibility a corresponds to the widely accepted mechanism for cytochrome P450 reactivity^{619–623} and has also frequently been assumed to hold for FeBLM chemistry.⁴⁷⁶ Loew and co-workers have studied the energetics of O–O heterolysis in cytochrome P450 through gradient-corrected DFT calculations and have shown that the reaction is highly favorable.⁶²⁴ Similar methods were used to study a wide range of non-heme iron hydroperoxide intermediates and BLM.⁶¹⁷ The result shows that heterolytic O–O bond cleavage of ABLM is predicted to be unfavorable by at least 40 kcal mol⁻¹. This is more than 150 kcal mol⁻¹ less likely than for cytochrome P450. Insight into this large difference in driving force can be obtained by analyzing the electronic structure differences between the BLM and cytochrome P450 ligand sets. High-valent oxo-porphyrins are known to be best described as $\text{Fe}^{\text{IV}}=\text{OP}^{+\bullet}$ radical species ('com-

pound I').^{619–623} The calculations show that an analogous situation exists in the hypothetical compound I analogue of FeBLM. The total spin density in Figure 56B shows that the hole on the ligand is created on the deprotonated amide and does not extend over the pyrimidine ring. Thus, the compound I analogue of FeBLM is best described as $\text{Fe}^{\text{IV}}=\text{OBLM}^{+\bullet}$ with the hole on the deprotonated amide. In the case of cytochrome P450, the hole is delocalized over the entire porphyrin moiety, while in BLM it is largely localized. Therefore, the oxidation of the ligand is energetically more costly in the case of BLM, and consequently, the ligand is much more difficult to oxidize. This is emphasized in Figure 56C which shows schematic potential energy surfaces for heterolytic O–O bond cleavage and demonstrates that this is much less favorable in ABLM than for cytochrome P450. This energetic difference is directly reflected in the CT data. Low-spin Fe^{III} porphyrins have LMCT bands in the near-infrared region (5000–10000 cm⁻¹) of the spectrum that are conveniently detected by MCD spectroscopy (Figure 56D, bottom^{109,625–629}), whereas the deprotonated amide to iron CT occurs in the near-UV ($\sim 25\,000$ cm⁻¹; Figure 56D, top) in Fe^{III} BLM.⁶¹⁷ This discrepancy accounts for ~ 54 kcal mol⁻¹ difference in heterolytic bond cleavage energy. In addition to the presence of an easy to create hole, the cytochrome P450 ligand set provides a doubly negatively charged porphyrin ring as well as an anionic axial thiolate that both help to stabilize the high charge of the Fe–oxo unit. By contrast, the only anionic ligand in the case of BLM is the deprotonated amide. On the basis of the above discussion it is considered unlikely that ABLM reacts via a cytochrome P450 like heterolytic cleavage mechanism with a formally $\text{Fe}^{\text{IV}}=\text{OBLM}^{+\bullet}$ intermediate as an active species.

The alternative possibility (b) is also discarded on the basis of (i) the cleavage leads to OH radicals that are expected to show less selectivity than observed with BLM⁴⁷⁶ and (ii) it has been speculated that the homolytic cleavage of the O–O bond may have an exceedingly high activation barrier.⁶³⁰ This has also been observed in preliminary calculations.

This leaves possibility c as a new working hypothesis for BLM chemistry, namely, the direct reaction of the hydroperoxide with DNA. This reaction is predicted to be close to thermoneutral. Calculations provide insight into the electronic structure contributions to this reaction (Figure 56E,F). The calculations show that protonation of the peroxide greatly lowers the energy of its antibonding σ^* orbital and therefore increases the electrophilicity of the peroxide. This activates the peroxide for electrophilic attack on the C–H bond (Figure 56E). CT from the C–H σ -bonding into the O_2^{2-} σ^* orbital leads to a weakening of both the C–H and the O–O bond (Figure 56F). This promotes H-atom transfer to form water, $\text{Fe}^{\text{IV}}=\text{OBLM}$, and a DNA radical.

In summary, the combination of spectroscopic analyses and electronic structure calculations has led to a new working hypothesis for the reactivity of ABLM, to date the only well-characterized mononuclear non-heme iron–oxygen intermediate. On the basis of this

hypothesis, new experiments can be designed that probe the possibility of the direct reaction between coordinated hydroperoxide and C–H bonds. It is also important to evaluate how this mechanism relates to other non-heme Fe–hydroperoxo systems.

III. Binuclear Non-Heme Iron

Binuclear non-heme iron enzymes involved in O₂ activation primarily exist in two oxidation states: the fully reduced biferrrous [Fe^{II}]₂ and the oxidized biferric [Fe^{III}]₂ form. During turnover, higher valent intermediates are also generated, possessing novel core geometric and electronic structures that can be probed by a variety of spectroscopic and analytical methods.

A. Spectroscopic Methodology

1. [Fe^{III}]₂

While the electronic structures of the binuclear ferric systems are built upon those of their component monomer halves (section II.A.2), their spectroscopic and magnetic features can be quite distinct. In particular, magnetic interactions among the two metal centers through the bridging ligation give rise to an exchange-coupled dimer ground state that is typically diamagnetic at LT even though each Fe^{III} monomer half formally possesses five unpaired electrons (section II.A.2).⁶³¹

a. Magnetism within a Dimeric Unit. 1. *Phenomenological Description of Magnetic Exchange.* In biferric complexes, the ground state splits into six total spin states, $S_{\text{tot}} = 0, 1, 2, 3, 4,$ and 5 , obtained from vector coupling of the individual spins, $S_{\text{tot}} = |\mathbf{S}_1 + \mathbf{S}_2|, |\mathbf{S}_1 + \mathbf{S}_2 - 1|, \dots, |\mathbf{S}_1 - \mathbf{S}_2|$.⁶³² These spin states are split in energy and produce a spin ladder that can be modeled by the Heisenberg–Dirac–Van Vleck (HDVV) phenomenological Hamiltonian⁶³³

$$H = -2J\mathbf{S}_1 \cdot \mathbf{S}_2 \quad (19)$$

with J the exchange coupling constant. The corresponding eigenvalues

$$E(S_{\text{tot}}) = -J[S_{\text{tot}}(S_{\text{tot}} + 1) - S_1(S_1 + 1) - S_2(S_2 + 1)] \quad (20)$$

define a simple Landé pattern where $J > 0$ relates to ferromagnetic coupling producing a ${}^{2(S_1 + S_2) + 1} = {}^{11}\Gamma$ ground state and $J < 0$ corresponds to antiferromagnetic coupling resulting in a ${}^{2(|S_1 - S_2|) + 1} = {}^1\Gamma$ ground state (Figure 58). This exchange splitting of spin states also applies to the electronic excited states. The magnitude of the excited-state coupling need not be the same as that of the ground state and may even be of opposite sign (vide infra). Note that in general the exchange splittings of excited states cannot be described properly by the HDVV Hamiltonian (eq 19).^{634–636}

The value of J can be obtained from a fit of magnetic susceptibility data measured as a function of temperature in a nonsaturating magnetic field. The measured susceptibility comprises three terms:

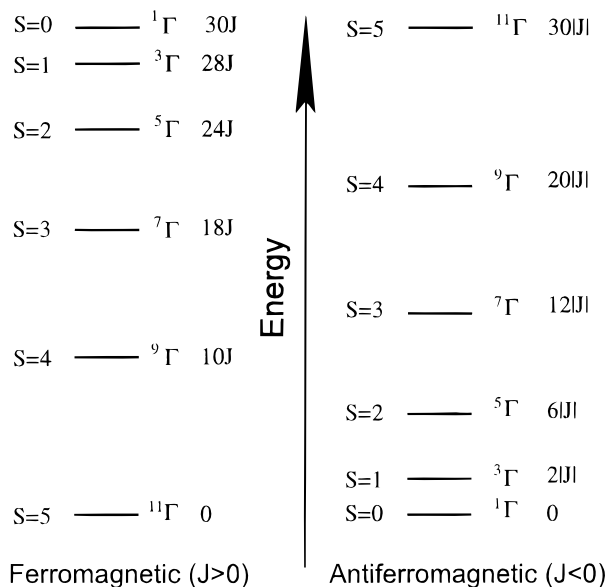


Figure 58. Ground-state spin ladder for ferromagnetically (left) and antiferromagnetically (right) exchange-coupled dimers consisting of two $S = 5/2$ monomer halves.

$\chi_{\text{exp}} = \chi_{\text{para}}(T) + \chi_{\text{dia}} + \chi_{\text{TIP}}$.⁶³⁷ $\chi_{\text{para}}(T)$ is the paramagnetic (temperature-dependent) contribution, χ_{dia} is the diamagnetic contribution that can be expressed in terms of a sum of individual contributions from each atom of the molecule, and χ_{TIP} is the temperature-independent paramagnetism, arising from mixing of excited states into the ground state by the magnetic field. χ_{dia} and χ_{TIP} are temperature independent and are accounted for by a constant offset when fitting experimental data. Typically J is determined from a fit of the susceptibility data using Van Vleck's equation including only the first-order Zeeman effect⁶³⁸

$$\chi(T) = \frac{N_A g^2 \beta^2}{kT} \cdot \frac{\sum_S \sum_{M_S=-S}^S M_S^2 e^{-E(S)/kT}}{\sum_S \sum_{M_S=-S}^S e^{-E(S)/kT}} \quad (21)$$

where N_A is Avogadro's number, g is the free electron g -value, 2.0023 , β is the Bohr magneton, k is the Boltzmann constant, T is the temperature, and S represents S_{tot} . Evaluation of eq 21 for an exchange-coupled high-spin biferric complex ($S_1 = 5/2$, $S_2 = 5/2$) yields

$$\chi(T) = \frac{2N_A g^2 \beta^2}{kT} \cdot \frac{e^{-2J/kT} + 5e^{-6J/kT} + 14e^{-12J/kT} + 30e^{-20J/kT} + 55e^{-30J/kT}}{1 + 3e^{-2J/kT} + 5e^{-6J/kT} + 7e^{-12J/kT} + 9e^{-20J/kT} + 11e^{-30J/kT}} \quad (22)$$

Representative simulations of χ as a function of T obtained with eq 22 for different J values are shown in Figure 59.

2. *Superexchange Pathways.* Although J is a phenomenological parameter, it can be related to the extent of delocalization of electron density from one

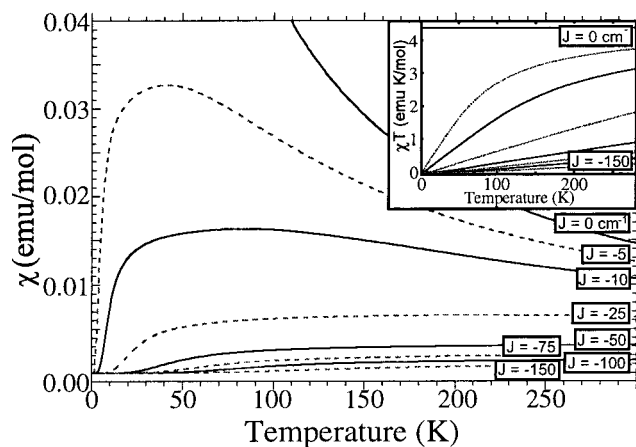


Figure 59. Susceptibility versus temperature plots for an exchange-coupled ($S_1 = 5/2$, $S_2 = 5/2$) system calculated using van Vleck's expression (eq 22) for a variety of antiferromagnetic coupling strengths (from largest to smallest susceptibility, $J = 0$, -5 , -10 , -25 , -50 , -75 , -100 , -150 cm^{-1} , respectively). In the 0 K temperature limit, the susceptibility of coupled systems goes to zero while uncoupled ($J = 0$ cm^{-1}) systems saturate as all electronic spins align. Inset: A χT versus T plot illustrates the deviation from uncoupled (Curie) behavior, which appears as a constant.

metal center of the dimer onto its partner through the bridging ligand orbitals. This mechanism is called superexchange and requires bridging ligand covalency.^{633,639} The ligand orbitals can be fully occupied or unoccupied, corresponding to hole and ET superexchange mechanisms, respectively.^{640,641} For biferrous and biferric complexes in which the two iron centers Fe1 and Fe2 are linked by a diamagnetic bridging ligand, four cases of superexchange interactions can be distinguished, all of which require that the metal orbitals on the two different centers overlap with the same bridging ligand orbital: (i) half-occupied orbitals on Fe1 and Fe2, (ii) a half-occupied orbital on Fe1 and an unoccupied orbital on Fe2, (iii) a fully occupied orbital on Fe1 and a half-occupied orbital on Fe2, and (iv) a fully occupied orbital on Fe1 and an empty orbital on Fe2.⁶⁴² Case i always produces an antiferromagnetic contribution to J because delocalization of an unpaired electron from one metal center into a half-occupied orbital on the other metal requires the two electrons to be spin paired (Pauli principle). Alternatively, case ii leads to a ferromagnetic contribution because the interaction of an electron delocalized onto the neighboring

metal with the other unpaired electrons on that center favors parallel spin alignment due to intra-atomic exchange (Hund's rule). Cases iii and iv only produce minor contributions to J and will not be considered here.

In high-spin ferric dimers, the ground-state exchange coupling constant J has contributions from the 25 different orbital pathways involving all possible combinations of the five half-occupied d-orbitals, i and j , localized on adjacent irons:⁶³⁵

$$J = \frac{1}{25} \sum_{i,j=1}^5 J_{ij} \quad (23)$$

Because all d-orbitals on the two Fe^{III} centers are half-occupied in the ground state, only the antiferromagnetic case (i), above, applies to biferric complexes. Yet it is important to note that antiferromagnetic contributions to J arise only from superexchange pathways involving d-orbitals of the two irons that overlap with the *same* ligand orbital. Therefore, most of the J_{ij} are negligibly small, their net contribution to J being weakly ferromagnetic due to true two-center two-electron exchange.⁶³³ Generally, a few key pathways do have overlap with a given ligand orbital, however, and these pathways are sufficiently effective in mediating an exchange interaction to produce an antiferromagnetically coupled ground state in most ferric dimers. The effectiveness of the dominant antiferromagnetic superexchange pathways strongly depends on the nature of the Fe–ligand bonding interaction and, therefore, on the core geometry and on the identities of the bridging ligands. This is key to the large variation in J across the series of known biferric complexes (Table 15).⁶³⁹

b. The Bent $\text{Fe}^{\text{III}}\text{--O--Fe}^{\text{III}}$ Unit: A Paradigm of a Dimeric Structure. The bent $\text{Fe}^{\text{III}}\text{--O--Fe}^{\text{III}}$ unit (the angle depends on the presence of additional μ -1,3-carboxylate bridges) occurs at the oxidized active sites of most of the binuclear iron metalloproteins involved in reversible binding or activation of O_2 (Table 2). A broad variety of spectroscopic methods have been employed to probe the electronic structure of this unit that has also been modeled in a remarkable number of synthetic Fe_2^{III} complexes.⁶³¹ These ferric oxo dimers are ideal systems in which to explore the effects of the strong coupling of two Fe centers together in a binuclear site.

1. *Unique Spectral Features. Ground State.* In the ground state of ferric oxo dimers, strong antiferro-

Table 15. Magnetic and Vibrational Parameters for $[\text{Fe}^{\text{III}}]_2$ Dimers with a Variety of Core Geometries and Ligands (Adapted from refs 643–647 and references therein)

core structure	Fe–O–Fe	J (cm^{-1})	ν_s^a	ν_{as}^a
$\text{Fe}_2(\mu\text{-O})_2$	92 → 94	–27		656, 676
$\text{Fe}_2(\text{O})$	180 → 150	–90 → –155	380 → 425	795 → 885
$\text{Fe}_2(\text{O})(\text{OH})$	98 → 106	–53 → –57	591 → 600	656 → 672
$\text{Fe}_2(\text{O})(\text{OAc})_2$	119 → 128	–120 → –122	525 → 540	725 → 751
$\text{Fe}_2(\text{O})(\text{O}_2\text{CR})_2$	129 → 138	–101 → –119	499 → 461	763 → 778
$\text{Fe}_2(\text{OH})_2$	103 → 105	–7 → –11	680	900
$\text{Fe}_2(\text{OH})(\text{OR})_2$	123 → 131	–15 → –17		
$\text{Fe}_2(\text{OR})_2$	104 → 107	–2.5 → –25		
$\text{Fe}_2(\mu\text{-O})_2$ (III,IV)	94.1	>80		635 → 676

^a ν_s and ν_{as} are the symmetric and antisymmetric Fe–O–Fe stretch modes.

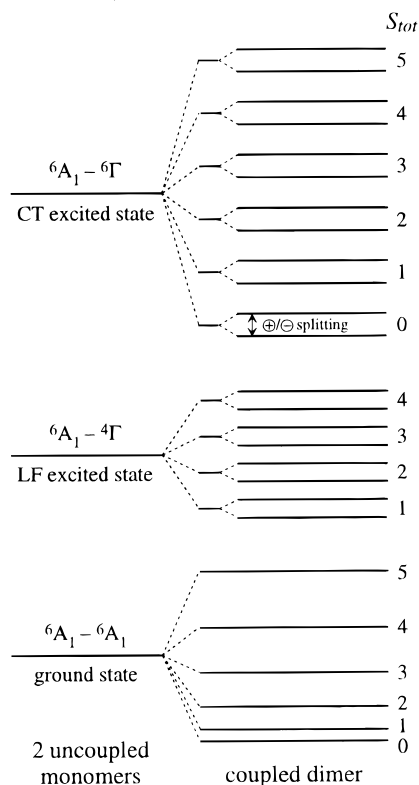


Figure 60. Schematic energy level diagram for the ground state and a LF and a CT excited state of Fe^{III} showing the effects of the dimer formation.

magnetic exchange coupling between the two $S = 5/2$ monomers gives rise to the $S_{\text{tot}} = 0, 1, 2, 3, 4, 5$ spin ladder shown in the right bottom half of Figure 60. The splitting can be modeled using the phenomenological spin Hamiltonian, eq 19, with J in the range between -80 and -120 cm^{-1} .⁶³¹ Thus, at 4 K only the singlet component of the exchange-split dimer ground state is thermally populated, whereas at 300 K the singlet, triplet, and quintet sublevels have significant population. While the singlet state is EPR silent, the higher spin states exhibit EPR signals that grow in with increasing temperature. Recent single-crystal EPR studies on $\text{enH}_2[(\text{FeHEDTA})_2\text{O}]\cdot 6\text{H}_2\text{O}$, possessing a roughly linear Fe–O–Fe unit, $\angle(\text{Fe–O–Fe}) = 165^\circ$, have provided accurate spin Hamiltonian parameters, such as ZFS parameters for the $S_{\text{tot}} = 1, 2,$ and 3 states as well as the orientation of the ZFS tensor relative to the dimer structure.⁶⁴⁸ There is the potential for more information to be obtained from single-crystal EPR studies on ferric oxo dimers in the future by using high-field EPR spectroscopy.

In ferric oxo dimers, the ground-state exchange coupling constant shows only a minor dependence on $\angle(\text{Fe–O–Fe})$ (Table 15) because individual contributions to J (eq 23) maximize and minimize for different Fe–O–Fe angles.^{649,650} In contrast to the case of oxo-bridged $[\text{Mn}^{\text{III}}]_2$ dimers where J exhibits a marked angular dependence,^{651,652} little information on the core geometries of structurally ill-defined oxo-bridged biferric sites can be derived from J . An alternative approach for the study of ferric oxo dimer core structures has been developed⁶⁴⁵ from the observed

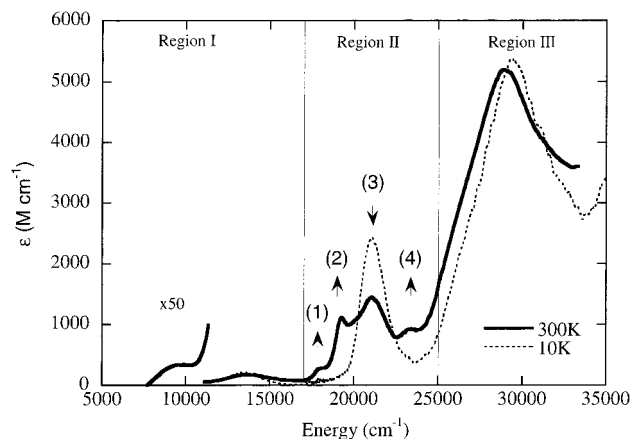


Figure 61. Unpolarized 300 K (—) and 10 K (---) absorption spectra of $[\text{Fe}(\text{III})_2\text{O}(\text{OAc})_2(\text{Me}_3\text{tacn})_2]^{2+}$ ($\angle(\text{Fe–O–Fe}) = 120^\circ$). Bands 1 and 2 correspond to the $S = 2$ and $S = 1$ components, respectively, of the ${}^4\text{A}_1$ LF excited state, and band 3 is due to the singlet, in-plane π oxo-to-Fe^{III} CT transition. (Reprinted with permission from ref 639. Copyright 1995 American Chemical Society.)

Raman shift of the symmetric and antisymmetric Fe–O–Fe stretching modes, ν_s and ν_{as} , respectively, which exhibit a roughly linear dependence on $\angle(\text{Fe–O–Fe})$. As the core angle changes from 90° to 180° , ν_s decreases from ~ 600 to 400 cm^{-1} concomitant with an increase of ν_{as} from ~ 700 to $\sim 900 \text{ cm}^{-1}$. Correlations such as this allow key structural features of transient, nonisolable enzyme intermediates to be identified, aiding determination of the mechanism in binuclear non-heme iron enzymes.

Excited States. Unpolarized electronic absorption spectra of $[\text{Fe}^{\text{III}}_2\text{O}(\text{OAc})_2(\text{Me}_3\text{tacn})_2]^{2+}$ ($\angle(\text{Fe–O–Fe}) = 120^\circ$) at 10 and 300 K are shown in Figure 61.⁶³⁹ The spectra are divided into three regions according to band intensities and temperature effects. In region I, two weak bands are observed with maxima at ~ 9500 and 13500 cm^{-1} . On the basis of the Tanabe–Sugano diagram for octahedral d^5 ions (Figure 12), these features were assigned to the ${}^6\text{A}_1 \rightarrow {}^4\text{T}_1^a$ and ${}^6\text{A}_1 \rightarrow {}^4\text{T}_2^a$ LF transitions. Strikingly, in ferric oxo dimers these formally spin-forbidden LF transitions are at least 1 order of magnitude more intense than for roughly octahedral Fe^{III} monomers and they are almost exclusively polarized along the Fe \cdots Fe vector.

Region II in Figure 61 is dominated by at least four overlapping bands that exhibit a remarkable temperature dependence. Upon cooling to 10 K the most intense feature at $\sim 21000 \text{ cm}^{-1}$ (band 3) almost doubles in intensity, indicating that it arises from a transition originating from the $S_{\text{tot}} = 0$ component of the dimer ground state (Figure 60, bottom). On the basis of the high absorption intensity and rR excitation profile data for the symmetric Fe–O–Fe stretching mode ν_s , this feature was assigned to an oxo-to-Fe CT transition. In ferric dimers, the CT excited states are obtained by coupling the ${}^6\text{A}_1$ ground state of one iron center with the ${}^6\Gamma$ CT excited state of the other iron.⁶⁵³ Since either of the two metal ions can be excited, the proper dimer wave functions are given by the symmetric and antisymmetric combinations of the locally excited configurations and the corresponding states are split in energy by Coulomb and

exchange-mediated excitation transfer (Figure 60, top).^{634,636,654} The other features in region II virtually disappear at LT, indicating that they arise from transitions originating from the $S_{\text{tot}} = 1$ and 2 ground-state components. The fact that the temperature dependence of band 3 follows the expected behavior for a pure singlet transition requires that the other S_{tot} components are significantly higher in energy, indicating that the corresponding oxo-to-Fe CT excited state is subject to a large antiferromagnetic energy splitting. From their temperature dependencies, bandwidths, and spectral positions, bands 1 and 2 in Figure 61 (region II) correspond to LF transitions. These features are much sharper than the LF bands in region I, which led to their assignments as components of the LF-independent ${}^6A_1 \rightarrow {}^4A_1$ spin flip transition.⁶³⁹ The variable-temperature behavior of bands 1 and 2 indicates that the $S = 2$ component is $\sim 1350 \text{ cm}^{-1}$ lower in energy than the $S = 1$ component, consistent with ferromagnetic coupling in the 4A_1 excited state.

Region III of the absorption spectrum of $[\text{Fe}^{\text{III}}_2\text{O}(\text{OAc})_2(\text{Me}_3\text{tacn})_2]^{2+}$ (Figure 61) consists of a series of intense CT absorption features, the so-called “oxo dimer bands”, that exhibit a moderate temperature dependence (note that in linear ferric oxo dimers the number of allowed oxo-to-Fe CT transitions is smaller than in bent dimers; thus, the extent of band overlaps in region III is greatly reduced in the former spectrum, which results in a far more dramatic temperature dependence⁶³⁹). From polarized single-crystal specular reflectance data (not shown), the major absorption bands below $30\,000 \text{ cm}^{-1}$ are polarized parallel to the $\text{Fe}\cdots\text{Fe}$ vector, which permitted their assignments as oxo-to-Fe CT transitions.⁶³⁹ Significantly, similar bands are not present in the absorption spectra of oxo-coordinated ferric monomers; e.g., the onset to the lowest-energy CT absorption in the spectrum of Fe^{III} doped into Al_2O_3 is observed above $40\,000 \text{ cm}^{-1}$.⁶⁵⁵

In summary, the most remarkable features in the electronic absorption spectrum of ferric oxo dimers (Figure 61) are (i) the LF transitions are unusually intense, (ii) the nature of the superexchange interaction can change upon excitation, as is seen on going from the antiferromagnetic ground state to the ferromagnetic 4A_1 LF excited state, and (iii) several oxo-to-Fe CT bands peak below $30\,000 \text{ cm}^{-1}$ that exhibit a strong temperature dependence and have no counterparts in the spectra of monomeric analogues. These bands are associated with the singlet components of CT excited states that are stabilized in energy due to large excited-state antiferromagnetism (ESAF).

2. Origin of Unique Spectral Features. Ferromagnetism in the 4A_1 LF Excited State: Significance of the Mixed π/σ Fe–O–Fe Superexchange Pathway. The ground-state exchange coupling constant J of a ferric oxo dimer is readily obtained from a fit of the experimental susceptibility data using eq 22.⁶³¹ In general the effectiveness of individual superexchange pathways contributing to J (eq 23), however, are not determined experimentally and must be inferred from electronic structure calculations. $[\text{Fe}^{\text{III}}_2\text{O}(\text{OAc})_2$ -

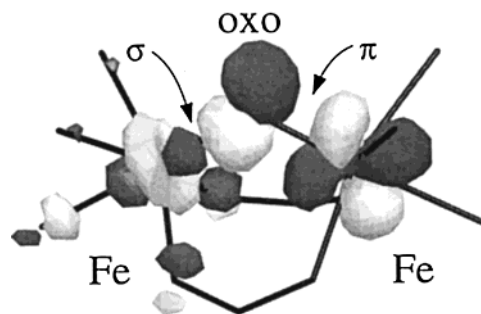


Figure 62. Boundary surface plot of the mixed Fe–O–Fe π/σ superexchange pathway that produces the dominant contribution to the strong antiferromagnetic coupling in the ground state of $[\text{Fe}^{\text{III}}_2\text{O}(\text{OAc})_2(\text{Me}_3\text{tacn})_2]^{2+}$ ($\angle(\text{Fe}–\text{O}–\text{Fe}) = 120^\circ$).

$(\text{Me}_3\text{tacn})_3]^{2+}$ possessing a bent Fe–O–Fe unit, $\angle(\text{Fe}–\text{O}–\text{Fe}) = 120^\circ$, provides a rare example where the dominant pathways were identified on the basis of the electronic absorption spectrum (Figure 61). According to the Tanabe model for LF excited states of dimers, ${}^6A_1 \rightarrow {}^4A_1$ excitation primarily reduces the efficiency of the mixed Fe–O–Fe π/σ superexchange pathway illustrated in Figure 62. Thus, the observed ferromagnetic exchange coupling in the 4A_1 LF excited state (Figure 61, region II, bands 1, 2) demonstrates that this pathway produces the dominant contribution to the ground state J in bent oxo-bridged ferric dimers.⁶³⁹ This model is consistent with experimental results obtained on $\text{Fe}^{\text{III}}–\text{O}–\text{Mn}^{\text{III}}$ ^{656,657} and $\text{Mn}^{\text{III}}–\text{O}–\text{Mn}^{\text{III}}$ ⁶⁵⁸ dimers and supported by DFT calculations.^{639,659,660} The significance of the mixed Fe–O–Fe π/σ superexchange pathway (Figure 62) with respect to protein function is discussed in section III.B.

Dimer Intensity Mechanisms for LF Transitions: Importance of a Highly Covalent Fe–O Bond. There are two dominant mechanisms that can be responsible for a relative increase in intensity of LF transitions in dimers (Figure 61, region I).⁶³⁹ The first mechanism involves thermal population of higher spin components of the exchange-split dimer ground state, from which spin-allowed transitions exist to the LF excited states.⁶⁶¹ This is illustrated in Figure 60 (center right). The LF excited states in ferric dimers are obtained by coupling the 6A_1 ground state of one Fe^{III} center with the ${}^4\Gamma$ excited states of its partner; thus, each LF excited state generates the four total spin levels $S_{\text{tot}} = 1, 2, 3,$ and 4 in the dimer (Figure 60, center right).⁶⁵³ Analogous to the CT excited states (vide supra), the LF excited states are further split by excitonic interactions,^{634,636,654} yielding a total of eight spin-allowed transitions in the dimer for each (spin-forbidden) monomer LF transition. While this exchange model properly accounts for the increase in intensity of the LF transitions with increasing temperature (gradual population of the $S_{\text{tot}} = 1$ and 2 components of the ground state), it fails to explain the high absorption intensity observed at 10 K.

The second intensity mechanism involves single-site SOC and leads to the spin selection rules $\Delta S = 0$ and ± 1 .⁵⁵ The same mechanism is operative in monomers, however, requiring that features unique

to the ferric oxo dimers exist that greatly increase the efficiency of SOC. The two terms contributing to the intensity of formally spin-forbidden transitions of Fe^{III} complexes are (i) SO mixing of quartet LF character (⁴T₁) into the sextet ground state and (ii) SO mixing of sextet CT character (⁶T₁) into the quartet LF excited states:⁶⁴

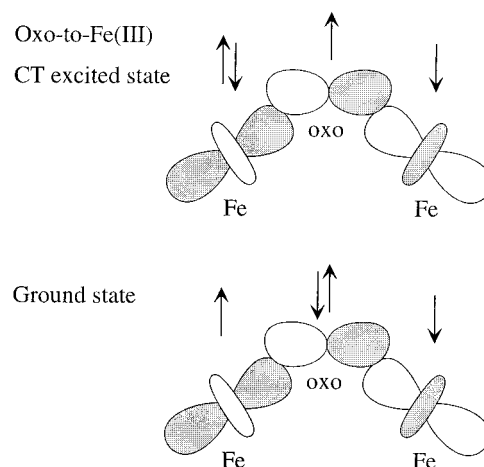
$$\begin{aligned} \langle {}^6A_1M_S|M_q|{}^4\Gamma M_S'\theta' \rangle = & \frac{\langle {}^6A_1M_S|H_{SO}|{}^4T_1M_S''\theta'' \rangle \langle {}^4T_1M_S''\theta''|M_q|{}^4\Gamma M_S'\theta' \rangle}{(E({}^4T_1) - E({}^6A_1))} + \\ & \frac{\langle {}^6A_1M_S|M_q|{}^6T_1M_S''\theta'' \rangle \langle {}^6T_1M_S''\theta''|H_{SO}|{}^4\Gamma M_S'\theta' \rangle}{(E({}^6T_1) - E({}^4\Gamma))} \quad (24) \end{aligned}$$

M_S , $M_S'(\theta')$, and $M_S''(\theta'')$ are the spin (and orbital) components of the ⁶A₁, ⁴Γ, and ⁶T₁ or ⁴T₁ states. H_{SO} is the SO operator, and M_q ($q = x, y, z$) is the electric dipole operator in the q direction. Evaluation of the first term in eq 24 indicates that this contribution, which is usually dominant in monomers, is virtually unchanged in dimers. In contrast, the contribution from the second term increases dramatically in oxo-bridged [Fe^{III}]₂ dimers due to the close energetic proximity of the ⁴T LF and ⁶T₁ oxo-to-Fe CT excited states and the high covalency of the Fe–oxo bond (note that in the ionic limit the relevant SOC matrix elements vanish).⁶³⁹

Exchange Coupling in CT Excited States: Experimental Probe of Superexchange Pathways. The “oxo dimer bands” (Figure 61, region II band 3 and region III) have no counterparts in the spectra of oxo-coordinated Fe^{III} monomers, causing them to be originally assigned as simultaneous pair excitations (SPEs),⁶⁶¹ corresponding to one-photon excitations of LF transitions on both Fe centers that become allowed through exchange interactions.⁶⁶² More recently these features were assigned as oxo-to-Fe CT transitions whose low energies were explained in terms of large antiferromagnetic energy splittings in the corresponding excited states.^{639,663} Formally, each oxo-to-Fe CT excitation leaves an unpaired electron in an oxo p orbital that has strong covalent overlap and that directly couples with the unpaired electron in one of the half-occupied d-orbitals on the second iron (Scheme 20). Therefore, CT excited-state exchange coupling with direct orbital overlap is greatly enhanced over ground-state exchange coupling that is due to superexchange. This is the origin of large ESAF that leads to a substantial stabilization of the singlet oxo-to-Fe CT excited states and, therefore, to the appearance of the ferric oxo dimer absorption bands at low energy (region II, band 3 and region III, Figure 61).

Quantitative insight into the origin of the strong CT ESAF in ferric oxo dimers was obtained by employing the recently developed valence-bond configuration interaction (VBCI) model of Tuzek and Solomon.⁶⁶⁴ In the VBCI formalism, ground-state antiferromagnetism (GSAF) arises from CI mixing of metal-to-metal CT (MMCT) and double CT (DCT) excited-state character into oxo-to-Fe CT excited states, which in turn CI mix into the ground state. Thus, in this formalism, superexchange is described

Scheme 20. Illustration of Superexchange (Ground State, Bottom) versus Direct Exchange (oxo-to-Fe^{III} CT Excited State, top) for a Ferric Oxo Dimer



as involving an oxo-to-Fe(1) CT transition, followed by either an Fe(2)-to-oxo CT transition (yielding an MMCT excited state) or an oxo-to-Fe(2) CT transition (corresponding to a DCT excited state). The relevant configurations are illustrated in Figure 63 (left). The MMCT and DCT excited states arise from coupling of two $S = 2$ monomer units, yielding total spin values ranging from $S_{\text{tot}} = 0$ to 4. Significantly, there are no $S_{\text{tot}} = 5$ MMCT and DCT states; thus, the $S_{\text{tot}} = 5$ components of the CT excited states are not stabilized in energy, which is key to the large observed ESAF in ferric oxo dimers. The effects of CI on the $S_{\text{tot}} = 0$ and 5 states are schematically illustrated in Figure 63 (right). Because GSAF derives from CI mixing of the ground state with CT excited states subject to ESAF, the ground-state J value can be approximated by a sum of individual contributions J_i^{CT} from all CT excited states Γ_i^{CT} as follows:⁶⁶⁵

$$-2J \cong \sum_i \lambda_i^2 (-2J_i^{\text{CT}}) \quad (25)$$

The λ_i 's are the first-order mixing coefficients given by

$$\lambda_i = \langle {}^1A_1^{\text{GS}}|H|{}^1\Gamma_i^{\text{CT}} \rangle / (E({}^1A_1^{\text{GS}}) - E({}^1\Gamma_i^{\text{CT}})) \quad (26)$$

where the Hamiltonian H comprises a sum of one-electron operators and the electron–electron repulsion e^2/r_{lm} and λ_i^2 reflects the covalent mixing into the ground state of the CT excited states associated with the bridging ligand. Because the mixing coefficients (eq 26) are on the order of ~ 0.1 , antiferromagnetic coupling in CT excited states can be 1–2 orders of magnitude larger than the ground-state exchange coupling. Note from Figure 63 and eq 25 that the VBCI formalism correlates the efficiency of a given superexchange pathway in mediating GSAF with the extent of antiferromagnetic energy splitting of the CT excited-state involved in that pathway. Thus, analysis of the CT absorption spectrum can

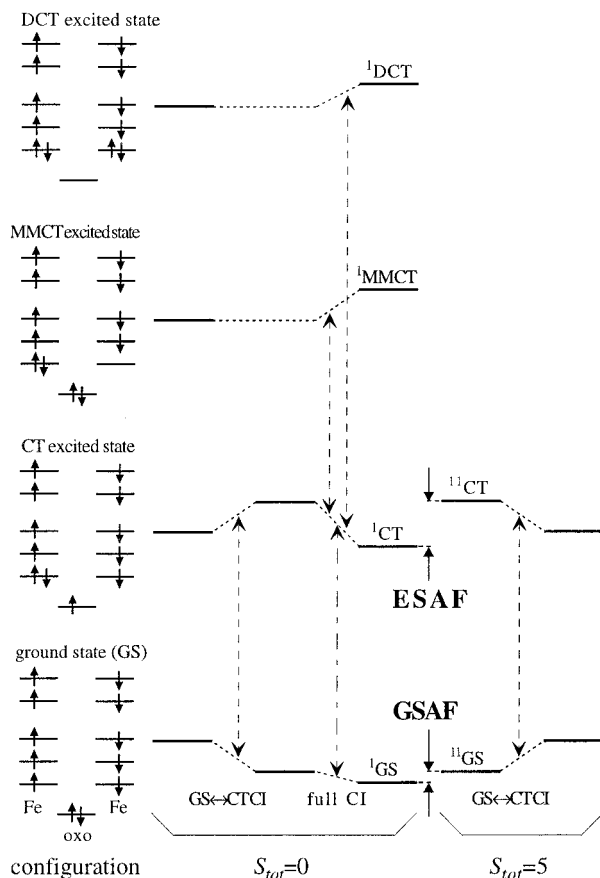


Figure 63. Schematic energy level diagram for a ferric dimer showing the relevant CIs that give rise to antiferromagnetic coupling in the dimer ground state. In this VBCI formalism, GSAF arises from CI mixing of *singlet* MMCT and DCT excited-state character into *singlet* oxo-to-Fe CT excited states, which in turn CI mix into the *singlet* ground state.

provide unique insight into the specific superexchange pathways associated with ground-state exchange coupling in dimers.

Application of the VBCI model to the $[\text{Fe}^{\text{III}}_2\text{O}(\text{OAc})_2(\text{Me}_3\text{tacn})_3]^{2+}$ complex permitted assignment of the prominent feature at $\sim 21\,000\text{ cm}^{-1}$ in region II (band 3) to the singlet, in-plane π oxo-to- Fe^{III} CT transition, with the corresponding out-of-plane π oxo-to- Fe^{III} CT transition being $\sim 5000\text{ cm}^{-1}$ higher in energy,^{639,666} contrary to what is expected from $\chi\alpha$ -DFT calculations that do not include dimer effects. This inverted ordering scheme for the singlet CT transition indicates that the ESAF splitting of the in-plane π oxo-to- Fe^{III} CT excited state is larger than that of the out-of-plane π oxo-to- Fe^{III} CT excited state. From eq 25 the contribution J^{CT} from the in-plane π CT excited state to the ground state J value is therefore significant, consistent with the observation of ferromagnetic coupling in the $^4\text{A}_1$ LF excited states that requires the existence of a dominant in-plane σ/π superexchange pathway (Figure 62). This superexchange pathway plays a key role in ET through the oxo-bridge (section III.B).

3. Nature of the $\text{Fe}^{\text{III}}\text{--O--Fe}^{\text{III}}$ Bond. In addition to defining superexchange pathways for ET, the oxo-to- Fe^{III} CT spectrum provides a sensitive probe of the nature of the $\text{Fe}^{\text{III}}\text{--O}$ bond. This CT spectrum

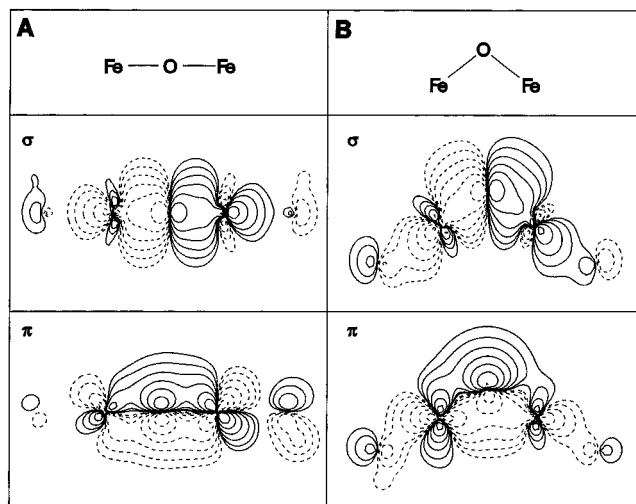


Figure 64. Contour plots of the relevant Fe–O–Fe bonding orbitals in ferric oxo dimers: (A) linear and (B) bent ($\angle(\text{Fe–O–Fe}) = 120^\circ$) structures. (Adapted from ref 699.)

changes dramatically on going from a linear Fe–O–Fe structure to the bent structure of $[\text{Fe}^{\text{III}}_2\text{O}(\text{OAc})_2(\text{Me}_3\text{tacn})_3]^{2+}$ ($\angle(\text{Fe–O–Fe}) = 120^\circ$), indicating that the Fe–O bond is greatly affected by $\angle(\text{Fe–O–Fe})$.⁶³⁹ In the linear unit, the dominant bonding interactions involve the oxygen p_z orbital oriented along the Fe–O–Fe vector and σ -bonding to the Fe^{III} 3d, 4s, and $4p_z$ orbitals (Figure 64, top left) and the oxygen p_x , p_y orbitals that are π -bonding to iron $d\pi$ (and $\text{O}p_x/p_y$) orbitals (Figure 64, bottom left). On going to the bent structure, the σ - and out-of-plane π -bonding interactions do not change significantly (Figure 64, top right), whereas the in-plane π -bonding interaction loses considerable Fe d character and becomes more localized on the bridging oxide (Figure 64, bottom right).⁶⁶⁷ This localization increases the net electron density on the oxo bridge, which would raise its pK_a value by stabilizing the protonated over the deprotonated form.⁶³⁹

A key result from our studies on ferric oxo dimers is that the $\text{Fe}^{\text{III}}\text{--O}$ bond is extremely covalent, as reflected in the high intensities and low energies of the oxo-to- Fe^{III} CT transitions.⁶³⁹ This indicates that the Fe–O–Fe unit is very stable, which has important biological implications. In Hr an oxo bridge is already present at the biferric, hydroperoxide-bound oxyHr level (vide infra). This site is therefore stabilized against further activation of peroxide. In contrast, such an oxo bridge is likely absent in the biferric peroxo intermediates of MMO and R2. Consequently, these species are activated for further reduction of the peroxide, which leads to the formation of oxo-bridged sites in the corresponding high-valent intermediates, as evidenced by EXAFS experiments (vide infra). These results suggest that binuclear non-heme iron proteins can limit the possible Fe oxidation states traversed during catalysis through the formation of a highly covalent oxo bridge.

In summary, ferric oxo dimers have been ideal systems to explore the effects of coupling two Fe centers in a binuclear site. This is primarily due to the high covalency of the Fe–oxo–Fe bond and the

Table 16. Summary of Exchange Coupling Constant for Reduced Binuclear Non-Heme Iron Proteins and Model Complexes

protein	type of bridges	J^a (cm ⁻¹)	ref
deoxy Hr	(μ -hydroxo)bis(μ -1,3-carboxylato)	-14 ± 2	660
deoxy N ₃ ⁻ Hr	(μ -aquo)bis(μ -1,3-carboxylato)	+2.2 ± 0.4	668
reduced RR	bis(μ -1,3-carboxylato)	-0.5	669
one azide bound reduced RR	bis(μ -1,3-carboxylato)	-2.5 ± 1.0	669
two azide bound reduced RR I	μ -1,3-carboxylato	-2.0 to +2.0	669
two azide bound reduced RR II	bis(carboxylato)	+1.0 ± 0.5	669
reduced MMOH	(μ -1,1-carboxylato)(μ -1,3-carboxylato)	+0.3 ± 0.1	670
reduced MMOH–MMOB	(μ -1,1-carboxylato)(μ -1,3-carboxylato)	+0.4 ± 0.1	670
reduced Δ^9 D	bis(μ -1,3-carboxylato)	< -0.5	671
reduced stearyl–ACP Δ^9 D	bis(μ -1,3-carboxylato)	< -1.5	671

model complexes	type of bridges	J (cm ⁻¹)	ref
[Fe ₂ (OH)(OAc) ₂ (Me ₃ TACN) ₂](ClO ₄)	(μ -hydroxo)bis(μ -1,3-carboxylato)	-13	672,673
[Fe ₂ (H ₂ O)(OAc) ₄ (tmen) ₂]	(μ -aquo)bis(μ -1,3-carboxylato)	< 1.0	674
(Et ₄) ₂ [Fe(salmp) ₂]	bis(μ -phenoxo)	+7	675
[Fe ₂ (OH) ₂ (HB(3,5-Pr ₂ pz) ₃) ₂]	bis(μ -hydroxo)	< 0	676
[Fe ₂ (O ₂ CC(CH ₃) ₃) ₄ (Pyr) ₂]	4-(μ -1,3-carboxylato)	-25	677
[Fe ₂ (μ -XDK)(μ -OBz)(Im) ₂ (OBz)(MeOH)]	tri(μ -1,3-carboxylato)	-1	677
[Fe ₂ (O ₂ CPh) ₄ (Pyr) ₄]	bis(μ -1,3-carboxylato)	+2	678
[Fe ₂ (O ₂ CH) ₄ (BIPhMe) ₂]	(μ -1,1-carboxylato)bis(μ -1,3-carboxylato)	~0	678

^a $H = -2JS_1S_2$.

associated large antiferromagnetic energy splittings in the ground and CT excited states, which can be probed experimentally. The other known bridging ligands occurring at binuclear non-heme iron active sites involved in reversible binding or activation of O₂ develop much weaker bonding interactions with the Fe centers. Therefore, the electronic spectra of sites lacking a bridging oxide (which includes the hydroxo- and carboxylato-bridged diferric and all diferrous sites) are essentially a superposition of two monomer spectra, one for each iron of the dimer. Nevertheless, exchange interactions between the two Fe centers are typically sufficiently strong to produce a magnetically coupled dimer whose electronic structure can be explored through magnetic susceptibility, EPR, and MCD spectroscopic experiments.

2. [Fe^{II}]₂

Fully reduced binuclear non-heme iron sites contain two exchange-coupled high-spin ferrous ions. The geometric and electronic structure of each ferrous site can be determined through the excited-state methodology described in the mononuclear non-heme iron section (vide supra, section II.A.1). Thus, the LT MCD spectrum is the sum of contributions from each iron, and the observation of more than two LF transitions immediately indicates significantly different geometric and electronic structures for each ferrous center.

The electronic structure of the ground state can be described by the ZFS parameters of the individual ferrous centers and the exchange-coupling interaction between the two irons through bridging ligands. From LF theory and experimental results, the largest reasonable magnitude for the axial ZFS parameter (D) of a mononuclear ferrous center should be approximately $|15|$ cm⁻¹. The exchange-coupling interaction (J) between the two ferrous ions is generally much smaller than that for binuclear ferric systems due to the fact that the bridging ligand interactions

with the iron atoms are less covalent, as they involve mainly carboxylate and hydroxo ligands for the relevant biological systems. Thus, the magnitudes of J and D become comparable and have to be considered together in order to describe the electronic structures of the ground states of fully reduced binuclear non-heme iron sites. J values for binuclear ferrous proteins and model complexes are summarized in Table 16.

a. Electronic Structure. Equation 27 gives the spin Hamiltonian for an exchange-coupled biferrous system

$$H = -2J\mathbf{S}_1 \cdot \mathbf{S}_2 + D_1(\mathbf{S}_{z1}^2 - 1/3S(S+1)) + E_1(\mathbf{S}_{x1}^2 - \mathbf{S}_{y1}^2) + D_2(\mathbf{S}_{z2}^2 - 1/3S(S+1)) + E_2(\mathbf{S}_{x2}^2 - \mathbf{S}_{y2}^2) + g_{z1}\beta H_z \mathbf{S}_{z1} + g_{x1}\beta H_x \mathbf{S}_{x1} + g_{y1}\beta H_y \mathbf{S}_{y1} + g_{z2}\beta H_z \mathbf{S}_{z2} + g_{x2}\beta H_x \mathbf{S}_{x2} + g_{y2}\beta H_y \mathbf{S}_{y2} \quad (27)$$

where the subscripts denote the different ferrous ions, J is the exchange-coupling constant, D and E are the axial and rhombic ZFS parameters from each ferrous ion, and H is the magnetic field strength. We assume that the exchange coupling is isotropic and small anisotropic terms can be combined with the ZFS parameters.^{679–683} The single site $g_{i,Fe^{2+}}$ can be approximately related to the ZFS parameters using LF theory as described by eq 28,¹³ where λ is the Fe^{II} ground-state SOC constant (~ 100 cm⁻¹) and k^2 is the Stevens orbital reduction factor, which is < 1 and quantifies covalency effects.

$$D_{Fe^{2+}} = \frac{-k^2\lambda}{4}(g_{xFe^{2+}} + g_{yFe^{2+}} - 2g_{zFe^{2+}}) \quad (28a)$$

$$E_{Fe^{2+}} = \frac{-k^2\lambda}{4}(g_{yFe^{2+}} - g_{xFe^{2+}}) \quad (28b)$$

This Hamiltonian is applied to an uncoupled basis set $|S_1, S_2, M_{S_1}, M_{S_2}\rangle$. As described in section II.A.1, a high-spin ferrous ion with an $S_i = 2$ and $M_{S_i} = 0$,

± 1 , ± 2 will split due to ZFS as defined by the parameters D and E . In an exchange-coupled system, the two ferrous centers can also interact through the bridging ligands to give $S_{\text{tot}} = |\mathbf{S}_1 + \mathbf{S}_2|$, $|\mathbf{S}_1 + \mathbf{S}_2 - 1|$, ..., $|\mathbf{S}_1 - \mathbf{S}_2| = 4, 3, 2, 1$, and 0 levels. These levels are split in energy by the exchange coupling $H = -2JS_1S_2$ to generate $(2S_{\text{tot}} + 1)$ degenerate M_S levels, which are further split in energy and mixed with other (S_{tot}, M_S) levels by ZFS. Application of eq 27 to the uncoupled basis generates a 25×25 matrix. Diagonalization of this matrix in zero magnetic field gives the wave functions of the binuclear ferrous spin states and their energies, which are dependent on the relative magnitudes and signs of the exchange-coupling and ZFS parameters and the relative orientation of the D tensors. The magnitude of D is constrained to be less than $|15| \text{ cm}^{-1}$; the maximum $|E/D|$ value is $1/3$. Figure 65 shows a series of representative energy-level diagrams generated from different combinations of the sign and magnitude of the exchange-coupling (J) and ZFS parameters (D_1 , D_2 , E_1 , and E_2). Each combination gives unique ground-state properties. Figure 65A shows the energy-level diagram for systems with weak axial ligation, thus negative ZFSs as a function of the sign and magnitude of J . The center of the figure gives the limiting case of two $S_i = 2$ ions having large ZFS (indicated by uncoupled basis functions (M_{S_1}, M_{S_2})) but no exchange coupling. These states split in energy when the two ferrous centers are allowed to couple ($|J| > 0$), resulting in dimer wave functions expressed as $(S_{\text{tot}}, |M_S|)$. The left side of the figure gives antiferromagnetic coupling ($J < 0$), which generates two accidentally energetically degenerate $(S_{\text{tot}}, |M_S|) = (0, 0)/(1, 0)$ levels as the ground state and $(4, 4)$ or $(1, 1)$ as the first excited state depending on the magnitude of J . The right side gives the ferromagnetic case ($J > 0$), producing an $(S_{\text{tot}}, |M_S|) = (4, 4)$ non-Kramers doublet ground state and different excited states dependent on the magnitude of J . Thus, when $J < 0$ and the ZFS is negative, the ground state is a singlet and would not show MCD intensity at LT and low magnetic field (vide infra). For $J > 0$ with negative ZFS, the ground state will be paramagnetic with $M_S = \pm 4$, thus $g_{\parallel} = 16$.

Strong axial ligation and thus a positive ZFS dramatically alters the energy-level diagram. Figure 65B presents the energy diagram with $D_1 = D_2 = +10 \text{ cm}^{-1}$ and axial symmetry ($E_1 = E_2 = 0$) for a range of J values from -5 to $+5 \text{ cm}^{-1}$. The right side of the diagram gives ferromagnetic coupling ($J > 0$) with an $(S_{\text{tot}}, |M_S|) = (4, 0)$ ground state and an $(S_{\text{tot}}, |M_S|) = (4, 1)$ first excited state regardless of the magnitude of J . The left side gives antiferromagnetic coupling ($J < 0$) with an $(S_{\text{tot}}, |M_S|) = (0, 0)$ ground state and $(S_{\text{tot}}, |M_S|) = (1, 1)$ first excited state independent of the magnitude of J . The $M_S = 0$ ground state is MCD-inactive but can gain intensity by mixing with the excited sublevels if the energy difference between the ground and excited levels is small.

Systems with two significantly different ferrous centers have unequal ZFSs. Figure 65C shows the energy-level diagram generated for $D_1 = -10 \text{ cm}^{-1}$, $D_2 = -5 \text{ cm}^{-1}$, and axial ($E_1 = E_2 = 0$) symmetry over

a range of J values from -5 to $+5 \text{ cm}^{-1}$. As observed for the symmetric case in Figure 65A, the ground state remains $(S_{\text{tot}}, |M_S|) = (4, 4)$ for ferromagnetic coupling ($J > 0$) and $(0, 0)$ for antiferromagnetic coupling ($J < 0$). Alternatively, when the D values associated with each ferrous site have opposite signs, the energy-level diagram significantly changes. Figure 65D presents the energy-level diagram generated for $D_1 = -10 \text{ cm}^{-1}$, $D_2 = +5 \text{ cm}^{-1}$, and axial ($E_1 = E_2 = 0$) symmetry for a range of J values from -5 to $+5 \text{ cm}^{-1}$. The right side of the figure corresponds to ferromagnetic coupling ($J > 0$). This results in an $(S_{\text{tot}}, |M_S|) = (2, 2)$ ground state when J is small but changes to $(3, 3)$ when $J > \sim 1 \text{ cm}^{-1}$, with different excited states dependent on the magnitude of J . The left side gives the antiferromagnetic coupling case ($J < 0$), which generates a different ground state as $-J$ increases: $(S_{\text{tot}}, |M_S|) = (2, 2)$, $(1, 1)$, or $(0, 0)$. Thus, different VTVH MCD saturation behavior associated with different g -values will be observed depending on the magnitude of $-J$ (vide infra).

Inclusion of a rhombic perturbation (to $E = 1/3D$, vide supra) in the energy diagram removes all degeneracy and produces mixed wave functions, as shown in Figure 65E. The relative energy order of the spin states, however, is not significantly affected. The possibility of noncollinearity of the ZFS tensors of the two ferrous centers also needs to be considered. Figure 65F presents the energy-level diagram for a dihedral angle (β) of 45° of the z axis of each ferrous center relative to the Fe-Fe axis while fixing all other parameters as in Figure 65A. The order of the sublevels within the energy range of interest (up to $\sim 40 \text{ cm}^{-1}$) does not change, but the energy differences do vary.

The sublevels generated above split in energy and interact upon the application of a magnetic field. Figure 66 presents a series of representative calculations performed over a range of antiferromagnetic J values for the axial ($D_1 = D_2 = -10 \text{ cm}^{-1}$) (Figure 65A, left) and rhombic ($|E/D| = 1/3$) (Figure 65E, left) cases for the lowest energy sublevels of the ground state in the presence of a magnetic field of up to 7 T. When J is small relative to the ZFS ($-J = 0.5 \text{ cm}^{-1}$, Figure 66A), a crossover of energy levels occurs at low magnetic field. This changes the ground state from $|M_S| = 0$ to 4. Turning on the rhombicity (Figure 66B) retains the energy order of the ground and excited states at 0 T, but one $M_S = 0$ state and the $M_S = -4$ state mix as the magnetic field is increased, which gives the ground state $M_S = -4$ character. Both cases result in a change of the VTVH MCD saturation behavior as the magnetic field is increased (vide supra).

From the above summary, different combinations of the parameters J , D , and E with different magnitudes, extents of noncollinearity, and variation in magnetic field give different energy splitting patterns. Thus, each specific case has to be considered separately to gain insight into its ground-state electronic structure.

b. Variable-Temperature, Variable-Field Magnetic Circular Dichroism. VTVH MCD can be used to probe the exchange-coupled ground state of high-

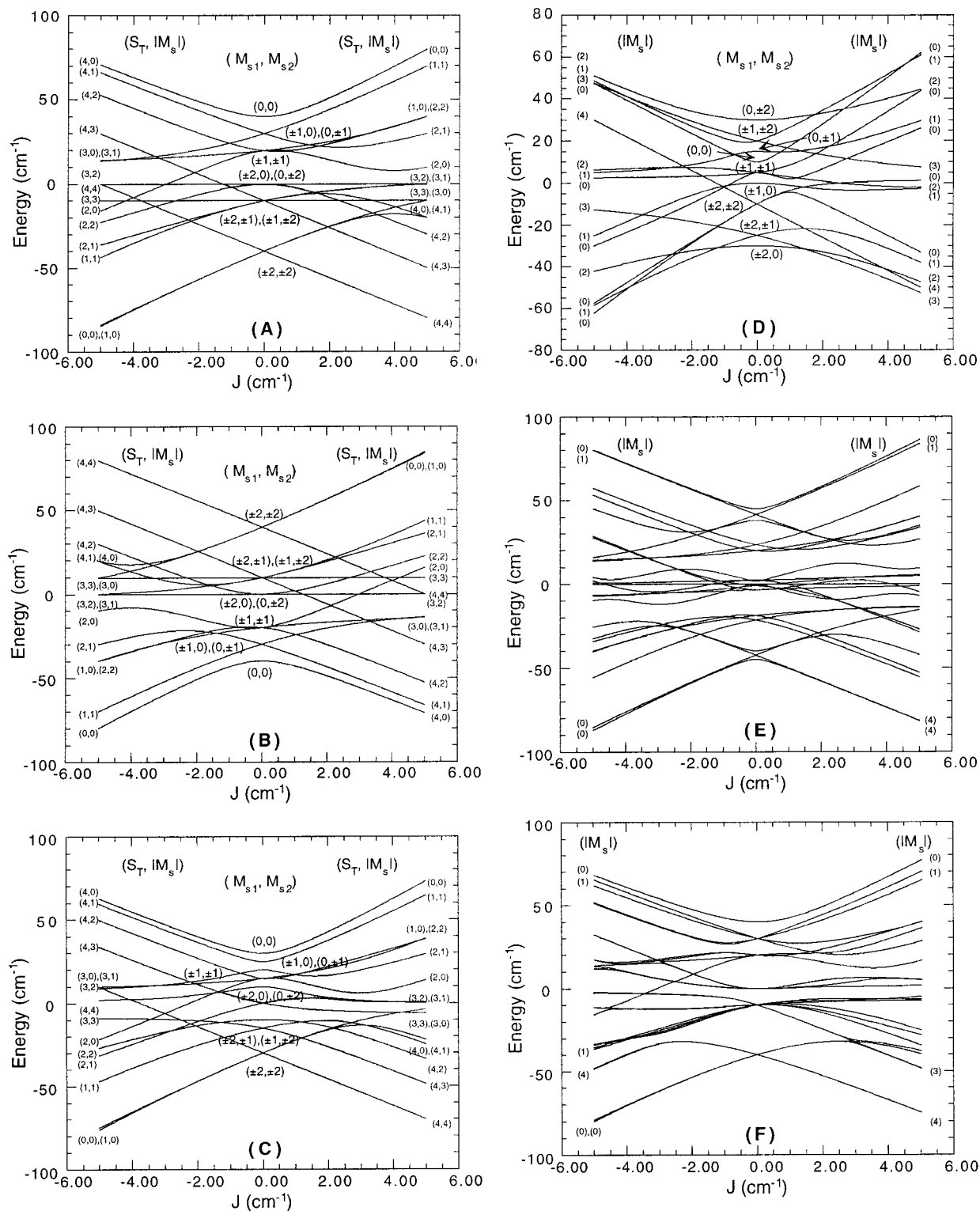


Figure 65. Correlation diagrams of the energy levels of the binuclear ferrous ground state including exchange coupling and single-site ZFS. The exchange coupling (J) is varied from -5 to $+5$ cm^{-1} . The central portion gives the pure ZFS limit with states labeled with M_{S_i} values for each uncoupled Fe^{II} (M_{S_1} , M_{S_2}). The right side indicates a ferromagnetic interaction ($J > 0$) between the ferrous atoms and the left an antiferromagnetic interaction ($J < 0$) with each state labeled as (S_T , $|M_S\rangle$). The M_S is continuous from the left to right, while the S_T changes. The spin Hamiltonian used for calculating the levels is given in eq 27, with (A) $D_1 = D_2 = -10$ cm^{-1} , and $E_1 = E_2 = 0$, (B) $D_1 = D_2 = +10$ cm^{-1} and $E_1 = E_2 = 0$, (C) $D_1 = -10$, $D_2 = -5$ cm^{-1} , and $E_1 = E_2 = 0$, (D) $D_1 = -10$, $D_2 = +5$ cm^{-1} , and $E_1 = E_2 = 0$, (E) $D_1 = -10$, $D_2 = -10$ cm^{-1} , and $E = \frac{1}{3}|D|$, and (F) $D_1 = D_2 = -10$ cm^{-1} , $E_1 = E_2 = 0$, and $\beta = 45^\circ$. $H = 0$ for all figures. (Adapted from ref 671.)

spin ferrous active sites to extract the parameters in eq 27. As described in section II.A.1, the saturation-magnetization curves for ferrous systems are nested

with the high-temperature data offset from the LT data. Such behavior is associated with rhombic ZFS of the ground state doublet and arises from nonlinear

field-induced mixing between the partners of the non-Kramers doublet. In addition, at LT and high field where the non-Kramers doublet is saturated, the MCD intensity still increases linearly with increasing field. This behavior reflects the additional presence of a **B**-term derived from mixing with higher energy sublevels of the ground state (and with excited states).

The MCD intensity expression for a non-Kramers system, allowing for the effects of a linear **B**-term and the presence of excited sublevels of the ground state, is given in eq 29^{12,13,17,22,23}

$$\Delta\epsilon = \sum_i \left[(A_{\text{sat}})_i \left(\int_0^{\pi/2} \frac{\cos^2 \theta \sin \theta}{\Gamma_i} g_{\parallel i} \beta H \alpha_i d\theta - \sqrt{2} \frac{M_z}{M_{xy}} \int_0^{\pi/2} \frac{\sin^3 \theta}{\Gamma_i} g_{\perp i} \beta H \alpha_i d\theta \right) + B_i H \gamma_i \right] \quad (29)$$

where

$$\Gamma_i = \sqrt{\delta_i^2 + (g_{\parallel i} \beta H \cos \theta)^2 + (g_{\perp i} \beta H \sin \theta)^2}$$

$$\alpha_i = \frac{e^{-(E_i - \Gamma/2)/kT} - e^{-(E_i + \Gamma/2)/kT}}{\sum_j e^{-(E_j - \Gamma/2)/kT} + e^{-(E_j + \Gamma/2)/kT}}$$

$$\gamma_i = \frac{e^{-(E_i - \delta/2)/kT} + e^{-(E_i + \delta/2)/kT}}{\sum_j e^{-(E_j - \delta/2)/kT} + e^{-(E_j + \delta/2)/kT}}$$

$(A_{\text{sat}})_i$, B_i , δ_i , $g_{\parallel i}$, and $g_{\perp i}$ are the **C**-term and **B**-term MCD intensity, the rhombic ZFS, and the dimer effective g -values of the i th doublet, respectively. E_i is the energy of the i th sublevel, and the factors α_i and γ_i are the Boltzmann populations for the **C**-term and **B**-term, respectively. H is the applied magnetic field, β is the Bohr magneton, k is the Boltzmann constant, T is the absolute temperature, and M_z and M_{xy} are the transition dipole moments for the direction indicated. Different combinations of these parameters lead to different VTVH behaviors. Thus, VTVH MCD gives the polarization of the LF transition from which the VTVH MCD data are collected. It also provides the electronic structure of the ground state, in particular the energy splittings and g_{\parallel} parameters for the ground and excited sublevels. These parameters often cannot be obtained from EPR due to the large rhombicity of ferrous centers and the exchange coupling.

Figure 67 shows representative VTVH MCD behaviors for the different ground states in Figures 65 and 66 which have different g_{\parallel} values, rhombicity (δ), and energy splittings. From eq 29, the polarization ratio M_z/M_{xy} also affects these saturation magnetization curves. Generally, large g_{\parallel} values of the ground doublet result in more rapid saturation of the VTVH MCD spectra. Figure 67A–C represent the VTVH MCD behavior with ground sublevels having $g_{\parallel} = 16$, 8, and 4, respectively. These correspond to different ground states: (A) $g_{\parallel} = 16$ (right of Figure 65A), $|M_S|$

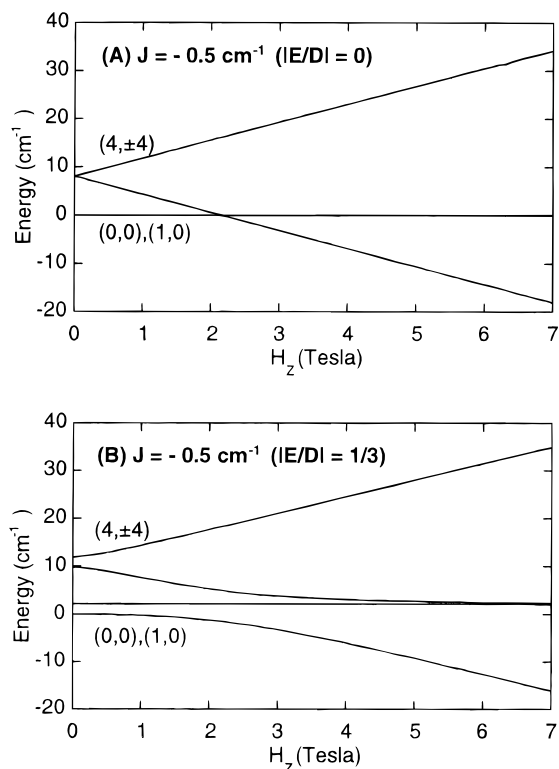
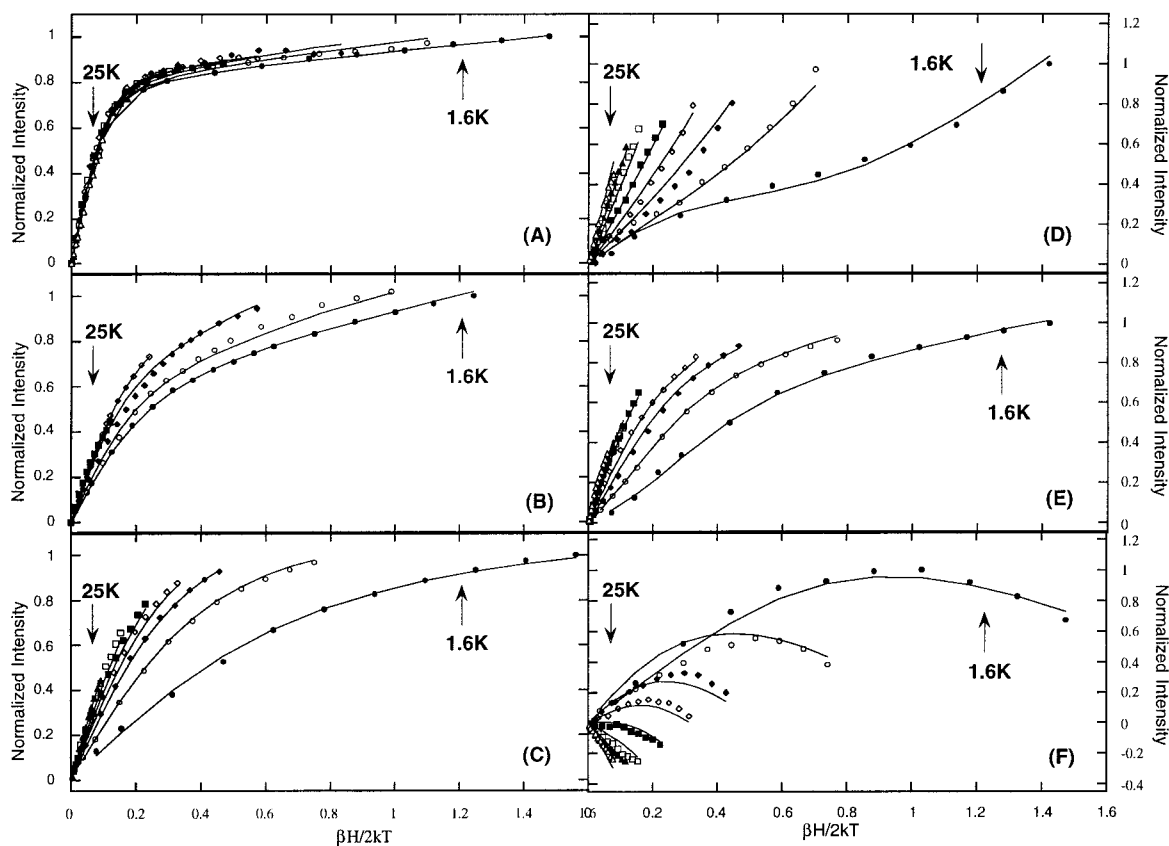


Figure 66. Energy splittings of the binuclear ferrous ground and excited sublevels with negative ZFS in the presence of a magnetic field along the z -axis. The axial ZFS parameters on the two iron atoms are $D_1 = D_2 = -10 \text{ cm}^{-1}$. The rhombic ZFS (E) and the exchange coupling (J) are (A) $J = -0.5 \text{ cm}^{-1}$, $|E/D| = 0$ and (B) $J = -0.5 \text{ cm}^{-1}$, $|E/D| = 1/3$. The ground and excited sublevels are labeled as $(S_{\text{tot}}, \pm M_S)$. The spin Hamiltonian used for calculating the levels is given in eq 27, with $H_x = H_y = 0$ and H_z varied from 0 to 7 T. (Reprinted with permission from ref 671. Copyright 1999 American Chemical Society.)

$= 4$; (B) $g_{\parallel} = 8$ ($-J < 1$ from the left of Figure 65D), $|M_S| = 2$; and (C) $g_{\parallel} = 4$ ($-J > 1$ from the left of Figure 65D), $|M_S| = 1$. The magnitude of the nesting behavior reflects the rhombic splitting (δ) of the ground state (Figure 67A, $\delta < 1 \text{ cm}^{-1}$; Figure 67B–F, $\delta > 2 \text{ cm}^{-1}$). However, when a low-lying excited state is present, there can be a crossover of the ground state in the presence of a magnetic field (Figure 66) which will significantly modify the VTVH MCD data. Figure 67D shows the VTVH MCD behavior of a ground-state crossover of the $|M_S| = 1$ and 2 sublevels of Figure 65E, left with $-J \approx 1.5 \text{ cm}^{-1}$, and Figure 67E presents the ground-state crossover of the $|M_S| = 0$ and 4 sublevels from Figure 65A, left, with $-J < \sim 1 \text{ cm}^{-1}$. From these cases one observes a change of the slope in the LT saturation curves corresponding to the change of ground state.

Thus, the results of the VTVH MCD data can be correlated with the spin Hamiltonian analysis described above to estimate the ground-state spin Hamiltonian parameters. Figure 67A is associated with a $g_{\parallel} = 16$ ($M_S = \pm 4$) ground state which must result from a combination of two ferrous sites with negative ZFSs and ferromagnetic coupling ($D_1 < 0$, $D_2 < 0$, $J > 0$). Figure 67B–D represents a $g_{\parallel} = 8$ ($M_S = \pm 2$) or a $g_{\parallel} = 4$ ($M_S = \pm 1$) ground state, indicating that the ZFSs of the two ferrous sites must have opposite signs and be antiferromagnetically



Summary of the saturation magnetization parameters:

VTVH MCD parameters	(A)	(B)	(C)	(D)	(E)	(F)
ground state g_{\parallel}	16	8	4	4	0	4
first excited state g_{\parallel}	—	—	—	8	16	8
rhombic splitting δ (cm^{-1})	< 1	> 2	> 2	> 2	> 2	> 2
first e.s. energy E_{es} (cm^{-1})	8	6	8	1.5	10	1.5
polarization ratio M_z/M_{xy}	0	0	0	0	0	> 2
spin-Hamiltonian parameters	(A)	(B)	(C)	(D)	(E)	(F)
J^a (cm^{-1})	+0.5	-0.5	-2.5	-1.5	-1.0	-1.5
D_1 (cm^{-1})	-9	+4	+4	+5	-10	-10
D_2 (cm^{-1})	-4	-10	-13	-10	-10	+5

$$^a H = -2JS_1S_2$$

Figure 67. Representative saturation magnetization behaviors of MCD signals of exchange-coupled binuclear ferrous systems. The MCD signal amplitude at fixed wavelength (symbol) for a range of magnetic fields (0–7.0 T) at a series of fixed temperatures is plotted as a function of $\beta H/2kT$. The fit to the VTVH MCD data (—) was obtained using eq 29 with the parameters presented in the table. (Adapted from refs 669–671.)

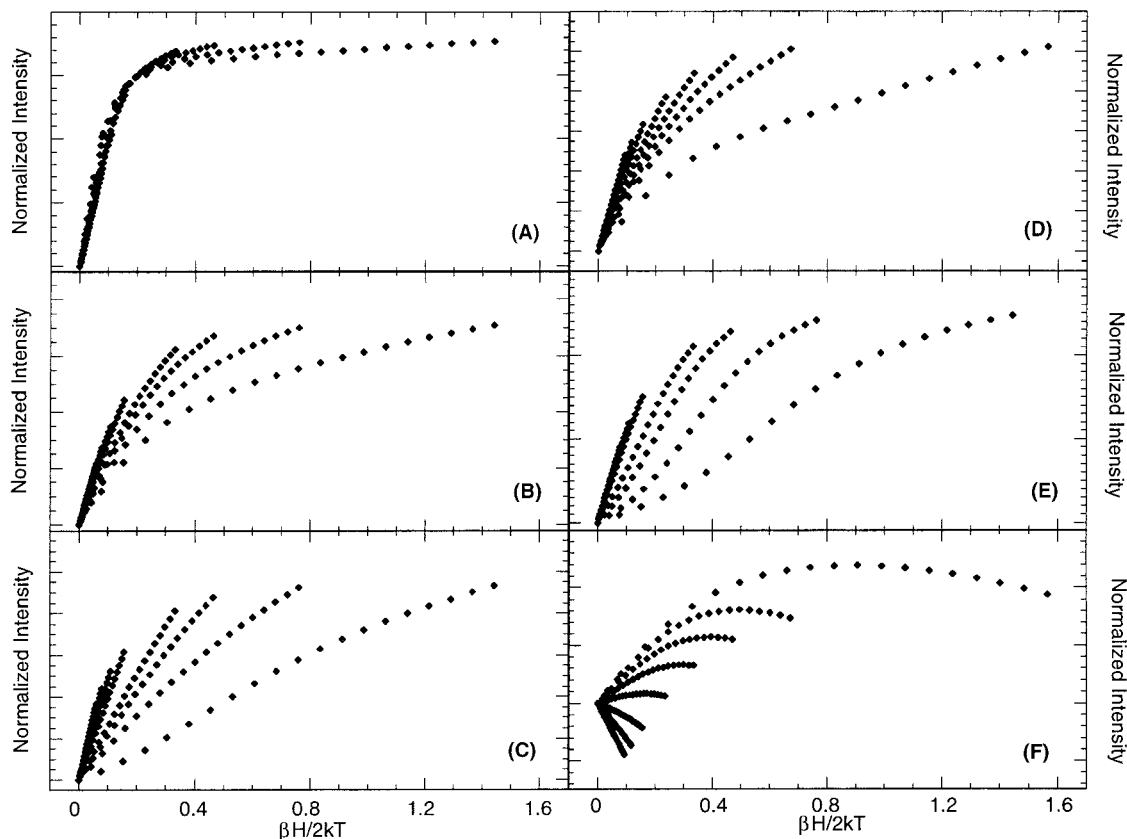
coupled ($D_1 > 0$, $D_2 < 0$, $J < 0$). Figure 67E shows a ground-state crossover of $|M_S| = 0$ and 4 from the spin Hamiltonian analysis in the presence of a magnetic field (Figure 66). This indicates that the two ferrous centers have negative ZFSs and are antiferromagnetically coupled ($D_1 < 0$, $D_2 < 0$, $J < 0$). It should be noted that the magnitude of the exchange coupling can thus be evaluated from the excited-state energy obtained from the VTVH analysis.

Figure 67A–E presents the VTVH MCD behavior for purely xy -polarized transitions (polarization ratio $M_z/M_{xy} \approx 0$ in eq 29). A z -polarized transition is affected by the Zeeman effect in the perpendicular direction (i.e., $g_{\perp} \neq 0$), resulting in a dramatic change in the VTVH MCD behavior. Figure 67F presents data from the same ground-state parameters as in Figure 67D but obtained from a different LF transition having a different polarization.

The above analysis using eq 29 includes an experimentally fit B -term contribution to account for the field-induced mixing between sublevels of the ground state. The VTVH MCD intensity can alternatively be calculated directly using the dimer wave functions from eq 27 and the fact that the MCD intensity is proportional to the spin-expectation values of the single iron center (for which the LF transition is being studied by MCD) projected on the dimer states.⁶⁵ This is given by eq 30

$$\frac{\Delta\epsilon}{E} = \frac{\gamma}{4\pi S} \int_0^\pi \int_0^{2\pi} \sum_i N_i (I_x \langle S_x \rangle_i M_{yz}^{\text{eff}} + I_y \langle S_y \rangle_i M_{xz}^{\text{eff}} + I_z \langle S_z \rangle_i M_{yx}^{\text{eff}}) \sin \theta \, d\theta \, d\varphi \quad (30)$$

where $\Delta\epsilon/E$ is the MCD intensity, I_s are direction cosines, θ is the angle between the magnetic field and



Summary of the saturation magnetization simulation parameters:

spin-Hamiltonian parameters	(A)	(B)	(C)	(D)	(E)	(F)
J^a (cm ⁻¹)	+0.5	-0.5	-2.0	-2.0	-0.5	-2.5
D_1^b (cm ⁻¹)	-10	+3	+3	+3	-15	-7
D_2 (cm ⁻¹)	-7	-7	-7	-7	-15	+3
M_{xy}	1	1	1	1	1	0
M_{xz}	1	1	1	1	0	1
M_{yz}	0	0	0	0	0	0

$$^a H = -2JS_1S_2$$

^b D_1 refers to the ferrous center associated with the ligand field transition from which the saturation magnetization behavior is obtained.

Figure 68. Simulations using the complete spin-Hamiltonian in eq 27 for saturation magnetization behavior of the MCD signal of exchange-coupled binuclear ferrous systems. The MCD signal amplitude at fixed wavelength (symbol) for a range of magnetic fields (0–7.0 T) at a series of fixed temperatures is plotted as a function of $\beta H/2kT$. Parameters used are listed in the inset table. Details of the simulation program are given in ref 65. (Adapted from ref 671.)

molecular z -axis, ϕ is the angle of the xy -projection of the magnetic field with molecular y -axis, the M_s are effective transition dipole moment products, and $\langle S_i \rangle$ s are the components of the spin-expectation value of the i th ground-state sublevel localized on the ferrous site for which the transition is studied. Figure 68A–F gives a series of fits to the data shown in Figure 67A–F using eq 30 obtained by varying the spin Hamiltonian parameters D_1 , D_2 , and J in eq 27. The spin Hamiltonian parameters derived from both methods are consistent with each other in sign and their magnitudes are within their error ranges. The combined VTVH MCD and spin Hamiltonian analysis in eq 27 provide detailed ground-state electronic structure insight for exchange-coupled biferrous systems.

c. Integer Spin Electronic Paramagnetic Resonance. Exchange-coupled binuclear ferrous systems

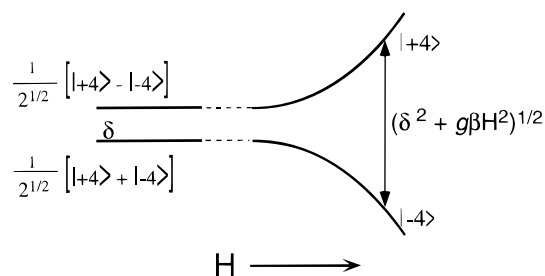


Figure 69. Rhombic splitting of an $M_S = \pm 4$ non-Kramers doublet at zero magnetic field (left) and with increasing applied field (right).

having $S_{\text{tot}} = 4$, $M_S = \pm 4$ non-Kramers doublets can show an integer spin EPR signal if δ is less than ~ 0.3 cm⁻¹ (the microwave energy at X band, Figure 69) or if ZFS strain results in some molecules with δ in this range. This dimer doublet is split by the mono-

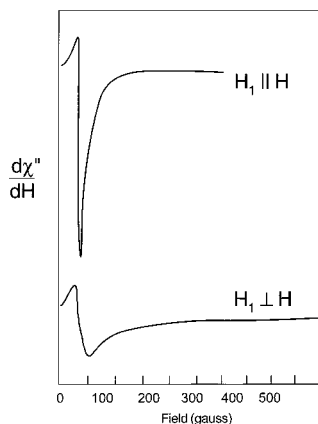


Figure 70. Integer spin EPR spectra of fully reduced methane monooxygenase taken with the microwave field applied parallel (top) and perpendicular (bottom) to the static field H . (Reprinted with permission from ref 684. Copyright 1990 American Chemical Society.)

mer rhombic term E in eq 27 only in fourth order, and thus, δ is small. The resonance between the $M_S = +4$ and -4 sublevels generates a formally $\Delta M_S = 8$ transition, which is forbidden in the normal configuration of EPR experiments. Equation 31 gives the expression for EPR intensity.

$$I \propto |\langle M_S' | g\beta \vec{H} \cdot \vec{S} | M_S \rangle|^2 \quad (31)$$

The normal (transverse mode) EPR experiment involves the magnetic dipole selection rule $\Delta M_S = \pm 1$. For a transverse-mode experiment, the oscillating magnetic field of the microwave radiation H is perpendicular to the external magnetic field and thus projects out the S_x or S_y operator, where $S_x = 1/2(S_+ + S_-)$ and $S_y = 1/2(S_+ - S_-)$. S_+ and S_- operating on M_S require that $M_S' = M_S \pm 1$ for the integral in eq 31 to be nonzero, i.e., $\Delta M_S = \pm 1$. Alternatively, for a longitudinal mode configuration, H is parallel to the external magnetic field and thus projects out the S_z operator, where S_z operating on M_S requires that $M_S' = M_S$ for the integral in eq 31 to be nonzero, i.e., $\Delta M_S = 0$. For the coupled binuclear ferrous system with $-ZFS$ and $+J$, the $M_S = +4$ and -4 wave functions are strongly mixed by the rhombic term in the spin-Hamiltonian. This leads to a $\Delta M_S = 0, 4 \rightarrow 4$ and $-4 \rightarrow -4$, magnetic dipole allowed component in the formally $\Delta M_S = 8$ transition, thus this transition becomes allowed. Figure 70 shows the EPR spectra for fully reduced methane monooxygenase⁶⁸⁴ where $g_{\parallel} = 16$ signals have been observed. It should be noted that the observed resonance position in the EPR spectrum is highly dependent on the value of δ (Figure 69). For systems with a large δ , this rhombicity leads to a decrease in the resonance frequency which results in an apparent increase in the g_{\parallel} value. Thus, the observed g_{\parallel} value may not directly reflect the g_{\parallel} value of the ground state. Alternatively, VTVH MCD data can provide detailed insight into both g_{\parallel} and δ as each has a different effect on the saturation magnetization curves (vide supra).

B. Reversible O_2 Binding to Hemerythrin

Hemerythrin (Hr), which was the first characterized binuclear non-heme iron protein,^{685–687} belongs

to the class of metalloproteins capable of reversible O_2 binding that also includes hemoglobin⁶⁸⁸ (possessing a heme-iron active site) and hemocyanin⁶⁸⁹ (having a binuclear Cu active site). The function of Hr as a dioxygen carrier was first recognized in 1873.⁶⁹⁰ In the past decades Hr has been the subject of extensive biochemical, spectroscopic, and theoretical studies that were aimed at obtaining molecular-level insight into the mechanism of reversible O_2 binding. Because recent excellent review articles^{685–687} provide extensive discussions of the chemistry and molecular structure of Hr, this article will primarily focus on electronic structure contributions to the reaction of Hr with O_2 .

Biochemical Characterization. Hr is found in four phyla of invertebrates and usually occurs as an octamer of virtually identical subunits; however, monomeric (myoHr) as well as dimeric, trimeric, and tetrameric proteins have also been identified.^{685–687} The molecular weight of myoHr is 13.9 kDa, similar to that of the octamer subunit (13.5 kDa). The sequences for a number of Hr species have been determined. In addition to the iron ligands (vide infra) there are other conserved residues that are also believed to be of direct relevance for proper functioning of the protein.⁶⁸⁷ This hypothesis was tested in the case of a conserved leucine residue (103 in the *T. zostericola* myoHr sequence).^{691,692} The corresponding side-chain methyl groups are in van der Waals contact with bound O_2 , suggesting that Leu103 might play a role in stabilizing bound dioxygen with respect to autoxidation. Two mutants of myoHr were prepared, L103V and L103N. Neither mutant forms a stable oxy adduct; instead, rapid autoxidation results in formation of the met forms.

Early experiments on Hr indicated that two iron centers are involved in binding one dioxygen molecule.⁶⁹³ By improving the purification and physical characterization of the protein, Klotz et al.⁶⁹⁴ were able to identify the two physiologically relevant forms of Hr as deoxyHr, containing a diferrous site, and oxyHr, possessing a two-electron-reduced O_2 species bound to an oxo-bridged diferric site. Using rR spectroscopy, Loehr and Klotz et al.^{695–697} were able to show that the O_2 moiety in oxyHr is a hydroperoxide, terminally bound to one Fe center and exhibiting a hydrogen-bond interaction with the bridging oxide. A third form of Hr that has been extensively studied is metHr, which is the most stable form of the protein.^{685–687} Similar to oxyHr, this physiologically irrelevant form also contains a diferric site but lacks the peroxide moiety.⁶⁸⁷

While allosteric effectors and cooperativity play a major role in the process of O_2 binding to hemoglobin and hemocyanin, the best characterized octameric Hr species, i.e., those of the sipunculid phyla, are non-cooperative in their reactivity toward dioxygen.^{698,699} In contrast, the octameric brachiopod proteins do exhibit cooperative O_2 binding with a Hill coefficient of ~ 2 .^{698,699} This difference may relate to the fact that the brachiopod proteins have two different types of subunits ($\alpha_4\beta_4$). Alternatively, there may be allosteric effector sites in the sipunculids present only in vivo that have yet to be identified.

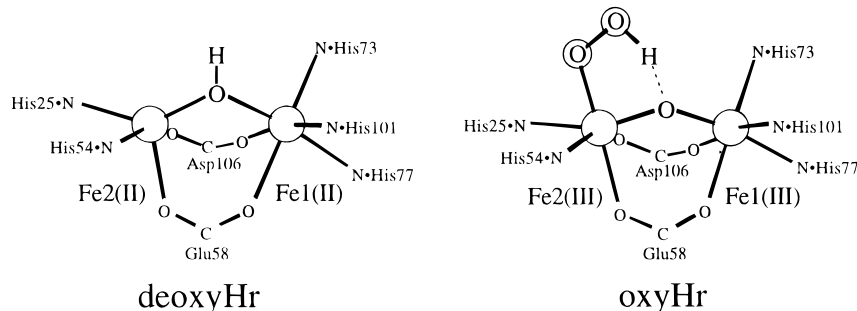


Figure 71. First coordination spheres of the diiron sites in deoxyHr (left) and oxyHr (right). (Reprinted with permission from ref 660. Copyright 1999 American Chemical Society.)

Kinetics. Kinetic studies of dioxygen binding to Hr have been performed *in vitro* by using temperature jump, stopped flow, and laser flash photolysis techniques.^{686,700–702} In the case of the octameric sipunculid *P. gouldii*, the most studied Hr species *in vitro*, the rate constants for O₂ binding and dissociation are $k_{\text{on}} = 7.4 \times 10^6 \text{ M}^{-1} \text{ s}^{-1}$ and $k_{\text{off}} = 51 \text{ s}^{-1}$, respectively ($K_{\text{eq}} = 1.5 \times 10^5 \text{ M}^{-1}$), and are pH independent.⁷⁰⁰ Upon replacement of H₂O by D₂O, k_{on} is unchanged whereas k_{off} decreases by about 20%.⁷⁰² These results were interpreted as indicating that the proton of the hydroperoxide at the oxyHr site is provided by the protein rather than the solvent and that the PT in the process of O₂ binding and release is not the rate-limiting step (*vide infra*).

In addition to O₂, several other small molecules, including N₃⁻, F⁻, and OCN⁻, bind to the active site of deoxyHr.^{685,686} In the corresponding adducts the two Fe centers remain in the divalent oxidation state. Alternatively, binding of NO causes a change in the oxidation state of one iron, yielding an antiferromagnetically coupled site consisting of an $S = 3/2$ {FeNO}⁷ (formally Fe^{III}–NO⁻) and an $S = 2$ Fe^{II} center.⁷⁰³ This deoxyHrNO complex has been proposed to serve as an analogue to the putative “ $1/2$ -metHr superoxide” mixed-valence intermediate in the oxygenation of deoxyHr; however, the occurrence of such an intermediate is not supported by electronic structure studies of O₂ binding (*vide infra*). MetHr also binds a number of monovalent anions, e.g., N₃⁻, OCN⁻, SCN⁻, F⁻, Cl⁻, Br⁻, I⁻, NO₂⁻, CN⁻, and OH⁻.^{685,686} The rates of formation of the corresponding adducts are of the same order as those for Fe^{III} in aqueous solution, but the dissociation rates are generally lower, so that the Hr complexes are more stable than their simple Fe^{III} counterparts.

Mixed-valence $1/2$ metHr species can be prepared upon one-electron reduction and oxidation of metHr and deoxyHr, respectively.⁶⁸⁶ The rapid reduction of metHr leads to $1/2$ metHr_R that is characterized by a rhombic EPR spectrum.⁷⁰⁴ Further reduction of $1/2$ -metHr_R is biphasic and slow, with the highest rates at low and high pH and a minimum near pH 7.⁷⁰⁵ Oxidation of deoxyHr results in the formation of $1/2$ -metHr_O that exhibits an axial EPR spectrum.⁷⁰⁴ Further oxidation of $1/2$ metHr_O to metHr is slow. In contrast to the reduction of $1/2$ metHr_R, however, this reaction has a simple pH dependence; it is fastest at high pH and slows down with decreasing pH.⁷⁰⁶ Insight into the puzzling redox properties of Hr was obtained from spectroscopic studies employing ab-

sorption, CD, MCD, and EPR techniques.⁷⁰⁷ A key observation in these studies was that there is a 5C Fe^{II} center present in deoxyHr (*vide infra*) and $1/2$ -metHr_O which binds an OH⁻ ligand and becomes 6C in $1/2$ metHr_R. As a result, the redox potential of that iron drops below the redox potential of its partner, so that the “extra” electron of Fe^{II} is transferred to the other center upon conversion of $1/2$ metHr_O into $1/2$ metHr_R. From these studies the reduction of $1/2$ metHr_R to deoxyHr is slow because this conversion requires dissociation of the OH⁻ ligand. Conversely, oxidation of $1/2$ metHr_O is slow as this transformation proceeds through the slow initial binding of OH⁻ to form $1/2$ metHr_R, which is then rapidly oxidized to metHr.

Structure. The three-dimensional molecular structures of myoHr and several octameric Hr species have been determined by X-ray crystallography at 2 Å resolution.⁶⁸⁷ The folding of the polypeptide chain in the monomeric subunits is fairly simple, consisting of four α -helices that pack roughly parallel to one another. One characteristic of this packing is that there is in fact only one small close-contact region, and the helices slightly diverge from one another away from the contact region. This produces a channel between the helices that can accommodate the heme group in cytochromes and the binuclear iron cluster in Hr. The interior of the channel is very hydrophobic, providing a suitable binding environment for dioxygen.

The active site of Hr consists of two iron centers separated by roughly 3.25–3.50 Å. In deoxyHr (Figure 71, left), the ferrous ions are bridged by two carboxylates and an exogenous hydroxide ligand.^{687,708} The coordination spheres of the two irons are completed by five His•N ligands, three binding to the 6C Fe1 and two to the 5C Fe2, leaving an open coordination site on Fe2. In the reaction of deoxyHr with dioxygen, one electron from each Fe^{II} center and the proton from the bridging hydroxide are transferred to O₂ binding to Fe2, yielding an oxo-bridged diferric site possessing a terminal hydroperoxide in oxyHr (Figure 71, right).^{687,708} The two-electron reduction of O₂ and deprotonation of the bridging hydroxide in oxyHr are evidenced by a number of spectral features discussed below.

Structural information on the active site has also been obtained from EXAFS experiments.⁷⁰⁹ In general there is a fairly good agreement between X-ray crystallographic and EXAFS data.⁶⁸⁷ The major discrepancy concerns the Fe•••Fe distance in deoxyHr

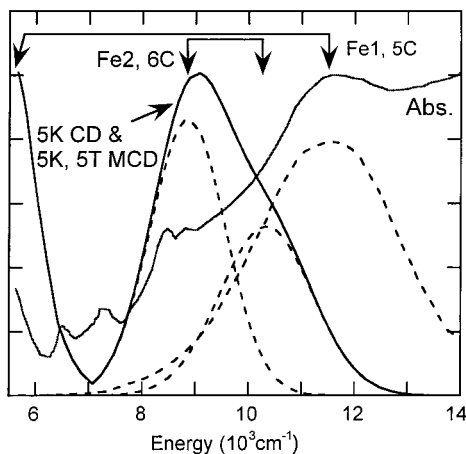


Figure 72. LT absorption, CD, and MCD spectra of deoxyHr. Dashed lines indicate peak positions. Note that the CD and MCD spectra at LT are superimposable, indicating that the two Fe^{II} centers are antiferromagnetically coupled. Arrows indicate LF transitions of each iron. (Adapted from ref 668.)

(where the value obtained from EXAFS is larger by 0.25 Å).

Spectroscopy. In studies of deoxyHr employing absorption, CD, and MCD spectroscopies,^{668,710} a total of four LF transitions were identified in the near-IR region (Figure 72), consistent with the presence of one 6C, roughly octahedral Fe^{II} center (Fe1) and one 5C, trigonal-bipyramidal Fe^{II} center (Fe2) (section II.A.1). Interestingly, the difference in coordination number between the two iron sites is not reflected in the Mössbauer spectrum, which exhibits only a single quadrupole doublet with an isomeric shift typical of high-spin ferrous iron ($\delta = 1.14 \text{ mm s}^{-1}$, $\Delta E_Q = 2.76 \text{ mm s}^{-1}$).⁷¹¹ Using variable-temperature MCD^{668,710} and ¹H NMR spectroscopic methods,⁷¹² the two irons were found to be antiferromagnetically coupled, $-J = 12\text{--}38$ and $10\text{--}20 \text{ cm}^{-1}$, respectively. These values were interpreted as indicating the presence of a hydroxide bridge at the reduced site, a model that has been subsequently supported by crystallographically characterized hydroxo-bridged model complexes^{676,713} and X-ray crystallographic studies.^{687,708} Using SQUID magnetic susceptibility, which permitted a more direct estimate of the exchange-coupling constant, a value of $J = -14(2) \text{ cm}^{-1}$ was obtained for deoxyHr.⁶⁶⁰ Thus, at 300 K, the entire manifold of ground-state spin sublevels is thermally populated (i.e., the entire exchange splitting is 280 cm^{-1}) and can thus participate in the reaction with O₂, a triplet.

Of particular interest with respect to the reaction of deoxyHr with O₂ are the orientations of the redox-active MOs containing the extra electron on each iron relative to the dimer structure. This was explored through density functional calculations on an approximate model of the deoxyHr site with formates and NH₃ groups replacing the carboxylates and histidines, respectively.⁶⁶⁰ Evaluation of the computational results on the basis of experimental data, which is an absolute requirement to validate analysis of electronic structure calculations, indicated that this approximate model provides a reasonable description of the deoxyHr active site. From Figure 73, the redox-

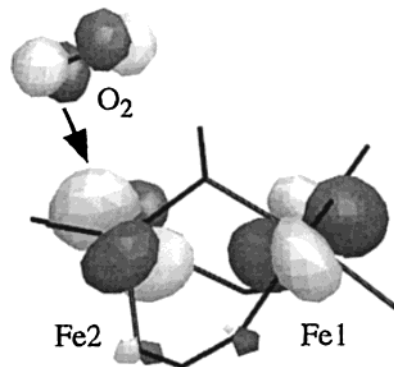


Figure 73. Boundary surface plots of the redox-active orbitals containing the "extra" electrons on Fe1 and Fe2, obtained from a DFT calculation on deoxyHr. Also indicated is the favorable orientation of the Fe2-centered orbital for a π -bonding interaction with one of the π^* orbitals of O₂ approaching along the open coordination site of that center. (Reprinted with permission from ref 660. Copyright 1999 American Chemical Society.)

active spin-down orbital localized on the 5C Fe^{II}2 is properly oriented for a π -bonding interaction with one of the two half-occupied π^* orbitals of dioxygen approaching along the open coordination site of that center. The redox-active orbital on the 6C Fe^{II}1 is oriented perpendicular to the Fe1–O (hydroxide) bond that might be anticipated to play a key role for ET from Fe1 to O₂ via Fe2 (vide infra). The LUMO of that iron is only $\sim 390 \text{ cm}^{-1}$ higher in energy, however, and that orbital has a good orientation for a π -bonding interaction with the hydroxide. Thus, re-orientation of the redox-active MO on Fe1 for efficient superexchange to Fe2 is energetically accessible.

For oxyHr, solution absorption and CD spectra,⁶⁶³ rR excitation profiles for the symmetric Fe–O–Fe, the Fe–hydroperoxide, and the O–OH stretching modes⁶⁹⁵ (denoted $\nu(\text{Fe–O})$, $\nu(\text{Fe–O}_2\text{H})$, and $\nu(\text{O–OH})$, respectively), along with polarized single-crystal electronic absorption spectra⁷¹⁴ are shown in Figure 74. Three dominant features denoted 1, A, and B are observed in the absorption spectra. Band 1 peaking at $\sim 19\,300 \text{ cm}^{-1}$ was assigned to a hydroperoxide-to-Fe CT transition because it is primarily E \perp c polarized (i.e., perpendicular to the Fe \cdots Fe vector) and greatly enhances the $\nu(\text{Fe–O}_2\text{H})$ and $\nu(\text{O–OH})$ modes in the rR spectrum.^{663,695,714} Bands A and B are predominantly E \parallel c polarized and were therefore assigned to oxo-to-Fe CT transitions.^{663,714}

Two features in the oxyHr absorption and rR data (Figure 74) require further consideration: (i) both the oxo-related $\nu(\text{Fe–O})$ and the hydroperoxide-related $\nu(\text{Fe–O}_2\text{H})$ modes are resonance enhanced under band A and (ii) the corresponding rR excitation profiles steadily decrease on approaching band B despite the increase in absorption intensity. This prompted an analysis of the spectroscopic data of oxyHr within the framework of the time-dependent Heller theory^{71,72,715} (see section II.A.2.a.2). Simulated absorption and rR excitation profile data are plotted on top of the experimental data in Figure 74.⁶⁶⁰ The simulation nicely reproduces the experimentally observed decrease in the rR excitation profiles for $\nu(\text{Fe–O})$ and $\nu(\text{Fe–O}_2\text{H})$ above $27\,000 \text{ cm}^{-1}$, indicating that this behavior is due to interference effects among

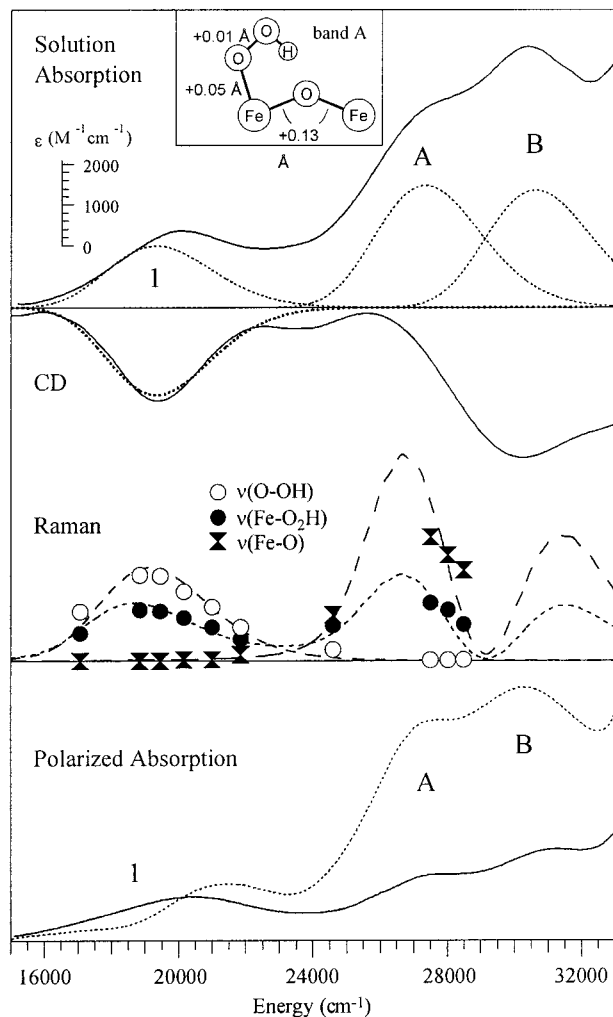


Figure 74. Experimental (300 K) and simulated absorption, CD, and rR excitation profile data for oxyHr. Top: solution absorption and CD spectra (solid lines, adapted from ref 663), band shape simulations for transitions 1, A, and B (dotted lines), and nuclear distortions in the excited state corresponding to band A (inset). Center: experimental rR excitation profiles (symbols, adapted from ref 695) and corresponding simulations (broken lines). Bottom: single-crystal absorption spectra for the E vector of light polarized parallel (dotted line) and perpendicular (solid line) to the $\text{Fe}\cdots\text{Fe}$ vector (adapted from ref 663). Parallel polarization has a large projection along $\text{Fe}-\text{O}-\text{Fe}$, and perpendicular polarization has a large projection along the $\text{Fe}-\text{O}_2\text{H}$ bond. (Reprinted with permission from ref 660. Copyright 1999 American Chemical Society.)

the oxo-to-Fe CT excited states assigned to bands A and B.⁷¹⁶ The CT excited state corresponding to band A was further characterized through an excited-state distortion analysis (section II.A.2.a.2).⁷¹⁵ The nuclear distortions of the $\text{HO}_2-\text{Fe}-\text{O}-\text{Fe}$ unit (Figure 74, inset) indicate that the corresponding excited state has predominantly oxo-to-Fe CT character. The strong enhancement of $\nu(\text{Fe}-\text{O}_2\text{H})$ in that region (● in Figure 74) actually arises from significant mechanical coupling between the $\text{Fe}-\text{O}(\text{oxo})$ and $\text{Fe}-\text{O}_2\text{H}$ stretch motions.

On the basis of the large body of spectroscopic data on oxyHr, an experimentally calibrated bonding description of the oxidized site could be generated.⁶⁶⁰ The calculated electronic structure of Fe1 indicates that the LF felt by this iron is dominated by the

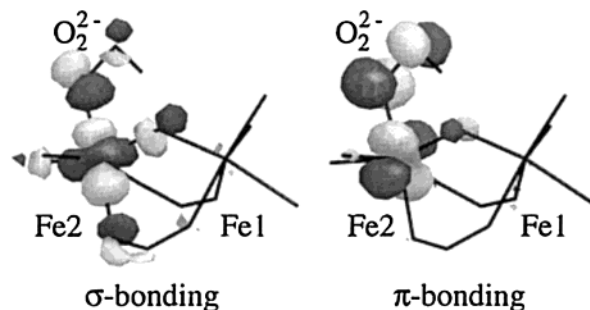


Figure 75. Boundary surface plots of the unoccupied Fe2 d-based orbitals involved in σ - and π -bonding interactions with the hydroperoxide π^* orbitals, obtained from a DFT calculation on oxyHr. Note that the corresponding peroxide-based occupied MOs are bonding with respect to the $\text{Fe}-\text{peroxide}$ bond. (Reprinted with permission from ref 782. Copyright 1997 American Chemical Society.)

bonding interactions with the bridging oxide, which is typical for Fe^{III} in oxo-bridged dimers⁶³⁹ (section III.A.1.b). Alternatively, Fe2 is involved in additional strong bonding interactions with the hydroperoxide (Figure 75). While the σ -donor interaction of the hydroperoxide with Fe2 is mitigated by the proton that stabilizes the peroxide π^* orbital oriented in the $\text{Fe}-\text{O}_2\text{H}$ plane (Figure 75, left), the π -donor strength even exceeds that of the bridging oxide (Figure 75, right). The net result of three strong π -bonding interactions of Fe2, i.e., one with the hydroperoxide and two with the bridging oxide, is a fairly symmetrical electronic surrounding for that iron. This model of distinct LF environments of the two Fe^{III} centers in oxyHr is consistent with Mössbauer data. Typically, the strong axial LF component associated with the bridging oxide in oxo-bridged diferric sites gives rise to a large quadrupole splitting, $\Delta E_Q = 1.5-2.0 \text{ mm s}^{-1}$.⁷¹⁷ In oxyHr, the quadrupole splitting of one iron is also large, $\Delta E_Q \approx 2.0 \text{ mm s}^{-1}$, whereas the second iron exhibits an unusually small ΔE_Q value of $\sim 1.0 \text{ mm s}^{-1}$, reflecting a less distorted electronic surroundings of that iron.⁷¹¹

The presence of an oxo bridge at the active site of oxyHr gives rise to strong antiferromagnetic coupling between the two ferric centers, $J = -77 \text{ cm}^{-1}$.⁷¹⁸ Compared to other oxo-bridged diferric sites, however, the coupling strength is weaker.⁶³¹ Also, the vibrational frequency of the symmetric $\text{Fe}-\text{O}-\text{Fe}$ stretching mode $\nu(\text{Fe}-\text{O})$ is lower in oxyHr than in oxo-bridged diferric model complexes and metHr derivatives.⁶⁴⁵ These results were interpreted as indicating a perturbed $\text{Fe}-\text{oxo}$ bonding interaction in oxyHr, ascribed to the strong hydrogen bond between the hydroperoxide and the bridging oxide that was identified by Loehr et al.^{695,719} using rR spectroscopy (Figure 71, right). Alternatively, DFT calculations suggest that the relatively weak exchange coupling in oxyHr is due primarily to the strong donor interaction of the hydroperoxide with Fe2 that localizes this center and reduces the $\text{Fe1} \rightarrow \text{Fe2}$ electron delocalization. The fairly strong hydrogen bond appears to be of minor importance with respect to the reduced exchange coupling; however, it produces a substantial reduction in the total oxo $\rightarrow \text{Fe}$ charge donation, which is reflected in the low $\nu(\text{Fe}-\text{O})$ frequency.⁶⁹⁵

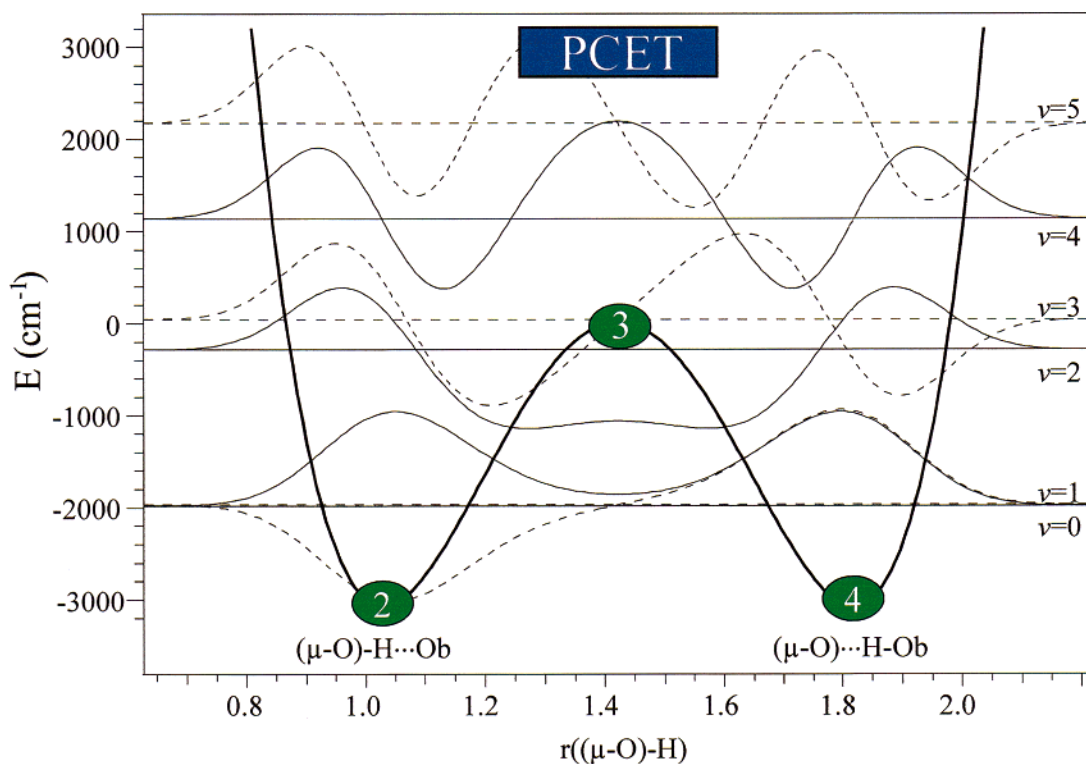
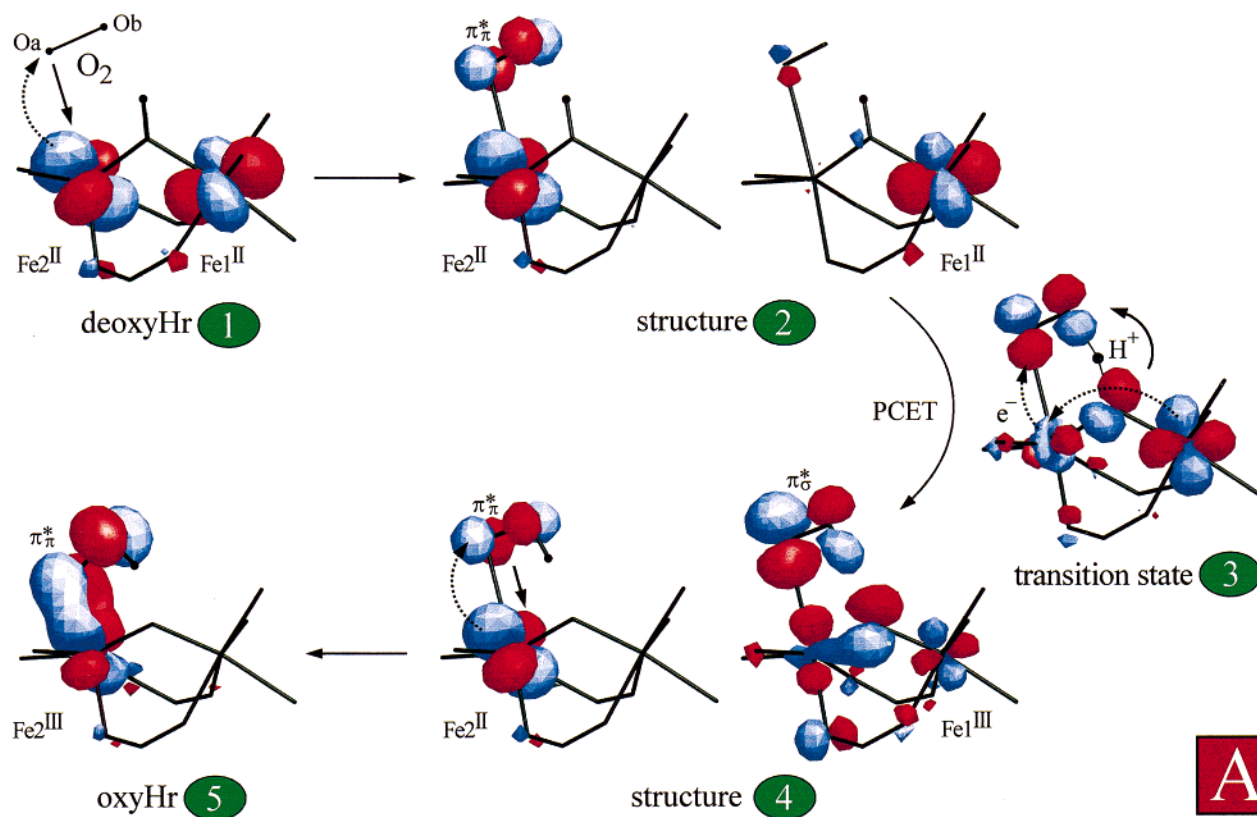


Figure 76. (A) Schematic illustration of the relevant steps for O_2 binding to deoxyHr. Pathways for the two ETs and the PT are indicated by curved dotted and solid arrows, respectively (PCET, concerted proton-coupled ET). (B) Proton PES as a function of the Ob-H distance (with $r(\text{Fe}2\text{-Oa}) = 2.95 \text{ \AA}$) Energies and wave functions of the protonic states are shown by solid lines (even states) and broken lines (odd states). (Reprinted with permission from ref 660. Copyright 1999 American Chemical Society.)

Molecular Mechanism. In an effort to obtain molecular-level insight into proton-coupled two-ET process associated with the interconversion of deoxyHr and oxyHr, the corresponding reaction coordinate was explored through DFT calculations evaluated and calibrated by the experimental data described above.⁷²⁰ A schematic representation of the resulting model for O₂ binding to deoxyHr is shown in Figure 76A. The dioxygen molecule approaches along the open coordination position of the 5C Fe2 center of deoxyHr (**1**). With decreasing Fe2–O_a distance, a weak bonding interaction develops between the redox-active orbital on Fe2 and one π* orbital of O₂ (designated π_π* since it π bonds to Fe2). As a consequence, some charge is transferred from this iron to the O₂ and the pK_a of the bridging hydroxide decreases while that of the partially reduced dioxygen increases and, eventually, a situation is found (*r*(Fe2–O_a) ≅ 2.95 Å) in which the two proton positions are isoenergetic and the proton can tunnel⁷²¹ from the bridging hydroxide (structure **2**) to the O₂ species (structure **4**). In the course of this event, the redox-active orbital of Fe1 rotates to maximize the π-bonding interaction with the bridging oxide (whose orbitals shift to higher energy upon deprotonation) and the extra electron of Fe1 gradually transfers to the second π* orbital of the O₂ moiety (denoted π_σ* since it σ bonds to Fe2) through the Fe1–O–Fe2 mixed π/σ superexchange pathway (structure **3**). This process corresponds to a concerted proton-coupled ET (PCET)^{722,723} where the distortion along the proton coordinate drives the oxidation of Fe^{II} (structure **2**) to Fe^{III} (structure **4**). It is distinct from an hydrogen-atom transfer in which case the electron would transfer along with the proton. Significantly, the ET pathway in the PCET process affords a large electronic coupling matrix element between the π_σ* orbital of O₂ binding to Fe2 and the low-lying (i.e., π-antibonding) redox-active orbital on Fe1. In linear dimers a similar mixed π/σ superexchange pathway is eliminated by symmetry,⁶³⁹ emphasizing the importance of a multiply bridged active site in Hr to produce the bent Fe–O–Fe unit ($\angle = 125^\circ$).^{687,708} As considered in section III.A.1.b, this π/σ pathway is the most efficient for mediation of exchange coupling in bent Fe–O–Fe dimers with these studies directly coupling the antiferromagnetic interaction with the superexchange pathway for ET.

To quantify the tunneling rate for the PT process **2** → **4**, the proton potential energy surface (PES) was estimated through DFT calculations for *r*(Fe2–O_a) = 2.95 Å (the bond length for structures **2**–**4** in Figure 76A) and modeled by a quartic potential, which is plotted in Figure 76B along with the corresponding vibrational energy levels and wave functions.⁷²⁰ From the splitting between the *v* = 0 and 1 levels, Δ*E*_± = 11 cm⁻¹, a tunneling rate constant of *k*_{PT} = 6.9 × 10¹¹ s⁻¹ was obtained. The PT step is therefore not expected to make a significant contribution to the rate constants for O₂ binding and release (7.4 × 10⁶ M⁻¹ s⁻¹ and 51 s⁻¹, respectively⁷⁰⁰) consistent with the small KIE observed (1.0 and 1.2, respectively).⁷⁰²

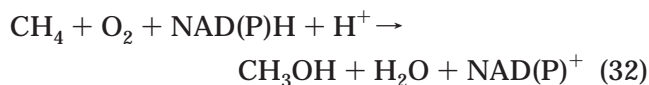
In the final step of the O₂ binding process (**4** → **5**), a further decrease in the Fe2–O_a distance to the

equilibrium value of ~2.0 Å formally completes the second ET, from Fe2 to the π_π* orbital of O₂H, yielding the terminal hydroperoxide at the oxo-bridged diferric site of oxyHr (**5**). The thermodynamic driving force for O₂ binding to deoxyHr (**1** → **5**) is high,⁷⁰⁰ largely because of the formation of the very stable μ-oxo [Fe^{III}]₂ unit⁶³⁹ (section III.A.1.b.3) and the associated increase in antiferromagnetic coupling with progress along the reaction coordinate, which leads to a net stabilization of the singlet ground state in oxyHr by |30*J*| (Figure 58).^{720,724}

C. O₂ Activation

1. Methane Monooxygenase

Biochemical Characterization. Methane monooxygenase (MMO) catalyzes NADH-dependent dioxygen activation and the insertion of an oxygen atom into the exceptionally stable C–H bond of methane (bond dissociation energy = 104 kcal mol⁻¹) to form methanol.^{643,725,726}

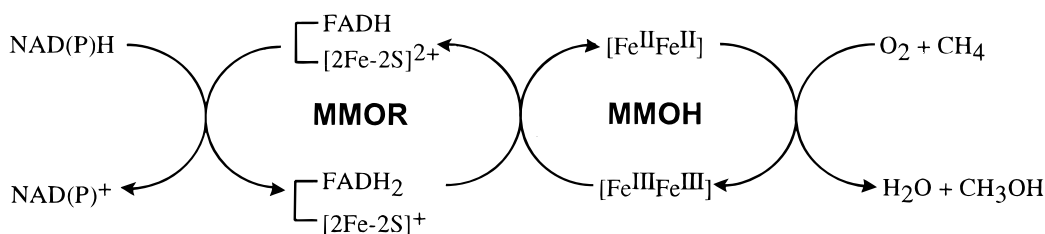


This reaction is the first and energetically most difficult step in the methane oxidation pathway. Subsequently, methanol is converted to formaldehyde by methanol dehydrogenase. Continued oxidation of formaldehyde to formate is catalyzed by formaldehyde dehydrogenase in concert with NAD⁺ reduction. Finally, formate is oxidized to CO₂ by formate dehydrogenase, which also utilizes NAD⁺ as an oxidant. This pathway allows the methanotroph to grow on methane as the sole source of carbon and energy.^{725,727,728}

Methanotrophs are classified into type I, II, or X according to the metabolic pathway utilized, their morphology, and types of MMO expressed.^{727,728} Types I and X methanotrophs utilize a ribulose biphosphate pathway in which ribulose 5-phosphate is condensed with formaldehyde, whereas type II methanotrophs utilize a serine pathway in which glycine is condensed with formaldehyde to initiate carbon assimilation. Type I methanotrophs possess only a particulate, membrane-bound form of MMO. In types II and X methanotrophs, either a particulate (pMMO) or a soluble (sMMO) form of the enzyme is expressed depending on growth conditions.^{725,727,728} When the growth media contains a high concentration of copper and a low concentration of iron, the particulate form is exclusively expressed.^{729,730} Less is known about pMMOs because of difficulties in purification of active enzyme.^{731–736} However, there has been some recent progress toward the more detailed characterization of pMMO chemistry.^{737–745} Alternatively, the soluble form is exclusively expressed when the growth media contains a low concentration of copper and a high concentration of iron. Much is known about sMMOs based on studies on two systems: *Methylosinus trichosporium* (OB3b) from type II and *Methylococcus capsulatus* (Bath) from type X.^{643,726,728,746,747}

In addition to methane oxidation, the soluble MMO catalyzes reactions with a broad range of substrates

Scheme 21



including saturated, unsaturated, linear, branched, aromatic, cyclic, and halogenated hydrocarbons.^{748–751} The products of these reactions yield alcohols, epoxides, and phenols. These adventitious substrates do not support bacterial growth. However, this broad reactivity allows the use of different substrates for mechanistic studies as well as industrial applications such as in xenobiotic biosynthesis or environmental pollution biodegradation.

sMMO is comprised of three protein components: a hydroxylase component (MMOH), a regulatory component termed B (MMOB), and a reductase component (MMOR). The molecular mass of MMOH is 245 kDa for its $(\alpha\beta\gamma)_2$ quaternary structure.^{752–756} MMOH contains the active site where methane oxygenation occurs. Metal analysis, Mössbauer spectroscopy, and X-ray crystallography show that there are two carboxylate- and hydroxo-bridged binuclear ferric clusters per $\alpha_2\beta_2\gamma_2$ molecule. The binuclear iron clusters in MMOH can be stabilized in three redox states: the oxidized $[\text{Fe}^{\text{III}}\text{Fe}^{\text{III}}]$, the mixed-valence $[\text{Fe}^{\text{III}}\text{Fe}^{\text{II}}]$, and the fully reduced $[\text{Fe}^{\text{II}}\text{Fe}^{\text{II}}]$ states.

The MMOR component is a 40 kDa monomer that contains one FAD and one $[\text{Fe}_2\text{S}_2]$ cluster per molecule. MMOR functions to couple oxidation of NADH to reduction of MMOH using the ET chain shown in Scheme 21.^{757–761} Many other multicomponent oxygenase enzymes are also known to utilize similar reductase components.⁷⁶² Green and Dalton have proposed that the two electrons required for the hydroxylation reaction are provided by the FADH/FADH₂ and $[2\text{Fe}-2\text{S}]^{2+}/[2\text{Fe}-2\text{S}]^{1+}$ redox couples of the reductase based on stopped-flow studies.⁷⁶³ A detailed study of the electron transfer process from MMOR to MMOH has recently appeared.⁷⁶⁴ On the basis of stopped-flow experiments, Lippard and co-workers proposed that three NADH molecules are used to fully reduce the MMOH–MMOR complex via formation of intermediates that include semiquinone MMOR and mixed-valence MMOH.

MMOB is a 16 kDa monomer with no associated metal ions or organic cofactors. Steady-state kinetic experiments indicate that MMOB can both activate and inactivate catalysis.^{756,765} During a titration with component B, the turnover rate of MMOH with a fixed amount of MMOR increases to a maximum at approximately a 2:1 B/H ratio then decreases. This observation suggests that distinct complexes between components are formed as an essential part of efficient catalysis by the reconstituted enzyme system coupled to NADH.⁷⁶⁵ At a low concentration of MMOB, kinetic modeling predicts increased formation of this ternary complex resulting in increased turnover rate. However, at a high concentration of

MMOB, the effective concentration of this ternary complex decreases due to formation of inhibitory complexes such as MMOH complexed to two MMOB per active site and a nonproductive MMOR–MMOB complex. Some of these predicted complexes have been demonstrated using chemical cross-linking techniques.⁷⁶⁵ Complexes have also been detected and their K_D values measured using fluorescence spectroscopy.⁷⁶⁵ These measurements on sMMO from *M. trichosporium* (OB3b) show the components have very high affinities for each other in the nanomolar range. Alternatively, studies on sMMO isolated from *M. capsulatus* (Bath) showed no evidence for MMOR–MMOB complexation. Instead, MMOR and MMOB interact noncompetitively with MMOH.⁷⁶⁴ MMOB alters the regioselectivity of MMOH-catalyzed reactions.⁷⁶⁶ It is possible that MMOB modulates sMMO catalysis by altering the oxidation–reduction potential of MMOH or the accessibility of reductants and/or substrates to the active site.

Indeed, addition of a stoichiometric amount of MMOB alters the redox potential of MMOH isolated from *M. trichosporium*,^{767,768} the redox potentials for MMOH ($E_1^{\circ'} = +76$ mV, $E_2^{\circ'} = +21$ mV, SHE) shift negatively ($E_1^{\circ'} = -52$ mV, $E_2^{\circ'} = -115$ mV, SHE). Thus, the MMOH–MMOB complex becomes more difficult to reduce. However, in the presence of MMOR, the changes in the MMOH redox potentials are reversed ($E_1^{\circ'} = +76$ mV, $E_2^{\circ'} = +125$ mV, SHE).⁷⁶⁸ This switches the potentials such that the system favors the two-electron reduction process. Addition of substrate to this system does not significantly perturb the redox potentials.^{767,768} Thus, the effect of MMOR is to poise the correct potentials for two-ET into MMOH. MMOH isolated from *M. capsulatus* shows somewhat different results.^{769–771} The redox potential values for MMOH ($E_1^{\circ'} = +100$ mV, $E_2^{\circ'} = -100$ mV, NHE) also shift more negatively when MMOB is added ($E_1^{\circ'} = +50$ mV, $E_2^{\circ'} = -170$ mV, NHE). The potentials for the MMOH–MMOB–MMOR complex were reported to be too low to measure. However, when substrate was added to the MMOH–MMOR–MMOB complex, the system potential changed to $E_1^{\circ'} < +100$ mV and $E_2^{\circ'} \approx 100$ mV, indicating that substrate must bind in order for electron transport to occur.

Kinetics. Classical steady-state kinetic modeling of MMO is difficult to address because of the complexity of the three-component system as well as involvement of three substrates (NADH, methane, and O₂). However, transient kinetic modeling of MMO reactions was developed using a single turnover reaction.^{756,772–775} Lipscomb and co-workers have established that the stoichiometrically reduced hy-

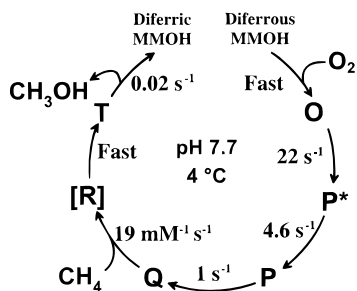


Figure 77. The catalytic cycle of methane monooxygenase intermediates described in text. (Adapted from refs 728 and 643.)

droxylase (2 but not 1 e^-) alone would catalyze the oxygenation of all known types of MMO substrates. In this manner, a number of transient intermediates in the MMO catalytic cycle were trapped in high yields. Valuable structural information thus became obtainable through spectroscopic characterizations of these intermediates. Figure 77 illustrates a current proposal of the MMO catalytic cycle in which either the enzymatically reduced or chemically reduced diiron cluster of MMOH is exposed to dioxygen in the presence of MMOB.⁷⁷⁶ Note that MMOB is required for the generation of the observed intermediates in high yields.

Upon reaction of fully reduced diiron cluster with dioxygen, a Michaelis–Menten-type complex, intermediate **O**, is proposed to form.⁷⁷³ This proposal was based on the observation that the $g = 16$ EPR signal, which has been shown to originate from the ferromagnetically coupled diferrous state (section III.A.2.c and *vide infra*), disappears at a rate independent of the dioxygen concentration. This is compatible with formation of a species such as an enzyme–dioxygen complex that precedes the oxidation of diferrous cluster since intermediate **O** retains the $g = 16$ EPR signal. Intermediate **O** decays at 22–26 s^{-1} at 4 °C independent of pH to an intermediate designated as **P***.⁷⁷⁵ This transient species was required by the observation that the decay of the diferrous EPR signal $g = 16$ is faster than the formation rate of the first optically detected intermediate designated as intermediate **P**, a diferric peroxy intermediate. Direct optical detection of intermediate **P*** has not been successful, perhaps due to its short lifetime or lack of a visible chromophore.⁷⁷⁵ Intermediate **P** (also has been referred to as intermediate **L** or H_{peroxo} in the Bath system^{777–779}) is formed ($\sim 4.6 s^{-1}$, 4 °C, pH 7.7) upon decay of intermediate **P***. It has a broad absorption band around 700 nm.^{775,780} Further decay of intermediate **P** at 1 s^{-1} (pH 7.7) produces intermediate **Q**, a brightly colored species with absorption features at 330 and 430 nm.^{772,775,777,778} On the basis of spectroscopic analysis (*vide infra*), intermediate **Q** is proposed to be a high-valent oxo-bridged intermediate.^{778,781,782} Intermediate **Q** reacts with substrate in an apparent bimolecular fashion.^{772,774,780} The linear relationship between intermediate **Q** decay rates and substrate concentration indicates that initial substrate reaction is a collisional event.

Substrate activation by intermediate **Q** is thought to involve the C–H bond cleavage in which case a substantial KIE is expected. However, in steady-state

turnover experiments using methane (CH_4 versus CD_4), sMMO from *M. trichosporium* showed very little KIE on V_{max} ($V_{\text{m,app,H}}/V_{\text{m,app,D}} = 1.7$) but large effects on K_m ($(V/K)_{\text{H}}/(V/K)_{\text{D}} = 8.4$ or $K_{\text{m,H}}/K_{\text{m,D}} = 0.2$).⁷⁸³ Similar experiments using MMO from *M. capsulatus* showed a small isotope effect on V_{max} ($V_{\text{m,app,H}}/V_{\text{m,app,D}} = 1.75$) and an inverse isotope effect on K_m ($K_{\text{m,H}}/K_{\text{m,D}} = 0.88$).⁷⁸⁴ These experiments showed that steps other than C–H bond cleavage are rate limiting in the overall enzymatic reactions. When decay of intermediate **Q** is monitored directly in a single turnover experiment, a very large deuterium KIE ($k_{\text{H}}/k_{\text{D}} \approx 50\text{--}100$) is observed indicating that the complete C–H bond breaking occurs in the transition state.⁷⁷⁴ Decay of intermediate **Q** is the only step showing a deuterium KIE during methane turnover. Because of the very large KIE, exceeding the classical limit, the presence of tunneling of the hydrogen atom during the abstraction process was invoked. Similar experiments using sMMO from *M. capsulatus* also revealed a large KIE of ~ 28 .⁷⁸⁰

Using alternate substrates such as nitrobenzene,^{766,772,778} an enzyme–product complex has been identified and designated as intermediate **T** in *M. trichosporium*.⁷⁷² Formation of product followed by a slow dissociation from the active site in a rate-limiting step was confirmed by chemically quenching the single turnover reaction. Less is known about the structure of intermediate **T**. It is a chromophoric intermediate with an absorption band at 325 nm and a shoulder at 395 nm, which appears to arise from the product (nitrophenol) bound in the active site.

One of the most prominent effects of MMOB was found to be gating of dioxygen reactivity with the fully reduced hydroxylase component.⁷⁷³ Although very slow, MMOH is capable of catalyzing all alternative substrates in the absence of MMOB when reducing equivalents are supplied by MMOR/NADH⁷⁵⁵ or H_2O_2 in a so-called peroxide shunt reaction.^{785,786} However, when MMOB is added to the NADH-coupled system, the initial O_2 binding is dramatically accelerated by approximately 1000-fold.^{768,773} In addition, the formation rate of intermediate **Q** is increased by about 40-fold.⁷⁶⁸ Upon addition of MMOB, the product yield also increases from roughly 40% to 80%, indicating that some uncoupled pathway is present which is decreased by MMOB.^{766,768} Recently, it has been found that MMOR also plays some role in reducing the rate of the uncoupled pathway.⁷⁶⁸ One possible candidate for the uncoupled pathway is the loss of H_2O_2 before the formation of intermediate **Q**.

Structure. X-ray crystal structures of MMOH have been reported for both the *M. trichosporium*⁷⁸⁷ and *M. capsulatus* enzymes.^{788–790} The crystal structures of MMOH from both sources show that it is almost exclusively helical (60%), consisting of 19 helices in the α subunit, 12 helices in the β subunit, and 8 helices in the γ subunit. Only 1% of the total residues is found in three short β strands. The overall structure resembles a heart-shaped dimer with a wide cleft running along the interface of the two protomers, toward the interior of the enzyme. The α and β subunits of MMOH form the inner walls of this cleft.

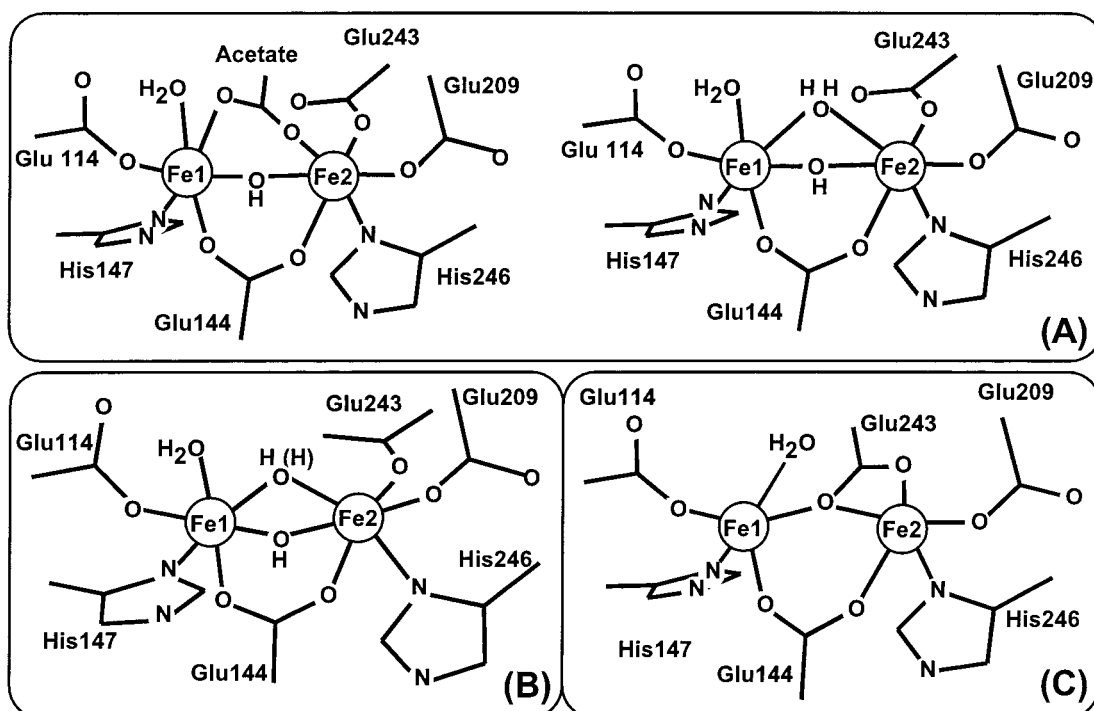


Figure 78. Representation of the crystallographically determined binuclear active sites of MMOH. (A) Diferric MMOH with (1MTY, right) and without (1MMO, left) acetate bound from *M. capsulatus*. (B) Diferric MMOH (1MHY and 1MHZ) from *M. trichosporium*. (C) Diferrous MMOH from *M. capsulatus*. (The oxidized structures were generated using the crystallographic coordinates from the indicated PDB files. The reduced structure was adapted from ref 789.)

The active site of MMOH is situated in immediate proximity to the cleft in the α subunit of MMOH. Each active site containing one diiron cluster is situated between four long α -helices (α B, α C, α E, and α F) which align next to each other in the structure. This structural motif has been found or implicated as a common feature of all of the diiron-containing proteins^{791–795} with the exception of an α/β sandwich structure found in purple acid phosphatase.⁷⁹⁶ Helices B and C contribute ligands to Fe1 and helices E and F contribute ligands to the Fe2 site. Two conserved segments of Glu–X–His are found.⁷⁹⁷ The iron–iron axis in MMO is oriented parallel to the long axis of the four-helix bundle.

Adjacent to the diiron cluster toward the interior of protein, a hydrophobic cavity has been identified. This pocket is lined by mostly non-hydrogen-bonding residues and is proposed to be the site of substrate approach.^{787,789,790} However, no obvious channel for the passage of substrate from the medium to this cavity is identified in resting MMOH. Xe binding to a remote hydrophobic pocket, which is separated from the active-site pocket by Leu110, has been observed.⁷⁸⁸ It is speculated that component interactions and/or redox-state changes of the diiron cluster may alter the protein structure such that it may form such a channel for methane and/or dioxygen entry.⁷⁸⁸

Two distinct core structures have been reported for the oxidized MMOH isolated from *M. capsulatus* (Figure 78A) depending on the temperature at which the data were recorded, 4 °C (2.2 Å resolution) and –160 °C (1.7 Å resolution).⁷⁸⁹ In the 4 °C structure, the two iron atoms are triply bridged by one hydroxo, one μ -1,3-endogenous carboxylate bridge (Glu144), and a second carboxylate bridge from an exogenous

acetate ion presumed to derive from the crystallization buffer. The Fe–Fe distance of this structure was reported to be \sim 3.4 Å. In the –160 °C structure, an aquo bridge has been assigned in place of the acetate bridge resulting in a μ -OH or μ -OH₂ structure with a shorter Fe–Fe distance of \sim 3.1 Å. The terminal ligands are His147 and Glu114 (monodentate) for Fe1 and His246, Glu209 (monodentate), and Glu243 (monodentate) for Fe2. For MMOH from *M. trichosporium* OB3b, two different oxidized crystalline forms have been solved to 2.0 and 2.7 Å resolutions.⁷⁸⁷ Only the shorter Fe–Fe distance of 3.0 Å was observed for both crystalline forms consistent with the presence of either two hydroxo bridges or one aquo and one hydroxo bridge (Figure 78B). These various crystal structures are perhaps indicative of the flexibility of the MMOH core structure, and this characteristic has been postulated as an important factor for the proper functioning of the enzyme.⁷⁸⁹

The reduced structure of MMOH (Figure 78C) from *M. capsulatus* has also been reported.⁷⁸⁹ MMOH crystals that contained the resting state diferric cluster were soaked with dithionite and redox mediator under anaerobic conditions. One protomer of the resulting structure was found to be different from the resting state.⁷⁸⁹ In this structure, the two hydroxo/aquo ligands have moved out of the bridging positions and Glu-243 has shifted to form a monodentate bridge between the two metals as well as coordinating to Fe2 in a bidentate fashion. Consequently, the two iron atoms are changed from 6C to 5C. The two vacant coordination sites are located adjacent to one another on the two irons, suggesting that they may form a bridged binding site for O₂ intermediates. In accord with the crystal structure, earlier CD and

MCD spectroscopic studies^{670,798} of MMO showed that the fully reduced state of MMOH contains two 5C ferrous centers with different geometries (vide infra).⁷⁸⁹

Since the crystal structures of MMO-component complexes are not yet available, the actual locations and structural effects of component interactions remain to be determined. However, the interactions between MMOH and MMOB and MMOR have been postulated to occur in the cleft that runs along the MMOH interior.⁷⁹⁰ Covalent cross-linking experiments showed that MMOB interacts with the α subunit of MMOH and MMOR interacts with the β subunit.⁷⁶⁵ Another potential MMOR binding site to the α subunit was proposed in the Bath system based on modeling the binding of a small peptide segment of MMOR to MMOH.⁷⁸⁸ Modeling of the MMOH–MMOB complex also has been attempted based on the recently reported solution structures of MMOB from *M. trichosporium*⁷⁹⁹ and *M. capsulatus*.⁸⁰⁰ High-resolution heteronuclear NMR spectroscopy of MMOB from two organisms revealed homologous secondary structures with very compact α/β folds devoid of cofactors. On the basis of preliminary studies, electrostatic interaction between MMOH and MMOB is proposed to be important in the case of *M. trichosporium*⁷⁹⁹ whereas mostly hydrophobic interactions are thought to be important in the case of *M. capsulatus*.^{800,801} It was also found for *M. trichosporium* that substrate addition to MMOB does not significantly alter chemical shifts, thus excluding a role for a MMOB–substrate complex in the catalytic cycle.⁷⁹⁹

Spectroscopy. Earlier spectroscopic studies on oxidized MMOH played a vital role in determining the nature of the bridging ligand. Oxidized MMOH as isolated exhibits no distinct absorption features below 33 000 cm⁻¹ (above 300 nm) in energy (precluding rR experiments), as expected for protonated (or substituted) oxo-bridged diiron-containing proteins.^{756,802} Each cluster of MMOH contains two high-spin Fe(III) ($S = 5/2$) that are antiferromagnetically coupled to give an $S_{\text{tot}} = 0$ spin system. Zero-field Mössbauer spectra of the oxidized MMOH from *M. trichosporium* indicate two slightly inequivalent high-spin iron sites ($\Delta E_{\text{Q}1} = 0.87 \text{ mm s}^{-1}$ with $\delta_1 = 0.51 \text{ mm s}^{-1}$ and $\Delta E_{\text{Q}2} = 1.16 \text{ mm s}^{-1}$ with $\delta_2 = 0.5 \text{ mm s}^{-1}$) in a roughly 50:50 mixture.^{761,803} The small quadrupole splitting also suggested the presence of a protonated (or substituted) oxo bridge. Similar zero-field Mössbauer analysis on the oxidized MMOH from *M. capsulatus* shows an unresolved single-quadrupole doublet with apparent $\Delta E_{\text{Q}} = 1.05 \text{ mm s}^{-1}$ and $\delta = 0.5 \text{ mm s}^{-1}$.⁸⁰² A high-field Mössbauer analysis of MMOH from *M. trichosporium* suggested that the J value is substantially smaller than that of known oxo-bridged diiron proteins, again consistent with the bridging ligand being protonated or substituted. The exact J value could not be extracted from the Mössbauer spectra because of broadening of the magnetic hyperfine splitting at higher temperature.⁷⁶¹ This derived from the presence of a small paramagnetic admixture in the ground state with applied magnetic fields and was explained in terms of the ZFS in the

presence of substantial antisymmetric exchange.⁸⁰⁴ Because of the small exchange coupling, an EPR signal from a presumably $S = 2$ excited state has been detected.⁷⁶¹ Parallel-mode EPR revealed a small but sharp resonance at $g = 8.0$, which maximized in intensity around 30 K. The temperature dependency of this signal gives a J value of -7.5 cm^{-1} ($H_{\text{ex}} = -2JS_1 \cdot S_2$). The small exchange-coupling constant, combined with crystallographic data, indicate a μ -hydroxo instead of an oxo bridge is present in the MMOH oxidized state. Further, the lack of short Fe–O or Fe–Fe distances that are fingerprints for oxo-bridged diiron clusters is apparent from the Fe K-edge EXAFS of MMOH.^{802,805–807} EXAFS analysis showed two Fe–Fe distances, 3 and 3.4 Å in the case of MMOH from *M. trichosporium*,⁸⁰⁷ and a single Fe–Fe distance of 3.42 Å in the case of MMOH from *M. capsulatus*.^{802,805}

Partial reduction of MMOH to the mixed-valence Fe^{III}Fe^{II} state results in a paramagnetic coupled iron cluster. The EPR spectrum of this state exhibits resonances at $g = 1.94, 1.86,$ and 1.75 ($g_{\text{ave}} = 1.85$) arising from antiferromagnetically coupled $S_1 = 2$ and $S_2 = 5/2$ to give an $S_{\text{tot}} = 1/2$ system.^{802,803,808} Mössbauer spectra showed that the two iron clusters are in a trapped valence state with an exchange coupling, J , of -30 cm^{-1} ($H_{\text{ex}} = -2JS_1 \cdot S_2$). A more complete picture of the mixed-valence state of MMOH was developed through advanced EPR studies. Proton ENDOR^{761,809,810} as well as pulsed EPR (ESEEM and Davies ENDOR) studies^{811,812} identified three classes of proton resonances associated with the diiron cluster of MMOH. Resonances with small hyperfine coupling values below 5 MHz are nonexchangeable with buffer D₂O and primarily associated with the protons of the endogenous ligands. The other two resonances exhibit unusually large hyperfine coupling constants of ~ 8 and ~ 13 MHz. The protons associated with these resonances exchange with D₂O only after 15–25 h of incubation at 4 °C.^{811,812} This indicates that the diiron site is sequestered from the solvent. The 8 MHz resonance is nearly isotropic (i.e., the resonance position does not change at different g -values). Alternately, the 13 MHz resonance exhibits a large anisotropy with $A_{\text{max}} \approx 30 \text{ MHz}$ at g_2 . On the basis of the comparison of the isotropic hyperfine constant with that of known $1/2$ metHr, the 8 MHz resonance was attributed to a terminal hydroxide ligand. Similarly, the magnitude and anisotropy of the 13 MHz resonance is attributable to a proton on the oxygen bridge. The presence of a protonated bridge (μ -OH) in the mixed-valence state strongly suggested that the same protonated bridge is also present in the oxidized state.^{761,809–813}

Combined CD and MCD data for reduced MMOH in Figure 79A revealed three bands at 7500, 9100, and 9900 cm⁻¹ assigned as d \rightarrow d transitions originating from two inequivalent 5C ferrous ions.⁶⁷⁰ VTVH MCD data in Figure 79B show saturation–magnetization behavior dramatically different from that of other known binuclear ferrous sites such as deoxyHr (vide supra). The system behaves as having a paramagnetic ground state with the rapid saturation magnetization giving a $g_{\text{H}} = 14.7$, which is

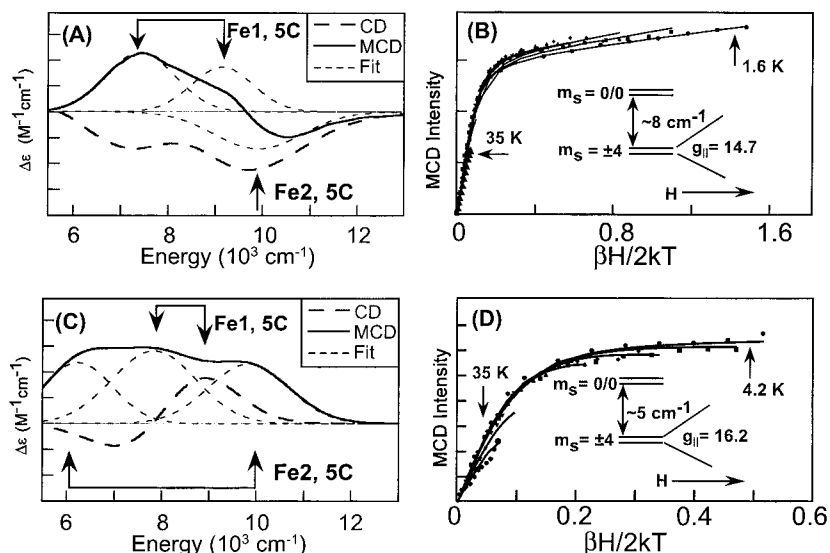


Figure 79. CD and LT MCD spectra of the reduced MMOH without and with MMOB bound. (A) CD (---) and LT MCD (—) spectra and the fit for the MCD spectra (---) of the reduced MMOH, recorded at 5 °C and 5 K and 7 T, respectively. (B) Saturation magnetization behavior of the MCD signal in the LF region for the reduced MMOH at 7500 cm^{-1} . The signal intensity (symbols) for a range of magnetic fields (0–7.0 T) at a series of fixed temperatures is plotted as a function of $\beta H/2kT$. The fit to the VTVH MCD data (—) was obtained using eq 29 giving the energy level diagram in inset. (C) The CD (---) and LT MCD (—) spectra and the fit for the MCD spectra (---) spectra of the reduced MMOH–MMOB complex, recorded at 5 °C and 5 K and 7 T, respectively. (D) Saturation magnetization behavior of the MCD signal in the LF region for the reduced MMOH–MMOB complex at 7500 cm^{-1} . The signal intensity (symbols) for a range of magnetic fields (0–7.0 T) at a series of fixed temperatures is plotted as a function of $\beta H/2kT$. The fit to the VTVH MCD data (—) was obtained using eq 29 giving the energy level diagram in inset. (Adapted from ref 670.)

consistent with an $S_{tot} = 4$ and $M_s = \pm 4$ ground state. From Figure 65A, this represents a ferromagnetically coupled site ($J \approx 0.3\text{--}0.5 cm^{-1}$) with two negative ZFS parameters ($D_1 = -4.0 cm^{-1}$ and $D_2 = -9.0 cm^{-1}$). This required that the μ -OH bridge present in the oxidized and mixed-valence forms is lost in the fully reduced site. Correlation to the crystal structure⁷⁸⁹ and model complexes^{814,815} suggests that ferromagnetic coupling is associated with the μ -1,1-oxygen bridge of carboxylate.

An intense integer-spin EPR signal is observed at $g = 16$ (Figure 70), which is also consistent with ferromagnetic coupling between two high-spin ferrous ions.⁶⁸⁴ The Mössbauer spectrum of the reduced MMOH from *M. trichosporium* exhibits two quadrupole doublets typical of high-spin Fe^{II} : $\Delta E_{Q1} = 3.1 mm s^{-1}$ with $\delta_1 = 1.3 mm s^{-1}$ and $\Delta E_{Q2} = 2.4\text{--}3.0 mm s^{-1}$ with $\delta_2 = 1.3 mm s^{-1}$ in roughly 50:50 mixture.⁷⁶¹ The Mössbauer spectrum of reduced MMOH from *M. capsulatus* only revealed a single species with $\Delta E_Q = 3.01 mm s^{-1}$ and $\delta = 1.3 mm s^{-1}$.⁸⁰² The lack of any Fe–Fe interactions probed by EXAFS spectroscopy indicates an increased Debye–Waller factor due to uncorrelated vibrations of the metal atoms, consistent with the loss of a hydroxo bridge upon complete reduction of the cluster.

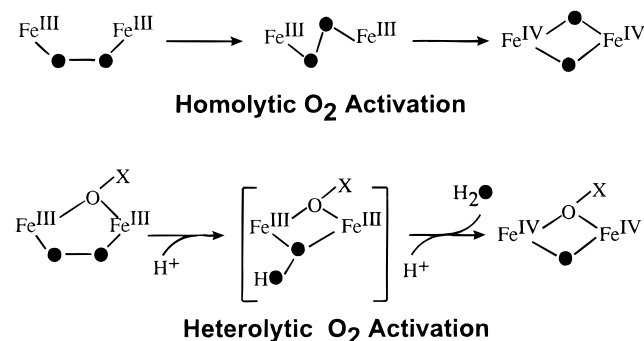
Addition of MMOB significantly changes the CD and MCD spectra with a new band detectable at 6260 cm^{-1} as well as bands at 7700, 8800, and 9800 cm^{-1} as shown in Figure 79C.^{670,798} Further VTVH MCD indicates that the ferrous centers are still ferromagnetically coupled with $J \approx 0.4 cm^{-1}$ but one of the ferrous ions is altered ($g_{||} = 16.2$, $D_1 = -6.0 cm^{-1}$, and $D_2 = -6.0 cm^{-1}$).^{670,798} These results clearly show that the active site of the reduced MMOH changes

when component B is present. This correlates with the observed increase in O_2 reactivity and suggests that the active site of reduced MMOH from the crystallography (Figure 78C) changes upon going to the highly reactive form of the enzyme. Addition of substrate to MMOH–MMOB complex results in marked changes in the CD spectrum. However, addition of substrate to MMOH alone does not perturb the CD spectrum, indicating that a conformational change of the active site occurs upon addition of substrate only in the presence of MMOB.⁷⁹⁸

Intermediate **P** is characterized by a broad absorption band at 700 nm ($\epsilon = 2500 M^{-1} cm^{-1}$) for *M. trichosporium*⁷⁷⁵ or 725 nm ($\epsilon = 1800 M^{-1} cm^{-1}$) for *M. capsulatus*.^{778,780,816} The band is proposed to arise from the peroxo-to-iron(III) CT transition, based on the comparison to a number of structurally characterized peroxo model complexes (refs 643, 815, and 659 and references therein). This intermediate is thus far only characterized by Mössbauer spectroscopy,^{778,782} which showed that both iron atoms are in the high-spin ferric state with a sharp quadrupole doublet ($\Delta E_Q = 1.51 mm s^{-1}$ and $\delta = 0.66 mm s^{-1}$) similar to end-on peroxo-bridged biferric model complexes.

Intermediate **Q** is characterized by intense absorption bands at 330 and 430 nm ($\epsilon = 7500 M^{-1} cm^{-1}$), features likely to arise from oxo-to- $Fe(IV)$ CT transition bands.^{778,779,781} From section II.A.2.a.2, rR data would be expected to provide valuable information about the nature of these transitions; however, despite concerted efforts in several laboratories, it has not yet been possible to obtain reproducible Raman data of intermediate **Q**. The zero-field Mössbauer spectrum of intermediate **Q** exhibits one well-defined doublet with $\delta = 0.17 mm s^{-1}$ and $\Delta E_Q = 0.53 mm$

Scheme 22



s^{-1} . The δ value of intermediate **Q** is substantially smaller than that for the diferric species, indicating both iron atoms possess mostly ferryl character. Moreover, the Mössbauer spectra of intermediate **Q** in applied magnetic fields up to 8.0 T show that the Fe^{IV} centers are diamagnetic with $-J > 30 \text{ cm}^{-1}$ ($H = -2JS_1 \cdot S_2$).

The EXAFS spectrum of intermediate **Q** shows two new features, a short Fe–Fe distance of 2.46 Å and one short Fe–O distance of 1.77 Å consistent with a proposed $\text{Fe}_2(\mu\text{-O})_2$ diamond core structure.⁷⁸² These novel features are not present in reduced and oxidized MMOH control samples. A crystallographically characterized synthetic model complex $\text{Fe}(\text{III})_2(\mu\text{-O})_2\text{-}(6\text{-Me}_3\text{-TPA})(\text{ClO}_4)_2$ exhibits a similar $\text{Fe}_2(\mu\text{-O})_2$ diamond core structure with a short Fe–Fe distance of 2.7 Å and Fe–O distances of 1.84 and 1.92 Å (vide infra).^{646,817} From the XAS experiments at the Fe K-edge on rapid freeze–quench samples,⁷⁸² the area of the preedge $1s \rightarrow 3d$ feature of **Q** is large, indicating that the Fe^{IV} centers have highly distorted surroundings and are likely to have coordination numbers no greater than 5.

Molecular Mechanism. The initial phase of the sMMO mechanism involves dioxygen activation by a binuclear ferrous site in the presence of MMOB but independent of the substrate.^{772,774,780} The reaction with dioxygen leads to formation of a peroxo intermediate (thought to have a $\mu\text{-}1,2\text{-peroxo}$ -bridged structure), which then spontaneously converts to a high-valent ferryl intermediate, intermediate **Q**. Once this reactive species is formed, methane enters the reaction cycle and oxygenation of the substrate occurs. There has been a general consensus regarding the formation of intermediate **Q** from intermediate **P**.^{776,818,819} The two favored mechanisms, Scheme 22, invoke either the heterolytic cleavage of the O–O bond assisted by asymmetric double protonation of an end-on bridging peroxide⁶⁵⁹ or the homolytic cleavage of the O–O bond through rearrangement to a side-on bridged structure, reminiscent of bis- $\mu\text{-oxo}$ formation in dicopper compounds (section III.D).

Support for the heterolytic cleavage of the O–O bond is available from kinetic studies of sMMO from *M. trichosporium*.⁷⁷⁵ The MMO reaction (eq 32) requires that a proton is supplied from the medium for each oxygenation reaction. Studies of the effect of pH and of proton inventory show that two protons are required in the O_2 reaction in the absence of substrate, one in the formation of intermediate **P** and a

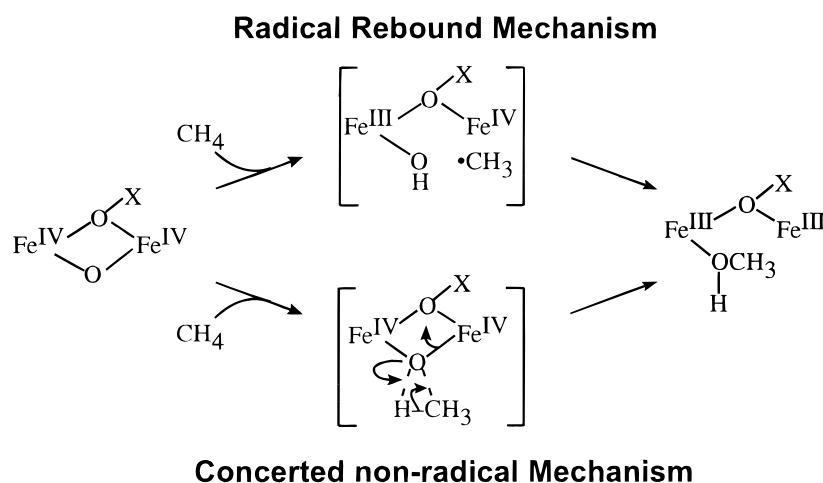
second for the intermediate **P** to intermediate **Q** conversion.⁷⁷⁵ Lipscomb and co-workers have proposed that a water molecule dissociates at this point as the O–O bond of intermediate **P** is heterolytically cleaved in forming intermediate **Q**.^{643,728,749,756,766,772,773,775,785,820} Support for the homolytic mechanism largely comes from theoretical modeling of the conversion of intermediate **P** to intermediate **Q** (see section III.D for discussion). While there are different proposed structures for intermediate **P** in the different calculations ($\mu\text{-}\eta^2\text{:}\eta^2\text{-peroxo}$ by Shteinman,^{821,822} an end-on *cis*- $\mu\text{-}1,2\text{-peroxo}$ or a side-on $\mu\text{-}\eta^2\text{:}\eta^2\text{-peroxo}$ by Yoshizawa and Hoffmann,^{823–825} and a distorted *cis*- $\mu\text{-}1,2\text{-peroxo}$ (with an additional weak bonding interaction between the peroxo ligand and one iron) by Siegbahn and Crabtree^{826,827}), all lead to a bis- $\mu\text{-oxo}$ [$\text{Fe}^{\text{IV}}\text{Fe}^{\text{IV}}$] species for intermediate **Q**, consistent with the diamond core observed experimentally in model studies (see section III.D).

The immediate product of the intermediate **Q** reaction with substrate cannot be trapped; thus, spectroscopic characterization of the substrate activation steps has not been possible. Instead, a number of different reactivity approaches have been applied to discern the various mechanistic steps proposed for the hydroxylation of hydrocarbons in MMO. Activation of the stable C–H bond of methane is thought to occur via either a radical rebound mechanism or a concerted insertion of an oxygen atom (Scheme 23).^{776,818,819,828,829}

Arguments for the radical rebound mechanism initially proposed by Lipscomb and co-workers have been presented by a number of research groups. Frey, Donnelly, and co-workers⁸³⁰ used 1,1-dimethylcyclopropane as a radical clock in sMMO from *M. trichosporium* and observed formation of both a ring-opened product (3-methyl-3-butene-1-ol, 6%) and a ring-expansion product (1-methylcyclobutanol, 13%) in addition to a nonrearranged product ((1-methylcyclopropyl)methanol, 81%). The ring-opened product was proposed to form from a substrate radical intermediate, while the ring-expansion product was proposed to arise from a second oxidation of the radical to form a carbocation. Lipscomb, Floss, and co-workers⁸³¹ applied a chiral ethane to detect rearrangements during catalysis in sMMO from *M. trichosporium*. This small substrate closely resembles methane compared to other bulky radical clock molecules and is expected to be unconstrained in the MMO active site. The product analysis showed 35% inversion of configuration, indicating that a radical intermediate is formed such that it can rotate in the active site before the completion of oxygen insertion. When this technique was applied by Lippard, Floss, and co-workers to sMMO from *M. capsulatus*, similar results (28% inversion) were obtained with chiral ethane.⁸³² Lipscomb and co-workers⁸³³ also applied methylcubane as a radical clock to sMMO from *M. trichosporium* and identified rearranged products, suggesting the mechanism of MMO involves hydrogen abstraction via a radical mechanism.

Arguments for the concerted mechanism were presented by Lippard, Newcomb, and co-workers^{834,835} studying sMMO from *M. capsulatus* applying meth-

Scheme 23



ylcubane as a radical clock. Only the methyl position was hydroxylated (0.5% total yield) with no rearrangement product.⁸³⁴ The lack of reactivity at the cubyl C–H position was taken to indicate that a conventional hydrogen abstraction to form a substrate radical intermediate was not involved. They have also applied the ultrafast radical clock substrate, *trans*-1-methyl-2-phenyl-cyclopropane, to the MMO system from *M. capsulatus* and found no rearranged products.⁸³⁵ Lippard, Newcomb, and co-workers computed the expected lifetime of the putative radical intermediate indicated by the partial rearrangement product distribution observed in the chiral ethane turnover experiments. Using the estimated rate constant for the C–C bond rotation and considering the ratio of rearranged products, a lifetime of roughly 150 fs was obtained for the putative radical intermediate.^{834,835} This extremely short lifetime argues against formation of discrete radical species. Instead, a nonsynchronous concerted mechanism with partial radical character was proposed to explain observed rearrangements. In this process, C–H bond breaking and C–O bond formation are almost concerted but not synchronized.

Siegbahn and Crabtree proposed a radical rebound mechanism based on theoretical studies⁸²⁷ and subsequent refinement.⁸²⁶ Their model predicts further activation of intermediate **Q** to an asymmetric [Fe^{III}–Fe^{IV}]-oxyl radical species. This species undergoes an H-atom abstraction reaction with CH₄ to form a transient methyl radical species bound to an [Fe^{III}–Fe^{IV}]-hydroxyl. This step is followed by a rapid recombination of •CH₃ with the Fe^{IV} center to form a weak Fe^V–CH₃ bond. The recombination of free methyl radical with Fe^{IV} to form an Fe–C bond is found to be very exothermic with no barrier. Basch, Mogi, Musaev, and Morokuma also recently published DFT calculations in support of H-atom abstraction.⁸³⁶ However, in their studies, the H-atom abstraction occurs at the edge of the bridging oxygen atom of the high-valent bis- μ -oxo species instead of the terminal oxyl radical. The resulting hydroxide bridge in the [Fe^{III}Fe^{IV}] mixed-valence state interacts weakly with the methyl radical. In their model, recombination of methyl radical with the hydroxy

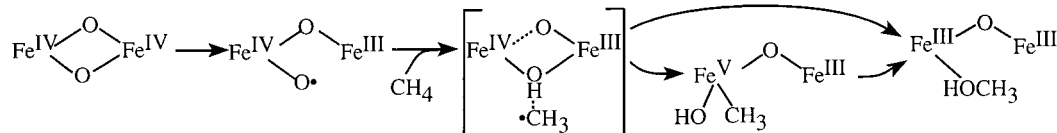
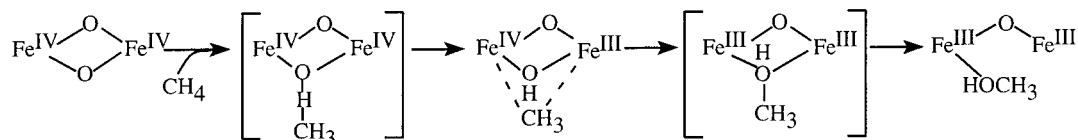
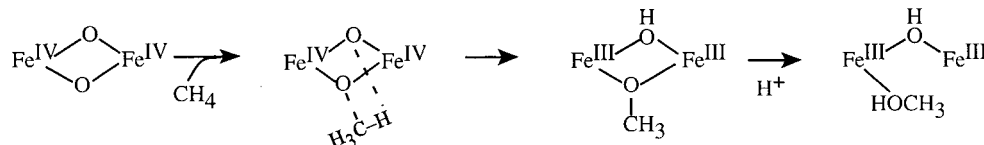
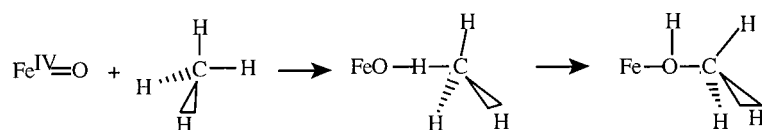
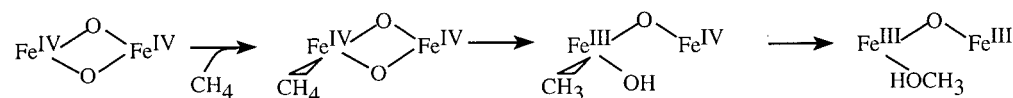
intermediate occurs without first forming an Fe–C bond. Alternatively, a number of theoretical studies have supported the concerted oxygen insertion mechanism. In line with an earlier proposal by Shestakov and Shilov⁸³⁷ and by Shteinman,^{821,822} Yoshizawa and Hoffmann used the extended Hückel method to argue against an oxygen rebound mechanism that invokes formation of a discrete radical species.^{824,825} Instead, they propose initial coordination of methane to Fe^{IV} forming a pentacoordinate carbon center followed by two-step concerted hydrogen and methyl shifts to generate methanol. To explain partial inversion of the chiral ethane during turnover, pseudorotation of Fe–CH₄ was proposed. A summary of the proposed mechanisms are listed in Scheme 24.

In recent years, much progress has been made toward understanding the mechanism of dioxygen and methane activation by MMO. In particular, spectroscopic characterization of reactive intermediates in MMO has significantly contributed to our current understanding. Further spectroscopic characterization of the peroxo biferric species, intermediate **P**, and the high-valent intermediate, intermediate **Q** are required for fundamental insight into the dioxygen activation processes. In addition, more experimental data describing the conversion of intermediate **P** to intermediate **Q** are needed to evaluate possible mechanisms.

2. Ribonucleotide Reductase

Biochemical Characterization. The enzymatic reduction of ribonucleotides catalyzed by ribonucleotide reductase (RR, EC 1.17.4.1) generates deoxyribonucleotides, which are essential for DNA synthesis.^{838–840} This involves reduction of the hydroxyl group on the 2'-carbon of the ribose moiety of nucleoside diphosphates and triphosphates.^{841,842} There are at least four classes of RR.^{842,843} Each class has its unique composition and cofactor requirement, but all contain a metal site and involve radical chemistry.^{842–844} Class I has an $\alpha_2\beta_2$ quaternary structure with a total molecular weight of 258 kDa.^{845,846} Homodimers α_2 and β_2 are usually referred as R1 and R2. Each R1 contains one substrate-binding site and two separate allosteric sites, and each R2 contains a binu-

Scheme 24

Siegbahn and Crabtree*Basch, Mogi, Musaev and Morokuma**Shteinman**Shestakov and Shilov**Yoshizawa and Hoffmann*

clear non-heme iron active site with a stable tyrosyl radical essential for enzymatic reactivity.^{838,845–850} This class of RR requires dioxygen to generate the binuclear active site and the radical and thus does not function under anaerobic conditions.^{851–853} They are found in all eukaryotes and some microorganisms, with RR from *E. coli* being the most characterized.⁸⁵⁴ Class II RR has an α or α_2 homodimer structure and a molecular weight of 82 kDa. The radical required for reactivity is generated by adenosyl cobalamin.^{855,856} This class of RR functions both aerobically and anaerobically and is found in some microorganisms but not in higher organisms. The most characterized enzyme is from *Lactobacillus leichmannii*.⁸⁵⁷ Class III RR is also found in *E. coli* and only functions anaerobically.^{842,858–860} This class of enzymes are iron–sulfur proteins with a glycy radical and have an $\alpha_2\beta_2$ quaternary structure with a molecular weight of 160 kDa.^{861,862} The α subunits contain the active site including the substrate-binding site, the allosteric sites, and the glycy radical, while the peptides of β subunits are held by a 4Fe–4S iron–sulfur center.^{861,862} Class IV RR was discovered in *coryneform* bacteria.^{863,864} This class of enzymes contain a putative binuclear manganese cluster and a tyrosyl radical.⁸⁶⁵ The structure and function of the Class I RR from *E. coli* will be considered below unless noted, and information on other classes can be obtained from recent reviews.^{794,843,844,854,866–870}

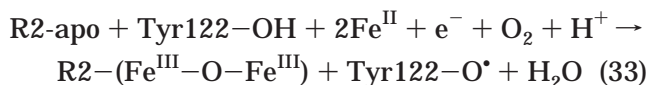
As described above, Class I RR has a tetrameric structure composed of the R1 and R2 homodi-

mers.^{845,846} The stable tyrosyl (Tyr122) radical in R2 is located in the interior of the protein surrounded by a tightly packed, hydrophobic environment and is shielded from electron-donor groups that are not part of the ET chain.^{845,871–873} This radical is stable for several weeks at 4 °C. It has been identified as an oxidized deprotonated Tyr122[•] radical, which stores an equivalent for subsequent turnover at a remote catalytic site on R1.^{871–873} Tyr122[•] along with the binuclear non-heme iron center are about 35 Å away from the active site of R1.⁸⁴⁵ Thus, a long-range ET chain is required, and the terminal group of the ET chain involved in catalysis has been identified from mutagenesis studies to be a radical on Cys439 at the R1 substrate-binding site.^{838,845,874}

Dioxygen is required for the formation of the tyrosyl radical along with oxidation of a binuclear ferrous center to an oxo-bridged binuclear ferric site which is thought to stabilize the tyrosyl radical (vide infra).^{852,875–883} Prior to the formation of the Tyr122[•], two intermediates **U** and **X** in the WT enzyme^{876–878,882,883} and one peroxo intermediate in the R2–D84E and R2–W48F/D84E mutants^{884,885} have been observed. The oxidized [Fe^{III}Fe^{III}], mixed-valent [Fe^{II}Fe^{III}], and reduced [Fe^{II}Fe^{II}] forms from *E. coli* and other systems have also been characterized. The structure and function of these sites are discussed below.

Kinetics. The reaction of R2 involved in formation of the Tyr122[•] and the oxo-bridged binuclear ferric non-heme site is shown in eq 33. R2-apo refers to the

subunit without bound iron atoms, and R2-(Fe^{III}-O-Fe^{III}) is the oxidized active site.



The binding of Fe^{II} by the apo protein has been investigated using Mössbauer spectroscopy with different amounts of ⁵⁶Fe and ⁵⁷Fe.⁸⁸⁶ The results show that the two metal-binding sites have different affinities for ferrous ions. By correlating the Mössbauer parameters of the two sites to their geometric structures,⁸⁷⁸ it has been suggested that the metal-binding site farther from the Tyr122* is preferentially occupied at a low Fe^{II}/R2 ratio (<1.7). This is in accord with the X-ray crystallography studies on mouse R2 (vide infra).⁸⁸⁷

As noted above, intermediates **U** and **X** have been observed in WT RR during the reaction shown in eq 33. Reaction of R2-apo, reductant ascorbate, and limited Fe^{II} (Fe^{II}/R2-apo = 2.0–2.4) with O₂ leads to the accumulation of intermediate **U** with an absorption maximum at 560 nm and a formation constant of $k = 5\text{--}10\text{ s}^{-1}$.⁸⁷⁷ This decays to intermediate **X** with a rate of $3.4\text{--}5.5\text{ s}^{-1}$. Decay of intermediate **X** with a rate constant of 0.8 s^{-1} is associated with the one-electron oxidation of Tyr122 and leads to the formation of a stable radical and oxo-bridged binuclear ferric active site. Reaction of R2-apo, reductant ascorbate, excess Fe^{II} (Fe^{II}/R2-apo ≥ 5), or limited Fe^{II} and excess ascorbate with O₂ leads to the formation of intermediate **X** with a rate constant of $5\text{--}10\text{ s}^{-1}$.⁸⁷⁶ Intermediate **U** is not observed under these conditions and is thought to decay to intermediate **X** too rapidly to accumulate ($k > 20\text{ s}^{-1}$). The formation constants ($5\text{--}10\text{ s}^{-1}$) of both intermediates **U** and **X** are not affected by the concentration of Fe^{II}, O₂, and R2-apo. Combined with the fact that reaction of Fe^{II}-preloaded R2 (reduced R2) and excess reductant with O₂ increases the formation constant of intermediate **X** to $k = 60\text{--}80\text{ s}^{-1}$, these results suggest that the rate constant of $5\text{--}10\text{ s}^{-1}$ reflects a conformational reorganization required for the binding of Fe^{II} by the apo protein.⁸⁸⁸

The formation of intermediate **X** is 2 times slower for the R2-Y122F mutant.⁸⁸⁹ In this mutant Tyr122 is replaced by a phenylalanine which is more difficult to oxidize. Reaction of R2-Y122F with dioxygen generates intermediate **X**, which is spectroscopically indistinguishable from but has longer lifetime than intermediate **X** observed in WT R2. Decay of this intermediate leads to a normal binuclear ferric center as observed for WT, along with generation of at least six paramagnetic species.^{890,891} At least two of these are tryptophan radicals, and another is proposed to be Tyr356*, which is part of the long-range ET chain and is conserved in all R2s. These results suggest that when Tyr122* is eliminated, other residues from the ET chain can supply the electron associated with the formation of the free radical essential for catalysis. It should be noted that the Y122F mutant has an altered midpoint potential relative to the native protein (from -115 to -178 mV), indicating that

Tyr122 does affect the environment of the binuclear center.⁸⁹²

In contrast to MMOH and Δ^9 desaturase ($\Delta^9\text{D}$), a peroxo-level intermediate is not observed for WT R2. However, it can be trapped from both the R2-D84E and R2-W48F/D84E mutants.^{884,885} The Asp84 ligand is replaced with a glutamate to correct the only difference in ligation among the four carboxylates and two histidines bound to the active site of *E. coli* R2 relative to MMOH (vide supra), and the Trp48 residue was substituted with phenylalanine to block ET to the binuclear non-heme iron center during O₂ activation to increase the lifetime of the intermediate. In the WT form, the peroxo intermediate either does not form or decays very rapidly ($k > 150\text{ s}^{-1}$ at 5 °C).⁸⁸⁵ The D84E mutation stabilizes the peroxo intermediate with a decay rate constant of $k = 0.9\text{--}1.2\text{ s}^{-1}$, and the W48F/D84E mutation further increases its lifetime ($k = 0.24\text{--}0.28\text{ s}^{-1}$).^{884,885} However, it should be noted that in contrast to $\Delta^9\text{D}$ (section III.C.3),⁷⁹³ reaction of the reduced binuclear non-heme iron of R2 with ¹⁸O₂ results in incorporation of ¹⁸O into the μ -oxo bridge of the biferric active site, requiring that O₂ must be coordinated to the binuclear center during O–O bond cleavage.²²⁴

It should also be noted that the reaction of another mutant, R2-F208Y, with O₂ leads to a partitioning between the production of Tyr122 radical and the hydroxylation of Tyr208.^{893–895} The former dominates in the presence of high concentration of reductant and undergoes a one-electron oxidation, while the latter leads to a two-electron oxidation to generate a catechol that is bidentate bound to one of the ferric ions, which gives an intense absorption band centered near 675 nm. The oxygen atom inserted into Tyr208, however, was shown to originate from a water molecule and not from dioxygen.⁸⁹⁵ This is in contrast to the results for similar experiments on the R2-W48F/D84E mutant.⁸⁹⁶ As described above, the W48F mutation shuts down the transfer of the extra electron to prevent the formation of Tyr122 radical. Resonance Raman studies show that the final product is an Fe^{III}-phenolate species with the inserted oxygen derived from dioxygen. These results should ultimately lead to insight into the structural basis for protein modulation of dioxygen reactivity among the O₂ activating enzymes.

Structure. Structures of R2 proteins in different oxidation states and from various sources have been determined by X-ray crystallography.^{845,846,887,897–902} The overall structure of the R2 homodimer is heart-shaped with the two equivalent binuclear non-heme iron centers about 25 Å apart. The structure contains more than 70% α helix, which forms an 8-stranded barrel in a similar arrangement to that of MMOH.⁹⁰³ The active site also exhibits the conserved EXXH motif that is found in MMOH and $\Delta^9\text{D}$.^{903,904}

The apo form of R2 from *E. coli* RR contains Asp84, His118, Glu115, Glu238, His241, and Glu204 in the metal-binding pocket.⁸⁹⁷ Compared to the iron-bound forms (vide infra), these amino acids move in slightly to occupy the space vacated by the iron atoms. Four of them, His118, Glu115, Glu238, and His 241, are protonated to maintain the overall charge neutrality,

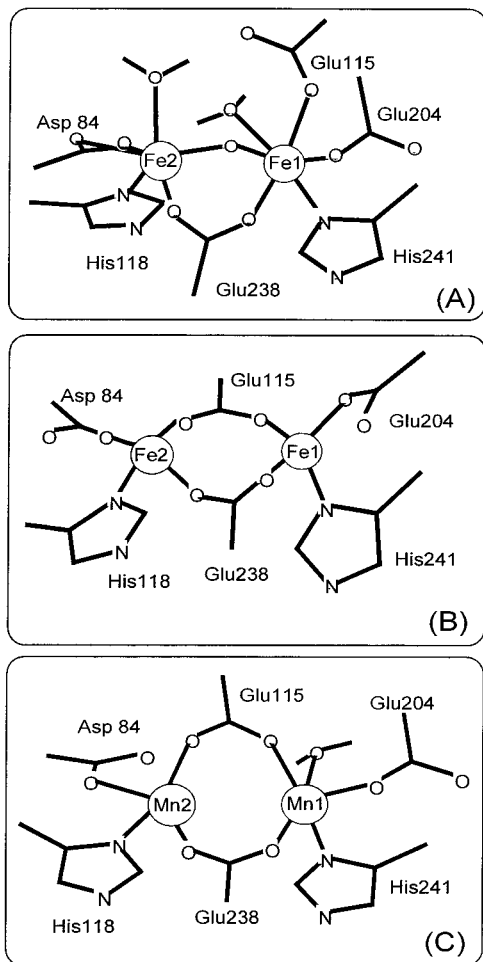


Figure 80. Representation of the crystallographically determined binuclear active sites of the R2 subunit of ribonucleotide reductase. (A) Binuclear oxidized $[\text{Fe}^{\text{III}}\text{Fe}^{\text{III}}]$ active site from *E. coli* (1RIB), (B) binuclear reduced $[\text{Fe}^{\text{II}}\text{Fe}^{\text{II}}]$ active site from *E. coli* (1XIK), and (C) binuclear $[\text{Mn}^{\text{II}}\text{Mn}^{\text{II}}]$ active site from *E. coli* (1MRR). (The structures were generated using the crystallographic coordinates from the indicated PDB files.)

which also keeps these side chains and Tyr122 connected via hydrogen bonds. The metal-binding sites can be occupied with two iron or manganese atoms, with the site farther from the tyrosine residue labeled Fe1 (Mn1) and the other Fe2 (Mn2).

The oxidized R2 structure was determined to a resolution of 2.2 Å (Figure 80A, PDB ID: 1RIB).⁸⁴⁶ The active site contains two ferric ions separated by about 3.3 Å (Fe–Fe distance = 3.2 Å from EXAFS studies,⁹⁰⁵ vide infra). Fe1 is bound with His241, Glu204, and Glu238, all monodentate. Fe2 is bound with His118 and bidentate with Asp84. Between the two iron atoms is one μ -1,3-carboxylate bridge from Glu115 and a μ -oxo bridge. Both iron atoms have additional solvent-derived ligation resulting in two 6C centers. The Tyr122 is buried inside the protein about 10 Å from the surface and is about 3.2 Å to Asp84 on Fe2.

Reduced R2 (Figure 80B, PDB ID: 1XIK)⁸⁹⁸ exhibits a similar ligand environment to that of the oxidized form at the binuclear active site with conformational changes in three of the carboxylate ligands.

The crystal structure for the protein reduced by X irradiation at 110 K (resolution of 1.7 Å) is very similar to the one obtained from chemical reduction at room temperature (resolution of 2.1 Å). Fe1 is bound to His241 and Glu204 monodentate. Fe2 is bound to His118 and Asp84 monodentate. Glu238 and Glu115 bridge between the two iron atoms in a μ -1,3 configuration. There is no μ -O(H) or other solvent-derived ligand detected. Both iron atoms can be described as distorted tetrahedral. The distance between the two iron atoms has increased to 3.9 Å, in agreement with the absence of a μ -O(H) bridge. The distance between the Tyr122 and Asp84 is also shortened to 2.7 Å, which may facilitate ET between these two moieties in the formation of the active site. It should be noted that this active-site structure does not completely agree with the one observed in solution from MCD studies (vide infra).⁶⁶⁹ This may relate to (1) disorder on Glu204 which could be bidentate, (2) the possibility of an unobserved solvent-derived ligand bound to Fe1 (similar to Mn–R2, vide infra),⁹⁰⁰ or (3) the different conditions used to obtain the crystal structure relative to those used for the MCD studies.

The structure of the R2–D84E mutant was determined to a resolution of 2.2 Å.⁹⁰¹ The oxidized binuclear active site closely resembles that in WT R2 except that Glu84 is monodentate bound to Fe2 and hydrogen-bonded to the neighboring solvent-derived ligand bound to the same iron atom. The two iron atoms are 5C and 6C, and the distance between them is 3.3 Å. This mutant was chemically reduced to the biferrous form, and the structure was determined crystallographically at 1.98 Å resolution. Comparison to the reduced form of WT R2 reveals three significant differences: (1) Glu84 is bidentate bound to Fe2 (Asp84 is monodentate in reduced WT), (2) the conformation of Glu204 has changed considerably with the unbound oxygen farther away from Fe1, and (3) Glu238 bridges the iron atoms in a μ -1,1 configuration with its second oxygen atom also bound to Fe1, which decreases the distance between the two iron atoms from 3.9 to 3.5 Å. Both iron atoms are 5C in R2–D84E. The reduced binuclear active site of this D84E mutant has a structure very similar to that of MMOH.

The structure of the azide-bound reduced form of the R2–F208A/Y122F mutant of *E. coli* RR has been determined at a resolution of 2.0 Å.⁸⁹⁹ Azide binds terminally to Fe1 with a change of the bridging Glu238 to a μ -1,1 configuration. The second oxygen atom of Glu238 also binds to Fe1, resulting in the two iron atoms being 6C and 4C with an Fe–Fe distance of 3.4 Å.

The binuclear active-site structure of manganese-substituted *E. coli* (Figure 80C, PDB ID: 1MRR)⁹⁰⁰ was determined at 2.5 Å resolution. The overall R2 structure of this Mn-substituted form is very similar to the Fe-occupied form, with a distance between the two Mn atoms of 3.6 Å. The binuclear active-site structure is different from that of the oxidized site⁸⁴⁶ but similar to the reduced Fe site.⁸⁹⁸ The Glu238 bound to Fe2 of the biferric form shifts in the Mn1 of Mn–R2 to bridge both manganese ions in a μ -1,3

configuration with Glu115 serving as the second μ -1,3 bridge. The Mn1 is bound with Glu204 and His241 along with one water ligand. The Mn2 is bound with His118 and Asp84 monodentate. There is no μ -oxo bridge and no solvent-derived ligand bound on Mn2. The two Mn atoms are 5C and 4C.

The structure of oxidized R2 from mammalian (mouse) RR was determined at pH 4.7 (resolution of 2.3 Å).⁸⁸⁷ The overall $\alpha_2\beta_2$ structure of mouse RR is very similar to that of *E. coli* RR, except that mouse R2 is mainly composed of β -strands. Both the oxidized and reduced forms contain only one iron atom bound at the active site. This iron atom is in the metal-binding site farther from the tyrosine residue and is bound with Glu170, Glu233, Glu267, and His270 with Glu267 bound bidentate, which results in a 5C distorted trigonal-bipyramidal geometry. The structure also reveals that the iron-radical site is more accessible and has less hydrogen bonds than in *E. coli* R2, which may contribute to the low stability of the iron center of mouse R2.⁹⁰⁶

Spectroscopy. The oxidized form of the binuclear non-heme iron center of R2 contains two ferric ions in the active site separated by 3.22 Å, from EXAFS.⁹⁰⁵ Mössbauer spectroscopy demonstrates that the sites have two high-spin ferric ions which are antiferromagnetically coupled.⁸⁷⁵ The magnitude of the exchange coupling is estimated from magnetic susceptibility and saturation-recovery EPR studies to be -90 to -108 cm^{-1} .^{852,907,908} This strong coupling originates from the presence of the oxo bridge between the two iron atoms. A short Fe–O distance of 1.78 Å, from EXAFS, is consistent with the presence of a μ -oxo bridge.⁹⁰⁵ The intense CD⁹⁰⁹ and absorption⁸⁵² transitions at 325 and 370 nm are oxo to ferric CT transitions (see section II.A.2), and the rR frequencies at 493 and 756 cm^{-1} arise from the symmetric and asymmetric stretching vibrations of the Fe–O–Fe core.^{910,911}

The nature of the Tyr122 \cdot has been studied with a variety of spectroscopic methods. UV–vis absorption shows the narrow, characteristic band at 412 nm for the tyrosyl radical.⁸⁵² The EPR spectrum shows no signal for the antiferromagnetically coupled binuclear non-heme iron center but does exhibit a $g = 2.0047$, $S = 1/2$ signal associated with the Tyr122 \cdot .^{881,912,913} ENDOR studies show that the Tyr122 \cdot is uncharged.⁸⁷¹ It lacks interaction with hydrogen-bonding protons and shows a strong hyperfine coupling with the β -methylene proton. CD studies show intense features around 410 and 800 nm for the Tyr122 \cdot with the former associated with the absorption feature at 410 nm.⁹⁰⁹ rR spectra obtained with excitation close to this 410-nm band further show a strongly enhanced mode at about 1500 cm^{-1} .^{872,914} This high frequency for a C–O stretch indicates that Tyr122 \cdot is not protonated, in accord with the ENDOR results. The interaction between the radical and the binuclear non-heme iron center is very weak. The magnitude of the exchange coupling estimated from saturation-recovery EPR is about $|0.0047 \pm 0.0003$ cm^{-1}], which may arise from a hydrogen-bonding interaction between these centers.⁹¹⁵

One-electron reduction of oxidized R2 with X-ray irradiation at LT produces the mixed-valent form, which gives three EPR signals at $g = 14.0$, 6.6, and 5.4 arising from a ferromagnetically coupled [Fe^{II}–Fe^{III}] center with an $S = 9/2$ Kramers doublet ground state.^{916,917} The mixed-valent form of R2 can also be obtained with low yield (5%) through chemical reduction with diimide, generating EPR signals at $g = 1.93$, 1.85, 1.83, and 1.64.⁹¹⁸ These figures result from an antiferromagnetically coupled [Fe^{II}Fe^{III}] center with an $S_{\text{tot}} = 1/2$ Kramers doublet ground state as observed for mixed-valent Hr,⁷⁰⁴ MMOH,^{802,810} and PAP,^{919–921} suggesting that there is a μ -hydroxo bridge between the two iron atoms. Measurement of the magnitude of the exchange coupling is in accord with the presence of a protonated bridge ($J \approx -17$ cm^{-1}).⁹¹⁷ The mixed-valent forms from mouse and herpes simplex virus upon mild chemical reduction are also observed and stable at room temperature.^{922,923} This parallels the μ -hydroxo bridge observed for the mixed-valent form of MMOH.^{802,810} However, oxidized RR has a μ -oxo bridge⁸⁴⁶ while oxidized MMOH retains the μ -hydroxo bridge.⁷⁹⁰ (vide supra, section III.C.1). It is of great importance to understand how the different electronic structures resulting from different bridging environments affect different catalytic functions.

The [Fe^{II}Fe^{II}] reduced form is colorless, thus only showing an absorption maximum at 282 nm deriving from the protein residues.⁹²⁴ The two iron atoms are high-spin ferrous ions based on Mössbauer studies.⁸⁷⁵ Magnetic susceptibility and NMR data suggest that the exchange-coupling interaction between the two iron atoms is weak.^{907,924} EPR studies show a very weak integer spin signal at $g = 14.4$, which is considered to derive from a small fraction of molecules having ferromagnetically coupled sites.⁹²⁵ CD and MCD studies show three transitions in the near-IR region (Figures 81A and 78) with one at high energy (9000 cm^{-1}) and two at low energy (5500 and 7500 cm^{-1}).⁶⁶⁹ This demonstrates that the active site contains one 5C and one 4C high-spin ferrous ion. VTVH MCD data (Figure 81B) show a paramagnetic center with a saturation behavior similar to that of a mononuclear ferrous center, indicating that the two exchange-coupled iron centers have a ground state with $M_S = \pm 2$.⁶⁶⁹ A spin Hamiltonian analysis of the saturation magnetization behavior indicates that the two iron atoms are weakly antiferromagnetically coupled with a magnitude of the exchange coupling of $J \approx -0.5$ cm^{-1} , and two sites have unequal ZFS parameters with opposite signs (vide supra, Figure 65D). This is consistent with the fact that the two iron atoms are 5C and 4C, which further indicates that there is an open coordination position on each ferrous center leading to the possibility of dioxygen bridging. It should be noted that the binuclear active-site structure obtained from crystallography contains two approximately equivalent 4C iron centers,⁸⁹⁸ which is not in agreement with the presence of three LF transitions in the near-IR region of the CD and MCD spectra.

Small-molecule binding to the reduced site is of importance for understanding the dioxygen reactivity

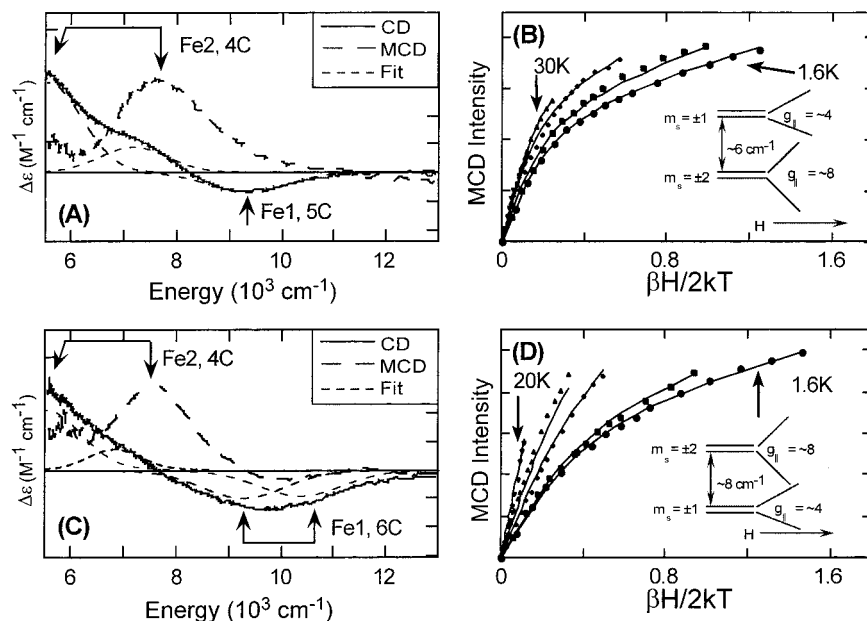


Figure 81. CD and LT MCD spectra of the reduced R2 without and with azide bound. (A) CD (—) and LT MCD (— —) spectra and the fit for the CD spectra (- - -) of the reduced R2, recorded at 5 °C and 5 K and 7 T, respectively. (B) Saturation magnetization behavior of the MCD signal in the LF region for the reduced R2 at 7700 cm^{-1} . The signal intensity (symbols) for a range of magnetic fields (0–7.0 T) at a series of fixed temperatures is plotted as a function of $\beta H/2kT$. The fit to the VTVH MCD data (—) was obtained using eq 29 giving the energy level diagram in inset. (C) CD (—) and LT MCD (— —) spectra and the fit for the CD spectra (- - -) of the azide-bound reduced R2, recorded at 5 °C and 5 K and 7 T, respectively. (D) Saturation magnetization behavior of the MCD signal in the LF region for the azide-bound reduced R2 at 7700 cm^{-1} . The signal intensity (symbols) for a range of magnetic fields (0–7.0 T) at a series of fixed temperatures is plotted as a function of $\beta H/2kT$. The fit to the VTVH MCD data (—) was obtained using eq 29 giving the energy level diagram in inset. (Adapted from ref 669.)

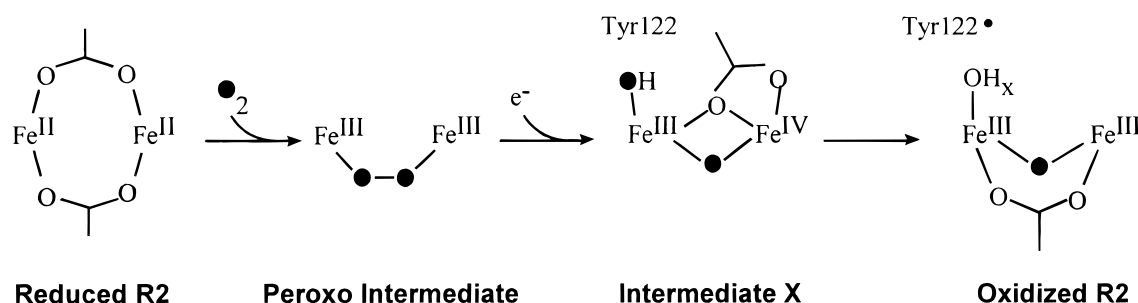
of the active site. CD and MCD studies show that with low-molar excess of azide, one azide binds to the 5C iron atom of the reduced site to convert it to 6C (Figure 81C).⁶⁶⁹ VTVH MCD data and analysis show that the ground state of this exchange-coupled center is altered to $M_S = \pm 1$ (Figure 81D).⁶⁶⁹ The two iron atoms remain weakly antiferromagnetically coupled ($J \approx -2.5 \text{ cm}^{-1}$), indicating that the bridging environment is not significantly perturbed. Compared to the crystal structure of the azide-bound R2–F208A/Y122F mutant, both studies are in agreement that the two ferrous centers are 4C and 6C, while the crystallographic results indicate that there is a carboxylate shift for one of the bridging ligands to a μ -1,1 bridging mode. CD and MCD studies also show that addition of high-molar excess of azide leads to two distinct two-azide-bound active sites.⁶⁶⁹ The one that can be spectroscopically defined contains one 5C and one 6C iron with the two iron atoms weakly ferromagnetically coupled, indicating that each iron atom is bound with one azide and the bridging interaction is perturbed. VTVH analysis shows that the ground state of this species is $|M_S| = \pm 4$, which is consistent with the presence of a $g = 17.0$ signal in the EPR spectrum.⁹²⁵ The above results demonstrate that the binuclear ferrous active site has open coordination positions on both ferrous centers capable of small-molecule (i.e., dioxygen) binding in a bridging mode. This is in accord with the data available for peroxo-level intermediates that have been trapped for the mutants of R2 (vide infra).^{884,885}

The first intermediate (U) observed in the reaction of the reduced R2 site with dioxygen shows an

absorption maximum around 560 nm.⁸⁷⁷ Mössbauer studies show that the active site remains binuclear ferrous, indicating that this species is not a peroxo biferric intermediate. The lack of the 412 nm absorption band further suggests that it does not contain the Tyr122*. The 560 nm absorption feature is, however, eliminated when a tryptophan near the surface of R2 (W48) is mutated to phenylalanine.⁹²⁶ Intermediate U is thought to be a protonated tryptophan radical, in accord with the presence of an EPR feature with a $g \approx 2$ signal at an early phase of the reconstitution process.

The second intermediate (X) has an absorption maximum at 360 nm.^{876,882} The lack of the 412 nm band indicates that it does not contain the Tyr122*. Freeze–quench studies show an $S = 1/2$ isotropic EPR signal at $g = 2.00$ which is different from that observed for the Tyr122* based on spectral line shape and time dependence of formation.^{878,882} The signal shows hyperfine broadening with $^{17}\text{O}_2$ or H_2^{17}O labeling and with a ^{57}Fe incorporation, indicating that the spin is coupled to both the binuclear non-heme iron active site and oxygen from H_2O and dioxygen.⁹²⁷ Q-band EPR studies show significant anisotropy of this $g = 2$ signal.⁹²⁷ From the results from rapid freeze–quench Q-band ^{57}Fe ENDOR, the oxidation state of X is thought to be $[\text{Fe}^{\text{III}}\text{Fe}^{\text{IV}}]$. This is based on the anisotropy of the ^{57}Fe hyperfine tensor of one of the iron sites and is consistent with the Mössbauer data, indicating a significantly smaller isomer shift ($\delta = 0.26 \text{ mm s}^{-1}$) in accord with an Fe^{IV} oxidation state.⁹²⁷ Thus, intermediate X can be best described as a spin-coupled $[\text{Fe}^{\text{III}}\text{Fe}^{\text{IV}}]$ center with

Scheme 25



significant spin delocalization onto oxygen ligands.

Numerous ENDOR studies have been performed to characterize the active-site structure of intermediate **X**.^{928–932} CW and pulsed Q-band ^{1,2}H-ENDOR studies performed with H₂O and D₂O show the presence of terminal aqua ligand bound to Fe^{III}.⁹²⁸ Q-band ¹⁷O₂ and H₂¹⁷O-ENDOR and S-band EPR studies reveal the two oxygen atoms initially derived from O₂: one is present as a μ -oxo bridge and the second as the terminal aqua ligand.⁹³¹ The latter is exchangeable with solvent, and no second μ -oxo bridge is observed. Along with the unusually short distances of Fe–Fe (2.5 Å) and Fe–O (1.8 Å) observed from EXAFS studies,⁹³² these results suggest that the intermediate **X** contains a single oxo bridge and one or two additional mono-oxo bridges provided by the carboxylate ligands. Parallel studies on model complexes have also provided insight into intermediate **X** and will be discussed in section III.D.2.

The peroxo intermediate present in R2–D84E and R2–W48F/D84E mutants exhibits a broad absorption band at 700 nm and diamagnetic ferric Mössbauer features,^{884,885} which are the characteristics of a peroxo–biferric core and are very similar to what has been observed for the peroxo intermediates of MMOH,^{779,782,816} Δ^9 D,⁹³³ and several μ -peroxo–biferric model complexes.^{659,934} Resonance Raman studies for the R2–W48F/D84E mutant show three peaks at 458, 499, and 870 cm⁻¹ assigned as the $\nu_s(\text{Fe}-\text{O}_2)$, $\nu_{\text{as}}(\text{Fe}-\text{O}_2)$, and $\nu(\text{O}-\text{O})$ vibrational modes, respectively.⁸⁸⁵ A similar frequency of $\nu_{\text{O}-\text{O}}$ (890 cm⁻¹) has also been observed for the R2–D84E mutant.⁹³⁵ The high frequency of $\nu_{\text{O}-\text{O}}$ along with the isotope shifts from ¹⁷O₂, ¹⁸O₂, and ¹⁶O¹⁸O labeling experiments for the R2–W48F/D84E mutant demonstrate that the peroxo is bound to the biferric center in a μ -1,2 mode. Decay of the peroxo intermediate in the R2–D84E mutant leads to the appearance of absorption maxima at about 409, 325, and 365 nm, suggesting the formation of the Tyr122• and the oxidized [Fe^{III}–O–Fe^{III}] center.⁸⁸⁴ It should be noted that intermediate **X** does not accumulate after the decay of the peroxo intermediate for the R2–D84E mutant, which may result from the change in the rate constants for the constituent steps. A detailed electronic structure description of the peroxo intermediate will be presented in section III.D.1.

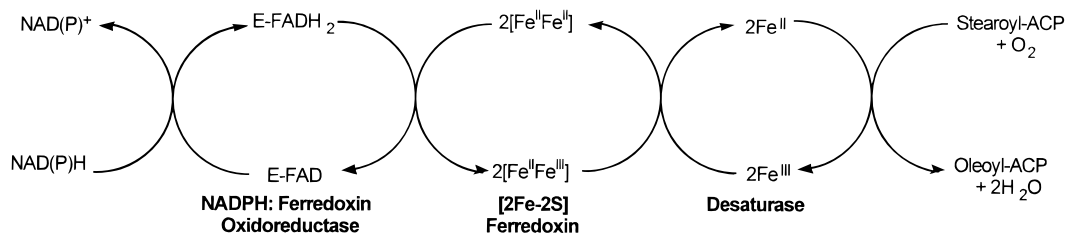
Molecular Mechanism. On the basis of the extensive information available from crystallography and spectroscopy on wild-type and mutant RRs, several key steps of the reaction of the binuclear ferrous site with dioxygen to generate the stable

tyrosyl radical have been derived (Scheme 25). Fe^{II} binding to the apo protein to form the reduced site requires a conformational rearrangement.⁸⁸⁸ The active-site geometric and electronic structure of the reduced form is best described as one 4C and one 5C ferrous center with two μ -1,3-carboxylate bridges between the two iron atoms, resulting in a weak antiferromagnetic coupling.⁶⁶⁹ This reduced form can rapidly react with dioxygen as the substrate (Tyr122) is a residue already present at the site, which is dramatically different from the lack of reactivity observed for MMOH and Δ^9 D (see sections III.C.1 and III.C.3). Reaction of the reduced site in WT R2 with dioxygen either leads to intermediate **U** with limited amount of Fe^{II}⁸⁷⁷ or directly generates intermediate **X** with excess of Fe^{II} or reductant.⁸⁷⁶ Intermediate **U** is a protonated tryptophan radical which can shuttle the extra electron into the binuclear active site to generate intermediate **X**.⁸⁷⁷ Reaction of the reduced R2–D84E and R2–D84E/W48F mutants with dioxygen generates the peroxo intermediate, in which dioxygen bridges the two ferric centers in a *cis*- μ -1,2 configuration.^{884,885} For the R2–D84E/W48F mutants, decay of the peroxo intermediate leads to intermediate **X**, with the extra electron provided either by excess Fe^{II} or reductant or by protein residues (see section III.D.2). Intermediate **X** contains an oxo-bridged [Fe^{III}Fe^{IV}] binuclear center, and its decay generates an oxidized oxo-bridged binuclear ferric center along with a stable unprotonated Tyr122•.

The fact that the two metal-binding sites have different affinity allows one to further distinguish that the site with Asp84 binds weaker and is the Fe^{III} in intermediate **X** while the site away from the Tyr122• binds stronger and has partial Fe^{IV} character in **X**.⁸⁸⁶ Thus, the more oxidized iron atom is farther from Tyr122•, and formation of Tyr122• by decay of intermediate **X** likely occurs by proton-coupled ET rather than direct hydrogen-atom abstraction. The electron is transferred to the Fe^{IV} center (Fe1), and the proton could be associated with formation of a solvent-derived ligand bound to Fe2 in the resulting binuclear ferric form. The stable tyrosyl radical generated is then stored and can be transferred through the long-range ET chain to the R1 subunit to generate a thiyl radical which then generates a reactive substrate radical essential for catalysis.⁸⁴³

3. Δ^9 Desaturase

Biochemical Characterization. The acyl-bound acyl carrier protein (acyl-ACP) desaturases activate dioxygen in a desaturation reaction involving the

Scheme 26. Electron Transfer Chain for Stearoyl-ACP Δ^9 Desaturase

insertion of a *cis* (or *Z*) double bond. Desaturation is an essential step in fatty acid biosynthesis. In eukaryotes, desaturation is a postsynthetic modification catalyzed by NADPH- and dioxygen-dependent binuclear non-heme iron enzymes. Both membrane-bound and soluble enzymes have been identified, and a large variety of isoforms that vary in substrate specificity and regioselectivity are known.^{936–938} The number and position of double bonds in fatty acids profoundly affects their physical and, therefore, physiological properties.^{939–942} Free fatty acids are not desaturated *in vivo* but must be attached by a phosphopantetheine thioester linkage to ACP for the soluble desaturases,⁹⁴³ to coenzyme A (CoA) for some membrane-bound desaturases,^{936,937} or to sugar or phospholipid moieties for other membrane-bound enzymes.^{936,937} Up to eight histidine residues are found to be conserved and are essential for catalytic activity for non-heme integral-membrane desaturases, hydroxylases, and monooxygenases.⁹⁴⁴ Some of these histidine residues have been demonstrated to be ligands for the iron atoms in their active sites.^{944–947} The similar histidine-rich motifs have also been found for integral-membrane enzymes performing other catalytic functions, including oxidases, decarboxylases, acetylenases, and epoxygenases.^{946,948–950} Site-directed mutagenesis studies for higher plants demonstrated that as few as four amino acid substitutions can convert an integral-membrane desaturase to an integral-membrane hydroxylase, and as few as six can convert a hydroxylase to a desaturase.⁹⁵¹ There is no significant sequence identity between the soluble and membrane-bound classes of enzymes.^{952–955} However, the soluble and membrane desaturases do have several important similarities: (1) the presence of the binuclear non-heme active site is required for catalysis;⁹⁵⁶ (2) inhibition by metal chelators;⁹⁵⁷ (3) stereospecificity of the substrate;⁹⁵⁸ and (4) large KIEs for C–H bond cleavage.⁹⁵⁹ Thus, it is believed that there is a partitioning among these different catalytic reaction pathways after the first hydrogen-atom abstraction from the substrates.

Stearoyl-acyl carrier protein Δ^9 desaturase (Δ^9 D) isolated from *Ricinus communis* (castor) seeds is the most well-characterized desaturase (EC 1.14.99.6). Δ^9 D is also the only soluble desaturase identified to date, as the others are integral membrane enzymes. This enzyme inserts the *cis* double bond between the 9 and 10 position of stearoyl-ACP to form oleoyl-ACP using the ET chain shown in Scheme 26.^{956,960–962} Δ^9 D is a homodimer with each subunit having one binuclear iron site and a molecular weight of about 84 kDa.^{955,963} Both the oxidized [$\text{Fe}^{\text{III}}\text{Fe}^{\text{III}}$] and fully reduced [$\text{Fe}^{\text{II}}\text{Fe}^{\text{II}}$] forms along with a peroxo inter-

mediate have been characterized, and their spectroscopic features will be discussed below.

Kinetics. Δ^9 D is isolated in a binuclear ferric state, which can be reduced to the catalytically active biferrous form either chemically or biologically.⁹³³ Steady-state kinetic experiments^{793,933} show that the rate of autoxidation of chemically reduced Δ^9 D in a single turnover is slow ($<0.002 \text{ min}^{-1}$) but is significantly increased in the presence of substrate (stearoyl-ACP) to $k \approx 0.027 \text{ min}^{-1}$, which is 10^3 -fold slower than the rate determined for biologically reduced Δ^9 D with $k \approx 20\text{--}30 \text{ min}^{-1}$. It should be noted that the slow autoxidation rate ($<0.002 \text{ min}^{-1}$) is not affected by addition of pantothenate coenzyme A, methyl stearate, apo-ACP (lacking the functionally essential phosphopantetheine group), or holo-ACP (lacking the stearoyl chain attached to the phosphopantetheine sulfhydryl group),⁹³³ which is in accord with observations from CD and MCD studies (vide infra).⁶⁷¹ It has been found that during the autoxidation of chemically reduced Δ^9 D in the presence of stearoyl-ACP, a peroxo-level intermediate can be trapped with a formation rate of $k = 46 \text{ s}^{-1}$ at 6°C .⁹⁶⁴ Decay of the intermediate leads to the resting biferrous state with a rate of 0.004 min^{-1} .⁹⁶⁴ Alternatively, the absence of desaturation product, 18:1 oleoyl-ACP, suggests that this chemically reduced form undergoes oxidase chemistry.⁹³³ Catalytic oxidation of biologically reduced Δ^9 D using ferredoxin reductase and [2Fe-2S] ferredoxin produces desaturation product, but no intermediate has yet been trapped.⁹³³ The different reactivity between these two forms remains to be understood. It should also be noted that in contrast to RR,²²⁴ ^{18}O is not detected in the oxo bridge (vide infra) after a single turnover of chemically reduced Δ^9 D with $^{18}\text{O}_2$.⁷⁹³

Several other kinetic experiments have also been performed to investigate the nature of substrate-binding specificity.^{965,966} Kinetic deuterium isotope experiments for the yeast Δ^9 CoA desaturase show that the maximum isotope effects occur at the 9-position of the substrates ($k_{\text{H}}/k_{\text{D}} = 7.1 \pm 0.2$) with no detectable effect at the 10-position ($k_{\text{H}}/k_{\text{D}} = 1.03 \pm 0.09$), and similar experiments for the plant oleate Δ^{12} desaturase also show that the maximum isotope effects occur at the 12-position of the substrates ($k_{\text{H}}/k_{\text{D}} = 7.3 \pm 0.4$) with a negligible effect at the 13-position ($k_{\text{H}}/k_{\text{D}} = 1.05 \pm 0.04$). These results provide insight into the mechanism and will be discussed. Recent steady-state kinetic studies give an estimate of $k_{\text{cat}}/K_{\text{M}}$ for different acyl chain lengths.⁹⁶⁷ The results show that the substrate-binding pocket can accommodate at least one more methylene group than the natural substrate and that the hydrophobic

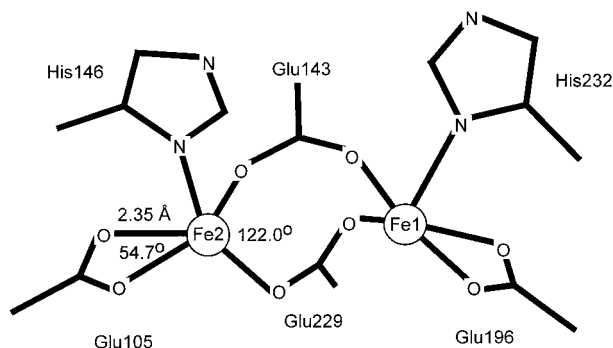


Figure 82. Representation of the crystallographically determined binuclear $\text{Fe}^{\text{II}}\text{Fe}^{\text{II}}$ active site of stearoyl-acyl carrier protein Δ^9 desaturase from castor seed (1AFR). (The structures were generated using the crystallographic coordinates from the indicated PDB files.)

binding energy increases upon increase in chain length.

Structure. The three-dimensional structure of reduced $\Delta^9\text{D}$ from castor seeds has been determined by X-ray crystallography to a resolution of 2.4 Å (PDB ID 1AFR).⁹⁰⁴ The form studied was obtained by photochemical reduction of the metal center by X-ray radiation. The active-site structure (Figure 82) shows that the two Fe^{II} atoms are bound in a highly symmetric environment: one iron is coordinated by Glu196 and His232, while the other iron is coordinated by Glu105 and His146, with both Glu196 and Glu105 binding in a bidentate mode. The two irons are μ -1,3-bridged by two carboxylate ligands (Glu229 and Glu143). The long distance between the irons (4.2 Å) indicates that a μ -O(H) bridge is not present, which is consistent with the lack of electron density in this region of the structure. The orientation of the iron ligands is maintained by side-chain hydrogen bonds. The solvent molecule bound in the vicinity of the iron center is also suggested to be located in a small hydrophobic pocket which is part of the substrate-binding channel, and a similar cavity has been found in MMO.⁷⁸⁹ A deep hydrophobic channel, which possibly binds the fatty acid, extends from the surface into the interior of the enzyme. Molecular modeling of the substrate, stearic acid, in this channel places its Δ^9 carbon close to one of the iron atoms with a distance of about 5.5 Å.

Spectroscopy. The oxidized [$\text{Fe}^{\text{III}}\text{Fe}^{\text{III}}$] form of $\Delta^9\text{D}$ has a μ -oxo bridge between the two ferric ions based on (1) the presence of oxo to ferric CT transitions in the UV-vis absorption spectrum between 300 and 500 nm with $\epsilon = 8000 \text{ M}^{-1} \text{ cm}^{-1}$ ⁷⁹³ and (2) the observation of Fe-O-Fe symmetric and asymmetric vibrational modes in the resonance Raman spectrum at $\nu_s = 519 \text{ cm}^{-1}$ and $\nu_{\text{as}} = 747 \text{ cm}^{-1}$.⁷⁹³ In H_2^{18}O , these vibrations shift by -18 and -34 cm^{-1} , respectively, indicating that the bridging ligand is exchangeable with solvent ($t_{1/2} = 7 \text{ min}$).⁷⁹³ Mössbauer spectroscopy indicates that the two ferric ions are strongly antiferromagnetically coupled with $-J > 30 \text{ cm}^{-1}$ ($H = -2JS_1S_2$),⁹⁶⁸ providing further evidence for the existence of μ -oxo ligation. The isomer shifts of the quadrupole doublets also suggest that the iron atoms have an oxygen-rich coordination environment. It should be noted that there is another minor quad-

rupole doublet detected, which may be associated with a binuclear ferric center containing a μ -hydroxo bridge.⁹⁶⁹ This is in accord with X-ray absorption studies of the oxidized $\Delta^9\text{D}$,⁹⁶⁹ which show two distinct binuclear centers that have Fe-Fe distances of 3.12 and 3.41 Å. The species having a short Fe-O bond of 1.8 Å shows an Fe-Fe distance of 3.12 Å, which is consistent with the presence of one μ -oxo bridge in the active site (72%). The species having the 3.41 Å Fe-Fe distance has no short Fe-O feature and is thought to contain a μ -hydroxo bridge (21%). The distribution of the two conformations is independent of pH between 6 and 10 and solvents,⁹⁶⁹ which indicates that other protein structural factors maintain this conformational change. A similar conformational distribution has also been observed for oxidized MMOH.⁸⁰⁷

The azide adduct of the oxidized $\Delta^9\text{D}$ active site shows a large change with pH.⁹⁷⁰ At pH higher than 7.8, rR spectroscopy shows a dominant $^{14}\text{N}_3^-$ asymmetric stretch $\nu_{\text{as}} = 2073 \text{ cm}^{-1}$ resolved into two bands with $^{15}\text{N}^{14}\text{N}_2^-$; thus, it is proposed to arise from an η^1 -terminal azide adduct. Alternatively, when the pH is decreased to <7 , the dominant $^{14}\text{N}_3^-$ feature of $\nu_{\text{as}} = 2100 \text{ cm}^{-1}$ shifted as a single band with $^{15}\text{N}^{14}\text{N}_2^-$ and is suggested to arise from the μ -1,3 bridging azide adduct. Both species show an Fe-N₃ stretching mode but lack the Fe-O-Fe stretching mode indicating protonation or loss of the μ -oxo bridge. Thus, the high-pH form contains a η^1 -terminal azide with a μ -hydroxo bridge, while the low-pH form has a μ -1,3-azide bridge. The ability to form a μ -1,3-azide bridge suggests that dioxygen can bind to the active site in a μ -1,2 configuration to form a peroxo-level intermediate in the $\Delta^9\text{D}$ catalytic cycle.

Reduced, [$\text{Fe}^{\text{II}}\text{Fe}^{\text{II}}$], $\Delta^9\text{D}$ contains two high-spin ferrous ions bound with oxygen and nitrogen ligands based on the Mössbauer studies.⁹⁶⁸ No EPR signal is observed. CD and MCD spectroscopies⁶⁷¹ (Figure 83A) show only two LF transitions in the near-IR region which are split by more than 2000 cm^{-1} , demonstrating that the active site contains two approximately equivalent 5C ferrous ions. The two LF transitions are separated by 3000 cm^{-1} compared to the generally observed splitting of larger than 5000 cm^{-1} for a 5C site (section II.A.1). A LF calculation using the crystal structure coordinates⁶⁷¹ shows that the two irons have a distorted square-pyramidal geometry with a weak axial interaction and a large two-in-two-out distortion in the equatorial plane due to the small bite angle of the terminal bidentate glutamate residue that leads to the usually small excited-state splitting. Analysis of VTVH MCD data⁶⁷¹ (Figure 83B) gives an $M_S = 0$ ground state and $|M_S| = 4$ excited substate at $\sim 10 \text{ cm}^{-1}$ above the ground state in the absence of a magnetic field. The iron centers are rhombic such that application of a magnetic field results in an energy splitting of the $|M_S| = 4$ doublet and its strong interaction with the $M_S = 0$ ground state (see Figure 67B). This is consistent with the lack of an EPR signal. Spin Hamiltonian analysis⁶⁷¹ shows that the two iron atoms are weakly antiferromagnetically coupled with $-J = < \sim 1 \text{ cm}^{-1}$ and both irons have similar -ZFS

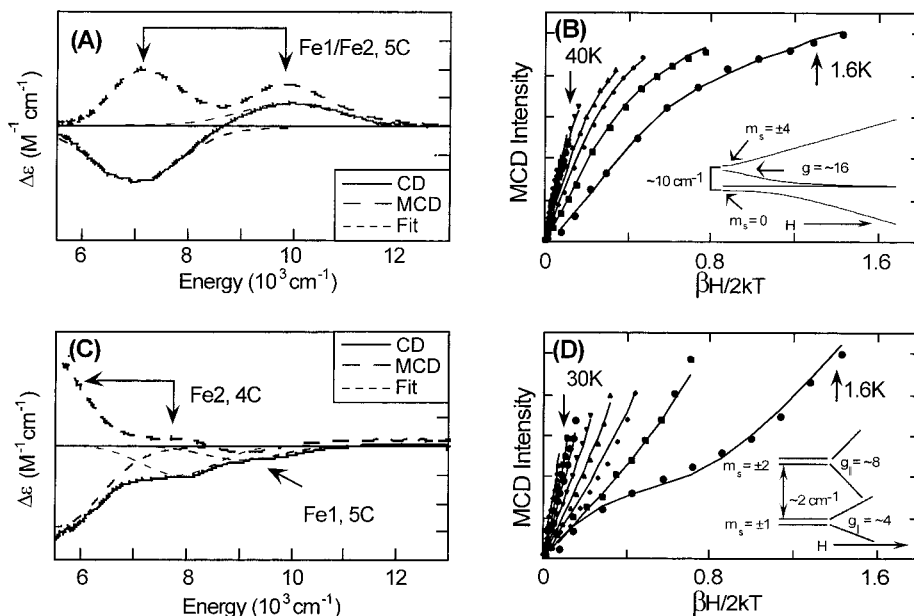


Figure 83. CD and LT MCD spectra of the reduced $\Delta^9\text{D}$ without and with substrate bound. (A) CD (—) and LT MCD (---) spectra and the fit for the CD spectra (- - -) of the reduced $\Delta^9\text{D}$, recorded at 5 °C and 5 K and 7 T, respectively. (B) Saturation-magnetization behavior of the MCD signal in the LF region for the reduced $\Delta^9\text{D}$ at 10 000 cm^{-1} . The signal intensity (symbols) for a range of magnetic fields (0–7.0 T) at a series of fixed temperatures is plotted as a function of $\beta H/2kT$. The fit to the VTVH MCD data (—) was obtained using eq 29, giving the energy level diagram in inset. (C) CD (—) and LT MCD (---) spectra and the fit for the CD spectra (- - -) of the substrate-bound reduced $\Delta^9\text{D}$, recorded at 5 °C and 5 K and 7 T, respectively. (D) Saturation magnetization behavior of the MCD signal in the LF region for the substrate-bound reduced $\Delta^9\text{D}$ at 5700 cm^{-1} . The signal intensity (symbols) for a range of magnetic fields (0–7.0 T) at a series of fixed temperatures is plotted as a function of $\beta H/2kT$. The fit to the VTVH MCD data (—) was obtained using eq 29, giving the energy level diagram in inset. (Adapted from ref 671.)

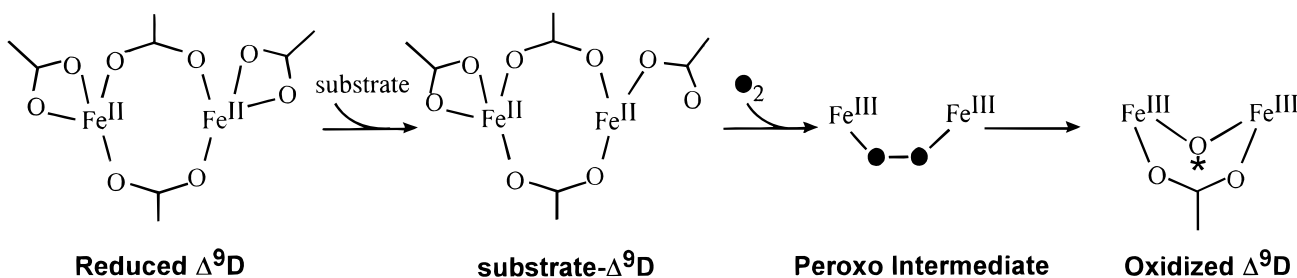
with $D_1 \approx D_2 \approx -10 \pm 5 \text{ cm}^{-1}$, further demonstrating that the two ferrous centers are approximately equivalent with a weak axial square-pyramidal geometry. It should be noted that the magnitude of the observed exchange-coupling constant is consistent with the presence of two μ -1,3-carboxylate bridges. The CD/MCD data above are consistent with the reduced $\Delta^9\text{D}$ crystal structure and are distinct from the CD/MCD data for reduced MMO^{670,798} and RR.⁶⁶⁹

The combination of CD/MCD/VTVH MCD studies further provided the first evidence that the substrate (stearoyl-ACP) binding strongly perturbs the active site.⁶⁷¹ From Figure 83C in which the substrate is bound to the active-site pocket, three LF transitions are observed in the CD/MCD spectra with one in the high-energy region (9500 cm^{-1}) and two in the low-energy region (7500 and 5500 cm^{-1}). The presence of more than two transitions indicates that upon the substrate binding, the two irons become inequivalent. One iron atom remains 5C but is distorted toward a trigonal-bipyramidal structure, while the other iron atom changes to 4C. VTVH MCD data (Figure 83D) also show a dramatic change upon substrate binding. The inverse saturation behavior is observed, which is associated with a change of the ground state from a lower $|M_S|$ value to a higher one with increase in the magnetic field (see section III.A.2). Thus, this behavior shows that the substrate bound form has a ground state of $|M_S| = 1$ which changes to an $|M_S| = 2$ at high field due to a crossover of these two sublevels indicating that the energy difference between them is very small. Spin Hamiltonian analysis⁶⁷¹ further demonstrates that the two iron centers

have ZFSs differing in sign and magnitude. The 5C iron center is associated with a $-ZFS$ while the 4C iron center has a $+ZFS$ (Figure 65D, left). The two iron atoms remain antiferromagnetically coupled, but the exchange-coupling increases to $-J \leq \sim 2.5 \text{ cm}^{-1}$, which is still within the range observed for two μ -1,3-carboxylate bridges. Thus, the substrate binding greatly alters both the geometric and electronic structure of the active site. The presence of the 4C site results in an additional open coordination position on one iron center for dioxygen binding and can alter the redox-active ground-state orbital to an orientation having better overlap with dioxygen, which would enhance ET from the binuclear iron center, increasing the dioxygen reactivity. It should be noted that there is no spectral change upon the addition of apo-ACP or holo-ACP, which is in accord with the observations from steady-state kinetic studies (vide supra).⁹³³

The peroxo intermediate that was trapped upon exposure of chemically reduced $\Delta^9\text{D}$ to stearoyl-ACP and 1 atm O_2 shows a broad absorption band at 700 nm.⁹³³ rR excitation into this band shows vibrational modes at $\nu_s(\text{Fe}-\text{O}_2) = 442 \text{ cm}^{-1}$, $\nu_{as}(\text{Fe}-\text{O}_2) = 490 \text{ cm}^{-1}$, and $\nu(\text{O}-\text{O}) = 898 \text{ cm}^{-1}$, which undergo mass-dependent isotope shifts for $^{16}\text{O}^{18}\text{O}$ and $^{18}\text{O}_2$.⁹³³ Each Fe-O₂ vibration exhibits one peak of intermediate frequency with $^{16}\text{O}^{18}\text{O}$. Along with the Mössbauer data⁹⁶⁴ and the high $\nu(\text{O}-\text{O})$, these results indicate that the peroxo is bridged symmetrically between the two ferric ions in a *cis*- μ -1,2 configuration.

Molecular Mechanism. Several key steps of the reaction of the binuclear ferrous site of $\Delta^9\text{D}$ with the substrate and dioxygen can be derived based on the

Scheme 27^a

^a Note that the bridging oxygen does not incorporate ^{18}O from dioxygen; see ref 793.

extensive information available from crystallography and spectroscopy (Scheme 27). The active-site geometric and electronic structure of reduced $\Delta^9\text{D}$ have been well-defined by both spectroscopy^{671,968} and crystallography.⁹⁰⁴ The dramatic perturbation on the active site upon substrate binding observed from CD/MCD studies indicated the presence of an additional open coordination position at one of the ferrous centers. On the basis of kinetic studies, these two forms have different dioxygen reactivity.^{793,933} MCD studies demonstrate that substrate binding greatly perturbs the LF of the active site in a manner which can control orbital overlap with dioxygen, resulting in enhanced reactivity.⁶⁷¹ Reaction of dioxygen with chemically reduced $\Delta^9\text{D}$ leads to a peroxo intermediate.⁹³³

A similar peroxo intermediate has also been obtained for the D84E and W48F/D84E mutants of ribonucleotide reductase,^{884,885} suggesting that the catalytic cycles of the oxygen-activating binuclear non-heme iron enzymes including MMO, RR, and $\Delta^9\text{D}$ may be closely related. This is consistent with their similar protein folds, ligation environments, and hydrophobic active sites. Thus, a high-valent intermediate may be formed in $\Delta^9\text{D}$ after decay of the peroxo intermediate. Alternatively, the failure to detect any incorporation of label in the μ -oxo bridge position of $\Delta^9\text{D}$, which is in contrast to the RR results, also suggests differences in certain aspects of their dioxygen reactivities.

The deuterium KIE^{965,966} observed for yeast $\Delta^9\text{D}$ and plant oleate $\Delta^{12}\text{D}$ suggest the possibility that the intermediate catalyzes hydrogen-atom abstraction from substrate to form a substrate radical intermediate. This mechanism could be shared among the range of soluble, membrane-bound desaturases, hydroxylases, and other enzymes related to fatty acid chemistry. These enzymes have a high specificity for the appropriate substrate for efficient catalysis. After the formation of the substrate radical intermediate, subtle differences in active-site or substrate structures can lead to different catalytic reactions and thus different products, which is supported by the interconversion between the desaturase and hydroxylase functions for the integral-membrane enzymes.⁹⁵¹ While it has been generally believed that a nitrogen-rich environment as in Hr may not donate sufficient charge to cleave the O–O bond compared to a carboxylate-rich environment for MMOH, RR, and $\Delta^9\text{D}$, the discovery of the integral-membrane O_2 -activating enzymes with nitrogen-rich environment lead to a new perspective on this important issue.

4. General Strategy

Figure 84A summarizes the structural information available for the reduced sites of the three binuclear non-heme iron dioxygen-activating enzymes. While all generate peroxy intermediates with apparently similar spectral and structural features, these re-

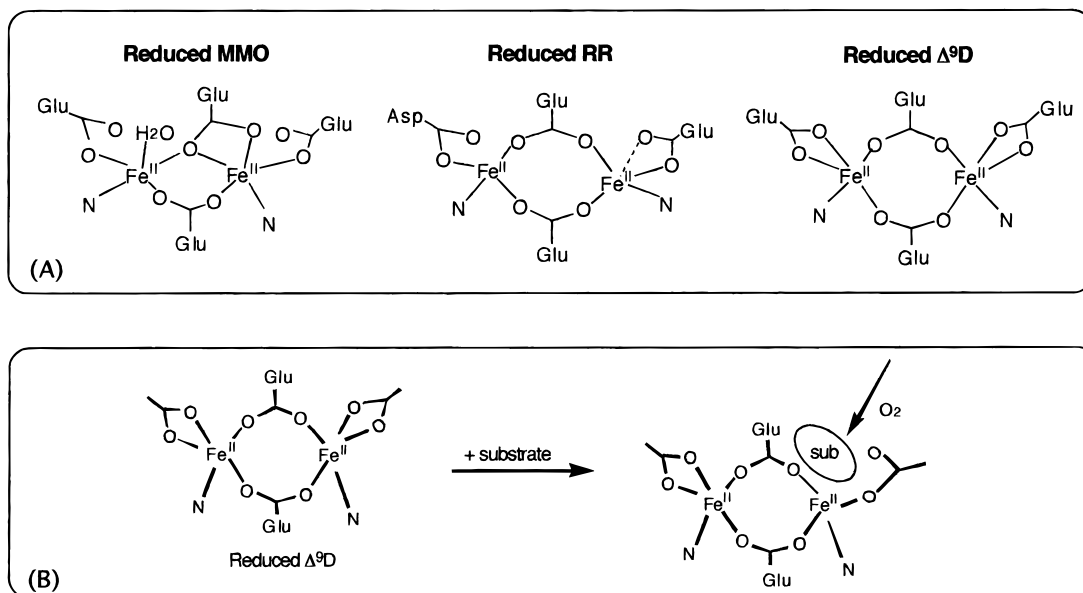


Figure 84. (A) Schematic structural comparison of the reduced sites of the three binuclear non-heme iron dioxygen activating enzymes. (B) Structural changes of the reduced $\Delta^9\text{D}$ active site upon substrate binding.

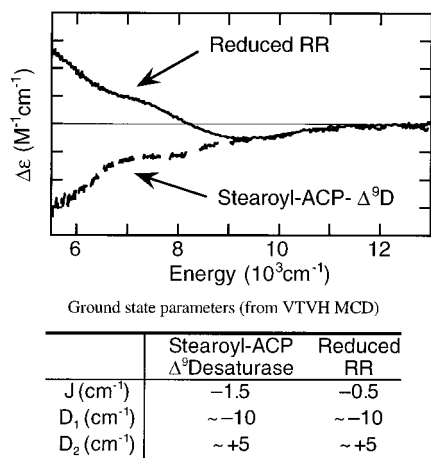


Figure 85. Comparison of the CD spectra of substrate (stearoyl-ACP)-bound reduced $\Delta^9\text{D}$ (---) and reduced R2 (—) recorded at 5 °C. The spin-Hamiltonian parameters of substrate-bound reduced $\Delta^9\text{D}$ and reduced RR are compared in the inset table.

duced sites have different geometric structures: methane monooxygenase has two 5C irons with μ -1,1- and μ -1,3-carboxylate bridges; ribonucleotide reductase has two μ -1,3-carboxylate bridges and two 4C irons from crystallography, while spectroscopy indicates one iron is 5C in solution; Δ^9 desaturase has similar 5C irons with two μ -1,3-carboxylate bridges. However, it is important to emphasize that the only resting reduced active-site structure that rapidly reacts with dioxygen is that of ribonucleotide reductase. In MMO, interaction with the coupling protein, component B, is required for a rapid O_2 reaction and spectroscopy indicates that the resting MMO active-site structure in Figure 84A changes when component B is present. The nature of this structural change must still be elucidated. For Δ^9 desaturase, substrate (i.e., stearoyl-ACP) must be bound for a rapid reaction with dioxygen. From the spectroscopy presented in section III.C.3, the reduced Δ^9 desaturase active-site geometric and electronic structures dramatically change upon substrate binding, Figure 84B. This behavior parallels the general strategy utilized by many of the mononuclear non-heme ferrous enzymes summarized in section II.C.6. Substrate binding results in an additional open coordination position at the active-site iron, allowing the direct reaction with dioxygen. Further, the spectral features of the Δ^9 desaturase-substrate complex indicate that this reactive site is very similar to that of the resting reduced active site of ribonucleotide reductase (Figure 85). The presence of the 4C site results in a new ligand field, thus an orientation of the redox-active orbital that provides better overlap a bridged dioxygen. This defines a similar reactive-site geometric and electronic structure for both dioxygen-activating enzymes and is consistent with the fact that for ribonucleotide reductase the substrate is a Tyr residue already present at the active site. Small-molecule binding studies of reduced ribonucleotide reductase further show that there are open coordination positions at both irons. This allows O_2 to react in a bridged structure and thus undergo two-electron reduction by the two Fe(II) without the need for the additional oxo bridge present in Hr

where O_2 reacts at a single Fe center. The lack of an additional highly covalent oxo bridge in the biferric-peroxy intermediates would destabilize this oxidation state relative to oxyHr toward the further reductive cleavage of the O-O bond to form oxo-bridged high-valent intermediates as considered below.

D. O_2 Intermediates

As presented above, an increasing number of intermediates in the reaction of the reduced diferrous sites with O_2 have recently been identified that could be studied spectroscopically by using stopped-flow and freeze-quench techniques. In this section the geometric and electronic structures of key intermediates in the O_2 activation process are considered and correlated with corresponding data on relevant model complexes. On the basis of these results, possible reaction coordinates for O_2 activation by binuclear non-heme iron enzymes are considered.

1. Peroxo Intermediates

In contrast to deoxyHr (section III.B), the reduced sites of O_2 -activating enzymes react with dioxygen in an irreversible process forming peroxide intermediates that have been trapped and studied spectroscopically for a number of proteins. From Table 17, the peroxide intermediates of the binuclear non-heme iron oxygen-activating enzymes appear to be very similar.⁹⁷¹ Their electronic absorption spectra exhibit an intense broad band centered around 600–750 nm ($\epsilon = 1500\text{--}2500 \text{ M}^{-1} \text{ cm}^{-1}$), assigned to a peroxide-to- Fe^{III} CT transition on the basis of rR data and by reference to a similar feature in the spectra of peroxo- $[\text{Fe}^{\text{III}}]_2$ model complexes (vide infra). Mössbauer data show that both irons are ferric and suggest that peroxide binds to the two Fe^{III} centers in a bridging mode. This was further explored through rR experiments on isotopically labeled peroxo intermediates obtained upon reaction of the reduced sites with $^{16}\text{O}^{18}\text{O}$. An asymmetric end-on μ -1,1 bridging mode will give rise to a set of two features in the region of the O-O stretch, one band for $^{16}\text{O}\text{--}^{18}\text{O}\text{--}[\text{Fe}^{\text{III}}]_2$ and another for $^{18}\text{O}\text{--}^{16}\text{O}\text{--}[\text{Fe}^{\text{III}}]_2$. Alternatively, a symmetric end-on μ -1,2 or side-on μ - η^2 : η^2 binding mode would be characterized by a single rR feature in the corresponding region. Thus far, all but one of the peroxo intermediates prepared with $^{16}\text{O}^{18}\text{O}$ exhibit a single peak in the O-O stretch region, consistent with a symmetric bridging mode of the peroxide moiety. In contrast, the $^{16}\text{O}^{18}\text{O}$ peroxo species of the R2-W48F/D84E double mutant studied by Loehr and Bollinger et al.⁸⁸⁵ shows two bands in that region, initially suggesting that the peroxide is bound in a μ -1,1 bridging mode. In samples prepared with $^{17}\text{O}_2$, the same two features are observed, however, indicating that the peroxide actually also binds in a symmetric bridging mode and that the appearance of two bands in the O-O stretch region is due to Fermi resonance arising from an accidental near-degeneracy of the O-O stretch and an underlying mode not normally resonance enhanced.⁸⁸⁵

Significant effort has been undertaken to prepare synthetic non-heme diiron(II) model complexes that can bind O_2 as peroxide and thus mimic the reactions

Table 17. Spectroscopic and Kinetic Properties of Protein Peroxo Biferric Intermediates and the Crystallographically Characterized Bis- μ -1,3-phenylacetato *cis*- μ -1,2-Peroxo Fe(III)₂ Dimer

	MMO (OB3b)	MMO (Bath)	R2	R2-D84E	R2-D84E/W48F	Δ^9D^a	<i>cis</i> - μ -1,2-peroxo Fe(III) ₂ dimer
optical, refs	<i>b</i>	<i>d</i>	<i>f</i>	<i>i</i>	<i>k</i>	<i>l</i>	<i>n</i>
λ_{\max} (nm)	700	725	700	700	700	700	694
ϵ_{\max} (M ⁻¹ cm ⁻¹)	2500	1800		1500		1200	2650
Mössbauer, refs	<i>c</i>	<i>e</i>	<i>g</i>	<i>i</i>		<i>m</i>	<i>n</i>
δ (mm s ⁻¹)	0.67	0.66	0.66	0.63		0.68/0.64	0.66
ΔE_Q (mm s ⁻¹)	1.51	1.51	1.51	1.58		1.90/1.06	1.40
Raman, refs			<i>g</i>	<i>j</i>	<i>k</i>	<i>l</i>	<i>l</i>
$\nu(\text{Fe-O})$ (cm ⁻¹)					458	442	415
$\nu(\text{O-O})$ (cm ⁻¹)				890	870	898	888
kinetics, refs	<i>b</i>	<i>e</i>	<i>h</i>	<i>i</i>	<i>k</i>	<i>l</i>	<i>n</i>
k_{form} (s ⁻¹)	8	22		5.4–10	2	>1	
k_{decay} (s ⁻¹)	2.4	0.5	>130	0.59–0.93	0.26	0.027 min ⁻¹	

^a Obtained upon reaction of fully (i.e., 4 e⁻) reduced protein with O₂. ^b Reference 775. ^c References 643 and 782. ^d Reference 780. ^e Reference 778. ^f Footnote 8 in ref 884. ^g Footnote 12 in ref 888. ^h Footnote 5 in ref 885. ⁱ Reference 884. ^j Reference 935. ^k Reference 885. ^l Reference 933. ^m Reference 964. ⁿ Reference 972.

of binuclear non-heme iron enzymes with dioxygen. A large number of proposed μ -1,2-peroxide-bridged [Fe^{III}]₂ dimers have been characterized in solution, which all exhibit an intense absorption band peaking at \sim 600–700 nm and a high O–O stretching frequency in the 850–900 cm⁻¹ range,⁶⁴³ similar to the protein intermediates (Table 17). Recently, the crystal structures of three binuclear peroxo [Fe^{III}]₂ complexes have been obtained.^{972–974} In these dimers peroxide binds in a *cis*- μ -1,2 bridging mode, with Fe–O–O–Fe dihedral angles ranging from 0° to 53°. Strikingly, the Fe–O–O bond angles of 120–129° are significantly larger than the metal–O–O angles in related μ -1,2-peroxo [Cu^{II}]₂ and [Co^{III}]₂ dimers (\sim 110°).^{688,975} From Table 17, absorption, rR, and Mössbauer data of the crystallographically defined *cis*- μ -1,2-peroxo [Fe^{III}]₂ complex of Lippard et al.⁹⁷² closely match the protein data, which led to the proposal that in the protein intermediates the peroxide also binds in an end-on μ -1,2 rather than a side-on μ - η^2 : η^2 bridging mode. To validate and refine this model, electronic structure studies were undertaken on the benzoate analogue of the structurally characterized bis- μ -1,3-phenylacetato *cis*- μ -1,2-peroxo [Fe^I]₂ dimer and on the side-on η^2 peroxo Fe^{III}–EDTA monomer (see section II.A.2). Figure 86 compares the absorption and rR excitation profile data for the R2–W48F/D84E peroxo species⁹⁷⁶ (a representative protein peroxo intermediate) and the *cis*- μ -1,2-[Fe^{III}]₂ dimer. While the rR excitation profiles for the protein and the *cis*- μ -1,2-[Fe^{III}]₂ dimer are almost superimposable, they are very distinct from that of the side-on η^2 -Fe^{III} monomer⁶⁰ (see section II.A.2). Significantly, this difference can be directly correlated with the different electronic structures associated with the different binding modes of peroxide in the *cis*- μ -1,2-[Fe^{III}]₂ dimer and the side-on η^2 -Fe^{III} monomer. Thus, the spectroscopic data in Figure 86 provide further support for a μ -1,2 binding mode of the peroxide moiety in the protein intermediates and indicate that the *cis*- μ -1,2-[Fe^{III}]₂ dimer is a reasonable geometric and electronic structural model for these species. Results obtained on the electronic structure of *cis*- μ -1,2-[Fe^{III}]₂ dimers summarized below can therefore have important implications for O₂ activation by non-heme iron enzymes.⁶⁵⁹

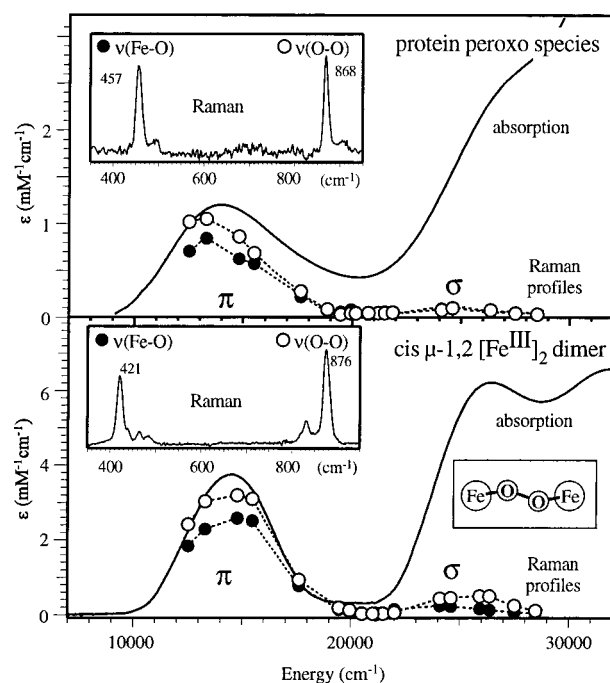


Figure 86. Absorption and rR excitation profile data for the O–O and symmetric Fe–O stretching modes of the R2–W48F/D84E peroxo intermediate (top) and the *cis*- μ -1,2-peroxo [Fe^{III}]₂ dimer (bottom). Note the dominant π versus σ intensity, which is characteristic of end-on peroxide–Fe^{III} bonding. Insets show the rR spectra taken at 676 nm. (Adapted from ref 976.)

Despite the small ground-state exchange-coupling constant for the *cis*- μ -1,2-[Fe^{III}]₂ dimer, $J = -33$ cm⁻¹, the temperature dependence of the absorption bands is weak. This precludes large antiferromagnetic energy splittings in the excited states, which is distinct from the large observed ESAF splittings in oxo-bridged analogues⁶³⁹ and consistent with the VBCI model introduced in section III.A.1.b.2. These differences can be ascribed to the lower covalency of the Fe–O (peroxide) bond as well as intraperoxide bonding that opposes reorientation of the oxygen p-orbitals for better overlap with the Fe d-orbitals. From a combined analysis of absorption, MCD, and rR excitation profile data, all peroxide-to-iron CT transitions could be resolved that contribute to the absorption spectrum of the *cis*- μ -1,2-[Fe^{III}]₂ dimer in

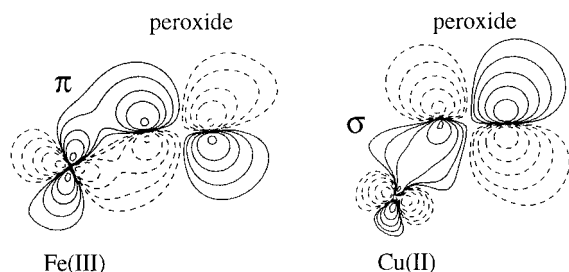


Figure 87. Contour plots for end-on peroxide–Fe^{III} bonding (left) and peroxide–Cu^{II} bonding (right), showing the dominant π - and σ -donor interactions, respectively, of peroxide. (Plot for peroxide–Cu^{II} bonding is adapted from ref 608.)

the $<30\,000\text{ cm}^{-1}$ region. Identifying the donor and acceptor orbitals involved in each transition permitted separation of the π and σ contributions to the total peroxide \rightarrow Fe charge donation. Significantly, the high π versus σ peroxide-to-Fe^{III} CT absorption intensity and the strong rR enhancement of the Fe–O stretch in the visible region (Figure 86) indicate that the π -donor interaction of peroxide in this dimer is dominant, which is very distinct from the situation found in related μ -1,2-[Cu^{II}]₂⁶⁰⁸ and -[Co^{III}]₂⁹⁷⁷ dimers where the σ -donor interaction makes the dominant contribution (Figure 87). This unique peroxide–metal bonding interaction in the *cis*- μ -1,2-[Fe^{III}]₂ dimer has important implications. It allows for a larger metal–O–O bond angle (120 – 130° ^{972–974} versus $\sim 110^\circ$ in Cu and Co peroxide complexes),^{688,975} which was found from a NCA to result in significant mechanical coupling between the Fe–O and O–O stretch motions. It is this coupling rather than a strong O–O bond that leads to the high O–O stretching frequency, $\nu(\text{O–O}) \approx 850$ – 900 cm^{-1} , generally observed for μ -1,2-peroxo [Fe^{III}]₂ complexes.⁶⁴³ In fact, the O–O force constants for the *cis*- μ -1,2-[Fe^{III}]₂ dimer, $\nu(\text{O–O}) = 876\text{ cm}^{-1}$, and a well-studied *trans*- μ -1,2-[Cu^{II}]₂ dimer,⁹⁷⁸ $\nu(\text{O–O}) = 832\text{ cm}^{-1}$, are practically identical, although $\nu(\text{O–O})$ differs by 44 cm^{-1} . This is consistent with the comparable donor strengths of the peroxide in these dimers as charge is primarily removed from the peroxide π^* orbitals that are antibonding with respect to the O–O bond. Given the relatively basic character of the bridging peroxide in the [Cu^{II}]₂ dimer,⁹⁷⁹ these results suggest that the peroxide in the μ -1,2-[Fe^{III}]₂ dimer and, by analogy, in the protein intermediates (Table 17) is *activated for nucleophilic attack*.⁶⁵⁹

2. High-Valent Intermediates

In comparison with the peroxide species (Table 17), little is known about the geometric and electronic structures of high-valent [Fe^{IV}]₂ and Fe^{III}Fe^{IV} intermediates that have thus far been identified in MMO (intermediate **Q**) and R2 (intermediate **X**), respectively (Table 18).⁶⁴³ This is primarily due to the fact that there are only a few Fe^{III}Fe^{IV} and no [Fe^{IV}]₂ model complexes known to date because the Fe^{IV} oxidation state is rather difficult to stabilize using biologically relevant ligands.

The major experimental insight presently available into the geometric and electronic structures of inter-

Table 18. Spectroscopic and Kinetic Properties of the High-Valent [Fe^{IV}]₂ and Fe^{III}Fe^{IV} Intermediates of MMO (Intermediate **Q) and R2 (Intermediate **X**), Respectively**

	MMO Q (OB3b)	MMO Q (Bath)	R2 X ^a
optical, refs	<i>c</i>	<i>d</i>	<i>e</i>
λ_{max} (nm)	330, 430	350, 420	365
Mössbauer, refs	<i>f</i>	<i>g</i>	<i>h</i>
δ (mm s ⁻¹), Fe1	0.17	0.21 (0.14) ^b	0.26
ΔE_{Q} (mm s ⁻¹), Fe1	0.53	0.68 (–0.6) ^b	–0.6
δ (mm s ⁻¹), Fe2	0.17	0.14 (0.48) ^b	0.56
ΔE_{Q} (mm s ⁻¹), Fe2	0.53	0.55 (–0.9) ^b	–0.9
$-J$ (cm ⁻¹)	>60		
EXAFS, refs	<i>i</i>		<i>j</i>
Fe \cdots O (Å)	1.77		1.8
Fe \cdots Fe (Å)	2.46		2.5
kinetics, refs	<i>k</i>	<i>l</i>	<i>m</i>
k_{form} (s ⁻¹)	2.4	0.5	8
k_{decay} (s ⁻¹)	0.04	0.07	1

^a EPR and ENDOR parameters for **X** are given in section III.C.2. ^b Obtained upon γ -irradiation of **Q** (ref 980). ^c References 772 and 781. ^d Reference 778. ^e References 877, 878, and 981. ^f References 772 and 781. ^g Reference 778. ^h Reference 927. ⁱ Reference 782. ^j Reference 932. ^k Reference 775. ^l Reference 778. ^m References 877, 878, and 981.

mediate **Q** derives from EXAFS and Mössbauer data.^{643,772,779,781} These show that intermediate **Q** is best described as a strongly exchange-coupled Fe^{IV} dimer with an Fe–Fe distance of 2.46 Å and both short and long Fe–O bonds of 1.77 and 2.0 Å.^{772,781} This would be consistent with the (μ -O)₂[Fe^{IV}]₂ core, referred to as a diamond core, which has been structurally defined in a (μ -O)₂Fe^{IV}Fe^{III} model complex (vide infra). Since EXAFS data only reflect the presence of at least two single-atom oxygen bridges, structures that utilize monodentate carboxylates as bridges (as proposed for **X**, below) are also possible. Representative core structures for **Q** that are consistent with currently available experimental data are shown in Figure 88 (top). Using LT radiolytic reduction,⁹⁸⁰ a fraction of **Q** could be converted into a paramagnetic Fe^{III}Fe^{IV} species. The Mössbauer parameters obtained for that species are very similar to those of R2 intermediate **X**. This, combined with the similar EXAFS results for **X** and **Q**, support the proposal that the diiron centers in MMO and R2 share a similar mechanism for O₂ activation.^{982–984} Intermediate **X** has a paramagnetic $S = 1/2$ ground state, permitting spectroscopic studies employing EPR and ENDOR methods (section III.C.2), which allow the fate of O₂ during the formation of this high-valent species in the reaction of a diferrous center with dioxygen to be determined.^{877,878,981} These studies show that **X** contains a single oxo bridge from O₂ (the second atom from dioxygen is coordinated terminally as H₂O to the Fe^{III}) and one or two additional mono-oxo bridges provided by carboxylate oxygens (structure d in Figure 88).⁹²⁸ The bis- μ -oxo diamond core structure was strongly disfavored.⁹³¹

From a theoretical perspective, structures considered for intermediates **X** and **Q** are given in the bottom of Figure 88. Generally, the bis- μ -oxo [Fe^{IV}]₂ core (f) is favored for **Q** and its one-electron-reduced form with one oxo bridge protonated for charge neutrality (g) has been considered for **X**.^{824–828,836} It

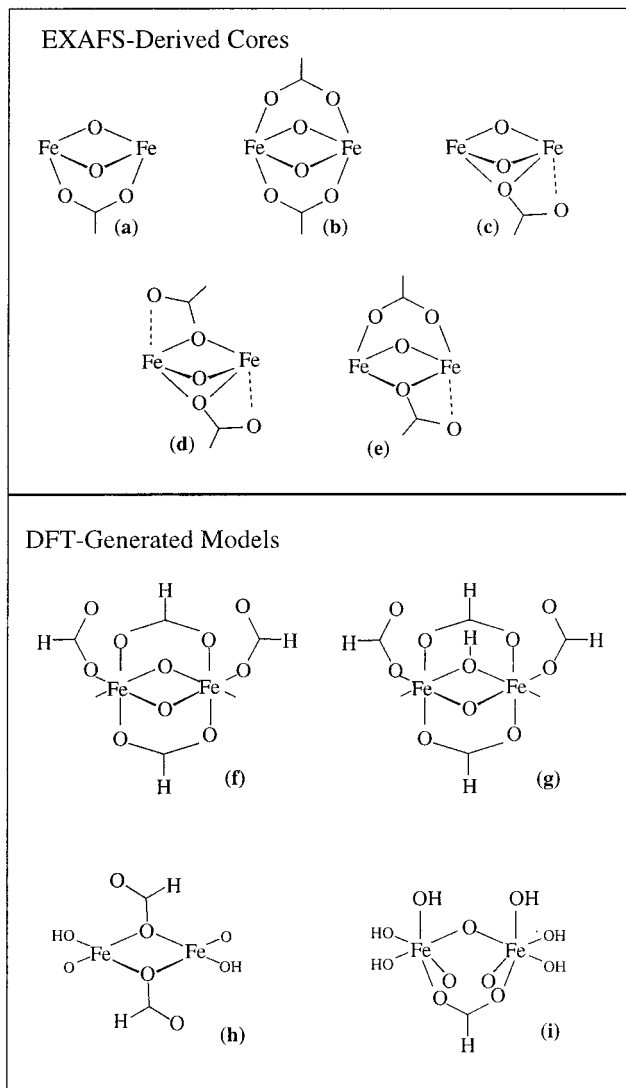


Figure 88. EXAFS-derived (top) and DFT-generated (bottom) active-site models for intermediates **Q** ($[\text{Fe}^{\text{IV}}]_2$) and **X** ($\text{Fe}^{\text{III}}\text{Fe}^{\text{IV}}$). ENDOR data⁹³¹ suggest that d is the best model at present for **X**.

should be noted that the presence of a proton on the bridge is not consistent with ENDOR data. The Fe–Fe bond length for structure f can successfully reproduce the EXAFS data on **Q**; it is found to be dependent on the number of bridging carboxylates and the ground spin state employed (the optimized antiferromagnetic structure has a 0.2 Å shorter bond length than the ferromagnetic structure).⁸²⁶ Note that the preedge XAS data support an iron coordination number of five or less. An interesting finding in Siegbahn's study is that geometry optimization of a structure with a single oxo and two monodentate carboxylate bridges (d), as is proposed for **X** on the basis of EXAFS and ENDOR data, does not afford a short Fe···Fe distance; rather, the bridging oxygen becomes terminal and the Fe···Fe distance increases to a final value of 3.12 Å (h), which is inconsistent with the EXAFS data.^{826,827}

Definitive descriptions of the transient intermediates **Q** and **X** will be greatly aided by comparison to the spectroscopic signatures of relevant model complexes. Both Que et al. and Caradonna et al. have

synthesized oxo-bridged high-valent iron dimers which are able to partially replicate the oxidation reactions of mono-oxygenases, fatty acid desaturases, and ribonucleotide reductases.^{817,985–988} The Que et al. complexes possess $\text{Fe}^{\text{III}}\text{Fe}^{\text{IV}}$ bis- μ -oxo cores with a tetradentate exogenous ligand, TPA (tris(2-pyridylmethyl)amine), which coordinates via one tertiary amine and three pyridine nitrogens. The substitution of methyl or ethyl groups onto each of the pyridine rings at the 5- or 6-positions greatly affects the magnetic properties of the core. The unsubstituted complex, $[\text{Fe}_2\text{O}_2(\text{TPA})_2]^{3+}$, the 5-methyl derivative, $[\text{Fe}_2\text{O}_2(5\text{-Me}_3\text{TPA})_2]^{3+}$, and the 5-ethyl species, $[\text{Fe}_2\text{O}_2(5\text{-Et}_3\text{TPA})_2]^{3+}$, all have a valence-delocalized $S = 3/2$ ground state which is generated by a strong interaction between the t_{2g} set of d-orbitals in two low-spin irons with nine valence electrons. The crystal structure of the 5-ethyl derivative identifies an Fe–Fe distance of 2.683 Å and Fe–O length of 1.805 Å.⁸¹⁷ This would be consistent with EXAFS data on intermediate **X** of R2 (short Fe···Fe separation of 2.5 Å and Fe–O distance of 1.8 Å) and intermediate **Q** of MMO (2.46 and 1.77 Å for Fe···Fe and Fe–O, respectively). The delocalized $S = 3/2$ ground spin state is not consistent with the $S = 1/2$ nature of **X**. However, the 6-methylated derivative $[\text{Fe}_2\text{O}_2(6\text{-Me}_3\text{TPA})_2]^{3+}$, whose structure has not yet been determined, has a valence-localized $S = 1/2$ ground state due to antiferromagnetic coupling of high-spin Fe^{III} and Fe^{IV} ions. The spectral features of this $S = 1/2$ complex compares favorably with intermediate **X**; it exhibits an isotropic $g = 2$ EPR spectrum and the ENDOR signal of Fe^{IV} in an anisotropic environment. This model is believed to have a ~ 0.40 Å longer Fe–Fe separation than **X** (inferred from EXAFS data for the $[\text{Fe}^{\text{III}}\text{Fe}^{\text{IV}}(\text{O})_2(5\text{-Me}_3\text{TPA})_2]^{3+}$ ⁶⁴⁶ and $[\text{Fe}^{\text{III}}\text{Fe}^{\text{III}}(\text{O})_2(6\text{-Me}_3\text{TPA})_2]^{2+}$ complexes⁹⁸⁶) and also a larger Mössbauer isomer shift (0.26 in the protein versus 0.08 mm s^{-1}). These differences may be attributed to the different exogenous ligands (pyridine and amine nitrogens in the model versus carboxylate and imidazole coordination in the protein) or the presence of a different core structure.

The Caradonna et al. complex has a quite different coordination environment, with the tridentate $\text{H}_2\text{-bamb}$ (2,3-bis(2-hydroxylbenzamido)-2,3-dimethylbutane) and imidazole ligands forming a doubly bridged dimer in the structurally characterized biferrous form.⁹⁸⁵ The irons have square-pyramidal coordination with imidazole normal to the plane of the diferrous Fe_2O_2 core and phenoxyl oxygens forming the bridges. This complex is capable of catalyzing the oxidation of a wide range of organic substrates including alkanes, alkenes, and sulfides using an oxygen-atom donor such as OIPh. The high-valent intermediate thought to be involved in catalysis has not been definitively characterized but is believed to be a ferryl $[\text{Fe}^{4+}=\text{O}]$ species based upon parallels between product distributions of the complex and those of iron porphyrin catalysts.

Detailed spectroscopic studies on these model systems parallel to those described above on peroxo-bridged biferric complexes are now required to define the electronic structure of the high-valent Fe–oxo

bond and its contribution to the reactivity of the binuclear non-heme iron active site.

3. Conversion of Peroxo Intermediates into High-Valent Fe–Oxo–Fe Species

In recent years, significant research effort in bioinorganic chemistry has focused on the molecular mechanism of O₂ activation by binuclear non-heme iron sites. Though the spectroscopic characterization of the metastable key intermediates, i.e., the peroxo species, **Q**, and **X**, has afforded extremely valuable information for evaluating possible reaction coordinates, the mechanism by which the O–O is cleaved remains a topic of current debate. While the formation of the high-valent oxo species **Q** and **X** has generally been interpreted as indicating reductive O–O bond cleavage, it has not yet been established whether this bond is homolytically or heterolytically cleaved. Also, it is puzzling that available experimental data on MMO and R2 (WT protein and mutants) strongly suggest that the peroxo intermediates may be similar (Table 17) yet the binuclear iron clusters of intermediates **Q** (MMO) and **X** (R2) have different oxidation states. This difference raises two important questions: (i) where is the “extra” electron coming from in R2 and (ii) at what stage is it transferred to the binuclear iron site. From stopped-flow experiments on the WT R2 protein under conditions of limiting Fe^{II}, a transient absorption develops at 560 nm that decays concomitant with the formation of **X**. On the basis of a similar absorption band in the electronic spectrum of Trp radicals, Bollinger et al.⁸⁸³ were able to assign this feature to a W48[•] radical species, which strongly implies that the “extra” electron in R2 is provided by W48. Support for this model is provided by recent studies on the phenylalanine, which is more difficult to oxidize) which does not develop the 560 nm feature during O₂ activation.⁹⁸⁹ In an effort to elucidate when the “extra” electron is transferred to the diiron cluster in the oxygen activation process, a number of R2 mutants have been studied. Of particular significance are the results obtained on the D84E single mutant,⁸⁸⁴ in which one of the aspartate ligands on Fe is replaced by a glutamate (which formally converts the R2 site into the MMO site) and the D84E/W48F double mutant.⁸⁸⁵ Upon reaction of the reduced sites with dioxygen, peroxo intermediates are observed for both the single and double mutants that appear to be very similar based on spectroscopic studies. Significantly, the rate constant for the decay of the R2–D84E peroxo species is 4 times greater than that of the R2–D84E/W48F analogue,⁸⁸⁵ which might suggest that transfer of the “extra” electron to the [Fe^{III}]₂ cluster is the rate-determining step in the formation of **X**. Thus, conversion of the peroxo species into **X** could occur without prior formation of an [Fe^{IV}]₂ spe-

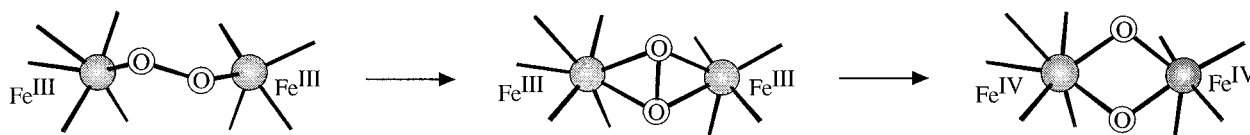
cies, consistent with the fact that (i) the peroxo intermediate of WT R2 decays at least an order of magnitude faster than the peroxo species of MMO⁸⁸⁸ and (ii) an [Fe^{IV}]₂ intermediate has not yet been observed for R2. Further studies on both WT protein and mutants of R2 should elucidate the sequence in which the O–O bond cleavage and the ET events occur.

In the case of MMO, two fundamentally different mechanisms are currently considered as the most likely pathways for the conversion of the peroxo species (designated **P**) into **Q**: (i) formation of a side-on biferric species followed by homolytic O–O bond cleavage, yielding a bis- μ -oxo [Fe^{IV}]₂ “diamond” core and (ii) 2-fold protonation of the same oxygen atom of the peroxide species followed by heterolytic O–O bond cleavage and formation of a mono-oxo-bridged [Fe^{IV}]₂ species in concert with release of a water molecule. These two mechanisms are considered below. Note that these are limiting descriptions with a number of possible intermediate structures within each class.

a. The Side-On \rightarrow Bis- μ -Oxo Pathway: Homolytic O–O Bond Cleavage. The side-on [Fe^{III}]₂ \rightarrow bis- μ -oxo [Fe^{IV}]₂ pathway (Scheme 28) is analogous to the mechanism of O₂ activation for binuclear copper enzymes where the facile interconversion between side-on peroxo [Cu^{II}]₂ and bis- μ -oxo [Cu^{III}]₂ species has been experimentally observed.⁹⁹⁰ The key question thus becomes whether it is justified to use a model derived for copper complexes as the basis to support a similar O–O bond cleavage mechanism for iron dimers. A striking spectral feature of side-on peroxo [Cu^{II}]₂ species is their inherently low O–O stretching frequency, typically in the 740–760 cm⁻¹ range. From a NCA, this low value reflects an unusually weak O–O bond; i.e., the corresponding force constant is only $k(\text{O–O}) = 2.4 \text{ mdyn } \text{\AA}^{-1}$.⁶² Insight into the origin of the weak O–O bond was obtained from X α DFT calculations that showed significant π -back-bonding from Cu^{II} into the peroxide σ^* orbital.⁶⁰⁸ This bonding interaction is unique to side-on peroxo [Cu^{II}]₂ complexes; it is neither observed experimentally nor computationally for end-on μ -1,2-peroxo [Cu^{II}]₂ complexes.^{608,978} It is this back-bonding into σ^* that permits facile conversion of the side-on peroxo [Cu^{II}]₂ dimers into bis- μ -oxo [Cu^{III}]₂ species.⁹⁹¹

A direct comparison between binuclear copper and iron complexes is complicated by the fact that a side-on peroxo [Fe^{III}]₂ dimer has not yet been reported. However, a reasonable model for this structure is provided by the side-on η^2 -Fe^{III}–EDTA monomer (see section II.A.2).⁶⁰ Significantly, the O–O stretch of this species peaks at 816 cm⁻¹, which has been shown by a NCA to reflect a high O–O force constant of $k(\text{O–O}) = 3.1 \text{ mdyn } \text{\AA}^{-1}$. Consistent with a relatively strong O–O bond, studies on the electronic structure

Scheme 28. Side-On \rightarrow Bis- μ -oxo Pathway (Adapted from ref 976.)



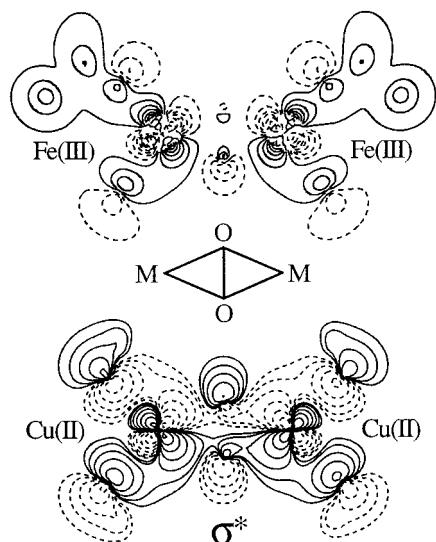


Figure 89. Contour plots for $\mu\text{-}\eta^2\text{:}\eta^2$ side-on peroxide– $[\text{Fe}^{\text{III}}]_2$ bonding (top) and peroxide– $[\text{Cu}^{\text{II}}]_2$ bonding (bottom), illustrating the large differences in metal d \rightarrow peroxide σ^* back-bonding in biferric and bicupric complexes. (Adapted from refs 976 and 608.)

of the side-on Fe^{III} monomer indicate that there is virtually no back-bonding from the occupied Fe^{III} d-orbitals into the peroxide σ^* orbital.⁶⁰ Starting from this experimentally defined reference electronic structure, the effects of dimerization upon the electronic structure of the side-on peroxide– Fe^{III} bond were explored. In contrast to copper complexes where dimerization significantly affects the nature of the side-on peroxo– Cu^{II} bond,⁶⁰⁸ our calculations suggest that these effects are minor in Fe^{III} complexes; rather, the two ferric centers are fairly uncoupled from one another and the Fe^{III} –peroxide bonding interactions are virtually unchanged by binding the second iron.⁹⁷⁶ A key result from these studies is that the side-on peroxo– Fe^{III} bond is almost purely σ in character, which is grossly different from the dominant π -donor interaction of the peroxide with Fe^{III} in the *cis*- μ -1,2- $[\text{Fe}^{\text{III}}]_2$ dimer.⁶⁵⁹ Thus, while most attention in evaluating the side-on \rightarrow bis- μ -oxo pathway for iron dimers has been given to the actual O–O bond-cleavage step analyzed below, it should be recognized that the preceding step, corresponding to the rearrangement from an end-on μ -1,2 to a side-on peroxo $[\text{Fe}^{\text{III}}]_2$ dimer, presuming that intermediate **P** in MMO has an end-on structure from its limited spectral characterization, involves complex electronic structure changes. Unlike $[\text{Cu}^{\text{II}}]_2$ dimers where σ -bonding is dominant in either case,⁶⁰⁸ interconversion between the two binding modes of peroxide in $[\text{Fe}^{\text{III}}]_2$ dimers would involve a π to σ bond change and thus be expected to be associated with a large barrier.⁹⁷⁶

From Figure 89, the extent of back-bonding into the unoccupied peroxide σ^* orbital in the side-on $\mu\text{-}\eta^2\text{:}\eta^2$ - $[\text{Fe}^{\text{III}}]_2$ dimer is considerably lower than that in a similar $[\text{Cu}^{\text{II}}]_2$ complex. Two dominant factors have been identified as being responsible for the differences in side-on peroxide– Cu^{II} versus side-on peroxide– Fe^{III} bonding: (i) the effective nuclear charge of Fe^{III} is greater than that of Cu^{II} , giving rise to a relative stabilization of the metal d-orbitals in the former case; and (ii) in high-spin d^5 Fe^{III} complexes

the occupied majority spin d-orbitals are significantly stabilized in energy by single-site exchange relative to their unoccupied minority spin counterparts, which is referred to as spin polarization.^{60,976} Both factors contribute to a larger energy separation from the peroxide σ^* orbital of the Fe^{III} d-orbitals than the Cu^{II} d-orbitals, which virtually eliminates $\text{Fe}^{\text{III}} \rightarrow$ peroxide σ^* -back-bonding (Figure 89). These results strongly suggest that conclusions reached from studies on copper complexes are not necessarily transferable to structurally related iron complexes. Indeed, DFT calculations for the conversion of side-on peroxo $[\text{Cu}^{\text{II}}]_2$ into bis- μ -oxo $[\text{Cu}^{\text{III}}]_2$ species yield a substantial enthalpic driving force,^{992–994} whereas analogous calculations on diiron sites suggest that $\mu\text{-}\eta^2\text{:}\eta^2$ -peroxo $[\text{Fe}^{\text{III}}]_2$ species are more stable than their bis- μ -oxo $[\text{Fe}^{\text{IV}}]_2$ analogues.^{826,827,976} Presumably by introducing certain geometric constraints upon the active-site model employed, the peroxo species can be sufficiently destabilized in energy that the formation of a bis- μ -oxo diiron^{IV} diamond core becomes energetically favorable. Under these conditions, the peroxo structures obtained may exhibit significant side-on character, however, which would not appear to be compatible with the present experimental data on the protein intermediates (see section III.B).¹⁰¹¹

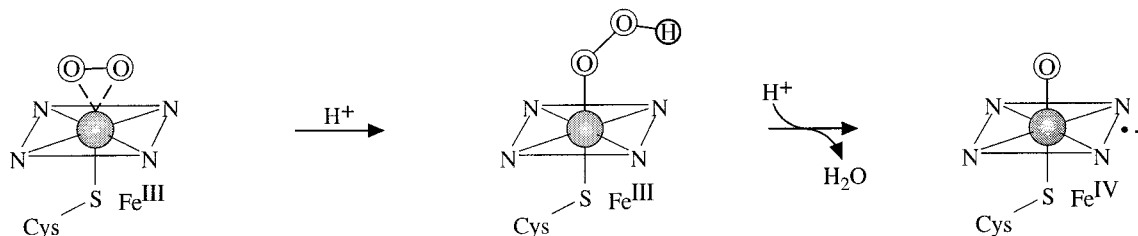
In summary, both experimental and computational studies on copper and iron complexes indicate that the two metals develop distinct bonding interactions with peroxide. In copper dimers, conversion of a side-on peroxo $[\text{Cu}^{\text{II}}]_2$ into a bis- μ -oxo $[\text{Cu}^{\text{III}}]_2$ species is energetically accessible because Cu^{II} d \rightarrow peroxide σ^* -back-bonding is substantial. Alternatively, in ferric dimers Fe^{III} d \rightarrow peroxide σ^* -back-bonding is insignificant and the conversion of a side-on peroxo $[\text{Fe}^{\text{III}}]_2$ into a bis- μ -oxo $[\text{Fe}^{\text{IV}}]_2$ species becomes energetically less favorable. Though available experimental results are insufficient to rule out this mechanism, alternate pathways also need to be considered for the transformation of **P** into **Q**.

b. The Proton-Triggered Pathway: Heterolytic O–O Bond Cleavage. A key result from studies on the end-on μ -1,2- $[\text{Fe}^{\text{III}}]_2$ model complex is that the peroxo species is activated for nucleophilic attack (vide supra).⁶⁵⁹ Given that the peroxide moiety in the protein intermediates appears to bind in a similar μ -1,2 bridging mode,⁹⁹⁵ a mechanism can be devised for the conversion of **P** into **Q** that parallels that proposed for cytochrome P450, in which protonation of the peroxide species leads to heterolytic O–O bond cleavage concomitant with release of a water molecule (Scheme 29).^{622,996} Starting from the experimentally calibrated bonding description for the *cis*- μ -1,2-peroxo $[\text{Fe}^{\text{III}}]_2$ model complex, this pathway has been evaluated through DFT calculations.⁹⁷⁶ Substitution of the nitrogen ligation in the synthetic complex by oxygen ligands to properly model the protein active site⁶⁴³ leads to only minor changes in electronic structure, consistent with the similar spectroscopy of the *cis*- μ -1,2-peroxo $[\text{Fe}^{\text{III}}]_2$ model and the protein intermediates (Table 17).

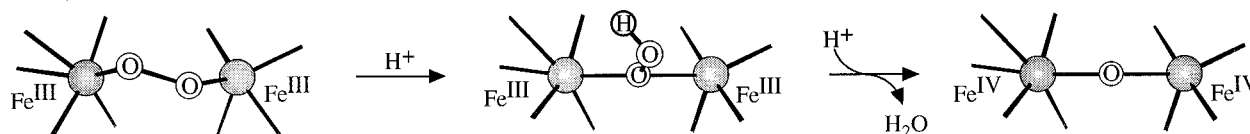
In the first step of this possible pathway, protonation and reorientation of the peroxide results in the formation of a μ -1,1-hydroperoxo $[\text{Fe}^{\text{III}}]_2$ species,

Scheme 29. Proton-Trigged Pathway Proposed for Cytochrome P450 (top) and MMO (bottom) (Adapted from ref 976.)

P450



MMO



paralleling the mechanism of peroxide activation observed for peroxo $[\text{Co}^{\text{III}}]_2$ complexes.^{997–1000} Consistent with our results obtained from an experimental study of a μ -1,1-hydroperoxo $[\text{Cu}^{\text{II}}]_2$ species,¹⁰⁰¹ protonation of the O_2 species in the $[\text{Fe}^{\text{III}}]_2$ dimer gives rise to a large stabilization of the peroxide orbitals including the unoccupied σ^* orbital, indicating that the hydroperoxide is activated for further reduction. There are interesting differences in hydroperoxide– Fe^{III} bonding between the μ -1,1-hydroperoxo species (Scheme 29) and oxyHr, possessing a terminal hydroperoxide (see section III.B). Both vibrational and computational data indicate that the O–O bond in oxyHr is strong, which can be ascribed to a partial disruption of the intraperoxide π -bonding and π -antibonding interactions that results from protonation of one oxygen. Alternatively, in the geometry-optimized μ -1,1-hydroperoxo species (Scheme 29), the O–O bond appears to be weak given the long O–O distance of 1.59 Å, compared to 1.41 Å in oxyHr. Factors are being evaluated that might contribute to this difference in O–O bond strength, including the presence of an oxo bridge at the oxyHr site that greatly stabilizes the two Fe^{III} ions toward further oxidation.^{639,660} In the μ -1,1-hydroperoxo species, further oxidation of the ferric centers upon reductive O–O bond cleavage would allow the formation of a stable $\text{Fe}^{\text{IV}}\text{--O--Fe}^{\text{IV}}$ unit in a high-valent species (vide infra). It is interesting to note that a small but significant shift of charge density from the occupied Fe^{III} d-orbitals into the hydroperoxide σ^* orbital is observed in the μ -1,1-hydroperoxo dimer but not in oxyHr.⁹⁷⁶

In the next step, transfer of a second proton yields a transient μ -1,1-dihydroperoxo $[\text{Fe}^{\text{III}}]_2$ species that spontaneously converts into a mono-oxo-bridged $[\text{Fe}^{\text{IV}}]_2$ species by heterolytic O–O bond cleavage and release of a water molecule. In this reaction scheme, the second iron center of the binuclear active site fulfills the role of the porphyrin in cytochrome P450 by supplying the second electron. It serves the further role of providing a second coordination site for the O_2 species and thus permits formation of a μ -oxo bridge at the active site of the high-valent intermediate. Formation of this stable $\text{Fe}^{\text{IV}}\text{--O--Fe}^{\text{IV}}$ unit, along with the formation of a water molecule, would

produce a substantial thermodynamic driving force for the two-electron reduction of the peroxo species that is required to overcome the large Franck–Condon barrier associated with reductive cleavage of the O–O bond¹⁰⁰² (section II.D). Calculation of the energy profile for this proton-triggered reaction pathway (Scheme 29) is complicated by the fact that the relative energies of the singly and doubly protonated intermediates strongly depend on the proton source used. Given the requirement of two protons in this mechanism, amino acid residues in the second coordination sphere, defining the active-site cavity, might also play an important role in the process of O_2 activation.^{775,780} Thr213, in particular, has been implicated as a critical amino acid residue because it is highly conserved among the O_2 -activating enzymes in both the heme P450 and the binuclear non-heme iron MMOs.⁷⁷⁵

An important feature of the model presented in Scheme 29 relates to the fact that one O atom of dioxygen forms the single oxo bridge in the high-valent intermediate and the second oxygen is incorporated into water, which would be consistent with Stubbe and Hoffman et al. ENDOR results on **X** (vide supra).⁹³¹ Thus, if **Q** and **X** have similar core structures as suggested by Mössbauer data on γ -irradiated **Q**,⁹⁸⁰ the proton-triggered heterolytic cleavage pathway (Scheme 29) would be favored over the side-on \rightarrow bis- μ -oxo pathway (Scheme 28). Further support for the former mechanistic scheme is provided by studies of the solvent pH and deuteration effects on the rates of formation and decay of intermediates **P** and **Q** performed by Lee and Lipscomb.⁷⁷⁵ From their studies it is rather unlikely that the O–O bond is cleaved without prior protonation of the O_2 species.

In summary, the proton-triggered pathway, which is based upon the observation that the peroxide in the *cis*- μ -1,2-peroxo $[\text{Fe}^{\text{III}}]_2$ dimer and presumably in the protein intermediates is activated for nucleophilic attack, bears striking similarities to the mechanism of O_2 activation implicated for cytochrome P450 (see Scheme 29, top and bottom). In this scenario the second iron would serve the role of the porphyrin in providing the second electron for reductive O–O bond cleavage. In addition to serving as an electron donor, however, this iron would also permit formation of a

stable $\text{Fe}^{\text{IV}}\text{--O--Fe}^{\text{IV}}$ unit in a high-valent species, which will produce a substantial thermodynamic driving force for the two-electron reduction of the peroxo species that is required to overcome the large Franck–Condon barrier associated with reductive O–O bond cleavage. Ongoing investigations in a number of laboratories seek to distinguish between possible mechanisms, including those in Schemes 28 and 29, for the conversion of **P** into **Q**.

IV. Concluding Comments

In the past few years there have been huge advances in the field of non-heme iron enzymes. Crystal structures are now available for most members of this class, spectroscopic methodologies have been developed which allow these to be studied in detail with maximum electronic structure insight, hybrid DFT programs are available for complementary insight, a range of intermediates has been trapped for the key steps in a number of the catalytic reactions, and highly relevant model systems have been developed by several groups that are now becoming structurally defined. In the mononuclear enzymes, it is becoming clear that a major difference relative to the heme enzymes is that the non-heme ligand environment is much more difficult to oxidize, making compound I equivalents less likely in a non-heme environment. This insight has come from spectroscopy on the hydroperoxy-intermediate, activated bleomycin; it is now important to have similar insight into the molecular mechanisms of the non-heme iron enzymes through the generation and study of their oxygen intermediates and analogues. VTVH MCD spectroscopy has elucidated the general mechanistic strategy for the coupled hydroxylation of substrate(s) where substrate binding results in an open coordination position for the dioxygen reaction. It is now important to develop insight into the molecular mechanisms of uncoupled reactions and of functional differences (oxygenation, oxidation, and desaturation) for apparently similar active sites. The electronic mechanisms of substrate and site activation and of selectivity in the intra- and extradiol dioxygenases still need to be understood as well. The electronic structure of oxy- and deoxy-hemerythrin are understood and have defined the mechanism and ET pathway for the coupled proton plus two-electron transfer to dioxygen binding at one Fe of an oxo-bridged binuclear center. For the binuclear non-heme iron enzymes, the second iron serves the role of the porphyrin and makes the two-electron reductive cleavage of the peroxide O–O bond favorable. Whether this involves homolytic or proton-triggered heterolytic cleavage still needs to be determined experimentally, and it is now important to define the electronic structures of the resultant high-valent oxo-bridged intermediates to understand their reactivity with substrates. Electronic structure changes associated with substrate activation of the biferrrous site in Δ^9 desaturase and component B activation in methane monooxygenase must still be determined, and molecular-level insight is required for understanding the differences in reactivity of apparently similar oxygen intermediates in the binuclear enzymes. Major ad-

vances have been made, but much still needs to be achieved at the beginning of the new millennium.

V. Abbreviations

[2Fe–2S]	two iron–two sulfur cluster
1,2-CCD	chlorocatechol 1,2-dioxygenase, EC 1.13.11.1
1,2-CTD	catechol 1,2-dioxygenase, EC 1.13.11.1
1,2-DHBD	2,3-dihydroxybiphenyl 1,2-dioxygenase, EC 1.13.11.39
1,2-DHPPD	2,3-dihydroxyphenylpropionate 1,2-dioxygenase
1,2-GTD	gentisate 1,2-dioxygenase, EC 1.13.11.4
1,2-HGTD	homogentisate 1,2-dioxygenase, EC 1.13.11.5
1,2-HQD	hydroquinol 1,2-dioxygenase, EC 1.13.11.37
2,3-CTD	catechol 2,3-dioxygenase, EC 1.13.11.2
2,4-D	2,4-dichlorophenoxyacetic acid
3,4-PCD	protocatechuate 3,4-dioxygenase, EC 1.13.11.3
3-HAO	3-hydroxyanthranilate 3,4-dioxygenase, EC 1.13.11.6
4C	four-coordinate
4,5-PCD	protocatechuate 4,5-dioxygenase, EC 1.13.11.8
5C	five-coordinate
6MPH ₄	6-methyltetrahydropterin
6C	six-coordinate
7,8-BH ₂	7,8-dihydrobiopterin
α -KG	α -ketoglutarate or 2-oxoglutarate
ABLM	activated bleomycin
ACC	1-amino-1-cyclopropane carboxylic acid
ACCO	1-amino-1-cyclopropane carboxylic acid oxidase
ACP	acyl carrier protein
ACV	δ -(L- α -aminoadipoyl)-L-cysteinyl-D-valine
apo (protein)	protein with metal removed
BDO	benzene dioxygenase, EC 1.14.12.3
BH ₄	tetrahydrobiopterin
BLM	bleomycin
CAT	catechol
CC	coupled cluster
CI	configuration interaction
CS2	clavaminate synthase 2
CT	charge transfer
Δ^9 D	stearoyl-acyl carrier protein Δ^9 desaturase
Δ	axial splitting of the d_{xy} and $d_{xz,yz}$ t_{2g} orbitals
ΔE_Q	Mössbauer quadrupole splitting
δ	splitting of the $M_S = \pm 2$ non-Kramers doublet
δ_{Fe}	Mössbauer isomer shift
DAOCS	deacetoxycephalosporin C synthase
DBC	3,4-di- <i>tert</i> -butylcatecholate
DCT	double charge transfer
DFT	density functional theory
DGPC	deoxyguanidinoproclavaminate acid
DHB	dihydroxybiphenyl
DHPP	dihydroxyphenylpropionate
DP–PEPLM	depyruvamide–PEPLM, without the β -aminoalanine moiety
E°	reduction potential
$E_1^{\circ'}$	formal potential value for first electron transfer
$E_2^{\circ'}$	formal potential value for second electron transfer
$E_{1/2}$	half wave reduction potential
EFE	ethylene-forming-enzyme
E_{HOMO}	energy of the highest occupied molecular orbital
ENDOR	electron nuclear double resonance
EPR	electron paramagnetic resonance
ES	enzyme–substrate complex
ESAF	excited-state antiferromagnetic coupling
ESEEM	electron spin–echo envelope modulation

ESO ₂	enzyme–substrate–dioxygen ternary complex; first intermediate for 3,4-PCD + PCA + O ₂	PT	proton transfer
ESO ₂ *	second intermediate for 3,4-PCD–PCA + O ₂	q-BH ₂	quinonoid dihydrobiopterin
ET	electron transfer	R1	large subunit of ribonucleotide reductase
EXAFS	extended X-ray absorption fine structure	R2	iron-containing subunit of ribonucleotide reductase
FADH	one-electron-reduced flavin adenine dinucleotide	RLO	rabbit lipoxygenase
FADH ₂	two-electron-reduced flavin adenine dinucleotide	rR	resonance Raman spectroscopy
FHB	3-fluoro, 4-hydroxybenzoate	RR	ribonucleotide reductase
\tilde{g}	effective <i>g</i> -value	SLO	soybean lipoxygenase
g_{eff}	effective <i>g</i> -value	sMMO	soluble form of methane monooxygenase
GSAF	ground-state antiferromagnetism	SO	spin–orbit
HDVV	Heisenberg–Dirac–Van Vleck (Hamiltonian)	SOC	spin–orbit coupling
HF	Hartree–Fock	SPE	simultaneous pair excitation
HLO	human lipoxygenase	TACN	triazacyclononane
HOMO	highest occupied molecular orbital	TfdA	2,4-dichlorophenoxyacetic acid/ α -KG dioxygenase
HPCA	homoprotocatechuate	TPA	tris(2-pyridylmethyl)amine
HPOD	13-(<i>S</i>)-hydroperoxy-9,11-(<i>E,Z</i>)-octadecadienoic acid	triphos	MeC(CH ₂ PPh ₂) ₃
Hr	hemerythrin	TrpH	tryptophan hydroxylase, EC 1.14.16.4
IHB	3-iodo, 4-hydroxybenzoate	TyrH	tyrosine hydroxylase, EC 1.14.16.2
INDO	intermediate neglect of differential overlap	V	rhombic splitting of the d _{xz} and d _{yz} t _{2g} orbitals
INO	2-hydroxyisonicotinic acid <i>N</i> -oxide	V _{max}	maximum enzyme velocity
IPNS	isopenicillin <i>N</i> -synthase	VBCI	valence-bond configuration interaction
<i>iso</i> -PEPLM	PEPLM with 2- <i>O</i> -carbamoyl (versus 3- <i>O</i>)	VTVH	variable-temperature, variable-field
<i>J</i>	exchange coupling constant	WT	wild-type
<i>k</i> ²	Stevens orbital reduction factor	XAS	X-ray absorption spectroscopy
KIE	kinetic isotope effect	ZFS	zero-field splitting
<i>K</i> _m	Michaelis constant		
λ	spin–orbit coupling constant		
L-Dopa	3,4-dihydroxyphenylalanine		
LF	ligand field		
LMCT	ligand-to-metal charge transfer		
LO	lipoxygenase, EC 1.13.11.12		
LT	low temperature		
LUMO	lowest unoccupied molecular orbital		
μ_z	Zeeman operator, $\mu_z = L_z + 2S_z$		
MCD	magnetic circular dichroism		
MLCT	metal-to-ligand charge transfer		
MMCT	metal-to-metal charge transfer		
MMO	methane monooxygenase		
MMOB	methane monooxygenase “protein B” component		
MMOH	methane monooxygenase hydroxylase component		
MMOR	methane monooxygenase reductase component		
NAD(P)H	reduced nicotinamide adenine dinucleotide (phosphate)		
NAD ⁺	nicotinamide adenine dinucleotide		
NCA	normal coordinate analysis		
NDO	naphthalene 1,2-dioxygenase, EC 1.14.12.12		
NNO	6-hydroxynicotinic acid <i>N</i> -oxide		
π_{ip}	in-plane phenolate oxygen valence orbital		
π_{op}	out-of-plane phenolate oxygen valence orbital		
PAH	phenylalanine hydroxylase, EC 1.14.16.1		
PC	proclavaminc acid		
PCA	protocatechuate		
PCBs	polychlorinated biphenyls		
PCET	proton-coupled electron transfer		
PDO	phthalate dioxygenase		
PEPLM	peplomycin (pepleomycin), BLM derivative with altered tail		
PES	potential energy surface		
phenSQ	9,10-phenanthrene semiquinone		
PKU	phenylketonuria		
pMMO	particulate form of methane monooxygenase		

VI. Acknowledgments

E.I.S. thanks his collaborators and past students as indicated in the references cited for their outstanding contributions to this field. This research is generously funded by the NIH (E.I.S. Grant GM40392 for mononuclear non-heme iron) and the NSF (E.I.S. Grant MCB-9816051 for binuclear non-heme iron). The following fellowships are also gratefully acknowledged: J.N.K., NIH biotechnology training grant; N.L., Deutscher Akademischer Austauschdienst postdoctoral fellowship; F.N., Deutsche Forschungsgemeinschaft postdoctoral fellowship; A.J.S., NSF predoctoral fellowship; and Y.-S.Y., Evelyn Laing McBain fellowship.

VII. References

- (1) Klabunde, T.; Sträter, N.; Fröhlich, R.; Witzel, H.; Krebs, B. *J. Biol. Chem.* **1996**, *259*, 737–748.
- (2) Klabunde, T.; Krebs, B. *Struct. Bonding* **1997**, *89*, 177–198.
- (3) Bonomi, F.; Kurtz, D. M., Jr.; Cui, X. *J. Bioinorg. Chem.* **1996**, *1*, 67–72.
- (4) Coulter, E. D.; Shenvi, N. V.; Kurtz, D. M., Jr. *Biochem. Biophys. Res. Commun.* **1999**, *255*, 317–323.
- (5) deMaré, F.; Kurtz, D. M., Jr.; Nordlund, P. *Nat. Struct. Biol.* **1996**, *3*, 539–546.
- (6) Takagi, H.; Shi, D. S.; Ha, Y.; Allewell, N. M.; Theil, E. C. *J. Biol. Chem.* **1998**, *273*, 18685–18688.
- (7) Moënné-Loccoz, P.; Krebs, C.; Herlihy, K.; Edmondson, D. E.; Theil, E. C.; Huynh, B. H.; Loehr, T. M. *Biochemistry* **1999**, *38*, 5290–5295.
- (8) Ha, Y.; Shi, D. S.; Small, G. W.; Theil, E. C.; Allewell, N. M. *J. Bioinorg. Chem.* **1999**, *4*, 243–256.
- (9) Gdaniec, Z.; Sierzputowska, G. H.; Theil, E. C. *Biochemistry* **1999**, *38*, 5676.
- (10) Small, F. J.; Ensign, S. A. *J. Biol. Chem.* **1997**, *272*, 24913–24920.
- (11) Whittaker, J. W.; Solomon, E. I. *J. Am. Chem. Soc.* **1988**, *110*, 5329–5339.
- (12) Zhang, Y.; Gebhard, M. S.; Solomon, E. I. *J. Am. Chem. Soc.* **1991**, *113*, 5162–5175.
- (13) Solomon, E. I.; Pavel, E. G.; Loeb, K. E.; Campochiaro, C. *Coord. Chem. Rev.* **1995**, *144*, 369–460.
- (14) Pavel, E. G.; Kitajima, N.; Solomon, E. I. *J. Am. Chem. Soc.* **1998**, *120*, 3949–3962.

- (15) Piepho, S. B.; Schatz, P. N. *Group Theory in Spectroscopy: With Applications to Magnetic Circular Dichroism*; Wiley: New York, 1983.
- (16) Stephens, P. J. *J. Chem. Phys.* **1970**, *52*, 3489–3516.
- (17) Stephens, P. J. *Annu. Rev. Phys. Chem.* **1974**, *25*, 201–232.
- (18) Stephens, P. J. *Adv. Chem. Phys.* **1976**, *35*, 197–264.
- (19) To be rigorously correct, the magnetic flux density \vec{B} should be used, since it measures the total magnetic field (external plus contributions from the medium) at the center of interest, whereas the magnetic field strength (H) only deals with the external field. These quantities are related by the permeability μ_m of the medium considered: $\vec{B} = \mu_m \vec{H}$ (refs 1003 and 1004). For diluted paramagnetic media, it is reasonable to assume that $\mu_m \approx 1$ and, therefore, H can be used instead of \vec{B} , which is the notation in most literature.
- (20) Note that heme centers, even when diamagnetic, can have very large \mathbf{A} - and \mathbf{B} -terms.
- (21) Campochiaro, C.; Pavel, E. G.; Solomon, E. I. *Inorg. Chem.* **1995**, *34*, 4669–4675.
- (22) Schatz, P. N.; Mowery, R. L.; Krausz, E. R. *Mol. Phys.* **1978**, *35*, 1537–1557.
- (23) Bennett, D. E.; Johnson, M. K. *Biochim. Biophys. Acta* **1987**, *911*, 71–80.
- (24) Note that the \mathbf{g} matrix is not a mathematically true second-rank tensor, because it connects two vector operations (H and \vec{S} ; vide supra, eq 10) which have different reference systems.
- (25) Thomson, A. J.; Johnson, M. K. *Biochem. J.* **1980**, *191*, 411–420.
- (26) Whittaker, J. W.; Solomon, E. I. *J. Am. Chem. Soc.* **1986**, *108*, 835–836.
- (27) Abragam, A.; Bleaney, B. *Electron Paramagnetic Resonance of Transition Ions*; Dover: New York, 1986.
- (28) Since wave functions are changing with magnetic field, this behavior formally corresponds to a temperature-dependent \mathbf{B} -term that is nonlinear with magnetic field. This is different from the \mathbf{B} -term given in eq 3 that is temperature-independent and linear with field and is a special case for non-Kramers systems.
- (29) Gütllich, P.; Link, R.; Trautwein, A. *Mössbauer Spectroscopy and Transition Metal Chemistry*; Springer-Verlag: Berlin, 1978; Vol. 3 (Inorganic Chemistry Concepts).
- (30) Gütllich, P.; Enslin, J. In *Inorganic Electronic Structure and Spectroscopy*; Solomon, E. I., Lever, A. B. P., Eds.; Wiley: New York, 1999; Vol. 1, pp 161–211.
- (31) Trautwein, A. X.; Bill, E.; Bominaar, E. L.; Winkler, H. *Struct. Bonding* **1991**, *78*, 1–95.
- (32) Roe, A. L.; Schneider, D. J.; Mayer, R. J.; Pyrz, J. W.; Widom, J.; Que, L., Jr. *J. Am. Chem. Soc.* **1984**, *106*, 1676–1681.
- (33) Westre, T. E.; Kennepohl, P.; DeWitt, J. G.; Hedman, B.; Hodgson, K. O.; Solomon, E. I. *J. Am. Chem. Soc.* **1997**, *119*, 6297–6314.
- (34) Sugiura, Y.; Suzuki, T.; Kawabe, H.; Tanaka, H.; Watanabe, K. *Biochim. Biophys. Acta* **1982**, *716*, 38–44.
- (35) Burger, R. M.; Kent, T. A.; Horwitz, S. B.; Münck, E.; Peisach, J. *J. Biol. Chem.* **1983**, *258*, 1559–1564.
- (36) Chen, V. J.; Orville, A. M.; Harpel, M. R.; Frolik, C. A.; Surerus, K. K.; Münck, E.; Lipscomb, J. D. *J. Biol. Chem.* **1989**, *264*, 21677.
- (37) Dunham, W. R.; Carroll, R. T.; Thompson, J. F.; Sands, R. H.; Funk, M. O., Jr. *Eur. J. Biochem.* **1990**, *190*, 611–617.
- (38) Kappock, T. J.; Caradonna, J. P. *Chem. Rev.* **1996**, *96*, 2659–2756.
- (39) Arciero, D. M.; Lipscomb, J. D.; Huynh, B. H.; Kent, T. A.; Münck, E. *J. Biol. Chem.* **1983**, *258*, 14981–14991.
- (40) Haavik, J.; Bill, E.; Lengen, M.; Martinez, A.; Flatmark, T.; Trautwein, A. X. In *Chemistry and Biology of Pteridines and Foliates*; Ayling, J. E., Ed.; Plenum: New York, 1993; pp 71–76.
- (41) Meyer-Klaucke, W.; Winkler, H.; Schünemann, V.; Trautwein, A. X.; Nolting, H.-F.; Haavik, J. *Eur. J. Biochem.* **1996**, *241*, 432–439.
- (42) Schünemann, V.; Meier, C.; Meyer-Klaucke, W.; Winkler, H.; Trautwein, A. X.; Knappskog, P. M.; Toska, K.; Haavik, J. *J. Biol. Inorg. Chem.* **1999**, *4*, 223–231.
- (43) Loeb, K. E.; Zaleski, J. M.; Westre, T. E.; Guajardo, R. J.; Mascharak, P. K.; Hedman, B.; Hodgson, K. O.; Solomon, E. I. *J. Am. Chem. Soc.* **1995**, *117*, 4545–4561.
- (44) Shu, L.; Chiou, Y.-M.; Orville, A. M.; Miller, M. A.; Lipscomb, J. D.; Que, L., Jr. *Biochemistry* **1995**, *34*, 6649–6659.
- (45) Scott, R. A.; Wang, S.; Eidsness, M. K.; Kriauciunas, A.; Frolik, C. A.; Chen, V. J. *Biochemistry* **1992**, *31*, 4596–4601.
- (46) Pavlosky, M. A.; Zhang, Y.; Westre, T. E.; Gan, Q.-F.; Pavel, E. G.; Campochiaro, C.; Hedman, B.; Hodgson, K. O.; Solomon, E. I. *J. Am. Chem. Soc.* **1995**, *117*, 4316–4327.
- (47) Loeb, K. E.; Westre, T. E.; Kappock, T. J.; Mitic, N.; Glasfeld, E.; Caradonna, J. P.; Hedman, B.; Hodgson, K. O.; Solomon, E. I. *J. Am. Chem. Soc.* **1997**, *119*, 1901–1915.
- (48) Davis, M. I.; Wasinger, E. C.; Westre, T. E.; Zaleski, J. M.; Orville, A. M.; Lipscomb, J. D.; Hedman, B.; Hodgson, K. O.; Solomon, E. I. *Inorg. Chem.* **1999**, *38*, 3676–3683.
- (49) Sugano, S.; Tanabe, Y.; Kamimura, H. *Multiplets of Transition-Metal Ions in Crystals*; Academic: New York, 1970.
- (50) Griffith, J. S. *The Theory of Transition-Metal Ions*; Cambridge University: Cambridge, U.K., 1964.
- (51) Aasa, R. *J. Chem. Phys.* **1970**, *52*, 3919–3930.
- (52) Castner, T., Jr.; Newell, G. S.; Holton, W. C.; Slichter, C. P. *J. Chem. Phys.* **1960**, *32*, 668–673.
- (53) Wickman, H. H.; Klein, M. P.; Shirley, D. A. *J. Chem. Phys.* **1965**, *42*, 2113–2117.
- (54) Griffith, J. S. *Mol. Phys.* **1964**, *8*, 213–216.
- (55) Gebhard, M. S.; Deaton, J. C.; Koch, S. A.; Millar, M.; Solomon, E. I. *J. Am. Chem. Soc.* **1990**, *112*, 2217–2231.
- (56) Neese, F.; Solomon, E. I. *Inorg. Chem.* **1998**, *37*, 6568–6582.
- (57) Gaffney, B. J.; Silverstone, H. J. In *EMR of Paramagnetic Molecules*; Berliner, L. J., Reuben, J., Eds.; Plenum: New York, 1993; p 1.
- (58) This is only correct in terms of the second-order spin Hamiltonian of eq 11. Taking into account fourth-order contributions, the ${}^6A_{1g}$ ground state is zero-field split into one 4-fold (Γ_8) and one 2-fold degenerate level (Γ_7) even in a perfect octahedron.
- (59) Deaton, J. C.; Gebhard, M. S.; Koch, S. A.; Millar, M.; Solomon, E. I. *J. Am. Chem. Soc.* **1988**, *110*, 6241–6243.
- (60) Neese, F.; Solomon, E. I. *J. Am. Chem. Soc.* **1998**, *120*, 12829–12848.
- (61) Solomon, E. I.; Hanson, M. A. In *Inorganic Electronic Structure and Spectroscopy*; Solomon, E. I., Lever, A. B. P., Eds.; Wiley: New York, 1999; Vol. 2, pp 1–129.
- (62) Baldwin, M. J.; Root, D. E.; Pate, J. E.; Fujisawa, K.; Kitajima, N.; Solomon, E. I. *J. Am. Chem. Soc.* **1992**, *114*, 10421–10431.
- (63) Lever, A. B. P. *Inorganic Electronic Spectroscopy*, 2nd ed.; Elsevier: Amsterdam, 1984; Vol. 33 (Studies in Physical and Theoretical Chemistry).
- (64) Deaton, J. C.; Gebhard, M. S.; Solomon, E. I. *Inorg. Chem.* **1989**, *28*, 877–889.
- (65) Neese, F.; Solomon, E. I. *Inorg. Chem.* **1999**, *38*, 1847–1865.
- (66) Oganessian, V. S.; George, S. J.; Cheesman, M. R.; Thomson, A. J. *J. Chem. Phys.* **1999**, *110*, 762–777.
- (67) Browett, W. R.; Fucaloro, A. F.; Morgan, T. V.; Stephens, P. J. *J. Am. Chem. Soc.* **1983**, *105*, 1868–1872.
- (68) Gerstman, B. S.; Brill, A. S. *J. Chem. Phys.* **1985**, *82*, 1212–1230.
- (69) Czernuszewicz, R. S.; Spiro, T. G. In *Inorganic Electronic Structure and Spectroscopy*; Solomon, E. I., Lever, A. B. P., Eds.; Wiley: New York, 1999; Vol. 1, pp 353–441.
- (70) Lee, S. Y.; Heller, E. J. *J. Chem. Phys.* **1979**, *71*, 4777–4788.
- (71) Tannor, D. J.; Heller, E. J. *J. Chem. Phys.* **1982**, *77*, 202–218.
- (72) Zink, J. I.; Shin, K.-S. K. *Adv. Photochem.* **1991**, *16*, 119–214.
- (73) Myers, A. B.; Mathies, R. A. In *Biological Applications of Raman Spectroscopy*; Spiro, T. G., Ed.; Wiley: New York, 1987; Vol. 2, pp 1–58.
- (74) Kramers, H. A.; Heisenberg, W. *Z. Phys.* **1925**, *31*, 681.
- (75) Dirac, P. A. M. *Proc. R. Soc. London* **1927**, *114*, 710.
- (76) Tang, J.; Albrecht, A. C. In *Raman Spectroscopy*; Szymanski, H. A., Ed.; Plenum: New York, 1970; Vol. 2.
- (77) Clark, R. J. H.; Stewart, B. *Struct. Bonding* **1979**, *36*, 1–80.
- (78) Griffith, J. S. *Nature* **1957**, *180*, 30–31.
- (79) Kotani, M. *Prog. Theor. Phys. Suppl.* **1961**, *17*, 4.
- (80) Weissbluth, M. *Hemoglobin: Cooperativity and Electronic Processes*; Springer-Verlag: Berlin, 1973.
- (81) Taylor, C. P. S. *Biochim. Biophys. Acta* **1977**, *491*, 137–149.
- (82) Soltis, S. M.; Strouse, C. E. *J. Am. Chem. Soc.* **1988**, *110*, 2824–2829.
- (83) Palmer, G. In *The Porphyrins*; Lever, A. B. P., Gray, H. B., Eds.; Addison-Wesley: London, 1983; Vol. 2, pp 43–88.
- (84) Shokirev, N. V.; Walker, F. A. *J. Am. Chem. Soc.* **1998**, *120*, 981–990.
- (85) Blumberg, W. E.; Peisach, J. *J. Adv. Chem. Ser.* **1971**, *100*, 271.
- (86) Blumberg, W. E.; Peisach, J. In *Magnetic Resonances in Biological Research*; Franconi, C., Ed.; Gordon and Breach: New York, 1971; p 65.
- (87) Blumberg, W. E.; Peisach, J. In *Structure and Bonding of Macromolecules and Membranes*; Chance, B., Yonetani, T., Eds.; Academic: New York, 1971; p 215.
- (88) Peisach, J.; Blumberg, W. E.; Adler, A. *Ann. N. Y. Acad. Sci.* **1973**, *206*, 310.
- (89) Bendix, J.; Brorson, M.; Schäffer, C. E. *Inorg. Chem.* **1993**, *32*, 2838–2849.
- (90) de Vries, S.; Albracht, S. *Biochim. Biophys. Acta* **1979**, *546*, 334–340.
- (91) Gibson, J. F. In *ESR and NMR of Paramagnetic Species in Biological and Related Systems*; Bertini, I., Drago, R. S., Eds.; D. Reidel Publishing Co., Inc.: Dordrecht, Holland, 1980; pp 225–253.
- (92) Baker, J. M.; Bleaney, B.; Bowers, K. D. *Proc. Phys. Soc., London* **1956**, *B69*, 1205.
- (93) Merrithew, P.; Lo, C. C.; Modestino, A. J. *Inorg. Chem.* **1973**, *12*, 1927–1930.
- (94) Reif, W. M.; DeSimone, R. E. *Inorg. Chem.* **1973**, *12*, 1793–1796.

- (95) Meyer, K.; Bill, E.; Mlenert, B.; Weyermüller, T.; Wieghardt, K. *J. Am. Chem. Soc.* **1999**, *121*, 4859–4876.
- (96) Koch, S.; Holm, R. H.; Frankel, R. B. *J. Am. Chem. Soc.* **1975**, *97*, 6714–6723.
- (97) Nishida, Y.; Oshio, S.; Kida, S. *Inorg. Chim. Acta* **1977**, *23*, 59–61.
- (98) Shoner, S. C.; Kovacs, J. A. *Inorg. Chem.* **1995**, *34*, 4517–4518.
- (99) Noveron, J. C.; Olmstead, M. M.; Mascharak, P. K. *Inorg. Chem.* **1998**, *37*, 1138–1139.
- (100) Burger, R. M.; Peisach, J.; Horwitz, S. B. *J. Biol. Chem.* **1981**, *256*, 11636–11644.
- (101) Sugiura, Y.; Kuwahara, J.; Nagasawa, T.; Yamada, H. *J. Am. Chem. Soc.* **1987**, *109*, 5848–5850.
- (102) Zang, Y.; Kim, J.; Dong, Y.; Wilkinson, E. C.; Appelman, E. H.; Que, L., Jr. *J. Am. Chem. Soc.* **1997**, *119*, 4197–4205.
- (103) Lubben, M.; Meetsma, A.; Wilkinson, E. C.; Feringa, B.; Que, L., Jr. *Angew. Chem., Int. Ed. Engl.* **1995**, *34*, 1512–1514.
- (104) Nguyen, C.; Guajardo, R. J.; Mascharak, P. K. *Inorg. Chem.* **1996**, *35*, 6273–6281.
- (105) de Vries, M. E.; La Crois, R. M.; Roelfes, G.; Kooijman, H.; Spek, A. L.; Hage, R.; Feringa, B. L. *Chem. Commun.* **1997**, 1549–1550.
- (106) Bernal, I.; Jensen, I. M.; Jensen, K. B.; McKenzie, C. J.; Toftlund, H.; Tuchagues, J.-P. *J. Chem. Soc., Dalton Trans.* **1995**, 3667–3675.
- (107) Otsuka, T.; Ohya, T.; Sato, M. *Inorg. Chem.* **1985**, *24*, 776–782.
- (108) Quinn, R.; Nappa, M.; Valentine, J. S. *J. Am. Chem. Soc.* **1982**, *104*, 4, 2588–2595.
- (109) Gadsby, P. M. A.; Thomson, A. J. *J. Am. Chem. Soc.* **1990**, *112*, 5003–5011.
- (110) Hill, H. A. O.; Roder, A.; Williams, R. J. P. *Struct. Bonding* **1970**, *8*, 123–151.
- (111) Harris-Loew, G. M. *Biophys. J.* **1970**, *10*, 196–212.
- (112) Safo, M. K.; Gupta, G. P.; Watson, C. T.; Simonis, U.; Walker, F. A.; Scheidt, W. R. *J. Am. Chem. Soc.* **1992**, *114*, 7066–7075.
- (113) Jäger, E. G.; Keutel, H. *Inorg. Chem.* **1997**, *36*, 3512–3519.
- (114) Gewirth, A. A.; Solomon, E. I. *J. Am. Chem. Soc.* **1988**, *110*, 3811–3819.
- (115) Ziegler, T. *Chem. Rev.* **1991**, *91*, 651–667.
- (116) Ziegler, T. *Can. J. Chem.* **1995**, *73*, 743–761.
- (117) Martin, C. H.; Zerner, M. C. In *Inorganic Electronic Structure and Spectroscopy*; Solomon, E. I., Lever, A. B. P., Eds.; Wiley: New York, 1999; Vol. 1, pp 555–659.
- (118) Li, J.; Noodleman, L.; Case, D. A. In *Inorganic Electronic Structure and Spectroscopy*; Solomon, E. I., Lever, A. B. P., Eds.; Wiley: New York, 1999; Vol. 1, pp 661–724.
- (119) Andzelm, J.; Wimmer, E. *J. Chem. Phys.* **1992**, *96*, 1280–1303.
- (120) Scheiner, A.; Baker, J.; Andzelm, J. W. *J. Comput. Chem.* **1997**, *18*, 775–795.
- (121) Wong, M. W. *Chem. Phys. Lett.* **1996**, *256*, 391–399.
- (122) Siegbahn, P. E. M. *Adv. Chem. Phys.* **1996**, *93*, 333–387.
- (123) Slater, J. C. *The Self-Consistent Field for Molecules and Solids: Quantum Theory of Molecules and Solids*; McGraw-Hill: New York, 1974; Vol. 4.
- (124) Gross, E. K. U.; Dobson, J. F.; Petersilka, M. *Top. Curr. Chem.* **1996**, *181*, 81–172.
- (125) Gardner, H. W. *Biochim. Biophys. Acta* **1991**, *1084*, 221–239.
- (126) Siedow, J. N. *Annu. Rev. Plant Physiol. Plant Mol. Biol.* **1991**, *42*, 145–188.
- (127) Yamamoto, S. *Biochim. Biophys. Acta* **1992**, *1128*, 117–131.
- (128) Ford-Hutchinson, A. W.; Gresser, M.; Young, R. N. *Annu. Rev. Biochem.* **1994**, *63*, 383–417.
- (129) Kühn, H.; Borngreber, S. In *Lipoxygenases and Their Metabolites*; Nigam, S., Pace-Asciak, C. R., Eds.; Plenum: New York, 1999.
- (130) Brash, A. R. *J. Biol. Chem.* **1999**, *274*, 23679–23682.
- (131) Kuhn, H.; Thiele, B. *J. FEBS Lett.* **1999**, *449*, 7–11.
- (132) van Leyen, K.; Duvoisin, R. M.; Engelhardt, H.; Wiedmann, M. *Nature* **1998**, *395*, 392–395.
- (133) Honn, K. V.; Tang, D. G.; Gao, X.; Butovich, I. A.; Liu, B.; Timar, J.; Hagmann, W. *Cancer Metastasis Rev.* **1994**, *13*, 365–396.
- (134) Sorkness, C. A. *Pharmacotherapy* **1997**, *17*, 50S–54S.
- (135) Musser, J. H.; Kreft, A. F. *J. Med. Chem.* **1992**, *35*, 2501–2524.
- (136) Axelrod, B.; Cheesbrough, T. M.; Laakso, S. *Methods Enzymol.* **1981**, *71*, 441–451.
- (137) Sloane, D. L. In *Lipoxygenase Lipoxygenase Pathway Enzymes*; Piazza, G., Ed.; American Oil Chemists' Society: Champaign, IL, 1996; pp 57–79.
- (138) Steczko, J.; Donoho, G. P.; Clemens, J. C.; Dixon, J. E.; Axelrod, B. *Biochemistry* **1992**, *31*, 4053–4057.
- (139) Boyington, J. C.; Gaffney, B. J.; Amzel, L. M. *Science* **1993**, *260*, 1482–1486.
- (140) Minor, W.; Steczko, J.; Stec, B.; Otwinowski, Z.; Bolin, J. T.; Walter, R.; Axelrod, B. *Biochemistry* **1996**, *35*, 10687–10701.
- (141) Gillmor, S. A.; Villasenor, A.; Fletterick, R.; Sigal, E.; Browner, M. *Nat. Struct. Biol.* **1997**, *4*, 1003–1009.
- (142) Sigal, E.; Craik, C. S.; Highland, E.; Grunberger, D.; Costello, L. L.; Dixon, R. A. F.; Nadel, J. A. *Biochem. Biophys. Res. Commun.* **1988**, *157*, 457.
- (143) Holman, T. R.; Zhou, J.; Solomon, E. I. *J. Am. Chem. Soc.* **1998**, *120*, 12564–12572.
- (144) Glickman, M. H.; Klinman, J. P. *Biochemistry* **1995**, *34*, 14077–14092.
- (145) Van der heijdt, L. M.; Schilstra, M. J.; Feiters, M. C.; Nolting, H. F.; Hermes, C.; Veldink, G. A.; Vliegthart, J. F. G. *Eur. J. Biochem.* **1995**, *231*, 186–191.
- (146) Gan, Q.-F.; Browner, M. F.; Sloane, D. L.; Sigal, E. *J. Biol. Chem.* **1996**, *271*, 25412–25418.
- (147) Lagock, J. W.; Emken, E. A.; Law, J. H.; Kezdy, F. J. *J. Biol. Chem.* **1976**, *251*, 6001–6006.
- (148) Egmond, M. E.; Fasella, P. M.; Veldink, G. A.; Vliegthart, J. F. G.; Boldingh, J. *Eur. J. Biochem.* **1977**, *76*, 469–479.
- (149) Veldink, G. A.; Vliegthart, J. F. G. *Adv. Inorg. Biochem.* **1984**, *6*, 139–161.
- (150) Schilstra, M. J.; Veldink, G. A.; Vliegthart, J. F. G. *Biochemistry* **1993**, *32*, 7686–7691.
- (151) Schilstra, M. J.; Veldink, G. A.; Vliegthart, J. F. G. *Biochemistry* **1994**, *33*, 3974–3979.
- (152) Schilstra, M. J.; Veldink, G. A.; Verhagen, J.; Vliegthart, J. F. G. *Biochemistry* **1992**, *31*, 7692–7699.
- (153) Jonsson, T.; Glickman, M. H.; Sun, S. J.; Klinman, J. P. *J. Am. Chem. Soc.* **1996**, *118*, 10319–10320.
- (154) Glickman, M. H.; Klinman, J. P. *Biochemistry* **1996**, *35*, 12882–12892.
- (155) Moiseyev, N.; Rucker, J.; Glickman, M. H. *J. Am. Chem. Soc.* **1997**, *119*, 3853–3860.
- (156) Rickert, K. W.; Klinman, J. P. *Biochemistry* **1999**, *38*, 12218–12228.
- (157) Skrzypczak-Jankun, E.; Amzel, L. M.; Kroa, B. A.; Funk, M. O., Jr. *Proteins: Struct. Funct. Genet.* **1997**, *29*, 15–31.
- (158) Monaco, H. L.; Zanotti, G. *Biopolymers* **1992**, *32*, 457–465.
- (159) Gardner, H. W. *Biochim. Biophys. Acta* **1989**, *1001*, 274–281.
- (160) Sloane, D. L.; Leung, R.; Craik, C. S.; Sigal, E. *Nature* **1991**, *354*, 149–152.
- (161) Petersson, L.; Slappendel, S.; Vliegthart, J. F. G. *Biochim. Biophys. Acta* **1985**, *828*, 81.
- (162) van der Heijdt, L. M.; Feiters, M. C.; Navaratnam, S.; Nolting, H. F.; Hermes, C.; Veldink, G. A.; Vliegthart, J. F. G. *Eur. J. Biochem.* **1992**, *207*, 793–802.
- (163) Scarrow, R. C.; Trimitsis, M. G.; Buck, C. P.; Grove, G. N.; Cowling, R. A.; Nelson, M. J. *Biochemistry* **1994**, *33*, 15023–15035.
- (164) Petersson, L.; Slappendel, S.; Feiters, M. C.; Vliegthart, J. F. G. *Biochim. Biophys. Acta* **1987**, *913*, 228–237.
- (165) Slappendel, S.; Veldink, G. A.; Vliegthart, J. F. G.; Aasa, R.; Malmström, B. G. *Biochim. Biophys. Acta* **1980**, *642*, 30–39.
- (166) Gaffney, B. J.; Mavrophilipos, D. V.; Doctor, K. S. *Biophys. J.* **1993**, *64*, 773–783.
- (167) De Groot, J. J. M. C.; Veldink, G. A.; Vliegthart, J. F. G.; Boldingh, J.; Wever, R.; van Gelder, B. F. *Biochim. Biophys. Acta* **1975**, *377*, 71–79.
- (168) Nelson, M. J. *J. Am. Chem. Soc.* **1988**, *110*, 2985–2986.
- (169) Solomon, E. I.; Zhou, J.; Neese, F.; Pavel, E. G. *Chem. Biol.* **1997**, *4*, 795–808.
- (170) Zhang, Y.; Gan, Q.-F.; Pavel, E. G.; Sigal, E.; Solomon, E. I. *J. Am. Chem. Soc.* **1995**, *117*, 7422–7427.
- (171) Prigge, S. T.; Boyington, J. C.; Gaffney, B. J.; Amzel, L. M. In *Lipoxygenase and Lipoxygenase Pathway Enzymes*; Piazza, G., Ed.; American Oil Chemists' Society: Champaign, IL, 1996; pp 1–32.
- (172) Lewinski, K.; Steczko, J.; Holman, T.; Sigal, E.; Stec, B.; Axelrod, B.; Minor, W. *XVII Congress and General Assembly of the International Union of Crystallography*, Seattle, WA, 1996; p C-580.
- (173) Spaepen, L. J. M.; Veldink, G. A.; Liefkens, T. J.; Vliegthart, J. F. G.; Kay, C. M. *Biochim. Biophys. Acta* **1979**, *574*, 301–311.
- (174) Corey, E. J.; Nagata, R. *J. Am. Chem. Soc.* **1987**, *109*, 8107–8108.
- (175) Corey, E. J.; Walker, C. *J. Am. Chem. Soc.* **1987**, *109*, 8108–8109.
- (176) Nelson, M. J.; Seitz, S. P. *Curr. Opin. Struct. Biol.* **1994**, *4*, 878–884.
- (177) Gardner, K. A.; Mayer, J. M. *Science* **1995**, *269*, 1849–1851.
- (178) Nelson, M. J. *Biochemistry* **1988**, *27*, 4273–4278.
- (179) Roth, J. P.; Mayer, J. M. *Inorg. Chem.* **1999**, *38*, 2760–2761.
- (180) Jonas, R. T.; Stack, T. D. P. *J. Am. Chem. Soc.* **1997**, *119*, 8566–8567.
- (181) Garssen, G. J.; Vliegthart, J. F. G.; Boldingh, J. *Biochem. J.* **1972**, *130*, 435–442.
- (182) Bugg, T. D. H.; Winfield, C. J. *Nat. Prod. Rep.* **1998**, 513–530.
- (183) Dagley, S. *Am. Sci.* **1975**, *63*, 681–689.
- (184) Glick, B. R.; Pasternak, J. J. *Molecular Biotechnology: Principles and Applications of Recombinant DNA*, 2nd ed.; American Society for Microbiology: Washington, DC, 1998.
- (185) Lipscomb, J. D.; Orville, A. M. In *Degradation of Environmental Pollutants by Microorganisms and Their Metalloenzymes*; Sigel,

- H., Sigel, A., Eds.; Marcel Dekker: New York, 1992; Vol. 28 (Metal Ions in Biological Systems), pp 243–298.
- (186) Hofer, B.; Eltis, L. D.; Dowling, D. N.; Timmis, K. N. *Gene* **1993**, *130*, 47–55.
- (187) Harayama, S.; Rekik, M. *J. Biol. Chem.* **1989**, *264*, 15328–15333.
- (188) Durham, D. R.; Stirling, L. A.; Ornston, L. N.; Perry, J. J. *Biochemistry* **1980**, *19*, 149–155.
- (189) Fujiwara, M.; Golovleva, L. A.; Saeki, Y.; Nozaki, M.; Hayaishi, O. *J. Biol. Chem.* **1975**, *250*, 4848–4855.
- (190) Bull, C.; Ballou, D. P.; Otsuka, S. *J. Biol. Chem.* **1981**, *256*, 12681–12686.
- (191) Fujisawa, H.; Hayaishi, O. *J. Biol. Chem.* **1968**, *243*, 2673–2681.
- (192) Hartnett, C.; Niedle, E. L.; Ngai, K.-L.; Ornston, L. N. *J. Bacteriol.* **1990**, *172*, 956–966.
- (193) van der Meer, J. R.; Eggen, R. I. L.; Zehnder, A. J. B.; de Vos, W. M. *J. Bacteriol.* **1991**, *173*, 2425–2434.
- (194) Ohlendorf, D. H.; Lipscomb, J. D.; Weber, P. C. *Nature* **1988**, *336*, 403–405.
- (195) Bhat, M. A.; Ishida, T.; Horiike, K.; Vaidyanathan, C. S.; Nozaki, M. *Arch. Biochem. Biophys.* **1993**, *300*, 738–746.
- (196) Fetzner, S.; Lingens, F. *Microbiol. Rev.* **1994**, *58*, 641–685.
- (197) Que, L., Jr. In *Iron Carriers and Iron Proteins*; Loehr, T. M., Ed.; Physical Bioinorganic Chemistry Series; VCH: New York, 1989; Vol. 5, pp 467–524.
- (198) Fujisawa, H.; Hiromi, K.; Uyeda, M.; Okuno, S.; Nozaki, M.; Hayaishi, O. *J. Biol. Chem.* **1972**, *247*, 4422–4428.
- (199) Whittaker, J. W.; Lipscomb, J. D.; Kent, T. A.; Münck, E. *J. Biol. Chem.* **1984**, *259*, 4466–4475.
- (200) Frazee, R. W.; Orville, A. M.; Dolbeare, K. B.; Yu, H.; Ohlendorf, D. H.; Lipscomb, J. D. *Biochemistry* **1998**, *37*, 2131–2144.
- (201) Walsh, T. A.; Ballou, D. P.; Mayer, R.; Que, L., Jr. *J. Biol. Chem.* **1983**, *258*, 14422–14427.
- (202) Que, L., Jr.; Mayer, R. *J. Am. Chem. Soc.* **1982**, *104*, 875–877.
- (203) Nakata, H.; Yamauchi, T.; Fujisawa, H. *Biochim. Biophys. Acta* **1978**, *527*, 171–181.
- (204) Whittaker, J. W.; Lipscomb, J. D. *J. Biol. Chem.* **1984**, *259*, 4487–4495.
- (205) Whittaker, J. W.; Lipscomb, J. D. *J. Biol. Chem.* **1984**, *259*, 4476–4486.
- (206) Orville, A. M.; Lipscomb, J. D.; Ohlendorf, D. H. *Biochemistry* **1997**, *36*, 10052–10066.
- (207) Ohlendorf, D. H.; Weber, P. C.; Lipscomb, J. D. *J. Mol. Biol.* **1987**, *195*, 225–227.
- (208) Ohlendorf, D. H.; Orville, A. M.; Lipscomb, J. D. *J. Mol. Biol.* **1994**, *244*, 586–608.
- (209) Orville, A. M.; Elango, N.; Lipscomb, J. D.; Ohlendorf, D. H. *Biochemistry* **1997**, *36*, 10039–10051.
- (210) Elgren, T. E.; Orville, A. M.; Kelly, K. A.; Lipscomb, J. D.; Ohlendorf, D. H.; Que, L., Jr. *Biochemistry* **1997**, *36*, 11504–11513.
- (211) Lipscomb, J. D.; Orville, A. M.; Frazee, R. W.; Dolbeare, K. B.; Elango, N.; Ohlendorf, D. H. In *Spectroscopic Methods in Bioinorganic Chemistry*; Solomon, E. I., Hodgson, K. O., Eds.; ACS Symposium Series 692; American Chemical Society: Washington, DC, 1998; pp 387–402.
- (212) Siu, D. C.-T.; Orville, A. M.; Lipscomb, J. D.; Ohlendorf, D. H.; Que, L., Jr. *Biochemistry* **1992**, *31*, 10443–10448.
- (213) Felton, R. H.; Barrow, W. L.; May, S. W.; Sowell, A. L.; Goel, S. *J. Am. Chem. Soc.* **1982**, *104*, 6132–6134.
- (214) Felton, R. H.; Gordon, S. L.; Sowell, A. L.; May, S. W. *Biochemistry* **1984**, *23*, 3955–3959.
- (215) True, A. E.; Orville, A. M.; Pearce, L. L.; Lipscomb, J. D.; Que, L., Jr. *Biochemistry* **1990**, *29*, 10847–10854.
- (216) Orville, A. M.; Lipscomb, J. D. *J. Biol. Chem.* **1989**, *264*, 8791–8801.
- (217) Fujisawa, H.; Uyeda, M.; Kojima, Y.; Nozaki, M.; Hayaishi, O. *J. Biol. Chem.* **1972**, *247*, 4414–4421.
- (218) Que, L., Jr.; Lipscomb, J. D.; Zimmermann, R.; Münck, E.; Orme-Johnson, N. R.; Orme-Johnson, W. H. *Biochim. Biophys. Acta* **1976**, *452*, 320–334.
- (219) Davis, M. I.; Orville, A. M.; Neese, F.; Zaleski, J. M.; Lipscomb, J. D.; Solomon, E. I. Manuscript in preparation.
- (220) Briganti, F.; Mangani, S.; Pedocchi, L.; Scozzafava, A.; Golovleva, L. A.; Jadan, A. P.; Solyanikova, I. P. *FEBS Lett.* **1998**, *433*, 58–62.
- (221) Salama, S.; Stong, J. D.; Neilands, J. B.; Spiro, T. G. *Biochemistry* **1978**, *17*, 3781–3785.
- (222) Öhrström, L.; Michaud-Soret, I. *J. Am. Chem. Soc.* **1996**, *118*, 3283–3284.
- (223) Michaud-Soret, I.; Andersson, K. K.; Que, L., Jr.; Haavik, J. *Biochemistry* **1995**, *34*, 5504–5510.
- (224) Ling, J. S.; Sahlin, M.; Sjöberg, B.-M.; Loehr, T. M.; Sanders-Loehr, J. *J. Biol. Chem.* **1994**, *269*, 5595–5601.
- (225) Lauffer, R. B.; Que, L., Jr. *J. Am. Chem. Soc.* **1982**, *104*, 7324–7325.
- (226) Que, L., Jr.; Lauffer, R. B.; Lynch, J. B.; Murch, B. P.; Pyrz, J. W. *J. Am. Chem. Soc.* **1987**, *109*, 5381–5385.
- (227) Orville, A. M.; Lipscomb, J. D. *J. Biol. Chem.* **1993**, *268*, 8596–8607.
- (228) Lipscomb, J. D.; Orville, A. M.; Frazee, R. W.; Miller, M. A.; Ohlendorf, D. H. In *Oxygen Homeostasis and Its Dynamics*; Ishimura, Y., Shimada, H., Suematsu, M., Eds.; Springer-Verlag: New York, 1998; Vol. 1, pp 263–275.
- (229) Smith, R. M.; Martell, A. E. *Critical Stability Constants*; Plenum: New York, 1982; Vol. 5.
- (230) Barbaro, P.; Bianchini, C.; Mealli, C.; Meli, A. *J. Am. Chem. Soc.* **1991**, *113*, 3181–3183.
- (231) Barbaro, P.; Bianchini, C.; Frediani, P.; Meli, A.; Vizza, F. *Inorg. Chem.* **1992**, *31*, 1523–1529.
- (232) Barbaro, P.; Bianchini, C.; Linn, K.; Mealli, C.; Meli, A.; Vizza, F.; Laschi, F.; Zanello, P. *Inorg. Chim. Acta* **1992**, *198–200*, 31–56.
- (233) Bianchini, C.; Frediani, P.; Laschi, F.; Meli, A.; Vizza, F.; Zanello, P. *Inorg. Chem.* **1990**, *29*, 3402–3409.
- (234) Westre, T. Ph.D. Thesis, Stanford University, 1996.
- (235) Fujii, S.; Ohya-Nishiguchi, H.; Hirota, N.; Nishinaga, A. *Bull. Chem. Soc. Jpn.* **1993**, *66*, 1408–1419.
- (236) Hamilton, G. A. In *Molecular Mechanisms of Oxygen Activation*; Hayaishi, O., Ed.; Academic: New York, 1974; pp 405–451.
- (237) Saeki, Y.; Nozaki, M.; Senoh, S. *J. Biol. Chem.* **1980**, *255*, 8465–8471.
- (238) Mayer, R. J.; Que, L., Jr. *J. Biol. Chem.* **1984**, *259*, 13056–13060.
- (239) Ridder, L.; Briganti, F.; Boersma, M. G.; Boeren, S.; Vis, E. H.; Scozzafava, A.; Veeger, C.; Rietjens, I. M. C. M. *Eur. J. Biochem.* **1998**, *257*, 92–100.
- (240) Pierpont, C. G.; Lange, C. W. *Prog. Inorg. Chem.* **1994**, *41*, 331–442.
- (241) Funabiki, T.; Mizoguchi, A.; Sugimoto, T.; Tada, S.; Tsuji, M.; Sakamoto, H.; Yoshida, S. *J. Am. Chem. Soc.* **1986**, *108*, 2921–2932.
- (242) Funabiki, T.; Sakamoto, H.; Yoshida, S.; Tamara, K. *J. Chem. Soc., Chem. Commun.* **1979**, 754–755.
- (243) Ito, M.; Que, L., Jr. *Angew. Chem., Int. Ed. Engl.* **1997**, *36*, 1342–1344.
- (244) Dei, A.; Gatteschi, D.; Pardi, L. *Inorg. Chem.* **1993**, *32*, 1389–1395.
- (245) Ogihara, T.; Hikichi, S.; Akita, M.; Moro-oka, Y. *Inorg. Chem.* **1998**, *37*, 2614–2615.
- (246) Pascaly, M.; Duda, M.; Rompel, A.; Sift, B. H.; Meyer-Klaucke, W.; Krebs, B. *Inorg. Chim. Acta* **1999**, *291*, 289–299.
- (247) Que, L., Jr. *Chem. Rev.* **1996**, *96*, 2607–2624.
- (248) Que, L., Jr.; Kolanczyk, R. C.; White, L. S. *J. Am. Chem. Soc.* **1987**, *109*, 5373–5380.
- (249) Cox, D. D.; Que, L., Jr. *J. Am. Chem. Soc.* **1988**, *110*, 8085–8092.
- (250) Jang, H. G.; Cox, D. D.; Que, L., Jr. *J. Am. Chem. Soc.* **1991**, *113*, 9200–9204.
- (251) Wasinger, E. C.; Davis, M. I.; Westre, T. E.; Zaleski, J. M.; Orville, A. M.; Lipscomb, J. D.; Hedman, B.; Hodgson, K. O.; Solomon, E. I. Unpublished results.
- (252) Karpishin, T. B.; Gebhard, M. S.; Solomon, E. I.; Raymond, K. N. *J. Am. Chem. Soc.* **1991**, *113*, 2977–2984.
- (253) Tatsuno, Y.; Saeki, Y.; Nozaki, M.; Otsuka, S.; Maeda, Y. *FEBS Lett.* **1980**, *112*, 83–85.
- (254) Boldt, Y. R.; Sadowsky, M. J.; Ellis, L. B. M.; Que, L., Jr.; Wackett, L. P. *J. Bacteriol.* **1995**, *177*, 1225–1232.
- (255) Que, L., Jr.; Widom, J.; Crawford, R. L. *J. Biol. Chem.* **1981**, *256*, 10941–10944.
- (256) Whiting, A. K.; Boldt, Y. R.; Hendrich, M. P.; Wackett, L. P.; Que, L., Jr. *Biochemistry* **1996**, *35*, 160–170.
- (257) Bertini, I.; Briganti, F.; Mangani, S.; Nolting, H. F.; Scozzafava, A. *Coord. Chem. Rev.* **1995**, *144*, 321–345.
- (258) Hrywna, Y.; Tsoi, T. V.; Maltseva, O. V.; Quensen, J. F., III; Tiedje, J. M. *Appl. Environ. Microbiol.* **1999**, *65*, 2163–2169.
- (259) Brühlmann, F.; Chen, W. *Biotechnol. Bioeng.* **1999**, *63*, 544–551.
- (260) Nakai, C.; Hori, K.; Kagamiyama, H.; Nakazawa, T.; Nozaki, M. *J. Biol. Chem.* **1983**, *258*, 2916–2922.
- (261) Kojima, Y.; Itada, N.; Hayaishi, O. *J. Biol. Chem.* **1961**, *236*, 2223–2228.
- (262) Wallis, M. G.; Chapman, S. K. *Biochem. J.* **1990**, *266*, 605–609.
- (263) Kaschabek, S. R.; Kasberg, T.; Müller, D.; Mars, A. E.; Janssen, D. B.; Reineke, W. *J. Bacteriol.* **1998**, *180*, 296–302.
- (264) Wogel, S. A.; Dege, J. E.; Perkins-Olson, P. E.; Juarez-Garcia, C. H.; Crawford, R. L.; Münck, E.; Lipscomb, J. D. *J. Bacteriol.* **1993**, *175*, 4414–4426.
- (265) Senoh, S.; Kita, H.; Kamimoto, M. In *Biological and Chemical Aspects of Oxygenases*; Bloch, K., Hayaishi, O., Eds.; Maruzen: Tokyo, 1966; pp 378–389.
- (266) Bugg, T. D. *Biochim. Biophys. Acta* **1993**, *1202*, 258–264.
- (267) Xu, L.; Resing, K.; Lawson, S. L.; Babbitt, P. C.; Copley, S. D. *Biochemistry* **1999**, *38*, 7659–7669.
- (268) Happe, B.; Eltis, L. D.; Poth, H.; Hedderich, R.; Timmis, K. N. *J. Bacteriol.* **1993**, *175*, 7313–7320.
- (269) Eltis, L. D.; Hofmann, B.; Hecht, H.-J.; Lünsdorf, H.; Timmis, K. N. *J. Biol. Chem.* **1993**, *268*, 2727–2732.
- (270) Kuhm, A. E.; Stolz, A.; Ngai, K.-L.; Knackmuss, H.-J. *J. Bacteriol.* **1991**, *173*, 3795–3802.

- (271) Adachi, K.; Iwayama, Y.; Tanioka, H.; Takeda, Y. *Biochim. Biophys. Acta* **1966**, *118*, 88–97.
- (272) Harpel, M. R.; Lipscomb, J. D. *J. Biol. Chem.* **1990**, *265*, 6301–6311.
- (273) Crawford, R. L.; Hutton, S. W.; Chapman, P. J. *J. Bacteriol.* **1975**, *121*, 794–799.
- (274) Malherbe, P.; Köhler, C.; Prada, M. d.; Lang, G.; Kiefer, V.; Schwarcz, R.; Lahm, H.-W.; Cesura, A. M. *J. Biol. Chem.* **1994**, *269*, 13792–13797.
- (275) Eltis, L. D.; Bolin, J. T. *J. Bacteriol.* **1996**, *178*, 5930–5937.
- (276) Heiss, G.; Stolz, A.; Kuhm, A. E.; Müller, C.; Klein, J.; Altenbuchner, J.; Knackmuss, H.-J. *J. Bacteriol.* **1995**, *177*, 5865–5871.
- (277) Spence, E. L.; Kawamukai, M.; Sanvoisin, J.; Braven, H.; Bugg, T. D. H. *J. Bacteriol.* **1996**, *178*, 5249–5256.
- (278) Han, S.; Eltis, L. D.; Timmis, K. N.; Muchmore, S. W.; Bolin, J. T. *Science* **1995**, *270*, 976–980.
- (279) Takemori, S.; Komiyama, T.; Katagiri, M. *Eur. J. Biochem.* **1971**, *23*, 178–184.
- (280) Nozaki, M.; Kagamiyama, H.; Hayaishi, O. *Biochem. Z.* **1963**, *23*, 582–590.
- (281) Hegg, E. L.; Que, L., Jr. *Eur. J. Biochem.* **1997**, *250*, 625–629.
- (282) Boldt, Y. R.; Whiting, A. K.; Wagner, M. L.; Sadowsky, M. J.; Que, L., Jr.; Wackett, L. P. *Biochemistry* **1997**, *36*, 2147–2153.
- (283) Harpel, M. R.; Lipscomb, J. D. *J. Biol. Chem.* **1990**, *265*, 22187–22196.
- (284) Beltrán-Valero de Bernabé, D.; Granadino, B.; Chiarelli, I.; Porfirio, B.; Mayatepek, E.; Aquaron, R.; Moore, M. M.; Festen, J. J. M.; Sanmarti, R.; Penalva, M. A.; Rodríguez de Córdoba, S. *Am. J. Hum. Genet.* **1998**, *62*, 776–784.
- (285) Beltrán-Valero de Bernabé, D.; Jimenez, F. J.; Aquaron, R.; Rodríguez de Córdoba, S. *Am. J. Hum. Genet.* **1999**, *64*, 1316–1322.
- (286) Bugg, T. D. H.; Sanvoisin, J.; Spence, E. L. *Biochem. Soc. Trans.* **1997**, *25*, 81–85.
- (287) Hori, K.; Hashimoto, T.; Nozaki, M. *J. Biochem.* **1973**, *74*, 375–384.
- (288) Nozaki, M.; Ono, K.; Nakazawa, T.; Kotani, S.; Hayaishi, O. *J. Biol. Chem.* **1968**, *243*, 2682–2690.
- (289) Vaillancourt, F. H.; Han, S.; Fortin, P. D.; Bolin, J. T.; Eltis, L. D. *J. Biol. Chem.* **1998**, *273*, 34887–34895.
- (290) Wogel, S. A. Ph.D. Thesis, University of Minnesota, 1989.
- (291) Arciero, D. M.; Orville, A. M.; Lipscomb, J. D. *J. Biol. Chem.* **1985**, *260*, 14035–14044.
- (292) Miller, M.; Lipscomb, J. D. *J. Biol. Chem.* **1996**, *271*, 5524–5535.
- (293) Kobayashi, T.; Ishida, T.; Horiike, K.; Takahara, Y.; Numao, N.; Nakazawa, A.; Nakazawa, T.; Nozaki, M. *J. Biochem.* **1995**, *117*, 614–622.
- (294) Cerdan, P.; Wasserfallen, A.; Rekik, M.; Timmis, K. N.; Harayama, S. *J. Bacteriol.* **1994**, *176*, 6074–6081.
- (295) Cerdan, P.; Rekik, M.; Harayama, S. *Eur. J. Biochem.* **1995**, *229*, 113–118.
- (296) Bartels, I.; Knackmuss, H.-J.; Reineke, W. *Appl. Environ. Microbiol.* **1984**, *47*, 500–505.
- (297) Klecka, G. M.; Gibson, D. T. *Appl. Environ. Microbiol.* **1981**, *21*, 1159–1165.
- (298) Senda, T.; Sugiyama, K.; Narita, H.; Yamamoto, T.; Kimbara, K.; Fukuda, M.; Sato, M.; Yano, K.; Mitsui, Y. *J. Mol. Biol.* **1996**, *255*, 735–752.
- (299) Bolin, J. T. Personal communication.
- (300) Sugiyama, K.; Senda, T.; Narita, H.; Yamamoto, T.; Kimbara, K.; Fukuda, M.; Yano, K.; Mitsui, Y. *Proc. Jpn. Acad., Ser. B* **1995**, *71*, 32–35.
- (301) Sugimoto, K.; Senda, T.; Aoshima, H.; Masai, E.; Fukuda, M.; Mitsui, Y. *Struct. Folding Design* **1999**, *7*, 953–965.
- (302) Kita, A.; Kita, S.-i.; Fujisawa, I.; Inaka, K.; Ishida, T.; Horiike, K.; Nozaki, M.; Miki, K. *Structure* **1998**, *7*, 25–34.
- (303) Bertini, I.; Capozzi, F.; Dikiy, A.; Happe, B.; Luchinat, C.; Timmis, K. N. *Biochem. Biophys. Res. Commun.* **1995**, *215*, 855–860.
- (304) Mabrouk, P. A.; Orville, A. M.; Lipscomb, J. D. *J. Am. Chem. Soc.* **1991**, *113*, 4053–4061.
- (305) Davis, M. I.; Orville, A. M.; Lipscomb, J. D.; Solomon, E. I. Unpublished results.
- (306) Bertini, I.; Briganti, F.; Mangani, S.; Nolting, H. F.; Scozzafava, A. *Biochemistry* **1994**, *33*, 10777–10784.
- (307) Chiou, Y. M.; Que, L., Jr. *Inorg. Chem.* **1995**, *34*, 3577–3578.
- (308) Bertini, I.; Briganti, F.; Mangani, S.; Nolting, H. F.; Scozzafava, A. *FEBS Lett.* **1994**, *350*, 207–212.
- (309) Arciero, D. M.; Lipscomb, J. D. *J. Biol. Chem.* **1986**, *261*, 2170–2178.
- (310) Brown, C. A.; Pavlovsky, M. A.; Westre, T. E.; Zhang, Y.; Hedman, B.; Hodgson, K. O.; Solomon, E. I. *J. Am. Chem. Soc.* **1995**, *117*, 715–732.
- (311) Spence, E. L.; Langley, G. J.; Bugg, T. D. H. *J. Am. Chem. Soc.* **1996**, *118*, 8336–8343.
- (312) Suckling, C. J. *Angew. Chem., Int. Ed. Engl.* **1988**, *27*, 537–552.
- (313) Hirose, J.; Kimura, N.; Suyama, A.; Kobayashi, A.; Hayashida, S.; Furukawa, K. *FEMS Microbiol. Lett.* **1994**, *118*, 273–278.
- (314) Zabinski, R.; Munck, E.; Champion, P. M.; Wood, J. M. *Biochemistry* **1972**, *11*, 3212–3219.
- (315) Sanvoisin, J.; Langley, G. J.; Bugg, T. D. H. *J. Am. Chem. Soc.* **1995**, *117*, 7836–7837.
- (316) Weiner, H.; Hayashi, Y.; Finke, R. G. *Inorg. Chim. Acta* **1999**, *291*, 426–437.
- (317) Kaufman, S. *Adv. Enzymol.* **1971**, *35*, 245–319.
- (318) Shiman, R. In *Chemistry and Biochemistry of Pterins*; Blakley, R. L., Benkovic, S. J., Eds.; Wiley: New York, 1985; Vol. 2 (Folates and Pterins), pp 179–249.
- (319) Kaufman, S. *Adv. Enzymol. Relat. Areas Mol. Biol.* **1993**, *67*, 77–264.
- (320) Kaufman, S. *Adv. Enzymol. Relat. Areas Mol. Biol.* **1995**, *70*, 103–220.
- (321) Nair, P. M.; Vaidyanathan, C. S. *Biochim. Biophys. Acta* **1965**, *110*, 521–531.
- (322) Baran, H.; Schwarcz, R. *Adv. Exp. Med. Biol.* **1991**, *294*, 485–488.
- (323) Kuhn, D. M.; Lovenberg, W. In *Chemistry and Biochemistry of Pterins*; Blakley, R. L., Benkovic, S. J., Eds.; Wiley: New York, 1985; Vol. 2 (Folates and Pterins), pp 353–382.
- (324) Moran, G. R.; Daubner, S. C.; Fitzpatrick, P. F. *J. Biol. Chem.* **1998**, *273*, 12259–12266.
- (325) Bhat, S. G.; Vaidyanathan, C. S. *Arch. Biochem. Biophys.* **1976**, *176*, 314–323.
- (326) Hufton, S. E.; Jennings, I. G.; Cotton, R. G. H. *Biochem. J.* **1995**, *311*, 353–366.
- (327) Flatmark, T.; Stevens, R. C. *Chem. Rev.* **1999**, *99*, 2137–2160.
- (328) Fitzpatrick, P. F. *Annu. Rev. Biochem.* **1999**, *68*, 355–381.
- (329) Weinstein, M.; Eisensmith, R. C.; Abadie, V.; Avigad, S.; Lyonnet, S.; Schwartz, G.; Munnich, A.; Woo, S. L. C.; Shiloh, Y. *Hum. Genet.* **1993**, *90*, 645–649.
- (330) Eiken, H. G.; Knappskog, P. M.; Apold, J.; Flatmark, T. *Hum. Mutat.* **1996**, *7*, 228–238.
- (331) Knappskog, P. M.; Eiken, H. G.; Martinez, A.; Bruland, O.; Apold, J.; Flatmark, T. *Hum. Mutat.* **1996**, *8*, 236–246.
- (332) Ellingsen, S.; Knappskog, P. M.; Eiken, H. G. *Hum. Mutat.* **1997**, *9*, 88–90.
- (333) Bjørge, E.; Knappskog, P. M.; Martinez, A.; Stevens, R. C.; Flatmark, T. *Eur. J. Biochem.* **1998**, *257*, 1–10.
- (334) Waters, P. J.; Parniak, M. A.; Akerman, B. R.; Jones, A. O.; Scriver, C. R. *J. Inherited Metab. Dis.* **1999**, *22*, 208–212.
- (335) Carr, R. T.; Balasubramanian, S.; Hawkins, P. C. D.; Benkovic, S. J. *Biochemistry* **1995**, *34*, 7525–7532.
- (336) Chen, D.; Frey, P. A. *J. Biol. Chem.* **1998**, *273*, 25594–25601.
- (337) Kaufman, S.; Pollock, R. J.; Summer, G. K.; Das, A. K.; Hajra, A. K. *Biochim. Biophys. Acta* **1990**, *1040*, 19–27.
- (338) Taguchi, H.; Paal, B.; Armarego, W. L. F. *Pteridines* **1995**, *6*, 45–57.
- (339) Armarego, W. L. F. *Pteridines* **1996**, *7*, 90.
- (340) Fisher, D. B.; Kirkwood, R.; Kaufman, S. *J. Biol. Chem.* **1972**, *247*, 5161–5167.
- (341) Gottschall, D. W.; Dietrich, R. F.; Benkovic, S. J.; Shiman, R. *J. Biol. Chem.* **1982**, *257*, 845–849.
- (342) Tourian, A. *Biochim. Biophys. Acta* **1971**, *242*, 345–354.
- (343) Shiman, R. *J. Biol. Chem.* **1980**, *255*, 10029–10032.
- (344) Shiman, R.; Gray, D. W. *J. Biol. Chem.* **1980**, *255*, 4793–4800.
- (345) Shiman, R.; Xia, T.; Hill, M. A.; Gray, D. W. *J. Biol. Chem.* **1994**, *269*, 24647–24656.
- (346) Kappock, T. J.; Harkins, P. C.; Friedenber, S.; Caradonna, J. P. *J. Biol. Chem.* **1995**, *270*, 30532–30544.
- (347) Fisher, D. B.; Kaufman, S. *J. Biol. Chem.* **1973**, *248*, 4345–4353.
- (348) Parniak, M. A.; Kaufman, S. *J. Biol. Chem.* **1981**, *256*, 6876–6882.
- (349) Phillips, R. S.; Parniak, M. A.; Kaufman, S. *Biochemistry* **1984**, *23*, 3836–3842.
- (350) Døskeland, A. P.; Døskeland, S. O.; Øgreid, D.; Flatmark, T. *J. Biol. Chem.* **1984**, *259*, 11242–11248.
- (351) Xia, T.; Gray, D. W.; Shiman, R. *J. Biol. Chem.* **1994**, *269*, 24657–24665.
- (352) Marota, J. J. A.; Shiman, R. *Biochemistry* **1984**, *23*, 1303–1311.
- (353) Wallick, D. E.; Bloom, L. M.; Gaffney, B. J.; Benkovic, S. J. *Biochemistry* **1984**, *23*, 1295–1302.
- (354) Hill, M. A.; Marota, J. J. A.; Shiman, R. *J. Biol. Chem.* **1988**, *263*, 5646–5655.
- (355) Shiman, R.; Gray, D. W.; Hill, M. A. *J. Biol. Chem.* **1994**, *269*, 24637–24646.
- (356) Dix, T. A.; Benkovic, S. J. *Biochemistry* **1985**, *24*, 5839–5846.
- (357) Bloom, L. M.; Benkovic, S. J.; Gaffney, B. J. *Biochemistry* **1986**, *25*, 4204–4210.
- (358) Lazarus, R. A.; DeBrosse, C. W.; Benkovic, S. J. *J. Am. Chem. Soc.* **1982**, *104*, 6869–6871.
- (359) Dix, T. A.; Bollag, G. E.; Domanico, P. L.; Benkovic, S. J. *Biochemistry* **1985**, *24*, 2955–2958.
- (360) Siegmund, H.-U.; Kaufman, S. *J. Biol. Chem.* **1991**, *266*, 2903–2910.
- (361) Fitzpatrick, P. F. *Biochemistry* **1991**, *30*, 3658–3662.

- (362) Bailey, S. W.; Dillard, S. B.; Ayling, J. E. *Biochemistry* **1991**, *30*, 10226–10235.
- (363) Lazarus, R. A.; Dietrich, R. F.; Wallick, D. E.; Benkovic, S. J. *Biochemistry* **1981**, *20*, 6834–6841.
- (364) Davis, M. D.; Kaufman, S. *Arch. Biochem. Biophys.* **1993**, *304*, 9–16.
- (365) Erlandsen, H.; Fusetti, F.; Martinez, A.; Hough, E.; Flatmark, T.; Stevens, R. C. *Nat. Struct. Biol.* **1997**, *4*, 995–1000.
- (366) Fusetti, F.; Erlandsen, H.; Flatmark, T.; Stevens, R. C. *J. Biol. Chem.* **1998**, *273*, 16962–16967.
- (367) Gibbs, B. S.; Wojchowski, D.; Benkovic, S. J. *J. Biol. Chem.* **1993**, *268*, 8046–8052.
- (368) Kobe, B.; Jennings, I. G.; House, C. M.; Michell, B. J.; Goodwill, K. E.; Santarsiero, B. D.; Stevens, R. C.; Cotton, R. G. H.; Kemp, B. E. *Nat. Struct. Biol.* **1999**, *6*, 442–448.
- (369) Goodwill, K. E.; Sabatier, C.; Marks, C.; Raag, R.; Fitzpatrick, P. F.; Stevens, R. C. *Nat. Struct. Biol.* **1997**, *4*, 578–585.
- (370) Goodwill, K. E.; Sabatier, C.; Stevens, R. C. *Biochemistry* **1998**, *37*, 13437–13445.
- (371) Ellis, H. R.; Daubner, S. C.; McCulloch, R. I.; Fitzpatrick, P. F. *Biochemistry* **1999**, *38*, 10909–10914.
- (372) Erlandsen, H.; Flatmark, T.; Stevens, R. C.; Hough, E. *Biochemistry* **1998**, *37*, 15638–15646.
- (373) Cox, D. D.; Benkovic, S. J.; Bloom, L. M.; Bradley, F. C.; Nelson, M. J.; Que, L., Jr.; Wallick, D. E. *J. Am. Chem. Soc.* **1988**, *110*, 2026–2032.
- (374) Andersson, K. K.; Cox, D. D.; Que, L., Jr.; Flatmark, T.; Haavik, J. *J. Biol. Chem.* **1988**, *263*, 18621–18626.
- (375) Kemsley, J. N.; Mitic, N.; Loeb Zaleski, K.; Caradonna, J. P.; Solomon, E. I. *J. Am. Chem. Soc.* **1999**, *121*, 1528–1536.
- (376) Martinez, A.; Olafsdottir, S.; Flatmark, T. *Eur. J. Biochem.* **1993**, *211*, 259–266.
- (377) Martinez, A.; Abeygunawardana, C.; Haavik, J.; Flatmark, T.; Mildvan, A. S. *Biochemistry* **1993**, *32*, 1–6390.
- (378) Dix, T. A.; Benkovic, S. J. *Acc. Chem. Res.* **1988**, *21*, 101–107.
- (379) Lange, S. J.; Miyake, H.; Que, L., Jr. *J. Am. Chem. Soc.* **1999**, *121*, 6330–6331.
- (380) Francisco, W. A.; Tian, G.; Fitzpatrick, P. F.; Klinman, J. P. *J. Am. Chem. Soc.* **1998**, *120*, 4057–4062.
- (381) Fitzpatrick, P. F. *Biochemistry* **1991**, *30*, 6386–6391.
- (382) Guroff, G.; Daly, J. W.; Jerina, D. M.; Renson, J.; Witkop, B.; Udenfriend, S. *Science* **1967**, *157*, 1524–1530.
- (383) De Carolis, E.; De Luca, V. *Phytochemistry* **1994**, *36*, 1093–1107.
- (384) Hedden, P. *Biochem. Soc. Trans.* **1992**, *20*, 373–377.
- (385) Prescott, A. G. *J. Exp. Bot.* **1993**, *44*, 849–861.
- (386) Kivirikko, K. I.; Myllylä, R. In *The Enzymology of Posttranslational Modification of Proteins*; Freedman, R. B., Hawkins, H. C., Eds.; Academic: London, 1980; Vol. 1, pp 53–104.
- (387) Chrispeels, M. J. *Methods Enzymol.* **1984**, *107*, 361.
- (388) Wang, Q.; VanDusen, W. J.; Petroski, C. J.; Garsky, V. M.; Stern, A. M.; Friedman, P. A. *J. Biol. Chem.* **1991**, *253*, 1654.
- (389) Hulse, J. D.; Ellis, S. R.; Henderson, L. M. *J. Biol. Chem.* **1978**, *253*, 1654.
- (390) Lindstedt, G.; Lindstedt, S.; Nordin, I. *Biochemistry* **1977**, *16*, 2181.
- (391) Holme, E. *Biochemistry* **1975**, *14*, 4.
- (392) Bankel, L.; Holme, E.; Lindstedt, G.; Lindstedt, S. *FEBS Lett.* **1972**, *21*, 135.
- (393) Streber, W. R.; Timmis, K. N.; Zenk, M. H. *J. Bacteriol.* **1987**, *169*, 2950–2955.
- (394) Fukumori, F.; Hausinger, R. P. *J. Biol. Chem.* **1993**, *268*, 24311–24317.
- (395) Thornburg, L. D.; Lai, M.-T.; Wishnok, J. S.; Stubbe, J. *Biochemistry* **1993**, *32*, 14023–14033.
- (396) Baldwin, J. E.; Abraham, E. *Nat. Prod. Rep.* **1988**, *5*, 129–145.
- (397) Baldwin, J. E.; Merritt, K. D.; Schofield, C. J.; Elson, S. W.; Baggaley, K. H. *J. Chem. Soc., Chem. Commun.* **1993**, 1301–1302.
- (398) Elson, S. W.; Baggaley, K. H.; Gillett, J.; Holland, S.; Nicholson, N. H.; Sime, J. T.; Woronicki, S. R. *J. Chem. Soc., Chem. Commun.* **1987**, 1736–1740.
- (399) Krol, W. J.; Basak, A.; Salowe, S. P.; Townsend, C. A. *J. Am. Chem. Soc.* **1989**, *111*, 7625–7627.
- (400) Kovacevic, S.; Miller, J. R. *J. Bacteriol.* **1991**, *173*, 398.
- (401) Salowe, S. P.; Marsh, E. N.; Townsend, C. A. *Biochemistry* **1990**, *29*, 6499–6508.
- (402) Marsh, E. N.; Chang, M. D.-T.; Townsend, C. A. *Biochemistry* **1992**, *31*, 12648–12657.
- (403) Roach, P. L.; Clifton, I. J.; Fülöp, V.; Harlos, K.; Barton, G. J.; Hajdu, J.; Andersson, I.; Schofield, C. J.; Baldwin, J. E. *Nature* **1995**, *375*, 700–704.
- (404) Britsch, L.; Dedio, J.; Saedler, H.; Forkmann, G. *Eur. J. Biochem.* **1993**, *217*, 745–754.
- (405) Lukacin, R.; Britsch, L. *Eur. J. Biochem.* **1997**, *249*, 748–757.
- (406) Baldwin, J. E.; Bradley, M. *Chem. Rev.* **1990**, *90*, 1079–1088.
- (407) Baldwin, J. E.; Lynch, G. P.; Schofield, C. J. *J. Chem. Soc., Chem. Commun.* **1991**, 736.
- (408) Abeles, F. B.; Morgan, P. W.; Saltveit, M. E., Jr. *Ethylene in Plant Biology*; Academic: San Diego, CA, 1992.
- (409) Kende, H. *Annu. Rev. Plant Physiol. Plant Mol. Biol.* **1993**, *44*, 283–307.
- (410) Adams, D. O.; Yang, S. F. *Proc. Natl. Acad. Sci. U.S.A.* **1979**, *76*, 170–174.
- (411) John, P. *Physiol. Plant.* **1997**, *100*, 583–592.
- (412) Dong, J. G.; Fernandez-Maculet, J. C.; Yang, S. F. *Proc. Natl. Acad. Sci. U.S.A.* **1992**, *89*, 9789–9793.
- (413) Tuderman, L.; Myllylä, R.; Kivirikko, K. I. *Eur. J. Biochem.* **1977**, *80*, 341–348.
- (414) Myllylä, R.; Tuderman, L.; Kivirikko, K. I. *Eur. J. Biochem.* **1977**, *80*, 349–357.
- (415) Puistola, U.; Turpeenniemi-Hujanen, T. M.; Myllylä, R.; Kivirikko, K. I. *Biochim. Biophys. Acta* **1980**, *611*, 40–50.
- (416) Holme, E.; Lindstedt, S.; Nordin, I. *Biochem. Biophys. Res. Commun.* **1982**, *107*, 518–524.
- (417) Webbie, R. S.; Punekar, N. S.; Lardy, H. A. *Biochemistry* **1988**, *27*, 2222–2228.
- (418) Hsu, C.-A.; Saewert, M. D.; Polsinelli, L. F., Jr.; Abbott, M. T. *J. Biol. Chem.* **1981**, *256*, 6098–6101.
- (419) Myllylä, R.; Majamaa, K.; Günzler, V.; Hanauske-Abel, H. M.; Kivirikko, K. I. *J. Biol. Chem.* **1984**, *259*, 5403–5405.
- (420) Myllylä, R.; Kuutti-Savolainen, E.-R.; Kivirikko, K. I. *Biochem. Biophys. Res. Commun.* **1977**, *83*, 441–448.
- (421) Valegard, K.; Vansheltinga, A. C. T.; Lloyd, M. D.; Hara, T.; Ramaswamy, S.; Perrakis, A.; Thompson, A.; Lee, H. J.; Baldwin, J. E.; Schofield, C. J.; Hajdu, J.; Andersson, I. *Nature* **1998**, *394*, 805–809.
- (422) Roach, P. L.; Clifton, I. J.; Hensgens, C. M. H.; Shibata, N.; Schofield, C. J.; Hajdu, J.; Baldwin, J. E. *Nature* **1997**, *387*, 827–830.
- (423) De Jong, L.; Albracht, S. P. J.; Kemp, A. *Biochim. Biophys. Acta* **1982**, *704*, 326–331.
- (424) Whiting, A. K.; Que, L., Jr.; Saari, R. E.; Hausinger, R. P.; Fredrick, M. A.; McCracken, J. *J. Am. Chem. Soc.* **1997**, *119*, 3413–3414.
- (425) Pavel, E. G.; Zhou, J.; Busby, R. W.; Gunsior, M.; Townsend, C. A.; Solomon, E. I. *J. Am. Chem. Soc.* **1998**, *120*, 743–753.
- (426) Chiou, Y.-M.; Que, L., Jr. *J. Am. Chem. Soc.* **1995**, *117*, 3999–4013.
- (427) Ng, S.-F.; Hanauske-Abel, H. M.; Englard, S. *J. Biol. Chem.* **1991**, *266*, 1526–1533.
- (428) Majamaa, K.; Hanauske-Abel, H. M.; Günzler, V.; Kivirikko, K. I. *Eur. J. Biochem.* **1984**, *138*, 239–245.
- (429) Zhou, J.; Gunsior, M.; Bachmann, B. O.; Townsend, C. A.; Solomon, E. I. *J. Am. Chem. Soc.* **1998**, *120*, 13539–13540.
- (430) Zhou, J.; Gunsior, M.; Kelly, K.; Bachmann, B. O.; Townsend, C. A.; Solomon, E. I. *J. Am. Chem. Soc.* **1999**, submitted.
- (431) Ming, L.-J.; Que, L., Jr.; Kriauciunas, A.; Frolik, C. A.; Chen, V. J. *Biochemistry* **1991**, *30*, 11653.
- (432) Jiang, F.; Peisach, J.; Ming, L.-J.; Que, L., Jr.; Chen, V. J. *Biochemistry* **1991**, *30*, 11437.
- (433) Ming, L.-J.; Que, L., Jr.; Kriauciunas, A.; Frolik, C. A.; Chen, V. J. *Inorg. Chem.* **1990**, *29*, 1111.
- (434) Randall, C. R.; Zang, Y.; True, A. E.; Que, L., Jr.; Charnock, J. M.; Garner, C. D.; Fujishima, Y.; Schofield, C. J.; Baldwin, J. E. *Biochemistry* **1993**, *32*, 6664.
- (435) Rocklin, A. M.; Tierney, D. L.; Kofman, V.; Brunhuber, N. M. W.; Hoffman, B. M.; Christoffersen, R. E.; Reich, N. O.; Lipscomb, J. D.; Que, L., Jr. *Proc. Natl. Acad. Sci. U.S.A.* **1999**, *96*, 7905–7909.
- (436) Hanauske-Abel, H. M.; Günzler, V. *J. Theor. Biol.* **1982**, *94*, 421–455.
- (437) Wu, M.; Moon, H.-S.; Begley, T. P. *J. Am. Chem. Soc.* **1999**, *121*, 587–588.
- (438) Zhang, Z.; Barlow, J. N.; Baldwin, J. E.; Schofield, C. J. *Biochemistry* **1997**, *36*, 15999–16007.
- (439) Pirrung, M. C.; Cao, J.; Chen, J. *Chem. Biol.* **1998**, *5*, 49–57.
- (440) Zhou, J.; Rocklin, A. M.; Lipscomb, J. D.; Que, L., Jr.; Solomon, E. I. Unpublished results.
- (441) Link, T. A. In *Advances in Inorganic Chemistry*; Academic: New York, 1999; Vol. 47, pp 83–157.
- (442) Bertini, I.; Cermonini, M. A.; Ferretti, S.; Lozzi, I.; Luchinat, C.; Viezzoli, M. S. *Coord. Chem. Rev.* **1996**, *151*, 145–160.
- (443) Ballou, D.; Batie, C. *Prog. Clin. Biol. Res.* **1988**, *274*, 211–26.
- (444) Crutcher, S. E.; Geary, P. J. *Biochem. J.* **1979**, *177*, 393–400.
- (445) Batie, C. J.; LaHaie, E.; Ballou, D. P. *J. Biol. Chem.* **1987**, *262*, 1510–1518.
- (446) Gibson, D. T.; Yeh, W.-K.; Liu, T.-N.; Subramanian, V. In *Oxygenases and Oxygen Metabolism*; Nozaki, M., Yamamoto, S., Ishimura, Y., Coon, M. J., Ernster, L., Estabrook, R. W., Eds.; Academic: New York, 1982; pp 51–62.
- (447) Ensley, B. D.; Gibson, D. T. *J. Bacteriol.* **1983**, *155*, 505–511.
- (448) Bundy, B. M.; Campbell, A. L.; Neidle, E. L. *J. Bacteriol.* **1998**, *180*, 4466–4474.
- (449) Markus, A.; Krekel, D.; Lingens, F. *J. Biol. Chem.* **1986**, *261*, 12883–12888.
- (450) Bernhardt, F.-H.; Heymann, E.; Traylor, P. S. *Eur. J. Biochem.* **1978**, *92*, 209–223.

- (451) Correll, C. C.; Batie, C. J.; Ballou, D. P.; Ludwig, M. L. *Science* **1992**, *258*, 1604–1610.
- (452) Lee, K. *J. Bacteriol.* **1999**, *181*, 2719–2725.
- (453) Kauppi, B.; Lee, K.; Carredano, E.; Parales, R. E.; Gibson, D. T.; Eklund, H.; Ramaswamy, S. *Structure* **1998**, *6*, 571–586.
- (454) Carredano, E.; Kauppi, B.; Choudhury, D.; Parales, R. E.; Lee, K.; Gibson, D. T.; Eklund, H.; Ramaswamy, S. *J. Inorg. Biochem.* **1999**, *74*, 21.
- (455) Parales, R. E.; Parales, J. V.; Gibson, D. T. *J. Bacteriol.* **1999**, *181*, 1831–1837.
- (456) Gurbiel, R. J.; Batie, C. J.; Sivaraja, M.; True, A. E.; Fee, J. A.; Hoffman, B. M.; Ballou, D. P. *Biochemistry* **1989**, *28*, 4861–4871.
- (457) Kuila, D.; Schoonover, J. R.; Dyer, R. B.; Batie, C. J.; Ballou, D. P.; Fee, J. A.; Woodruff, W. H. *Biochim. Biophys. Acta* **1992**, *1140*, 175–183.
- (458) Kuila, D.; Fee, J. A.; Schoonover, J. R.; Woodruff, W. H.; Batie, C. J.; Ballou, D. P. *J. Am. Chem. Soc.* **1987**, *109*, 1559–1561.
- (459) Cline, J. F.; Hoffman, B. M.; Mims, W. B.; LaHaie, E.; Ballou, D. P.; Fee, J. A. *J. Biol. Chem.* **1985**, *260*, 3251–3254.
- (460) Tsang, H. T.; Batie, C. J.; Ballou, D. P.; Penner-Hahn, J. E. *Biochemistry* **1989**, *28*, 7233–7240.
- (461) Penner-Hahn, J. E. In *Synchrotron Radiation in Structural Biology*; Sweet, R. M., Woodhead, A. D., Eds.; Plenum: New York, 1989; Vol. 51 (Basic Life Sciences), pp 177–186.
- (462) Axcell, B. C.; Geary, P. J. *Biochem. J.* **1975**, *146*, 173.
- (463) Geary, P. J.; Saboowalla, F.; Patil, D.; Cammack, R. *Biochem. J.* **1984**, *217*, 667.
- (464) Fee, J. A.; Findling, K. L.; Yoshida, T.; Hille, R.; Tarr, G. E.; Hearshen, D. O.; Dunham, W. R.; Day, E. P.; Kent, T. A.; Münck, E. *J. Biol. Chem.* **1984**, *259*, 124–133.
- (465) Gurbiel, R. J.; Ohnishi, T.; Robertson, D. E.; Daldal, F.; Hoffman, B. M. *Biochemistry* **1991**, *30*, 11579–11584.
- (466) Tsang, H.-T.; Batie, C. J.; Ballou, D. P.; Penner-Hahn, J. E. *J. Biol. Inorg. Chem.* **1996**, *1*, 24–33.
- (467) Coulter, E. D.; Moon, N.; Batie, C. J.; Dunham, W. R.; Ballou, D. P. *Biochemistry* **1999**, *38*, 11062–11072.
- (468) Pavel, E. G.; Martins, L. J.; Ellis, W. R., Jr.; Solomon, E. I. *Chem. Biol.* **1994**, *1*, 173–183.
- (469) Bertini, I.; Luchinat, C.; Mincione, G.; Parigi, G.; Gassner, G. T.; Ballou, D. P. *J. Biol. Inorg. Chem.* **1996**, *1*, 468–475.
- (470) Umezawa, H. *Gann Monogr. Cancer Res.* **1976**, *19*, 3–36.
- (471) Hecht, S. M. *Acc. Chem. Res.* **1986**, *19*, 383–391.
- (472) Stubbe, J.; Kozarich, J. W. *Chem. Rev.* **1987**, *87*, 1107–1136.
- (473) Petering, D. H.; Byrnes, R. W.; Antholine, W. E. *Chem.-Biol. Interact.* **1990**, *73*, 133–182.
- (474) Stubbe, J.; Kozarich, J. W.; Wu, W.; Vanderwall, D. E. *Acc. Chem. Res.* **1996**, *29*, 322–330.
- (475) Petering, D. H.; Mao, Q.; Li, W.; DeRose, E.; Antholine, W. E. In *Probing of Nucleic Acids by Metal Ion Complexes of Small Molecules*; Sigel, A., Sigel, H., Eds.; Marcel Dekker: New York, 1996; Vol. 33 (Metal Ions in Biological Systems), pp 619–648.
- (476) Burger, R. M. *Chem. Rev.* **1998**, *98*, 1153–1169.
- (477) Claussen, C. A.; Long, E. C. *Chem. Rev.* **1999**, *99*, 2797–2816.
- (478) Radtke, K.; Lornitzo, F. A.; Byrnes, R. W.; Antholine, W. E.; Petering, D. H. *Biochem. J.* **1994**, *302*, 655–664.
- (479) Lazo, J. S.; Humphreys, C. J. *Proc. Natl. Acad. Sci. U.S.A.* **1983**, *80*, 3064–3068.
- (480) Hecht, S. M. *Bioconjugate Chem.* **1994**, *5*, 513–526.
- (481) Battigello, J.-M.; Cui, M.; Carter, B. J. In *Probing of Nucleic Acids by Metal Ion Complexes of Small Molecules*; Sigel, A., Sigel, H., Eds.; Marcel Dekker: New York, 1996; Vol. 33 (Metal Ions in Biological Systems), pp 593–617.
- (482) Lim, S. T.; Jue, C. K.; Moore, C. W.; Lipke, P. N. *J. Bacteriol.* **1995**, *177*, 3534–3539.
- (483) Murugesan, N.; Hecht, S. M. *J. Am. Chem. Soc.* **1985**, *107*, 493–500.
- (484) Padbury, G.; Sligar, S. G. *J. Biol. Chem.* **1985**, *260*, 7820–7823.
- (485) Povirk, L. F.; Wübker, W.; Köhnlein, W.; Hutchinson, F. *Nucleic Acids Res.* **1977**, *4*, 3573–3580.
- (486) Povirk, L. F.; Köhnlein, W.; Hutchinson, F. *Biochim. Biophys. Acta* **1978**, *521*, 126–133.
- (487) Burger, R. M.; Berkowitz, A. R.; Peisach, J.; Horwitz, S. B. *J. Biol. Chem.* **1980**, *255*, 11832–11838.
- (488) Breen, A. P.; Murphy, J. A. *Free Radical Biol. Med.* **1995**, *18*, 1033–1077.
- (489) Giloni, L.; Takeshita, M.; Johnson, F.; Iden, C.; Grollman, A. P. *J. Biol. Chem.* **1981**, *256*, 8608–8615.
- (490) Haidle, C. W.; Weiss, K. K.; Kuo, M. T. *Mol. Pharmacol.* **1972**, *8*, 531–537.
- (491) D'Andrea, A. D.; Haseltine, W. A. *Proc. Natl. Acad. Sci. U.S.A.* **1978**, *75*, 3608–3612.
- (492) Takeshita, M.; Kappen, L. S.; Grollman, A. P.; Eisenberg, M.; Goldberg, I. H. *Biochemistry* **1981**, *20*, 7599–7606.
- (493) Bailly, C.; Waring, M. J. *J. Am. Chem. Soc.* **1995**, *117*, 7311–7316.
- (494) Shipley, J. B.; Hecht, S. M. *Chem. Res. Toxicol.* **1988**, *1*, 25–27.
- (495) Povirk, L. F.; Han, Y.-H.; Steighner, R. J. *Biochemistry* **1989**, *28*, 8, 5808–5814.
- (496) Steighner, R. J.; Povirk, L. F. *Proc. Natl. Acad. Sci. U.S.A.* **1990**, *87*, 8350–8354.
- (497) Absalon, M. J.; Wu, W.; Kozarich, J. W.; Stubbe, J. *Biochemistry* **1995**, *34*, 2076–2086.
- (498) Burger, R. M.; Horwitz, S. B.; Peisach, J.; Wittenberg, J. B. *J. Biol. Chem.* **1979**, *254*, 12299–12302.
- (499) Albertini, J.-P.; Garnier-Suillerot, A.; Tosi, L. *Biochem. Biophys. Res. Commun.* **1982**, *104*, 557–563.
- (500) Kuramochi, H.; Takahashi, K.; Takita, T.; Umezawa, H. *J. Antibiot.* **1981**, *34*, 576–582.
- (501) Sam, J. W.; Tang, X.-J.; Peisach, J. *J. Am. Chem. Soc.* **1994**, *116*, 5250–5256.
- (502) Burger, R. M.; Tian, G.; Drlica, K. *J. Am. Chem. Soc.* **1995**, *117*, 1167–1168.
- (503) Veselov, A.; Sun, H.; Sienkiewicz, A.; Taylor, H.; Burger, R. M.; Scholes, C. P. *J. Am. Chem. Soc.* **1995**, *117*, 7508–7512.
- (504) Chien, M.; Grollman, A. P.; Horwitz, S. B. *Biochemistry* **1977**, *16*, 3641–3647.
- (505) Povirk, L. F.; Hogan, M.; Dattagupta, N.; Buechner, M. *Biochemistry* **1981**, *20*, 665–670.
- (506) Rao, E. A.; Saryan, L. A.; Antholine, W. E.; Petering, D. H. *J. Med. Chem.* **1980**, *23*, 1310–1318.
- (507) Roy, S. N.; Horwitz, S. B. *Cancer Res.* **1984**, *44*, 1541–1546.
- (508) Sausville, E. A.; Peisach, J.; Horwitz, S. B. *Biochemistry* **1978**, *17*, 2740–2746.
- (509) Sausville, E. A.; Stein, R. W.; Peisach, J.; Horwitz, S. B. *Biochemistry* **1978**, *17*, 2746–2754.
- (510) Buettner, G. R.; Moseley, P. L. *Biochemistry* **1992**, *31*, 9784–9788.
- (511) Ciriolo, M. R.; Magliozzo, R. S.; Peisach, J. *J. Biol. Chem.* **1987**, *262*, 6290–6295.
- (512) Sugiyama, H.; Ohmori, K.; Saito, I. *J. Am. Chem. Soc.* **1994**, *116*, 10326–10327.
- (513) Burger, R. M.; Projan, S. J.; Horwitz, S. B.; Peisach, J. *J. Biol. Chem.* **1986**, *261*, 15955–15959.
- (514) Burger, R. M.; Drlica, K.; Birdsall, B. *J. Biol. Chem.* **1994**, *269*, 25978–25985.
- (515) McGall, G. H.; Rabow, L. E.; Ashley, G. W.; Wu, S. H.; Kozarich, J. W.; Stubbe, J. *J. Am. Chem. Soc.* **1992**, *114*, 4958–4967.
- (516) Rabow, L. E.; McGall, G. H.; Stubbe, J.; Kozarich, J. W. *J. Am. Chem. Soc.* **1990**, *112*, 3203–3208.
- (517) Rabow, L.; Stubbe, J.; Kozarich, J. W.; Gerlt, J. A. *J. Am. Chem. Soc.* **1986**, *108*, 7130–7131.
- (518) Iitaka, Y.; Nakamura, H.; Nakatani, T.; Muraoka, Y.; Fujii, A.; Takita, T.; Umezawa, H. *J. Antibiot.* **1978**, *31*, 1070–1072.
- (519) Brown, S. J.; Mascharak, P. K. *J. Am. Chem. Soc.* **1988**, *110*, 1996–1997.
- (520) Tan, J. D.; Hudson, S. E.; Brown, S. J.; Olmstead, M. M.; Mascharak, P. K. *J. Am. Chem. Soc.* **1992**, *114*, 3841–3853.
- (521) Farinas, E.; Tan, J. D.; Baidya, N.; Mascharak, P. K. *J. Am. Chem. Soc.* **1993**, *115*, 2996–2997.
- (522) Kurosaki, H.; Hayashi, K.; Ishikawa, Y.; Goto, M. *Chem. Lett.* **1995**, 691–692.
- (523) Kurosaki, H.; Hayashi, K.; Ishikawa, Y.; Goto, M.; Inada, K.; Taniguchi, I.; Shionoya, M.; Kimura, E. *Inorg. Chem.* **1999**, *38*, 2824–2832.
- (524) Oppenheimer, N. J.; Rodriguez, L. O.; Hecht, S. M. *Proc. Natl. Acad. Sci. U.S.A.* **1979**, *76*, 5616–5620.
- (525) Akkerman, M. A. J.; Haasnoot, C. A. G.; Pandit, U. K.; Hilbers, C. W. *Magn. Reson. Chem.* **1988**, *26*, 793–802.
- (526) Akkerman, M. A. J.; Haasnoot, C. A. G.; Hilbers, C. W. *Eur. J. Biochem.* **1988**, *173*, 211–225.
- (527) Akkerman, M. A. J.; Neijman, E. W. J. F.; Wijmenga, S. S.; Hilbers, C. W.; Bermel, W. J. *J. Am. Chem. Soc.* **1990**, *112*, 7462–7474.
- (528) Manderville, R. A.; Ellena, J. F.; Hecht, S. M. *J. Am. Chem. Soc.* **1994**, *116*, 10851–10852.
- (529) Wu, W.; Vanderwall, D. E.; Stubbe, J.; Kozarich, J. W.; Turner, C. J. *J. Am. Chem. Soc.* **1994**, *116*, 10843–10844.
- (530) Xu, R. X.; Nettesheim, D.; Otvos, J. D.; Petering, D. H. *Biochemistry* **1994**, *33*, 907–916.
- (531) Manderville, R. A.; Ellena, J. F.; Hecht, S. M. *J. Am. Chem. Soc.* **1995**, *117*, 7891–7903.
- (532) Mao, Q.; Fulmer, P.; Li, W.; DeRose, E. F.; Petering, D. H. *J. Biol. Chem.* **1996**, *271*, 6185–6191.
- (533) Otvos, J. D.; Antholine, W. E.; Wehrli, S.; Petering, D. H. *Biochemistry* **1996**, *35*, 1458–1465.
- (534) Wu, W.; Vanderwall, D. E.; Lui, S. M.; Tang, X.-J.; Turner, C. J.; Kozarich, J. W.; Stubbe, J. *J. Am. Chem. Soc.* **1996**, *118*, 1268–1280.
- (535) Wu, W.; Vanderwall, D. E.; Turner, C. J.; Kozarich, J. W.; Stubbe, J. *J. Am. Chem. Soc.* **1996**, *118*, 1281–1294.
- (536) Caceres-Cortes, J.; Sugiyama, H.; Ikudome, K.; Saito, I.; Wang, A. H.-J. *Eur. J. Biochem.* **1997**, *244*, 818–828.
- (537) Caceres-Cortes, J.; Sugiyama, H.; Ikudome, K.; Saito, I.; Wang, A. H.-J. *Biochemistry* **1997**, *36*, 9995–10005.
- (538) Calafat, A. M.; Won, H.; Marzilli, L. G. *J. Am. Chem. Soc.* **1997**, *119*, 3656–3664.

- (539) Lehmann, T. E.; Ming, L.-J.; Rosen, M. E.; Que, L., Jr. *Biochemistry* **1997**, *36*, 2807–2816.
- (540) Lui, S. M.; Vanderwall, D. E.; Wu, W.; Tang, X.-J.; Turner, C. J.; Kozarich, J. W.; Stubbe, J. *J. Am. Chem. Soc.* **1997**, *119*, 9603–9613.
- (541) Vanderwall, D. E.; Lui, S. M.; Wu, W.; Turner, C. J.; Kozarich, J. W.; Stubbe, J. *Chem. Biol.* **1997**, *4*, 373–387.
- (542) Sucheck, S. J.; Ellena, J. F.; Hecht, S. M. *J. Am. Chem. Soc.* **1998**, *120*, 7450–7460.
- (543) Wu, W.; Vanderwall, D. E.; Teramoto, S.; Lui, S. M.; Hoehn, S. T.; Tang, X. J.; Turner, C. J.; Boger, D. L.; Kozarich, J. W.; Stubbe, J. *J. Am. Chem. Soc.* **1998**, *120*, 2239–2250.
- (544) Loeb, K. E.; Zaleski, J. M.; Hess, C. D.; Hecht, S. M.; Solomon, E. I. *J. Am. Chem. Soc.* **1998**, *120*, 1249–1259.
- (545) Lehmann, T. E.; Ming, L.-J.; Rosen, M. E.; Serrano, M. L.; Que, L., Jr. *J. Inorg. Biochem.* **1999**, *74*, 205.
- (546) Carter, B. J.; Murty, V. S.; Reddy, K. S.; Wang, S.-N.; Hecht, S. M. *J. Biol. Chem.* **1990**, *265*, 4193–4196.
- (547) Carter, B. J.; Reddy, K. S.; Hecht, S. M. *Tetrahedron* **1991**, *47*, 2463–2474.
- (548) Boger, D. L.; Ramsey, T. M.; Cai, H.; Hoehn, S. T.; Kozarich, J. W.; Stubbe, J. *J. Am. Chem. Soc.* **1998**, *120*, 53–65.
- (549) Sam, J. W.; Takahashi, S.; Lippai, I.; Peisach, J.; Rousseau, D. L. *J. Biol. Chem.* **1998**, *273*, 16090–16097.
- (550) Kemsley, J. N.; Loeb Zaleski, K.; Solomon, E. I. Unpublished results.
- (551) Burger, R. M.; Blanchard, J. S.; Horwitz, S. B.; Peisach, J. *J. Biol. Chem.* **1985**, *260*, 15406–15409.
- (552) Westre, T. E.; Loeb, K. E.; Zaleski, J. M.; Hedman, B.; Hodgson, K. O.; Solomon, E. I. *J. Am. Chem. Soc.* **1995**, *117*, 1309–1313.
- (553) Sugiura, Y.; Ishizu, K. *J. Inorg. Biochem.* **1979**, *11*, 171–180.
- (554) Lever, A. B. P.; Gray, H. B. *Iron Porphyrins*; Addison-Wesley: Reading, MA, 1983; Vol. 1.
- (555) Wu, J. C.; Kozarich, J. W.; Stubbe, J. *J. Biol. Chem.* **1983**, *258*, 4694–4697.
- (556) MacFaul, P. A.; Ingold, K. U.; Wayner, D. D. M.; Que, L., Jr. *J. Am. Chem. Soc.* **1997**, *119*, 10594–10598.
- (557) Bull, C.; McClune, G. J.; Fee, J. A. *J. Am. Chem. Soc.* **1983**, *105*, 5290–5300.
- (558) Ahmad, S.; McCallum, J. D.; Shiemke, A. K.; Appelman, E. H.; Loehr, T. M.; Sanders-Loehr, J. *Inorg. Chem.* **1988**, *27*, 2230–2233.
- (559) De Groot, J. J. M. C.; Garssen, G. J.; Veldink, G. A.; Vliegthart, J. F. G.; Boldingh, J. *FEBS Lett.* **1975**, *56*, 50–54.
- (560) Slappendel, S.; Veldink, G. A.; Vliegthart, J. F. G.; Aasa, R.; Malmström, B. G. *Biochim. Biophys. Acta* **1983**, *747*, 32–36.
- (561) Nelson, M. J.; Chase, D. B.; Seitz, S. P. *Biochemistry* **1995**, *34*, 6159–6163.
- (562) Wada, A.; Ogo, S.; Watanabe, Y.; Mukai, M.; Kitagawa, T.; Jitsukawa, K.; Masuda, H.; Einaga, H. *Inorg. Chem.* **1999**, *38*, 3592–3593.
- (563) Kim, C.; Chen, K.; Kim, J.; Que, L., Jr. *J. Am. Chem. Soc.* **1997**, *119*, 5964–5965.
- (564) Ho, R. Y. N.; Roelfes, G.; Feringa, B. L.; Que, L., Jr. *J. Am. Chem. Soc.* **1999**, *121*, 264–265.
- (565) Simaan, A. J.; Banse, F.; Mialane, P.; Boussac, A.; Un, S.; Kargar-Grisel, T.; Bouchoux, G.; Girerd, J.-J. *Eur. J. Inorg. Chem.* **1999**, 993–996.
- (566) Cheng, K. L.; Lott, P. F. *Anal. Chem.* **1956**, *28*, 462–465.
- (567) McClune, G. J.; Fee, J. A.; McClusky, G. A.; Groves, J. T. *J. Am. Chem. Soc.* **1977**, *99*, 5220–5222.
- (568) Marusak, R. A.; Mears, C. F. In *Active Oxygen in Biochemistry*; Valentine, J. S., et al., Eds.; Blackie: London, 1995; pp 336–400.
- (569) Walling, C.; Kurz, M.; Schugar, H. J. *Inorg. Chem.* **1970**, *9*, 931–937.
- (570) Walling, C.; Kato, S. *J. Am. Chem. Soc.* **1971**, *93*, 4275–4281.
- (571) Walling, C. *Acc. Chem. Res.* **1975**, *8*, 125–131.
- (572) Walling, C.; Partch, R. E.; Weil, T. *Proc. Natl. Acad. Sci. U.S.A.* **1975**, *72*, 140–142.
- (573) Kim, J.; Larka, E.; Wilkinson, E. C.; Que, L., Jr. *Angew. Chem., Int. Ed. Engl.* **1995**, *34*, 2048–2051.
- (574) Menage, S.; Wilkinson, E. C.; Que, L., Jr.; Fontecave, M. *Angew. Chem., Int. Ed. Engl.* **1995**, *34*, 203–205.
- (575) Zang, Y.; Elgren, T. E.; Dong, Y.; Que, L., Jr. *J. Am. Chem. Soc.* **1993**, *115*, 811–813.
- (576) Gütlich, P. *Struct. Bonding* **1981**, *44*, 83–195.
- (577) Gütlich, P.; Hauser, A.; Spiering, H. *Angew. Chem., Int. Ed. Engl.* **1994**, *33*, 2024–2054.
- (578) Guajardo, R. J.; Hudson, S. E.; Brown, S. J.; Mascharak, P. K. *J. Am. Chem. Soc.* **1993**, *115*, 7971–7977.
- (579) Roelfes, G.; Lubben, M.; Chen, K.; Ho, R. Y. N.; Meetsma, A.; Genseberger, S.; Hermant, R. M.; Hage, R.; Mandal, S. K.; Young, J. V. G.; Zang, Y.; Kooijman, H.; Spek, A. L.; Que, L., Jr.; Feringa, B. L. *Inorg. Chem.* **1999**, *38*, 1929–1936.
- (580) Kitajima, N.; Komatsuzaki, H.; Hikichi, S.; Osawa, M.; Moro-oka, Y. *J. Am. Chem. Soc.* **1994**, *116*, 11596–11597.
- (581) Chiaroni, A.; Pascard-Billy, C. *Bull. Soc. Chim. Fr.* **1973**, 781–787.
- (582) Alcock, N. W.; Golding, B. T.; Mwesigye-Kibende, S. *J. Chem. Soc., Dalton Trans.* **1985**, 1997–2000.
- (583) Mikolański, W.; Baum, G.; Massa, W.; Hoffmann, R. W. *J. Organomet. Chem.* **1989**, *376*, 397–405.
- (584) Chavez, F. A.; Nguyen, C. V.; Olmstead, M. M.; Mascharak, P. K. *Inorg. Chem.* **1996**, *35*, 6282–6291.
- (585) Chavez, F. A.; Rowland, J. M.; Olmstead, M. M.; Mascharak, P. K. *J. Am. Chem. Soc.* **1998**, *120*, 9015–9027.
- (586) Chavez, F. A.; Briones, J. A.; Olmstead, M. M.; Mascharak, P. K. *Inorg. Chem.* **1999**, *38*, 1603–1608.
- (587) Kitajima, N.; Katayama, T.; Fujisawa, K.; Iwata, Y.; Moro-oka, Y. *J. Am. Chem. Soc.* **1993**, *115*, 7872–7873.
- (588) Fujisawa, K.; Tanaka, M.; Moro-oka, Y.; Kitajima, N. *J. Am. Chem. Soc.* **1994**, *116*, 12079–12080.
- (589) Harata, M.; Jitsukawa, K.; Masuda, H.; Einaga, H. *J. Am. Chem. Soc.* **1994**, *116*, 10817–10818.
- (590) Wada, A.; Harata, M.; Hasegawa, K.; Jitsukawa, K.; Masuda, H.; Mukai, M.; Kitagawa, T.; Einaga, H. *Angew. Chem., Int. Ed. Engl.* **1998**, *37*, 798–799.
- (591) Carmona, D.; Lamata, M. P.; Ferrer, J.; Modrego, J.; Perales, M.; Lahoz, F. J.; Atencio, R.; Oro, L. A. *Chem. Commun.* **1994**, 575–576.
- (592) Note that the hydrated ferric ion itself shows catalase activity; the reaction is believed to follow a radical mechanism (refs 571 and 1005–1007).
- (593) Melnyk, A. C.; Kjeldahl, N. K.; Rendina, A. R.; Busch, D. H. *J. Am. Chem. Soc.* **1979**, *101*, 3232–3240.
- (594) Nishida, Y.; Nasu, M.; Akamatsu, T. *Z. Naturforsch.* **1992**, *47B*, 115–120.
- (595) Sugimoto, H.; Sawyer, D. T. *J. Am. Chem. Soc.* **1984**, *106*, 4283–4285.
- (596) Barton, D. H. R.; Doller, D. *Acc. Chem. Res.* **1992**, *25*, 504–512.
- (597) Nam, W.; Ho, R.; Valentine, J. S. *J. Am. Chem. Soc.* **1991**, *113*, 7052–7054.
- (598) Leising, R. A.; Brennan, B. A.; Que, L., Jr.; Fox, B. G.; Münck, E. *J. Am. Chem. Soc.* **1991**, *113*, 3988–3990.
- (599) Leising, R. A.; Kim, J.; Perez, M. A.; Que, L., Jr. *J. Am. Chem. Soc.* **1993**, *115*, 9524–9530.
- (600) Kim, J.; Harrison, R. G.; Kim, C.; Que, L., Jr. *J. Am. Chem. Soc.* **1996**, *118*, 4373–4379.
- (601) Arends, I. W. C. E.; Ingold, K. U.; Wayner, D. D. M. *J. Am. Chem. Soc.* **1995**, *117*, 4710–4711.
- (602) Rana, T. M.; Meares, C. F. *J. Am. Chem. Soc.* **1990**, *112*, 2457–2458.
- (603) Rana, T. M.; Meares, C. F. *J. Am. Chem. Soc.* **1991**, *113*, 1859–1861.
- (604) Mialane, P.; Nivorokine, A.; Pratiel, G.; Azèma, L.; Slany, M.; Godde, F.; Simaan, A.; Banse, F.; Kargar-Grisel, T.; Bouchoux, G.; Sainion, J.; Horner, O.; Guilhem, J.; Tchertanova, L.; Meunier, B.; Girerd, J.-J. *Inorg. Chem.* **1999**, *38*, 1085–1092.
- (605) Ringbom, A.; Saxen, B. *Anal. Chim. Acta* **1957**, *16*, 541–545.
- (606) Kachanova, Z. P.; Purmal, A. P. *Russ. J. Phys. Chem.* **1964**, *38*, 1342.
- (607) Hester, R. E.; Nour, E. M. *J. Raman Spectrosc.* **1981**, *11*, 35–38.
- (608) Ross, P. K.; Solomon, E. I. *J. Am. Chem. Soc.* **1991**, *113*, 3246–3259.
- (609) Shadle, S. E.; Hedman, B.; Hodgson, K. O.; Solomon, E. I. *J. Am. Chem. Soc.* **1995**, *117*, 2259–2272.
- (610) Butcher, K. D.; Didziulis, S. V.; Briat, B.; Solomon, E. I. *J. Am. Chem. Soc.* **1990**, *112*, 2231–2242.
- (611) Slappendel, S.; Veldink, G. A.; Vliegthart, J. F. G.; Aasa, R.; Malmström, B. G. *Biochim. Biophys. Acta* **1981**, *667*, 77–86.
- (612) De Groot, J. J. M. C.; Garssen, G. J.; Vliegthart, J. F. G.; Boldingh, J. *Biochim. Biophys. Acta* **1973**, *326*, 279–284.
- (613) Chamulitrat, W.; Mason, R. P. *J. Biol. Chem.* **1989**, *264*, 20968–20973.
- (614) Nelson, M. J.; Cowling, R. A. *J. Am. Chem. Soc.* **1990**, *112*, 2820–2821.
- (615) Nelson, M. J.; Seitz, S. P.; Cowling, R. A. *Biochemistry* **1990**, *29*, 6897–6903.
- (616) Heimbrook, D. C.; Mulholland, R. L., Jr.; Hecht, S. M. *J. Am. Chem. Soc.* **1986**, *108*, 7839–7840.
- (617) Neese, F.; Zaleski, J. M.; Loeb, K. E.; Solomon, E. I. Manuscript in preparation.
- (618) Takahashi, S.; Sam, J. W.; Peisach, J.; Rousseau, D. L. *J. Am. Chem. Soc.* **1994**, *116*, 4408–4413.
- (619) Traylor, T. G.; Traylor, P. S. In *Active Oxygen in Chemistry and Biology*; Blackie: New York, 1995; p 84.
- (620) Groves, J. T. *J. Chem. Educ.* **1985**, *62*, 928–931.
- (621) Dawson, J. H. *Science* **1988**, *240*, 433–439.
- (622) Sono, M.; Roach, M. P.; Coulter, E. D.; Dawson, J. H. *Chem. Rev.* **1996**, *96*, 2841–2887.
- (623) Ortiz-de Montellano, P. R. *Cytochrome P450: Structure, Mechanism and Biochemistry*; Plenum: New York, 1985.
- (624) Harris, D. L.; Loew, G. H. *J. Am. Chem. Soc.* **1998**, *120*, 8941–8948.
- (625) Cheesman, M. R.; Greenwood, C.; Thomson, A. J. *Adv. Inorg. Chem.* **1991**, *36*, 201–255.

- (626) Williams, R. J. P. *Chem. Rev.* **1956**, *56*, 299–328.
- (627) Cheng, J. C.; Osborne, G. A.; Stephens, P. J.; Eaton, E. A. *Nature (London)* **1973**, *241*, 193–194.
- (628) Day, P.; Smith, D. W.; Williams, R. J. P. *Biochemistry* **1967**, *6*, 1563–1566, 3747–3750.
- (629) Makinen, M. W.; Churg, A. K. In *The Porphyrins*; Gray, H. B., Lever, A. B. P., Eds.; Addison-Wesley: Reading, MA, 1983; Vol. 1, pp 141–235.
- (630) Solomon, E. I.; Sundaram, U. M.; Machonkin, T. E. *Chem. Rev.* **1996**, *96*, 2563–2605.
- (631) Kurtz, D. M. *Chem. Rev.* **1990**, *90*, 535–606.
- (632) Note that we assume here that the ZFS is much smaller than the exchange coupling which is generally the case for high-spin ferric sites.
- (633) Van Vleck, J. H. *The Theory of Electric and Magnetic Susceptibilities*; Oxford University Press: Oxford, 1932.
- (634) Ross, P. K.; Allendorf, M. D.; Solomon, E. I. *J. Am. Chem. Soc.* **1989**, *111*, 4009–4021.
- (635) Ferguson, J.; Guggenheim, H. J.; Tanabe, Y. *J. Phys. Soc. Jpn.* **1966**, *21*, 692–704.
- (636) Güdel, H. U.; Weihe, H. In *Molecular Magnetism: From Molecular Assemblies to the Devices*; Coronado, E., et al., Eds.; Kluwer: Norwell, MA, 1996; pp 173–197.
- (637) Carlin, R. L. *Magnetochemistry*; Springer-Verlag: New York, 1986.
- (638) Wojciechowski, W. *Inorg. Chim. Acta* **1967**, *1*, 319–323.
- (639) Brown, C. A.; Remar, G. J.; Musselman, R. L.; Solomon, E. I. *Inorg. Chem.* **1995**, *34*, 688–717.
- (640) Newton, M. D. *Chem. Rev.* **1991**, *91*, 767–792.
- (641) Barbara, P. F.; Meyer, T. J.; Ratner, M. A. *J. Phys. Chem.* **1996**, *100*, 13148–13168.
- (642) Weihe, H.; Güdel, H. U. *Inorg. Chem.* **1997**, *36*, 3632–3639.
- (643) Wallar, B. J.; Lipscomb, J. D. *Chem. Rev.* **1996**, *96*, 2625–2657.
- (644) Fontecave, M.; Menage, S.; Duboc-Toia, C. *Coord. Chem. Rev.* **1998**, *178*, 1555–1572.
- (645) Sanders-Loehr, J.; Wheeler, W. D.; Shiemke, A. K.; Averill, B. A.; Loehr, T. M. *J. Am. Chem. Soc.* **1989**, *111*, 8084–8093.
- (646) Zang, Y.; Dong, Y. H.; Que, L., Jr.; Kauffmann, K.; Munck, E. *J. Am. Chem. Soc.* **1995**, *117*, 1169–1170.
- (647) Zheng, H.; Zang, Y.; Dong, Y.; Young, V. G., Jr.; Que, L., Jr. *J. Am. Chem. Soc.* **1999**, *121*, 2226–2235.
- (648) Holgate, S. J. W.; Bondarenko, G.; Collison, D.; Mabbs, F. E. *Inorg. Chem.* **1999**, *38*, 2380–2385.
- (649) Weihe, H.; Güdel, H. U. *J. Am. Chem. Soc.* **1998**, *120*, 2870–2879.
- (650) Weihe, H.; Güdel, H. U. *J. Am. Chem. Soc.* **1997**, *36*, 66539–6543.
- (651) Wieghardt, K. *Angew. Chem., Int. Ed. Engl.* **1989**, *28*, 1153–1172.
- (652) Kipke, C. A.; Scott, M. J.; Gohdes, J. W.; Armstrong, W. H. *Inorg. Chem.* **1989**, *28*, 3–2194.
- (653) Hirst, L. L.; Ray, T. *Proc. R. Soc. London, Ser. A* **1982**, *384*, 191–203.
- (654) Eickman, N. C.; Himmelwright, R. S.; Solomon, E. I. *Proc. Natl. Acad. Sci. U.S.A.* **1979**, *76*, 2094–2098.
- (655) Lehmann, G. Z. Z. *Phys. Chem. Neue Folge* **1970**, *72*, 279–283.
- (656) Bossek, U.; Weyer Müller, T.; Wieghardt, K.; Bonvoisin, J.; Girerd, J.-J. *J. Chem. Soc., Chem. Commun.* **1989**, 633–636.
- (657) Hotzelmann, R.; Wieghardt, K.; Flörke, U.; Haupt, H.-J.; Weatherburn, D. C.; Bonvoisin, J.; Blondin, G.; Girerd, J.-J. *J. Am. Chem. Soc.* **1992**, *114*, 1681–1696.
- (658) Brunold, T. C.; Gamelin, D. R.; Solomon, E. I. Manuscript in preparation.
- (659) Brunold, T. C.; Tamura, N.; Kitajima, N.; Moro-oka, Y.; Solomon, E. I. *J. Am. Chem. Soc.* **1998**, *120*, 5674–5690.
- (660) Brunold, T. C.; Solomon, E. I. *J. Am. Chem. Soc.* **1999**, *121*, 8277–8287.
- (661) Schugar, H. J.; Rossman, G. R.; Barraclough, C. G.; Gray, H. B. *J. Am. Chem. Soc.* **1972**, *94*, 2683–2689.
- (662) Dexter, D. L. *Phys. Rev.* **1962**, *126*, 1962–1967.
- (663) Reem, R. C.; McCormick, J. M.; Richardson, D. E.; Devlin, F. J.; Stephens, P. J.; Musselman, R. L.; Solomon, E. I. *J. Am. Chem. Soc.* **1989**, *111*, 4688–4704.
- (664) Tuzek, F.; Solomon, E. I. *Inorg. Chem.* **1993**, *32*, 2850–2862.
- (665) Tuzek, F. In *Spectroscopic Methods in Bioinorganic Chemistry*; Solomon, E. I., Hodgson, K. O., Eds.; ACS Symposium Series 692; American Chemical Society: Washington, DC, 1997; pp 98–118.
- (666) In-plane and out-of-plane relates to the orientations of the oxo- π and Fe-d orbitals relative to the Fe–O–Fe plane; both transitions are allowed with E in-plane polarized.
- (667) The large spectral changes observed on going from a linear to a bent structure provide further support to the assignments of the lowest-energy ferric oxo dimer bands to in-plane π oxo-to-Fe^{III} CT transitions as only the in-plane π -bonding interaction is significantly perturbed along this structural coordinate.
- (668) Reem, R. C.; Solomon, E. I. *J. Am. Chem. Soc.* **1987**, *109*, 1216–1226.
- (669) Pulver, S. C.; Tong, W. H.; Bollinger, M. J., Jr.; Stubbe, J.; Solomon, E. I. *J. Am. Chem. Soc.* **1995**, *117*, 12664–12678.
- (670) Pulver, S.; Froland, W. A.; Fox, B. G.; Lipscomb, J. D.; Solomon, E. I. *J. Am. Chem. Soc.* **1993**, *115*, 12409–12422.
- (671) Yang, Y.-S.; Broadwater, J. A.; Pulver, S. C.; Fox, B. G.; Solomon, E. I. *J. Am. Chem. Soc.* **1999**, *121*, 2770–2783.
- (672) Chauduri, P.; Wieghardt, K. *Angew. Chem., Int. Ed. Engl.* **1985**, *24*, 4, 778–779.
- (673) Hartman, J. R.; Rardin, R. L.; Chauduri, P.; Pohl, K.; Wieghardt, K.; Nuber, B.; Weiss, J.; Papaefthymiou, G. C.; Frankel, R. B.; Lippard, S. J. *J. Am. Chem. Soc.* **1987**, *109*, 7387.
- (674) Hagen, K. S.; Lachicotte, R. *J. Am. Chem. Soc.* **1992**, *114*, 8741–8742.
- (675) Hendrich, M. P.; Day, E. P.; Wang, C.-P.; Synder, B. S.; Holm, R. H.; Münck, E. *Inorg. Chem.* **1994**, *33*, 2848–2856.
- (676) Kitajima, N.; Tamura, N.; Tanaka, M.; Moro-oka, Y. *Inorg. Chem.* **1992**, *31*, 3342–3343.
- (677) Herold, S.; Lippard, S. J. *J. Am. Chem. Soc.* **1997**, *119*, 145–156.
- (678) Tolman, W. B.; Liu, S.; Bentsen, J. G.; Lippard, S. J. *J. Am. Chem. Soc.* **1991**, *113*, 152–164.
- (679) Kahn, O. In *Molecular Magnetism*; VCH: New York, 1993.
- (680) Weltner, W., Jr. *Magnetic Atoms and Molecules*; Dover: New York, 1983.
- (681) Bencini, A.; Gatteschi, D. In *Electron Paramagnetic Resonance of Exchanged Coupled System*; Springer-Verlag: Berlin, 1990; pp 20–47.
- (682) Moriya, T. *Weak Ferromagnetism*; Academic: New York, 1963; Vol. 1 (Magnetism).
- (683) Moriya, T. *Phys. Rev.* **1960**, *120*, 91–98.
- (684) Hendrich, M. P.; Munck, E.; Fox, B. G.; Lipscomb, J. D. *J. Am. Chem. Soc.* **1990**, *112*, 5861–5865.
- (685) Klotz, I. M.; Kurtz, D. M. *Acc. Chem. Res.* **1984**, *17*, 16–22.
- (686) Wilkins, P. C.; Wilkins, R. G. *Coord. Chem. Rev.* **1987**, *79*, 195–214.
- (687) Stenkamp, R. E. *Chem. Rev.* **1994**, *94*, 715–726.
- (688) Niederhoffer, E. C.; Timmons, J. H.; Martell, A. E. *Chem. Rev.* **1984**, *84*, 137–203.
- (689) Solomon, E. I.; Baldwin, M. J.; Lowery, M. D. *Chem. Rev.* **1992**, *92*, 521–542.
- (690) Lankester, E. R. *Proc. R. Soc. London* **1873**, *21*, 71.
- (691) Raner, G. M.; Martins, L. J.; Ellis, W. R., Jr. *Biochemistry* **1997**, *36*, 7037–7043.
- (692) Martins, L. J.; Hill, C. P.; Ellis, W. R., Jr. *Biochemistry* **1997**, *36*, 7044–7049.
- (693) Boeri, E.; Ghirelli-Magaldi, A. *Biochim. Biophys. Acta* **1957**, *23*, 489–493.
- (694) Klotz, I. M.; Klotz, T. A.; Fiess, H. A. *Arch. Biochem. Biophys.* **1957**.
- (695) Shiemke, A. K.; Loehr, T. M.; Sanders-Loehr, J. *J. Am. Chem. Soc.* **1984**, *106*, 4951–4956.
- (696) Dunn, K. M.; Shriver, D. F.; Klotz, I. M. *Proc. Natl. Acad. Sci. U.S.A.* **1973**, *70*, 2852–2854.
- (697) Kurtz, D. M.; Shriver, D. F.; Klotz, I. M. *Coord. Chem. Rev.* **1977**, *24*, 145–178.
- (698) Richardson, D. E.; Emad, M.; Reem, R. G.; Solomon, E. I. *Biochemistry* **1987**, *25*, 1003–1013.
- (699) Holm, R. H.; Kennepohl, P.; Solomon, E. I. *Chem. Rev.* **1996**, *96*, 2239–2314.
- (700) de Waal, D. J. A.; Wilkins, R. G. *J. Biol. Chem.* **1976**, *251*, 2339–2343.
- (701) Alberding, N.; Lavalette, D.; Austin, R. H. *Proc. Natl. Acad. Sci. U.S.A.* **1981**, *78*, 2301–2309.
- (702) Armstrong, G. D.; Sykes, A. G. *Inorg. Chem.* **1986**, *25*, 3135–3139.
- (703) Nocek, J. M.; Kurtz, D. M., Jr.; Sage, J. T.; Xia, Y.-M.; Debrunner, P.; Shiemke, A. K.; Sanders-Loehr, J.; Loehr, T. M. *Biochemistry* **1988**, *27*, 1014–1024.
- (704) Muhoberac, B. B.; Wharton, D. C.; Babcock, L. M.; Harrington, P. C.; Wilkins, R. G. *Biochim. Biophys. Acta* **1980**, *626*, 337–345.
- (705) Armstrong, G. D.; Sykes, A. G. *Inorg. Chem.* **1986**, *25*, 3725–3729.
- (706) Armstrong, G. D.; Sykes, A. G. *Inorg. Chem.* **1987**, *25*, 3392–3398.
- (707) McCormick, J. M.; Reem, R. C.; Solomon, E. I. *J. Am. Chem. Soc.* **1991**, *113*, 9066–9079.
- (708) Holmes, M. A.; Le Trong, I.; Turley, S.; Sieker, L. C.; Stenkamp, R. E. *Biochemistry* **1991**, *30*, 583.
- (709) Zhang, K.; Stern, E. A.; Ellis, F.; Sanders-Loehr, J.; Shiemke, A. K. *Biochemistry* **1988**, *27*, 7470–7479.
- (710) Reem, R. C.; Solomon, E. I. *J. Am. Chem. Soc.* **1984**, *106*, 8323–8325.
- (711) Clark, P. E.; Webb, J. *Biochemistry* **1981**, *20*, 4628–4632.
- (712) Maroney, M. J.; Kurtz, D. M., Jr.; Nocek, J. M.; Pearce, L. L.; Que, L., Jr. *J. Am. Chem. Soc.* **1986**, *108*, 6871–6879.
- (713) Lachicotte, R.; Kaitaygorodskiy, A.; Hagen, K. S. J. *J. Am. Chem. Soc.* **1993**, *115*, 8883–8884.

- (714) Gay, R. R.; Solomon, E. I. *J. Am. Chem. Soc.* **1978**, *100*, 1972–1973.
- (715) Myers, A. B.; Mathies, R. A. In *Biological Applications of Raman Spectroscopy*; Spiro, T. G., Ed.; Wiley: New York, 1987; Vol. 2, pp 1–58.
- (716) Wootton, J. L.; Zink, J. I. *J. Am. Chem. Soc.* **1997**, *119*, 1895–1900.
- (717) Que, L., Jr.; True, A. E. In *Progress in Inorganic Chemistry: Bioinorganic Chemistry*; Lippard, S. J., Ed.; Wiley: New York, 1990; Vol. 1, pp 97–200.
- (718) Dawson, J. W.; Gray, H. B.; Hoenig, H. E.; Rossman, G. R.; Schredder, J. M.; Wang, R. H. *Biochemistry* **1972**, *11*, 461–465.
- (719) Shiemke, A. K.; Loehr, T. M.; Sanders-Loehr, J. *J. Am. Chem. Soc.* **1986**, *108*, 2437–2443.
- (720) Brunold, T. C.; Solomon, E. I. *J. Am. Chem. Soc.* **1999**, *121*, 8288–8295.
- (721) Cukier, R. I.; Zhu, J. *J. Phys. Chem., Ser. B* **1997**, *101*, 7180–7190.
- (722) Cukier, R. I. *J. Phys. Chem.* **1995**, *99*, 16101–16115.
- (723) Cukier, R. I. *J. Phys. Chem.* **1996**, *100*, 15428–15443.
- (724) Note that, in the framework of the VBCI model, the ground-state exchange coupling arises from spin-dependent CI of the ground state with MMCT excited states. In ferric dimers, the $S = 5$ ground-state component cannot interact with MMCT excited states (Figure 63). Thus, this state defines the energy of the ground state in the absence of exchange coupling. Therefore the full stabilization of the $S = 0$ state ($=30|J|$) is due to the exchange coupling rather than that of the spin barycenter ($=18|J|$) in Figure 60.
- (725) Dalton, H. *Adv. Appl. Microbiol.* **1980**, *26*, 71–87.
- (726) Valentine, A. M.; Lippard, S. J. *J. Chem. Soc., Dalton Trans.* **1997**, 3925–3931.
- (727) Anthony, C. *The Biochemistry of Methylotrophs*; Academic: London, 1982.
- (728) Lipscomb, J. D. *Annu. Rev. Microbiol.* **1994**, *48*, 371–399.
- (729) Stanley, S. H.; Prior, S. D.; Leak, D. J.; Dalton, H. *Biotechnol. Lett.* **1983**, *5*, 487–492.
- (730) Leak, D. J.; Dalton, H. *Appl. Microbiol. Biotechnol.* **1986**, *23*, 470–476.
- (731) Lontoh, S.; DiSpirito, A. A.; Semrau, J. D. *Arch. Microbiol.* **1999**, *171*, 301–308.
- (732) Nguyen, H. H. T.; Elliott, S. J.; Yip, J. H. K.; Chan, S. I. *J. Biol. Chem.* **1998**, *273*, 7957–7966.
- (733) Nguyen, H. H. T.; Shiemke, A. K.; Jacobs, S. J.; Hales, B. J.; Lidstrom, M. E.; Chan, S. I. *J. Biol. Chem.* **1994**, *269*, 14995–15005.
- (734) Tikhvatullin, I. A.; Korshunova, L. A.; Gvozdev, R. I.; Dalton, H. *Biochemistry (Moscow)* **1996**, *61*, 886–891.
- (735) Takeguchi, M.; Miyakawa, K.; Okura, I. *Biomaterials* **1998**, *11*, 229–234.
- (736) Takeguchi, M.; Miyakawa, K.; Okura, I. *J. Mol. Catal., Ser. A* **1998**, *132*, 145–153.
- (737) Takeguchi, M.; Miyakawa, K.; Okura, I. *J. Mol. Catal., Ser. A* **1999**, *137*, 161–168.
- (738) Takeguchi, M.; Ohashi, M.; Okura, I. *Biomaterials* **1999**, *12*, 123–129.
- (739) Yuan, H.; Collins, M. L. P.; Antholine, W. E. *Biophys. J.* **1999**, *76*, 2223–2229.
- (740) Yuan, H.; Collins, M. L. P.; Antholine, W. E. *J. Am. Chem. Soc.* **1997**, *119*, 5073–5074.
- (741) Elliott, S. J.; Randall, D. W.; Britt, R. D.; Chan, S. I. *J. Am. Chem. Soc.* **1998**, *120*, 3247–3248.
- (742) Wilkinson, B.; Zhu, M.; Priestley, N. D.; Nguyen, H. H. T.; Morimoto, H.; Williams, P. G.; Chan, S. I.; Floss, H. G. *J. Am. Chem. Soc.* **1996**, *118*, 921–922.
- (743) Nguyen, H. H. T.; Nakagawa, K. H.; Hedman, B.; Elliott, S. J.; Lidstrom, M. E.; Hodgson, K. O.; Chan, S. I. *J. Am. Chem. Soc.* **1996**, *118*, 12766–12776.
- (744) Elliott, S. J.; Zhu, M.; Tso, L.; Nguyen, H. H. T.; Yip, J. H. K.; Chan, S. I. *J. Am. Chem. Soc.* **1997**, *119*, 9949–9955.
- (745) Katterle, B.; Abudu, N.; Ljones, T.; Gvozdev, R.; Andersson, K. K. *J. Inorg. Biochem.* **1999**, *74*, 189–189.
- (746) Pilkington, S. J.; Dalton, H. *Methods Enzymol.* **1990**, *188*, 181–190.
- (747) Feig, A. L.; Lippard, S. J. *Chem. Rev.* **1994**, *94*, 759–805.
- (748) Colby, J.; Stirling, D. I.; Dalton, H. *Biochem. J.* **1977**, *165*, 395–402.
- (749) Fox, B. G.; Borneman, J. G.; Wackett, L. P.; Lipscomb, J. D. *Biochemistry* **1990**, *29*, 6419–6427.
- (750) Green, J.; Dalton, H. *J. Biol. Chem.* **1989**, *264*, 17698–17703.
- (751) Higgins, I. J.; Best, D. J.; Hammond, R. C. *Nature* **1980**, *286*, 561–564.
- (752) Colby, J.; Dalton, H. *Biochem. J.* **1978**, *171*, 461–468.
- (753) Woodland, M. P.; Dalton, H. *J. Biol. Chem.* **1984**, *259*, 53–59.
- (754) Green, J.; Dalton, H. *J. Biol. Chem.* **1985**, *260*, 5795–5801.
- (755) Fox, B. G.; Lipscomb, J. D. *Biochem. Biophys. Res. Commun.* **1988**, *154*, 165–170.
- (756) Fox, B. G.; Froland, W. A.; Dege, J. E.; Lipscomb, J. D. *J. Biol. Chem.* **1989**, *264*, 10023–10033.
- (757) Colby, J.; Dalton, H. *Biochem. J.* **1979**, *177*, 903–908.
- (758) Lund, J.; Woodland, M. P.; Dalton, H. *Eur. J. Biochem.* **1985**, *147*, 297–305.
- (759) Lund, J.; Dalton, H. *Eur. J. Biochem.* **1985**, *147*, 291–296.
- (760) Prince, R. C.; Patel, R. N. *FEBS Lett.* **1986**, *203*, 127–130.
- (761) Fox, B. G.; Hendrich, M. P.; Surerus, K. K.; Andersson, K. K.; Froland, W. A.; Lipscomb, J. D.; Munck, E. *J. Am. Chem. Soc.* **1993**, *115*, 3688–3701.
- (762) Gibson, D. T. *Microbial degradation of organic compounds*; Marcel Dekker: New York, 1984; Vol. 13.
- (763) Green, J.; Dalton, H. *Biochem. J.* **1989**, *259*, 167–172.
- (764) Gassner, G. T.; Lippard, S. J. *Biochemistry* **1999**, *38*, 12768–12785.
- (765) Fox, B. G.; Liu, Y.; Dege, J. E.; Lipscomb, J. D. *J. Biol. Chem.* **1991**, *266*, 540–550.
- (766) Froland, W. A.; Andersson, K. K.; Lee, S.-K.; Liu, Y.; Lipscomb, J. D. *J. Biol. Chem.* **1992**, *267*, 17588–17597.
- (767) Paulsen, K. E.; Liu, Y.; Fox, B. G.; Lipscomb, J. D.; Munck, E.; Stankovich, M. T. *Biochemistry* **1994**, *33*, 713–722.
- (768) Liu, Y.; Nesheim, J. C.; Paulsen, K. E.; Stankovich, M. T.; Lipscomb, J. D. *Biochemistry* **1997**, *36*, 5223–5233.
- (769) Liu, K. E.; Lippard, S. J. *Adv. Inorg. Chem.* **1995**, *42*, 263–289.
- (770) Liu, K. E.; Lippard, S. J. *J. Biol. Chem.* **1991**, *266*, 12836–12839.
- (771) Kazlauskaitė, J.; Hill, H. A. O.; Wilkins, P. C.; Dalton, H. *Eur. J. Biochem.* **1996**, *241*, 552–556.
- (772) Lee, S.-K.; Nesheim, J. C.; Lipscomb, J. D. *J. Biol. Chem.* **1993**, *268*, 21569–21577.
- (773) Liu, Y.; Nesheim, J. C.; Lee, S.-K.; Lipscomb, J. D. *J. Biol. Chem.* **1995**, *270*, 24662–24665.
- (774) Nesheim, J. C.; Lipscomb, J. D. *Biochemistry* **1996**, *35*, 10240–10247.
- (775) Lee, S.-K.; Lipscomb, J. D. *Biochemistry* **1999**, *38*, 4423–4432.
- (776) Lipscomb, J. D.; Que, L., Jr. *J. Biol. Inorg. Chem.* **1998**, *3*, 331–336.
- (777) Liu, K. E.; Valentine, A. M.; Qiu, D.; Edmondson, D. E.; Appelman, E. H.; Spiro, T. G.; Lippard, S. J. *J. Am. Chem. Soc.* **1997**, *119*, 11134.
- (778) Liu, K. E.; Valentine, A. M.; Wang, D. L.; Huynh, B. H.; Edmondson, D. E.; Salifoglou, A.; Lippard, S. J. *J. Am. Chem. Soc.* **1995**, *117*, 10174–10185.
- (779) Liu, K. E.; Wang, D. L.; Huynh, B. H.; Edmondson, D. E.; Salifoglou, A.; Lippard, S. J. *J. Am. Chem. Soc.* **1994**, *116*, 7465–7466.
- (780) Valentine, A. M.; Stahl, S. S.; Lippard, S. J. *J. Am. Chem. Soc.* **1999**, *121*, 3876–3887.
- (781) Lee, S.-K.; Fox, B. G.; Froland, W. A.; Lipscomb, J. D.; Munck, E. *J. Am. Chem. Soc.* **1993**, *115*, 6450–6451.
- (782) Shu, L. J.; Nesheim, J. C.; Kauffmann, K.; Munck, E.; Lipscomb, J. D.; Que, L., Jr. *Science* **1997**, *275*, 515–518.
- (783) Rataj, M. J.; Kauth, J. E.; Donnelly, M. I. *J. Biol. Chem.* **1991**, *266*, 18684–18690.
- (784) Wilkins, P. C.; Dalton, H.; Samuel, C. J.; Green, J. *Eur. J. Biochem.* **1994**, *226*, 555–560.
- (785) Andersson, K. K.; Froland, W. A.; Lee, S.-K.; Lipscomb, J. D. *New J. Chem.* **1991**, *15*, 411–415.
- (786) Jiang, Y.; Wilkins, P. C.; Dalton, H. *Biochim. Biophys. Acta* **1993**, *1163*, 105–112.
- (787) Elango, N.; Radhakrishnan, R.; Froland, W. A.; Wallar, B. J.; Earhart, C. A.; Lipscomb, J. D.; Ohlendorf, D. H. *Protein Sci.* **1997**, *6*, 556–568.
- (788) Rosenzweig, A. C.; Brandstetter, H.; Whittington, D. A.; Nordlund, P.; Lippard, S. J.; Frederick, C. A. *Proteins: Struct. Funct. Genet.* **1997**, *29*, 141–152.
- (789) Rosenzweig, A. C.; Nordlund, P.; Takahara, P. M.; Frederick, C. A.; Lippard, S. J. *Chem. Biol.* **1995**, *2*, 409–418.
- (790) Rosenzweig, A. C.; Frederick, C. A.; Lippard, S. J.; Nordlund, P. *Nature* **1993**, *366*, 537–543.
- (791) Degrado, W. F. *Adv. Protein Chem.* **1988**, *39*, 51–124.
- (792) Cohen, C.; Parry, D. A. D. *Proteins: Struct. Funct. Genet.* **1990**, *7*, 1–15.
- (793) Fox, B. G.; Shanklin, J.; Ai, J. Y.; Loehr, T. M.; Sandersloehr, J. *Biochemistry* **1994**, *33*, 12776–12786.
- (794) Nordlund, P.; Eklund, H. *Curr. Opin. Struct. Biol.* **1995**, *5*, 758–766.
- (795) Summa, C. M.; Lombardi, A.; Lewis, M.; DeGrado, V. F. *Curr. Opin. Struct. Biol.* **1999**, *9*, 500–508.
- (796) Strater, N.; Klabunde, T.; Tucker, P.; Witzel, H.; Krebs, B. *Science* **1995**, *268*, 1489–1492.
- (797) Kurtz, D. M. *J. Biol. Inorg. Chem.* **1997**, *2*, 159–167.
- (798) Pulver, S. C.; Froland, W. A.; Lipscomb, J. D.; Solomon, E. I. *J. Am. Chem. Soc.* **1997**, *119*, 387–395.
- (799) Chang, S. L.; Wallar, B. J.; Lipscomb, J. D.; Mayo, K. H. *Biochemistry* **1999**, *38*, 5799–5812.
- (800) Walters, K. J.; Gassner, G. T.; Lippard, S. J.; Wagner, G. *Proc. Natl. Acad. Sci. U.S.A.* **1999**, *96*, 7877–7882.
- (801) Brandstetter, H.; Whittington, D. A.; Lippard, S. J.; Frederick, C. A. *Chem. Biol.* **1999**, *6*, 441–449.

- (802) Dewitt, J. G.; Bentsen, J. G.; Rosenzweig, A. C.; Hedman, B.; Green, J.; Pilkington, S.; Papaefthymiou, G. C.; Dalton, H.; Hodgson, K. O.; Lippard, S. J. *J. Am. Chem. Soc.* **1991**, *113*, 9219–9235.
- (803) Fox, B. G.; Surerus, K. K.; Munck, E.; Lipscomb, J. D. *J. Biol. Chem.* **1988**, *263*, 10553–10556.
- (804) Kauffmann, K. E.; Popescu, C. V.; Dong, Y. H.; Lipscomb, J. D.; Que, L., Jr.; Munck, E. *J. Am. Chem. Soc.* **1998**, *120*, 8739–8746.
- (805) Ericson, A.; Hedman, B.; Hodgson, K. O.; Green, J.; Dalton, H.; Bentsen, J. G.; Beer, R. H.; Lippard, S. J. *J. Am. Chem. Soc.* **1988**, *110*, 2330–2332.
- (806) Dewitt, J. G.; Rosenzweig, A. C.; Salifoglou, A.; Hedman, B.; Lippard, S. J.; Hodgson, K. O. *Inorg. Chem.* **1995**, *34*, 2505–2515.
- (807) Shu, L. J.; Liu, Y.; Lipscomb, J. D.; Que, L., Jr. *J. Biol. Inorg. Chem.* **1996**, *1*, 297–304.
- (808) Woodland, M. P.; Patil, D. S.; Cammack, R.; Dalton, H. *Biochim. Biophys. Acta* **1986**, *873*, 237–242.
- (809) Derose, V. J.; Liu, K. E.; Kurtz, D. M.; Hoffman, B. M.; Lippard, S. J. *J. Am. Chem. Soc.* **1993**, *115*, 6440–6441.
- (810) Hendrich, M. P.; Fox, B. G.; Andersson, K. K.; Debrunner, P. G.; Lipscomb, J. D. *J. Biol. Chem.* **1992**, *267*, 261–269.
- (811) Hoffman, B. M.; Sturgeon, B. E.; Doan, P. E.; Derose, V. J.; Liu, K. E.; Lippard, S. J. *J. Am. Chem. Soc.* **1994**, *116*, 6023–6024.
- (812) Thomann, H.; Bernardo, M.; McCormick, J. M.; Pulver, S.; Andersson, K. K.; Lipscomb, J. D.; Solomon, E. I. *J. Am. Chem. Soc.* **1993**, *115*, 8881–8882.
- (813) Derose, V. J.; Liu, K. E.; Lippard, S. J.; Hoffman, B. M. *J. Am. Chem. Soc.* **1996**, *118*, 121–134.
- (814) Lee, D. W.; Lippard, S. J. *J. Am. Chem. Soc.* **1998**, *120*, 12153–12154.
- (815) Lecloux, D. D.; Barrios, A. M.; Mizoguchi, T. J.; Lippard, S. J. *J. Am. Chem. Soc.* **1998**, *120*, 9001–9014.
- (816) Liu, K. E.; Valentine, A. M.; Qiu, D.; Edmondson, D. E.; Appelman, E. H.; Spiro, T. G.; Lippard, S. J. *J. Am. Chem. Soc.* **1995**, *117*, 4997–4998.
- (817) Hsu, H. F.; Dong, Y. H.; Shu, L. J.; Young, V. G.; Que, L., Jr. *J. Am. Chem. Soc.* **1999**, *121*, 5230–5237.
- (818) Deeth, R. J.; Dalton, H. *J. Biol. Inorg. Chem.* **1998**, *3*, 302–306.
- (819) Whittington, D. A.; Valentine, A. M.; Lippard, S. J. *J. Biol. Inorg. Chem.* **1998**, *3*, 307–313.
- (820) Lipscomb, J. D.; Nesheim, J. C.; Lee, S.-K.; Liu, Y. *FASEB J.* **1997**, *11*, 65.
- (821) Shteinman, A. A. *Russ. Chem. Bull.* **1995**, *44*, 975–984.
- (822) Shteinman, A. A. *FEBS Lett.* **1995**, *362*, 5–9.
- (823) Yoshizawa, K.; Hoffmann, R. *Inorg. Chem.* **1996**, *35*, 2409–2410.
- (824) Yoshizawa, K.; Yamabe, T.; Hoffmann, R. *New J. Chem.* **1997**, *21*, 151–161.
- (825) Yoshizawa, K.; Ohta, T.; Yamabe, T.; Hoffmann, R. *J. Am. Chem. Soc.* **1997**, *119*, 12311–12321.
- (826) Siegbahn, P. E. M. *Inorg. Chem.* **1999**, *38*, 2880–2889.
- (827) Siegbahn, P. E. M.; Crabtree, R. H. *J. Am. Chem. Soc.* **1997**, *119*, 3103–3113.
- (828) Siegbahn, P. E. M.; Crabtree, R. H.; Nordlund, P. *J. Biol. Inorg. Chem.* **1998**, *3*, 314–317.
- (829) Yoshizawa, K. *J. Biol. Inorg. Chem.* **1998**, *3*, 318–324.
- (830) Ruzicka, F.; Huang, D. S.; Donnelly, M. I.; Frey, P. A. *Biochemistry* **1990**, *29*, 1696–1700.
- (831) Priestley, N. D.; Floss, H. G.; Froland, W. A.; Lipscomb, J. D.; Williams, P. G.; Morimoto, H. *J. Am. Chem. Soc.* **1992**, *114*, 7561–7562.
- (832) Valentine, A. M.; Wilkinson, B.; Liu, K. E.; Komarpanicucci, S.; Priestley, N. D.; Williams, P. G.; Morimoto, H.; Floss, H. G.; Lippard, S. J. *J. Am. Chem. Soc.* **1997**, *119*, 1818–1827.
- (833) Jin, Y.; Lipscomb, J. D. *Biochemistry* **1999**, *38*, 6178–6186.
- (834) Liu, K. E.; Johnson, C. C.; Newcomb, M.; Lippard, S. J. *J. Am. Chem. Soc.* **1993**, *115*, 939–947.
- (835) Valentine, A. M.; LeTadicBiadatti, M. H.; Toy, P. H.; Newcomb, M.; Lippard, S. J. *J. Biol. Chem.* **1999**, *274*, 10771–10776.
- (836) Basch, H.; Mogi, K.; Musaev, D. G.; Morokuma, K. *J. Am. Chem. Soc.* **1999**, *121*, 7249–7256.
- (837) Karasevich, E. I.; Shestakov, A. F.; Shilov, A. E. *Kinet. Katal.* **1997**, *38*, 782–789.
- (838) Stubbe, J. *J. Biol. Chem.* **1990**, *265*, 5329–5332.
- (839) Sjöberg, B.-M.; Gräslund, A. In *Advances in Inorganic Biochemistry*; Theil, E. C., Eichorn, G. L., Marzilli, L. G., Eds.; Elsevier: 1983; Vol. 5, pp 87–110.
- (840) Reichard, P.; Ehrenberg, A. *Science* **1983**, *221*, 514–519.
- (841) Lammers, M.; Follmann, H. *Struct. Bonding* **1983**, *54*, 27–91.
- (842) Reichard, P. *Science* **1993**, *260*, 1773–1777.
- (843) Stubbe, J.; van der Donk, W. A. *Chem. Rev.* **1998**, *98*, 705–762.
- (844) Mulliez, E.; Fontecave, M. *Coord. Chem. Rev.* **1999**, *185*–186, 775–793.
- (845) Nordlund, P.; Sjöberg, B.-M.; Eklund, H. *Nature* **1990**, *45*, 593–598.
- (846) Nordlund, P.; Eklund, H. *J. Mol. Biol.* **1993**, *232*, 123–164.
- (847) von Döbeln, U.; Reichard, P. *J. Biol. Chem.* **1976**, *251*, 3616–3622.
- (848) Brown, N. C.; Reichard, P. *J. Biol. Chem.* **1969**, *244*, 39–42.
- (849) Thelander, L. *J. Biol. Chem.* **1974**, *249*, 4858–4862.
- (850) Uhlin, U.; Eklund, H. *Nature* **1994**, *370*, 533–539.
- (851) Barlow, T.; Eliasson, R.; Platz, A.; Reichard, P.; Sjöberg, B.-M. *Proc. Natl. Acad. Sci. U.S.A.* **1983**, *80*, 1492–1495.
- (852) Petersson, L.; Gräslund, A.; Ehrenberg, A.; Sjöberg, B.-M.; Reichard, P. *J. Biol. Chem.* **1980**, *255*, 6706–6712.
- (853) Fontecave, M.; Eliasson, R.; Reichard, P. *J. Biol. Chem.* **1987**, *262*, 12325–12331.
- (854) Fontecave, M.; Nordlund, P.; Eklund, H.; Reichard, P. *Adv. Enzymol. Relat. Areas Mol. Biol.* **1992**, *65*, 147–183.
- (855) Licht, S.; Gerfen, G. J.; Stubbe, J. *Science* **1996**, *271*, 477–481.
- (856) Booker, S.; Licht, S.; Broderick, J.; Stubbe, J. *Biochemistry* **1994**, *33*, 12626–12685.
- (857) Booker, S.; Stubbe, J. *Proc. Natl. Acad. Sci. U.S.A.* **1993**, *90*, 8352–8356.
- (858) Fontecave, M.; Eliasson, R.; Reichard, P. *Proc. Natl. Acad. Sci. U.S.A.* **1989**, *86*, 2147–2151.
- (859) Barlow, T. *Biochem. Biophys. Res. Commun.* **1988**, *155*, 747–753.
- (860) Yang, F.-D.; Spanevello, R. A.; Celiker, I.; Hirschmann, R.; Rubin, H.; Cooperman, B. S. *FEBS Lett.* **1990**, *272*, 61–64.
- (861) Mulliez, E.; Fontecave, M.; Gaillard, J.; Reichard, P. *J. Biol. Chem.* **1993**, *268*, 2296–2299.
- (862) Ollangnier, S.; Mulliez, E.; Gaillard, J.; Eliasson, R.; Fontecave, M.; Reichard, P. *J. Biol. Chem.* **1996**, *271*, 9410–9416.
- (863) Schimpff-Weiland, G.; Follmann, H.; Auling, G. *Biochem. Biophys. Res. Commun.* **1981**, *102*, 1276–1282.
- (864) Willing, A.; Follmann, H.; Auling, G. *Eur. J. Biochem.* **1988**, *178*, 603–611.
- (865) Gripenburg, U.; Lassmann, G.; Auling, G. *Free Radical Res.* **1996**, *26*, 473–481.
- (866) Sjöberg, B.-M. *Structure* **1994**, *2*, 793–796.
- (867) Sjöberg, B.-M. In *Structure of Ribonucleotide Reductase from Escherichia coli*; Eckstein, F., Lilley, D. M. J., Eds.; Springer-Verlag: Berlin, 1995; Vol. 9, pp 192–221.
- (868) Andersson, K. K.; Gräslund, A. *Diiron–Oxygen Proteins*; Academic: New York, 1995; Vol. 43.
- (869) Gräslund, A.; Sahlin, M. *Annu. Rev. Biophys. Biomol. Struct.* **1996**, *25*, 259–286.
- (870) Stubbe, J. *Adv. Enzymol. Relat. Areas Mol. Biol.* **1990**, *63*, 349–419.
- (871) Bender, C. J.; Sahlin, M.; Babcock, G. T.; Barry, B. A.; Chandrashekar, T. K.; Salowe, S. P.; Stubbe, J.; Lindström, B.; Petersson, L.; Ehrenberg, A.; Sjöberg, B.-M. *J. Am. Chem. Soc.* **1989**, *111*, 8076–8083.
- (872) Backes, G.; Sahlin, M.; Sjöberg, B.-M.; Loehr, T. M.; Sanders-Loehr, J. *Biochemistry* **1989**, *28*, 1923–1929.
- (873) Atkin, C. L.; Thelander, L.; Reichard, P.; Lang, G. *J. Biol. Chem.* **1973**, *248*, 7464–7472.
- (874) Rova, U.; Goodtzova, K.; Ingemarson, R.; Behravan, G.; Gräslund, A.; Thelander, L. *Biochemistry* **1995**, *34*, 4267–4275.
- (875) Lynch, J. B.; Juarez-Garcia, C.; Münck, E.; Que, L., Jr. *J. Biol. Chem.* **1989**, *264*, 8091–8096.
- (876) Bollinger, J. M., Jr.; Tong, W. H.; Ravi, N.; Huynh, B. H.; Edmondson, D. E.; Stubbe, J. *J. Am. Chem. Soc.* **1994**, *116*, 8024–8032.
- (877) Bollinger, J. M., Jr.; Tong, W. H.; Ravi, N.; Huynh, B. H.; Edmondson, D. E.; Stubbe, J. *J. Am. Chem. Soc.* **1994**, *116*, 8015–8023.
- (878) Ravi, N.; Bollinger, J. M., Jr.; Huynh, B. H.; Edmondson, D. E.; Stubbe, J. *J. Am. Chem. Soc.* **1994**, *116*, 8007–8014.
- (879) Sahlin, M.; Sjöberg, B.-M.; Backes, G.; Loehr, T. M.; Sanders-Loehr, J. *Biochem. Biophys. Res. Commun.* **1990**, *167*, 813–818.
- (880) Fontecave, M.; Gerez, C.; Atta, M.; Jeunet, A. *Biochem. Biophys. Res. Commun.* **1990**, *168*, 659–664.
- (881) Ochiai, E.-I.; Mann, G. J.; Gräslund, A.; Thelander, L. *J. Biol. Chem.* **1990**, *265*, 15758–15761.
- (882) Bollinger, J. M.; Edmondson, D. E.; Huynh, B. H.; Filley, J.; Norton, J. R.; Stubbe, J. *Science* **1991**, *253*, 292–298.
- (883) Bollinger, J. M., Jr.; Ravi, N.; Tong, W. H.; Edmondson, D. E.; Huynh, B. H.; Stubbe, J. *J. Inorg. Biochem.* **1993**, *51*, 6.
- (884) Bollinger, J. M., Jr.; Krebs, C.; Vicol, A.; Chen, S.; Ley, B. A.; Edmondson, D. E.; Huynh, B. H. *J. Am. Chem. Soc.* **1998**, *120*, 1094–1095.
- (885) Moëne-Loccoz, P.; Baldwin, J.; Ley, B. A.; Loehr, T. M.; Bollinger, J. M., Jr. *Biochemistry* **1998**, *37*, 14659–14663.
- (886) Bollinger, J. M., Jr.; Chen, S.; Parkin, S. E.; Mangravite, L. M.; Ley, B. A.; Edmondson, D. E.; Huynh, B. H. *J. Am. Chem. Soc.* **1997**, *119*, 5976–5977.
- (887) Kauppi, B.; Nielsen, B. B.; Ramaswamy, S.; Larsen, I. K.; Thelander, M.; Thelander, L.; Eklund, H. *J. Mol. Biol.* **1996**, *262*, 706–720.
- (888) Tong, W. H.; Chen, S.; Lloyd, S. G.; Edmondson, D. E.; Huynh, B.-H.; Stubbe, J. *J. Am. Chem. Soc.* **1996**, *118*, 2107–2108.
- (889) Tong, W.; Burdi, D.; Riggs-Gelasco, P.; Chen, S.; Edmondson, D.; Huynh, B. H.; Stubbe, J.; Han, S.; Arvai, A.; Tainer, J. *Biochemistry* **1998**, *37*, 5840–5848.
- (890) Sahlin, M.; Lassmann, G.; Potsch, S.; Slaby, A.; Sjöberg, B.-M.; Gräslund, A. *J. Biol. Chem.* **1994**, *269*, 11699–11702.

- (891) Sahlin, M.; Lassmann, G.; Potsch, S.; Sjöberg, B.-M.; Gräslund, A. *J. Biol. Chem.* **1995**, *270*, 12361–12372.
- (892) Silva, K. E.; Elgren, T. E.; Que, L., Jr.; Stankovich, M. T. *Biochemistry* **1995**, *34*, 14093–14103.
- (893) Parkin, S. E.; Chen, S.; Ley, B. A.; Mangravite, L.; Edmondson, D. E.; Huynh, B. H.; Bollinger, J. M., Jr. *Biochemistry* **1998**, *37*, 1124–1130.
- (894) Åberg, A.; Örmö, M.; Nordlund, P.; Sjöberg, B.-M. *Biochemistry* **1993**, *32*, 9845–9850.
- (895) Örmö, M.; deMaré, F.; Regnström, K.; Åberg, A.; Sahlin, M.; Ling, J.; Loehr, T. M.; Sanders-Loehr, J.; Sjöberg, B.-M. *J. Biol. Chem.* **1992**, *267*, 8711–8714.
- (896) Baldwin, J.; Moëne-Loccoz, P.; Krebs, C.; Ley, B. A.; Edmondson, D. E.; Huynh, B. H.; Loehr, T. M.; Bollinger, J. M., Jr. *J. Inorg. Biochem.* **1999**, *74*, 74.
- (897) Åberg, A.; Nordlund, P.; Eklund, H. *Nature* **1993**, *361*, 276–278.
- (898) Logan, D. T.; Su, X.-D.; Åberg, A.; Regnström, K.; Hajdu, J.; Eklund, H.; Nordlund, P. *Structure* **1996**, *4*, 1053–1064.
- (899) Andersson, M. E.; Högbom, M.; Rinaldo-Matthis, A.; Andersson, K. K.; Sjöberg, B.-M.; Nordlund, P. *J. Am. Chem. Soc.* **1999**, *121*, 2346–2352.
- (900) Atta, M.; Nordlund, P.; Åberg, A.; Eklund, H.; Fontecave, M. *J. Biol. Chem.* **1992**, *267*, 20682–20688.
- (901) Voegtli, W. C.; Khidekel, N.; Baldwin, J.; Ley, B. A.; Bollinger, J. M., Jr.; Rosenzweig, A. C. *J. Am. Chem. Soc.* Submitted for publication.
- (902) Logan, D. T.; deMaré, F.; Persson, B. O.; Slaby, A.; Sjöberg, B.-M.; Nordlund, P. *Biochemistry* **1998**, *37*, 10798–10807.
- (903) Rosenzweig, A. C.; Nordlund, P.; Takahara, P. M.; Frederick, C. A.; Lippard, S. J. *Chem. Biol.* **1995**, *2*, 409–418.
- (904) Lindqvist, Y.; Huang, W. J.; Schneider, G.; Shanklin, J. *EMBO J.* **1996**, *15*, 4081–4092.
- (905) Scarrow, R. C.; Maroney, M. J.; Palmer, S. M.; Que, L., Jr.; Roe, A. L.; Salowe, S. P.; Stubbe, J. *J. Am. Chem. Soc.* **1987**, *109*, 7857–7864.
- (906) Hanson, M. A.; Schmidt, P. P.; Strand, K. R.; Gräslund, A.; Solomon, E. I.; Andersson, K. K. *J. Am. Chem. Soc.* **1999**, *121*, 6755–6756.
- (907) Atta, M.; Scheer, C.; Fries, P. H.; Fontecave, M.; Latour, J.-M. *Angew. Chem., Int. Ed. Engl.* **1992**, *31*, 1513–1515.
- (908) Galli, C.; Atta, M.; Andersson, K. K.; Gräslund, A.; Brudvig, G. W. *J. Am. Chem. Soc.* **1995**, *117*, 740–746.
- (909) McCormick, J. M.; Reem, R. C.; Foroughi, J.; Bollinger, J. M., Jr.; Jensen, G. M.; Stephens, P. J.; Stubbe, J.; Solomon, E. I. *New J. Chem.* **1991**, *6*, 439–444.
- (910) Sjöberg, B.-M.; Loehr, T. M.; Sanders-Loehr, J. *Biochemistry* **1982**, *21*, 96–102.
- (911) Sjöberg, B.-M.; Sanders-Loehr, J.; Loehr, T. M. *Biochemistry* **1987**, *26*, 4242–4247.
- (912) Gerfen, G. J.; Bellew, B. F.; Un, S.; Bollinger, J. M., Jr.; Stubbe, J.; Griffin, R. G.; Singel, D. J. *J. Am. Chem. Soc.* **1993**, *115*, 6420–6421.
- (913) Un, S.; Atta, M.; Fontecave, M.; Rutherford, A. W. *J. Am. Chem. Soc.* **1995**, *117*, 10713–10719.
- (914) Tripathi, G. N. R.; Schuler, R. H. *J. Chem. Phys.* **1984**, *81*, 113–121.
- (915) Hirsh, D. J.; Beck, W. F.; Lynch, J. B.; Que, L., Jr.; Brudvig, G. W. *J. Am. Chem. Soc.* **1992**, *114*, 7475–7481.
- (916) Hendrich, M. P.; Elgren, T. E.; Que, L., Jr. *Biochem. Biophys. Res. Commun.* **1991**, *176*, 705–710.
- (917) Davydov, R.; Kuprin, S.; Gräslund, A.; Ehrenberg, A. *J. Am. Chem. Soc.* **1994**, *116*, 11120–11128.
- (918) Gerez, C.; Gaillard, J.; Latour, J.-M.; Fontecave, M. *Angew. Chem., Int. Ed. Engl.* **1991**, *30*, 1135–1136.
- (919) Debrunner, P. G.; Hendrich, M. P.; de Jersey, J.; Keough, D. T.; Sage, J. T.; Zerner, B. *Biochim. Biophys. Acta* **1983**, *745*, 103–106.
- (920) Davis, J. C.; Averill, B. A. *Proc. Natl. Acad. Sci. U.S.A.* **1982**, *49*, 4623–4627.
- (921) Antanaitis, B. C.; Aisen, P.; Lilienthal, H. R. *J. Biol. Chem.* **1983**, *258*, 3166–3172.
- (922) Atta, M.; Andersson, K. K.; Ingemarson, R.; Thelander, L.; Gräslund, A. *J. Am. Chem. Soc.* **1994**, *116*, 6429–6430.
- (923) Davydov, R. M.; Davydov, A.; Ingemarson, R.; Thelander, L.; Ehrenberg, A.; Gräslund, A. *Biochemistry* **1997**, *36*, 9093–9100.
- (924) Sahlin, M.; Gräslund, A.; Petersson, L.; Ehrenberg, A.; Sjöberg, B.-M. *Biochemistry* **1989**, *28*, 2618–2625.
- (925) Elgren, T. E.; Hendrich, M. P.; Que, L., Jr. *J. Am. Chem. Soc.* **1993**, *115*, 9291–9292.
- (926) Bollinger, J. M., Jr.; Ley, B. A.; Chen, S.; Huynh, B. H.; Edmondson, D. E. Conference on Oxygen Intermediates in Nonheme Metallobiochemistry Abstract, Minneapolis, MN, 1996.
- (927) Sturgeon, B. E.; Burdi, D.; Chen, S.; Huynh, B. H.; Edmondson, D. E.; Stubbe, J.; Hoffman, B. M. *J. Am. Chem. Soc.* **1996**, *118*, 7551–7557.
- (928) Willems, J.-P.; Lee, H.-I.; Burdi, D.; Doan, P. E.; Stubbe, J.; Hoffman, B. M. *J. Am. Chem. Soc.* **1997**, *119*, 9816–9824.
- (929) Burdi, D.; Sturgeon, B. E.; Tong, W. H.; Stubbe, J.; Hoffman, B. M. *J. Am. Chem. Soc.* **1996**, *118*, 281–282.
- (930) Veselov, A.; Scholes, C. P. *Inorg. Chem.* **1996**, *35*, 3702–3705.
- (931) Burdi, D.; Willems, J.-P.; Riggs-Gelasco, P.; Antholine, W. E.; Stubbe, J.; Hoffman, B. M. *J. Am. Chem. Soc.* **1998**, *120*, 12910–12919.
- (932) Riggs-Gelasco, P. J.; Shu, L.; Chen, S.; Burdi, D.; Huynh, B. H.; Que, L., Jr.; Stubbe, J. *J. Am. Chem. Soc.* **1998**, *120*, 849–860.
- (933) Broadwater, J. A.; Ai, J.; Loehr, T. M.; Sanders-Loehr, J.; Fox, B. G. *Biochemistry* **1998**, *37*, 14664–14671.
- (934) Kim, K.; Lippard, S. J. *J. Am. Chem. Soc.* **1995**, *118*, 4914–4915.
- (935) Skulan, A. J.; Brunold, T. C.; Baldwin, J.; Bollinger, J. M., Jr.; Solomon, E. I. Unpublished results.
- (936) Numa, S. *Fatty Acid Metabolism and Its Regulation*; Elsevier: New York, 1984.
- (937) Gunstone, F. D. *Fatty Acid and Lipid Chemistry*, 1st ed.; Blackie: London, 1996.
- (938) Shanklin, J.; Cahoon, E. B. *Annu. Rev. Plant Physiol. Plant Mol. Biol.* **1998**, *49*, 611–641.
- (939) Heinz, E. In *Lipid Metabolism in Plants*; Noore, T. S., Ed.; CRC: Boca Raton, FL, 1993; pp 34–89.
- (940) Murata, N.; Wada, H. *Biochem. J.* **1995**, *308*, 1–8.
- (941) Cahoon, E. B.; Lindqvist, Y.; Schneider, G.; Shanklin, J. *Proc. Natl. Acad. Sci. U.S.A.* **1997**, *94*, 4872–4877.
- (942) Schultz, D. J.; Cahoon, E. B.; Shanklin, J.; Craig, R.; Cox-Foster, D. L.; Mumma, R. O.; Medford, J. I. *Proc. Natl. Acad. Sci. U.S.A.* **1996**, *93*, 8771–8775.
- (943) Nagai, J.; Bloch, K. *J. Biol. Chem.* **1966**, *241*, 1925–1927.
- (944) Shanklin, J.; Whittle, E.; Fox, B. G. *Biochemistry* **1994**, *33*, 12787–12794.
- (945) Shanklin, J.; Achim, C.; Schmidt, H.; Fox, B. G.; Münck, E. *Proc. Natl. Acad. Sci. U.S.A.* **1997**, *94*, 2981–2986.
- (946) Avelange-Macherel, M. H.; Macherel, D.; Wada, H.; Murata, N. *FEBS Lett.* **1995**, *361*, 111–114.
- (947) Schmidt, H.; Dresselhaus, T.; Buck, F.; Heinz, E. *Plant Mol. Biol.* **1994**, *26*, 631–642.
- (948) Stuke, J. E.; McDonough, V. M.; Martin, C. E. *J. Biol. Chem.* **1990**, *265*, 20144–20149.
- (949) Suzuki, M.; Hayakawa, T.; Shaw, J. P.; Rekik, M.; Harayama, S. *J. Bacteriol.* **1991**, *173*, 1690–95.
- (950) Lee, M.; Lenman, M.; Banas, A.; Bafor, M.; Singh, S.; Schweizer, M.; Nilsson, R.; Liljeborg, C.; Dahlqvist, A.; Gummeson, P.-O.; Sjö Dahl, S.; Green, A.; Stymne, S. *Science* **1998**, *280*, 915–918.
- (951) Broun, P.; Shanklin, J.; Whittle, E.; Somerville, C. *Science* **1998**, *282*, 1315–1317.
- (952) Thiede, M. A.; Ozols, J.; Strittmatter, P. *J. Biol. Chem.* **1986**, *261*, 13230–13235.
- (953) Yadav, N. S.; Wierzbicki, A.; Aegerter, M.; Caster, C. S.; Pérez-Grau, L.; Kinney, A. J.; Hitz, W. D.; Booth, R., Jr.; Schweiger, B.; Stecca, K. L.; Allen, S. M.; Blackwell, M.; Reiter, R. S.; Carlson, T. J.; Russel, S. H.; Feldmann, K. A.; Pierce, J.; Browse, J. *Plant Physiol.* **1993**, *103*, 467–476.
- (954) Stuke, J. E.; McDonough, V. M.; Martin, C. E. *J. Biol. Chem.* **1989**, *265*, 16537–16544.
- (955) Shanklin, J.; Somerville, C. *Proc. Natl. Acad. Sci. U.S.A.* **1991**, *88*, 2510–2514.
- (956) Nagai, J.; Bloch, K. *J. Biol. Chem.* **1968**, *243*, 4626–4633.
- (957) Jaworski, J. G.; Stumpf, P. K. *Arch. Biochem. Biophys.* **1974**, *162*, 158–165.
- (958) Scheorper, G. J., Jr.; Bloch, K. *J. Biol. Chem.* **1965**, *240*, 54–63.
- (959) Morris, L. J. *Biochem. J.* **1970**, *118*, 681–693.
- (960) Holloway, P. W. In *The Enzymes*, 3rd ed.; Boyer, P. D., Ed.; Academic: New York, 1983; pp 63–83.
- (961) Wada, H.; Schmidt, H.; Heinz, E.; Murata, N. *J. Bacteriol.* **1993**, *175*, 544–547.
- (962) Schmidt, H.; Heinz, E. *Plant Physiol.* **1990**, *94*, 214–220.
- (963) McKeon, T. A.; Stumpf, P. K. *J. Biol. Chem.* **1982**, *257*, 12141–12147.
- (964) Broadwater, J. A.; Achim, C.; Münck, E.; Fox, B. G. *Biochemistry* **1999**, *38*, 12197–12204.
- (965) Buist, P. H.; Behrouzian, B. *J. Am. Chem. Soc.* **1996**, *118*, 6295–6296.
- (966) Buist, P. H.; Behrouzian, B. *J. Am. Chem. Soc.* **1998**, *120*, 871–876.
- (967) Haas, J. A.; Fox, B. G. *Biochemistry* **1999**, *38*, 12833–12840.
- (968) Fox, B. G.; Shanklin, J.; Somerville, C.; Münck, E. *Proc. Natl. Acad. Sci. U.S.A.* **1993**, *90*, 2486–2490.
- (969) Shu, L.; Broadwater, J. A.; Achim, C.; Fox, B. G.; Münck, E.; Que, L., Jr. *J. Bioinorg. Chem.* **1998**, *3*, 392–400.
- (970) Ai, J.; Broadwater, J. A.; Loehr, T. M.; Sanders-Loehr, J.; Fox, B. G. *J. Bioinorg. Chem.* **1997**, *2*, 37–45.
- (971) In the reaction of ferritin, a peroxide intermediate has recently been trapped and characterized spectroscopically (refs 7, 1008, and 1009). rR data on that species also appear to indicate that peroxide binds in a bridging mode, presumably an end-on μ -1,2 configuration. There are quantitative differences between the intermediates' spectroscopic signatures indicating a difference in their electronic structures, which correlates with differences in function (oxygen activation versus iron oxidation).

- (972) Kim, K.; Lippard, S. J. *J. Am. Chem. Soc.* **1996**, *118*, 4914–4915.
- (973) Ookubo, T.; Sugimoto, H.; Nagayama, T.; Masuda, H.; Sato, T.; Tanaka, K.; Maeda, Y.; Okawa, H.; Hayashi, Y.; Uehara, A.; Suzuki, M. *J. Am. Chem. Soc.* **1996**, *118*, 701–702.
- (974) Dong, Y. H.; Yan, S. P.; Young, V. G.; Que, L., Jr. *Angew. Chem., Int. Ed. Eng.* **1996**, *35*, 618–620.
- (975) Jacobson, R. R.; Tyeklár, Z.; Farooq, A.; Karlin, K. D.; Liu, S.; Zubieta, J. *J. Am. Chem. Soc.* **1988**, *110*, 3690–3692.
- (976) Brunold, T. C.; Baldwin, J.; Bollinger, J. M., Jr.; Solomon, E. I. Manuscript in preparation.
- (977) Tuzek, F.; Solomon, E. I. *Inorg. Chem.* **1992**, *31*, 944–953.
- (978) Baldwin, M. J.; Ross, P. K.; Pate, J. E.; Tyeklár, Z.; Karlin, K. D.; Solomon, E. I. *J. Am. Chem. Soc.* **1991**, *113*, 8671–8679.
- (979) Fox, S.; Karlin, K. In *Active Oxygen in Biochemistry*; Valentine, J. S., Foote, C. S., Greenberg, A., Liebman, J. F., Eds.; Blackie: Glasgow, U.K., 1995; pp 188–231.
- (980) Valentine, A. M.; Tavares, P.; Pereira, A. S.; Davydov, R.; Krebs, C.; Koffman, B. M.; Edmondson, D. E.; Huynh, B. H.; Lippard, S. J. *J. Am. Chem. Soc.* **1998**, *120*, 2190–2191.
- (981) Bollinger, J. M.; Stubbe, J.; Huynh, B. H.; Edmondson, D. E. *J. Am. Chem. Soc.* **1991**, *113*, 6289–6291.
- (982) Que, L., Jr.; Dong, Y. *Acc. Chem. Res.* **1996**, *29*, 190–196.
- (983) Que, L., Jr. *J. Chem. Soc., Dalton Trans.* **1997**, 3933–3940.
- (984) Edmondson, D. E.; Huynh, B. H. *Inorg. Chim. Acta* **1996**, *252*, 399–404.
- (985) Mukerjee, S.; Stassinopoulos, A.; Caradonna, J. P. *J. Am. Chem. Soc.* **1997**, *119*, 8097–8098.
- (986) Dong, Y. H.; Zang, Y.; Shu, L. J.; Wilkinson, E. C.; Que, L., Jr.; Kauffmann, K.; Munck, E. *J. Am. Chem. Soc.* **1997**, *119*, 12683–12684.
- (987) Kim, C.; Dong, Y.; Que, L., Jr. *J. Am. Chem. Soc.* **1997**, *119*, 3635–3636.
- (988) Dong, Y.; Fujii, H.; Hendrich, M. P.; Leising, R. A.; Pan, G.; Randall, C. R.; Wilkinson, E. C.; Zang, Y.; Que, L., Jr.; Fox, B. G.; Kauffmann, K.; Munck, E. *J. Am. Chem. Soc.* **1995**, *117*, 2778–2792.
- (989) Krebs, C.; Baldwin, J.; Chen, S.; Ley, B. A.; Edmondson, D. E.; Bollinger, J. M., Jr.; Huynh, B. H. *J. Inorg. Biochem.* **1999**, *74*, 195–195.
- (990) Halfen, J. A.; Mahapatra, S.; Wilkinson, E. C.; Kaderli, S.; Young, V. G., Jr.; Que, L., Jr.; Zuberbühler, A. D.; Tolman, W. B. *Science* **1996**, *271*, 1397–1400.
- (991) Henson, M. J.; Mukherjee, P.; Stack, T. D. P.; Solomon, E. I. *J. Am. Chem. Soc.* **1999**, *121*, 10332–10345.
- (992) Cramer, C. J.; Smith, B. A.; Tolman, W. B. *J. Am. Chem. Soc.* **1996**, *118*, 11283–11287.
- (993) Bérces, A. *Inorg. Chem.* **1997**, *36*, 4831–4837.
- (994) Flock, M. *J. Phys. Chem. A* **1999**, *103*, 95–102.
- (995) This assumption is based on the similarities between the spectroscopic data of wild-type and mutant protein intermediates and structurally characterized end-on μ -1,2-[Fe^{III}]₂ model complexes.
- (996) Ortiz de Montellano, P. R. In *Cytochrome P-450 Structure, Mechanism, and Biochemistry*; Ortiz de Montellano, P. R., Ed.; Plenum: New York, 1986; pp 217–271.
- (997) Mori, M.; Weil, J. A. *J. Am. Chem. Soc.* **1967**, *89*, 3732–3744.
- (998) Thewalt, U.; Marsh, R. *J. Am. Chem. Soc.* **1967**, *89*, 6364–6365.
- (999) Davies, R.; Sykes, A. G. *J. Chem. Soc. A* **1968**, *90*, 2840–2845.
- (1000) Davies, R.; Stevenson, M. B.; Sykes, A. G. *J. Chem. Soc. A* **1970**, *92*, 1261–1266.
- (1001) Root, D. E.; Mahroof-Tahir, M.; Karlin, K. D.; Solomon, E. I. *Inorg. Chem.* **1998**, *37*, 4838–4848.
- (1002) Shin, W.; Sundaram, U. M.; Cole, J. L.; Zhang, H. H.; Hedman, B.; Hodgson, K. O.; Solomon, E. I. *J. Am. Chem. Soc.* **1996**, *118*, 3202–3215.
- (1003) Quickenden, T. I.; Marshall, R. C. *J. Chem. Educ.* **1972**, *49*, 114–116.
- (1004) Weil, J. A.; Bolton, J. R.; Wertz, J. E. *Electron Paramagnetic Resonance*; Wiley: New York, 1994.
- (1005) Haber, F.; Weiss, J. *Naturwissenschaften* **1932**, *20*, 948.
- (1006) Haber, F.; Weiss, J. *Proc. R. Soc. London, Ser. A* **1934**, *147*, 332.
- (1007) Barb, W. C.; Baxendale, J. H.; George, P.; Hargrave, K. R. *Trans. Faraday Soc.* **1951**, *47*, 462–500, 591–616.
- (1008) Zhao, Z.; Treffry, A.; Quail, M. M.; Guest, J. R.; Harrison, P. M. *J. Chem. Soc., Dalton Trans.* **1997**, 3977–3978.
- (1009) Pereira, A. S.; Small, W.; Krebs, C.; Tavares, P.; Edmondson, D. E.; Theil, E. C.; Huynh, B. H. *Biochemistry* **1998**, *37*, 9871–9876.
- (1010) Kurtz, D. M., Jr. *Chemtracts, Inorg. Chem.* **1999**, *12*, 303–310.
- (1011) Dunitz, B. D.; Beachy, M. D.; Cao, Y.; Whittington, D. A.; Lippard, S. J.; Freisner, R. A. Manuscript in preparation.

CR9900275

